Precious Metals In The Fight Against Cancer

Rebecca Amelia Bedford

A thesis submitted to the

University of Birmingham for the degree of

DOCTOR OF PHILOSOPHY

February 2024

University of Birmingham Research Archive
e-theses repository

Declaration

I hereby declare that, except where specific reference is made to other sources, the work contained in this thesis is the original work of the author. It has been composed by myself, and has not been submitted, in whole or in part, for any other degree, diploma or other qualification.

R. Bedford

Rebecca Amelia Bedford

February 2024

COVID-19 impact statement

COVID-19 restrictions were in place at the start of the PhD programme in Oct 2020. Hence, Year 1 activities were re-structured to comply with restrictions. Of particular importance, experimental work was delayed until Jan 2021. Work conducted under restricted lab occupancy – particularly the synthetic chemistry side of the project – was highly disrupted. Year 1 finished without a full set of complexes to be tested for anticancer activity. This had to be completed during Year 2, causing delays to the start of biological testing. Further synthetic work was not carried out to minimise impact on the overall project.

Due to COVID-19 restrictions being in place at the start of the program, the schedule of the project was amended to allow the for early months to be dedicated to literature search and planning. Given the academic background of the candidate, this time was useful to familiarise themselves with the research field and plan for the experimental sections. This planning was useful to initiate reagent and chemical ordering. Deliveries were heavily affected and items that would normally be available in a couple of days had a long waiting time. In consequence of slow initial data collection, decisions on chapter structure and experimental content had to be reviewed. Having planned during these months and having done some reagent ordering ahead, later delays were mitigated.

In February 2021, experimental work was initiated. Timings were affected due to bubble rotas and room occupancy regulations, as well as external delays in the supply of chemical reagents and laboratory supplies, which were out of our control. Training was scheduled and achieved over several months on and off due to the bubble rota system which was in place in both the main pharmacy lab and tissue culture and staff self-isolating. Planning during the early months mitigated delays to some degree. Lab bubbles continued until August 2021, limiting synthesis capabilities. Nonetheless synthesis continued but at a slower rate than expected.

As tissue culture rooms remained single occupancy and were being used by multiple research groups, scheduling experiments was challenging. Early investigations continued, however, low tissue culture occupancy limited the ability to carry out larger experiments and larger batches of testing. This had a substantial impact on data collection which was severely limited in the initial days. Bubble rota allowances did not always align well with the experimental requirements which contributed heavily to delays (e.g. experiments that needed two consecutive days against rotas that were on intermittent days, or specific timings for the biological experiments against allowed lab hours). Also, being part of a vulnerable group due to a medical condition and family members being vulnerable, minimal contact and lone working at the university was conducted where possible. However, due to health and safety regulations this was not possible for chemical work, therefore planning for less busy periods was aimed for. In this time, only limited writing could be done due to uncertainty with methods available and results yet to be produced at the time.

Resulting from these challenges and setbacks, new chapter structures and the thesis overview were redesigned. In particular, the new structure allowed for the flexibility to reduce the number of series of complexes and accommodate for those that were not synthesised at the start of the project. This was a difficult decision, but it was a viable way of reducing the impact that the Covid-19 restrictions had on the synthetic chemistry work, while ensuring that the research requirements were met. The research is now focuses on a narrower family of complexes with a lower number of structural variations and more on the biological investigations pertaining the fate at cellular level of the metal complexes, rather than being evenly distributed between synthetic chemistry work and biological work.

Acknowledgements and thanks

Table of contents

Conferences attended

Dalton Joint Interest Group Conference & DYME 2021
Online Event
-Participant
29th June to 1st July 2021

Celebrating Women in Chemistry Conference and Careers Event 2022
University of Nottingham, UK
-Participant
22nd February 2022

HEFi 22 Conference
University of Birmingham, UK
-Participant
20th June 2022

EUROBIC 2022 – 16th European Biological Inorganic Chemistry Conference
Université Grenoble Alpes, France
-Participant
17th to 21st July 2022

Dalton 2023
University of Warwick, UK
-Presenter: "Ruthenium piano-stool complexes against ovarian cancer" (poster)
18th to 20th April 2023

PhD Scientific Days/EUniWell pilot conference 2023
Semmelweis University, Hungary
-Presenter: ""A Link to the Future! Linkers to increase potency of ruthenium complexes" (talk)
22nd to 24th June 2023
*Award won for best Pharmacy presentation

Transitioning from academia to industry conference 2023
Charnwood Campus, UK
-Presenter: "Ruthenium piano-stool complexes against ovarian cancer" (poster)
7th September 2023

ISBOMC 2023
Technische Universität, Germany
-Presenter: "A Link to the Future! Linkers to increase potency of ruthenium complexes" (poster)
18th to 21st September 2023

Table of figures

Table of tables

List of abbreviations

American Type Culture Collection	(ATCC)
4',6-diamidino-2-phenylindole	(DAPI)
9-Ethyl guanine	(9-EtG)
Azopyridine	(AzPy)
Base Excision Repair	(BER)
Bilateral Salpingo-Oophorectomy	(BSO)
Bovine Serum Albumin	(BSA)
Calf Thymus DNA	(ctDNA)
Carbonyl Cyanide Chlorophenylhydrazone	(CCCP)
Cell Cytoplasmic Membrane	(CCM)
Cisplatin	(CDDP)
COrrelated SpectroscopY	(COSY)
Cystine-Glutamate Antiporter	(system XC–)
Density Functional Theory	(DFT)
DiChlorodihydroFluorescein DiAcetate	(DCFDA)
Double Stand DNA	(dsDNA)
ElectroSpray Ionisation Mass Spectroscopy	(ESI-MS)
Enhanced Permeability and Retention	(EPR)
Enhanced Permeability and Retention	(EPR)
Epithelial Ovarian Cancer	(EOC)
Erastin	(ERA)
European Collection of Authenticated Cell Cultures	(ECACC)
Extracellular Matrix	(ECM)
Ferrostatin	(FER-1)
Foetal Bovine Serum	(FBS)
Glutathione	(GSH)
Glutathione Disulphide	(GSSG)
Heteronuclear Multiple Bond Correlation	(HMBC)
Heteronuclear Single Quantum Coherence	(HSQC)
High performance liquid chromatography	(HPLC)
Histone Deacetylase	(HDAC)

Homologous Recombination	(HRR)
-inhibitor	(-i)
Iminopyridine	(ImPy)
Inductively Coupled Plasma Mass Spectrometry	(ICP-MS)
L- Buthionine sulfoximine	(L-BSO)
Matrix MetalloProteinase	(MMP)
Mode of Action	(MOA)
Mechanism of Cell Death	(MOD)
Microtubule Targeting Agents	(MTA)
MisMatch Repair	(MMR)
Mitochondrial Inner Membrane Potential	(ΨIM)
Mitochondrial Membrane Potential	($\Delta\Psi m$)
n-Octanol saturated PBS	(O-PBS)
Non-Essential Amino Acid	(NEAA)
Non-Homologous End Joining	(NHEJ)
Nuclear Magnetic Resonance	(NMR)
Nucleotide Excision Repair	(NER)
Paclitaxel	(PTX)
PBS saturated with n-Octanol	(PBS-O)
Penicillin/Streptomycin	(Pen/Strep)
Phosphate Buffered Saline	(PBS)
Propidium Iodide	(PI)
Reactive Oxygen Species	(ROS)
Rhodamine123	(Rh123)
Single Cell Dilution	(SCD)
Single Cell Suspension	(SCS)
Single Strand DNA	(ssDNA)
Staurosporine	(STS)
The National Institute for Health and Care Excellence	(NICE)
Thiazolyl Blue Tetrazolium Bromide	(MTT)
Trichostatin A	(TriA)
Triple Negative Breast Cancer	(TNBC)

Abstract

Being the second biggest global killer, despite an array of pharmaceutical and treatment interventions, cancer is a prominent strain on healthcare. Currently, the precious metal complex cisplatin and its second-generation platinum complexes, carboplatin and oxaliplatin, are essential in the management of many cancers, being utilised in around 50% of all treatment regimens. Nonetheless, their use is fraught with deleterious side effects, a common problem with many non-targeted chemotherapies.

Platinum-based treatments are front line choices in malignancies such as ovarian cancer. As the sixth most common cancer, it tends to have a positive initial response from surgery and chemotherapy regimens, but relapse is frequent and often associated to resistance. This has led to ovarian cancer having a 66% death rate. Such treatment failures have inspired research into the potential of other precious metals. Ruthenium, for example, is a transition metal like platinum but it has the potential for improved qualities including wider coordination space, broader capacity to hold variations in chemical moieties and iron-mimicking. A large number of ruthenium complexes have been synthesised thus far with exceptional anticancer activity, and singular examples have reached clinical studies.

In this work, ruthenium piano-stool complexes with a bidentate iminopyridine ligand with differing bioisosteric replacements in the phenyl ring have been investigated. Replacing small moieties in drug-like molecules have shown to make significant differences in their potency. This work uses such strategy to investigate ruthenium-based complexes as anticancer agents. The research has successfully led to the synthesis, physiochemical and biological investigation of 22 piano-stool complexes differing in bioisosteric replacements, and their further investigation into the death mechanisms, DNA, and cell membrane targeting mechanisms of action of four lead complexes.

The complexes with modified ligands explored demonstrate the high potential of ruthenium piano-stools in the treatment of ovarian cancer and the potential of bioisosteric replacements.

Chapter 1 - Introduction

Overview Of Epithelial Ovarian Cancer, Current Treatments, And The Use Of Precious Metals Against Cancer

1-1: A growing problem

The development of abnormal, undifferentiated growths has been recorded as early as Egyptian times, nonetheless detailed scientific examination of cancer was not described until the 16th century, with in-depth documentation accompanying the development of autopsies and the field of pathology not appearing until 19th century[1]. With the increasing aging population and increased exposure to environmental risk factors, cancer is now one of the most prevalent healthcare concerns globally[2–4]. Screening and treatment advancements have increased ten-year survival rates of patients in the UK from 24% to 46% between 1971 and 2005 with survival now improving to 49%[5,6]. Yet, incidence has also increased by 12% from 1993 to 2017, culminating as a global 1:5 lifetime (before age 75) diagnosis risk with a total of 19.3 million cases being diagnosed in 2020[2,3,6,7]. There is now also increased incidence and mortality rates from developing countries where capability for care is lagging, demonstrating that cancer is now becoming a global concern[8]. The highest incidence cancers globally in 2020 were breast (11.7%), lung (11.4%), colorectal (9.8%), prostate (7.3%) and skin (non-melanoma, 6.2%). However, these percentages are not reflective of the highest causes of cancer death which were lung (18.0%), colorectal (9.2%), liver (8.3%), stomach (7.7%), and breast (6.9%)[4,6]. These differences in incidence and death rates can be attributed to a variety of reasons including ability for prevention, screening, treatment options, tumour heterogeneity and innate difficulty in treating the cancer type.

Prevention campaigns are dominated by the reduction of exposure to carcinogens. This includes the avoidance of exogenous carcinogens such as smoking, attributed to be the dominant preventable cause, but also promoting healthier lifestyles to reduce obesity through exercise and diet[9]. Many causes of cancer have been identified with lists of hundreds of compounds and agents being listed as carcinogens by groups such as the World Health Organisation and the U.S. Department of Health and Human Services[1,10,11]. These lists indict causes such as tobacco, UV radiation, alcohol, infection, obesity, and infection, yet only 30-50% of cancer is preventable by lifestyle changes[12]. While specific

carcinogens target certain tissues over others, at a molecular level, cancer often exhibits the same traits resulting from genomic mutations and aberrant protein expression[13–15]. These traits of cancer are also known as the Hallmarks of Cancer shown in Figure 1-1[16–18]. These hallmarks are required for the development of cancer, being an enabler or a product of cancer development, highlighting the highly complex and interlinked mechanisms required[19].
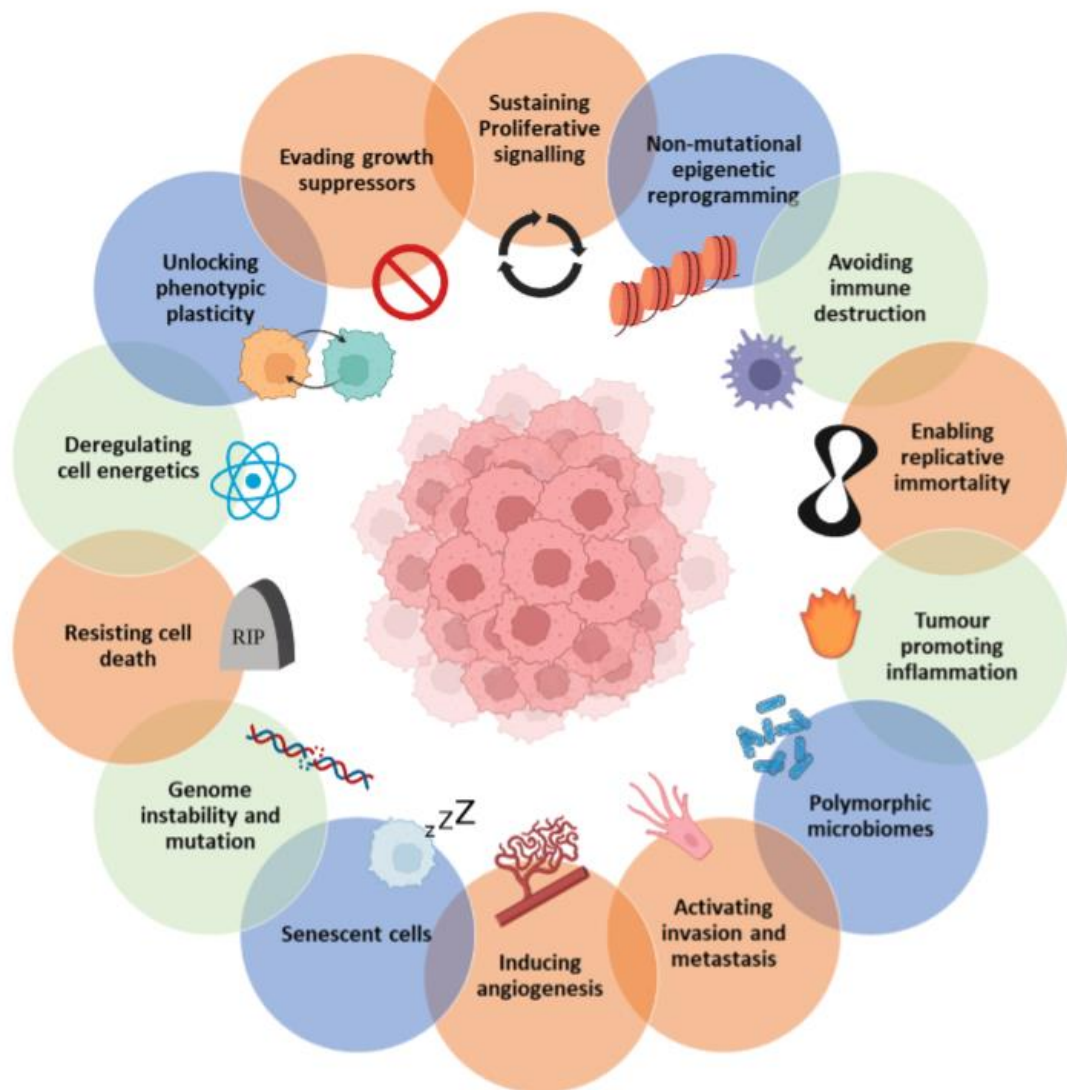
Figure 1-1: The Hallmarks of Cancer defined by Hanahan and Weinburg[16–18]. These traits have found to be essential to the development of cancer, regardless of type. Furthermore, these traits can be applied to the treatment of cancer by targeting the errant pathways utilised in these hallmarks. Figure modified and presented as the accumulation of the three updates to the hallmarks published; orange hallmarks identified in 2000[16], green hallmarks identified in 2011[17], and blue hallmarks identified in 2022[18].

With only a fraction of cancer incidences being preventable, early diagnosis screening has been effective for several cancers. One example is breast cancer screening by mammography, which can decrease death rates of women over the age of 40 by 40% with regular screening[20]. Furthermore, computational modelling has suggested that when breast screening availability is reduced by 50%, a six-month screening delay could lead to ~40,000 life-years lost[21]. Yet, more than 90% of cancer cases in the UK are diagnosed by symptomatic disease presentation, and screening is not effective for all cancer types such as with ovarian cancer[22]. A long-term ovarian cancer screening trial done in the United Kingdom (UKCTOCS) was conducted with 202,638 women enrolled concluded that neither CA125 and/or ultrasound screening significantly reduced deaths from ovarian or tubal cancer, despite earlier and lower stage diagnoses[23]. The limitations of prevention and early intervention are evident in insignificantly altered disease rates of ovarian cancer in recent years[2–4]. Therefore, new and improved treatments are required, especially in regard to ovarian cancer.

1-2: Ovarian Cancer

In this work, Epithelial Ovarian Cancer (EOC) was focused on for a variety of reasons. Ovarian cancer is the sixth most common cancer with globally; in 2020, 313,959 women were diagnosed and 207,252 died (66% death rate), with a five-year survival rate of stage IV patients is less than 20%[4]. Further, even if remission is achieved, many relapse within two years with rarely curable conditions. Death rates of relapsed patients are as high as 56-70% for clear cell carcinoma histology or late stage progression with peritoneal metastasis[24–29].

Ovarian cancer develops from three main areas: the epithelium, germ cells and sex-cord stromal tissue, 90%, 3% and 2% respectively, with the remaining 5% being uncharacterised[31]. EOC can be separated into five groups[30,31]:

- Serous – originates in the fallopian tube (52%)

- Endometrioid – originates from the womb endometrium (10%)

- Mucinous – histopathologically related to the endocervical epithelium and often remain confined to the ovary (6%)

- Clear cell – originates in the endometrium, but are characterised by their histological features of large "clear cells" (6%)

- Other – consists of rare types or are uncharacterised (27%)

Further, tumours can be divided by being type I, large unilateral tumours which are thought to be derived from benign ovarian lesions such as cysts that embed and mutate, or type II which are high grade bilateral tumours which are often aggressive and have low survival rates[31].

Ovarian cancer patients are often middle-aged women, with increasing age associated with higher risk of development, higher stage at diagnosis and higher risk of death[32,33]. This trend is attributed to increased toxin exposure and mutation accumulation over time, especially as there is no increased risk of ovarian cancer regarding tobacco and alcohol[34]. Other risk factors have been identified such as being

postmenopausal, increase in gonadotropin levels, menopausal hormone treatments, increased number of menstrual cycles, increased retrograde bleeding and ovary stress, and that protection against ovarian cancer increases with parity, breastfeeding and hormonal contraceptives [32,35]. These risk and protective factors were initially noted in 1971 as part of the Incessant Ovulation Hypothesis: mammals that underwent frequent and high number of ovulation cycles had a higher frequency of ovarian cancer[36]. This was demonstrated in chickens where increased ovulation to increase egg production resulted in 89% of chickens developing ovarian adenocarcinoma, but also in women that were not given ovulation rest periods by pregnancy, there was an increased risk of developing ovarian cancer[34,37]. However, there is evidence that fertility therapy does not increase risk of developing ovarian cancer[35]. This led to the evolution of the Incessant Ovulation Hypothesis to be based around the combination of ovulation, menstruation, menopause hormone therapy and age induced gonadotrophin to work in combination to result in the increase of inclusion cyst and follicular fluid formation, retrograde bleeding and signalling pathway alterations culminating in reactive oxygen species (ROS) generation, dysregulated iron and transferrin levels and inflammation causing damage to ovary cells causing proliferation which goes on to mutate into cancer[35].

While incidence is higher in middle-aged women, EOC can affect women of all ages due to other causes including hereditary genetic alterations which cause 36% of EOC[38]. Mutations in *BRCA1/2*, key genes in DNA strand break repair, occur in ~23% of cases and they are the most frequently documented mutation in EOC familial cases[32,38,39]. However, after high-grade serous carcinomas have established, *BRCA1/2* function can be regained following platinum treatments[35]. Mutation of key enzymes in mismatch repair have also been documented including *MSH2/6 MLH1, PMS1/2, STK11* and *MUTUH*[30,32]. Other genes that have been documented to be frequently mutated also include *TP53, CCNE1, RB1, BECN1* and *NRAS* leading to the deregulation of several pathways including genome damage surveillance, growth regulation, and autophagy causing the development of high-grade tumours[35].

Thus far in the UK, genetic testing is not routine in initial diagnosis or treatment, yet since the development of PARP inhibitors (PARPi) in recent years there has been a push for the use of *BRCA* testing for PARPi use, and is now utilised in recurrent cases only[40]. However, their use is still limited due to the low frequency of *BRCA* mutations in recurrent conditions[41]. The National Institute for Health and Care Excellence (NICE) guidelines surrounding ovarian cancer and familial risk newly updated in March 2024 has expanded the screening of the proband and relatives to test for mutations in BRCA1/2, SMARCA4, FOXL2, CTNNB1, APC, and DICER1, with a trial on whole genome sequencing on germline and tumour tissue[42–44]. However, no further guidance on the use of PARPi has been described. At this point in time, there is a delay in the research in this area and the knowledge gained being translated into clinical use, even then this work is limited as only a fraction of patients will benefit.

EOC patients suffer from a non-specific range of symptoms, earning it the title 'the silent killer'. Other cancers such as breast or lung cancer often have a prominent symptom that can be noticed by a clinician or a patient, for example the feeling of a mass or a persistent cough, respectively[45]. In contrast, EOC often is asymptomatic in early stages and late-stage cases often have non-specific symptoms such as abdominal bloating, early satiety, nausea, back pain, tiredness, weight loss, change in bowel and urinary functions, leading to late diagnosis[28,46].

As EOC suffers from limited familial diagnostics, lack of screening, an ambiguous symptom profile and inadequate treatment regimens, this has led to poor diagnosis and survival rates. Only 15% of EOC cases are identified in stage I whereas over 70% are detected in stage III or IV, additionally death rates have continued to increase over the last ten years[23,38,47].This demonstrates that even if EOC is diagnosed earlier, high death rates persist, highlighting the need for treatment advancement.

1-3: Cancer treatments currently in use

In 2012, the World Oncology Forum questioned "Are we winning the war against cancer?". While there have been many excellent successes in the development of many cancer treatments, the overarching sentiment was that while several battles have been won, the war continues, with each method of treatment significantly differing their positives and draw backs[48]. Example treatment regimens include surgery, chemotherapy, radiotherapy, ablation, and immunotherapy.

For ovarian cancer, most effective treatment types are surgical and chemotherapy treatments. Research into the benefits of radiotherapy, ablation, and immunotherapy therapy have been investigated with varying results. For radiotherapy, studies have found that its use has had limited effectiveness in clinical use[49–51]. Ablation has received limited investigation due to the limitations of the technique and preference for surgical resection of primary ovarian tumours, but the technique has potential for metastatic tumours in organs with functional reserve such as the liver[52–56]. Immunotherapy has gained significant interest, especially due to the immunogenic nature of ovarian tumours. Immunotherapy treatments include the use of PD1/PD-L1 inhibitors and chimeric antigen receptor (CAR) T cell therapies[57]. Despite its success in other cancers, immunotherapy has had limited success in ovarian cancer. For example, PD1/PD-L1 inhibitor studies have found that at best treatments exhibit a partial response in a small fraction of patients, with the majority of patients exhibiting disease progression[58,59]. However, research into this area is still limited therefore may improve with further research[57]. Therefore, surgical and chemotherapy treatment options will be focused on in more depth.

1-3.1: Surgical treatment options

With the invention of aesthetic and antiseptics, the ability to exorcise the bulk mass of a tumour has had great impact on the survival rates of patients and has become a cornerstone in cancer treatment being used for more than 80% of cases[60,61]. Depending on the cancer type and location, surgery can

also be used for preventative, diagnostic, curative and reconstructive purposes and can vary from partial to complete excision of a tumour in a curative manner[61]. For example, for breast cancer, surgery can be used for all the purposes above as mass debulking is possible as treatment which can then be submitted for further testing, as well as reconstruction of the breast which has been found to be helpful for patient wellbeing and mental health[61,62].

For EOC, surgery can be used in a preventative, diagnostic and curative purposes and is often used as part of gold standard treatment. Several surgical options are available depending on disease progression and any associated familial history. One option is a bilateral salpingo-oophorectomy where both ovaries and Fallopian tubes are removed[63]. This is considered a minimal risk surgery, achieved by keyhole surgery and can reduce risk by 80% in *BRCA* mutation positive patients[47]. Despite this large benefit, this option is not routinely recommended without extensive education to patients as side effects for women post-menopause includes minimal effects such as vaginal dryness, decreased sexual function and decreased ability to orgasm[47]. Further, this option is often recommended for pre-menopausal women, as surgery immediately begins menopause, therefore has additional side effects including, cardiovascular disease, osteoporosis and sterility[47,64]. Other surgical options include laparoscopic debulking which can involve unilateral oophorectomy (ovary removal), or unilateral salpingo-oophorectomy depending on the extent of disease progression with average 5-year reoccurrence rates as low as 11.6% for stage I diagnoses[65]. While this is beneficial for younger patients due to reproductive conservation, for more advanced cases effectiveness is much lower with increased rates of distant disease and recurrence[66].

Tumour removal not only aids reduction of the tumour mass but provides a sample for further testing for histological and genetic testing and disease staging. However, there is a very limited panel of genes to currently test for beyond *BRCA1/2* and limited approved targeted treatments for any mutations found[40]. Therefore, while there is potential in this area, subsequent options must be improved before any genetic testing becomes useful.

1-3.2: Currently approved chemotherapy for clinical use

With the previous options only providing part or not being suitable as a solution, chemotherapy is key. Due to the array of dysregulation and cellular targets within a cell, a wide variety of treatments have been developed targeting many different cellular elements. Two main categories of treatments have developed: non-targeted and targeted.

1-3.2.1: Non-targeted chemotherapy

Non-targeted chemotherapies are defined as agents that are cytotoxic to all actively dividing cells without discrimination, targeting both cancerous and non-cancerous tissue. Their versatility however is their downfall. Their untargeted nature can cause a wide variety of side effects including nausea, vomiting, fatigue, anaemia, lymphopenia, hair loss, fever, infection and bleeding, with additional side effects exclusive to the treatment given[67–69]. Therefore, usage is tightly controlled and monitored, and often given with an equally wide range of symptom alleviators such as antiemetics and broad range antibiotics[69].

1-3.2.2: Alkylating agents

During the First world war, chemical weapons were used to deal significant damage to the opposition before their prohibition in the Geneva convention due to their horrific effects[70,71]. However, during this time, the effectiveness of mustard gas on bone marrow depletion was seen, and its effectiveness the treatment of lymphoma was realised[70–72]. This gave rise to first generation alkylating agents such as mechlorethamine (Figure 1-2a), which was a highly potent agent given intravenously[71]. Further modifications were then made to improve the lipophilicity and reactivity lead to the development of later generation compounds such as chlorambucil (Figure 1-2b) which is less vulnerable to chlorine ion displacement and is better tolerated[71,73].
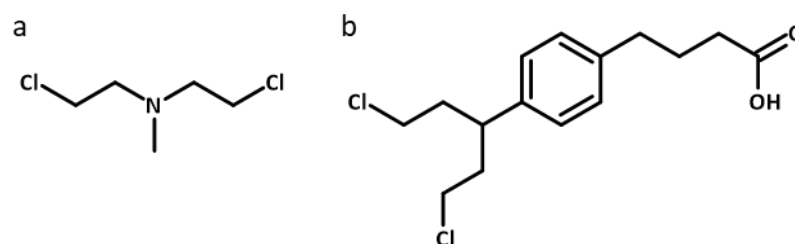
Figure 1-2: Examples of alkylating agents approved for clinical use. a). mechlorethamine, b). chlorambucil.

There are now broadly six classes of alkylating agents across two groups and are now the most commonly prescribed chemotherapy and are most effective in haematological cancers[70]. The two main groups are monofunctional Triazenes/Hydrazines and Nitrosoureas which attack one DNA strand forming adducts, and bifunctional Nitrogen Mustards, Oxazaphosphorines, alkyl alkane sulfonates and ethylene imines/aziridines which attack two strands forming crosslinks[70]. These agents broadly work by being metabolised from bis(2-chloroethyl) to an aziridinium derivative cyclopropyl electrophile that seek and attack electron rich, nucleophilic DNA. Attacks are dominantly on DNA with very little targeting of RNA and protein[72]. Several positions of nucleotides can be attacked by SN1 and SN2 reactions attacking nitrogen and oxygen atoms, however, Guanine-N7, Cytosine-N3, Adenine-N1 and Adenine-N3 are favoured targets[70,72]. Despite being the most used chemotherapy, alkylating agents struggle with resistance and significant side effects[70,71]. Intrinsic and acquired resistance has been documented by the increased activity of O^6-methylguanine transferase, which can remove the alkyl chains added to Guanine-N7[71,74,75]. Further, an abundance of side effects have been documented including diarrhoea, oral ulceration, nausea/vomiting, tremors, hallucinations, infertility, infection and in rare cases bone marrow failure. Most of these issues can be combatted with the co-treatment with other inhibitors and protective agents including O^6-benzyl guanine to inhibit alkyl removal and brefeldin A to prevent infection[71,74,75]. However, alkylating agents suffer from being less effective against fast-growing cancer cells, therefore less suitable for more aggressive cancer types[70].

1-3.2.3: Alkylating-like platinum agents

Originally, platinum agents were classified as alkylating agents due to the similar pattern of damage induced, however these complexes do not induce alkylation, but rather directly complex with DNA through co-ordination bonds, which are more difficult to repair[71]. With the improved knowledge of their mechanism of action and mode of action (MOA), platinum complexes are now considered to be their own category, and as alkylating-like agents. Globally, only three platinum complexes have been approved for clinical use: cisplatin (CDDP), oxaliplatin, and carboplatin (Figure 1-3a, b, c). Three others - nedaplatin, lobaplatin and heptaplatin have been approved for use in Japan, China and Korea, respectively (Figure 1-3d, e, f)[72,76]. Following the initial description of CDDP in 1844, its effectiveness as an anticancer agent was not identified until over 100 years later in 1965, and did not gain clinical approval until 1978[72,76]. Platinum complexes are now used in 50% of treatment regimens for a variety of haematological and solid cancers[77–80]. The clinically approved platinum complexes in Figure 1-3 are square planar complexes and are constructed of three main moieties; a). the amine carrier ligands, which, can adjust the pharmacokinetic properties of the complexes such as lipophilicity and uptake, b). the chloride/carboxylate labile ligands, which are aquated as part of the activation mechanism, and c). the platinum coordination sphere[77,81].

Here, CDDP will be focused on due to being the most frequently used platinum complex against cancer[82]. Following its delivery by intravenous catheter, 68-98% of CDDP is transported in the blood by transport proteins, primarily albumin via the hydrophobic site I subdomain IIA hydrophobic pocket[83,84]. Additionally, due to the chloride levels in the blood being at ~100 mM, the chlorine labile ligands are not aquated, meaning CDDP remains inactive[72]. Following uptake into the cell, primarily through active transport via the copper transporter Ctr1 in addition to some passive diffusion, CDDP is aquated to form $[Pt(NH_3)_2(H_2O)_2]$ because of the lower levels of chloride ions in the cell (being only ~3-20 mM) and is activated[72,85]. The aquated CDDP then binds to DNA though nucleophilic substitution, similar to

alkylating agents, however the platinum remains bound forming platinum adducts and inter-/intra-strand crosslinks predominantly on Guanine-N7[86]. These Pt-DNA adducts have been viewed to be more toxic than CH_3-DNA/alkyl chain-DNA adducts formed by traditional alkylating agents[86]. This is due to alkylating agents only transferring a alkyl chain to DNA while in comparison CDDP and other platinum complexes form co-ordination bond which are much stronger and harder to remove and repair as cells have designated repair enzymes such as O_6-methylguanine transferase which can remove alkyl adducts but not coordination adducts[72,71]. Adduct and crosslink formation encourages double and single strand breaks. DNA strand breaks are highly lethal forms of DNA damage, forcing the cell into cell cycle arrest, predominantly S phase and G_2/M for CDDP treated cells to attempt to repair the damage[87–89]. However, frequently this damage cannot be repaired, this initiates death signalling cascades to trigger intrinsic apoptosis through the activation and deactivation of several proteins including p53, BID, BAX, BAK, BH3 proteins, and BCL-2 family proteins. This leads to the development of mitochondrial membrane pores, the release of cytochrome C, causing the cleavage of Procaspase 9 to Caspase 9 via Apaf1, the subsequent cleavage of Procaspase 3/7 to Caspase 3/7 causing apoptosis and cell death through cell breakdown[90,91].
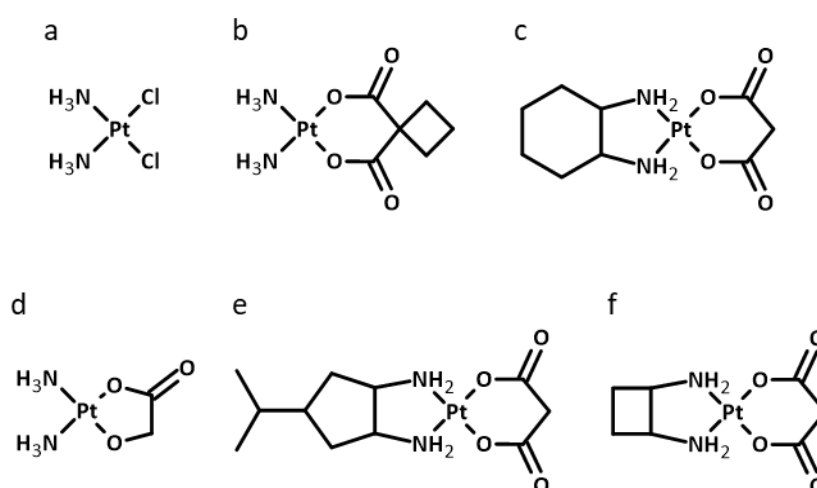
Figure 1-3: Platinum complexes approved for clinical use globally and locally. a). cisplatin (CDDP), b). carboplatin, c). oxaliplatin, d). nedaplatin approved in Japan, e). lobaplatin approved in China, f). heptaplatin approved in Korea.

It should be noted that while platinum complexes have been found to have a similar MOA and spectrum of activity, biological efficacy between them can differ. For example, carboplatin, has a similar spectrum of activity, but is substantially less effective due to the formation of ineffective active species and the reduced activity of the bidentate carboxylate liable ligand over the two monodentate ligands of CDDP[92,93]. Both differences are attributed to the difference in aquation method. It was originally believed that aquation of carboplatin was similar to that of CDDP using associative substitution of the carboxylate ligand with water, however upon further investigation, it was found that the rate constant of this reaction was too low to be feasible in an *in vivo* system[92]. While the full mechanism of aquation of carboplatin is still under debate, there are several theoretically feasible models including the utilisation of electron transfer hypothesis with the synthesis of several intermediates and the use of other biological nucleophiles such as GSH and carbonate to form the final aquated carboplatin complex[92,93].

Due to the uptake of platinum complexes being favoured by rapidly dividing cells, this makes them highly effective against cancerous cells. However, this does not provide accumulation specificity with other types of rapidly diving cells in the body such as hematopoietic and epithelial cells also accumulating substantial levels of complex, causing significantly debilitating side effects in patients. In addition to the general side effects induced by chemotherapy previously discussed, seven main categories have been determined; nephrotoxicity, ototoxicity, neurotoxicity, cardiotoxicity, haematological toxicity, hepatotoxicity, and gastrointestinal toxicity[69]. Of these, nephrotoxicity is most prominent as up to 50% of CDDP is excreted through the kidneys within 48 hours of treatment, causing high concentrations of CDDP in the nephrons leading to inflammation, oxidative damage, apoptosis and acute tubular necrosis[94]. Severe nephrotoxicity is seen in ~20% of patients, but can be as high at 66-70% in the elderly and in children due to decline in function and glomerular filtration rate[94,95]. Further, inter-patient genetic variation in genes including *ERCC1/2* and *SLC22A2,* coding XPD and OCT2

proteins used in DNA nucleotide excision repair and CDDP uptake respectively have been corrected with increased prevalence of nephrotoxicity[94,96].

Platinum complex regimens are also vulnerable to the development and intrinsic presence of resistance. Four main resistance mechanisms effect platinum complex. Decreased uptake occurs by reducing the amount of transporters including organic cation receptors, organic carnitine and zwitterion transporters, LRCC8 and copper transporter 1[86]. Increased efflux is promoted by the increase in MRP2 and other ATP-binding cassette transporters leading to the increased removal of complexes before they have change to move to the nucleus and inflict damage[86]. Increased detoxification is upregulated through increased levels of glutathione (GSH), glutathione-S-transferase, and metallothioneins[97]. Increased damage repair is also initiated by upregulating enzymes and effectors involved in translesion, nucleotide excision and homologous recombination repair including XPD variants, PARP1, BRCA1/2, CHK1/2, and p53[97,98].

Despite these setbacks, platinum complexes are still being widely investigated to improve potency and bioavailability while attempting to alleviate toxicity and resistance mechanisms. This has mainly been through the development of new structures and formulations. New structures include alternate carrier ligands, addition of active cargos and the oxidization from Pt(II) to Pt(IV) to change structure shape from square planar to octahedral. Examples of these include such as phenanthriplatin, Pt(IV) LA-12, Pt(II) sugar conjugates, Pt(II) hormone conjugates, Pt(IV) stataplatin, Pt(IV)-valporate conjugates, and many others[77,99,100]. Polymer complexes and nanoparticles have also been in development including BBR3464, triplatinNC and triplatinNC-A polymers which are extended chains of CDDP derivatives with three Pt(II) centres[99,100]. Nanoparticles include micelles such as NC-6004 and NC-4016, and the use of carbon nanotubes[99,101,102]. The predominant aim of these complexes and formulations is to circumvent the detoxification and accumulation mechanism observed in platinum resistant disease by protecting against detoxicants like GSH and efflux by MRP2, utilizing alternate uptake mechanisms such as endocytosis and other transporters like glucose transporters, prevent systemic platinum release, and

adding additional properties with the conjugation with other biologically active molecules. However, while several of these have been highly effective *in vitro*, *in vivo*, and in clinical trial, none thus far have achieved clinical approval.

1-3.2.4: Antimetabolites

In cancerous cells, metabolism is accelerated to match demands required for accelerated growth. Therefore, antimetabolites can provide some specificity targeting fast-growing and cycling cells[103]. As of 2017, 17 antimetabolites were approved for clinical use, divided into three groups; folate antagonists (methotrexate), purine antagonists (mercaptopurine), and pyrimidine antagonists (5-fluorouracil)(Figure 1-4)[103,104]. Originally, antimetabolites were found to be most effective in haematological cancers, but are now routinely and effectively used in the treatment of solid tumours including, colorectal, breast and pancreatic cancer[105]. Despite having different targets, these compounds have a similar MOA: to inhibit metabolic processes involved in the synthesis of DNA. For example, 5-fluorouracil is taken up into the cell as an inactive pro-drug, which is then converted to fluorodeoxy-uridine monophosphate, which covalently binds to the active site of thymidylate synthase, inhibiting the conversion of deoxy-uridine monophosphate to deoxy-thymidine monophosphate, preventing nucleotide synthesis[104,106,107]. Other secondary MOA have been shown including direct DNA damage and by RNA damage[106,107].

Despite the success that antimetabolites have had and the documented ability to be highly effective in late-stage disease progression, response rates are highly variable[103]. This has been attributed to the MOA of these treatments, interpatient genetic variability of the enzymes involved in the metabolism, intra-patient metabolic variability, and metabolic pathway cross-talk[103,105]. This variability coupled with the dose-limiting toxicity of these treatments introduce a high variability preventing consistent treatment. In addition, due to high metabolic processing in the body, only 3% of the final dose localises to cancer environment to exhibit anticancer effects[107]. This leads to significant side effects including

anaemia, bone marrow disorders, gastrointestinal issues, haemorrhage, alopecia, cardiac disorders, hepatic disorders, and parkinsonism[108]. These issues have led to the decline in pursuit of new antimetabolites for fear of developing new treatments with similar MOA and drawbacks[105].
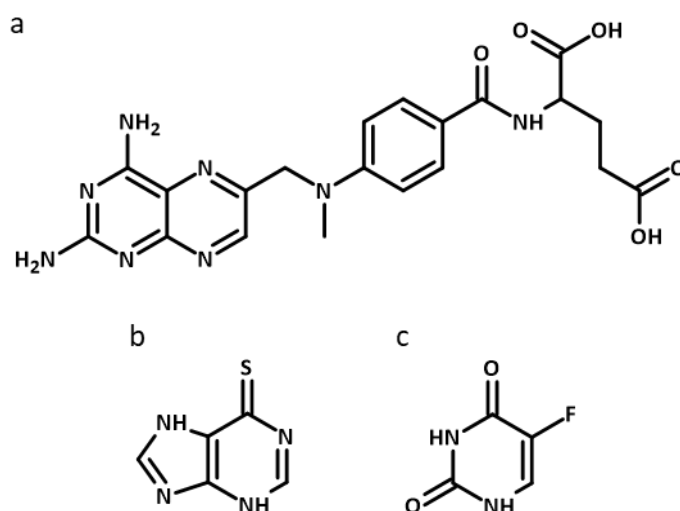
Figure 1-4: Select examples of the main groups of antimetabolite compounds. a). methotrexate, b). mercaptopurine, c). 5-fluorouracil.

1-3.2.5: Cytotoxic antibiotics

The natural world is often a source of inspiration for new effective treatments for many conditions, and cancer is no exception. Cytotoxic antibiotics are compounds that are derived from bacteria and fungi, so can be classified as natural products, that have profound cytotoxicity including anthracyclines and epipodophyllotoxins[109]. Despite cytotoxic antibiotic compounds having highly varying structures and origins, this class often have very general MOA of attacking DNA via intercalation or by DNA polymerase II inhibition to induce damage and apoptosis. Two primary examples are doxorubicin and etoposide (Figure 1-5).

Doxorubicin was originally derived from the bacteria *Streptomyces peucetius* in the 1970s and is now a highly effective non-specific treatment for many cancers including breast, lung, gastric, ovarian, thyroid, haematological and paediatric cancers[110–112]. Its primary MOAs are through DNA intercalation,

disruption of topoisomerase II and generation of ROS through the intermediate doxorubicin-semiquinone[110,112]. This leads to DNA strand breaks and cellular damage leading to apoptosis and autophagy[110,112]. However, being non-targeted, toxicity is a major issue with patients exhibiting many side effects including neurotoxicity, hepatotoxicity, nephrotoxicity, and dose limiting cardiotoxicity[110–112]. Cardiotoxicity presents as cardiac hypertrophy, and can present years after treatment[112]. Cardiotoxicity is suggested to be due to the reduced compound doxorubicinol which effects iron and calcium regulation in addition to ion pumps in the sarcoplasmic reticulum and the mitochondria[110,111]. While these can be alleviated with treatments such as metformin, this is a further increase to patient treatment load with its own associated side effects[111]. Further, doxorubicin is also plagued by the occurrence of resistance and inter-patient variation stemming from ABCB1, ABCC1 and other multi-drug resistance transporters[110].

Figure 1-5: Examples of cytotoxic antibiotics approved for clinical use. a). doxorubicin. b). etoposide.

Another example is etoposide, a semi-synthetic derivative of podophyllotoxin from the *Podophyllum peltatum* plant approved for use in 1966[113,114]. Etoposide reversibly poisons the active site of topoisomerase II, preventing the second transesterification reaction which ligates DNA strands after initial breakage, stalling repair and breaking the strand[113,114]. Similar to doxorubicin, many side effects are seen with etoposide treatment including alopecia, gastrointestinal toxicity, hypersensitivity,

however myelosuppression is the dose limiting toxicity, potentially leading to the development of secondary acute myelocytic leukaemia[113–115]. Antiproliferative effects are also reduced by efflux and deactivation methods similar to doxorubicin[113].

Both compounds rely on the recruitment of topoisomerase II. Meaning, these treatments are more effective with co-treatment with a direct DNA damaging agent such as CDDP and in more aggressive cancers with a faster cell cycle increasing topoisomerase II activity[112,113]. However, the contrary is also true, where tumours have low topoisomerase II activity, DNA repair is faulty or cell replication is slow/cells are in senescence, the activity of these complexes is diminished.

1-3.2.6: Microtubule targeting agents

Moving away from DNA targeting non-specific agents, the microtubule targeting agents (MTAs) are another highly effective family of compounds used against cancer preventing effective mitosis and other key processes including structure maintenance, motility, and cellular trafficking[116]. Due to their success, they are the second most commonly used class of cytotoxic treatment[117]. MTAs are a highly diverse group to match the wide variety of binding sites of microtubules available including vinca alkaloids and taxanes[116]. Vinca alkaloids such as vinblastine (Figure 1-6a) were derived from *Catharanus roseus* plant in the 1950s reversibly bind via non-covalent bonding to the vinca site of microtubules, inducing a destabilising effect, preventing the formation of microtubules[117,118]. On the contrary, taxanes such as paclitaxel (PTX, Figure 1-6b), derived from the *Taxus brevifolia* yew tree in 1992, bind to laulimalide/peloruside sites, stabilising the microtubule formation preventing disassembly[117,118]. The inhibition of assembly and disassembly activates the mitotic spindle checkpoint, initiating mitotic arrest, mitotic slippage, mitotic catastrophe and apoptosis via Caspase 2/8/9[118,119]. Despite most treatments in this family targeting the microtubule, there is wide binding variation within and across the categories of MTAs.
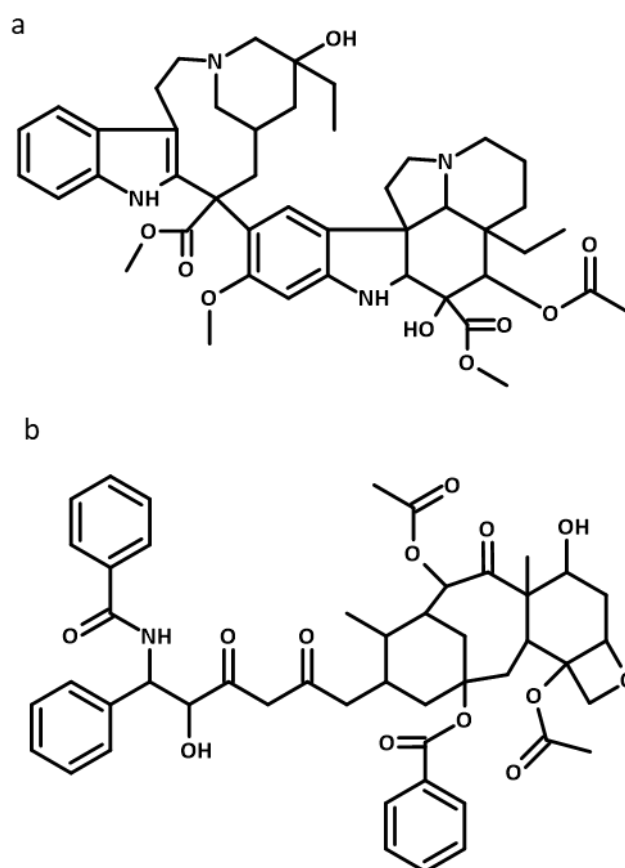
Figure 1-6: Examples of microtubule targeting agents approved for clinical use. a). vinblastine, b). paclitaxel (PTX).

Beneficially, MTAs are more effective at low concentrations, however toxicity is still an issue. MTAs often induce the canonical chemotherapy symptoms similar to the other families previously discussed including alopecia, nausea and vomiting and exhibit dose limiting neutropenia caused by myelosuppression, and neurotoxicity caused by neuronal degeneration which can only be treated with cessation of treatment[117,120]. MTA families are also subject to resistance in similar ways[121]. The main mechanism of resistance is increased efflux via ABCB1 and ABCC3 through P-glycoprotein recognition[118]. Resistance can also arise through tubulin unit mutations and increased detoxification and compound efflux. While there have been attempts to mitigate efflux by developing semi synthetic derivatives, their effectiveness in clinic has not yet been determined[122]. There has been success with albumin nanoparticles to improve solubility and cytotoxicity of PTX, gaining clinical approval for use in

pancreatic and breast cancer, but otherwise, further modifications have been not been as successful[122].

1-3.2.7: Targeted chemotherapy

With the recent explosion in genomics research and the ability of sequencing to determine cancerous mutations, so has the research into drugs to target those specific cancerous mutations. The two main classes are small molecule inhibitors and monoclonal antibodies[123]. Small molecules inhibitors (*target protein*-i) are considered to be the more dominant class and are characterised by their highly specific structures and <900 Da weight to allow their use both on the surface and to allow for uptake to take effect inside the cell with highly precise target binding[124]. Some examples include gefitinib (EGFRi), sorafenib (VEGFi), crizotinib (ALKi) and vemurafenib (V600E BRAFi)[123]. These inhibitors work by specifically and competitively binding to their target, preventing subsequent signalling of oncoproteins and activation of tumour suppressor proteins.

Monoclonal antibodies are also commonly used targeted therapies but differ from small molecule inhibitors significantly differ in terms of their mechanisms and modes of action. Due to the high weight and size, antibodies are not commonly internalised and elicit their MOA on the cell cytoplasmic membrane (CCM) by binding to receptors and signalling molecules[124]. Example antibodies include trastuzumab (anti-HER2), bevacizumab (anti-VEGFR) and cetuximab (anti-EGFR)[124,125]. Antibodies, once bound to their target, disrupt cellular communications and interactions by blocking complement proteins, attracting the immune system, inhibiting signalling and delivering any cargo attached to the antibody to the cell to cause additional damage[124].

These treatments boast the ability for increased effectiveness at treating cancer and decreased side-effects versus their non-targeted counterparts yet, these treatments come with significant drawbacks[123]. Due to the highly specific nature of these treatments, they are only effective against one target, vulnerable to treatment target mutations, and highly expensive to research and produce[123,124].

While often posed to be safer than non-targeted treatments by having less side effects due to less adverse target interactions, patients receiving targeted treatments can also experience side effects[126].

Targeted chemotherapy has been highly successful against lung and breast cancer with many viable options for these[125,127,128]. However, this is not the case for all cancer types, including EOC. There has been limited research in targeted therapy, likely due to the limited actionable targets as previously discussed. There has been approved use of PARPi such as olaparib and niraparib due to the defective BRCA1/2 pathways and the VEGFRi bevacizumab in the USA. Despite their approval, it has been documented that there is no significant extension in overall survival, and extended survival by an average of 7.8 months in late stage patients respectively with the use of PARPi[28,129,130]. Other interests have been into immune checkpoint inhibitors through PD1/PDL1, and oestrogen receptor targeting, but there have been no clinically significant results with response rates of less than 20%[129,131].

1-3.3: Current treatment regimens of EOC

According to the UK NICE guidelines for the treatment of ovarian cancer, stage I conditions should be treated with surgery for resection by total hysterectomy or mono/bi lateral salpingo-oophorectomy with lymph node assessment to rule out progression, with only high-risk patients receiving six cycles of adjuvant carboplatin chemotherapy[40]. For stage II-IV patients, surgery is recommended with neoadjuvant chemotherapy for macroscopy resection[40]. However, for second line treatments, there is very limit treatment guidance other than the use of genetic screening and the use of PARPi as previously described in appropriate cases[40]. The current chemotherapy standard of care is carboplatin and PTX[25,132,133]. Beyond this there is very little choice for alternate treatment for first line therapy other than the use of CDDP for patients experiencing carboplatin toxicity and the use of pegylated liposomal doxorubicin hydrochloride as a mono or combinational therapy with platinum treatment for second line therapy[129,131,132,134,135]. These limited treatment options in addition to there being no significantly promising targeted therapy options demonstrate the need for alternative treatments.

1-4: Metals in medicine

Trace metals are essential to life. They are intimately involved in a wide range of enzymatic reactions such as metabolism, nucleotide synthesis, and redox catalysis, in addition to being relied upon in many storage/transport roles[136]. Understanding the importance of metals in biology, attention has been drawn to other d group metals for use in medicine. As shown by the anticancer treatments reviewed above, the majority of pharmacological options are organic with a very small minority being metal containing complexes, yet this has not hindered the interest of metals in the treatment of cancer[137,138]. The use of metals in treatment stems back to the use of arsenic trioxide in potassium bicarbonate for the treatment of leukaemia in the 1700s[76,139]. However, metals for the treatment of cancer were not highly successful until the development of CDDP. Yet, due to the shortfalls of platinum complexes, there has also been an abundance of research into alternative metals including rhenium, titanium, osmium and iridium with varying structures, ligands and properties[140–144].

This work will focus on the use of ruthenium. Ruthenium has been widely investigated in the treatment of cancer due to a range of biological and chemical reasons including[145,146]:

- Being able to mimic iron and interact with many iron-using proteins/biochemical pathways

- Ruthenium complexes possessing innate prodrug qualities through slow ligand exchange activation, limiting off target interaction

- Ruthenium complexes exhibiting similar binding kinetics to platinum complexes

- Often exhibiting reduced complex toxicity compared to platinum complexes

- Ruthenium complexes exhibiting differential DNA binding compared to platinum complexes

- Ruthenium complexes often exhibiting multiple and differential MOA to platinum complexes

- Ruthenium often not sharing limiting cross resistance with platinum complexes

From the current literature, four main complexes/families have been identified with significant potential and substantially different behaviours.

1-4.1: KP1019/1339

KP1019 and KP1339 are traditional octahedral Ru(III) complexes originally developed from (ImH)[trans-RuCl$_4$(Imidazole)$_2$] the Keppler group[147]. KP1019 and KP1339 (Figure 1-7a) only differ in their cation with KP1019 having a less soluble indazole and KP1339 having a more soluble sodium and have been documented to have highly similar MOA[148]. The solubility limitations of KP1019 have led to the shift in focus to KP1339 as maximum tolerated dose could not be reached in phase I clinical trials due to the significant infusion volume required to provide doses over 600 mg[147]. Following intravenous infusion KP1019/1339 can bind to albumin and transferrin for transport in the blood through interaction with site I and site II of albumin, then can be taken up by active transport through transferrin receptors[149]. This allows a degree of specificity due to the upregulation of transferrin receptors on cancer cells to satiate the increased need for iron[150]. KP1019 and KP1339 are considered to be prodrugs as following uptake, they are reduced from Ru(III) to Ru(II) by the low pH and hypoxic tumour environment[151,152]. Following reduction, activation occurs similarly to CDDP with the aquation of two of the axial chlorine ligands to water[147,153,154]. These chemical properties provide the KP complexes with additional layers of specificity towards cancerous cells and the ability to prevent premature activation. However, they can be deactivated by cellular GSH levels[147].

Like many ruthenium complexes, KP1019 has been documented to have several MOA. The primary MOA is to induce depolarisation of the mitochondrial membrane potential ($\Delta\Psi$m) and generate ROS through the redox activity of the ruthenium centre[154]. This causes the cell to undergo intrinsic apoptosis through irreversible damage to the mitochondria, the release of cytochrome C, and Caspase 9/3/7 activation. However, other secondary MOA include the formation of monofunctional ruthenium adducts inducing low level DNA crosslinking and unwinding have been demonstrated intracellularly causing intrinsic apoptosis[147,155]. Additionally, KP1019 also prevented the formation of colony forming units and tumour propagation short and long term[156].
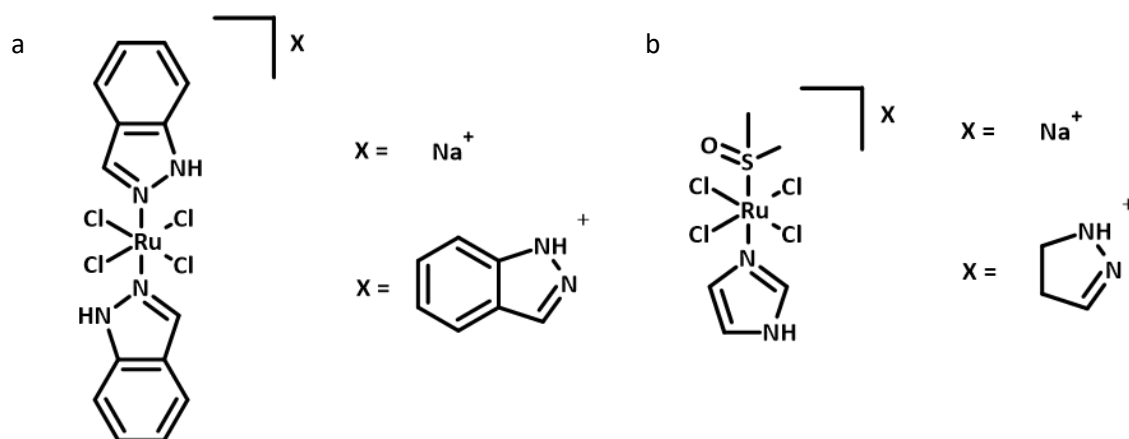
Figure 1-7: Structure of a). KP1019/1339 (KP1019 has an indazole counter ion while KP1339 has a sodium counter ion, allowing for differences in solubility of the complexes). b). NAMI/NAMI-A complexes (NAMI possesses a sodium counter ion while NAMI-A has an imidazole counter ion for improved solubility).

KP1019 has performed successfully in *in vivo* murine studies being more effective and less variable than the comparators CDDP and 5-fluorouracil[152,157]. Furthermore, the mice experienced low toxicity and mild adverse effects such as erythropoiesis interference. Due to these promising results KP1019 successfully reached phase I clinical trial for several tumour types where over two trials, only mild toxicity was reported and no dose limited toxicity was observed, pharmacokinetic properties such as long half-life and low clearance were reported, in addition to disease stabilisation being observed[147,158].

1-4.2: NAMI/NAMI-A

NAMI complexes (Figure 1-7b) were developed by the Alessio Sava research group, initially designed as NAMI with a sodium counter ion. To improve synthesis, solid stability, physiochemical properties, and solubility, the sodium was substituted with an imidazole counter ion and the complex named NAMI-A[159]. Similar to the KP1019/1339 complexes, NAMI-A is also a Ru(III) traditional octahedral complex, sharing similar intravenous transport bound to albumin and transferrin, and having a similar activation mechanism of being reduced from Ru(III) to Ru(II) followed by aquation of two axial chloride ligands[153,160–162]. NAMI-A is highly remarkable complex; despite being described as inactive in antiproliferative screening with IC_{50} values >500 μM, it has been highly effective in *in vivo* studies and

metastatic studies[100,160]. This probed further interest into the MOA of NAMI-A. The primary MOA is through the interference of the $\alpha_5\beta_1$ integrin, preventing fibronectin binding and FAK Try397 autophosphorylation[163]. This is likely due to predominant interference with the β_1 unit shown by unit expression assays, siRNA experimentations and additional reduced collagen IV binding to the $\alpha_2\beta_1$ integrin[163,164]. Additional MOA include the inhibition of matrix metalloproteinases (MMP) 2 and 9, cytoskeletal remodelling, G_2/M arrest, VEGF induced angiogenesis inhibition, MAPK/ERK signalling inhibition with limited DNA binding[145,165]. This has been documented to induce apoptosis via ERK1/2 downregulation, Hsp27 modulation, cytochrome C release, increase in Caspase 3 activity, and increase in apoptotic cells identified by propidium iodide/annexin V flow cytometry analysis[166,167].

Despite its inactivity against in antiproliferative screening, the benefits seen against secondary tumours and *in vivo* study encouraged the progression of NAMI-A to clinical trial. In Phase I trials, NAMI-A was successful with a dose suggestion of 300 mg/m^2/day, with a range of side effects being observed[168]. However, in a phase I/II trial as part of a combination treatment with gemcitabine for non-small cell lung cancer, the trial concluded that preliminary efficacy of NAMI-A was not convincing with several side effects including sudden onset nausea, vomiting and diarrhoea, constipation, elevated liver function tests and creatinine, fatigue, phlebitis at infusion, and vascular and portacath events, though the latter were completely resolved with urokinase or portacath replacement[145]. So, while NAMI-A does have the potential as a clinical agent, a treatment for only metastasis is highly limited. Therefore, next steps for NAMI-A have been to rebrand as an antimetastatic agent only and seek optimal treatment combinations to treat both the primary and secondary masses while simultaneously limiting toxicity.

1-4.3: RAPTA complexes and monodentate ligand piano-stool complexes

RAPTA complexes are pseudo-octahedral piano-stool Ru(II) complexes, with stabilisation of the Ru(II) by the η^6 coordinated arene ring developed by the Dyson group[169]. In contrast to the Ru(III) complexes, RAPTA complexes do not have to be reduced to be activated, but their labile chlorine ligands must be aquated similar to CDDP and the Ru(III) complexes[170]. RAPTA-C was synthesised first, following which several derivative complexes have been documented, however the primary derivatives differ in their arene ring with naming derivatives based on their arene ring (C – p-Cymene, B – benzene, T – toluene) (Figure 1-8)[169]. The remarkable ligand of the RAPTA complexes is the 1,3,5-triaza-7-phosphaadamantane (PTA) ligand being amphilic aiding the lipophilicity and hydrophilicity of these complexes, assisting solubility[169]. Interestingly, RAPTA complexes exhibit good antibiotic properties against several bacterial strains, however the most promising candidate, RAPTA-C, has been consistently documented to have low antiproliferative activity with IC_{50} values varying from 60 to >300 µM in *in vitro* studies[171–174]. However, in *ex vivo* and *in vivo* studies under optimal dosing conditions, primary tumour and metastasis reduction was achieved with minimal toxicity of vomiting and alopecia in mice although tumour apoptosis, necrosis and quiescence were observed[175]. Furthermore, highly significant synergy can be achieved with the co-treatment the EGFRi erlotinib and the PI3K/mTOR inhibitor BEZ-235 preventing proliferation and angiogenesis[176].

Complex	R^1	R^2
RAPTA-B	H	H
RAPTA-C	CH$_3$	CH(CH$_3$)$_2$
RAPTA-T	H	CH$_3$
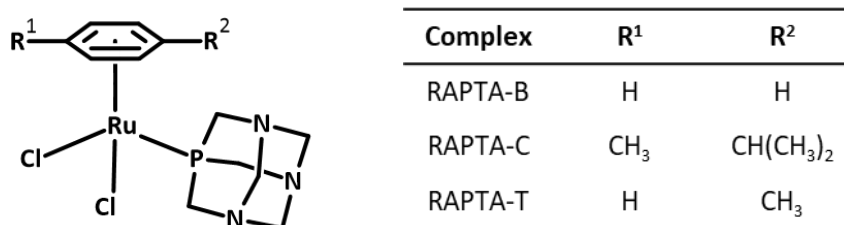
Figure 1-8: Structure of the predominant RAPTA complexes. RAPTA-B has a benzene arene, while RAPTA-C has a *p*-cymene ring and RAPTA-T has a toluene ring altering their activity.

The differences between *in vitro* and *in vivo* activity have been suggested to be due to the MOA of RAPTA-C. RAPTA-C has been documented to bind to a variety of both extracellular and intracellular proteins through the equated monodentate ligands forming coordination bonds with many plasma and cellular proteins transferrin, albumin, GSH, lysozyme, ubiquitin, cytochrome C, superoxide dismutase, PARP, metallothioneins and histones through nucleophilic attack[169,171,177]. Some DNA binding has been documented causing DNA crosslinking, but similar to NAMI-A, this is a secondary MOA and not corelated with potency and DNA damage is primarily through histone binding. Despite being described as cytostatic, apoptosis has been described. This includes increase in p53, JNK, p21, BAX, cytochrome C and ROS, and a decrease in cyclin E and decrease in Procaspase 9[169,172,175]. This leads to the induction of G_2/M arrest and intrinsic apoptosis via the mitochondria and the p53-JNK pathways[178]. These results show that RAPTA-C does have potential for clinical trials, however the issues surrounding dosing with the high variation in response and resultant mechanisms with the change in dose concentration need to be addressed beforehand[170].

1-4.4: RAED complexes and bidentate ligand piano-stool complexes

Similar to the RAPTA complexes, RAED complexes by the Sadler group are also Ru(II) pseudo-octahedral piano-stool complexes, but differ by overall charge, often possessing a bidentate ligand in addition to the labile halogen monodentate ligand developed [177]. One of the first examples of this class is RM175 (Figure 1-9). There is significant benefit of the bidentate ligand over monodentate ligands due to the chelate effect, where bidentate and polydentate chelation have increased stability, are substantially stronger, and are preferably formed[179,180]. However, this also limits biomolecule adduct formation, as the complex can only form monodentate adducts via the aquated ligand[177]. However, this does not affect the potency as RM175 has consistently demonstrated potent *in vitro* activity often with low to moderate IC_{50} values varying from 5 to 60 µM following 24 hours exposure in several cancer cell lines including ovarian, breast and lung while maintaining specificity towards cancerous lines with

concentrations needed to be a log higher to be toxic in normal hepatocytes[146,181–183]. This cytotoxicity also translates into xenograft and *in vivo* models demonstrating good efficacy against the primary tumour and metastatic lesions[146,183,184].
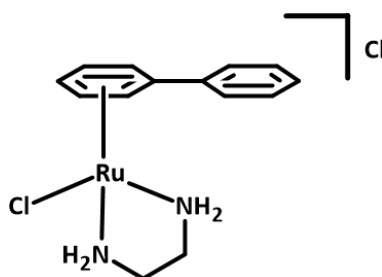
Figure 1-9: Structure of RM175, one of the original bidentate ligand piano-stool complexes which has inspired many subsequent complexes, including those in this work.

The efficacy of RM175 may be due to the differing MOA to the previous complexes. The primary MOA of RM175 has been suggested to be the formation monofunctional ruthenium adducts on DNA, primarily on Guanine-N7 though coordination bonding, which is then supported by hydrophobic and non-covalent bonding of the arene ring intercalating with the DNA strand, in a non-cross resistant method to CDDP[177,185–188]. While this DNA interaction has only been noted in physiochemical studies, it has been suggested that DNA damage does occur *in vitro*, causing the induction of death by apoptosis through the p53-p21-BAX pathway with extent of DNA damage correlation with extent of cell death[189]. Secondary MOA through protein adducts have been observed with adducts to GSH and ubiquitin, but protein binding is non-preferential due to monodentate binding[177]. Invasion through chemo- and haptotaxis, and metastasis inhibition has also been observed through increasing fibronectin adhesion and increase in MMP2 activity[183]v.

RM175 has had many significant successes in *in vitro* and *in vivo* studies, however rather than push towards clinical trials, interest has been directed towards structural changes to improve pharmacokinetic and pharmacodynamic properties. One example was the changing of the metal centre to osmium. This change maintained toxicity with an IC_{50} value <10 μM with 72 hours exposure,

however it was noted that the osmium complex exhibited much slower binding kinetics with DNA than the ruthenium complex, but had several binding points including Guanine and Cytosine forming mono-osmiated and di-osmiated adducts[186,190,191]. Slower interaction kinetics have been associated with decreased deactivation before interacting with DNA[190]. Other variations include ring substitutions from biphenyl to *p*-cymene and tetrahydroanthracene. However, it was reported that the *p*-cymene complex was marginally less cytotoxic than the biphenyl complex, but exhibited a similar MOA to RM175 by binding to guanine in DNA as mono-ruthenated adducts and are also capable of non-covalent, hydrophobic interaction with DNA, with increasing interaction corelating with cytotoxicity[192,193]. Other ligands include the chain extension from ethylenediamine to N-ethyl ethylenediamine, but very little difference between the cytotoxic activity in a variety of ovarian cancer cell lines, and it was noted that that arene ring changes had a greater influence on cytotoxicity than ligand extention[182].

1-4.5: Other complexes of interest

Inspired by RM175 and its second-generation complexes, there was increased interest in alternative metals and bidentate ligands. The primary metal of interest was osmium as a metal centre due to being documented to react 100X slower in hydrolysis/aquation and biomolecule reactions than ruthenium[194,195]. Other ligands of interest was the use of azopyridine (AzPy) ligands due to their strong pi-bond acidity, which stabilizes the oxidation state of the metal centre and their ability to catalyse the conversion of GSH to GSSG[196,197]. From the interest in AzPy ligands developed an interest in iminopyridine (ImPy) ligands due to the bioisosteric replacement of one nitrogen in the azo bond with a carbon[196]. From these interests, several comparative antiproliferative studies and MOA studies have been done with varying arene rings, monodentate halogen, and substitutions on the phenyl and pyridine rings[87,143,198–200]. From these investigations, one complex of interest arose [Os(η^6-*p*-cym)(AzPy-NMe$_2$)I]PF$_6$, known as FY26. Following antiproliferative investigation by the Sanger Institute's Cancer

Genome Project treatment screening program in 809 cancer cell lines, FY26 exhibited significant antiproliferative activity with a mean GI_{50} of 0.75 µM, compared to CDDP with a mean GI_{50} of 36.7 µM[201]. Biological evaluation found that the main MOA of FY26 was through ROS generation, GSH-GSSG conversion, G_1 arrest, ROS generation, mitochondrial compromise, and DNA damage, making it a highly effective multitargeting complex[201–204]. but by apoptosis flow cytometry no increase was observed in the apoptotic quadrants, yet a significant increase in the non-viable population indicating membrane compromise without an apoptotic phenotype, therefore an alternative mechanism of cell death to apoptosis[203]. However, $[Ru(\eta^6\text{-}p\text{-cym})(ImPy\text{-}NMe_2)I]PF_6$ which shares the dimethylamine phenyl ring substituent has also been found to be highly potent despite more facile synthetic methods[87].

1-5: Bioisosteres in drug development and design

In previous organometallic complex research, there is an attraction to more structurally complex ligands from metal centres for several reasons. One reason for this is the ability to take advantage of unique features of cancer cells to increase specificity, for example the addition of glucose derivatives to a complex to increase uptake of the complex through the increased upregulation of GLUT receptors on cancer cells and achieve significantly increased cell uptake of the complex and improved activity[205–207]. A second reason is to improve or restore toxicity. This can be observed in ferrocifen, where the conjugation of Tamoxifen-OH to a ferrocenyl group allows the complex to become effective against breast cancer cells regardless of their Oestrogen receptor status where tamoxifen is only effective against Oestrogen positive receptors through ferrocifen's redox activity[207–209]. A third reason is to increase the MOA targets of the complex which can be seen by the ruthenium piano-stool with the ciprofloxacin-derivative Cip-A bidentate ligand allowing the complex to have both improved anticancer and antibiotic activity[210].

While logical these large changes make significant changes to the activity of a structure, small specific changes can also have significantly profound effects. One example is the replacement of hydrogen with fluoride of cladribine to make clofarabine (Figure 1-10). The addition of the fluorine allows for activity against acute lymphoblastic leukaemia, while without it, cladribine is ineffective. Similarly, the addition of fluoride to uracil to synthesise 5-fluorouracil allows for a highly potent anticancer treatment[105]. These changes are known as bioisosteric replacements and are an essential tool in drug design. Bioisosteric replacements are defined as similar functional groups or structures that exhibit analogous structural, topological, electronic, physicochemical and biological properties[211,212]. In practice this definition is often not strictly applied as bioisosteric replacements and are often used to alter the biological properties of a structure and achieve more desirable traits including improved MOA, potency, toxicity/side effect profile, pharmacokinetics, metabolic stability and synthesis routes[211,212].

Therefore, bioisosteres can also be defined as substitutions, atom/group replacements and modifications to improve the desirable traits of a bioactive molecule. This means bioisosteres can widely vary, subsequently there are different categories (Table 1-1)[211–215]. The variety of replacements allows for highly precise molecule tuning, making a highly powerful tool in all areas of drug design.
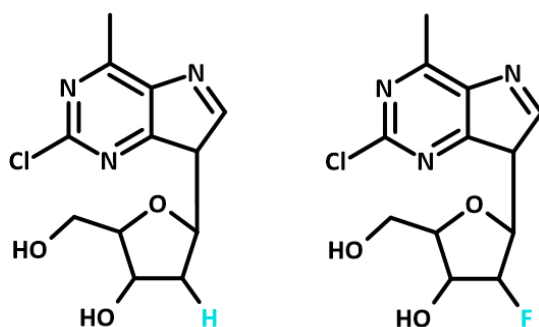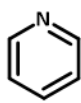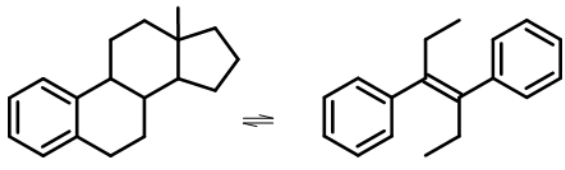
Figure 1-10: Example of bioisosteric replacement in small molecule drug design. a). cladribine. b). clofarabine. With the bioisosteric replacement of hydrogen with a fluorine in these compounds, there is a profound difference in activity where the latter is highly effective against acute lymphoid leukaemia while the former is ineffective.

The effect of small bioisosteric replacements are also seen in organometallic complexes. As previously mentioned, there has been a variety of piano-stool complexes based off RM175 varying their four main moieties. With many ImPy and AzPy being synthesised, most derivatives alter in their monodentate ligand, arene ring and substituents on the bidentate ligands. There have been many papers with series of complexes comparing bioisosteric replacements highlighting several trends including improved potency of iodo ligands over chloro ligands, that AzPy ligand containing complexes are more potent than ImPy ones and that larger arene rings improve lipophilicity, uptake and prevent oxidation of the ruthenium centre[87,182,199]. However, several bioisosteric replacements and small modifications have yet to be examined including methyl derivatives, extension of the ImPy ligand, and phenyl ring atom variants.

Table 1-1: The main categories of bioisosteric replacement used in drug design, being either classical– often substitution, or non-classical – where more complex transformations are often employed.

Classical	Non-Classical
• Monovalent H > F, Cl, OH, CH_3 • Divalent $-CH_2->$ -NH-, -S-, -O- • Trivalent =CH- > =N-, =P- • Tetravalent C > N^+, P^+ • Ring equivalents 	• Linear ⇌ Cyclic conversion • Functional group substitution Amide/Ester ⇌ di/triazoles • Retroisosterism

1-6: Aims and objectives

As small changes in molecular structure can cause significant differences in the activity of anticancer complexes, bioisosteric replacements could be used to improve currently established chemical entities and inform future design of second-generation treatments. Therefore, the aim of this work is to explore the potential of different bioisosteric moieties to improve the anticancer potency and shift the MOA of ruthenium piano-stool complexes. There will be focus on modifications of the phenyl ring in the ImPy ligand of p-cymene complexes. Based on this, the following specific objectives can be drawn:

- To synthesise and characterise 19 ImPy molecules with capability of being bidentate ligands

- To synthesise and characterise three series of $[Ru(\eta^6\text{-}p\text{-Cym})(ImPy)X]PF_6$ complexes as potential anticancer agents. Their physicochemical characterisation will be established using techniques such as Nuclear Magnetic Resonance (NMR), mass spectrometry, UV-Vis spectroscopy and Density Functional Theory (DFT) geometry optimisations

- To explore the anticancer activity of the complexes in tumour cell lines of different origins including several EOC, non-small cell lung, triple negative breast, epithelial colon, and ductal pancreatic cancers, as well as normal non-cancerous lung cells

- To determine suitable candidates in each series for further research in EOC based on potency and chemical structure qualities

- In Chapter 3, the benefits of the methyl group bioisostere will be explored with further experimentation into the MOA and mechanisms of cell death (MOD) activated paying particular attention to apoptosis, ferroptosis and autophagy

- In Chapter 4, the advantage of using a methylene linker bioisostere will be investigated with specific interest in the DNA strand and nuclear damage induced

- In Chapter 5, the effect of a singular atom substitution and the resultant shift in MOA will be explored with further evaluation of the effect on the CCM including morphology and binding

1-7: References

1. Blackadar, C. B. Historical review of the causes of cancer. *World J. Clin. Oncol.* **7**, 54–86 (2016).
2. Bray, F. *et al.* Global cancer statistics 2018: GLOBOCAN estimates of incidence and mortality worldwide for 36 cancers in 185 countries. *CA Cancer J Clin* **68**, 394–424 (2018).
3. Bray, F. *et al.* Erratum: Global cancer statistics 2018: GLOBOCAN estimates of incidence and mortality worldwide for 36 cancers in 185 countries. *CA Cancer J Clin* **70**, 313–313 (2020).
4. Sung, H. *et al.* Global Cancer Statistics 2020: GLOBOCAN Estimates of Incidence and Mortality Worldwide for 36 Cancers in 185 Countries. *CA Cancer J Clin* **71**, 209–249 (2021).
5. Quaresma, M., Coleman, M. P. & Rachet, B. 40-year trends in an index of survival for all cancers combined and survival adjusted for age and sex for each cancer in England and Wales, 1971-2011: A population-based study. *Lancet* **385**, 1206–1218 (2015).
6. Ferlay, J. *et al.* Cancer statistics for the year 2020: An overview. *Int. J. Cancer* **149**, 778–789 (2021).
7. Caul, S. & Broggio, J. Cancer registration statistics, England - Office for National Statistics. *Census 2021* https://www.ons.gov.uk/peoplepopulationandcommunity/healthandsocialcare/conditionsanddiseases /bulletins/cancerregistrationstatisticsengland/2017 (2019).
8. Vineis, P. & Wild, C. P. Global cancer patterns: causes and prevention. *Lancet* **383**, 549–557 (2014).
9. Soerjomataram, I. & Bray, F. Planning for tomorrow: global cancer incidence and the role of prevention 2020–2070. *Nat. Rev. Clin. Oncol.* **18**, 663–672 (2021).
10. World Health Organization. List of Classifications – IARC Monographs on the Identification of Carcinogenic Hazards to Humans. https://monographs.iarc.who.int/list-of-classifications (2023).
11. Lunn, R. M. *et al.* Cancer Hazard Evaluations for Contemporary Needs: Highlights From New National Toxicology Program Evaluations and Methodological Advancements. *JNCI J. Natl. Cancer Inst.* **114**, 1441–1448 (2022).
12. Shahab, L., McGowan, J. A., Waller, J. & Smith, S. G. Prevalence of beliefs about actual and mythical causes of cancer and their association with socio-demographic and health-related characteristics: Findings from a cross-sectional survey in England. *Eur. J. Cancer* **103**, 308–316 (2018).
13. Karimi, M. R., Karimi, A. H., Abolmaali, S., Sadeghi, M. & Schmitz, U. Prospects and challenges of cancer systems medicine: from genes to disease networks. *Brief. Bioinform.* **23**, 1–31 (2022).
14. Comment, L. A. *et al.* Evidence-Based Development and Clinical Use of Precision Oncology Therapeutics. *Clin. Pharmacol. Ther.* **108**, 440–443 (2020).
15. Berner, A. M., Morrissey, G. J. & Murugaesu, N. Clinical Analysis of Whole Genome Sequencing in Cancer Patients. *Curr. Genet. Med. Rep.* **7**, 136–143 (2019).
16. Hanahan, D. & Weinberg, R. A. The Hallmarks of Cancer. *Cell* **100**, 57–70 (2000).
17. Hanahan, D. & Weinberg, R. A. Hallmarks of Cancer: The Next Generation. *Cell* **144**, 646–674 (2011).
18. Hanahan, D. Hallmarks of Cancer: New Dimensions. *Cancer Discov.* **12**, 31–46 (2022).
19. Fernald, K. & Kurokawa, M. Evading apoptosis in cancer. *Trends Cell Biol.* **23**, 620–633 (2013).
20. Monticciolo, D. L. *et al.* Breast Cancer Screening Recommendations Inclusive of All Women at Average Risk: Update from the ACR and Society of Breast Imaging. *J. Am. Coll. Radiol.* **18**, 1280–1288 (2021).
21. Yong, J. H. E. *et al.* The impact of episodic screening interruption: COVID-19 and population-based cancer screening in Canada. *J. Med. Screen.* **28**, 100–107 (2020).
22. Whitaker, K. Earlier diagnosis: the importance of cancer symptoms. *Lancet Oncol.* **21**, 6–8 (2020).
23. Menon, U. *et al.* Ovarian cancer population screening and mortality after long-term follow-up in the UK Collaborative Trial of Ovarian Cancer Screening (UKCTOCS): a randomised controlled trial. *Lancet* **397**, 2182–2193 (2021).
24. NICE. Ovarian cancer: recognition and initial management. *[Online]* https://www.nice.org.uk/guidance/cg122 (2011).
25. Cancer Research, U. K. Ovarian cancer statistics. *[Online]* https://www.cancerresearchuk.org/health-professional/cancer-statistics/statistics-by-cancer-type/ovarian-cancer#heading-Zero (2022).
26. Hirose, S. *et al.* Retrospective analysis of sites of recurrence in stage I epithelial ovarian cancer. *J. Gynecol. Oncol.* **29**, 1–11 (2018).
27. Al-Alem, L. & Curry, T. E. Ovarian cancer: involvement of the matrix metalloproteinases. *Reproduction* **150**, 55–64 (2015).

28. Lheureux, S., Gourley, C., Vergote, I. & Oza, A. M. Epithelial ovarian cancer. *Lancet* **393**, 1240–1253 (2019).
29. Rocconi, R. P. *et al.* Long-Term Follow-Up of Gemogenovatucel-T (Vigil) Survival and Molecular Signals of Immune Response in Recurrent Ovarian Cancer. *Vaccines* **9**, 894–910 (2021).
30. Desai, A. *et al.* Epithelial ovarian cancer: An overview. *World J. Transl. Med.* **3**, 1–8 (2014).
31. Torre, L. A. *et al.* Ovarian cancer statistics, 2018. *CA. Cancer J. Clin.* **68**, 284–296 (2018).
32. Falzone, L. *et al.* A multidisciplinary approach remains the best strategy to improve and strengthen the management of ovarian cancer (Review). *Int. J. Oncol.* **59**, 1–14 (2021).
33. Barclay, M. E., Abel, G. A., Greenberg, D. C., Rous, B. & Lyratzopoulos, G. Socio-demographic variation in stage at diagnosis of breast, bladder, colon, endometrial, lung, melanoma, prostate, rectal, renal and ovarian cancer in England and its population impact. *Br. J. Cancer* **124**, 1320–1329 (2021).
34. La Vecchia, C. Ovarian cancer: epidemiology and risk factors. *Eur. J. Cancer Prev.* **26**, 55–62 (2017).
35. Otsuka, I. Mechanisms of High-Grade Serous Carcinogenesis in the Fallopian Tube and Ovary: Current Hypotheses, Etiologic Factors, and Molecular Alterations. *Int. J. Mol. Sci.* **22**, 4409–4424 (2021).
36. Fathalla, M. F. Incessant Ovulation—A Factor In Ovarian Neoplasia? *Lancet* **298**, 163–163 (1971).
37. Ferris, J. S. *et al.* Oral contraceptive and reproductive risk factors for ovarian cancer within sisters in the breast cancer family registry. *Br. J. Cancer* **110**, 1074–1080 (2014).
38. Reid, B. M., Permuth, J. B. & Sellers, T. A. Epidemiology of ovarian cancer: a review. *Cancer Biol. Med.* **14**, 9–32 (2017).
39. Toss, A. *et al.* Hereditary Ovarian Cancer: Not Only BRCA 1 and 2 Genes. *Biomed Res. Int.* **2015**, 1–11 (2015).
40. National Institute for Health and Care Excellence. Ovarian cancer: recognition and initial management. *NICE guidelines* https://www.nice.org.uk/guidance/cg122/chapter/Recommendations (2023).
41. Rose, M., Burgess, J. T., O'Byrne, K., Richard, D. J. & Bolderson, E. PARP Inhibitors: Clinical Relevance, Mechanisms of Action and Tumor Resistance. *Front. Cell Dev. Biol.* **8**, 1–22 (2020).
42. Vergote, I. *et al.* Current perspectives on recommendations for BRCA genetic testing in ovarian cancer patients. *Eur. J. Cancer* **69**, 127–134 (2016).
43. Fox, E. *et al.* The sooner the better: Genetic testing following ovarian cancer diagnosis. *Gynecol. Oncol.* **137**, 423–429 (2015).
44. National Institute for Health and Care Excellence. Project information | Ovarian cancer: identifying and managing familial and genetic risk | Guidance | NICE. *NICE guidelines* https://www.nice.org.uk/guidance/indevelopment/gid-ng10225 (2023).
45. Koo, M. M. *et al.* Presenting symptoms of cancer and stage at diagnosis: evidence from a cross-sectional, population-based study. *Lancet Oncol.* **21**, 73–79 (2020).
46. Doubeni, C. A., Doubeni, A. R. & Myers, A. E. Diagnosis and Management of Ovarian Cancer. *Am. Fam. Physician* **93**, 937–944 (2016).
47. Stewart, C., Ralyea, C. & Lockwood, S. Ovarian Cancer: An Integrated Review. *Semin. Oncol. Nurs.* **35**, 151–156 (2019).
48. Hanahan, D. Rethinking the war on cancer. *Lancet* **383**, 558–563 (2014).
49. Dembo, A. J. Epithelial ovarian cancer: The role of radiotherapy. *Int. J. Radiat. Oncol.* **22**, 835–845 (1992).
50. Fields, E. C., McGuire, W. P., Lin, L. & Temkin, S. M. Radiation Treatment in Women with Ovarian Cancer: Past, Present, and Future. *Front. Oncol.* **7**, 1–17 (2017).
51. Iorio, G. C., Martini, S., Arcadipane, F., Ricardi, U. & Franco, P. The role of radiotherapy in epithelial ovarian cancer: a literature overview. *Med. Oncol.* **36**, 63–78 (2019).
52. Lei, T. *et al.* High-intensity focused ultrasound ablation in the treatment of recurrent ovary cancer and metastatic pelvic tumors: a feasibility study. *Int. J. Hyperth.* **38**, 282–287 (2021).
53. Bojalian, M. O., Machado, G. R., Swensen, R. & Reeves, M. E. Radiofrequency ablation of liver metastasis from ovarian adenocarcinoma: case report and literature review. *Gynecol. Oncol.* **93**, 557–560 (2004).
54. Gervais, D. A., Arellano, R. S. & Mueller, P. R. Percutaneous Radiofrequency Ablation of Nodal Metastases . *Cardiovasc. Intervent. Radiol.* **25**, 547–549 (2002).
55. Yuan, F. *et al.* Image-Guided Percutaneous Thermal Ablation of Oligometastatic Ovarian and Non-Ovarian Gynecologic Tumors. *J. Vasc. Interv. Radiol.* **32**, 729–738 (2021).
56. Zhuo, S. *et al.* Percutaneous microwave ablation versus surgical resection for ovarian cancer liver metastasis. *Int. J. Hyperth.* **37**, 28–36 (2020).
57. Yang, C. *et al.* Immunotherapy for Ovarian Cancer: Adjuvant, Combination, and Neoadjuvant. *Front.*

Immunol. **11**, 1–18 (2020).

58. Hamanishi, J. *et al.* Safety and Antitumor Activity of Anti–PD-1 Antibody, Nivolumab, in Patients With Platinum-Resistant Ovarian Cancer. *J. Clin. Oncol.* **33**, 4015–4022 (2015).

59. Hinchcliff, E. *et al.* Characteristics and outcomes of patients with recurrent ovarian cancer undergoing early phase immune checkpoint inhibitor clinical trials. *Gynecol. Oncol.* **151**, 407–413 (2018).

60. Wyld, L., Audisio, R. A. & Poston, G. J. The evolution of cancer surgery and future perspectives. *Nat. Rev. Clin. Oncol.* **12**, 115–124 (2015).

61. Sullivan, R. *et al.* Global cancer surgery: delivering safe, affordable, and timely cancer surgery. *Lancet Oncol.* **16**, 1193–1224 (2015).

62. Markopoulos, C. *et al.* Impact of Breast Cancer Surgery on the Self-Esteem and Sexual Life of Female Patients. *J. Int. Med. Res.* **37**, 182–188 (2009).

63. Cusimano, M. C. *et al.* Association of bilateral salpingo-oophorectomy with all cause and cause specific mortality: population based cohort study. *BMJ* **375**, 1–13 (2021).

64. Eleje, G. U. *et al.* Risk-reducing bilateral salpingo-oophorectomy in women with BRCA1 or BRCA2 mutations. *Cochrane Database Syst. Rev.* **8**, 1–70 (2018).

65. Lheureux, S., Gourley, C., Vergote, I. & Oza, A. M. Epithelial ovarian cancer. *Lancet* **393**, 1240–1253 (2019).

66. Canlorbe, G., Chabbert-Buffet, N. & Uzan, C. Fertility-Sparing Surgery for Ovarian Cancer. *J. Clin. Med.* **10**, 4235–4257 (2021).

67. Olver, I. *et al.* The timeliness of patients reporting the side effects of chemotherapy. *Support. Care Cancer* **26**, 3579–3586 (2018).

68. Qiao, J., Liu, Z. & Fu, Y.-X. Adapting conventional cancer treatment for immunotherapy. *J. Mol. Med.* **94**, 489–495 (2016).

69. Oun, R., Moussa, Y. E. & Wheate, N. J. The side effects of platinum-based chemotherapy drugs: a review for chemists. *Dalt. Trans.* **47**, 6645–6653 (2018).

70. Chiorcea-Paquim, A.-M. & Oliveira-Brett, A. M. Electrochemistry of chemotherapeutic alkylating agents and their interaction with DNA. *J. Pharm. Biomed. Anal.* **222**, 1–17 (2023).

71. Lehmann, F. & Wennerberg, J. Evolution of Nitrogen-Based Alkylating Anticancer Agents. *Processes* **9**, 377–387 (2021).

72. Lajous, H., Lelièvre, B., Vauléon, E., Lecomte, P. & Garcion, E. Rethinking Alkylating(-Like) Agents for Solid Tumor Management. *Trends Pharmacol. Sci.* **40**, 342–357 (2019).

73. More, G. S., Thomas, A. B., Chitlange, S. S., Nanda, R. K. & Gajbhiye, R. L. Nitrogen Mustards as Alkylating Agents: A Review on Chemistry, Mechanism of Action and Current USFDA Status of Drugs. *Anticancer. Agents Med. Chem.* **19**, 1080–1102 (2019).

74. Chen, Y., Jia, Y., Song, W. & Zhang, L. Therapeutic Potential of Nitrogen Mustard Based Hybrid Molecules. *Front. Pharmacol.* **9**, 1–12 (2018).

75. Singh, R. K., Kumar, S., Prasad, D. N. & Bhardwaj, T. R. Therapeutic journery of nitrogen mustard as alkylating anticancer agents: Historic to future perspectives. *Eur. J. Med. Chem.* **151**, 401–433 (2018).

76. Kenny, R. G. & Marmion, C. J. Toward Multi-Targeted Platinum and Ruthenium Drugs—A New Paradigm in Cancer Drug Treatment Regimens? *Chem. Rev.* **119**, 1058–1137 (2019).

77. Apps, M. G., Choi, E. H. Y. & Wheate, N. J. The state-of-play and future of platinum drugs. *Endocr. Relat. Cancer* **22**, 219–233 (2015).

78. Thiabaud, G. *et al.* Oxaliplatin Pt(IV) prodrugs conjugated to gadolinium-texaphyrin as potential antitumor agents. *Proc. Natl. Acad. Sci.* **117**, 7021–7029 (2020).

79. Galanski, M., Jakupec, M. A. & Keppler, B. K. Update of the Preclinical Situation of Anticancer Platinum Complexes: Novel Design Strategies and Innovative Analytical Approaches. *Curr. Med. Chem.* **12**, 2075–2094 (2005).

80. Linares, J. *et al.* Long-term platinum-based drug accumulation in cancer-associated fibroblasts promotes colorectal cancer progression and resistance to therapy. *Nat. Commun.* **14**, 746 (2023).

81. Tetko, I. V, Jaroszewicz, I., Platts, J. A. & Kuduk-Jaworska, J. Calculation of lipophilicity for Pt(II) complexes: Experimental comparison of several methods. *J. Inorg. Biochem.* **102**, 1424–1437 (2008).

82. Makovec, T. Cisplatin and beyond: molecular mechanisms of action and drug resistance development in cancer chemotherapy. *Radiol. Oncol.* **53**, 148–158 (2019).

83. Romani, A. M. P. Cisplatin in cancer treatment. *Biochem. Pharmacol.* **206**, 1–11 (2022).

84. Dabrowiak, J. C. *Metals in medicine, second edition*. *Metals in Medicine, Second Edition* (2017).

85. Arnesano, F., Losacco, M. & Natile, G. An Updated View of Cisplatin Transport. *Eur. J. Inorg. Chem.* **2013**, 2701–2711 (2013).

86. Rottenberg, S., Disler, C. & Perego, P. The rediscovery of platinum-based cancer therapy. *Nat. Rev. Cancer* **21**, 37–50 (2021).

87. Romero-Canelón, I., Salassa, L. & Sadler, P. J. The Contrasting Activity of Iodido versus Chlorido Ruthenium and Osmium Arene Azo- and Imino-pyridine Anticancer Complexes: Control of Cell Selectivity, Cross-Resistance, p53 Dependence, and Apoptosis Pathway. *J. Med. Chem.* **56**, 1291–1300 (2013).

88. Chen, H., Landen, C. N., Li, Y., Alvarez, R. D. & Tollefsbol, T. O. Enhancement of Cisplatin-Mediated Apoptosis in Ovarian Cancer Cells through Potentiating G2/M Arrest and p21 Upregulation by Combinatorial Epigallocatechin Gallate and Sulforaphane. *J. Oncol.* **2013**, 1–9 (2013).

89. Ghosh, S. Cisplatin: The first metal based anticancer drug. *Bioorg. Chem.* **88**, 1–20 (2019).

90. Blankenberg, F. G. & Norfray, J. F. Multimodality Molecular Imaging of Apoptosis in Oncology. *Am. J. Roentgenol.* **197**, 308–317 (2011).

91. Xu, G. & Shi, Y. Apoptosis signaling pathways and lymphocyte homeostasis. *Cell Res.* **17**, 759–771 (2007).

92. Ciancetta, A., Coletti, C., Marrone, A. & Re, N. Activation of carboplatin by carbonate: a theoretical investigation. *Dalt. Trans.* **41**, 12960–12969 (2012).

93. Kuduk-Jaworska, J., Jański, J. J. & Roszak, S. Comparative study of hydrolytic and electron-driven processes in carboplatin biotransformation. *J. Inorg. Biochem.* **170**, 148–159 (2017).

94. Zazuli, Z. *et al.* Genetic Variations and Cisplatin Nephrotoxicity: A Systematic Review. *Front. Pharmacol.* **9**, 1–17 (2018).

95. Rodieux, F., Wilbaux, M., van den Anker, J. N. & Pfister, M. Effect of Kidney Function on Drug Kinetics and Dosing in Neonates, Infants, and Children. *Clin. Pharmacokinet.* **54**, 1183–1204 (2015).

96. Sprowl, J. A. *et al.* Cisplatin-Induced Renal Injury Is Independently Mediated by OCT2 and p53. *Clin. Cancer Res.* **20**, 4026–4035 (2014).

97. Köberle, B., Tomicic, M. T., Usanova, S. & Kaina, B. Cisplatin resistance: Preclinical findings and clinical implications. *Biochim. Biophys. Acta - Rev. Cancer* **1806**, 172–182 (2010).

98. Damia, G. & Broggini, M. Platinum Resistance in Ovarian Cancer: Role of DNA Repair. *Cancers,* **11**, 119 (2019).

99. Johnstone, T. C., Suntharalingam, K. & Lippard, S. J. The Next Generation of Platinum Drugs: Targeted Pt(II) Agents, Nanoparticle Delivery, and Pt(IV) Prodrugs. *Chem. Rev.* **116**, 3436–3486 (2016).

100. Sigel, A., Sigel, H., Freisinger, E. & Sigel, R. K. O. *Metallo-Drugs: Development and Action of Anticancer Agents*. (De Gruyter, 2018).

101. Yamamoto, Y. *et al.* Effect of combined treatment with the epirubicin-incorporating micelles (NC-6300) and 1,2-diaminocyclohexane platinum (II)-incorporating micelles (NC-4016) on a human gastric cancer model. *Int. J. Cancer* **135**, 214–223 (2014).

102. Plummer, R. *et al.* A Phase I clinical study of cisplatin-incorporated polymeric micelles (NC-6004) in patients with solid tumours. *Br. J. Cancer* **104**, 593–598 (2011).

103. Mehrmohamadi, M., Jeong, S. H. & Locasale, J. W. Molecular features that predict the response to antimetabolite chemotherapies. *Cancer Metab.* **5**, 1–13 (2017).

104. Konstantinov, S. M. & Berger, M. R. *Antimetabolites BT - Encyclopedia of Molecular Pharmacology*. (Springer Berlin Heidelberg, 2008).

105. Parker, W. B. Enzymology of Purine and Pyrimidine Antimetabolites Used in the Treatment of Cancer. *Chem. Rev.* **109**, 2880–2893 (2009).

106. Longley, D. B., Harkin, D. P. & Johnston, P. G. 5-Fluorouracil: mechanisms of action and clinical strategies. *Nat. Rev. Cancer* **3**, 330–338 (2003).

107. Vodenkova, S. *et al.* 5-fluorouracil and other fluoropyrimidines in colorectal cancer: Past, present and future. *Pharmacol. Ther.* **206**, 1–19 (2020).

108. National Institute for Health and Care Excellence. Fluorouracil | Drugs | BNF | NICE. *BNF* https://bnf.nice.org.uk/drugs/fluorouracil/#side-effects (2013).

109. Lash, B. W. & Gilman, P. B. *Cancer Immunotherapy*. (Academic Press, 2013).

110. Thorn, C. F. *et al.* Doxorubicin pathways: pharmacodynamics and adverse effects. *Pharmacogenet. Genomics* **21**, 440–446 (2011).

111. Rawat, P. S., Jaiswal, A., Khurana, A., Bhatti, J. S. & Navik, U. Doxorubicin-induced cardiotoxicity: An update on the molecular mechanism and novel therapeutic strategies for effective management. *Biomed. Pharmacother.* **139**, 1–14 (2021).

112.	Meredith, A.-M. & Dass, C. R. Increasing role of the cancer chemotherapeutic doxorubicin in cellular metabolism. *J. Pharm. Pharmacol.* **68**, 729–741 (2016).

113.	Hainsworth, J. D. & Greco, F. A. Etoposide: Twenty years later. *Ann. Oncol.* **6**, 325–339 (1995).

114.	Montecucco, A., Zanetta, F. & Biamonti, G. Molecular mechanisms of etoposide. *EXCLI J.* **14**, 95–108 (2015).

115.	Godley, L. A. & Larson, R. A. Therapy-Related Myeloid Leukemia. *Semin. Oncol.* **35**, 418–429 (2008).

116.	Zhang, D. & Kanakkanthara, A. Beyond the Paclitaxel and Vinca Alkaloids: Next Generation of Plant-Derived Microtubule-Targeting Agents with Potential Anticancer Activity. *Cancers,* **12**, 1721–1745 (2020).

117.	Moudi, M., Go, R., Yien, C. Y. S. & Nazre, M. Vinca alkaloids. *Int. J. Prev. Med.* **4**, 1231–1235 (2013).

118.	Čermák, V. *et al.* Microtubule-targeting agents and their impact on cancer treatment. *Eur. J. Cell Biol.* **99**, 1–14 (2020).

119.	Mukhtar, E., Adhami, V. M. & Mukhtar, H. Targeting Microtubules by Natural Agents for Cancer Therapy. *Mol. Cancer Ther.* **13**, 275–284 (2014).

120.	Guastalla III, J. P. & Diéras, V. The taxanes: toxicity and quality of life considerations in advanced ovarian cancer. *Br. J. Cancer* **89**, 16–22 (2003).

121.	Tangutur, A. D., Kumar, D., Krishna, K. V. & Kantevari, S. Microtubule Targeting Agents as Cancer Chemotherapeutics: An Overview of Molecular Hybrids as Stabilizing and Destabilizing Agents. *Curr. Top. Med. Chem.* **17**, 2523–2537 (2017).

122.	Tomao, S. Albumin-bound formulation of paclitaxel (Abraxane ABI-007) in the treatment of breast cancer. *Int. J. Nanomedicine* **4**, 99–105 (2009).

123.	Padma, V. V. An overview of targeted cancer therapy. *BioMedicine* **5**, 1–6 (2015).

124.	Lee, Y. T., Tan, Y. J. & Oon, C. E. Molecular targeted therapy: Treating cancer with specificity. *Eur. J. Pharmacol.* **834**, 188–196 (2018).

125.	Araghi, M. *et al.* Recent advances in non-small cell lung cancer targeted therapy; an update review. *Cancer Cell Int.* **23**, 1–26 (2023).

126.	Baldo, B. A. & Pham, N. H. Adverse reactions to targeted and non-targeted chemotherapeutic drugs with emphasis on hypersensitivity responses and the invasive metastatic switch. *Cancer Metastasis Rev.* **32**, 723–761 (2013).

127.	Middleton, G. *et al.* The National Lung Matrix Trial of personalized therapy in lung cancer. *Nature* **583**, 807–812 (2020).

128.	Goutsouliak, K. *et al.* Towards personalized treatment for early stage HER2-positive breast cancer. *Nat. Rev. Clin. Oncol.* **17**, 233–250 (2020).

129.	Morand, S., Devanaboyina, M., Staats, H., Stanbery, L. & Nemunaitis, J. Ovarian Cancer Immunotherapy and Personalized Medicine. *Int. J. Mol. Sci.* **22**, 1–19 (2021).

130.	Smith, M. & Pothuri, B. Appropriate Selection of PARP Inhibitors in Ovarian Cancer. *Curr. Treat. Options Oncol.* **23**, 887–903 (2022).

131.	Grunewald, T. & Ledermann, J. A. Targeted Therapies for Ovarian Cancer. *Best Pract. Res. Clin. Obstet. Gynaecol.* **41**, 139–152 (2017).

132.	Huang, C. Y. *et al.* Comparing paclitaxel-"carboplatin with paclitaxel-"cisplatin as the front-line chemotherapy for patients with FIGO IIIC serous-type tubo-ovarian cancer. *Int. J. Environ. Res. Public Health* **17**, 1–23 (2020).

133.	Blagden, S. P. & Nicum, S. A source of hope for platinum-resistant ovarian cancer? *Lancet* **397**, 254–256 (2021).

134.	Kurnit, K. C., Fleming, G. F. & Lengyel, E. Updates and New Options in Advanced Epithelial Ovarian Cancer Treatment. *Obstet. Gynecol.* **137**, 108–121 (2021).

135.	National Institute for Health and Care Excellence. Topotecan, pegylated liposomal doxorubicin hydrochloride, paclitaxel, trabectedin and gemcitabine for treating recurrent ovarian cancer. *NICE Guidelines* https://www.nice.org.uk/guidance/ta389/chapter/1-Recommendations (2016).

136.	Sun, H. & Chai, Z.-F. Metallomics: An integrated science for metals in biology and medicine. *Annu. Reports Sect. 'A' (Inorganic Chem.* **106**, 20–38 (2010).

137.	Galván-Hidalgo, J. M., Ramírez-Apan, T., Nieto-Camacho, A., Hernández-Ortega, S. & Gómez, E. Schiff base Sn(IV) complexes as cytotoxic agents: Synthesis, structure, isosteric and bioisosteric replacement. *J. Organomet. Chem.* **848**, 332–343 (2017).

138.	Mjos, K. D. & Orvig, C. Metallodrugs in Medicinal Inorganic Chemistry. *Chem. Rev.* **114**, 4540–4563 (2014).

139.	Antman, K. H. Introduction: The History of Arsenic Trioxide in Cancer Therapy. *Oncologist* **6**, 1–2 (2001).

140.   Bauer, E. B., Haase, A. A., Reich, R. M., Crans, D. C. & Kühn, F. E. Organometallic and coordination rhenium compounds and their potential in cancer therapy. *Coord. Chem. Rev.* **393**, 79–117 (2019).

141.   Mijatović, S. *et al.* Study of the anticancer properties of methyl- and phenyl-substituted carbon- and silicon-bridged ansa-titanocene complexes. *J. Organomet. Chem.* **751**, 361–367 (2014).

142.   Coverdale, J. P. C. *et al.* Asymmetric transfer hydrogenation by synthetic catalysts in cancer cells. *Nat. Chem.* **10**, 347–354 (2018).

143.   Fu, Y. *et al.* Structure–activity relationships for organometallic osmium arene phenylazopyridine complexes with potent anticancer activity. *Dalt. Trans.* **40**, 10553–10562 (2011).

144.   Liu, Z. *et al.* Contrasting Reactivity and Cancer Cell Cytotoxicity of Isoelectronic Organometallic Iridium(III) Complexes. *Inorg. Chem.* **50**, 5777–5783 (2011).

145.   Leijen, S. *et al.* Phase I/II study with ruthenium compound NAMI-A and gemcitabine in patients with non-small cell lung cancer after first line therapy. *Invest. New Drugs* **33**, 201–214 (2015).

146.   Guichard, S. M. *et al.* Anti-tumour activity in non-small cell lung cancer models and toxicity profiles for novel ruthenium(II) based organo-metallic compounds. *Biochem. Pharmacol.* **71**, 408–415 (2006).

147.   Hartinger, C. G. *et al.* KP1019, A New Redox-Active Anticancer Agent – Preclinical Development and Results of a Clinical Phase I Study in Tumor Patients. *Chem. Biodivers.* **5**, 2140–2155 (2008).

148.   Heffeter, P. *et al.* Intracellular protein binding patterns of the anticancer ruthenium drugs KP1019 and KP1339. *JBIC J. Biol. Inorg. Chem.* **15**, 737–748 (2010).

149.   Dömötör, O. *et al.* Characterization of the binding sites of the anticancer ruthenium(III) complexes KP1019 and KP1339 on human serum albumin via competition studies. *JBIC J. Biol. Inorg. Chem.* **18**, 9–17 (2013).

150.   Shen, Y. *et al.* Transferrin receptor 1 in cancer: a new sight for cancer therapy. *Am. J. Cancer Res.* **8**, 916–931 (2018).

151.   Kapitza, S. *et al.* Heterocyclic complexes of ruthenium(III) induce apoptosis in colorectal carcinoma cells. *J. Cancer Res. Clin. Oncol.* **131**, 101–110 (2005).

152.   Hartinger, C. G. *et al.* From bench to bedside – preclinical and early clinical development of the anticancer agent indazolium trans-[tetrachlorobis(1H-indazole)ruthenate(III)] (KP1019 or FFC14A). *J. Inorg. Biochem.* **100**, 891–904 (2006).

153.   Zhang, C. *et al.* Stimuli-responsive platinum and ruthenium complexes for lung cancer therapy. *Front. Pharmacol.* **13**, 1–21 (2022).

154.   Trondl, R. *et al.* NKP-1339, the first ruthenium-based anticancer drug on the edge to clinical application. *Chem. Sci.* **5**, 2925–2932 (2014).

155.   Frühauf, S. & Zeller, W. J. New platinum, titanium, and ruthenium complexes with different patterns of DNA damage in rat ovarian tumor cells. *Cancer Res.* **51**, 2943–2948 (1991).

156.   Depenbrock, H. *et al.* Preclinical activity of trans-indazolium [tetrachlorobisindazoleruthenate(III)] (NSC 666158; IndCR; KP 1019) against tumour colony-forming units and haematopoietic progenitor cells. *Eur. J. Cancer* **33**, 2404–2410 (1997).

157.   Keppler, B. K. *et al. New Ruthenium Complexes for the Treatment of Cancer*. (Springer Berlin Heidelberg, 1989).

158.   Lentz, F. *et al.* Pharmacokinetics of a novel anticancer ruthenium complex (KP1019, FFC14A) in a phase I dose-escalation study. *Anticancer. Drugs* **20**, 97–103 (2009).

159.   Alessio, E. & Messori, L. NAMI-A and KP1019/1339, two iconic ruthenium anticancer drug candidates face-to-face: A case story in medicinal inorganic chemistry. *Molecules* **24**, 1–20 (2019).

160.   Groessl, M. *et al.* Structure–Activity Relationships for NAMI-A-type Complexes (HL)[trans-RuCl4L(S-dmso)ruthenate(III)] (L = Imidazole, Indazole, 1,2,4-Triazole, 4-Amino-1,2,4-triazole, and 1-Methyl-1,2,4-triazole): Aquation, Redox Properties, Protein Binding, and Antiproli. *J. Med. Chem.* **50**, 2185–2193 (2007).

161.   Messori, L., Orioli, P., Vullo, D., Alessio, E. & Iengo, E. A spectroscopic study of the reaction of NAMI, a novel ruthenium(III)anti-neoplastic complex, with bovine serum albumin. *Eur. J. Biochem.* **267**, 1206–1213 (2000).

162.   Sava, G. *et al.* Influence of chemical stability on the activity of the antimetastasis ruthenium compound NAMI-A. *Eur. J. Cancer* **38**, 427–435 (2002).

163.   Pelillo, C. *et al.* Inhibition of adhesion, migration and of α5β1 integrin in the HCT-116 colorectal cancer cells treated with the ruthenium drug NAMI-A. *J. Inorg. Biochem.* **160**, 225–235 (2016).

164.   Khoshnoodi, J., Pedchenko, V. & Hudson, B. G. Mammalian collagen IV. *Microsc. Res. Tech.* **71**, 357–370

(2008).

165. Sava, G. *et al.* Dual Action of NAMI-A in inhibition of solid tumor metastasis: selective targeting of metastatic cells and binding to collagen. *Clin. Cancer Res.* **9**, 1898–905 (2003).

166. Sanna, B. *et al.* The anti-metastatic agent imidazolium trans-imidazoledimethylsulfoxide-tetrachlororuthenate induces endothelial cell apoptosis by inhibiting the mitogen-activated protein kinase/extracellular signal-regulated kinase signaling pathway. *Arch. Biochem. Biophys.* **403**, 209–218 (2002).

167. Pillozzi, S. *et al.* NAMI-A is highly cytotoxic toward leukaemia cell lines: evidence of inhibition of KCa 3.1 channels. *Dalt. Trans.* **43**, 12150–12155 (2014).

168. Rademaker-Lakhai, J. M., Van Den Bongard, D., Pluim, D., Beijnen, J. H. & Schellens, J. H. M. A phase I and pharmacological study with imidazolium-trans-DMSO-imidazole-tetrachlororuthenate, a novel ruthenium anticancer agent. *Clin. Cancer Res.* **10**, 3717–3727 (2004).

169. Murray, B. S., Babak, M. V, Hartinger, C. G. & Dyson, P. J. The development of RAPTA compounds for the treatment of tumors. *Coord. Chem. Rev.* **306**, 86–114 (2016).

170. Rausch, M., Dyson, P. J., Nowak-Sliwinska, P. & Nowak-Sliwinska, P. Recent Considerations in the Application of RAPTA-C for Cancer Treatment and Perspectives for Its Combination with Immunotherapies. *Adv. Ther.* **2**, 1–12 (2019).

171. Scolaro, C. *et al.* Tuning the hydrophobicity of ruthenium(ii)–arene (RAPTA) drugs to modify uptake, biomolecular interactions and efficacy. *Dalt. Trans.* **43**, 5065–5072 (2007).

172. Nowak-Sliwinska, P. *et al.* Organometallic Ruthenium(II) Arene Compounds with Antiangiogenic Activity. *J. Med. Chem.* **54**, 3895–3902 (2011).

173. Weiss, A. *et al.* In vivo anti-tumor activity of the organometallic ruthenium(ii)-arene complex [Ru(η 6 - p -cymene)Cl 2 (pta)] (RAPTA-C) in human ovarian and colorectal carcinomas. *Chem. Sci.* **5**, 4742–4748 (2014).

174. Scolaro, C. *et al.* In vitro and in vivo evaluation of ruthenium(II)-arene PTA complexes. *J. Med. Chem.* **48**, 4161–4171 (2005).

175. Chatterjee, S., Kundu, S., Bhattacharyya, A., Hartinger, C. G. & Dyson, P. J. The ruthenium(II)–arene compound RAPTA-C induces apoptosis in EAC cells through mitochondrial and p53–JNK pathways. *JBIC J. Biol. Inorg. Chem.* **13**, 1149–1155 (2008).

176. Berndsen, R. H. *et al.* Combination of ruthenium(II)-arene complex [Ru(η6-p-cymene)Cl2 (pta)] (RAPTA-C) and the epidermal growth factor receptor inhibitor erlotinib results in efficient angiostatic and antitumor activity. *Sci. Rep.* **7**, 1–16 (2017).

177. Artner, C., Holtkamp, H. U., Hartinger, C. G. & Meier-Menches, S. M. Characterizing activation mechanisms and binding preferences of ruthenium metallo-prodrugs by a competitive binding assay. *J. Inorg. Biochem.* **177**, 322–327 (2017).

178. Chatterjee, S., Kundu, S., Bhattacharyya, A., Hartinger, C. G. & Dyson, P. J. The ruthenium(II)–arene compound RAPTA-C induces apoptosis in EAC cells through mitochondrial and p53–JNK pathways. *J. Biol. Inorg. Chem.* **13**, 1149–1155 (2008).

179. Frausto da Silva, J. J. R. The chelate effect redefined. *J. Chem. Educ.* **60**, 390–392 (1983).

180. Breslow, R., Belvedere, S., Gershell, L. & Leung, D. The chelate effect in binding, catalysis, and chemotherapy. **72**, 333–342 (2000).

181. Guichard, S. M. *et al.* Anti-tumour activity in non-small cell lung cancer models and toxicity profiles for novel ruthenium(II) based organo-metallic compounds. *Biochem. Pharmacol.* **71**, 408–415 (2006).

182. Aird, R. E. *et al.* In vitro and in vivo activity and cross resistance profiles of novel ruthenium (II) organometallic arene complexes in human ovarian cancer. *Br. J. Cancer* **86**, 1652–1657 (2002).

183. Bergamo, A. *et al.* In vivo tumour and metastasis reduction and in vitro effects on invasion assays of the ruthenium RM175 and osmium AFAP51 organometallics in the mammary cancer model. *J. Inorg. Biochem.* **104**, 79–86 (2010).

184. Bergamo, A., Gaiddon, C., Schellens, J. H. M. M., Beijnen, J. H. & Sava, G. Approaching tumour therapy beyond platinum drugs: Status of the art and perspectives of ruthenium drug candidates. *J. Inorg. Biochem.* **106**, 90–99 (2012).

185. Chen, H. *et al.* Organometallic ruthenium(II) diamine anticancer complexes: Arene-nucleobase stacking and stereospecific hydrogen-bonding in guanine adducts. *J. Am. Chem. Soc.* **124**, 3064–3082 (2002).

186. Novakova, O. *et al.* DNA Interactions of Monofunctional Organometallic Ruthenium(II) Antitumor Complexes in Cell-free Media. *Biochemistry* **42**, 11544–11554 (2003).

187. Brabec, V. & Kasparkova, J. Ruthenium coordination compounds of biological and biomedical significance. DNA binding agents. *Coord. Chem. Rev.* **376**, 75–94 (2018).

188. Chen, H., Parkinson, J. A., Morris, R. E. & Sadler, P. J. Highly Selective Binding of Organometallic Ruthenium Ethylenediamine Complexes to Nucleic Acids: Novel Recognition Mechanisms. *J. Am. Chem. Soc.* **125**, 173–186 (2003).

189. Hayward, R. L. *et al.* Investigation of the role of Bax, p21/Waf1 and p53 as determinants of cellular responses in HCT116 colorectal cancer cells exposed to the novel cytotoxic ruthenium(II) organometallic agent, RM175. *Cancer Chemother. Pharmacol.* **55**, 577–583 (2005).

190. Kostrhunova, H. *et al.* DNA Interactions of Monofunctional Organometallic Osmium(II) Antitumor Complexes in Cell-Free Media. *J. Med. Chem.* **51**, 3635–3643 (2008).

191. Wootton, C. A. *et al.* Binding of an organo–osmium(ii) anticancer complex to guanine and cytosine on DNA revealed by electron-based dissociations in high resolution Top–Down FT-ICR mass spectrometry. *Dalt. Trans.* **44**, 3624–3632 (2015).

192. Novakova, O. *et al.* Conformation of DNA Modified by Monofunctional Ru(II) Arene Complexes: Recognition by DNA Binding Proteins and Repair. Relationship to Cytotoxicity. *Chem. Biol.* **12**, 121–129 (2005).

193. Morris, R. E. *et al.* Inhibition of Cancer Cell Growth by Ruthenium(II) Arene Complexes. *J. Med. Chem.* **44**, 3616–3621 (2001).

194. Gatti, A. *et al.* Half-Sandwich Arene Ruthenium(II) and Osmium(II) Thiosemicarbazone Complexes: Solution Behavior and Antiproliferative Activity. *Organometallics* **37**, 891–899 (2018).

195. Peacock, A. F. A. *et al.* Tuning the Reactivity of Osmium(II) and Ruthenium(II) Arene Complexes under Physiological Conditions. *J. Am. Chem. Soc.* **128**, 1739–1748 (2006).

196. Fu, Y. Organometallic Osmium Arene Anticancer Complexes. (University of Warwick, 2011).

197. Dougan, S. J., Habtemariam, A., McHale, S. E., Parsons, S. & Sadler, P. J. Catalytic organometallic anticancer complexes. *Proc. Natl. Acad. Sci.* **105**, 11628–11633 (2008).

198. Fu, Y. *et al.* Organometallic osmium arene complexes with potent cancer cell cytotoxicity. *J. Med. Chem.* **53**, 8192–8196 (2010).

199. Fu, Y. *et al.* The contrasting chemical reactivity of potent isoelectronic iminopyridine and azopyridine osmium(ii) arene anticancer complexes. *Chem. Sci.* **3**, 2485–2494 (2012).

200. Romero-Canelón, I., Pizarro, A. M., Habtemariam, A. & Sadler, P. J. Contrasting cellular uptake pathways for chlorido and iodido iminopyridine ruthenium arene anticancer complexes. *Metallomics* **4**, 1271–1279 (2012).

201. Hearn, J. M. *et al.* Potent organo-osmium compound shifts metabolism in epithelial ovarian cancer cells. *Proc. Natl. Acad. Sci.* **112**, 3800–3805 (2015).

202. Kumar, S. A. *et al.* Dose- and time-dependent tolerability and efficacy of organo-osmium complex FY26 and its tissue pharmacokinetics in hepatocarcinoma-bearing mice. *Metallomics* **13**, 1–11 (2021).

203. Romero-Canelón, I., Mos, M. & Sadler, P. J. Enhancement of Selectivity of an Organometallic Anticancer Agent by Redox Modulation. *J. Med. Chem.* **58**, 7874–7880 (2015).

204. Ballesta, A. *et al.* Kinetic analysis of the accumulation of a half-sandwich organo-osmium pro-drug in cancer cells. *Metallomics* **11**, 1648–1656 (2019).

205. Gottschaldt, M. *et al.* Sugar-Selective Enrichment of a D-Glucose-Substituted Ruthenium Bipyridyl Complex Inside HepG2 Cancer Cells. *ChemBioChem* **11**, 649–652 (2010).

206. Kacsir, I. *et al.* Ruthenium Half-Sandwich Type Complexes with Bidentate Monosaccharide Ligands Show Antineoplastic Activity in Ovarian Cancer Cell Models through Reactive Oxygen Species Production. *Int. J. Mol. Sci.* **22**, 1–38 (2021).

207. Vessières, A. *et al.* A ferrocenyl derivative of hydroxytamoxifen elicits an estrogen receptor-independent mechanism of action in breast cancer cell lines. *J. Inorg. Biochem.* **104**, 503–511 (2010).

208. Lee, H. Z. S. *et al.* Synthesis, Characterization, and Biological Properties of Osmium-Based Tamoxifen Derivatives – Comparison with Their Homologues in the Iron and Ruthenium Series. *Eur. J. Inorg. Chem.* **2015**, 4217–4226 (2015).

209. Gasser, G. & Metzler-Nolte, N. The potential of organometallic complexes in medicinal chemistry. *Curr. Opin. Chem. Biol.* **16**, 84–91 (2012).

210. Ude, Z. *et al.* A novel dual-functioning ruthenium(II)-arene complex of an anti-microbial ciprofloxacin derivative - Anti-proliferative and anti-microbial activity. *J. Inorg. Biochem.* **160**, 210–217 (2016).

211. Ali, G. *et al.* Input of isosteric and bioisosteric approach in drug design. *J. Chem. Soc. Pakistan* **36**, 150–

169 (2014).

212. Brown, N. Bioisosteres and Scaffold Hopping in Medicinal Chemistry. *Mol. Inform.* **33**, 458–462 (2014).
213. Patani, G. A. & LaVoie, E. J. Bioisosterism: A Rational Approach in Drug Design. *Chem. Rev.* **96**, 3147–3176 (1996).
214. Dick, A. & Cocklin, S. Bioisosteric Replacement as a Tool in Anti-HIV Drug Design. *Pharmaceuticals* **13**, 1–16 (2020).
215. Oladipupo, A. Toxin to medicine and bioisosterism in drug development: a study of the discovery and development of ACE inhibitors from snake venom. *Maced. Pharm. Bull.* **66**, 15–33 (2020).

Chapter 2 - General Experimental Methodology

General Chemical And Biological Methodology

Used Across Multiple Chapters

2-1: Materials

For chemical synthesis and analysis, all materials and solvents were purchased from commercial sources including Thermo Fisher Scientific and Sigma-Aldrich and used without further modification or purification unless otherwise specified.

For tissue culture maintenance, all media, supplements including foetal bovine serum (FBS), penicillin/streptomycin (Pen/Strep) solution, Non-Essential Amino Acid (NEAA) solution, glutamine and maintenance consumables including Phosphate Buffered Saline (PBS) and Trypsin/EDTA were all purchased from commercial sources including Gibco, Lonza and Sigma Aldrich.

Table 2-1: List of fluorescent stains and dyes used in this work, their excitation and emission wavelengths required for detection, and their preperation details.

Stain	Excitation (Ex), Emission (Em)	Preparation
DAPI (4',6-Diamidino-2-phenylindole)	Ex: 345 nm, Em: 455 nm	From solid, prepared as a 1 mg/mL solution in DMSO
Rh123 (Rhodamine 123)	Ex: 507 nm, Em: 529 nm	From solid, prepared as a 1 mg/mL solution in DMSO
DCFDA (DiChlorodihydroFluorescein DiAcetate)	Ex: 504 nm, Em: 540 nm	From solid, prepared as a 1 mg/mL solution in DMSO
Biotracker 490 green membrane dye	Ex: 484 nm, Em: 501 nm	Purchaced ready to use
JC1 (5,5',6,6'-Tetrachloro-1,1',3,3'-tetraethylbenzimidazolylcarbocyanine iodide)	Monomer - Ex: 510 nm, Em: 527 nm Dimer - Ex: 585 nm, Em: 590 nm	Purchaced ready to use
PI (Propidium Iodide)	Ex: 530 nm, Em: 618 nm	From solid, prepared as a 1 mg/mL solution in sterile type I water
Cell Brite Red membrane	Ex: 644 nm, Em: 665 nm	Purchaced ready to use
Gamma-H2A.X (Ser139) Monoclonal Antibody (CR55T33)	Ex: 482 nm, Em: 708 nm	Purchaced ready to use

Chemicals, comparator controls, and experimental consumables including test kits were obtained from similar commercial sources. Fluorescent stains used in this work include 4',6-Diamidino-2-phenylindole (DAPI), Rhodamine 123 (Rh123), DiChlorodihydroFluorescein DiAcetate (DCFDA), Propidium Iodide (PI), 5,5',6,6'-Tetrachloro-1,1',3,3'-tetraethylbenzimidazolylcarbocyanine iodide (JC1), biotracker 490 green membrane dye, Cell Brite red membrane dye, and gamma-H2A.X (Ser139) monoclonal antibody (CR55T33). Table 1-1 contains details of stock preparations and excitation and emission wavelengths of each stain.

2-2: Instrumentation

2-2.1: Nuclear Magnetic Resonance

All NMR were conducted using a Bruker 400 MHz NMR spectrometer with a 5 mm ^{1}H-^{13}C DUL probe and an Oxford Instruments 9.39 T magnet. Experimentation was carried out at room temperature. All experiments were internally referenced to DMSO-d$_6$ at 2.5 ppm. ^{1}H spectra were ran with a scale up to 20 ppm and ^{13}C spectra with a scale up to 200 ppm. For each imine ligand, a ^{1}H, ^{13}C and a Heteronuclear Single Quantum Coherence (HSQC) experiment was done. For each complex a ^{1}H, ^{13}C, H-^{1}H COrrelated SpectroscopY (COSY), HSQC and Heteronuclear Multiple Bond Correlation (HMBC) experiment was done. Spectra were processed using Bruker TopSpin 4.4.1 (Bruker UK ltd).

For the ligands synthesised, NMR experimentation was used to confirm the formation of the imine bond. For the complexes synthesised, NMR spectra were used to fully elucidate the structure of the proposed complexes.

2-2.2: Electrospray ionisation mass spectroscopy

Low resolution positive electrospray ionisation mass spectroscopy (ESI-MS) analysis was done on both the imine ligands and the ruthenium complexes using a Waters Xevo G2-XS analyser with samples dissolved in acetonitrile:water or acetonitrile alone prepared, analysed, and reported out by the Analytical Facility (Chemistry) at the University of Birmingham. Experimentation was run with a range up to 2500 m/z.

2-2.3: Elemental analysis

Elemental analysis samples were prepared, analysed, and reported by the Analytical Facility (Chemistry) at the University of Birmingham on the CE Instruments EA1110 elemental analyser.

2-2.4: High performance liquid chromatography

Reverse-phase high performance liquid chromatography (HPLC) was done using the Agilent Technologies 1260 Infinity II (Agilent). Purity determination was assessed using the details in Table 2-2 with peak integration at 254 nm corresponding to percentage purity.

Table 2-2: HPLC specifications used for complex purity determination.

Specification	Protocol Information
Column	Discovery C18, 15 cm X 4.6 mm dimensions, 5 µm particle size
Eluents	A: 0.1% (v/v) trifluoracetic acid in water B: 0.1% (v/v) trifluoracetic acid in acetonitrile
Flow Rate	1.0 mL/min
Injection volume	50 µL
Run time	35 minutes total
Detector	Diode Array Detector (DAD) Detection wavelengths: 210 nm and 254 nm Reference wavelength: 360 nm
Sample preparation	Complexes at 100 µM in 2.7% (v/v) DMSO in water
Mobile phase gradient	0 minutes ➔ A: 90%, B: 10% 30 minutes ➔ A: 20%, B:80% 35 minutes ➔ A: 90%, B: 10%

2-2.5: UV-Vis spectroscopy

Spectra for assay optimisation were collected on a Shimadzu UV-2600 UV-Vis spectrometer, using 1 cm light window, spectra measuring between 200-900 nm at room temperature and analysed using UV Probe (version 2.42) software (Shimadzu).

2-2.6: Colorimetric absorbance, fluorescence intensity and UV-Vis spectroscopy analysis of 96-well plates

All colorimetric absorbance, UV-Vis spectroscopy and fluorescence measurements taken in a 96-well plate format were done using a BMG Labtech Omega plate reader with Omega (v. 3.00 R2) and Mars

(v. 2.41 build 12) software (BMG Labtech). Absorbance wavelength is specified per protocol. Fluorescence intensity measured at Ex 330 nm Em 520 nm for blue probes, and Ex 485 nm Em 520 nm for green probes. All UV-Vis wavelength were collected between 200 – 900 nm. Processing of the data was then conducted using Microsoft Excel.

2-2.7: Fluorescence microscopy

All fluorescence microscopy was done on the EVOS XL Core Imaging System (Invitrogen) with magnifications varying between 2X and 40X. Images were collected and formatted in Microsoft PowerPoint. Stains and channels used in this work are shown in Table 2-1 and Table 2-3.

Table 2-3: EVOS XL Core Imaging System channels used in this study including channel name, colour, excitation (Ex) and emission (Em) wavelengths boundaries achieved with each channel, and the cellular stains and dyes used with each channel.

Filter	Wavelength	Stain
DAPI (blue)	Ex: 357/44 nm, Em: 447/60 nm	DAPI
GFP (green)	Ex: 482/25 nm, Em: 524/24 nm	Rh123 DCFDA Biotracker 490 green membrane dye
Texas Red (red)	Ex: 585/29 nm, Em: 628/32 nm	PI Cell Brite Red membrane
CY5 (dark red)	Ex: 628/40 nm, Em: 692/40 nm	Gamma-H2A.X (Ser139) Monoclonal Antibody (CR55T33)

2-2.8: Flow cytometry

Flow cytometry experiments were conducted on a Beckman Coulter CytoFLEX S using CytExpert software at the Technology Hub Flow Cytometry core facility at the University of Birmingham. Laser and filter information provided in Table 2-4. Subsequent data analysis was then preformed using FloJo 10.8.1 (FlowJo LLC.) and Microsoft Excel.

Table 2-4: Beckman Coulter CytoFLEX S lasers filters used in this study including filter name, colour, excitation, and emission wavelengths boundaries achieved with each laser and filter, and the cellular stains and dyes used with each filter.

Laser	Filter	Stain
Blue (488 nm)	FITC (525/40 nm)	Annexin V JC1 – monomerised
Yellow (561 nm)	PC5.5 (690/50 nm)	PI Gamma-H2A.X (Ser139) Monoclonal Antibody (CR55T33)
Red (638 nm)	PE DsRed (585/42 nm)	JC1 – polymerised

2-3: Statistical testing

All statistical testing in this work was preformed using a Welch's t-test comparing drug treated populations against the corresponding negative control unless stated otherwise. Significance levels are given as * for p<0.05, ** for p<0.01, and *** for p<0.001.

2-4: Ligand and complex synthesis

A structure guide of the complexes and ligands is provided in Appendix I. Synthesis of the ligands generally used the reaction shown in Scheme 2-1. Briefly, equimolar equivalents of an aniline derivative and 2-pyridinecarboxaldehyde were mixed in 5 mL of acetonitrile overnight under stirring. From this, the acetonitrile was removed by rotary evaporation and the crude product collected. This reaction is a nucleophilic addition of the amine to the aldehyde, eliminating water, to produce the iminium ion, which is then deprotonated to produce the final imine product. Specifics regarding individual ligand synthesis is detailed in Appendix II.
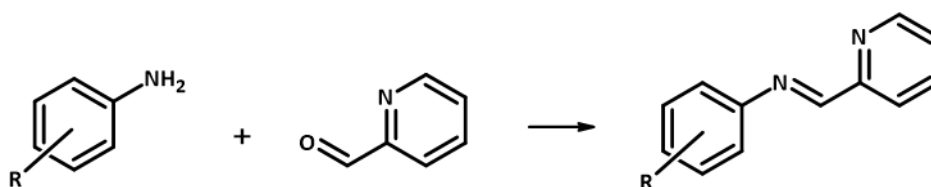
Scheme 2-1: Generalised reaction scheme for the synthesis of the bidentate iminopyridine ligands. Where the addition to the different amine derivatives to 2-pyridinecarboxaldehyde results in the formation of the ligand through nucleophilic addition.

Using the crude ligands produced following physiochemical characterisation, the complexes were synthesised using the reaction shown in Scheme 2-2. Briefly, 1:2 equimolar concentrations of the ruthenium dimer and crude ligand were mixed in 5 mL methanol and stirred overnight. To this, ammonium hexafluorophosphate in excess was added and the reaction was left to stir again overnight. The reaction mixture was then vacuum filtered and recrystalised using appropriate solvents including diethyl ether or water producing a pure solid product. This reaction is a chelation reaction of the ligand to the ruthenium centres of the dimer, replacing two monodentate chlorine groups with the bidentate ligand driven by the chelate effect. This is followed by the anion replacement of Cl^- by PF_6^-, which allows for the precipitation of the complexes by forced molecular ordering. Specifics regarding individual complex synthesis are detailed in their respective chapters.
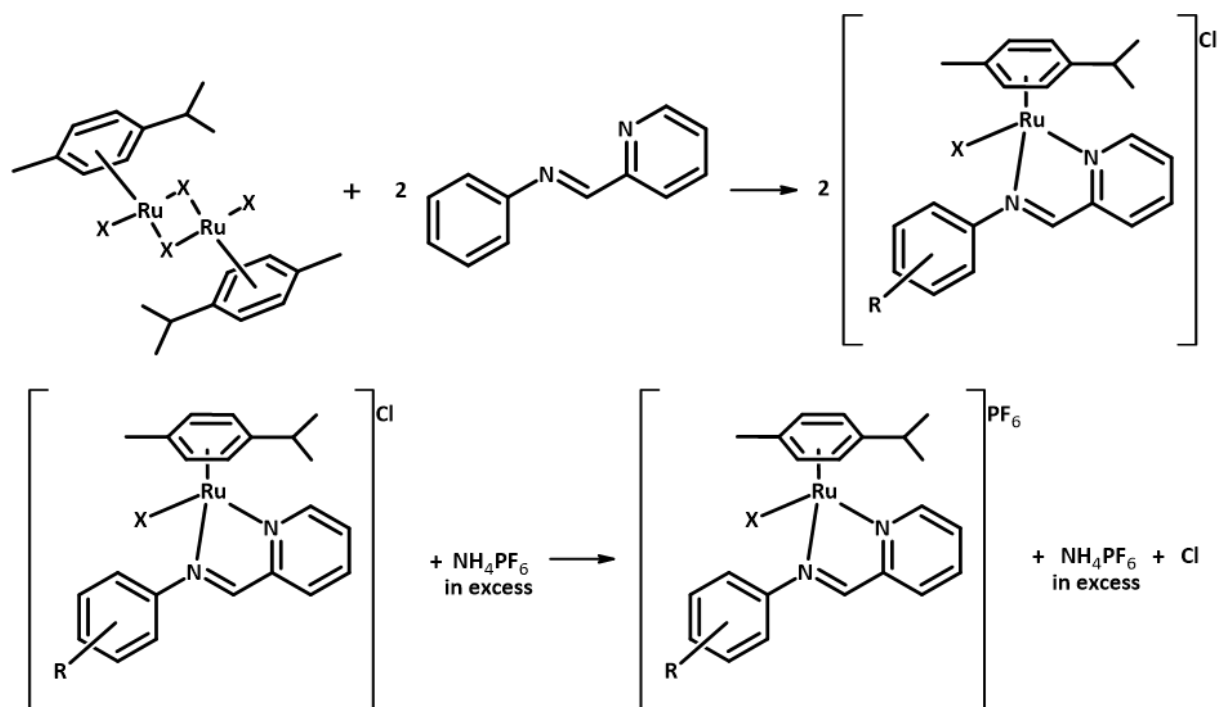
Scheme 2-2: Generalised reaction scheme for the synthesis of the complexes used in this study. The bidentate ligands are combined with the p-cymene ruthenium dimers in a chelation reaction, resulting in the formation of the complexes with a chlorine counter ion. The addition of ammonium hexafluorophosphate to this allows the precipitation of a solid complex which can be recrystallized for further analysis/biological studies.

2-5: Physiochemical characterisation

2-5.1: LogD at pH 7.4

To determine the lipophilicity of the compounds synthesised here and due to the ionisable nature of several of the compounds, $LogD_{7.4}$ was determined at physiologically relevant pH via the 'shake-flask' method and UV-Vis spectroscopy.

A solution of n-Octanol saturated with PBS (O-PBS) and a solution of PBS saturated with n-Octanol (PBS-O) were made by mixing 72 mL of both in a flask for 4 days until a saturated equilibrium was reached, then the aqueous PBS-O layer and the organic O-PBS layers were separated. 1.0 mg of each complex was dissolved in 1.5 mL of PBS-O to saturate the PBS-O solution with complex, any residual complex was filtered out using a 0.2 µm syringe filter. 500 µL of drug saturated PBS-O solution was mixed with 500 µL O-PBS and shaken for 24 hours. Following this, the aqueous PBS-O layer was removed. Both the aqueous layer before shaking with O-PBS and the aqueous layer after shaking with O-PBS were tested. 100 µL of sample was aliquoted per well in a 96 well plate allowing for triplicate testing. UV-Vis spectra were collected from 220 to 900 nm, and the data was processed in Microsoft Excel. Negative controls were both the PBS-O before shaking and post shaking without any complex. From the spectra data, Equation 2-1a and b were used to determine the ratio of complex in the organic and aqueous layers and the $LogD_{7.4}$ for each complex.

Equation 2-1: Equations used to calculate $LogD_{7.4}$ in this work. a). for the calculation of the concentration of complex in the organic layer and b). for the calculation of the $LogD_{7.4}$.

$$a). \, [Complex]_{organic} = [Complex]_{in \, PBS} - [Complex]_{aqueous}$$

$$b). \, LogD_{7.4} \, = Log\left(\frac{[Complex]_{organic}}{[Complex]_{aqueous}}\right)$$

2-5.2: Analytical stability in biologically relevant matrixes

Optimisation of analytical conditions for stability studies including the concentrations of the complexes and human plasma (Sigma) were conducted on the Shimadzu UV-2600 UV-Vis spectrometer with dilutions done in PBS. ctDNA purity was determined by 260/280 before each experiment with a minimum ratio of 1.8 to ensure samples were protein free. Final concentrations of ctDNA used was 0.5 mg/mL in 5% methanol in PBS and plasma was diluted 1:500 in PBS. Complex concentrations were chosen to be proportional to the absorption of ctDNA and plasma at 0.50-1.00 Abs., rounded to 100, 150 or 200 µM diluted in PBS. Final experimentation was done with a total volume of 200 µL with a matrix concentration of with 100, 150 or 200 µM, to be in a 1:1 ratio with the complex being tested in PBS with <5% (v/v) DMSO. Matrixes tested include 1:1 water to PBS, PBS, GSH, Bovine Serum Albumin (BSA), RPMI-1640, full RPMI-1640, PBS, 5% (v/v) NEAA in PBS, ctDNA and human plasma. Interaction of the complexes with water was done with the complexes in 5% (v/v) DMSO in water at 200 µM of complex. Interaction with DMSO was done with the complexes in 100% DMSO at 200 µM of complex.

Data was collected in a 96 well plate format with six replicates for each matrix. UV-Vis spectra was collected from 220 to 900 nm at 0 hour and 24 hours. The data was processed in Microsoft Excel to determine if any isosbestic points are present. Water was used as negative control for each matrix, with a minimum of eight replicates.

2-5.3: Density Functional Theory of the ruthenium complexes

DFT geometry optimisations were done by Dr James Coverdale. Optimizations were carried out in the gas phase using Gaussian 09 using previously reported crystallographic data on Ru(II) p-cymene azopyridine complex CCDC 616620 as a starting input, with structural modifications made using GaussView 16 (Gaussian 16, Wallingford CT, 2016)[1]. Calculations were carried out using the hybrid Perdew-Burke-Ernzerhof functional with the Lanl2DZ (effective core potential for Ru) and 6-31+G** (all other atoms) basis sets[2–5]. True energy minima were confirmed by the lack of imaginary values in

vibrational mode calculations. From these calculations, required data was extrapolated including bond

lengths, electron density and substituent rotations.

2-6: Cellular studies for cytotoxicity and mode of action

2-6.1: Cell maintenance

Cell lines used in this work are A2780, A549, UFH001, MIAPaCa, PEA1, PEA2, SKOV3, HCT116 p53+/+, HCT116 p53-/- and MRC5, details of which are in Table 2-5. A2780, A549, UFH001, PEA1, PEA2, SKOV3, HCT116 p53+/+, HCT116 p53-/- and MRC5 were purchased from the European Collection of Authenticated Cell Cultures (ECACC) or American Type Culture Collection (ATCC). MIAPaCa were kindly provided by Dr Marium Rana from the Institute of Biosciences at the University of Birmingham. Cells were maintained as adherent monolayers in their respective media at 37.5°C at 5% CO_2 humidified atmosphere. Cells were passaged at 70-90% confluence twice a week. All media variations were supplemented with 10% (v/v) FBS and 1% (v/v) 10,000 unit/mL penicillin/streptomycin solution. Additional supplements were added to media for UFH001 and MIAPaCa as detailed in Table 2-5.

Table 2-5: Cell lines used in this work detailing the cell type, media base and any supplementation to the media.

Cell line	Cell type	Media	Media Supplementation
A2780	Ovarian adenocarcinoma	RPMI-1640	10% FBS, 1% Pen/Strep
SKOV3	Ovarian adenocarcinoma	RPMI-1640	10% FBS, 1% Pen/Strep
PEA1	Ovarian adenocarcinoma	RPMI-1640	10% FBS, 1% Pen/Strep
PEA2	Ovarian adenocarcinoma	RPMI-1640	10% FBS, 1% Pen/Strep
A549	Lung alveolar type II adenocarcinoma	RPMI-1640	10% FBS, 1% Pen/Strep
HCT116 p53+/+	Colorectal carcinoma, known *p53* positive	RPMI-1640	10% FBS, 1% Pen/Strep
HCT116 p53-/-	Colorectal carcinoma, known *p53* negative	RPMI-1640	10% FBS, 1% Pen/Strep
UFH001	Triple negative CAIX+ breast	DMEM (High glucose, without pyruvate)	10% FBS, 1% Pen/Strep, 1% NEAA, 0.14 mM sodium pyruvate
MIAPaCa	Adherent pancreatic carcinoma	DMEM (High glucose, without pyruvate)	10% FBS, 1% Pen/Strep and 1% NEAA
MRC5	Adherent foetal lung fibroblast	DMEM (High glucose, with pyruvate)	10% FBS, 1% Pen/Strep

2-6.2: In vitro antiproliferative activity of complexes

Antiproliferative activity for all complexes was determined using the MTT assay.

96 well plates were seeded with 5×10^3 cells in 200 μL of media and incubated for 48 hours. The media was then removed, and the plates treated with either fresh media as a negative control, CDDP or complex concentrations ranging between 0.01 and 200 μM. Other comparator treatments including PTX ranges were used with appropriate six-point concentration dilutions. All drug concentrations were diluted from a freshly prepared DMSO-media stock with a final DMSO concentration <2.5% (v/v). Cells were exposed to treatment for 24 hours, after which treatment was replaced with fresh media and allowed 72 hours recovery. Following recovery, MTT assay was done by adding 50 μL of 1 mg/mL MTT

solution in PBS and incubated for 4 hours at 37.5°C. The MTT/media solution was then removed, and the formazan crystals formed were dissolved by addition of 100 μL of propanol to each well and shaken on a slow rolling belly dancer until fully dissolved. Formazan formation was measured via absorbance at 570 nm. Experiment was done with duplicate of triplicate repeats. From this IC_{50} values were calculated for each complex using Sigma plot 14.5 (Systat software inc., 2020).

2-6.3: Fluorescence microscopy for mitochondrial polarisation, membrane integrity, nuclear morphology and ROS generation

Fluorescence microscopy for ΔΨm polarisation, CCM integrity, nuclear morphology and ROS generation were conducted by seeding 24 well plates with $3X10^4$ SKOV3 or $4X10^4$ A2780 cells in 24 well plates and incubated for 24 hours. Following incubation, cells were treated with 500 μL of equipotent treatment concentrations for 24 hours in triplicate. ROS generation had additional positive controls of 1 mM hydrogen peroxide or 0.7 mM Luperox for two hours. Following treatment, cells were washed with PBS and stained for 45 minutes with 480 μL of 1% (v/v) 4',6-diamidino-2-phenylindole (DAPI), 1% (v/v) Propidium Iodide (PI) and 1% (v/v) Rhodamine123 (Rh123) in media for nuclear morphology, CCM integrity and ΔΨm depolarisation or 480 μL of 1% (v/v) 4',6-diamidino-2-phenylindole (DAPI), 1% (v/v) Propidium Iodide (PI) and 1% (v/v) dichlorodihydrofluorescein diacetate (DCFDA) in media for ROS generation. Following staining cells were washed a minimum of three times with PBS and imaged on the EVOS XL Core Imaging System (Invitrogen).

2-6.4: Fluorescence intensity for mitochondrial depolarisation and ROS generation

Fluorescence intensity for ΔΨm polarisation and ROS generation were conducted by seeding black bottom 96 well plates with $1X10^4$ SKOV3 or A2780 and incubated for 24 hours. Following incubation, cells were treated with 200 μL of equipotent treatment concentrations for 24 hours with a minimum

of six replicates. ROS generation had additional positive controls of 1 mM hydrogen peroxide or 0.7 mM Luperox for two hours. Following treatment, cells were washed with PBS and stained for 45 minutes with 200 µL of (v/v) Rh123 in media for ΔΨm depolarisation or 200 µL 1% (v/v) DCFDA in media for ROS generation. Following staining cells were washed with PBS and green fluorescence intensity measured. Crystal violet protein content was then determined by staining cells with 50 µL of 1 mg/mL crystal violet in 80% methanol for 30 minutes at 4°C. The plate was then washed with water, the crystal violet dissolved in 200 µL 10% (v/v) acetic acid in propanol per well, 100 µL was transferred to a clear 96 well plate and absorbance measured at 590 nm. Fluorescence intensity was normalised by crystal violet protein content and analysed in Microsoft Excel.

2-6.5: Wound healing assay

SKOV3 cells were seeded in 12 well plates with 8×10^4 cells and incubated for 48 hours. The monolayer was then wounded with a 5 mL pipette tip with 1 wound per well and cells drugged with 1 mL of equipotent treatment in quadruplicate. A2780 cells were seeded in 24 well plates with 6×10^4 cells per well and incubated for 24 hours. Cells were then wounded with a 1000 µL tip with 2 wounds per well and drugged with 500 µL of treatment in triplicate. Following 24 hours exposure, cells were washed, media replaced with full media and incubated for a further 72 hours. Following recovery time, cells were stained with 1 mg/mL crystal violet in 80% (v/v) methanol in PBS for 30 minutes. Following staining cells were washed with water.

Images of the wounds were taken on the EVOS at t=0 when monolayer was wounded, t=24 following 24 hours of treatment exposure and t=24+72 following 72 hours of recovery time. Wound widths were measured using the measure feature in Fiji and analysed in Microsoft Excel[6].

2-6.6: Colony formation assay

Protocol was adapted from Franken *et al* for colony formation immediately following treatment[7]. A 6 well plate was seeded with $5X10^4$ cells and incubated for 48 hours. Cells were then drugged equipotently with 2 mL of treatment and exposed for 24 hours. Following treatment, supernatant was removed, cells were washed with PBS and trypsinised to form a single cell suspension (SCS). The SCS was counted and diluted accordingly to single cell dilutions (SCD) to seed 500 cells per 2 mL in a 6 well plate with each treatment in triplicate for SKOV3 or sextuplicate for A2780. Cells were then incubated for 7 days after which the colonies were stained and fixed with 1 mL of 1 mg/mL crystal violet in 80% (v/v) methanol in PBS. Colonies were imaged at 1X magnification and on the EVOS XL Core Imaging System at 4X to determine number of colonies and colony density respectively using Fiji[6].

2-6.7: Cell cycle arrest

In a 6 well plates, $6.5X10^5$ SKOV3 or $1X10^6$ A2780 cells were seeded and incubated for 24 hours. Cells were drugged with 2 mL of treatment in triplicate and in addition to staurosporine (STS) at 1 μM in SKOV3 or 0.1 μM in A2780 as a positive control. Cells were exposed for 24 hours after which the drug media was removed and discarded. The cells were washed with PBS and trypsinised with 0.5 mL then quenched with 1mL of media, and this resulting SCS was transferred into 5 mL tubes and centrifuged for 5 minutes at 1000 RPM. The supernatant was removed and discarded, and the pellet was resuspended in 1 mL of cold 80% (v/v) methanol in PBS and the cells were allowed to fix on ice for 1 hour. Following fixation, the SCS was centrifuged for 5 minutes at 1000 RPM, and the supernatant removed. The pellet was washed in PBS and centrifuged again, with the supernatant being discarded. 480 μL of stain was then added per sample consisting of 10% (v/v) PI and 15% (v/v) RNase in PBS and allowed to stain at room temperature for 30 minutes in the dark. Once stained, the samples were centrifuged for 5 minutes at 1000 RPM, the supernatant was removed, and the pellet washed once in PBS before being suspended in suspended in 500 μL of PBS. These samples were then analysed by flow

cytometry. Subsequent analysis was then preformed using the cell cycle analysis feature in FloJo 10.8.1 (FlowJo LLC.).

2-6.8: Apoptosis assay

In a 6 well plates, $6.5X10^5$ SKOV3 or $1X10^6$ A2780 cells were seeded and incubated for 24 hours. Cells were drugged with 2 mL of treatment in triplicate, in addition, STS at 1 µM in SKOV3 or 0. 1 µM in A2780 was used as a positive control, with three additional STS treated samples as compensation controls. Cells were exposed for 24 hours after which the media was transferred into a 15 mL Falcon tube. The adherent cells were washed with PBS and trypsinised with 0.5 mL then quenched with 1mL of media, and this resulting SCS and all previous washes were added to the removed supernatant centrifuged for 5 minutes at 1000 RPM. The supernatant was removed and discarded, and the pellet was resuspended in 480 µL of Annexin V binding buffer with 1% (v/v) PI and 1% (v/v) Annexin V-FITC in addition to single channel staining for compensation purposes. Cells were stained at room temperature for 45 minutes in the dark. Samples were then centrifuged for 5 minutes at 1000 RPM, the supernatant was removed, and the pellet suspended in 500 µL of PBS. These samples were then analysed by flow cytometry.

2-6.9: Protein content by Bradford assay

Protein standard was made up to 2 mg/mL and serially diluted to 1.4, 1, 0.75, 0.5, 0.25 mg/mL with lysis buffer used as a 0 mg/mL value for the protein concentration standard curve. Cell lysate collection is detailed in respective chapters and lysates were diluted in PBS if required to fall in analytical range of the assay. The Bradford assay was ran in a 96 well plate format using 5 µL of diluted sample in 250 µL of Bradford solution per well. Each sample was ran in triplicate. After mixing, the plate was shaken for 5 minutes and incubated for 30 minutes. Absorbance was measured at 595 nm, from which data was exported to excel where protein concentration was calculated from the linear standard curve.

2-6.10: Caspase 3/7 activity

Caspase 3/7 activity was preformed using the Amplite caspase 3/7 activity kit (cat. no. 13507, AAT Bioquest) per manufacturer's instructions from step 3 due to cell lysate being collected previously (lysate collection detailed in respective chapters). Absorbance was exported to excel and normalised by protein content determined by Bradford assay to determine Caspase 3/7 activity.

2-6.11: Cellular membrane morphology

Fluorescence microscopy was conducted by seeding 24 well plates with $3X10^4$ SKOV3 or $4X10^4$ A2780 cells and incubated for 24 hours. Cells were drugged equipotently for 24 hours in triplicate. Following treatment exposure, cells were washed with PBS and stained with 500 μL of 1% (v/v) DAPI and 1% (v/v) Cell Brite Red membrane dye in 80% (v/v) methanol in PBS for 30 minutes at 37°C, following which cells were washed with PBS and imaged at 40X magnification on the EVOS XL Core Imaging System.

2-6.12: Spheroid assay

A2780 cells were seeded at $5X10^3$ cells in 250 μL per well in round bottom, repellent surface 96 well plates and incubated for 5 days until spheroids were developed. Following spheroid development, cells were drugged equipotently with eight replicates per treatment, then incubated for 24 hours exposure. Following exposure, cells were fixed with 2% (v/v) formaldehyde and imaged on the EVOS FL imaging system at 2X magnification. Spheroid area was measured using FUJI and data analysed in Microsoft Excel[6].

2-6.13: Inductively Coupled Plasma-Mass Spectroscopy

Cells were seeded at $4X10^6$ cells per p100 dishes and incubated for 24 hours. Following which cells were treated equipotently in triplicate. For total metal accumulation and metal distribution, cells were exposed for 24 hours at 37°C. After exposure cells were washed with PBS, trypsinised and quenched with media to a 7 mL SCS. This SCS was counted, and cells per 1 mL was noted for biological

normalisation. 6 mL of SCS was taken and centrifuged at 1000 RPM for 5 minutes, the supernatant was removed, the pellet was washed in 1 mL of PBS and centrifuged again. The supernatant was removed and frozen at -20°C until digestion.

All samples were digested using nitric acid. Firstly, after samples were defrosted, they were centrifuged at 13400 RPM for 2 minutes, to which 200 μL of 72% (v/v) ultrapure nitric acid was added. The samples were then heated to 60°C overnight. Samples were then allowed to cool, and the entire samples were transferred to a new fully labelled 15 mL falcon tube of 3.8 mL with ultrapure type I water.

Inductively Coupled Plasma Mass Spectrometry (ICP-MS) was performed by Dr James P. C. Coverdale at the University of Warwick on the Agilent 7900 series ICP-MS with data collected and analysed using MassHunter 4.4 (Version C.01.04, build 544.8). Briefly the analyser was calibrated using certified reference standards of ^{101}Ru and ^{195}Pt (1000 ppm) at concentrations of 0, 0.1, 0.25, 0.5, 1, 2.5, 5, 10, 25, 50, 100, 250, 500, 1000 ppb with an internal calibration to ^{166}Er. Samples were then run in no gas mode and results collected in ppb. From this metal content was normalised by cell count with metal content expressed as femtograms per cells. For fractional results, samples were normalised by total uptake and expressed as a percentage with raw values as fmol/cell given in Appendix III.

2-7: References

1. Dougan, S. J., Melchart, M., Habtemariam, A., Parsons, S. & Sadler, P. J. Phenylazo-pyridine and Phenylazo-pyrazole Chlorido Ruthenium(II) Arene Complexes: Arene Loss, Aquation, and Cancer Cell Cytotoxicity. *Inorg. Chem.* **45**, 10882–10894 (2006).
2. Adamo, C. & Barone, V. Toward reliable density functional methods without adjustable parameters: The PBE0 model. *J. Chem. Phys.* **110**, 6158–6170 (1999).
3. Millett, A. J., Habtemariam, A., Romero-Canelón, I., Clarkson, G. J. & Sadler, P. J. Contrasting Anticancer Activity of Half-Sandwich Iridium(III) Complexes Bearing Functionally Diverse 2-Phenylpyridine Ligands. *Organometallics* **34**, 2683–2694 (2015).
4. Wadt, W. R. & Hay, P. J. Ab initio effective core potentials for molecular calculations. Potentials for main group elements Na to Bi. *J. Chem. Phys.* **82**, 284–298 (1985).
5. McLean, A. D. & Chandler, G. S. Contracted Gaussian basis sets for molecular calculations. I. Second row atoms, Z=11–18. *J. Chem. Phys.* **72**, 5639–5648 (1980).
6. Schindelin, J. *et al.* Fiji: an open-source platform for biological-image analysis. *Nat. Methods* **9**, 676–682 (2012).
7. Franken, N. A. P., Rodermond, H. M., Stap, J., Haveman, J. & van Bree, C. Clonogenic assay of cells in vitro. *Nat. Protoc.* **1**, 2315–2319 (2006).

Chapter 3 - Methyl Bioisosteres

Mode Of Action And Mechanisms Of Cell Death

Induced By Methyl Group Bioisosteric

Replacements In The Iminopyridine Ligand Of

Ruthenium Piano-Stool Complexes

3-1: Introduction

3-1.1: Mechanisms of cell death

Cellular death is the irreversible stopping of biochemical processes in response to age, disease, exogenous substances, or injury, and is the end point of all cells[1]. Cytotoxic treatments specifically induce cell death through a diverse range of MOA targeting a variety of pathways. These MOA then converge into specific mechanisms of cell death (MOD) shown in Figure 3-1[1].

There are three main groups of cell death[1,2]. Type I – apoptotic-like death which has canonical features of cytoplasmic shrinkage, chromatin condensation, nuclear fragmentation, and CCM blebbing into the formation of smaller apoptotic bodies[1]. These features come from internal signals such as DNA or mitochondrial damage which leads to the activation of Caspase 9 to initiate intrinsic apoptosis or external signals through death receptors to FADD or TRADD to Caspase 8 to initiate extrinsic apoptosis[3]. Caspase 9 or 8 then can go on to cleave the effector pro-Caspase 3 through the DEVD motif, activating it, which goes onto cleave other proteins such as ICAD and ROCK1 which induce chromatin condensation and fragmentation, cell shrinkage and actinomycin contraction, leading to cell contraction outward blebbing formation apoptotic bodies to be endocytosed by leukocytes and other local cells[4].

The second group is type II - Non-apoptotic-like death that has features of cytoplasmic vacuolization followed by lysosomal degradation or phagocytosis. Induction and mechanisms are far more varied than type I with a diverse selection of mechanisms involving origins in vacuoles, mitochondria, detoxification system failures or immune responses[5]. However, type II is mainly based on intercellular system/signalling damage and failure, causing death without canonical apoptotic systems being involved. This is seen by autophagy which can be on a macro, micro or mitochondrial only scale where cells sequester damaged proteins and organelles into lysosomes for protein recycling when there is

damage or starvation[3]. From this, if damage is too extensive, mass recycling is initiated, leading to cellular recycling and blebbing which can be phagocytosed by the immune system or endocytosed by surrounding cells for materials. However other types of controlled cell death are included which share features with type III cell death such as necroptosis where after imitation of intrinsic apoptosis there is inhibition of Caspase 8 activation leading to RIPK3 activation and MLKL phosphorylation and oligomerisation, causing the formation of pores in the CCM and death[6].
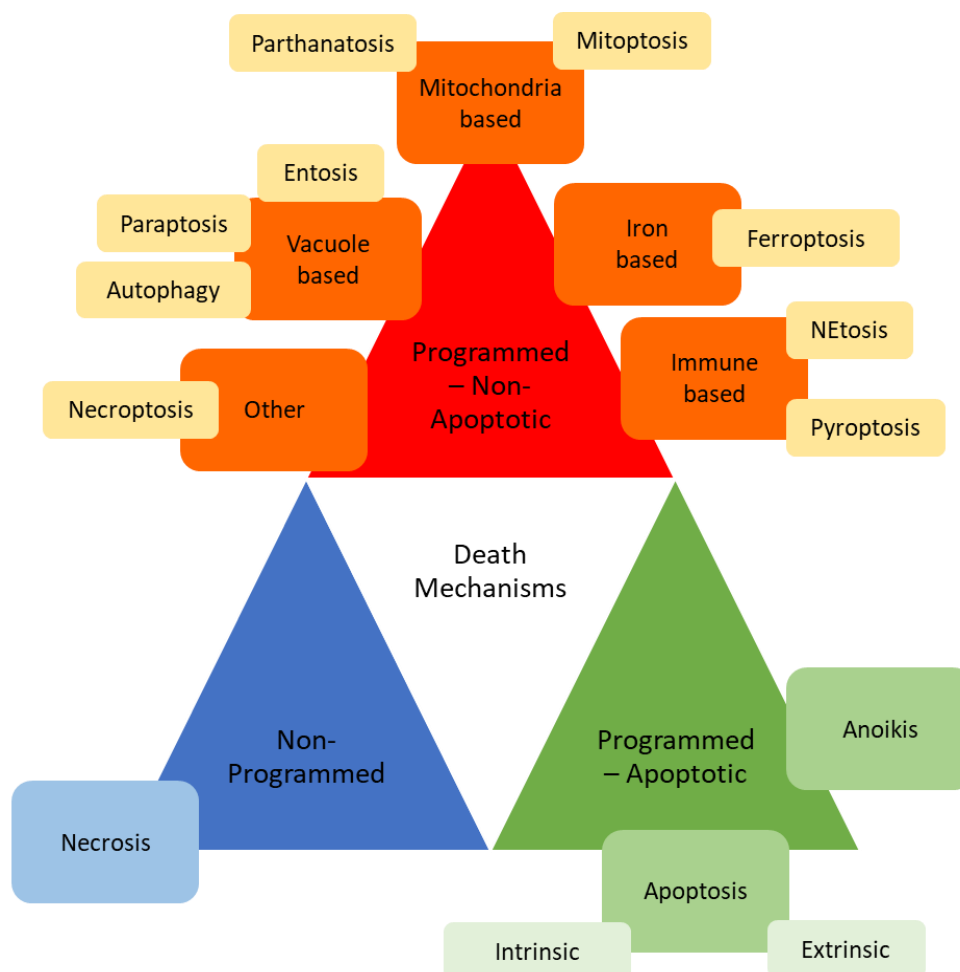
Figure 3-1: The main three categorises of death mechanisms used by cells; programmed apoptotic, programmed non-apoptotic, and non-programmed cell death, in addition to further subsequent types within each category[1]. Despite these main groupings, some mechanisms of cell death do have overlapping mechanistic features between these main groups.

Type III death is unique as it only encompasses uncontrolled death and is often sudden, so very little signalling is involved. Necrosis is initiated by external damage such as physical injury, heat, hypoxia

and xenobiotics, however necrosis has also been documented to be induced by extremely low levels of ATP[5,7]. Therefore, necrosis is often instantaneous, meaning rather than being a process of death, it is the end point state of the cell, characterised by cellular swelling, karyolyis, karyorrhexis, CCM leakage and inflammation signalling[8].

Cytotoxic treatments aim for type I and type II MOD as they are well understood, controlled, regulated forms of death to prevent further damage to the surrounding area and upregulation of inflammation response. However, this is a double-edged tactic due to cancer cells often being intrinsically resistant to apoptosis as a recognised hallmark of cancer[9,10]. This is a recognised flaw in the design of chemotherapy, and new treatment design is moving focus to other or multiple mechanisms of death to evade innate apoptosis resistance.

3-1.2: Mechanisms of cell death by organometallic complexes

Ruthenium co-ordination complexes can activate a range of MOA. For example, RM175 is documented to intercalate with DNA, induce $\Delta\Psi$m depolarisation, and generate ROS in addition to several other mechanisms to induce apoptosis[11]. These mechanisms go on to cause apoptosis in a p53 and BAX dependant manner[12]. RAPTA-C and other derivative complexes can also induce apoptosis through oxidative stress and the inhibition of JNK pathways[13]. To mitigate issues around apoptosis targeting and intrinsic inhibition contradiction, treatments can be designed to use a variety of MOA leading to a different or multifrontal MOD such as those shown in Figure 3-2. IrFN (Figure 3-2a) initiates ferroptotic death through mitochondrial localisation, proteomic alterations, increased expression of HMO1X resulting in the generation of ROS, lipid peroxidation and death which is inhibited with the co-treatment of the ferroptosis inhibitor ferrostatin (Fer-1)[14]. RuSora (Figure 3-2b) possesses a dual MOD by utilising apoptosis and ferroptosis shown by the presentation of phospholipid phosphatidylserine external CCM during apoptosis, but also the increase of ROS, GSH depletion, decreased GPX4 expression and lipid peroxidation which was prevented with Fer-1[15]. Other MOD include autophagy as

induced by Λ-WHO402 (Figure 3-2c), evident by the increase of Belcin-1 expression, conversion of LC3-I to LC3-II and decreased NAF-1 expression, decreased Bcl-2-Belcin-1 binding preventing Belcin-1 deactivation and an increase of autophagosomes and autolysosomes[16]. ToThyRu (Figure 3-2d), a nucleolytic derivative from the ineffective AziRu, also can initiate a dual MOD by exhibiting intrinsic apoptosis by the increase of Caspase 9, Caspase 3, Bax and decrease of Bcl-2 for apoptosis, but also autophagy by the increase of autolysosomes seen in late-stage autophagy[17].
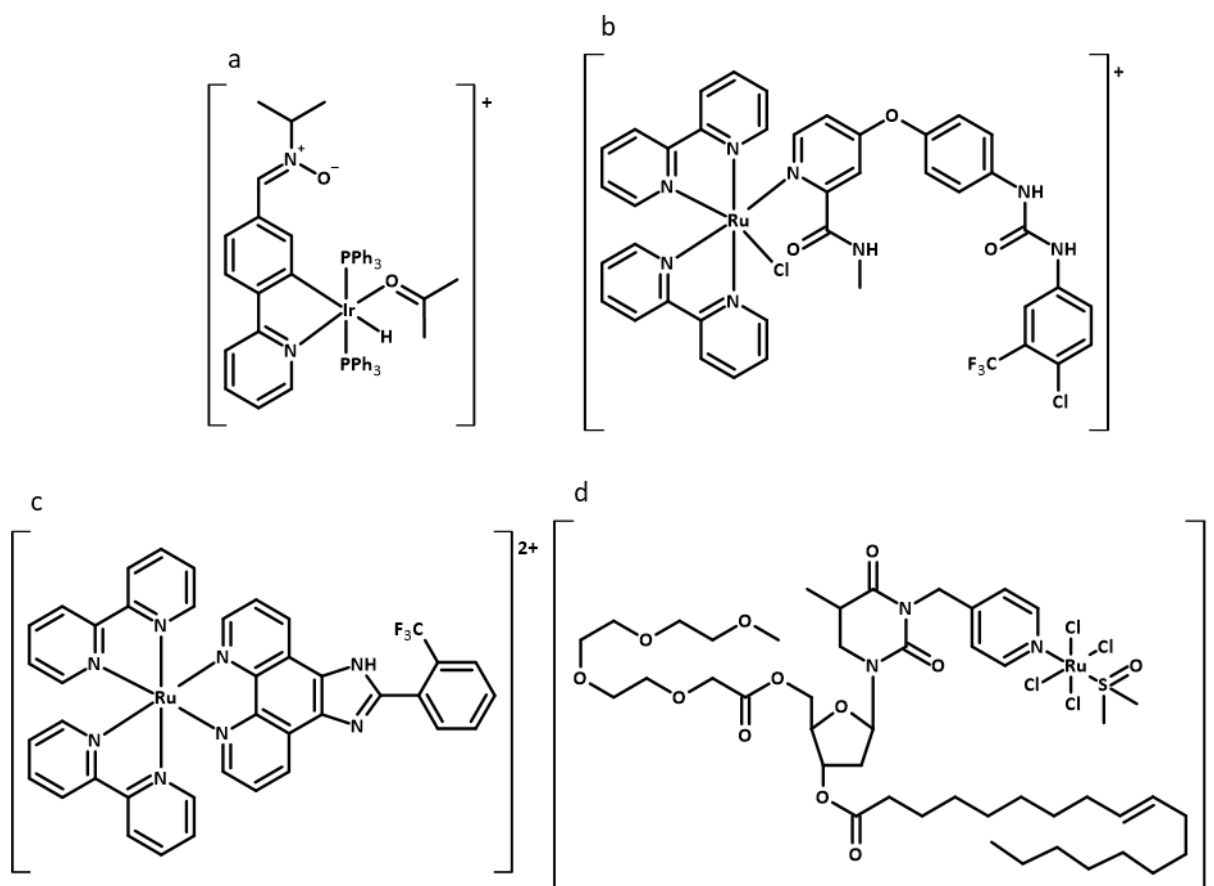
Figure 3-2: Examples of organometallic complexes which used alternative mechanisms to apoptosis to induce cell death. a). IrFN, b). RuSora, c). by Λ-WHO402, d). ToThyRu.

Yet, not all co-ordination complexes that are effective against cancer induce cell death. Several ruthenium complexes have cytostatic MOA, where the treatment arrests cell growth and proliferation without killing the cell, such as those shown in Figure 3-3. [(η6-*p*-cymene)Ru(2-hydroxyisoquinoline-3-(2H)-thionato)Cl] inhibits growth with potencies comparable to CDDP, however MOA testing

demonstrated no specific mechanisms bar G_1 arrest in conjunction with inhibition of wound healing and reduction of colony formation[18]. In cells treated with RAPTA complexes such as RAPTA-C, cytotoxicity has been documented to vary in apoptotic/cytostatic being concentration dependant due to having high IC_{50} concentrations, no cell cycle arrest and not showing apoptosis through western plot assays at lower concentrations, however DNA interaction forming DNA bridges has been documented along with significant reduction in tumour size and metastasis formation in *in vivo* models[11,19,20]. Helicate complexes such as VR54 and $[Ru(dppz)_2(21p\text{-}HPIP)]^{2+}$ have also been documented to be cytostatic due to not inducing apoptosis, subsequent Caspase 3 activity or other MOD like necrosis, however, G_1 arrest is induced by both complexes[21,22]. Cytostatic treatments often benefit from being more effective at lower doses than the maximal dosages leading to less side effects as seen by RAPTA-C, but also benefit patients to be able to undergo progression-free survival where a curative treatment may not be an option[20,23]. Cytostatic agents can also lead to a more vulnerable state in cancer cells and the availability to give lower doses of treatments and improved responses to cytotoxic therapies as seen by $[Ru(dppz)_2(p\text{-}HPIP)]^{2+}$ when co-treated with the CHK1 inhibitor CHIR-124 at nanomolar concentrations[21].
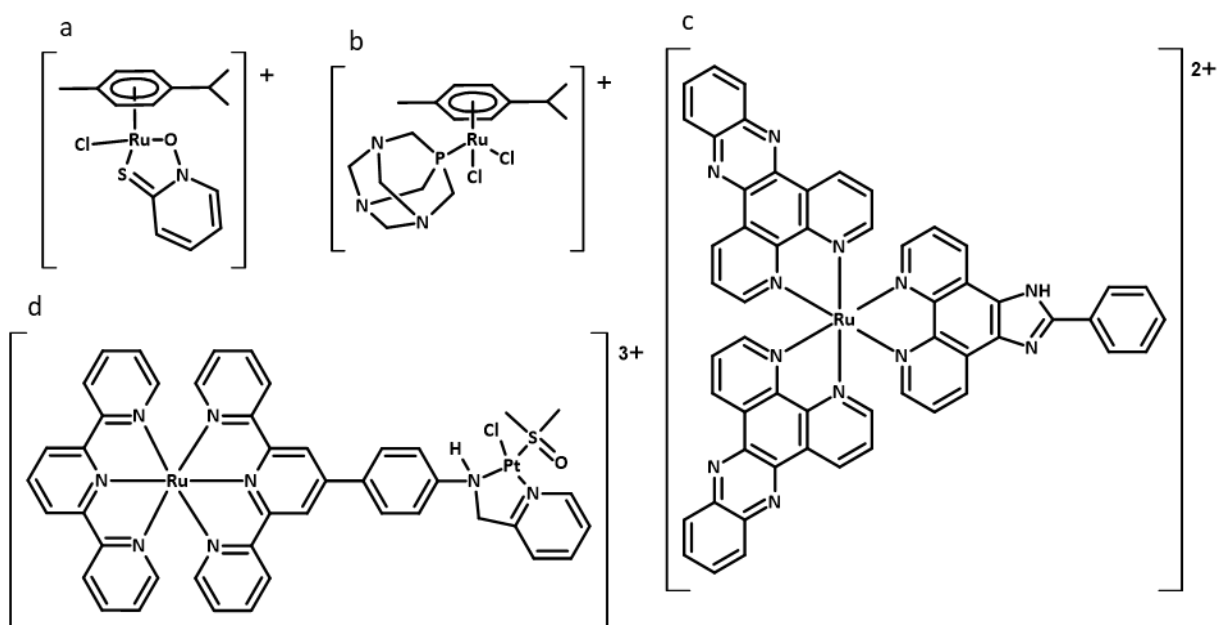
Figure 3-3: Complexes that are cytostatic and inhibit further cell proliferation. a). [(η^6-*p*-Cymene)Ru(2-hydroxyisoquinoline-3-(2H)-thionato)Cl], b). RAPTA-C, c). VR54, d). [Ru(dppz)$_2$(21p-HPIP)]$^{2+}$.

3-1.3: Methyl bioisosteres

Smart design of complexes encourages the development of highly intricate structures with several moieties, each with a specific function. This can lead to limited exploration into complexes with less complicated modifications from a core structure. One such modification is the addition of methyl groups and alkyl derivatives. Methyl substitutions are one of the smallest bioisosteric replacements employed in pharmaceutical design, with the ability to have a high impact on a structure's chemical and biological properties. These properties include effecting electrical structure, lipophilicity, entropy and water interactions while only adding 14 g/mol to overall molecular weight if substituting a hydrogen[24]. This is exemplified by benzene and toluene where the addition of a methyl increases molecular weight from 78.11 g/mol to 82.14 g/mol while increasing clogP by ~0.5 from 2.03 to 2.52[25]. Differences can be so profound, it has been dubbed the 'magic methyl effect'. The addition of a methyl can significantly improve potency due to conformational, energetic, metabolic and hydrophilic interaction changes, sometime leading to 1000-fold improvements in activity[26]. This effect has been

demonstrated by many drugs, including the Bcr-Abl inhibitor imatinib for chronic myeloid leukaemia, in which the methyl group promotes rotation around the pyridinyl-pyrimidine group enhancing interactions with the Bcr-Abl active site[24,27]. The effect has also been demonstrated in organoruthenium, organorhenium, and organoiridium complexes containing benzoyl thiourea derivatives [28]. In these complexes, addition of a methyl group increased potency by >2X, with *para* substitution being more effective than *ortho*. Additionally, the position of the methyl substitution also effected chelating properties of the ligand leading to the synthesis of a ionic complex with a bidentate ligand with a *para* methyl group or neutral structure with a monodentate ligand with an *ortho* methyl.

Thus far, there has been some investigation into the use of methyl derivatives, however these instances are in Pt(IV) and Ru(II) complexes with monodentate ligands[29–31]. One key example similar to the complexes synthesised in this work was explored by Fu *et al* in similar osmium complexes[32–34]. This methyl modification was used to assign isomerism and determine catalytic potential differences between differing isomers. Limited comparable biological screening of with and without the presence of the chiral carbon in A2780 was conducted, only covering antiproliferative activity. While potency did improve with the use of the methyl group, the methylated complexes also included a alkyl spacer which can also be highly effective at improving potency[32,33].

Previous work using imine bidentate ligands in ruthenium piano stool complexes has been predominantly focused on the other functional group substitutions including hydroxyl, carboxyl and dimethylamine[35,36]. These complexes were found to have varying activity in A2780 EOC, with unsubstituted complexes exhibiting the highest IC_{50} values by sulforhodamine B assay. This was followed by carboxyl complexes, then hydroxyl complexes, with dimethyl amine complexes being the most potent[36]. Following antiproliferative screening, the dimethylamine complexes were evaluated further by cellular accumulation followed by biological activity of the complexes including DNA replication inhibition, cell cycle arrest, requirement of p53, and GSH detoxification mechanisms. There was an increased focus on the use dimethylamine group due significant potency in both ImPy

complexes and in AzPy complexes[35] [37–39]. This has inadvertently limited the investigation into other functional groups by increasing focus on the dimethyl amine group. the use of a methyl group as a phenyl ring substituent. Additionally, for these ImPy complexes regarding MOD, only Caspase 3 activity and apoptosis induction was investigated[36]. Noting the range of biological activity these complexes exhibit and the breadth of MOD that can be induced by metallic complexes, this highlights a limitation to this current area.

3-1.4: Overview of work in Chapter 3

In this chapter, the potential of the methyl group bioisostere was evaluated in various positions on the phenyl ring of the parental structure [Ru(η^6-p-Cym)(ImPy)Cl]PF$_6$ by assessing the physiochemical and biological activity. This was achieved by the synthesis and characterisation of a series of six complexes, followed by antiproliferative activity screening in range of EOC cell lines to determine structure activity relationships. Being the best preforming complex of this series, complex **6** was taken forward for preliminary MOA screening in SKOV3 with particular attention to the MOD initiated due to the notable resistance to cell death and apoptosis seen in SKOV3.

3-2: Experimental section

3-2.1: Ligand and complex synthesis

ImPy ligands used in this chapter are shown in Figure 3-4. Ligands were synthesised using the synthetic scheme shown in Scheme 2-1. Full synthetic information is given in Appendix II.
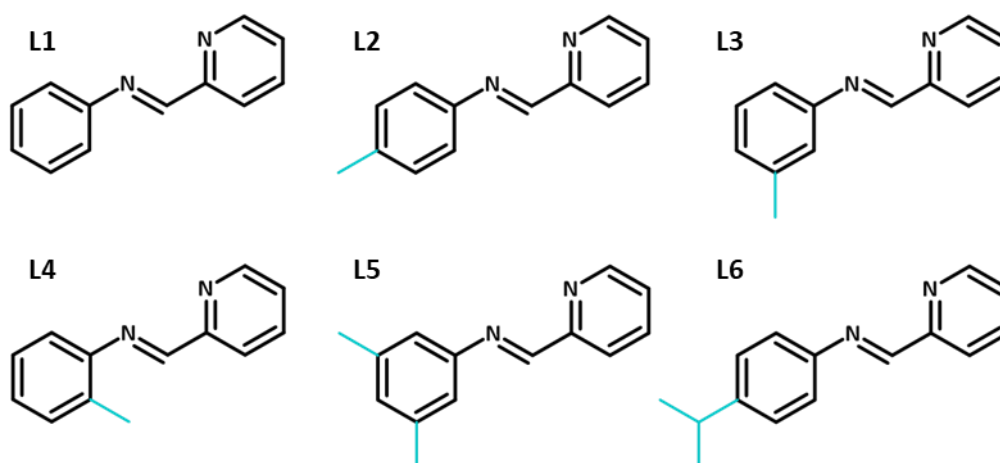
Figure 3-4: Structures of the six iminopyridine ligands used in Chapter 3 with the methyl bioisostere groups highlighted in blue.

Complexes were then synthesised using the synthetic scheme shown in Scheme 2-2.

3-2.1.1: *Complex 1 –* Ru(L1)Cl(PF$_6$), [Ru(η^6-*p*-Cym)(ImPy)Cl]PF$_6$

According to reaction scheme in Scheme 2-2, dichloro(p-cymene)ruthenium(II) dimer (101.6 mg, 0.17 mmol) was mixed with **L1** (60.5 mg, 0.33 mmol). Following which ammonium hexafluorophosphate (135.2 mg, 0.83 mmol) was added producing a solid weighing 183.9 mg (92.85%). ^{1}H NMR (400 MHz; DMSO-d$_6$) δ 0.98 (d, J=6.9 Hz, 6H), 2.16 (s, 3H), 2.51 (m, 1H), 5.58 (d, J=6.3 Hz, 1H), 5.63 (d, J=6.2 Hz, 1H), 5.76 (d, J=6.3 Hz, 1H), 6.09 (d, J=6.3 Hz, 1H), 7.62 (m, 3H), 7.81 (td, J=7.2, 1.4 Hz, 2H), 7.89 (qd, J=5.6, 1.8 Hz, 1H), 8.27 (dd, J=7.9, 1.4 Hz, 1H), 8.32 (td, J=7.6, 1.2 Hz, 1H), 8.93 (s, 1H), 9.58 (d, J=5.4 Hz, 1H). ^{13}C NMR (400 MHz; DMSO-d$_6$) δ 18.29, 21.59, 21.70, 30.49, 84.93, 85.12, 86.14, 86.55, 103.45, 105.09, 122.52, 128.93, 129.54, 129.81, 130.09, 139.97, 151.73, 154.55, 156.00, 167.92. m/z (ESI-MS)

found a highest intensity peak for the fragment of 453.07, with a calculated of 453.07 (M+ $[C_{22}H_{24}ClN_2Ru]^+$).

3-2.1.2: *Complex 2 -* Ru(L2)Cl(PF$_6$), [Ru(η^6-*p*-Cym)(ImPy-4-Me)Cl]PF$_6$

According to reaction scheme in Scheme 2-2, dichloro(p-cymene)ruthenium(II) dimer (100.9 mg, 0.16 mmol) was mixed with **L2** (64.7 mg, 0.33 mmol). Following which ammonium hexafluorophosphate (134.3 mg, 0.82 mmol) was added producing a solid weighing 201.4 mg (99.87%). ^{1}H NMR (400 MHz; DMSO-d$_6$) δ 0.98 (d, J=7.0 Hz, 6H), 2.16 (s, 3H), 2.44 (s, 3H), 2.51 (m, 1H), 5.58 (d, J=6.2 Hz, 1H), 5.62 (d, J=6.2 Hz, 1H), 5.76 (d, J=6.3 Hz, 1H), 6.09 (d, J=6.2 Hz, 1H), 7.44 (d, J=8.1 Hz, 2H), 7.70 (d, J=8.4 Hz, 2H), 7.88 (qd, J=5.7, 1.7 Hz, 1H), 8.26 (dd, J=7.8, 1.3 Hz, 1H), 8.31 (td, J=7.6, 1.2 Hz, 1H), 8.89 (s, 1H), 9.56 (d, J=5.5 Hz, 1H). ^{13}C NMR (400 M Hz; DMSO-d$_6$) δ 20.83, 21.59, 21.72, 30.50, 84.77, 85.10, 86.30, 86.53, 103.61, 104.93, 122.45, 128.79, 129.91, 139.66, 139.93, 149.45, 154.60, 155.96, 167.08. m/z (ESI-MS) found a highest intensity peak for the fragment of 467.08, with a calculated of 467.08 (M+ $[C_{23}H_{26}ClN_2Ru]^+$).

3-2.1.3: *Complex 3 -* Ru(L3)Cl(PF$_6$), [Ru(η^6-*p*-Cym)(ImPy-3-Me)Cl]PF$_6$

According to reaction scheme in Scheme 2-2, dichloro(p-cymene)ruthenium(II) dimer (100.9 mg, 0.16 mmol) was mixed with **L3** (64.7 mg, 0.33 mmol). Following which ammonium hexafluorophosphate (134.3 mg, 0.82 mmol) was added producing a solid weighing 186.8 mg (92.63%). ^{1}H NMR (400 MHz; DMSO-d$_6$) δ 0.99 (dd, J=5.3, 1.7 Hz, 6H), 2.15 (s, 3H), 2.47 (s, 3H), 2.52 (m, 1H), 5.58 (d, J=6.2 Hz, 1H), 5.65 (d, J=6.2 Hz, 1H), 5.76 (d, J=6.2 Hz, 1H), 6.06 (d, J=6.3 Hz, 1H), 7.41 (d, J=7.6 Hz, 1H), 7.52 (t, J=7.6 Hz, 1H), 7.60 (s, 2H), 7.89 (qd, J=5.7, 1.8 Hz, 1H), 8.26 (dd, J=7.9, 1.2 Hz, 1H), 8.32 (td, J=7.6, 1.3 Hz, 1H), 8.91 (s, 1H), 9.57 (d, J=5.4 Hz, 1H). ^{13}C NMR (400 MHz; DMSO-d$_6$) δ 18.21, 21.01, 21.50, 21.72, 30.48, 85.37, 85.76, 86.44, 102.89, 105.29, 119.80, 122.60, 128.89, 129.33, 129.98, 130.42, 139.13,

139.96, 151.84, 154.54, 155.97, 167.63. m/z (ESI-MS) found a highest intensity peak for the fragment of 467.08, with a calculated of 467.08 (M+ $[C_{23}H_{26}ClN_2Ru]^+$).

3-2.1.4: *Complex 4* - Ru(L4)Cl(PF$_6$), [Ru(η^6-*p*-Cym)(ImPy-2-Me)Cl]PF$_6$

According to reaction scheme in Scheme 2-2, dichloro(p-cymene)ruthenium(II) dimer (102.2 mg, 0.17 mmol) was mixed with **L4** (65.5 mg, 0.33 mmol). Following which ammonium hexafluorophosphate (136.0 mg, 0.83 mmol) was added producing a solid weighing 187.4 mg (92.93%). ^{1}H NMR (400 MHz; DMSO-d$_6$) δ 0.95 (d, J=6.7 Hz, 3H), 1.02 (d, J=6.7 Hz, 3H), 2.10 (s, 3H), 2.40 (s, 3H), 2.59 (m, 1H), 5.32 (d, J=5.4 Hz, 1H), 5.73 (dd, J=3.4, 2.6 Hz, 2H), 6.02 (d, J=6.1 Hz, 1H), 7.44 (m, 2H), 7.52 (m, 1H), 7.70 (t, J=4.5 Hz, 1H), 7.93 (qd, J=5.5, 1.5 Hz, 1H), 8.26 (dd, J=7.8, 1.1 Hz, 1H), 8.33 (td, J=7.6, 1.2 Hz, 1H), 8.91 (s, 1H), 9.63 (d, J=5.4 Hz, 1H). ^{13}C NMR (400 MHz; DMSO-d$_6$) δ 17.64, 18.07, 21.14, 22.06, 30.43, 86.08, 86.59, 87.10, 101.52, 105.49, 123.13, 126.75, 128.73, 129.24, 130.16, 131.65, 140.07, 151.27, 154.36, 155.98, 170.78. m/z (ESI-MS) found a highest intensity peak for the fragment of 467.08, with a calculated of 467.08 (M+ $[C_{23}H_{26}ClN_2Ru]^+$).

3-2.1.5: *Complex 5* - Ru(L5)Cl(PF$_6$), [Ru(η^6-*p*-Cym)(ImPy-3,5-Me$_2$)Cl]PF$_6$

According to reaction scheme in Scheme 2-2, dichloro(p-cymene)ruthenium(II) (110.7 mg, 0.18 mmol) was mixed with **L5** (71.0 mg, 0.36 mmol). Following which ammonium hexafluorophosphate (147.3 mg, 0.91 mmol) was added producing a solid weighing 199.2 mg (88.02%). ^{1}H NMR (400 MHz; DMSO-d$_6$) δ 0.98 (d, J=7.0 Hz, 3H), 1.01 (d, J=7.0 Hz, 3H), 2.14 (s, 3H), 2.42 (s, 6H), 2.54 (m, 1H), 5.57 (d, J=6.2 Hz, 1H), 5.66 (d, J=6.3 Hz, 1H), 5.75 (d, J=6.4 Hz, 1H), 6.03 (d, J=6.3 Hz, 1H), 7.23 (s, 1H), 7.40 (s, 2H), 7.88 (qd, J=5.6, 1.6 Hz, 1H), 8.25 (dd, J=7.7, 1.2 Hz, 1H), 8.31 (td, J=7.7, 1.3 Hz, 1H), 8.90 (s, 1H), 9.57 (d, J=5.4 Hz, 1H). ^{13}C NMR (400 MHz; DMSO-d$_6$) δ 18.14, 20.93, 21.40, 21.76, 30.47, 85.34, 85.68, 85.88, 86.33, 102.27, 105.53, 119.97, 128.86, 129.88, 131.14, 138.86, 139.96, 151.95, 154.55, 155.95, 167.36.

m/z (ESI-MS) found a highest intensity peak for the fragment of 481.99, with a calculated of 481.10 (M+ $[C_{24}H_{28}ClN_2Ru]^+$).

3-2.1.6: *Complex 6 -* Ru(L6)Cl(PF$_6$), [Ru(η^6-*p*-Cym)(ImPy-4-CH(CH$_3$)$_2$)Cl]PF$_6$

According to reaction scheme in Scheme 2-2, dichloro(p-cymene)ruthenium(II) (104.8 mg, 0.17 mmol) was mixed with **L6** (76.8 mg, 0.34 mmol). Following which ammonium hexafluorophosphate (139.5 mg, 0.86 mmol) was added producing a solid weighing 204.9 mg (97.83%). ^{1}H NMR (400 MHz; DMSO-d$_6$) δ 0.98 (d, J=6.9 Hz, 6H), 1.29 (d, J=6.8 Hz, 6H), 2.16 (s, 3H), 2.50 (m, 1H), 3.04 (m, 1H), 5.58 (d, J=6.2 Hz, 1H), 5.64 (d, J=6.2 Hz, 1H), 5.76 (d, J=6.3 Hz, 1H), 6.10 (d, J=6.4 Hz, 1H), 7.50 (d, J=8.5 Hz, 2H), 7.73 (d, J=8.5 Hz, 2H), 7.88 (qd, J=5.4, 1.5 Hz, 1H), 8.24 (dd, J=7.8, 1.1 Hz, 1H), 8.31 (td, J=7.7, 1.2 Hz, 1H), 8.90 (s, 1H), 9.57 (d, J=5.5 Hz, 1H). ^{13}C NMR (400 MHz; DMSO-d$_6$) δ 18.31, 21.52, 21.75, 23.71, 23.73, 30.49, 33.19, 84.81, 85.01, 86.08, 86.72, 103.55, 104.90, 122.54, 127.29, 128.79, 129.87, 139.94, 149.63, 150.39, 154.59, 155.96, 167.21. m/z (ESI-MS) found a highest intensity peak for the fragment of 495.11, with a calculated of 495.11 (M+ $[C_{25}H_{30}ClN_2Ru]^+$).

3-2.2: Aqueous solution behaviour studies

3-2.2.1: GSH titration interaction by UV-Vis spectroscopy

GSH was dissolved to prepare a stock solution of 1500 µM in 5% (v/v) methanol in PBS, from which final assay titre concentrations ranging from 750 to 3.2 µM were diluted. Complex **6** was diluted to the final concentration of 150 µM in 3.75% (v/v) DMSO in PBS. The GSH concentrations and **6** were mixed to a total volume of 200 µL in a clear 96 well plate with each concentration in quadruplicate. The plate was then shaken at room temperature before UV-Vis spectra were collected at 0.5, 1 and 24 hours.

3-2.3: Cell studies in SKOV3

For all following experiments, SKOV3 cells were treated with full media as a negative control. Unless stated otherwise treatments were used equipotently at 2X IC_{50} concentrations of CDDP and PTX, as positive and as EOC gold standard of treatments controls. Complex **6** was used at 0.5X IC_{50} concentration, with further concentrations of 1X and 2.5X IC_{50} in selected experiments. Cells were exposed to treatment for 24 hours.

3-2.3.1: Cell lysate collection

P150 dishes were seeded with $8X10^6$ SKOV3 cells and incubated for 24 hours then treated equipotently with the addition of 1 µM of STS as a positive control of apoptosis in triplicate. After 24 hours exposure, cells were washed with PBS and trypsinized to a SCS, washed twice with PBS and lysed using 2X Cell lysis buffer item J (Sigma) diluted 1:1 in cold PBS on ice for 30 minutes. Following digestion, the solution was centrifuged at 12,000 RPM at 4°C for 30 minutes with the supernatant collected for analysis. Cell lysate was divided between the Bradford assay, Caspase 3/7 as described in Chapter 2, and Caspase 9 kit.

3-2.3.2: Caspase 9 activity

Caspase 9 activity was assessed using the Caspase 9 Activity Assay Kit (by Colorimetric, Elabcsience) per manufactures instructions from step 6 as cell lysate had been previously prepared. Absorbance values were exported to Microsoft Excel and normalised by the negative control absorbance and protein content.

3-2.3.3: Autophagy activity

Black wall, clear glass bottom 96 well plates were seeded with $1.5X10^4$ SKOV3 cells per well and incubated for 24 hours. Cells were treated equipotently in addition to 1 µM STS as a positive control

of autophagy. Post exposure, cells were washed and stained with the ATT Bioquest Cell Meter™ Autophagy Assay Kit per manufacturer's instructions. Fluorescence intensity and fluorescence microscopy of cells was measured using blue fluorescence intensity and the DAPI channel respectively. Post fluorescence analysis, cells were stained with 50 µL 1mg/mL crystal violet in 80% (v/v) methanol in PBS for 30 minutes at 4°C. The plate was then washed with water, crystal violet was dissolved in 100 µL of 10% (v/v) acetic acid in isopropanol and absorbance measured at 590 nm for crystal violet protein content normalisation of fluorescence intensity.

3-2.3.4: Co-treatment for ferroptosis inhibition and activation

Protocol was based on the antiproliferative activity assay detailed in Chapter 2, with an altered treatment protocol. Co-treatment drugging protocols are shown in Table 3-1 for ferroptosis inhibition and Table 3-2 for ferroptosis enhancement using Fer-1 and erastin (ERA) as positive controls for inhibition and activation respectively. Co-treatments were added within 5 minutes of each other. Cell survival was calculated as a percentage of the negative control without co-treatment.

Table 3-1: Ferroptosis inhibition combinations used in this work given in final treatment concentrations. The ferroptosis inhibitor ferrostatin (Fer-1) was used increments of 0, 0.25, 0.49, and 1.2 µM. Fer-1 was co-treated with CDDP, PTX, STS, complex **6**, the ferroptosis inducer erastin (ERA) as a positive control or media as a negative control.

Treatment	Fer-1 concentration (µM)			
	0	0.25	0.49	1.2
Negative control – media	✓	✓	✓	✓
CDDP at 1X IC$_{50}$	✓	✓	✓	✓
STS at 1 µM	✓	✓	✓	✓
6 at 0.25X, 0.5X and 1.25X	✓	✓	✓	✓
PTX at 1X IC$_{50}$	✓	✓	✓	✓
ERA at 1X IC$_{50}$ (5.38 µM)	✓	✓	✓	✓

Table 3-2: Ferroptosis enhancement combinations used in this work given in final treatment concentrations. The ferroptosis inducer erastin (ERA) was used in increments of 0 X, 1X and, 3X IC_{50}. ERA was co-treated with CDDP, PTX, STS, complex *6*, or media as a negative control.

Treatment	ERA (IC_{50} = 5.38 µM)			
	0X IC_{50}	0.5X IC_{50}	1X IC_{50}	3X IC_{50}
Negative control – media	✓	✓	✓	✓
CDDP at 1X IC_{50}	✓	✓	✓	✓
STS at 1 µM	✓	✓	✓	✓
6 at 0.25X, 0.5X and 1.25X	✓	✓	✓	✓
PTX at 1X IC_{50}	✓	✓	✓	✓

3-2.3.5: Ruthenium piano-stool antiproliferative activity enhancement by L-buthionine sulfoximine cotreatment

Protocol was based on the antiproliferative activity assay detailed in Chapter 2, with an altered treatment protocol. A2780 and SKOV3 cells were co-treated with final concentrations ranging between 200 and 0.01 µM of CDDP, *1* or *6* in combination with 5 µM of L-buthionine sulfoximine (L-BSO). Co-treatments were added within 5 minutes of each other. Cell survival was then calculated from which IC_{50} values were determined.

3-3: Results

3-3.1: Physiochemical characterisation of methyl bioisostere complexes

3-3.1.1: Synthesis and characterisation of the iminopyridine ligands and piano-stool complexes used in Chapter 3

Following ImPy ligand synthesis, imine bond formation was confirmed, and ligand structure was elucidated using ^{1}H, ^{13}C and HSQC NMR experiments, specifically observing for the singlet imine proton shift at ~8.8 ppm.

Table 3-3: Complexes synthesised and evaluated in Chapter 3.
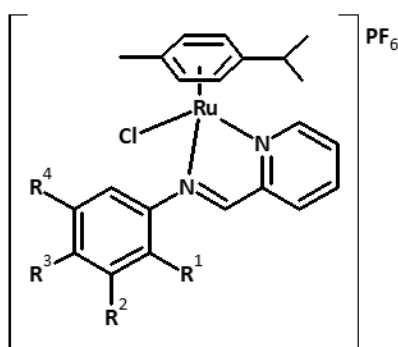
Complex	R^1	R^2	R^3	R^4
1 - Ru(L1)Cl(PF$_6$), [Ru(η^6-*p*-Cym)(ImPy)Cl]PF$_6$	H	H	H	H
2 - Ru(L2)Cl(PF$_6$), [Ru(η^6-*p*-Cym)(ImPy-4-Me)Cl]PF$_6$	H	H	CH$_3$	H
3 - Ru(L3)Cl(PF$_6$), [Ru(η^6-*p*-Cym)(ImPy-3-Me)Cl]PF$_6$	H	CH$_3$	H	H
4 - Ru(L4)Cl(PF$_6$), [Ru(η^6-*p*-Cym)(ImPy-2-Me)Cl]PF$_6$	CH$_3$	H	H	H
5 - Ru(L5)Cl(PF$_6$), [Ru(η^6-*p*-Cym)(ImPy-3,5-DiMe)Cl]PF$_6$	H	CH$_3$	H	CH$_3$
6 - Ru(L6)Cl(PF$_6$), [Ru(η^6-*p*-Cym)(ImPy-4-*i*Pr)Cl]PF$_6$	H	H	CH(CH$_3$)$_2$	H

The ligands were then used as starting materials for the six complexes shown in Table 3-3. Following synthesis, structure was elucidated using 1D and 2D NMR experiments reflected in Chapter 2 NMR, complimented with ESI-MS spectrometry, HPLC and elemental analysis. The experimental data was consistent with the proposed structures and purity was confirmed before biological analysis.

3-3.1.2: Chemical structure elucidation example using complex *6*

Elucidation of the proposed complex structures was done using a combination of the NMR experiments including ^{1}H, ^{13}C, ^{1}H COSY, ^{1}H^{13}C HSQC, and ^{1}H^{13}C HMBC. Proton assignment of complex *6* is shown in Figure 3-5. The ^{1}H NMR spectrums shows 16 proton signals with chemical shifts between 0.98 and 9.57 ppm. One of these signals can be assigned to the residual peak of the DMSO used as solvent. ^{13}C data spans between 18.31 and 167.21 ppm. Carbon to proton correlations at a single bond were determined using the ^{1}H^{13}C HSQC (Figure 3-6), while ^{1}H COSY and ^{1}H^{13}C HMBC allowed for establishing interactions at longer bond distances. 2D experiments also contain the corresponding solvent signals expected.

3-3.1.3: Complex interaction with biologically relevant matrixes by UV-Vis

Following synthesis and elucidation that the correct complexes had been produced, evaluation of complex interaction with biologically relevant matrixes was assess by UV-Vis spectroscopy changes in the charge transfer band region of the spectra to determine suitability for biological study (Table 3-4). All complexes here shown to interact with water, GSH, media and full media by exhibiting isosbestic points in the charge transfer band region of the spectra after 24 hours incubation. All complexes except *1* and *5* exhibit an isosbestic point with ctDNA. Hyperchromism was observed for all complexes bar complex *1* in DMSO. Complexes *1* and *5* also exhibited hypochromism with all other matrixes bar BSA. No precipitation of complex was observed in any matrix.
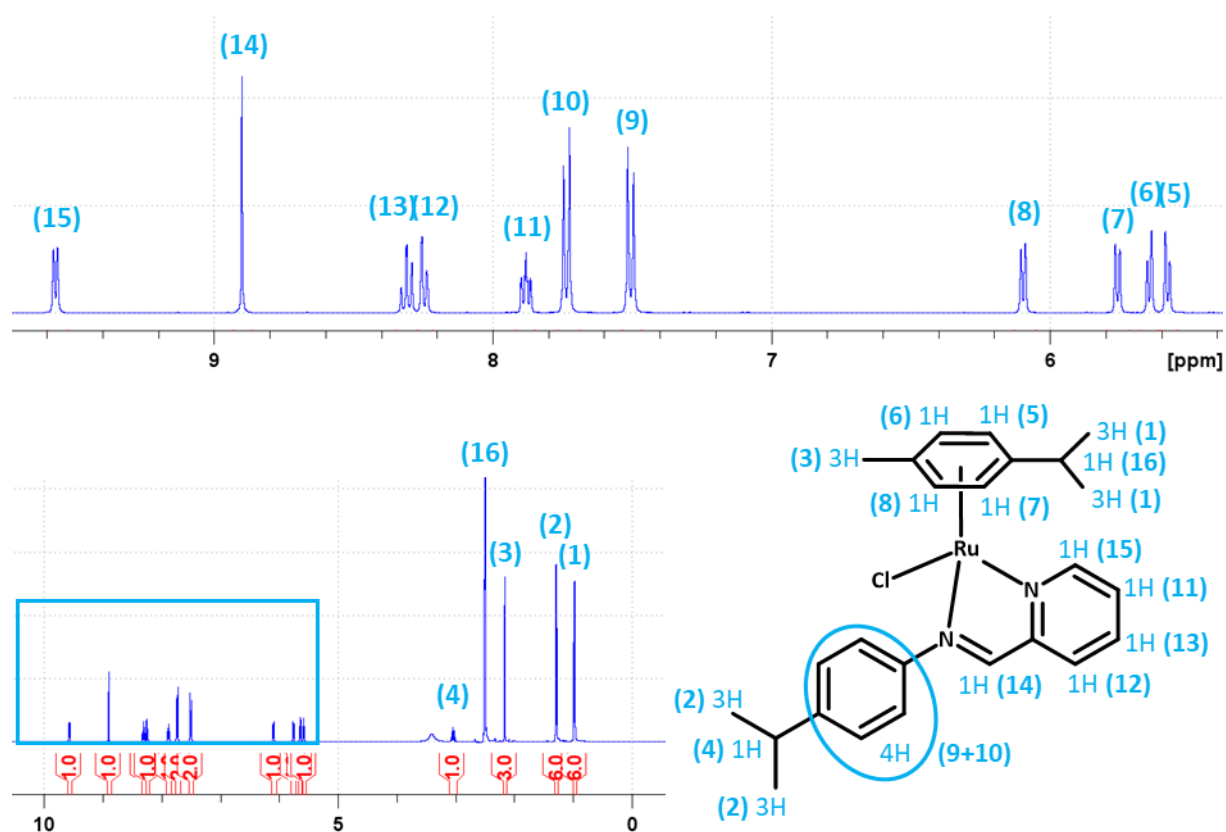
Figure 3-5: Proton assignment of complex **6.** a). structure of complex **6** with proton integral given as H and corresponding ¹H peak given in brackets. b). ¹H NMR at 400 MHz with expansion box of shifts from 5.5-10 ppm. Integrals given in red and proton assignment given in blue referenced to DMSO at 2.5 ppm.
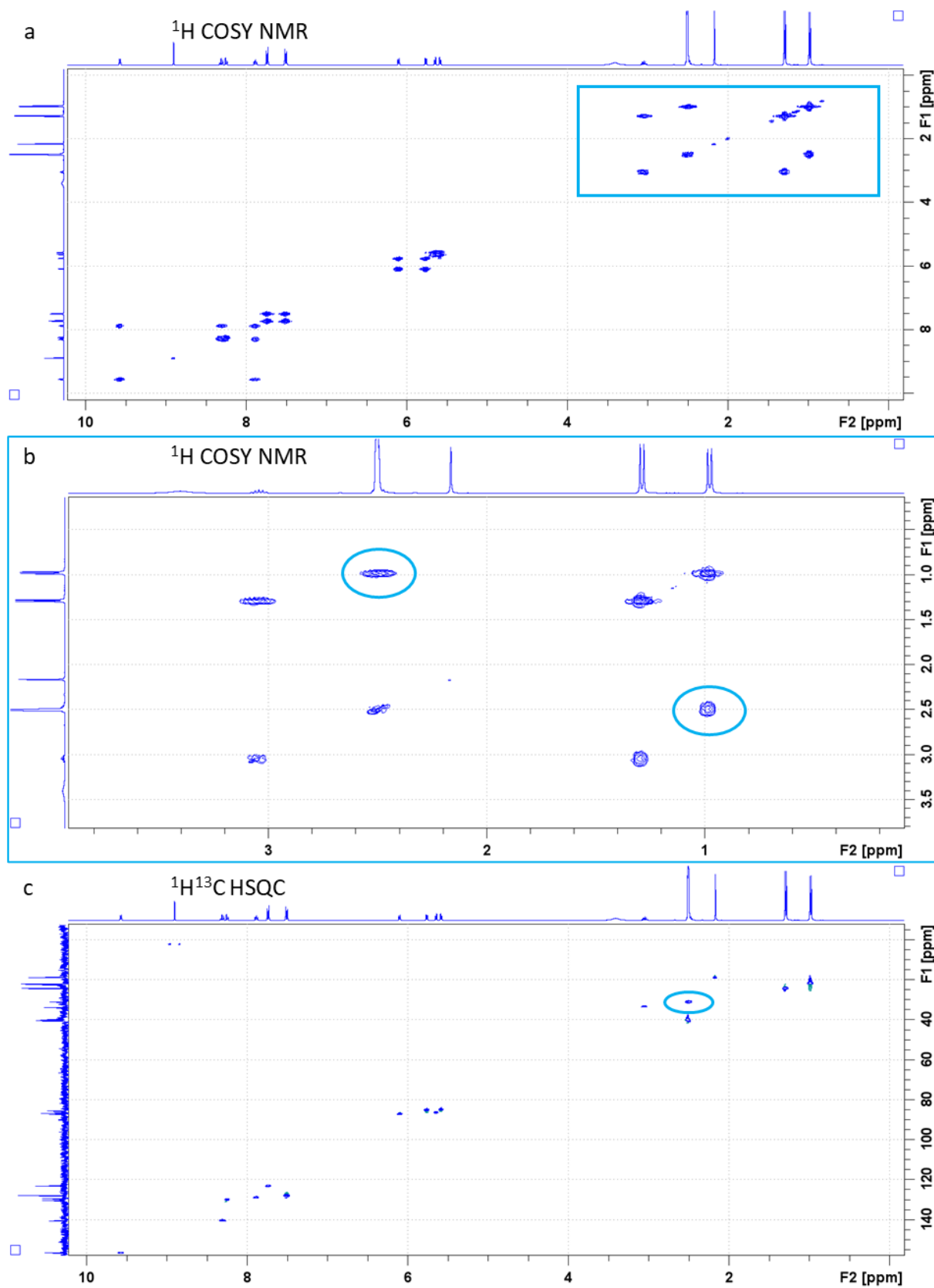
Figure 3-6: 400 Hz NMR spectra highlighting the overlap of the DMSO and proton 16 in complex **6**. a). Full ^{1}H COSY spectra of complex **6** from 0-10 ppm. b). Magnification of ^{1}H COSY NMR. Circled peaks highlight the presence of a proton corelation of shift 1 with a shift within the DMSO peak. c). ^{1}H^{13}C HSQC NMR spectra with highlighted proton-carbon corelation of a proton in addition to the DMSO proton-carbon corelation.

3-3.1.4: GSH interaction by UV-Vis titration

Noting the interaction with GSH, further in-depth experimentation was evaluated (Figure 3-7). Maintaining an equimolar concentration of complex **6** to GSH, UV-Vis spectra were collected (Figure 3-7a) a hyperchromic and hypsochromic effect is seen over the course of 24 hours. When titrating the concentration of GSH while maintaining complex **6** concentration at 150 µM, within 30 minutes of combination (Figure 3-7b), hypochromism is observed with a bathochromic shift. With the increased interaction time, the extent of hypochromism and bathochromism is increased with 24 hours exhibiting the greatest effect (Figure 3-7c and d).

Table 3-4: Summary of UV-Vis spectra changes of the complexes investigated in Chapter 3 with biologically relevant matrixes following 24 hours incubation. Abbreviations: dimethyl sulfoxide (DMSO), phosphate buffered saline (PBS), bovine serum albumin (BSA), glutathione (GSH), calf thymus DNA (ctDNA), non-essential amino acids (NEAA), no change (NC), isosbestic point (IP), hypochromism ($\downarrow$), and hyperchromism ($\uparrow$).

Complex	DMSO	H_2O	1:1 H_2O:PBS	PBS	BSA	GSH	Media	Full Media	ctDNA	Human plasma	NEAA
1	NC	IP	$\downarrow$	$\downarrow$	$\downarrow$	IP	IP	IP	$\downarrow$	$\downarrow$	$\downarrow$
2	$\uparrow$	IP	NC	NC	NC	IP	IP	IP	IP	NC	NC
3	$\uparrow$	IP	NC	NC	NC	IP	IP	IP	IP	NC	NC
4	$\uparrow$	IP	NC	NC	NC	IP	IP	IP	IP	NC	NC
5	$\uparrow$	IP	$\downarrow$	$\downarrow$	NC	IP	IP	IP	$\downarrow$	$\downarrow$	$\downarrow$
6	$\uparrow$	IP	NC	NC	NC	IP	IP	IP	IP	NC	NC
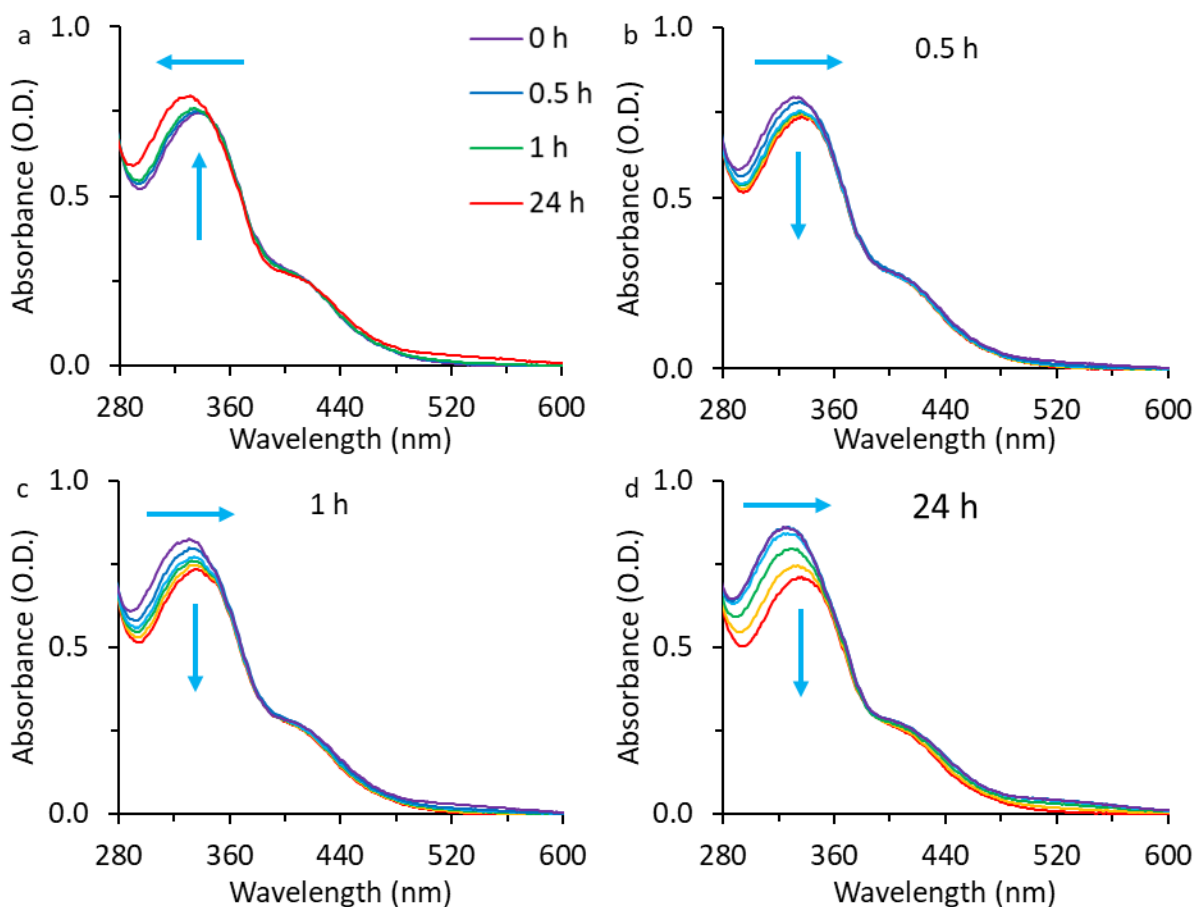
Figure 3-7: GSH interaction titration studies by UV-Vis spectroscopy. a). overlay of time dependant spectra of GSH and complex *6* in a 1:1 ratio showing an hyperchromic and hypsochromic over time, b). titration of 3.2 to 750 µM GSH with 150 µM of *6* showing a hypochromic and bathochromic shift with increasing concentration at 0.5 hours, c). at 1 hour, d). at 24 hours.

LogD$_{7.4}$ and lipophilicity

Lipophilicity being an important quality in the behaviour of a pharmacological agent, was determined by the shake flask method. All the complexes synthesised were shown to have a negative LogD$_{7,4}$ values ranging from -0.66 to -0.21 for complex *1* and *6* respectively (Table 3-5). Furthermore, several trends regarding substitution also appear. Methyl substitution position effects lipophilicity increasing unsubstituted>*para*>*meta*>*ortho*. Furthermore, increased substitution increases the lipophilicity by 0.28 with mono substitution and 0.37 with bi substitution in the 3, 5 positions. Lipophilicity was increased most in these complexes with the addition of the isopropyl group in the *para* position in complex *6*.

Table 3-5: LogD$_{7.4}$ of the six complexes evaluated in this chapter determined by the shake flask method using PBS and n-octanol.

Complex	LogD$_{7.4}$
1	-0.66
2	-0.38
3	-0.42
4	-0.51
5	-0.29
6	-0.21

3-3.1.5: Density Functional Theory of the ruthenium complexes

Noting the subtle differences in lipophilicity of the complexes, using DFT energy minimized, geometry optimised structure renders were calculated for complexes **1**, **2**, **3**, **4** and **6** shown in Figure 3-8 to assess for structural differences. From these the bond lengths around the ruthenium centre and the rotation of the phenyl ring were calculated (Table 3-6). Of the complexes compared here there were no predicted significant differences in the bond lengths between any of the complexes evaluated with all bond lengths being 2.390 Å, 2.064 Å and 2.084 Å. Regarding Phenyl ring rotation, **4** had a significant calculated rotation of 12.94° over **1**. However, **2**, **3** and **6** all experienced decreased rotation compared to **1** of 1.63°, 2.44° and 3.05° respectively.

Table 3-6: Calculated DFT bond lengths (Å) and phenyl ring rotation (°) determined from the lowest energy structures. (Calculated by Dr J.P.C. Coverdale).

Complex	Ru-Cl (Å)	Ru-N imino (Å)	Ru-N pyridine (Å)	N-Ph dihedral (°)
1	2.3872	2.0698	2.0806	52.6103
2	2.3893	2.0638	2.0839	50.1720
3	2.3891	2.0620	2.0853	50.9800
4	2.3919	2.0599	2.0853	65.5488
6	2.3889	2.0648	2.0839	49.5619
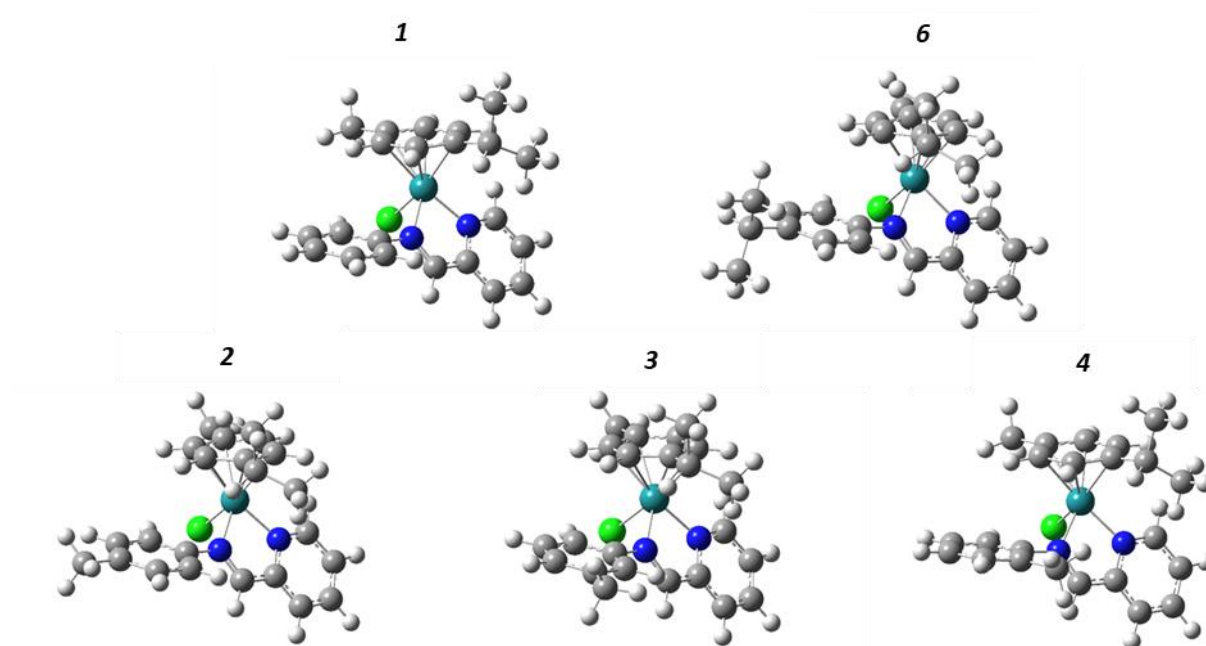
Figure 3-8: Calculated DFT structures of selected complexes in their lowest energy structures. (Rendered by Dr J.P.C. Coverdale).

3-3.2: Cell Studies of methyl bioisostere complexes

3-3.2.1: Antiproliferative screening

The complexes were screened in a variety of EOC lines to assess their antiproliferative activity (Table 3-7 and Figure 3-9). IC_{50} values were determined using the MTT assay following a 24-hour exposure and 72 hours recovery time regime with comparison to CDDP and PTX as standards for organometallic complexes and EOC respectively.

The complexes in this series largely demonstrates consistent activity across the EOC cell lines tested in this panel. Complex *1* (unsubstituted) was the least potent complex evaluated here with an IC_{50} >140 µM in all but one EOC cell line. Complex *1* was followed by complex *4* (*o*-CH$_3$) which was only effective in PEA1 and PEA2 with potencies <140 µM. Complexes *2* and *3* (*p*- and *m*-CH$_3$, respectively) exhibited similar moderate potencies in all EOC cell lines, bar SKOV3, generally being more potent than complex *4*. With the addition of a second methyl group in complex *5* (2,4-diCH$_3$), potency increased with IC_{50} values <100 µM in three of the EOC lines. Here, complex *6* (*i*Pr group) was the most potent complex

exhibiting moderate to significant activity in all of the EOC cell lines here with IC_{50} values <85 µM.

Table 3-7: Antiproliferative screening of the six complexes used in this chapter with efficacy displayed as IC_{50} values and the PEA factor (calculated as = IC_{50}(PEA2)÷IC_{50}(PEA1), therefore increasing PEA factor corelates with increased resistance in the PEA2). (n.d., no data).

Complex	IC_{50} Value (µM)					PEA Factor
	A2780	SKOV3	PEA1	PEA2	MRC5	
1	>140	>140	>140	98.45 (0.04)	>140	N.A.
2	76 (2)	>140	64 (2)	110 (2)	>140	1.73 (0.07)
3	84.0 (0.2)	>140	67 (1)	126 (1)	n.d.	1.87 (0.03)
4	>140	>140	73 (2)	117 (2)	n.d.	1.60 (0.05)
5	40.6 (0.2)	120 (1)	34 (1)	67.8 (0.7)	n.d.	1.94 (0.08)
6	44.6 (0.7)	84.5 (0.5)	10 (2)	26.5 (0.2)	>140	2.5 (0.4)
CDDP	3 (1)	11 (1)	2.72 (0.07)	8.08 (1)	5.6 (0.7)	3.0 (0.5)
PTX	0.32 nM (0.02)	0.56 nM (0.03)	3.5 nM (0.3)	4.28 nM (0.06)	n.d.	1.2 (0.1)

This series generally exhibits good potency in the EOC A2780, PEA1 and PEA2 lines meanwhile, activity varies greatly in the intrinsically CDDP-resistant SKOV3 line. Here, the complexes performed best in A2780 with all complexes except *1* and *4* achieving an IC_{50} value below 100 µM, followed by PEA1 with all but *1* achieving a measurable IC_{50} value below 100 µM. In contrast, the complexes did not perform as well in SKOV3 and PEA2 with most IC_{50} values being above 140 µM and 100 µM, respectively.

Here the PEA factor (the ratio between the IC_{50} values of PEA2 and PEA1 cells, corresponding to the effectiveness between first line and second line treatment) demonstrates that all the methyl derivative complexes synthesised here experienced between 0.5X and 1.4X less resistance than CDDP. However, in the intrinsically CDDP resistant line SKOV3, potencies generally halved compared to A2780.

Here, the MRC5 normal lung cells were used to model normal cells and provide a model for cancer cell to normal cell specificity. All three complexes tested did not exhibit antiproliferative activity with IC_{50} values of above 140 µM. Specifically, the activity of complex *6* in MRC5 is between 2.6X and 22.5X less effective in MRC5 than the EOC lines screens. This contrasts CDDP which maintained strong antiproliferative activity with an IC_{50} of 5.6 µM, comparable to the potency in the EOC cell lines.

Within the series, complex **6** is the most effective complex having the highest potency of all the complexes tested in most cell lines. However, **6** was also substantially affected by treatment resistance seen between PEA1 and PEA2 with the highest PEA factor.
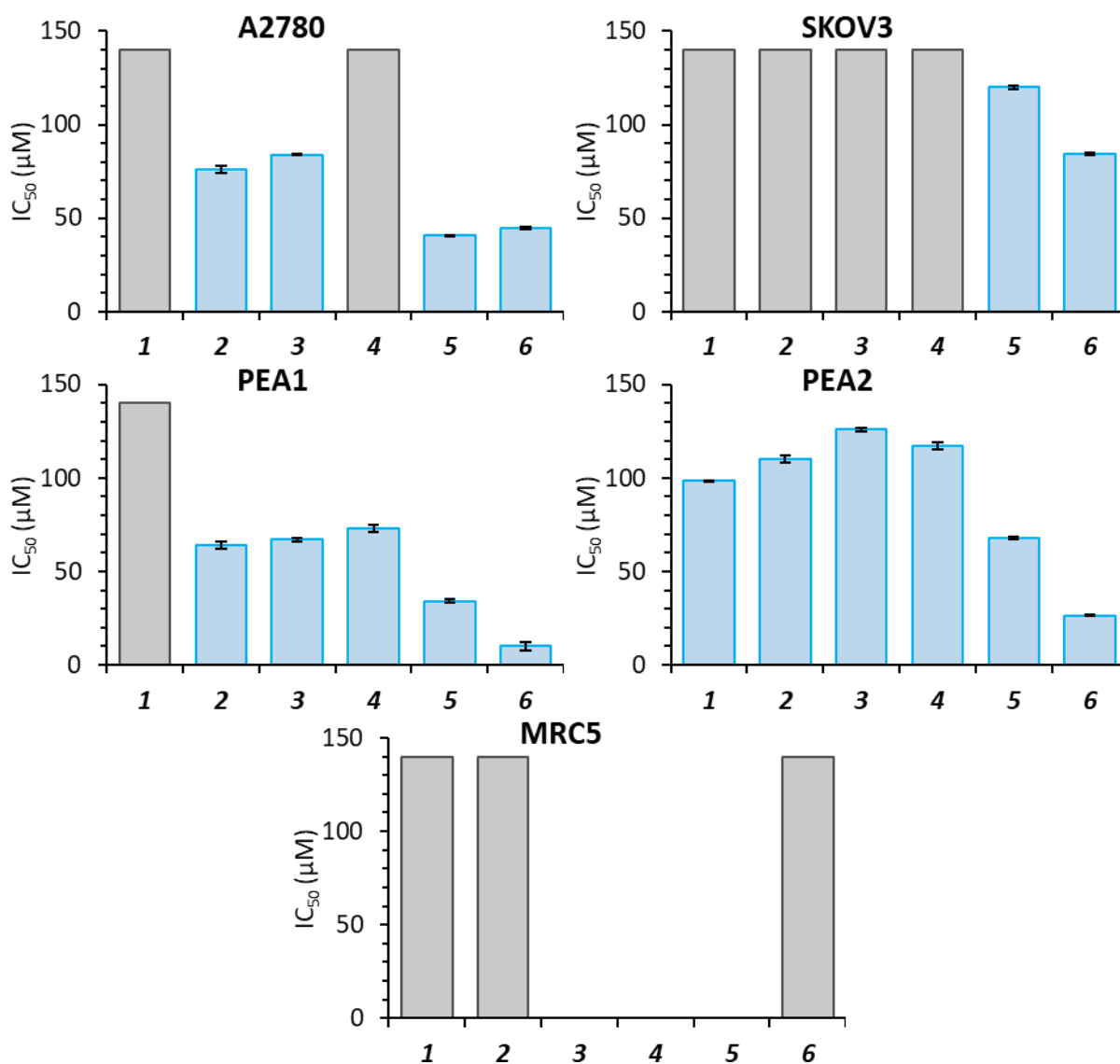
Figure 3-9: Antiproliferative screening of the six complexes used in this chapter with efficacy displayed as IC_{50} values. Bars in grey indicate an IC_{50} value of >140 µM.

When analysing the series as a whole, several trends can be seen. The first observation is the use of the methyl group around the phenyl ring does provide significant improvement to the potency of the complexes in A2780 and PEA1 but not SKOV3 and PEA2. The methyl group in A2780 and PEA1 allows for measurable IC_{50} below 100 µM. In PEA2, the methyl group does allow for some antiproliferative

activity improvement but is limited with all IC$_{50}$ concentrations of the methylated complexes being above 100 μM. Further in SKOV3, the methyl substitution did not provide any significant antiproliferative activity. However, the substitution position does have a significant influence on potency in all cell lines. In all almost all cases, methyl substitution in the *ortho* position significantly decreased potency over the *para* and *meta* positions with potency on average being ~1.5X less potent. This effect is seen greatest in A2780 where potency decreased to unmeasurable levels here in the *ortho* position from an IC$_{50}$ of 76 μM in the *para* position, therefore being 1.8X more potent.

In addition to the position of the methyl group, the number of methyl groups greatly effects potency where increased substitution, increases potency. This is This trend is further extended into the use of the *i*Pr group of **6** where potency doubles in SKOV3, and triples in PEA1 and PEA2. Yet this does not extend in A2780 where potency between **5** and **6** is comparable.

A further trend seen is the increase in potency with the increase in lipophilicity. While it must be acknowledged that the changes in lipophilicity are small, there is substantial increase in IC$_{50}$ with small decreases in lipophilicity (Figure 3-10). This trend is strongest in PEA2 where potency can double with an increase in lipophilicity from -0.29 to -0.21. Evaluating all the complexes synthesised here, complex **6** was selected for further testing in SKOV3 due to its high potency in all lines.
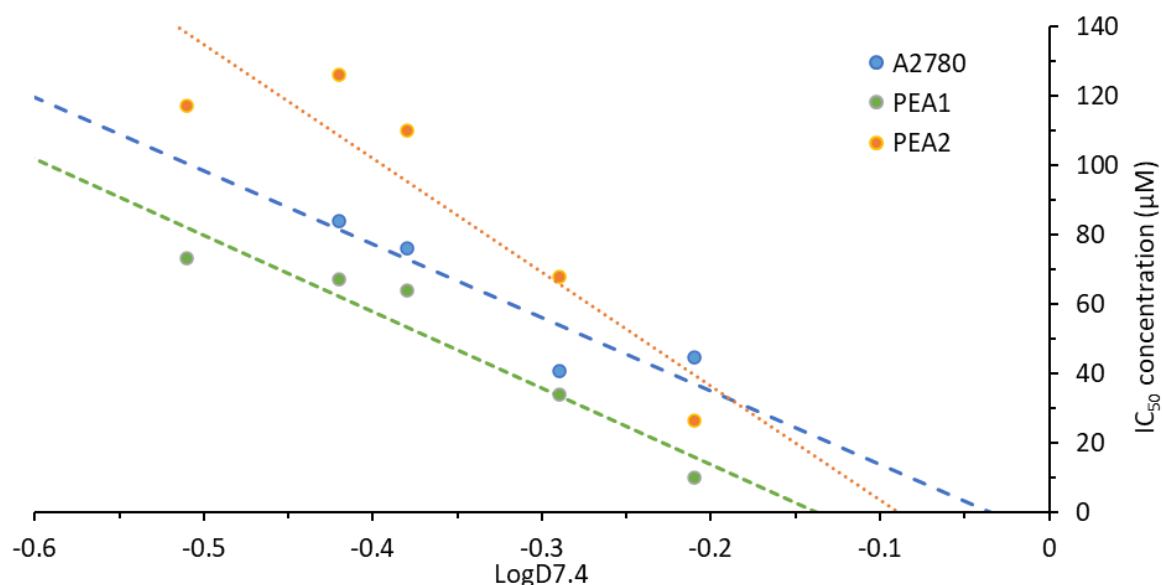
Figure 3-10: Graphical representation of the corelation between $LogD_{7.4}$ and IC_{50} value in cell lines where more than four IC_{50} values were less than 140 µM. In all three EOC cell lines, there is a remarkable trend with increasing lipophilicity and decreasing IC_{50} of the complexes screened.

3-3.3: Preliminary mode of action screening of complex 6

3-3.3.1: Mitochondrial depolarisation

As ΔΨm depolarisation is a common MOA of ruthenium piano-stool complexes, depolarisation was tested by fluorescence microscopy using Rh123 staining shown in Figure 3-11. Rh123 is a cationic dye which fluoresces green when the ΔΨm is polarised but does not fluoresce when polarisation is lost. The negative control, CDDP nor PTX treatments did not depolarise the ΔΨm, while complex *6* induced complete loss of fluorescence at 0.5X IC_{50} concentrations.
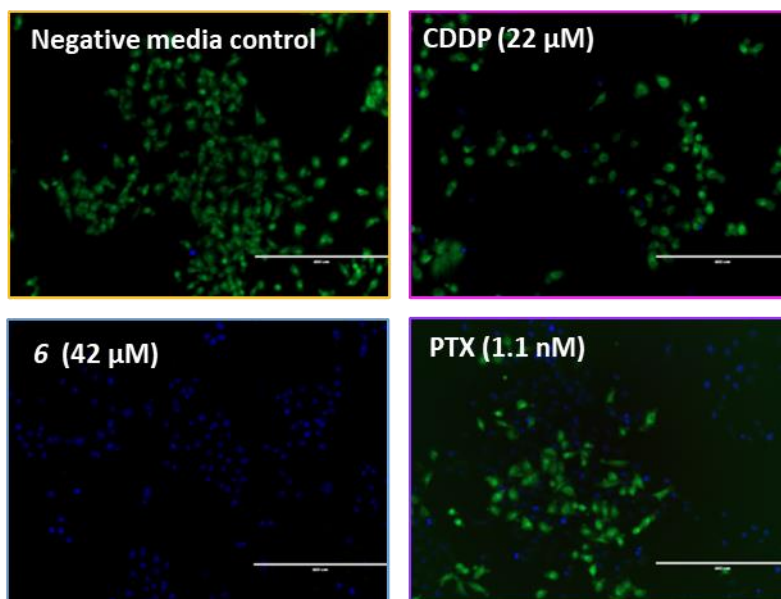
Figure 3-11: Evaluation of mitochondrial depolarisation in SKOV3 cells treated with media as negative control, CDDP 2X IC_{50} (22 µM), *6* 0.5X IC_{50} (42 µM) or PTX 2X IC_{50} (1.1 nM). Cells stained with Rh123 (green), DAPI (blue) and PI (red). Images presented as overlays of green, blue, and red channels at 10X magnification (scale bar 400 µm).

3-3.3.2: ROS generation

Often coupled with ΔΨm depolarisation and a common MOA of ruthenium complexes, ROS generation was tested by fluorescence microscopy, using DCFDA is shown in Figure 3-12. DCFDA is a fluorescent probe that fluoresces green in the presence of ROS species. The negative control, CDDP or PTX did not induce visible ROS levels, while complex *6*, Luperox and hydrogen peroxide induced ROS generation. Interestingly, *6* induced hotspots of ROS generation in ~35% of the cell population in comparison to hydrogen peroxide which has a consistent lower-level staining across all cells. Further investigation using fluorescence intensity of DCFDA (Figure 3-13) indicates that at 0.5X IC_{50}, *6* did not induce any significant difference in ROS generation compared to the control. However, generation is dose dependant with higher levels at 2.5X IC_{50} concentrations, ROS was induced in levels comparable to Luperox and hydrogen peroxide.
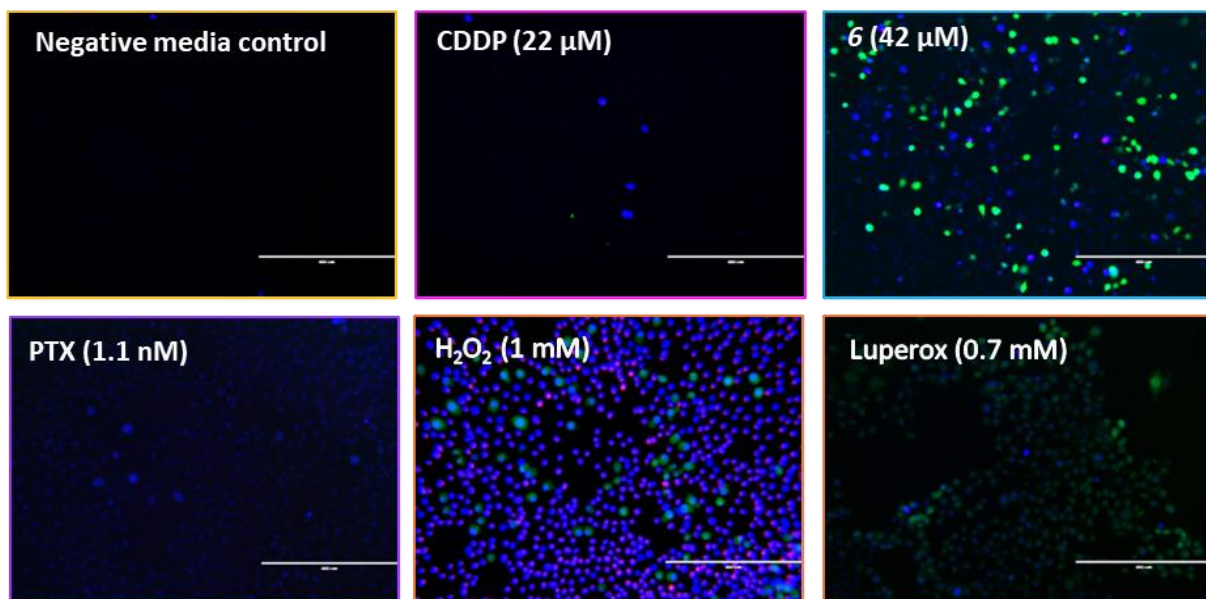
Figure 3-12: Evaluation of ROS generation in SKOV3 cells treated media as negative control, CDDP 2X IC$_{50}$ (22 µM), **6** 0.5X IC$_{50}$ (42 µM), PTX 2X IC$_{50}$ (1.1 nM), 1 mM hydrogen peroxide, or 0.7 mM Luperox, then stained with DCFDA (green), DAPI (blue) and PI (red). Images presented as overlays of the green, blue, and red channels at 10X magnification (scale bar: 400 µm).
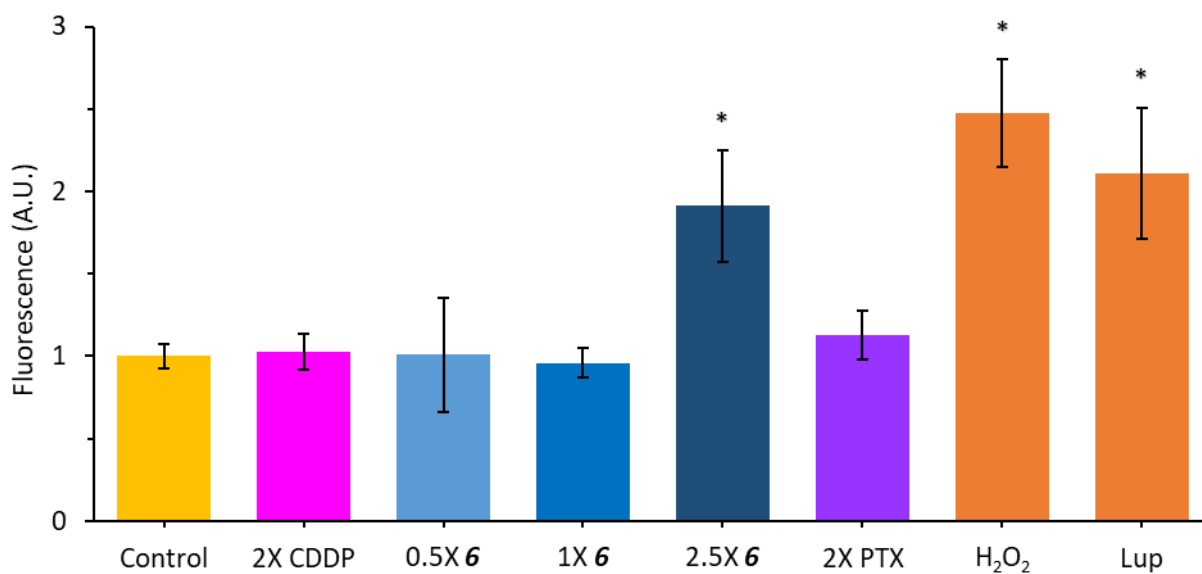
Figure 3-13: Evaluation of ROS generation in SKOV3 cells treated with media as negative control, CDDP 2X IC$_{50}$ (22 µM), **6** 0.5X IC$_{50}$ (42 µM), PTX 2X IC$_{50}$ (1.1 nM), 1 mM hydrogen peroxide, or 0.7 mM Luperox, stained with DCFDA and fluorescence intensity normalised by protein content. (Significance determined by Welch t-test where * indicates $p < 0.05$, ** indicates $p < 0.01$, and *** indicates $p < 0.001$ levels of significance).

Cell cycle arrest

With replication arrest being highly effective in the inhibition of cancer growth and indicative of MOA of a complex, cell cycle arrest was assessed by flow cytometry (Figure 3-14). Using PI and RNase, fluorescence intensity is directly proportional to DNA quantity, therefore when DNA doubles in replication, population proportions compared to a control population can indicate cell cycle arrest. CDDP at 2X IC_{50} significantly ($p<0.01$) induced S phase arrest by reducing the G_0/G_1 population. However, PTX at 2X IC_{50} and **6** at 0.5X IC_{50} did not induce significant cell cycle arrest.
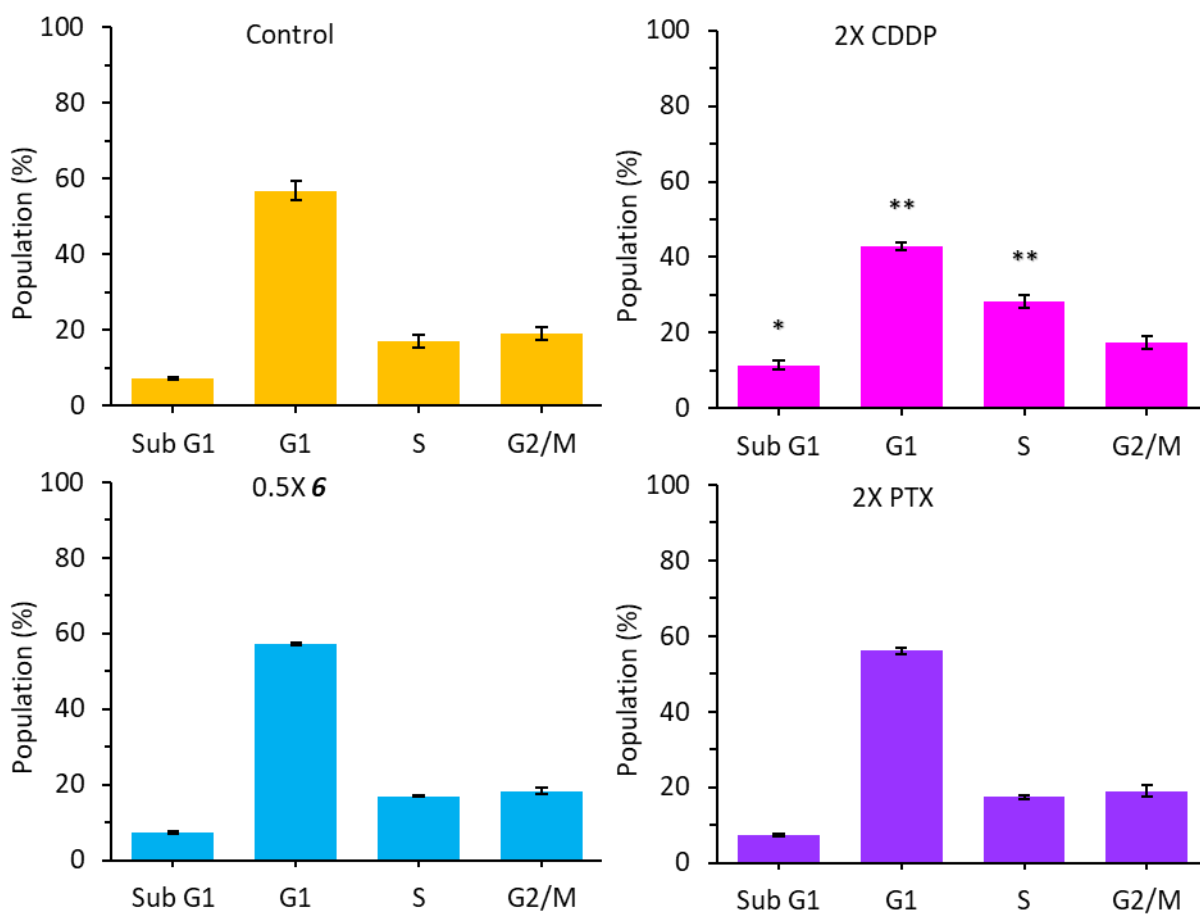
Figure 3-14: Cell cycle arrest of SKOV3 cells by flow cytometry treated with media as negative control, CDDP 2X IC_{50} (22 µM), **6** 0.5X IC_{50} (42 µM), or PTX 2X IC_{50} (1.1 nM), stained with PI and RNase. (Significance determined by Welch t-test where * indicates $p<0.05$, ** indicates $p<0.01$, and *** indicates $p<0.001$ levels of significance).

3-3.3.3: Wound healing assay

With invasion being a key process in the progression of cancer, the wound healing assay was used as an *in vitro* model. Wound closure was measured from T=0 (monolayer wounding when cells were drugged), to T=24 (after 24 hours treatment exposure), and T=24+72 (after 24 hours treatment exposure time followed by 72 hours recovery time). Wound measurements and images are shown in Figure 3-15 and Figure 3-16 respectively.

Only PTX prevented significant (p<0.05) wound closure following 24 hours of drug exposure with both CDDP and *6* treatment not preventing significant wound closure. Yet, with the inclusion of 72 hours recovery time, both *6* and PTX significantly (p<0.05 and p<0.01, respectively) prevent wound closure.
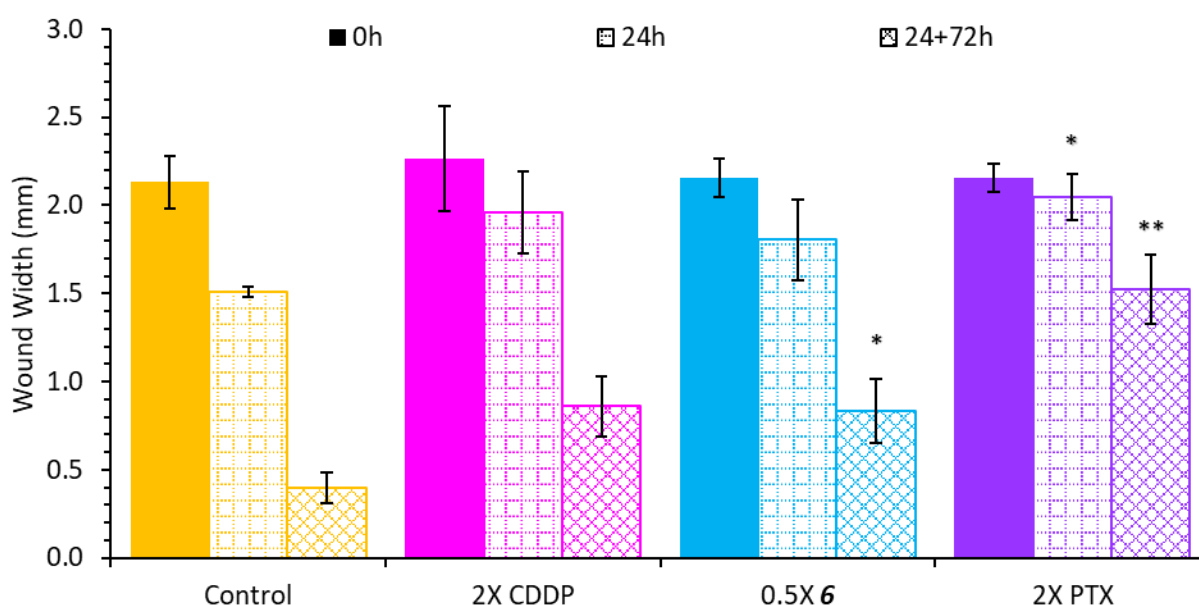
Figure 3-15: Averages of the wound widths of the wound healing assay of SKOV3 cells treated with media as negative control, CDDP 2X IC_{50} (22 µM), *6* 0.5X IC_{50} (42 µM), or PTX 2X IC_{50} (1.1 nM) at 0 hours (monolayer wounding and start of treatment exposure), 24 hours (following treatment exposure) and 24 + 72 hours (total wound closure including 24 hours treatment and 72 hours recovery time). (Significance determined by Welch t-test where * indicates p<0.05, ** indicates p<0.01, and *** indicates p<0.001 levels of significance).
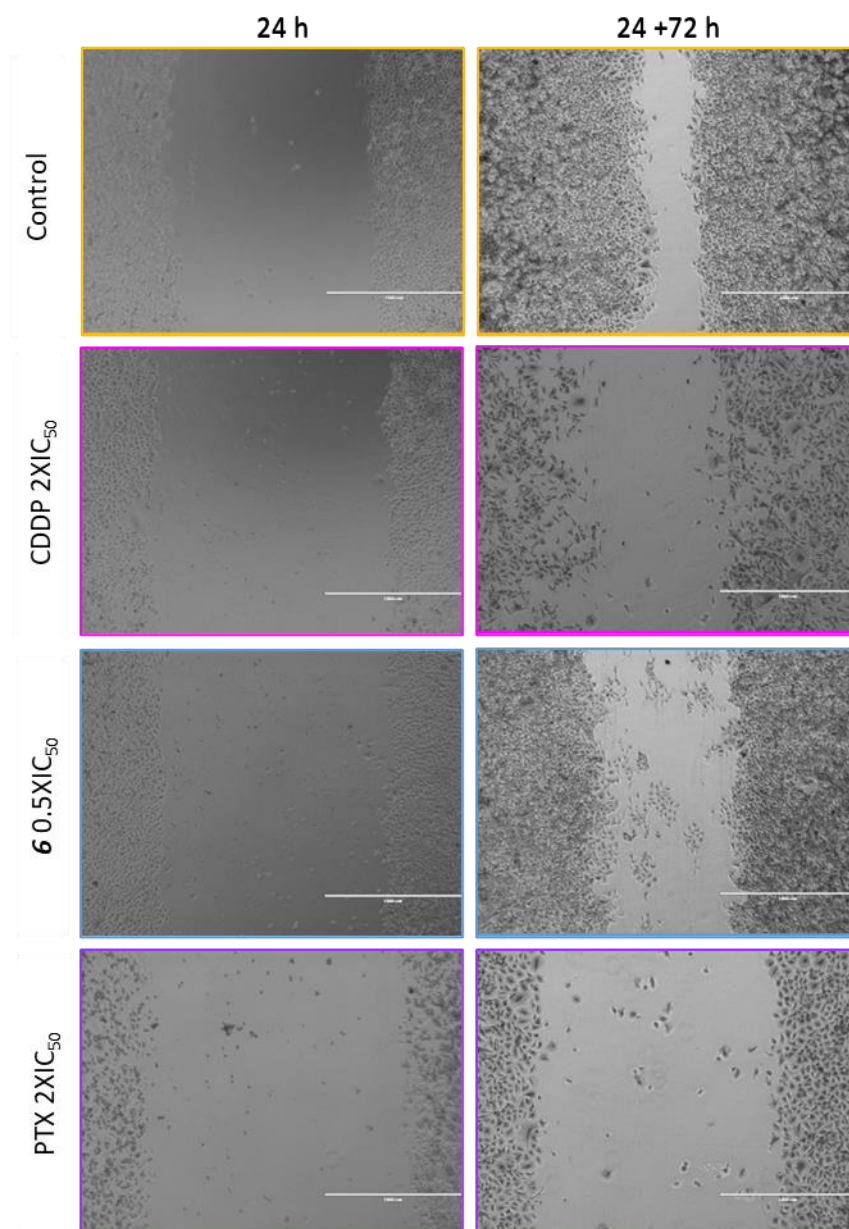
Figure 3-16: Wound healing assay of SKOV3 cells treated with media as negative control, CDDP 2X IC_{50} (22 μM), **6** 0.5X IC_{50} (42 μM), or PTX 2X IC_{50} (1.1 nM), with images taken at 24 hours (following treatment exposure) and 24 + 72 hours (total wound closure, including 24 hours treatment and 72 hours recovery time). Images taken at 4X magnification, scale bar: 1000 μm.

3-3.3.4: Colony formation

In tandem with invasion evaluation, colony formation is used as an *in vitro* model of metastatic potential. The colony formation assay was carried out using a 24-hour exposure period followed by a seven-day colony growth period).
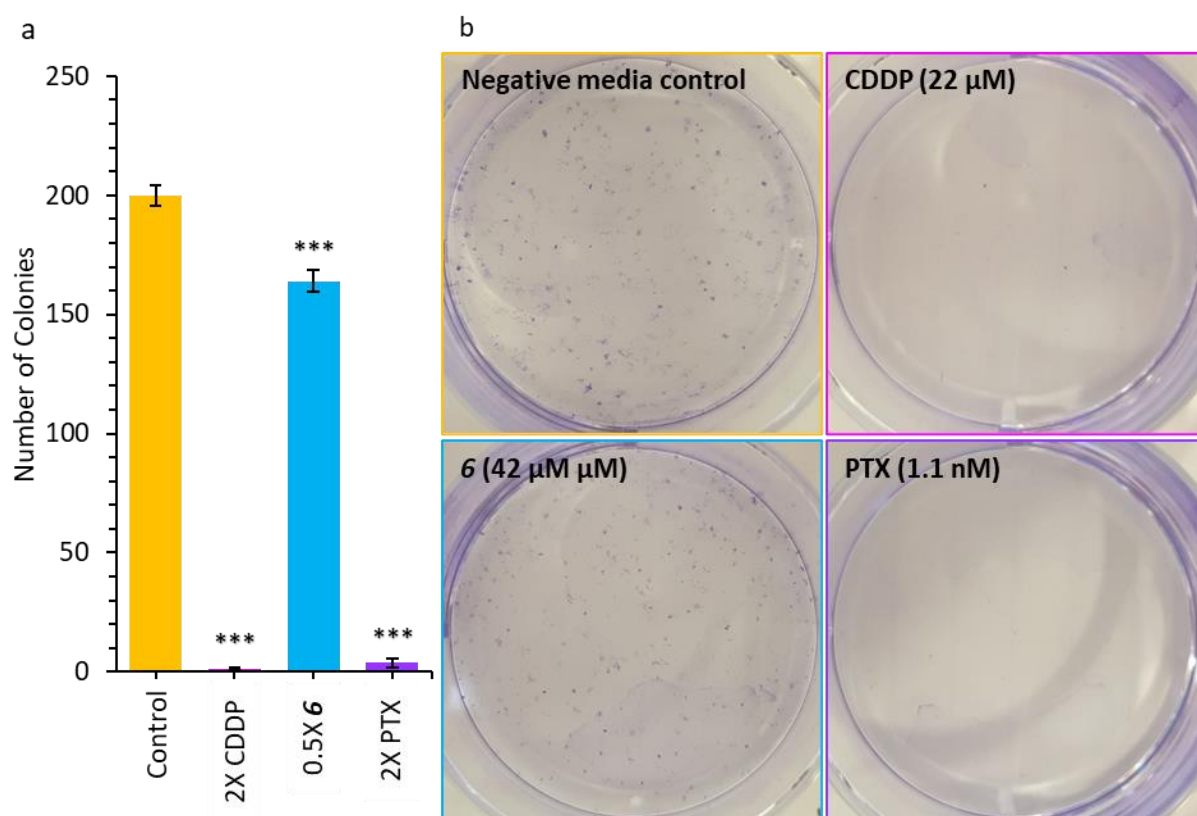
Figure 3-17: a). average colony counts and b). well images at 1X magnification of the colony formation assay of SKOV3 cells treated with media as negative control, CDDP 2X IC$_{50}$ (22 µM), **6** 0.5X IC$_{50}$ (42 µM), and PTX 2X IC$_{50}$ (1.1 nM) (significance determined by Welch t-test where *** indicates p<0.001 level of significance).

Colony count evaluation is shown in Figure 3-17. All treatments used here significantly (p<0.001) reduced growth. However, it must be noted that that an average of 164 colonies developed compared to the control of 200 colonies, whereas CDDP and PTX treatment led to the growth of an average of ten colonies per test.

In addition to the number of colonies, colony density was also evaluated to assess the effectiveness and growth following metastasis. All off the treatments significantly (P<0.001) decreased the density of the colonies that grew (Figure 3-18). Treatment with complex **6** induced a 48% decrease in colony density, while CDDP and PTX treated cells developed colonies with less than ten cells present. In addition, evaluation of colony morphology, **6** treated cells develop colonies that diffuse in nature in comparison to the control colonies.
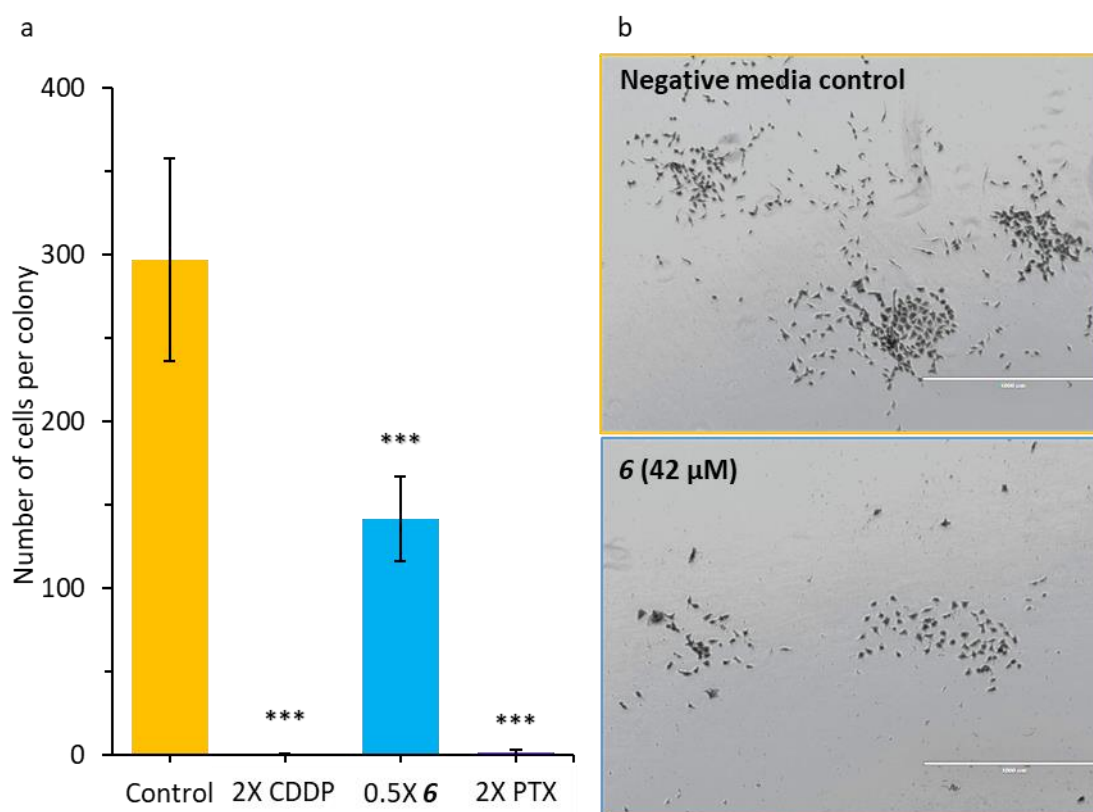
Figure 3-18: a). average colony density and b). images of the colonies formed in the colony formation assay of SKOV3 cells treated with media as negative control, CDDP X2 IC_{50}, *6* 0.5X, 1 and 2.5 IC_{50}, PTX X2 IC_{50}. (Significance determined by Welch t-test where * indicates $p<0.05$, ** indicates $p<0.01$, and *** indicates $p<0.001$ levels of significance). Images taken at 4X magnification, scale bar: 1000 μm.

3-3.4: Mechanism of cell death testing of 6

3-3.4.1: Apoptosis induction

As cells have several MOD to induce death appropriate to the cellular stimuli with apoptosis being one of the mostly observed and tested mechanisms, it was investigated by flow cytometry. Using Annexin V/PI staining, extent of apoptosis can be determined, demonstrated by Figure 3-19.

Apoptosis analysis populations of SKOV3 cells treated with *6* at 0.5X, 1X and 2.5X IC_{50}, CDDP 2X IC_{50}, PTX 2X IC_{50} and STS at 1 μM is shown in Figure 3-20. CDDP induced significant early and late-stage apoptosis ($p<0.05$ and $p<0.01$, respectively) without an increase in the non-viable population while PTX only induced a fractional but significant ($p<0.05$) early phase apoptosis. Complex *6* induces

apoptosis dose dependently with the late-stage population increasing from 1% (p<0.05) to 41% (p<0.001) in 0.5X IC_{50} and 2.5X IC_{50} treated cells, respectively. This similar trend is also observed in the early apoptotic population of **6** treated cells but to a lesser extent with the population increasing from 1% (p=0.1) to 13% (p<0.001) with increasing dose. This trend however is not observed in the non-viable population, where there is only a significant (p<0.05) increase in the non-viable population in **6** 2.5X IC_{50} treated cells.
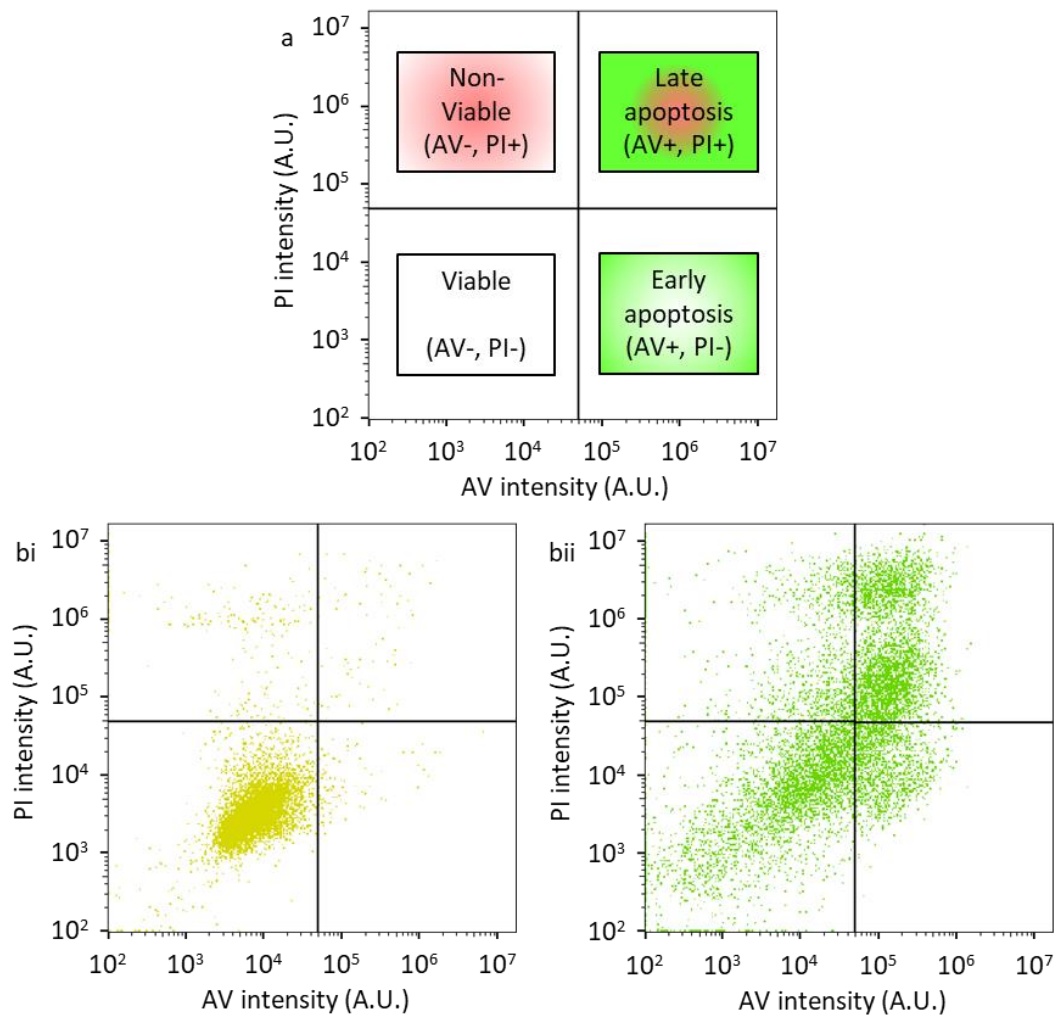
Figure 3-19: Apoptosis by flow cytometry theory and a). gating strategy and corresponding apoptotic populations by fluorescence intensity using bi). the untreated negative control, and bii). the positive control such as STS.
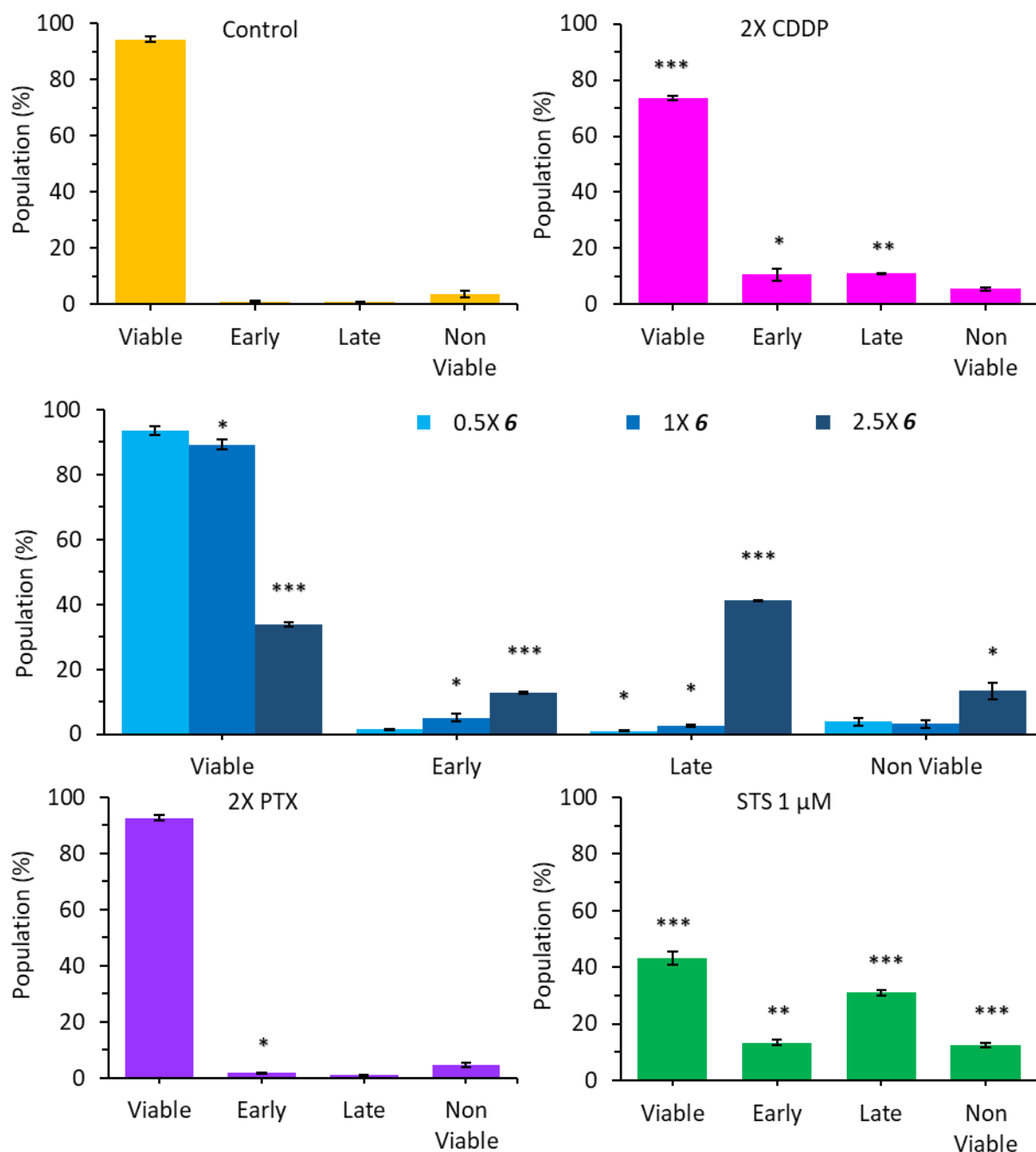
Figure 3-20: Apoptosis induction by flow cytometry of SKOV3 cells treated with media as negative control, CDDP 2X IC_{50} (22 µM), *6* at 0.5X (42 µM), 1X (84 µM) and 2.5X (211 µM) IC_{50}, PTX 2X IC_{50} (1.1 nM), or 1 µM STS, then stained with PI and Annexin V. (Significance determined by Welch t-test where * indicates $p<0.05$, ** indicates $p<0.01$, and *** indicates $p<0.001$ levels of significance).

3-3.4.2: Caspase activity

Due to the evidence in the apoptosis assay, caspase activity was investigated colourimetrically, normalised by protein content (Figure 3-21).
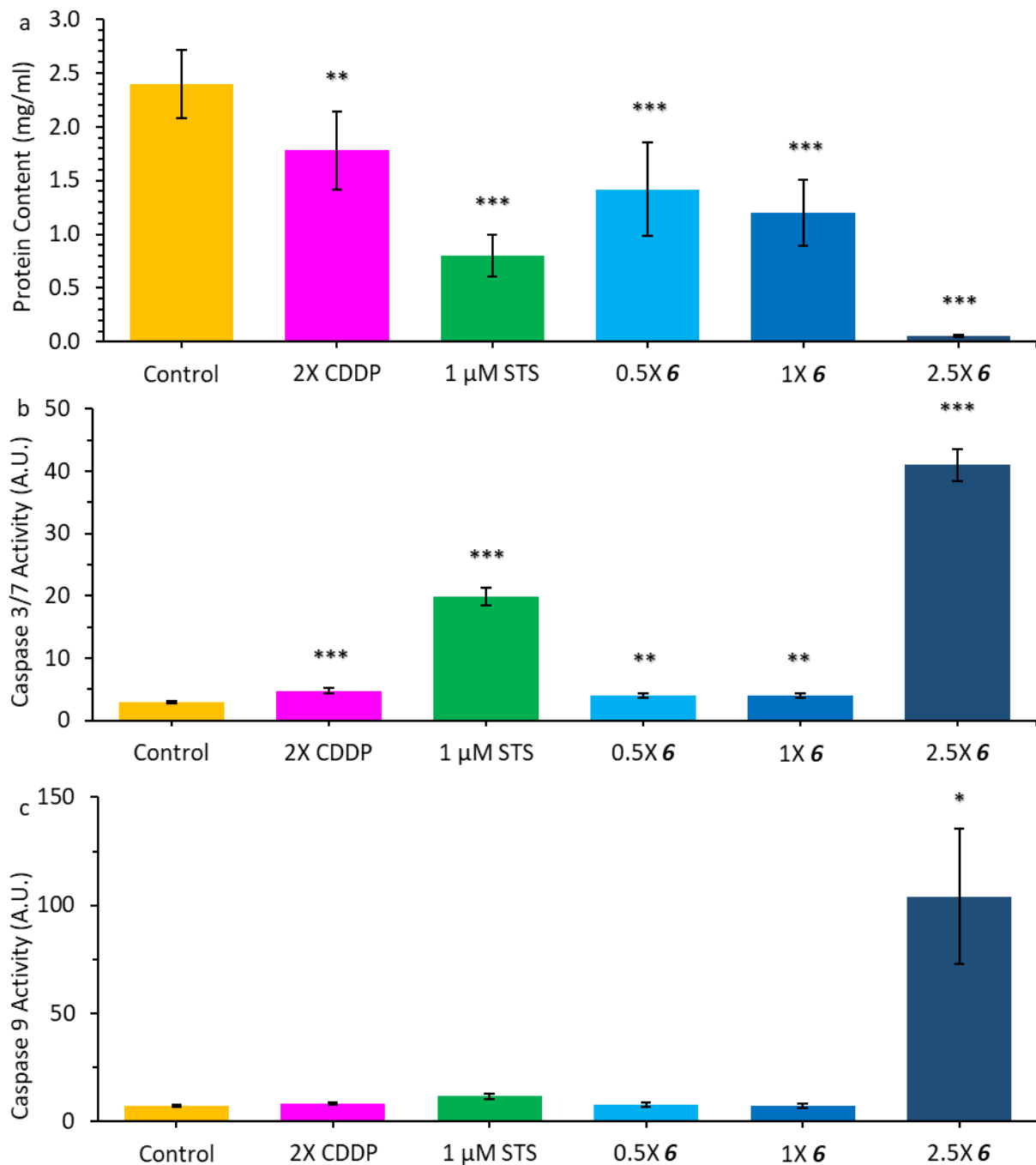
Figure 3-21: Quantitative assessment of a). protein content, b). Caspase 3/7 activity, c). Caspase 9 activity of SKOV3 cells treated with media as negative control, CDDP 2X IC_{50} (22 μM), **6** at 0.5X (42 μM), 1X (84 μM), and 2.5X (211 μM) IC_{50}, or 1 μM STS. (Significance determined by Welch t-test where * indicates $p<0.05$, ** indicates $p<0.01$, and *** indicates $p<0.001$ levels of significance).

Protein content decreased with cytotoxic treatment (Figure 3-21a). Interestingly, **6** treated cells exhibit

significantly lower protein levels dose dependently with content decreasing from 1.4 mg/mL to 0.1

mg/mL with concentration increasing from 0.5X IC_{50} to 2.5X IC_{50}. This decrease cannot be attributed to

103

cell death as cells treated with CDDP at 2X IC_{50} has been previously shown to induce more apoptosis than cells treated with *6* at 0.5X IC_{50}, yet protein content is lower in *6* treated cells being 1.8 mg/mL compared to 1.4 mg/mL.

Caspase 3/7 activity (Figure 3-21b) was increased in all treatments to a significant level ($p<0.01$). As expected, *6* treated cells Caspase 3/7 activity was dose dependent in a similar trend to the apoptosis assay with a 10.8X increase between *6* at 0.5X IC_{50} and 2X IC_{50}. However, there is no significant difference between the 0.5X and 1X IC_{50} doses.

Due to the indications of Caspase 3/7 having higher activity in *6* treated cells, Caspase 9 was also investigated as being a biochemical precursor and an indicator of intrinsic apoptosis often triggered by mitochondrial and DNA damage (Figure 3-21c). While CDDP and STS did induce an increase in Caspase 9 activity it was not statistically significant. However, *6* did induce significant ($p<0.05$) levels of Caspase 9 activity at 2.5X IC_{50} concentrations.

3-3.4.3: Cellular morphology by fluorescence microscopy

With the evidence that complex *6* treatment leads to decreased protein content, and CCM permeabilization, cell and CCM morphology was investigated by fluorescence microscopy using a CCM intercalating dye (Figure 3-22). Neither CDDP nor PTX treatment induces a loss of red fluorescence and cellular morphology remains intact similar to the untreated control. However, when treated with increasing concentrations of complex *6*, membrane dye fluorescence decreases. In addition to the alterations in the CCM, *6* treated cells exhibit a shrunken morphology, even at low treatment concentrations. To determine if CCM dye fluorescence loss is due to loss of CCM integrity, PI fluorescence from the apoptosis assay was collated (Figure 3-23). At 2.5X IC_{50}, *6* exhibits a significant ($p<0.01$) increase with 54% of the population exhibiting positive levels of PI fluorescence, corelating with CCM dye loss.
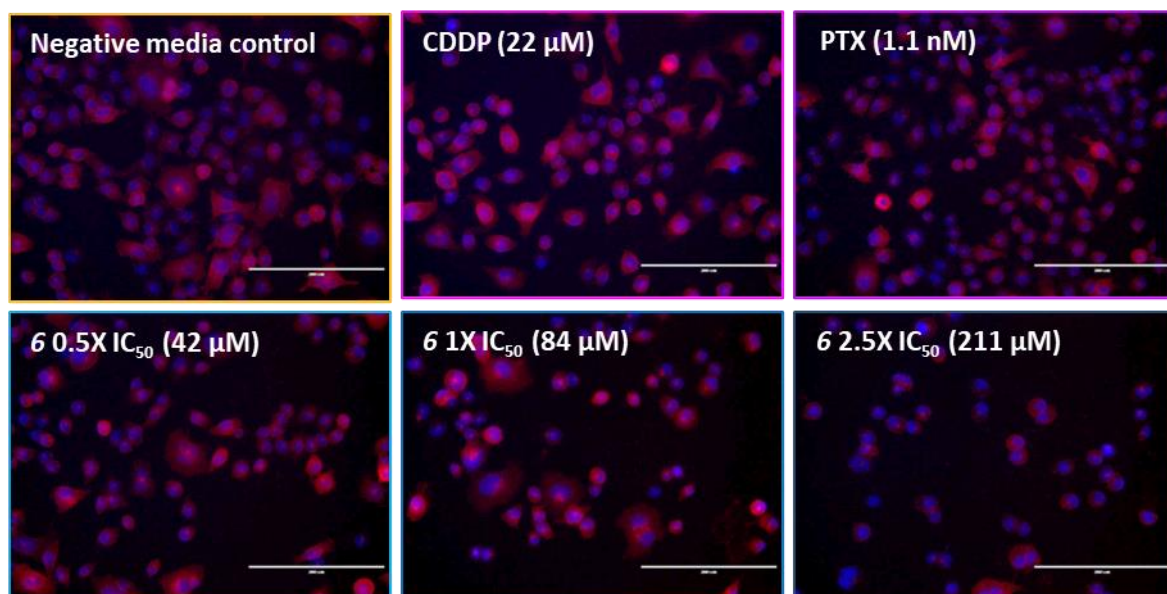
Figure 3-22: Cellular morphology of SKOV3 cells treated with media as negative control, CDDP 2X IC$_{50}$ (22 μM), PTX 2X IC$_{50}$ (1.1 nM), **6** at 0.5X (42 μM), 1X (84 μM), or 2.5X (211 μM) IC$_{50}$, stained with Cell Brite Red membrane dye (red) and DAPI (blue). Images presented as overlays of the red and blue channels the taken at 20X magnification, scale bar: 200 μm.
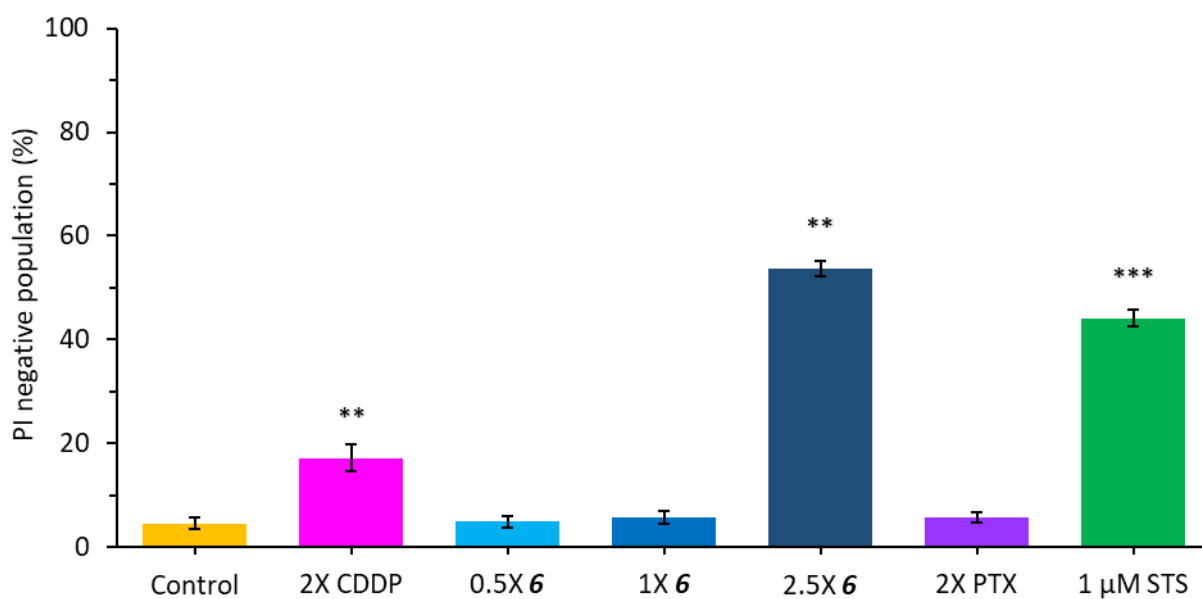
Figure 3-23: Membrane integrity by flow cytometry of SKOV3 cells treated with media as negative control, CDDP 2X IC$_{50}$ (22 μM), **6** at 0.5X (42 μM), 1X (84 μM), and 2.5X (211 μM) IC$_{50}$, PTX 2X IC$_{50}$ (1.1 nM), or 1 μM STS, then stained with PI. (Significance determined by Welch t-test where * indicates $p<0.05$, ** indicates $p<0.01$, and *** indicates $p<0.001$ levels of significance).

3-3.4.4: Autophagy activity

Type II MOD are also important in cancer cell death, including the under/over activation of autophagy. This was investigated by fluorescence microscopy and intensity (Figure 3-24 and Figure 3-25, respectively). CDDP, STS and *6* at 1X IC_{50} induced a significant (p<0.05) increase in autophagy. This contrasts PTX, *6* at 0.5X and 2.5X IC_{50} which did not induce any difference to the negative control.
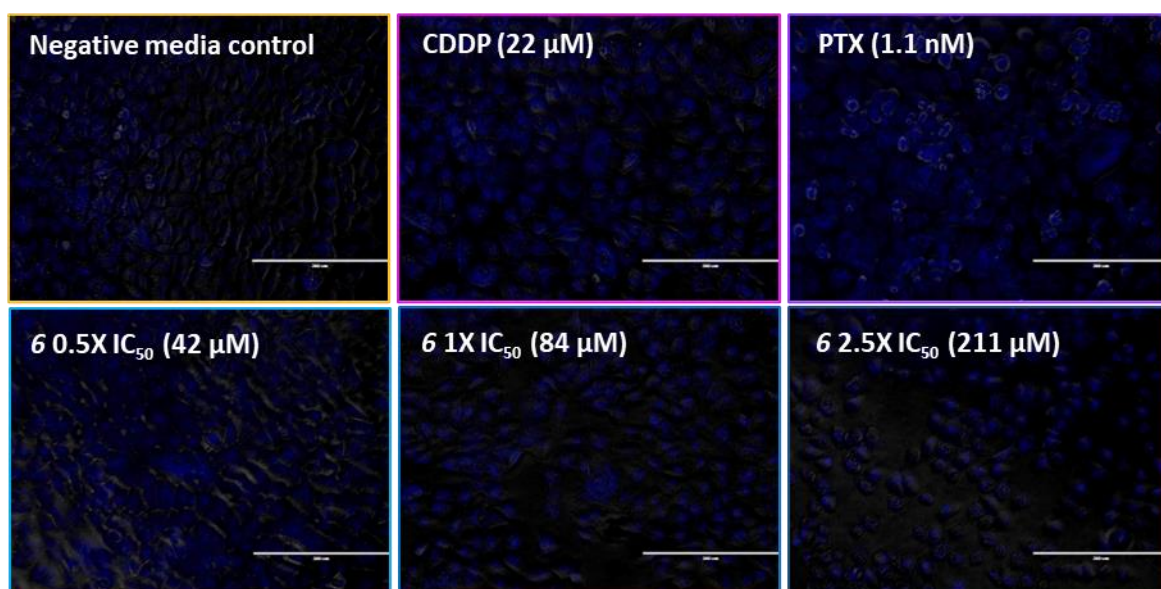
Figure 3-24: Autophagy microscopy of SKOV3 cells treated with a). media as negative control CDDP 2X IC_{50} (22 µM), PTX 2X IC_{50} (1.1 nM), *6* at 0.5X (42 µM), 1X (84 µM), or 2.5X (211 µM) IC_{50}, stained with ATT Bioquest Cell Meter™ Autophagy Assay Kit. Images presented as overlays of the blue and transmission channels the taken at 10X magnification, scale bar: 400 µm.
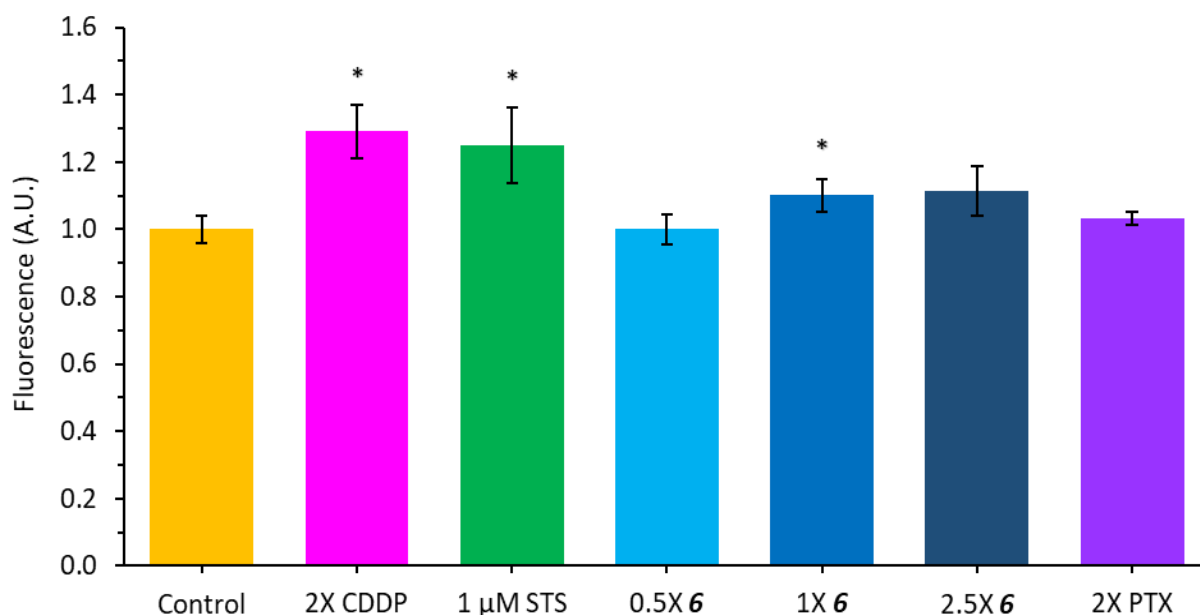
Figure 3-25: Autophagy activity in SKOV3 cells treated with media as negative control, CDDP 2X IC$_{50}$ (22 µM), **6** at 0.5X (42 µM), 1X (84 µM), and 2.5X (211 µM) IC$_{50}$, PTX 2X IC$_{50}$ (1.1 nM), or 1 µM STS. (Significance determined by Welch t-test where * indicates p<0.05, ** indicates p<0.01, and *** indicates p<0.001 levels of significance).

3-3.4.5: Ferroptosis inhibition

The induction of ferroptosis was investigated by growth inhibition by co-treatment with the ferroptosis inhibitor FER-1 (Figure 3-26). FER-1 was demonstrated to be an effective inhibitor of ferroptosis even at 0.25 µM co-treatment with all concentrations of ERA at IC$_{50}$. FER-1 induced very little improvement in survival in the control and STS treatment populations being 3% and 1% respectively. The maintained survival of the control population even at 1.2 µM doses of FER-1 indicate that FER-1 does not induce growth inhibition. Interestingly, FER-1 did provide some protection against CDDP and PTX at 0.25 µM of 28% and 18% respectively, however this subsides in a dose dependant manner with growth inhibition improving to 0 µM FER-1 concentrations in PTX. This trend is not observed in **6** treated cells in all three treatment concentrations tested. Remarkably, FER-1 does offer a marginal increase in survival of 6.4% in 0.25X IC$_{50}$ to 17% in 1.25X IC$_{50}$ treated cells. However, these increases in survival are lower than the inhibition seen in CDDP, PTX and ERA treated cells.
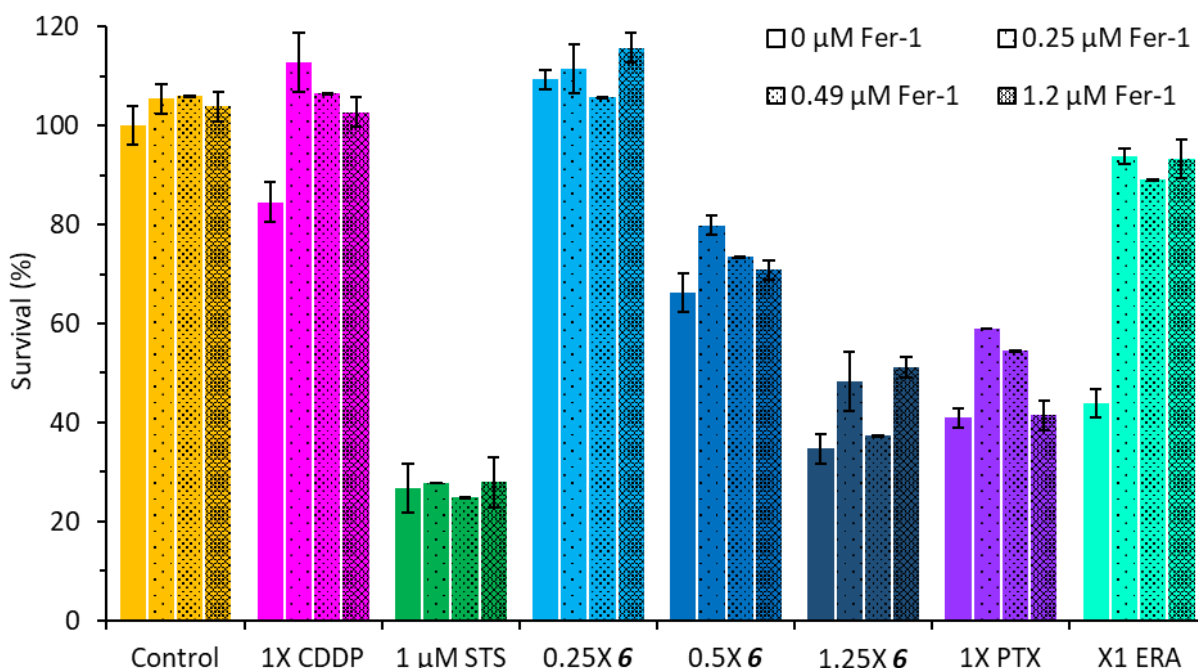
Figure 3-26: Ferroptosis inhibition using ferrostatin at 0, 0.25, 0.49, 1.2 µM of SKOV3 cells treated with media as negative control, CDDP 1X IC$_{50}$ (11 µM), **6** 0.25X (21 µM), 0.5X (42 µM), 1.25X IC$_{50}$ (105 µM), PTX 1X IC$_{50}$ (0.6 µM), 1 µM STS, and ERA 1X IC$_{50}$ (5.38 µM) shown through cell survival.

3-3.4.6: Co-treatment studies with complex 6

Due to the ROS induction and CCM effects previously observed, the co-treatment with the ferroptosis inducer ERA was also investigated by growth inhibition (Figure 3-27). As shown in the untreated control, with the increase in ERA concentration, survival decreases dose dependently. This similar trend is also observed to a lower extent in STS. CDDP also demonstrated a similar trend with survival not decreasing with increasing concentrations of ERA until a sharp increase at 3X IC$_{50}$. Remarkably, **6** induced sharp decreases in survival rates when co-treated with ERA. With co-treatment of SKOV3 with **6** 0.25X IC$_{50}$ and ERA 0.5X IC$_{50}$ a survival rate of 34%, with independent survival rates of 78% and 77% respectively. Furthermore, this enhancement effect is seen dose dependently in **6** 0.25X and 0.5X IC$_{50}$ treated cells achieving 5% survival in **6** 0.5X IC$_{50}$ and ERA 3X IC$_{50}$ treated cells. Yet, in **6** 1.25X IC$_{50}$ treated cells, as concentration of ERA was increased, survival marginally increased from 2±0.6% to 5±0.9%.
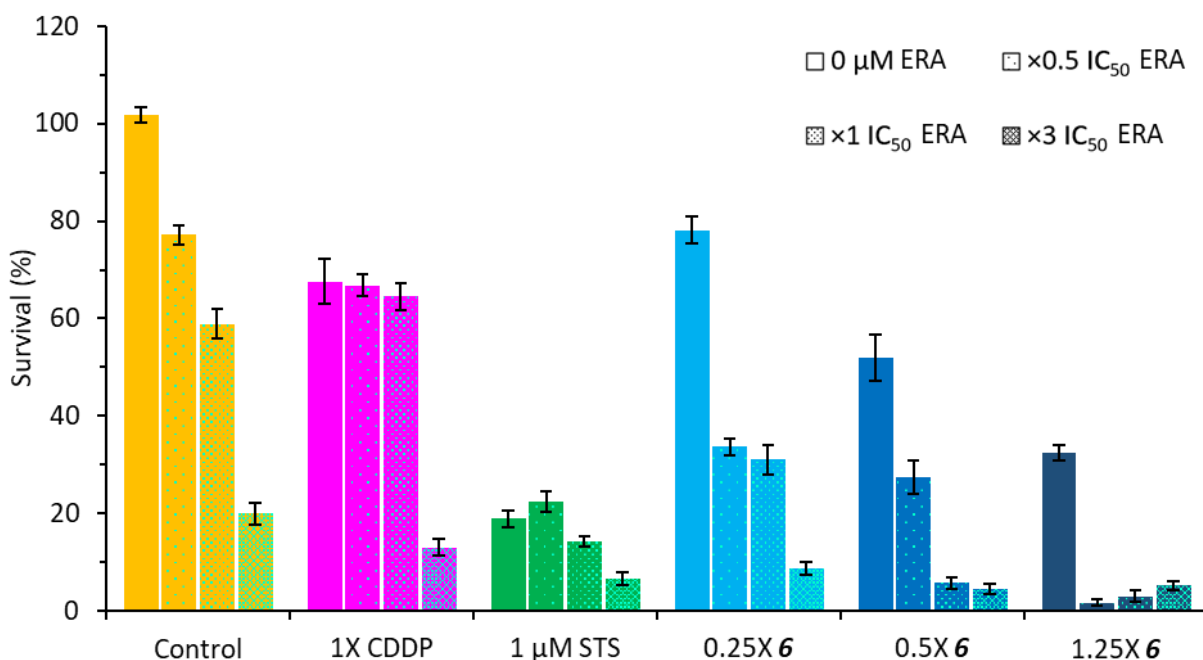
Figure 3-27: Co-treatment of SKOV3 cells treated with media as negative control, CDDP 1X IC_{50} (11 μM), *6* 0.25X (21 μM), 0.5X (42 μM), 1.25X IC_{50} (105 μM), or 1 μM STS with ERA 0.5X (2.7 μM), 1X (5.4 μM) and 3X (16.3 μM) IC_{50} to assess enhancement of complex activity shown through cell survival.

Observing the increased potency and the implicated mechanisms of *6* with ERA. Co-treatment of *6* with L-BSO was evaluated (Figure 3-28). Use of L-BSO was impotent with a cell survival of 105% (±3.4%) in A2780 compared to the negative control with a survival of 101.91% (±4.87). In SKOV3 (Figure 3-28a), with the addition L-BSO, potency of CDDP and *6* improved with the IC_{50} concentrations decreasing by 26% and 46%, achieving IC_{50} values of 7.6 μM and 45.8 μM respectively. This potential was also evaluated in A2780 (Figure 3-28b), with CDDP and *6* both achieving an improvement in potency with IC_{50} values decreasing by 47% and 87% with values of 1.9 μM and 5.63 μM respectively. In addition, the impotent and unsubstituted complex *1* was also evaluated in A2780, and with the co-treatment of L-BSO, *1* became significantly more potent achieving an IC_{50} value of 63.6 μM, a minimum of a 2.2X increase in potency.
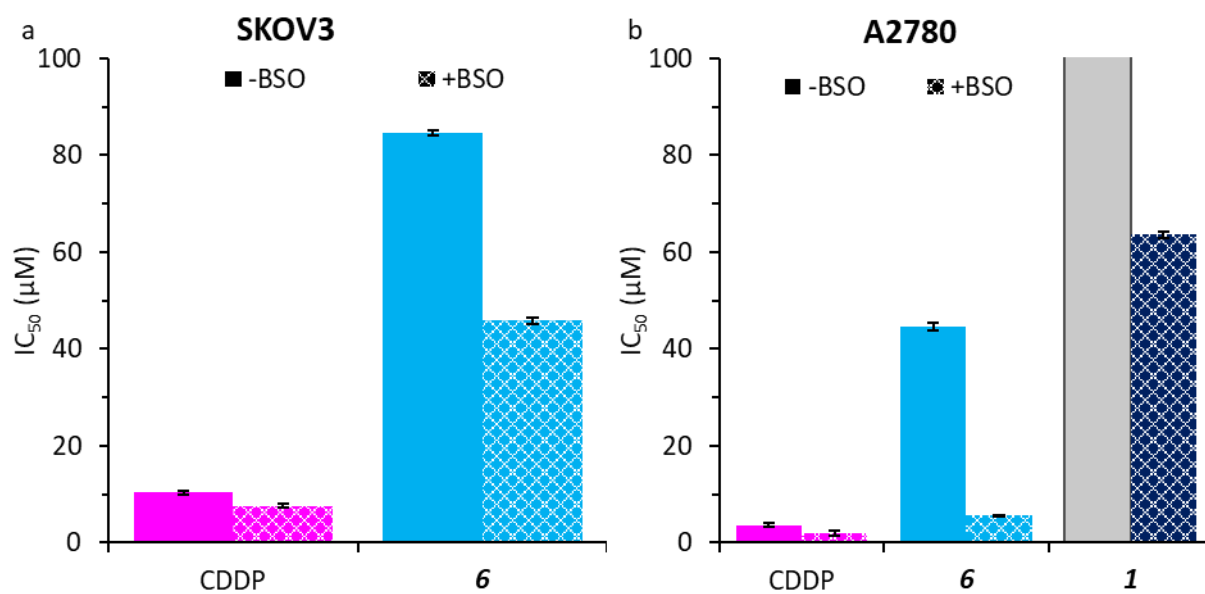
Figure 3-28: L-BSO co-treatment: Co-treatment of a). SKOV3 cells, b). A2780 cells treated with CDDP, **6**, or **1** with 5 µM L-Buthionine sulfoximine (BSO) to assess enhancement of complex activity shown through IC_{50} values. (IC_{50} value for **1** in A2780 is greater than 140 µM shown in grey).

3-4: Discussion

In this chapter, the potential of methyl derivatives in EOC was investigated, from this complex **6** due to its superior efficacy was selected for further death mechanism testing.

3-4.1: Preliminary physiochemical investigations of methyl bioisosteric complexes

The complexes proposed in Table 3-3 were successfully synthesised, in good yield and sufficient purity for initial physiochemical and growth inhibition screening. Structural elucidation was mostly based on NMR data. In particular the ^{1}H-NMR spectrum shows the expected patterns for a *p*-cymene unit in a piano-stool complex which includes symmetric methyl signals for the isopropylic group, as well as, a de-shielded methyl group as a singlet. The aromatic rings show the classical two-doublet signals that can be associated with a 1,4-di substituted benzene. The N,N-chelating ligand also contains two aromatic rings, the first pyridinic one with a 1,2- substitution and the second, derived from the aniline unit with para- substituents that generate two coupling doublets. This ligand also contains an isopropylic unit shifted downfield as a consequence of the latter ring. Signals with very characteristic chemical shift include the alpha proton to the pyridine nitrogen, appearing as a doublet at 9.57 ppm and most importantly the iminic proton as a singlet at low field in 8.90 ppm.

The complexes were then assessed for interactions with biologically relevant matrixes to identify any potential MOA, detoxification methods and alterations of the complexes during testing. Here, all complexes interacted with GSH, media and full media. Further interaction studies of **6** with GSH showed when in an equimolar system over time, **6** and GSH exhibit a hyperchromic and hypsochromic blue shift. However, when the concentration of GSH is titred, a significantly bathochromic red shift and hypochromism were seen. This behaviour is consistent with other reports of organometallics and the covalent interaction with GSH[40–44]. This has been hypothesized to be through the aquation of the

complex chlorine ligand, which is then directly substituted with GSH, forming the GSH-complex adduct[41]. The interaction of the complexes with GSH is not unexpected. Many chemotherapeutics such as CDDP interact with GSH, as part of cytoprotective mechanisms shown in Figure 3-29[45,46]. GSH can directly bind to CDDP and form Pt-GS adducts which can be exported by the multidrug resistance proteins, ABC transporters, for nephritic excretion[45]. ABCC2 is the primary channel used by GSH and is ATP dependant for activity[47]. In addition, GSH can also detoxify hydrogen peroxide by converting it to water and glutathione disulphide (GSSG) using GSH peroxidase. CDDP can also bind to GSSG forming $Pt(GS)_2$, which can also be actively transported from the cell.
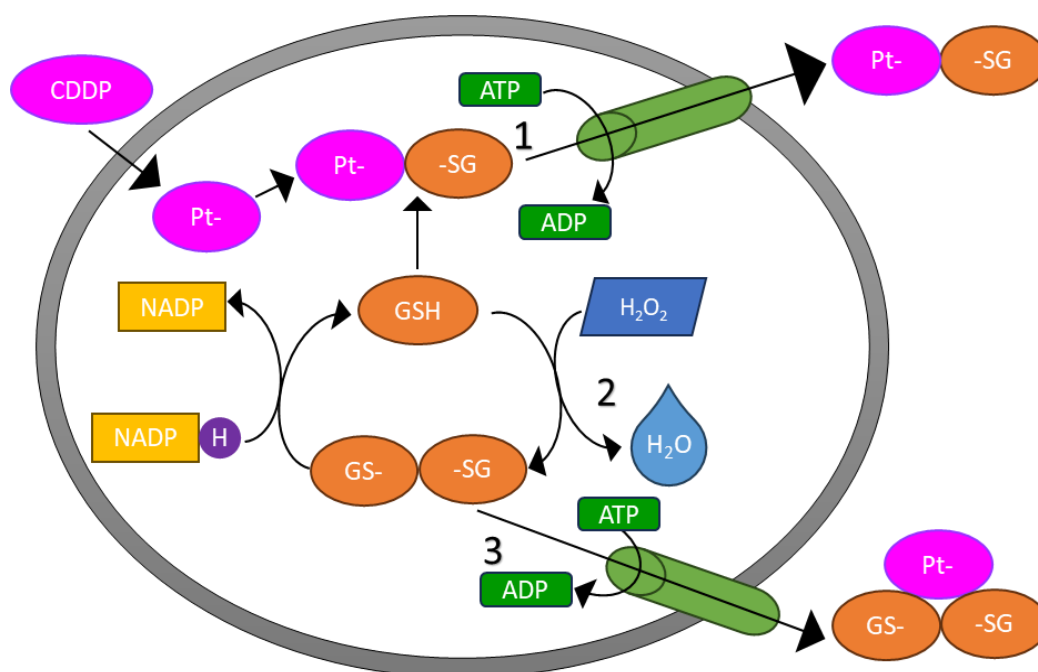
Figure 3-29: GSH cellular protective mechanisms in regards to the mechanisms of action of platinum complexes such as cisplatin. 1). The formation of Pt-GSH adducts and their export. 2). The detoxification of hydrogen peroxide by formation of glutathione disulfide (GSSG). 3). The export of PT-GSSG adducts.

The interaction between the complexes and media/full media here is unlikely to be due to GSH. RPMI-1640 formulations contain 1 mg/L of GSH, resulting in total amount of 1.6 µM in the final media matrix[48]. This is 94X lower than the 1:1 concentration tested in the GSH matrix. Further, RPMI-1640 has 45 components that could be the source of the interaction. Nonetheless, in growth inhibition testing, several complexes still exhibited good activity. This suggests that this interaction could be

liable, part of complex activation, aquation of the monodentate ligand or enable complex MOA in addition to potential detoxification and deactivation mechanisms. For example, interaction with GSH while maintaining potency has been documented. The complex $(\eta^6$-biphenyl)Ru(AzPy-NMe$_2$)I]PF$_6$ has been demonstrated to oxidise the conversion of GSH to GSSG through the AzPy azo bond to a hydrazo group, which goes on to regenerate the azo bond through the hydrogenation of dissolved O_2 to generate hydrogen peroxide[49].

Notably, most of these complexes do not exhibit spectra changes in BSA or plasma matrixes, the primary transport protein and transport media in the body. This is contrary to many ruthenium complexes including NAMI-A, KP1019, and many Ru piano-stool complexes which can be transported by albumin and transferrin[50–52]. Being bound to these macromolecules can consequently increase transport to the tumour microenvironment, aiding specificity. While these complexes cannot take advantage of these transport mechanisms, the hydrophilic nature of the complexes should aid their transport without being bound but may be vulnerable during transit to the tumour.

Of particular note, these complexes interacted with water with the formation of an isosbestic point, which did not appear in the 1:1 water to PBS matrix. This has been previously explored in similar complexes and demonstrated to be due to the aquation of the monodentate chlorine ligand, which is repressed with increasing sodium chloride[36]. Aquation is a process in metal complexes, especially those with halogen monodentate ligands, such as those used in this work, and similar previous generation complexes[35,53,54]. This aquation is suggested to be similar to that of CDDP, where the exchange of the halogen ligands with water is part of the activation mechanism, allowing for subsequent complex interactions[53,55,56].

Noting the formation of aqua adducts, the formation of isosbestic points of complexes *2*, *3*, *4*, and *6* with ctDNA, is not unexpected, agreeing with previously described mechanisms and agreement with previous results[36]. DNA targeting is a frequent target of antiproliferative treatments, including metal

complexes such as CDDP and RM175. CDDP is well documented to develop the formation of DNA adducts, which causes the stalling of DNA replication, strand damage and breakage, causing the induction of apoptosis and other MOD[57]. Yet, DNA interaction of metal complexes is not limited to the development of adducts, but other methods including intercalation, groove binding and electrostatic interactions[58]. However, more in-depth experimentation is required to determine the mode of interaction.

While these complexes did exhibit hyperchromism with pure DMSO, an isosbestic point did not form in these cases, but that does not rule out an interaction. CDDP has been documented to form a range of adducts with DMSO by substitution of the NH_3 and Cl ligands[59]. In addition, other metal complexes have also been documented to interact, but in these cases, isosbestic points in hypsochromism was evident[60]. Furthermore, repression of adduction formation can be induced with the introduction of chlorine ions in solution in the form of saline or lithium chloride[60,61]. In this work, similar hyperchromism is not observed in other matrixes, suggesting that DMSO adduct formation/interaction can be prevented in the diluted matrixes in the UV-Vis and biological activity assay making it an appropriate solvent for further use.

The lipophilicity of the complexes in this chapter varied with $LogD_{7.4}$ values ranging from -0.66 to -0.21 exhibiting a borderline lipophilic/hydrophilic nature due to the organic structures and being ions with a PF_6 counter anion. Organometallic complexes can widely vary in their lipophilicity with a range of logP values, however there is a consistent trend seen in many series of complexes that there is an inverse corelation between lipophilicity and IC_{50} value[29–31,39,62,63]. Furthermore, increasing potency with extent of methyl substitution and extension of the methyl to the isopropyl group is also observed in other series[29–31,62,63]. However, potency of the complexes explored in these series still widely varies from being highly potent in the case of FY26, to being ineffective in the case of Ru-1 to Ru-4 explored by Guo *et al*, despite having similar LogP values[39,62]. This likely due to lipophilicity being a contributary factor in potency, with lipophilicity of the specific substituents resulting in increased potencies[31].

3-4.2: Antiproliferative screening of methyl bioisosteric complexes

The complexes in this series exhibited good activity in a variety of EOC cell lines. With methyl substitution, potency improved in A2780 and PEA1, EOC lines that do not have resistance profiles, while methyl substitution was not as effective in SKOV3 or PEA2. A2780 is considered to be one the primary models of EOC as it was collected before patient treatment and also possesses a fully functional *TP53* gene and p53 proteins[64–66]. Therefore, A2780 is treatment naïve and can be used to investigate a variety of anticancer compounds. This contrasts SKOV3, a notoriously hardy EOC cell line which exhibits intrinsic resistant to CDDP and many other treatments. This has been attributed to the lack of *TP53*, increased GSH levels, reduced apoptotic pathway signalling when initiated, aberrant PUMA expression and Smac release, and increased anti-apoptotic protein levels including BCL-x$_L$ and MCL-1[67–71]. This provides some insight to that these complexes trend with many other treatments in effectively treating A2780 but facing difficulties in SKOV3.

The use of these complexes in resistant lines can be demonstrated using the PEA1 and PEA2 cell lines. PEA1 and PEA2 are sister lines derived from the same patient before and after treatment with CDDP and Prednimustine, an effective treatment regimen for EOC pre-millennia with 61% response rates[72,73]. Here, all the complexes synthesised experience some resistance with complex **6** experiencing the most cross-resistance with a PEA factor of 2.5, but this was still reduced compared to CDDP with a PEA factor of 3.0. PEA2 is considered to have similar properties to PEA1, while gaining mechanisms of resistance to CDDP and Prednimustine. Yet, further research into PEA1 and PEA2 genetic characterisations have concluded that these cell lines have diverged independently from one host with 5% derivative chromosomes and large differences in loss of heterozygosity events[74]**.** These changes suggest that other resistance mechanisms that are not CDDP dependant, possibly Prednimustine induced or developed through genomic instability, are utilised in the cell leading to decreased potency. For example, Prednimustine can lead to an increase in metallothionein levels, a small protein rich in

cysteine used in metal binding/absorbing and redox scavenging[75,76]. Therefore, the decrease in complex potency in PEA2 over PEA1 can potentially be attributed to these cellular profile differences.

The position of the methyl was also seen to influence potency. As shown, there is a trend of increasing potency with *o<m<p*. This is likely due to the steric hinderance of the *o*-methyl group and the imine bond in **4** forcing rotation of the phenyl ring in the predicted DFT structures. In solution, the unsubstituted **1** and the *para* substituted **2** would be able to experience full phenyl rotation, the o-methyl in **4** would limit rotation by due to collision with the chlorine monodentate ligand, the imine bond and potentially the *p*-cymene ring. This could limit interactions with potential biomolecule targets and/or prevent aquation of the chlorine monodentate ligand. Similar to CDDP, aquation of halogen monodentate ligand is an essential activation step of for many organometallic complexes, as aquation to an $-OH_2$ group allows for co-ordination of the metal centre with macromolecules[77–79]. Therefore, if aquation is inhibited due to steric hinderance, this could result in the prevention of activation of the complex.

One benefit of the complexes synthesised here is the inactivity in normal lung MRC5. MRC5 cells are derived from the lung tissue of a 14-week old male foetus from a genetically normal family with no neoplastic capability demonstrated[80]. Selectivity is a significant hinderance of many anticancer treatments. Here, none of the tested complexes exhibited any antiproliferative effects, in stark contrast to CDDP which was highly potent. This demonstrates that these complexes have specificity for neoplastic tissues. Specificity is widely varied in ruthenium organometallic complexes, therefore the ability of these complexes to maintain specificity is highly remarkable[81–83]. This specificity provides an edge over other non-targeted treatments as are often more well tolerated due to decreased toxicity.

SKOV3 was chosen for further work due being an aggressive cell line and intrinsically resistant to CDDP. Additionally, complex **6** was selected due to being the best preforming complex of this series.

3-4.3: Preliminary mode of action evaluation of complex 6

Organometallic complexes have the capabilities to affect several pathways in the cell. $\Delta\Psi m$ depolarisation is often induced by organometallic complexes and can be assessed by fluorescence microscopy with Rh123, which fluoresces in corelation with the extent of $\Delta\Psi m$ polarisation[84,85]. Here **6** induced $\Delta\Psi m$ depolarisation at 0.5X IC_{50}. The loss of $\Delta\Psi m$ is associated with the dysregulation of several processes. With the mitochondria regularly referred to as the 'powerhouse of the cell', depolarisation can be associated with the reduction in ATP production due to the loss of the proton gradient, meaning that ATP synthase cannot be powered, and in extreme circumstances induce ATPase activity[84,86]. Reduction of ATP in the cell has been associated with the increase in protease, nuclease and lipase activity, however this has only been noted in chronic decrease in ATP, therefore it is uncertain if this occurs in 24 hours exposure[84]. Alterations of as little as 10% in the $\Delta\Psi m$ can increase ROS generation by 90% in normal cells[87]. Loss of $\Delta\Psi m$ has also been noted to promote the dysregulation of Ca^{2+} and Fe^{2+}, which can go on to effect endoplasmic reticulum and thiol regulation, respectively[84,88]. Additionally, $\Delta\Psi m$ loss has also been linked to the stabilisation of PINK1, suggested to be due to inaccessibility PARL, which goes on to phosphorylate the E3 ligase Parkin via serine 65. Parkin then ubiquitinates mitochondrial substates, leading to mitophagy[84,89,90]. However, while these MOA cannot be ascertained without further experimentation, the loss of $\Delta\Psi m$ polarisation is a highly significant MOA as it loss of mitochondrial function is highly relied upon in several MOD.

As **6** induced the loss of $\Delta\Psi m$ polarisation, and due to the catalytic nature of many organometallic complexes including FY26 and η^6-C_6Me_6 derivatives of RM175, ROS generation was investigated[91,92]. By fluorescence microscopy, **6** induced hotspots of ROS in SKOV3 cells and further testing demonstrated that significantly increased levels of ROS were induced when cells were treated with high concentrations of **6**. ROS can interact with a wide variety of cellular components in both positive and negative ways. Cancer cells generally have an increased baseline level of ROS compared to normal

cells as ROS is used in the signalling of proliferation, differentiation, and migration, but also to induce low levels of consistent damage of proteins, DNA and lipids which aids disease progression[93–95]. However, due to cancer cells often surviving at the limit of ROS levels, further increase often exceeds the limit of what cells can tolerate, becoming deadly[93]. Therefore, when cells are treated with **6**, ROS concentrations can potentially reach intolerable levels in cells and cause irreparable cellular damage. This damage can then be detected by various systems and induce several different death mechanisms depending on what is damaged including apoptosis, autophagy and ferroptosis[3,5,14].

Cell cycle arrest occurs in several types of cell death with arrest phase dependant on the damage that has occurred. Here, complex **6** did not induce cell cycle arrest after 24 hours exposure. While this contrasts CDDP which induced significant S phase arrest, PTX also did not induce significant cell cycle arrest. The lack of cell cycle arrest in **6** treated cells is peculiar. Traditionally, cell cycle arrest occurs in parallel with many types of cell death including apoptosis and autophagy[96,97]. Therefore, the lack of cell cycle indicates that cell death may be occurring faster than cell cycle can be initiated or signalling for cycle inhibition/prevention of cycle initiation is not occurring. There are several possibilities for these to occur. For the former explanation, it could be that necrosis is potentially occurring, which would result in cell death without signalling for cell cycle arrest due to time restraints and lack of signalling[5,7]. Another possibility is that a MOD that does not rely on induce cell cycle is occurring. It has been observed that ferroptosis can be inhibited with the induction of cell cycle arrest due to increased lipid droplet formation[98]. However, there is also contradictory information stating that arrest can still be seen in ferroptotic cells[99]. Therefore, the lack of cell cycle arrest does not indicate any specific MOA or MOD at this point. A similar phenomenon may be possible with **6** where 24 hours exposure may be insufficient for cell cycle arrest at 0.5X IC_{50}, or that 0.5X IC_{50} may not be sufficient for arrest signalling at 24 hours.

Wound healing is a commonly used assay as a model for tissue invasion[100]. Here, complex **6** induced significant inhibition of wound closure over the course of four days as part of a 24-hour exposure plus

72 hours recovery protocol. However, **6** did not prevent wound closing in the initial 24 hours. This suggests that an initial activation period or a longer period is required for the MOA of complex **6**, which would further agree with the lack of cell cycle arrest after 24 hours. Inhibition of migration is a desirable trait of many anticancer treatments, and has been documented by other organometallic complexes, one being RAPTA-T[101–103]. Anti-migratory activity of RAPTA-T has been suggested to be due to inhibition of MMPs[101,102]. MMPs are zinc-dependent endopeptidases and work in the cleavage and remodelling of the extracellular matrix (ECM), allowing for tumour growth and simulating the development of neo-vasculature[104]. The inhibition of migration therefore is a desirable trait, especially in EOC where MMP1, MMP2 and MMP9 can be upregulated and associated, but also invasion and vascularisation is highly observed with stage III and IV patients often experiencing peritoneal invasion and metastasis[105,106]. However, many elements are responsible for invasion including many CCM qualities and signalling pathways. Therefore, without further experimentation into signalling and mechanism testing specific reasoning cannot be provided.

Colony formation was used as a model for metastasis by evaluation of cellular survival following treatment and produce colonies after reseeding, therefore evaluate long-term effects without treatment present[107]. Invasion and metastasis are canonical mechanisms in cancer development. Platinum complexes have been shown to be effective at preventing colony formation growth on multiple occasions, with effectiveness extending to oxaliplatin being approved for metastatic colorectal cancer[108–110]. This is contrary to several ruthenium complexes where activity has varied, one example which achieves metastasis inhibition is NAMI-A through α5β1 integrin and FAK auto-phosphorylation inhibition[110–112]. The delay in activity highlighted by cell cycle and would healing analysis is somewhat seen by the colony formation as **6** at 0.5X IC$_{50}$ did induce a decrease in the number and size of colonies formed, yet colonies still developed. This indicates that **6** could have a delayed activation, however after an extended period (greater than 72 hours), effectiveness of the complex subsides, or the MOA of **6** can be repaired or low enough for cells to continue replicating. This

phenomenon has also been observed in PTX treated cells where after treatment, cells can undergo death, arrest or continue to proliferate[113]. However, as **6** does not induce cell cycle arrest and the presence of colonies demonstrates cell survival, this indicates that cells are continuing to proliferate, but at a reduced capacity.

3-4.4: *Mechanism of cell death evaluation of 6*

Chemotherapies are often measured by their ability to induce death in cancerous cells. The primary method of controlled cell death is apoptosis, which can be investigated via annexin V and PI staining. The annexin V binds to phosphatidylserine which is flipped from the internal CCM to the external CCM during early phase apoptosis, while in late phase apoptosis the CCM becomes compromised allowing for the passage of PI into the cell to intercalate in DNA and fluorescence[114,115]. Complex **6** induced dose dependant apoptosis with high levels of early and late apoptosis at 2.5X IC_{50}, comparable to CDDP and STS. Apoptosis is the preferred MOD for anticancer treatments for several reasons. Apoptosis is a universal, often the most common MOD employed by cells, therefore can be applied to many different types of tissue types[116]. In addition, as it is a controlled MOD, residual cellular components can be cleared while causing minimal damage to surrounding tissues which can occur with other cell types that permeabilise the CCM such as necrosis[3]. Therefore, complex **6** being able to achieve apoptosis at IC_{50} by 24 hours exposure is highly beneficial as anticancer therapeutic, due to the notable resistance of SKOV3 to many antiproliferative treatments[117,118].

To investigate the dose dependant nature of apoptosis seen in flow cytometry and potential signalling cascade delays of lower doses of complex **6**, caspase activity was examined as prominent instigators and effectors of apoptosis. The activity of the effector caspases Caspase 3/7 was determined and found to be significantly expressed in all treatment doses of **6**. Caspase activation in conjunction with annexin V fluorescence heavily indicts that complex **6** induces apoptosis, further Caspase 3/7 activity is proportional to the extent of apoptosis occurring (i.e. low activity levels corelates with low apoptosis

levels). The ability to induce significant initiator caspase signalling within 24 hours is noteworthy, especially as previous experimentation indicates that recovery time is important to antiproliferative activity as it suggests that *6* may have an extended activity time in the cell. Additionally, Caspase 3/7 activity also indicates that *6* does not induce necrosis at 2.5X IC_{50}. As annexin V positive and PI positive stained cells cannot be differentiate between late apoptotic cells and primary necrotic cells *in vitro*, caspase activity suggests that apoptosis is occurring rather than necrosis[119]. This is highly beneficial as this indicates cells are dying in a manner that does not induce collateral damage to surrounding cells and tissues[3].

Due to the increased fraction of non-viable cells and decreased protein content, CCM morphology was investigated using the lipophilic carbocyanine dye Cell Brite Red membrane dye. Upon treatment with *6*, cellular size substantially decreased, and further CCM fluorescence decreased in a dose dependant manner, indicating a decrease in dye CCM integration. The shrinkage of cellular morphology and CCM decrease further supports the involvement of apoptosis as canonical morphological features[120].

To further investigation type of apoptosis, Caspase 9 activation was questioned due to the compromise of the ΔΨm. Initiator Caspase 9 activity was only significantly increased in 2.5X IC_{50} doses of *6*. This indicates that complex *6* only induces intrinsic apoptosis higher doses. This suggests that MOD is dose dependant and other cleavers of Caspase 3/7 such as Caspase 2, 4, 8, and 10 could be utilised at lower concentrations[121]. Further, as apoptosis induction relies upon many different signalling molecules as part of a wider web of signalling to induce apoptosis, there are many trigger points that can be activated[122]. Therefore, *6* could potentially affect several different steps in the apoptosis signalling cascade, meaning a specific variant of apoptosis for lower doses of complex *6* cannot be assigned at this point such as intrinsic, extrinsic or anoikis, reinforcing a potential multi-modal MOA.

As organometallic complexes can induce a variety of MOA, and the indication at lower concentrations that other mechanisms of death activating Caspase 3 and 7 being possible, the ability to induce several

mechanisms of death was also investigated. Due to the substantial decrease in protein content, cell size, $\Delta\Psi m$ depolarisation, and ROS generation the potential effect of autophagy was investigated. Complex **6** only induced statistically significant autophagy at 1X IC_{50}. However, while there was no statistically significant difference between **6** treated at 2.5X IC_{50} and the negative control (p=0.09) fluorescence was higher by 0.01 in 2.5X IC_{50} than in 1X IC_{50} treated cells. This is due to due to wider variation in the replicates of 2.5X IC_{50} treated cells. This suggests that the induction of autophagy is reliant on a minimum threshold of damage occurring, in addition to being a secondary MOD.

Autophagy is the main process of cellular recycling. Here autophagy was assessed by via autophagosome marking, therefore cannot differentiate between the three main types of autophagy; micro, macro and mitochondrial[3,123,124]. Due to the cellular damage indicated by $\Delta\Psi m$ depolarisation and ROS generation assay, coupled with the fractional increase in autophagy, suggests that selective micro-autophagy and mitophagy is most likely[3]. This recycling process makes autophagy an important mechanism in both the development and inhibition of cancer development[125]. Autophagy is used in cancer cells to regenerate materials for growth due to microenvironment stress, to recover from starvation, and remove damaged organelles and proteins[126]. The increase in autophagy seen in complex **6** treated SKOV3 cells could be due to the degradation of damaged cellular components caused by the MOA of **6**, or the degradation of cell components, damaged or undamaged, to aid recovery.

Due to the ROS inductive capacity of **6**, ferroptosis was investigated due to its involvement in lipid peroxidation, potentially being a cause for the decreased CCM fluorescence. Here, the ferroptosis inhibitor FER-1 did not notably prevent antiproliferative activity of **6** with only a maximal 17% survival improvement. FER-1 inhibits the final step of ferroptosis as a radical-trapping antioxidant which scavenges hydroperoxyl and alkoxyl radicals, which inhibits the chain of lipid peroxidation, preventing the integration of lipid hydroperoxides into the CCM, and by extension CCM comprimise[127,128]. Therefore, the 6.4-17% increase in survival with combination treatment of **6** and FER-1 may be due to

the scavenging of radicals in fraction of the cells that do experience ROS generation, preventing lipid peroxidation and ferroptosis. Therefore, lipid peroxidation and ferroptosis induction may only play a small part in the overall MOD of complex *6*.

3-4.5: Potency enhancement of 6 by co-treatment

Chemotherapeutics are rarely used alone to enable complete eradication due to heterogenous tumour microenvironments, to prevent the development of resistance, and combination therapy is viewed as the only way to counteract metastatic disease[129]. This is done by utilising therapeutics with differing MOA, to prevent resistance overlap and treatment redundancy. Additionally, ferroptosis is considered to be the only MOD cancer cells cannot escape from[130]. Therefore, the combination of apoptotic and ferroptotic MOD has the potential to be a highly effective antiproliferative regimen.

At current, ferroptosis inducers have had little success in clinical trial thus far. At current, Sorafenib is the only clinically approved treatment that can induce ferroptosis, yet it is branded as a multi-kinase inhibitor that can also induce ferroptosis[131]. In this work, the ferroptosis inducer ERA was used. Erastin named for its ability to irradicate RAS and ST-expressing cells, ERA works by irreversibly inhibiting the cystine-glutamate antiporter (system X_C^-) and binding to the mitochondrial voltage channels 2 and 3[132]. While ERA has been shown to be highly potent in many cell lines and here with a potent IC_{50} of 5.38 µM in SKOV3[131–133]. However, *in vivo* ERA has had documented issue with solubility, which can be solved with the imidazole ketone modification, which further improved potency[131]. Here the co-treatment of ERA with complex *6* produced highly potent antiproliferative activity achieving near complete eradication of cell survival. The enhancement in activity seen here could be due to the parallel signalling mechanism used in by ferroptosis and apoptotic signalling. Improved activity could also be due to GSH reduction by the system X_C^- inhibition. As demonstrated by the UV-Vis experimentation, complex *6* interacts with GSH, however at current, it is unknown if this is as part of a detoxification method or a catalytic method such as seen the biphenyl derivative of FY26 as

previously discussed[49]. However, if GSH concentration in the cell is reduced due to ERA, **6** is then available to induce other interactions in the cell. This observation of organometallic complex potency improvement has also been seen with the co-treatment with L-BSO which reduces GSH concentration by inhibiting γ-glutamylcysteine synthetase, the rate limiting enzyme of GSH synthesis[38,134]. Furthermore, L-BSO has successfully been used in a variety of chemotherapeutic and radiotherapeutic treatments with high success rates where in some cases potency increases by 2.3X in A2780[38,135–137].

With this knowledge, cells were co-treated with complex **6** or **1** with L-BSO in SKOV3 and A2780, and potency was significantly improved. This highly supports the previous suggestions of GSH binding to these complexes in the co-ordination sphere, leading to the decrease in their potency. Therefore, when GSH synthesis is inhibited, complex-GSH conjugate formation is prevented, allowing for the complexes to elicit their MOA[45,46]. However, the improvement of potency of **6** in SKOV3 was only ~54% of the improvement seen in A2780. This suggests that other intrinsic resistance mechanisms employed by SKOV3 cells may be preventing the full activity of **6** which are allowed in A2780. This can be attributed to the many differences between the SKVO3 and A2780 cell lines and highlights the importance of screening multiple in the assessment of complex and its MOA. This was highlighted in antiproliferative screening and the many features shown by the SKOV3 cell line which increase the difficulty to induce apoptosis and death[67–71]. This highlights that a multi-MOA of treatment is highly beneficial as a non-targeted treatment. This also highlights that the most impotent of treatments can be significantly improved with small, non-toxic, co-treatments such as L-BSO[138].

3-5: Conclusion

Organometallic complexes are gaining popularity as potential antiproliferative agents in difficult to treat cancers. However, with the desire to design more intricate complexes to achieve higher secondary functions, smaller modifications are often overlooked. In line with the aim of this chapter, methyl modifications of the phenyl ring of $[Ru(\eta^6\text{-}p\text{-Cym})(ImPy)Cl]PF_6$ complexes were investigated. Following the successful synthesis and chemical characterisation, these complexes were found to express moderate activity in a variety of EOC cell lines while maintaining inactivity in normal lung fibroblasts. Further, methyl modifications only enhanced activity due to improving lipophilicity of the complexes. However, complex **6** was found to have promising activity compared to the other complexes. Treatment with **6** can induce several MOA including ΔΨm depolarisation, ROS generation, wound healing inhibition and colony formation inhibition. Yet remarkably, **6** was found to induce several MOD including apoptosis, in addition to limited autophagy and ferroptosis, while not inducing uncontrolled death such as necrosis. Further, co-treatment of cells with complex **6** and GSH synthesis inhibitors was found to significantly improve the antiproliferative activity.

These findings highly suggest a multi-modal MOA of complex **6**, which can lead into the activation of multiple different MOD in SKOV3, making it a highly effective treatment in combination therapy. This quality is greatly beneficial in the treatment of EOC and other cancers which require a multi-targeted approach.

3-6: References

1. Galluzzi, L. *et al.* Molecular mechanisms of cell death: recommendations of the Nomenclature Committee on Cell Death 2018. *Cell Death Differ.* **25**, 486–541 (2018).
2. Nirmala, J. G. & Lopus, M. Cell death mechanisms in eukaryotes. *Cell Biol. Toxicol.* **36**, 145–164 (2020).
3. D'Arcy, M. S. Cell death: a review of the major forms of apoptosis, necrosis and autophagy. *Cell Biol. Int.* **43**, 582–592 (2019).
4. Eskandari, E. & Eaves, C. J. Paradoxical roles of caspase-3 in regulating cell survival, proliferation, and tumorigenesis. *J. Cell Biol.* **221**, 1–13 (2022).
5. Yan, G., Elbadawi, M. & Efferth, T. Multiple cell death modalities and their key features (Review). *World Acad Sci J* **2**, 39–48 (2020).
6. Dhuriya, Y. K. & Sharma, D. Necroptosis: a regulated inflammatory mode of cell death. *J. Neuroinflammation* **15**, 1–9 (2018).
7. Golstein, P. & Kroemer, G. Cell death by necrosis: towards a molecular definition. *Trends Biochem. Sci.* **32**, 37–43 (2007).
8. Khalid, N. & Azimpouran, M. *Necrosis*. (StatPearls Publishing, 2020).
9. Blagosklonny, M. V. Prospective strategies to enforce selectively cell death in cancer cells. *Oncogene* **23**, 2967–2975 (2004).
10. Hanahan, D. & Weinberg, R. A. Hallmarks of Cancer: The Next Generation. *Cell* **144**, 646–674 (2011).
11. Coverdale, J. P. C., Laroiya-McCarron, T. & Romero-Canelón, I. Designing Ruthenium Anticancer Drugs: What Have We Learnt from the Key Drug Candidates? *Inorganics* **7**, 1–15 (2019).
12. Hayward, R. L. *et al.* Investigation of the role of Bax, p21/Waf1 and p53 as determinants of cellular responses in HCT116 colorectal cancer cells exposed to the novel cytotoxic ruthenium(II) organometallic agent, RM175. *Cancer Chemother. Pharmacol.* **55**, 577–583 (2005).
13. Chatterjee, S., Kundu, S., Bhattacharyya, A., Hartinger, C. G. & Dyson, P. J. The ruthenium(II)-arene compound RAPTA-C induces apoptosis in EAC cells through mitochondrial and p53-JNK pathways. *J. Biol. Inorg. Chem.* **13**, 1149–1155 (2008).
14. Wang, X. *et al.* A ferroptosis-inducing iridium(III) complex. *Sci. China Chem.* **63**, 65–72 (2020).
15. Lai, Y., Lu, N., Luo, S., Wang, H. & Zhang, P. A Photoactivated Sorafenib-Ruthenium(II) Prodrug for Resistant Hepatocellular Carcinoma Therapy through Ferroptosis and Purine Metabolism Disruption. *J. Med. Chem.* **65**, 13041–13051 (2022).
16. Yuan, J., Lei, Z., Wang, X., Zhu, F. & Chen, D. Ruthenium complex Λ-WH0402 induces hepatocellular carcinoma LM6 (HCCLM6) cell death by triggering the Beclin-1-dependent autophagy pathway. *Metallomics* **7**, 896–907 (2015).
17. Irace, C. *et al.* Antiproliferative effects of ruthenium-based nucleolipidic nanoaggregates in human models of breast cancer in vitro: insights into their mode of action. *Sci. Rep.* **7**, 1–13 (2017).
18. Kladnik, J. *et al.* Organoruthenium Complexes with Benzo-Fused Pyrithiones Overcome Platinum Resistance in Ovarian Cancer Cells. *Cancers,* **13**, 1–21 (2021).
19. Berndsen, R. H. *et al.* Combination of ruthenium(II)-arene complex [Ru(η6-p-cymene)Cl2 (pta)] (RAPTA-C) and the epidermal growth factor receptor inhibitor erlotinib results in efficient angiostatic and antitumor activity. *Sci. Rep.* **7**, 1–16 (2017).
20. Scolaro, C. *et al.* In vitro and in vivo evaluation of ruthenium(II)-arene PTA complexes. *J. Med. Chem.* **48**, 4161–4171 (2005).
21. Gill, M. R. *et al.* A ruthenium polypyridyl intercalator stalls DNA replication forks, radiosensitizes human cancer cells and is enhanced by Chk1 inhibition. *Sci. Rep.* **6**, 1–15 (2016).
22. Ramu, V. *et al.* A cytostatic ruthenium(II)-platinum(II) bis(terpyridyl) anticancer complex that blocks entry into S phase by up-regulating p27KIP1. *Chem. - A Eur. J.* **21**, 9185–9197 (2015).
23. Millar, A. W. & Lynch, K. P. Rethinking clinical trials for cytostatic drugs. *Nat. Rev. Cancer* **3**, 540–545 (2003).
24. De Miranda, A. S. The methylation effect in medicinal chemistry. *Rev. Virtual Quim.* **3**, 228–232 (2011).
25. Sun, S. & Fu, J. Methyl-containing pharmaceuticals: Methylation in drug design. *Bioorganic Med. Chem. Lett.* **28**, 3283–3289 (2018).
26. Aynetdinova, D. *et al.* Installing the 'magic methyl'-C-H methylation in synthesis. *Chem. Soc. Rev.* **50**, 5517–5563 (2021).

27. Schindler, T. *et al.* Structural Mechanism for STI-571 Inhibition of Abelson Tyrosine Kinase. *Science,* **289**, 1938–1942 (2000).

28. Adhikari, S., Hussain, O., Phillips, R. M., Kaminsky, W. & Kollipara, M. R. Neutral and cationic half-sandwich arene d 6 metal complexes containing pyridyl and pyrimidyl thiourea ligands with interesting bonding modes: Synthesis, structural and anti-cancer studies. *Appl. Organomet. Chem.* **32**, 1–13 (2018).

29. Loh, S. Y., Mistry, P., Kelland, L. R., Abel, G. & Harrap, K. R. Reduced drug accumulation as a major mechanism of acquired resistance to cisplatin in a human ovarian carcinoma cell line: circumvention studies using novel platinum (II) and (IV) ammine/amine complexes. *Br. J. Cancer* **66**, 1109–1115 (1992).

30. Song, R. *et al.* Synthesis and cytotoxicity of new platinum(IV) complexes of mixed carboxylates. *J. Inorg. Biochem.* **96**, 339–345 (2003).

31. Pastuszko, A., Majchrzak, K., Czyz, M., Kupcewicz, B. & Budzisz, E. The synthesis, lipophilicity and cytotoxic effects of new ruthenium(II) arene complexes with chromone derivatives. *J. Inorg. Biochem.* **159**, 133–141 (2016).

32. Fu, Y. *et al.* Mirror-Image Organometallic Osmium Arene Iminopyridine Halido Complexes Exhibit Similar Potent Anticancer Activity. *Chem. – A Eur. J.* **19**, 15199–15209 (2013).

33. Fu, Y. Organometallic Osmium Arene Anticancer Complexes. (University of Warwick, 2011).

34. Fu, Y. *et al.* The contrasting chemical reactivity of potent isoelectronic iminopyridine and azopyridine osmium(ii) arene anticancer complexes. *Chem. Sci.* **3**, 2485–2494 (2012).

35. Romero-Canelón, I., Salassa, L. & Sadler, P. J. The Contrasting Activity of Iodido versus Chlorido Ruthenium and Osmium Arene Azo- and Imino-pyridine Anticancer Complexes: Control of Cell Selectivity, Cross-Resistance, p53 Dependence, and Apoptosis Pathway. *J. Med. Chem.* **56**, 1291–1300 (2013).

36. Romero-Canelón, I. DESIGN AND MECHANISM OF ACTION OF ORGANOMETALLIC ANTICANCER COMPLEXES. (University of Warwick, 2012).

37. Hearn, J. M. *et al.* Pharmaco-genomic investigations of organo-iridium anticancer complexes reveal novel mechanism of action. *Metallomics* **10**, 93–107 (2018).

38. Romero-Canelón, I., Mos, M. & Sadler, P. J. Enhancement of Selectivity of an Organometallic Anticancer Agent by Redox Modulation. *J. Med. Chem.* **58**, 7874–7880 (2015).

39. van Rijt, S. H., Romero-Canelón, I., Fu, Y., Shnyder, S. D. & Sadler, P. J. Potent organometallic osmium compounds induce mitochondria-mediated apoptosis and S-phase cell cycle arrest in A549 non-small cell lung cancer cells. *Metallomics* **6**, 1014–1022 (2014).

40. Aktara, M. N., Nayim, S., Sahoo, N. K. & Hossain, M. The synthesis of thiol-stabilized silver nanoparticles and their application towards the nanomolar-level colorimetric recognition of glutathione. *New J. Chem.* **43**, 13480–13490 (2019).

41. Kar, B. *et al.* GSH-resistant and highly cytoselective ruthenium(ii)-p-cymene-(imidazo[4,5-f][1,10]phenanthrolin-2-yl)phenol complexes as potential anticancer agents. *Dalt. Trans.* **50**, 10369–10373 (2021).

42. Kausar, H. *et al.* Cucurbitacin B potently suppresses non-small-cell lung cancer growth: Identification of intracellular thiols as critical targets. *Cancer Lett.* **332**, 35–45 (2013).

43. Mondal, A. & Paira, P. Hypoxia efficient and glutathione-resistant cytoselective ruthenium(ii)-p-cymene-arylimidazophenanthroline complexes: biomolecular interaction and live cell imaging. *Dalt. Trans.* **49**, 12865–12878 (2020).

44. Mondal, A. *et al.* DNA targeting half sandwich Ru(ii)-p-cymene-N^N complexes as cancer cell imaging and terminating agents: influence of regioisomers in cytotoxicity. *Dalt. Trans.* **50**, 979–997 (2021).

45. Chen, H. H. W. & Kuo, M. T. Role of Glutathione in the Regulation of Cisplatin Resistance in Cancer Chemotherapy. *Met. Based. Drugs* **2010**, 1–7 (2010).

46. Lan, D. *et al.* Exogenous glutathione contributes to cisplatin resistance in lung cancer A549 cells. *Am. J. Transl. Res.* **10**, 1295–1309 (2018).

47. Townsend, D. M., Marto, J. A., Deng, M., Macdonald, T. J. & Hanigan, M. H. High Pressure Liquid Chromatography And Mass Spectrometry Characterization Of The Nephrotoxic Biotransformation Products Of Cisplatin. *Drug Metab. Dispos.* **31**, 705–713 (2003).

48. Corning. Corning: RPMI 1640 Formulation. *Beginning-to-end Solutions for Cell Culture* 1–2 https://www.corning.com/catalog/cls/documents/formulations/CLS-CG-FM-031.pdf (2018).

49. Dougan, S. J., Habtemariam, A., McHale, S. E., Parsons, S. & Sadler, P. J. Catalytic organometallic anticancer complexes. *Proc. Natl. Acad. Sci.* **105**, 11628–11633 (2008).

50. Hairat, S. & Zaki, M. Half sandwiched RutheniumII complexes: En Route towards the targeted delivery by

Human Serum Albumin (HSA). *J. Organomet. Chem.* **937**, 1–40 (2021).

51. Dömötör, O. & Enyedy, É. A. Binding mechanisms of half-sandwich Rh(III) and Ru(II) arene complexes on human serum albumin: a comparative study. *JBIC J. Biol. Inorg. Chem.* **24**, 703–719 (2019).

52. Demoro, B. *et al.* Screening organometallic binuclear thiosemicarbazone ruthenium complexes as potential anti-tumour agents: cytotoxic activity and human serum albumin binding mechanism. *Dalt. Trans.* **42**, 7131–7146 (2013).

53. Wang, F. *et al.* Controlling ligand substitution reactions of organometallic complexes: Tuning cancer cell cytotoxicity. *Proc. Natl. Acad. Sci.* **102**, 18269–18274 (2005).

54. Wang, F. *et al.* Kinetics of Aquation and Anation of Ruthenium(II) Arene Anticancer Complexes, Acidity and X-ray Structures of Aqua Adducts. *Chem. – A Eur. J.* **9**, 5810–5820 (2003).

55. Rottenberg, S., Disler, C. & Perego, P. The rediscovery of platinum-based cancer therapy. *Nat. Rev. Cancer* **21**, 37–50 (2021).

56. Lau, J. K.-C. & Ensing, B. Hydrolysis of cisplatin—a first-principles metadynamics study. *Phys. Chem. Chem. Phys.* **12**, 10348–10355 (2010).

57. Dasari, S. & Bernard Tchounwou, P. Cisplatin in cancer therapy: Molecular mechanisms of action. *Eur. J. Pharmacol.* **740**, 364–378 (2014).

58. Almaqwashi, A. A., Paramanathan, T., Rouzina, I. & Williams, M. C. Mechanisms of small molecule–DNA interactions probed by single-molecule force spectroscopy. *Nucleic Acids Res.* **44**, 3971–3988 (2016).

59. Kerrison, S. J. S. & Sadler, P. J. Solvolysis of cis-[Pt(NH3)2Cl2] in dimethyl sulphoxide and reactions of glycine with [PtCl3 (Me2SO)] – as probed by 195 Pt nuclear magnetic resonance shifts and 195Pt– 15N coupling constants. *J. Chem. Soc., Chem. Commun.* **23**, 861–863 (1977).

60. Maikoo, S. *et al.* Biomolecular Interactions of Cytotoxic Ruthenium Compounds with Thiosemicarbazone or Benzothiazole Schiff Base Chelates. *ChemMedChem* **17**, 1–15 (2022).

61. Hall, M. D. *et al.* Say No to DMSO: Dimethylsulfoxide Inactivates Cisplatin, Carboplatin, and Other Platinum Complexes. *Cancer Res.* **74**, 3913–3922 (2014).

62. Guo, L. *et al.* Synthesis and biological evaluation of zwitterionic half-sandwich Rhodium(III) and Ruthenium(II) organometallic complexes. *Bioorg. Chem.* **116**, 105311 (2021).

63. Giringer, K. *et al.* Analysis of ruthenium anticancer agents by MEEKC-UV and MEEKC–ICP-MS: Impact of structural motifs on lipophilicity and biological activity. *Electrophoresis* **39**, 1201–1207 (2018).

64. UK Health Security Agency. Cell line profile Ovarian Cancer Cell Like A2780. *ECACC catalogue* https://www.culturecollections.org.uk/media/113526/a2780-cell-line-profile.pdf.

65. Lee, J.-G., Ahn, J.-H., Jin Kim, T., Ho Lee, J. & Choi, J.-H. Mutant p53 promotes ovarian cancer cell adhesion to mesothelial cells via integrin β4 and Akt signals. *Sci. Rep.* **5**, 1–12 (2015).

66. Lu, X., Errington, J., Curtin, N. J., Lunec, J. & Newell, D. R. The impact of p53 status on cellular sensitivity to antifolate drugs. *Clin. cancer Res.* **7**, 2114–2123 (2001).

67. Mullany, L. K. *et al.* Specific TP53 Mutants Overrepresented in Ovarian Cancer Impact CNV, TP53 Activity, Responses to Nutlin-3a, and Cell Survival. *Neoplasia* **17**, 789–803 (2015).

68. Yaginuma, Y. & Westphal, H. Abnormal structure and expression of the p53 gene in human ovarian carcinoma cell lines. *Cancer Res.* **52**, 4196–4199 (1992).

69. Yuan, Z. *et al.* The p53 Upregulated Modulator of Apoptosis (PUMA) Chemosensitizes Intrinsically Resistant Ovarian Cancer Cells to Cisplatin by Lowering the Threshold Set by Bcl-xL and Mcl-1. *Mol. Med.* **17**, 1262–1274 (2011).

70. Kelland, L. R. *et al.* Mini-review: discovery and development of platinum complexes designed to circumvent cisplatin resistance. *J. Inorg. Biochem.* **77**, 111–115 (1999).

71. Mon, M. T., Yodkeeree, S., Punfa, W., Pompimon, W. & Limtrakul, P. Alkaloids from *Stephania venosa* as Chemo-Sensitizers in SKOV3 Ovarian Cancer Cells *via* Akt/NF-κB Signaling. *Chem. Pharm. Bull.* **66**, 162–169 (2018).

72. Smyth, J. F. *et al.* Cisplatinum and prednimustine, an active regimen for advanced epithelial ovarian cancer. *Ann. Oncol. Off. J. Eur. Soc. Med. Oncol.* **2**, 755–758 (1991).

73. Langdon, S. P. *et al.* Characterization and properties of nine human ovarian adenocarcinoma cell lines. *Cancer Res.* **48**, 6166–6172 (1988).

74. Cooke, S. L. *et al.* Genomic analysis of genetic heterogeneity and evolution in high-grade serous ovarian carcinoma. *Oncogene* **29**, 4905–4913 (2010).

75. Wrigley, E., Verspaget, H. W., Jayson, G. C. & McGown, A. T. Metallothionein expression in epithelial ovarian cancer: effect of chemotherapy and prognostic significance. *J. Cancer Res. Clin. Oncol.* **126**, 717–721 (2000).

76. Ling, X.-B. *et al.* Mammalian Metallothionein-2A and Oxidative Stress. *Int. J. Mol. Sci.* **17**, 1–13 (2016).

77. Huang, H., Zhang, P., Chen, Y., Ji, L. & Chao, H. Labile ruthenium(ii) complexes with extended phenyl-substituted terpyridyl ligands: synthesis, aquation and anticancer evaluation. *Dalt. Trans.* **44**, 15602–15610 (2015).

78. Dougan, S. J., Melchart, M., Habtemariam, A., Parsons, S. & Sadler, P. J. Phenylazo-pyridine and phenylazo-pyrazole chlorido ruthenium(II) arene complexes: Arene loss, aquation, and cancer cell cytotoxicity. *Inorg. Chem.* **45**, 10882–10894 (2006).

79. Li, M., Lai, L., Zhao, Z. & Chen, T. Aquation Is a Crucial Activation Step for Anticancer Action of Ruthenium(II) Polypyridyl Complexes to Trigger Cancer Cell Apoptosis. *Chem. – An Asian J.* **11**, 310–320 (2016).

80. Jacobs, J. P., Jones, C. M. & Baille, J. P. Characteristics of a Human Diploid Cell Designated MRC-5. *Nature* **227**, 168–170 (1970).

81. Hildebrandt, J. *et al.* Highly Cytotoxic Osmium(II) Compounds and Their Ruthenium(II) Analogues Targeting Ovarian Carcinoma Cell Lines and Evading Cisplatin Resistance Mechanisms. *Int. J. Mol. Sci.* **23**, 4976–5005 (2022).

82. Păunescu, E., Soudani, M., Clavel, C. M. & Dyson, P. J. Varying the metal to ethacrynic acid ratio in ruthenium(ii)/osmium(ii)-p-cymene conjugates. *J. Inorg. Biochem.* **175**, 198–207 (2017).

83. Teixeira-Guedes, C., Brás, A. R., Teixeira, R. G., Valente, A. & Preto, A. Ruthenium(II)–Cyclopentadienyl-Derived Complexes as New Emerging Anti-Colorectal Cancer Drugs. *Pharmaceutics* **14**, 1293–1313 (2022).

84. Zorova, L. D. *et al.* Mitochondrial membrane potential. *Anal. Biochem.* **552**, 50–59 (2018).

85. Zorova, L. D. *et al.* Is the Mitochondrial Membrane Potential (∆Ψ) Correctly Assessed? Intracellular and Intramitochondrial Modifications of the ∆Ψ Probe, Rhodamine 123. *Int. J. Mol. Sci.* **23**, 1–14 (2022).

86. Zhao, R., Jiang, S., Zhang, L. & Yu, Z. Mitochondrial electron transport chain, ROS generation and uncoupling (Review). *Int. J. Mol. Med.* **44**, 3–15 (2019).

87. Bagkos, G., Koufopoulos, K. & Piperi, C. A new model for mitochondrial membrane potential production and storage. *Med. Hypotheses* **83**, 175–181 (2014).

88. Martínez-Reyes, I. *et al.* TCA Cycle and Mitochondrial Membrane Potential Are Necessary for Diverse Biological Functions. *Mol. Cell* **61**, 199–209 (2016).

89. Kondapalli, C. *et al.* PINK1 is activated by mitochondrial membrane potential depolarization and stimulates Parkin E3 ligase activity by phosphorylating Serine 65. *Open Biol.* **2**, 1–17 (2012).

90. Bernardini, J. P., Lazarou, M. & Dewson, G. Parkin and mitophagy in cancer. *Oncogene* **36**, 1315–1327 (2017).

91. Pizarro, A. M., Habtemariam, A. & Sadler, P. J. Activation Mechanisms for Organometallic Anticancer Complexes. in *Medicinal Organometallic Chemistry* vol. 32 21–56 (Springer, 2010).

92. Liu, Z. & Sadler, P. J. Organoiridium Complexes: Anticancer Agents and Catalysts. *Acc. Chem. Res.* **47**, 1174–1185 (2014).

93. Nakamura, H. & Takada, K. Reactive oxygen species in cancer: Current findings and future directions. *Cancer Sci.* **112**, 3945–3952 (2021).

94. Cui, Q. *et al.* Modulating ROS to overcome multidrug resistance in cancer. *Drug Resist. Updat.* **41**, 1–25 (2018).

95. Panieri, E. & Santoro, M. M. ROS homeostasis and metabolism: a dangerous liason in cancer cells. *Cell Death Dis.* **7**, 2253–2253 (2016).

96. Vermeulen, K., Berneman, Z. N. & Van Bockstaele, D. R. Cell cycle and apoptosis. *Cell Prolif.* **36**, 165–175 (2003).

97. Pucci, B., Kasten, M. & Giordano, A. Cell Cycle and Apoptosis. *Neoplasia* **2**, 291–299 (2000).

98. Lee, H. *et al.* Cell cycle arrest induces lipid droplet formation and confers ferroptosis resistance. *Nat. Commun.* **15**, 1–13 (2024).

99. Rodencal, J. *et al.* Sensitization of cancer cells to ferroptosis coincident with cell cycle arrest. *Cell Chem. Biol.* **31**, 234–248 (2024).

100. Rodriguez, L. G., Wu, X. & Guan, J.-L. Wound-Healing Assay. in *Cell Migration* 23–30 (Humana Press, 2005).

101. Lamač, M. *et al.* Harmless glucose-modified ruthenium complexes suppressing cell migration of highly invasive cancer cell lines. *Appl. Organomet. Chem.* **34**, 1–5 (2020).

102. Wang, Y. *et al.* New Organometallic Ruthenium(II) Compounds Synergistically Show Cytotoxic, Antimetastatic and Antiangiogenic Activities for the Treatment of Metastatic Cancer. *Chem. – A Eur. J.* **26**, 15170–15182 (2020).

103. Fandzloch, M. *et al.* New organometallic ruthenium(ii) complexes with purine analogs – a wide perspective on their biological application. *Dalt. Trans.* **50**, 5557–5573 (2021).

104. Conlon, G. A. & Murray, G. I. Recent advances in understanding the roles of matrix metalloproteinases in tumour invasion and metastasis. *J. Pathol.* **247**, 629–640 (2019).

105. Lheureux, S., Gourley, C., Vergote, I. & Oza, A. M. Epithelial ovarian cancer. *Lancet* **393**, 1240–1253 (2019).

106. Al-Alem, L. & Curry, T. E. Ovarian cancer: involvement of the matrix metalloproteinases. *Reproduction* **150**, 55–64 (2015).

107. Côrte-Real, L. *et al.* Biotinylated Polymer-Ruthenium Conjugates: In Vitro and In Vivo Studies in a Triple-Negative Breast Cancer Model. *Pharmaceutics* **14**, 1–22 (2022).

108. Bergamo, A. & Sava, G. Linking the future of anticancer metal-complexes to the therapy of tumour metastases. *Chem. Soc. Rev.* **44**, 8818–8835 (2015).

109. Yue, P. *et al.* Hyperactive EGF receptor, Jaks and Stat3 signaling promote enhanced colony-forming ability, motility and migration of cisplatin-resistant ovarian cancer cells. *Oncogene* **31**, 2309–2322 (2012).

110. Galanski, M. S., Arion, B. V, Jakupec, A. M. & Keppler, K. B. Recent Developments in the Field of Tumor-Inhibiting Metal Complexes. *Current Pharmaceutical Design* vol. 9 2078–2089 (2003).

111. Kostova, I. Ruthenium Complexes as Anticancer Agents. *Current Medicinal Chemistry* vol. 13 1085–1107 (2006).

112. Alessio, E. Thirty Years of the Drug Candidate NAMI-A and the Myths in the Field of Ruthenium Anticancer Compounds: A Personal Perspective. *Eur. J. Inorg. Chem.* **2017**, 1549–1560 (2017).

113. Zasadil, L. M. *et al.* Cytotoxicity of Paclitaxel in Breast Cancer Is due to Chromosome Missegregation on Multipolar Spindles. *Sci. Transl. Med.* **6**, 229–243 (2014).

114. Majtnerová, P. & Roušar, T. An overview of apoptosis assays detecting DNA fragmentation. *Mol. Biol. Rep.* **45**, 1469–1478 (2018).

115. Watanabe, M. *et al.* The Pros and Cons of Apoptosis Assays for Use in the Study of Cells, Tissues, and Organs. *Microsc. Microanal.* **8**, 375–391 (2002).

116. Pfeffer, C. & Singh, A. Apoptosis: A Target for Anticancer Therapy. *Int. J. Mol. Sci.* **19**, 1–10 (2018).

117. Wang, G., Jiang, M.-Y., Meng, Y., Song, H.-R. & Shi, W. Cellular Mechanisms of a New Pyrazinone Compound that Induces Apoptosis in SKOV-3 Cells. *Asian Pacific J. Cancer Prev.* **15**, 797–802 (2014).

118. Chan, H.-C., Liao, Y.-H., Chang, H.-W. & Liu, C.-H. The mechanism of anticancer activity of the new synthesized compound - 6,7-Methylenedioxy-4-(2,4-dimethoxyphenyl)quinolin −2(1H)-one(12e) in human ovarian cancer cell lines. *Taiwan. J. Obstet. Gynecol.* **60**, 266–272 (2021).

119. Brauchle, E., Thude, S., Brucker, S. Y. & Schenke-Layland, K. Cell death stages in single apoptotic and necrotic cells monitored by Raman microspectroscopy. *Sci. Rep.* **4**, 1–9 (2014).

120. Voss, A. K. & Strasser, A. The essentials of developmental apoptosis. *F1000Research* **9**, 1–12 (2020).

121. Degterev, A. & Yuan, J. Expansion and evolution of cell death programmes. *Nat. Rev. Mol. Cell Biol.* **9**, 378–390 (2008).

122. Paoli, P., Giannoni, E. & Chiarugi, P. Anoikis molecular pathways and its role in cancer progression. *Biochim. Biophys. Acta - Mol. Cell Res.* **1833**, 3481–3498 (2013).

123. Jacob, J. A. *et al.* Autophagy: An overview and its roles in cancer and obesity. *Clin. Chim. Acta* **468**, 85–89 (2017).

124. Levy, J. M. M., Towers, C. G. & Thorburn, A. Targeting autophagy in cancer. *Nat. Rev. Cancer* **17**, 528–542 (2017).

125. White, E. The role for autophagy in cancer. *J. Clin. Invest.* **125**, 42–46 (2015).

126. Yun, C. & Lee, S. The Roles of Autophagy in Cancer. *Int. J. Mol. Sci.* **19**, 1–18 (2018).

127. Cao, J. Y. & Dixon, S. J. Mechanisms of ferroptosis. *Cell. Mol. Life Sci.* **73**, 2195–2209 (2016).

128. Zilka, O. *et al.* On the Mechanism of Cytoprotection by Ferrostatin-1 and Liproxstatin-1 and the Role of Lipid Peroxidation in Ferroptotic Cell Death. *ACS Cent. Sci.* **3**, 232–243 (2017).

129. Mayer, L. D. & Janoff, A. S. Optimizing combination chemotherapy by controlling drug ratios. *Mol. Interv.* **7**, 216–223 (2007).

130. Szlasa, W., Zendran, I., Zalesińska, A., Tarek, M. & Kulbacka, J. Lipid composition of the cancer cell membrane. *J. Bioenerg. Biomembr.* **52**, 321–342 (2020).

131. Liang, C., Zhang, X., Yang, M. & Dong, X. Recent Progress in Ferroptosis Inducers for Cancer Therapy. *Adv. Mater.* **31**, 1–25 (2019).

132. Kwon, O.-S. *et al.* Systematic identification of a nuclear receptor-enriched predictive signature for erastin-induced ferroptosis. *Redox Biol.* **37**, 1–15 (2020).

133. Yagoda, N. *et al.* RAS–RAF–MEK-dependent oxidative cell death involving voltage-dependent anion channels. *Nature* **447**, 865–869 (2007).

134. Pernar, M. *et al.* Organometallic ruthenium(II)-arene complexes with triphenylphosphine amino acid bioconjugates: Synthesis, characterization and biological properties. *Bioorg. Chem.* **87**, 432–446 (2019).

135. Zhang, P. & Sadler, P. J. Redox-Active Metal Complexes for Anticancer Therapy. *Eur. J. Inorg. Chem.* **2017**, 1541–1548 (2017).

136. Tremlett, W. D. J. *et al.* Design concepts of half-sandwich organoruthenium anticancer agents based on bidentate bioactive ligands. *Coord. Chem. Rev.* **445**, 1–53 (2021).

137. Seršen, S. *et al.* Structure-Related Mode-of-Action Differences of Anticancer Organoruthenium Complexes with β-Diketonates. *J. Med. Chem.* **58**, 3984–3996 (2015).

138. Révész, L., Edgren, M. R. & Wainson, A. A. Selective toxicity of buthionine sulfoximine (BSO) to melanoma cells in vitro and in vivo. *Int. J. Radiat. Oncol.* **29**, 403–406 (1994).

Chapter 4 - Spacer Bioisosteres

Mode And Mechanism Of Action And DNA

Damage Differences Induced By The Inclusion Of

A Spacer Bioisostere In The Iminopyridine Ligand

Of Ruthenium Piano-Stool Complexes

4-1: Introduction

4-1.1: DNA control, damage, and repair

DNA is one of the most highly regulated and controlled elements in the cell, even when highly dysregulated in cancer[1]. Due to the many levels of DNA regulation from its synthesis to its expression, there is a wide range of targets available to non-targeted treatments shown in Figure 4-1[2].
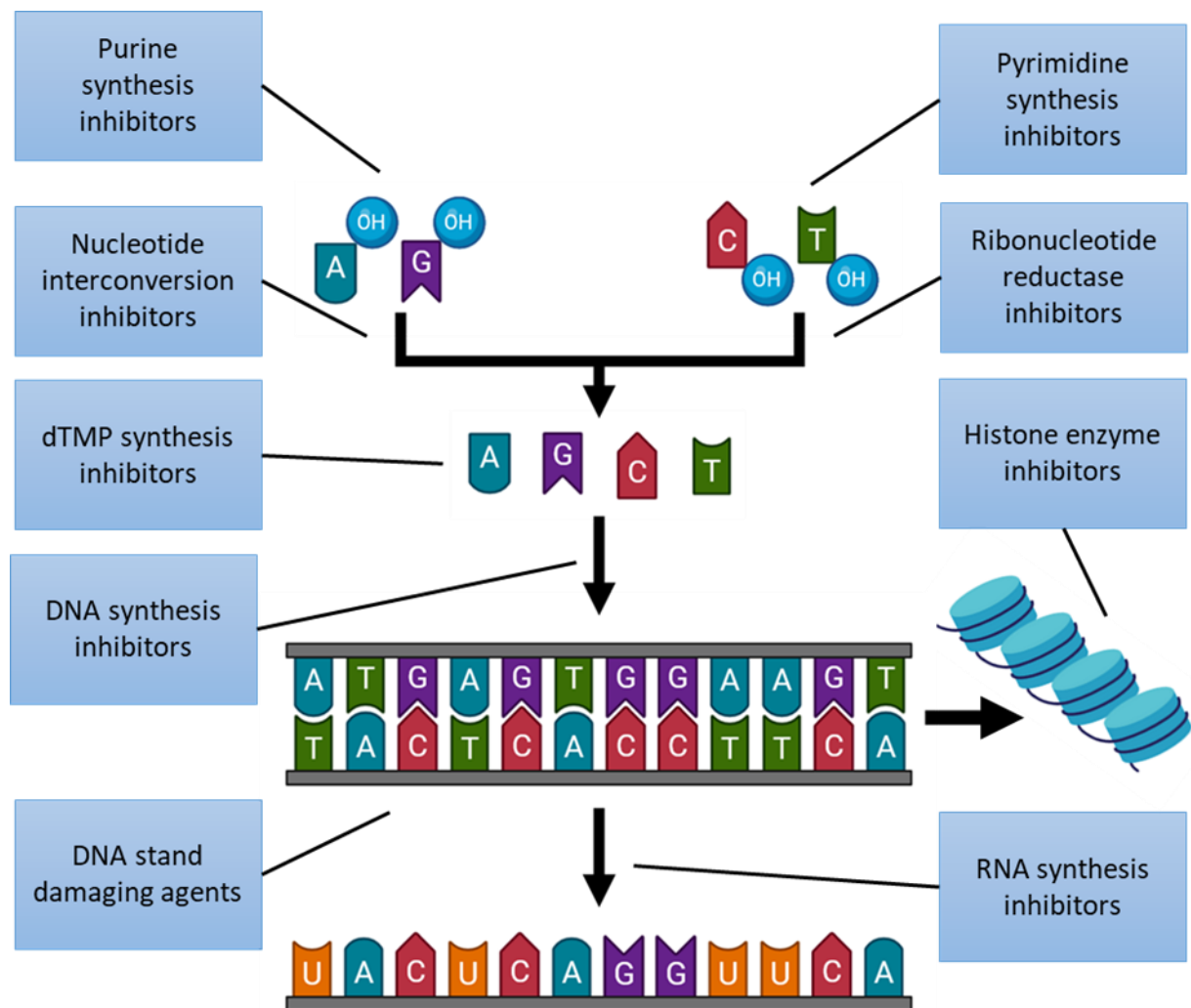
Figure 4-1: Variety of DNA-targeting treatment families that can be used in cancer treatment highlighting that DNA damage can occur from the prevention of successful DNA synthesis by preventing the effective synthesis of nucleobases to the inhibition of transcription preventing effective synthesis of RNA.

To allow for the multiple levels of control DNA has several layers of structure:

- Primary structure – single strand DNA (ssDNA) formation of the sugar-phosphate back bone of deoxynucleotides by phosphodiester bonds.

- Secondary structure – formation of double strand DNA (dsDNA) by hydrogen bonding between Adenine with Thymine and Guanine with Cytosine.

- Tertiary structure – winding of dsDNA to form helices.

- Quaternary structure – dsDNA helices are wound and unwound around histone proteins forming nucleosomes[3].

Furthermore, each of these layers of structure can be damaged in a multitude of ways (Figure 4-2)[4]. Damage types include nucleotide mutations, development of apurinic sites, nucleotide deletion, DNA adduct formation, mismatch pairing, ssDNA breaks, dsDNA breaks and DNA strand cross-links[4,5]. DNA damaging agents can directly affect the DNA strand, like CDDP along with its second-generation complexes Oxaliplatin and Carboplatin. These are effective at inducing DNA damage by directly binding to two Guanine-N7 and inducing mono, inter and intra-strand cross-links in addition to causing dsDNA breaks, the most lethal form of DNA damage[6–10]. CDDP has also been known to induce ROS and calcium release, all culminating in intrinsic apoptosis[6]. DNA damage can also occur through inhibition of associated DNA machinery. For example Etoposide induces ssDNA and dsDNA breaks by reversable inhibition of DNA topoisomerase II[11,12]. Topoisomerase II which unwinds, cleaves and reseals sdDNA, therefore when etoposide binds it causes stabilisation of the cleavable complex, preventing resealing of strand breaks, leading to intrinsic apoptosis p53 dependently and cell death[11,12]. Another example is Trichostatin A (TriA), a hydroxamic acid derivative[13–15]. As a bidentate zinc chelator with a rigid diene spacer, TriA inhibits histone deacetylase (HDAC) class I and II activity through occupying the HDAC substrate channel[14]. Furthermore, TriA has also been documented to induce anti-oxidant and anti-inflammatory activity by increasing GSH and catalyse levels, reducing interleukin and NF-κB, and inducing p53 dependant apoptosis and decreasing MMP enzyme activity[15,16].
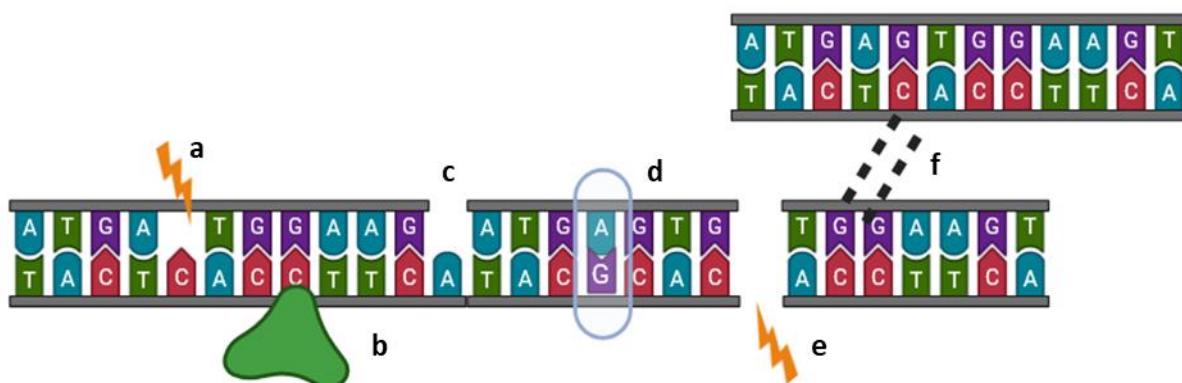
Figure 4-2: Different types of DNA strand damage possible due to endogenous and exogenous causes: a). Small scale nucleobase damage from oxidative, alkylating and deamination events, b). Large scale nucleotide damage causing bulky adducts, c). Single strand DNA (ssDNA) breaks due to backbone damage, d). Nucleotide base mismatch from faulty synthesis, e). Double strand DNA (dsDNA) breaks from large scale backbone damage, f). DNA cross linkage usually though di-adduct formation.

In cancer, there is a global alteration in genomic regulation to promote expression of oncogenes and reduce expression of tumour suppressors. To aid this, cancer cells develop defective DNA repair mechanisms to increase genomic instability and mutation to aid tumour development[17]. By taking advantage of compromises in repair, DNA is frequently targeted by cancer therapeutics due to DNA damage being a predominant inducer apoptosis and being a consistent viable target across all cancer types. Yet, DNA targeting treatments are coupled with significant side effects, for example CDDP induces significant gastrointestinal and nephrotoxicity while etoposide can induce secondary cancers[12,18]. Therefore, there is a continual need to develop new, DNA targeting complexes that do not share this toxicity, and organometallic complexes like RM175 can achieve this[19].

4-1.2: Spacers, linkers, and bridges used in organometallic complexes

The use of specialised functional groups to join two independently active groups in pharmaceuticals has been widely explored and exploited to improve the potency and efficacy of treatments, especially so in antibody-drug conjugates[20]. Dependant on their properties, these functional groups can be known as linkers, bridges, or spacers, and fall into two main categories: cleavable or non-cleavable. Cleavable

connectors can be chemically severed producing two daughter molecules, while non-cleavable connectors are transported and maintained as a singular molecule to their target.

In organometallic complexes, there has been interest in the binding of biologically relevant molecules to a complex to take advantage of potential uptake mechanisms and prevent detoxification using bridges, linkers, and spacers. One key example is the use of glucose and other sugar derivatives in auxiliary ligands designed to take advantage of the altered glucose uptake and metabolic regulation in cancer (Figure 4-3e). Using sugars such as glucose, mannose and rhamnose, complexes exhibited moderate to significant potency against prostate cancer[21]. Other examples include the use of nucleobase derivatives in the organometallic structures, which theoretically allows for DNA interactions and synthesis inhibition when integrated while also harnessing the MOA traits of organometallic complexes including $\Delta\Psi m$ depolarisation and ROS generation[22,23].

Bioactive groups have not been limited to biological molecules. There have been significant advancements in the conjugation of organometallic complexes to other cytotoxic treatments. Key examples are the conjugation of ferrocene to tamoxifen, to PTX and to 5-flurouracil (Figure 4-3a, b, and c)[22]. There are also instances of SAHA, a HDACi being conjugated to organometallic piano-stool complexes (Figure 4-3d)[24]. Shown by the variety of applications complexes with active cargos and linkers exhibit, there is potential for their use to improve current treatments. However, the use of linkers and cargo attachment on the potency of a complex is highly unpredictable. This is shown by the potencies of the Figure 4-3e sugar derivatives with the glucose form being highly ineffective while the mannose derivative is highly potent[21]. Furthermore, the SAHA derivatives are less potent than their HDACi unchelated derivatives, while the tamoxifen and PTX organometallic conjugates both exhibit nanomolar IC_{50} values[21,22,24,25].
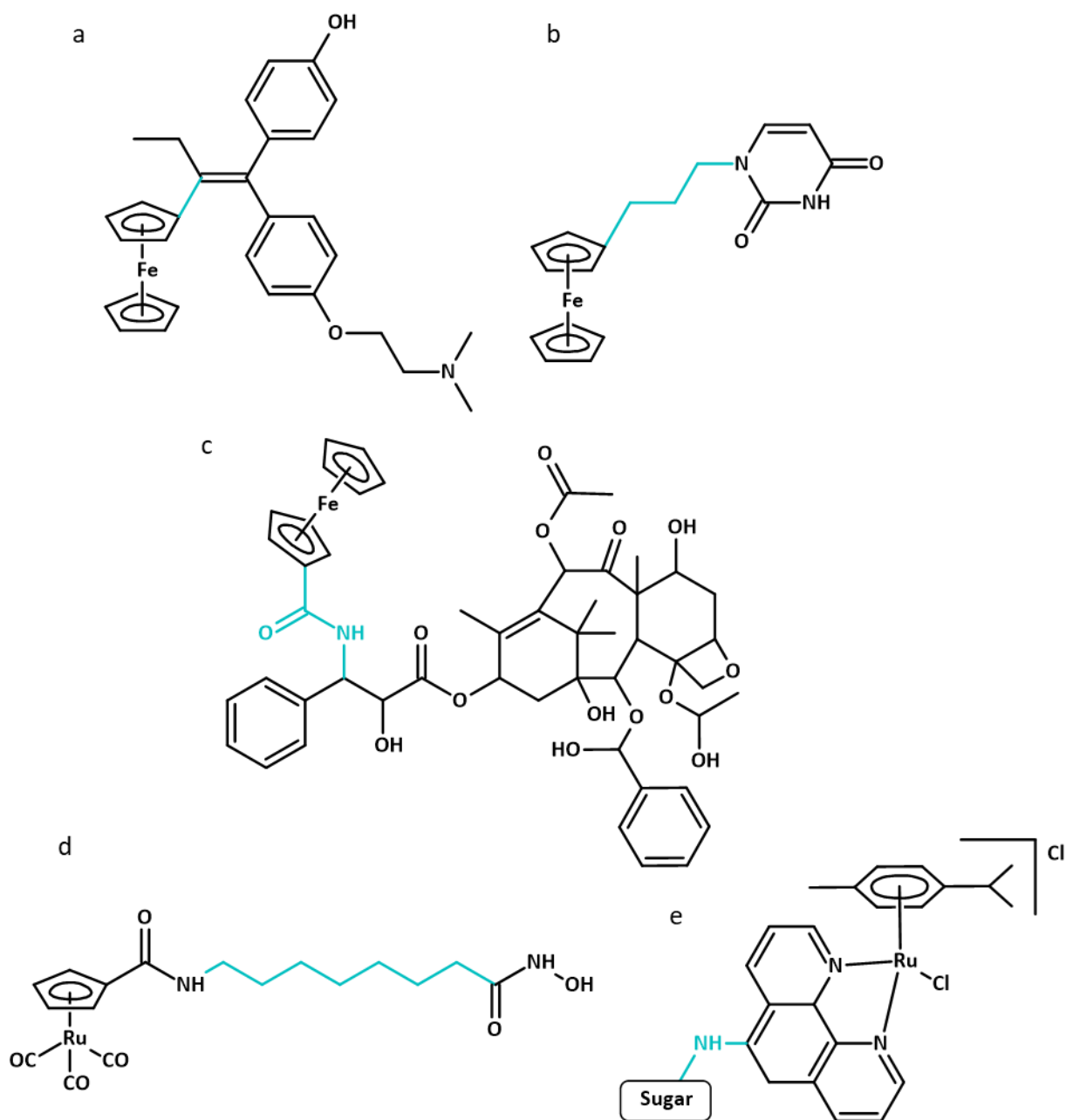
Figure 4-3: Selection of organometallic complexes that use linkers, spacers, or bridges between bioactive molecules and organometallic moieties. a). ferrocifen, b). ferrocene-5-fluorouracil conjugate, c). ferrocene-paclitaxel conjugate, d). ruthenium-SAHA conjugate, e). ruthenium-sugar conjugate.

4-1.3: Alkyl chain spacers

In the current literature, there are many examples of alkyl chains being used on the periphery of complexes to improve potency, alter structure and shift MOA[23,26–28]. These chains are most often used

as a spacer between the complex and an active cargo/moiety or to synthesise di/multi-nuclear complexes tot allow for enough steric space between the active moieties (Figure 4-4)[29,30].

There is very little research the use of a spacer within a bidentate ligand. Early work was done in osmium ImPy piano-stool complexes (Figure 4-5)[31]. These structures were used to assess transfer-hydrogenation catalysis and enable classical resolution for chirality differentiation[31]. While extensive antiproliferative screening was performed with the complexes with the added chiral carbon as part of the NCI-60 activity screen with highly efficacy for both isomers[31]. However, limited comparable antiproliferative screening between the complexes with and without the spacer have been done. Nonetheless, this screening in EOC A2780 indicated a substantial increase in potency both chlorine and iodine monodentate complexes is indicated[31–33].

Figure 4-4: Examples of complexes that use alkyl spacers to attach cargo. a). ferrocene-5-fluorouracil conjugates with varying methyl side chain length, b). cisplatin-derivative polymers, c). RAPTA-C derivative binuclear complexes with varying spacer length and type.
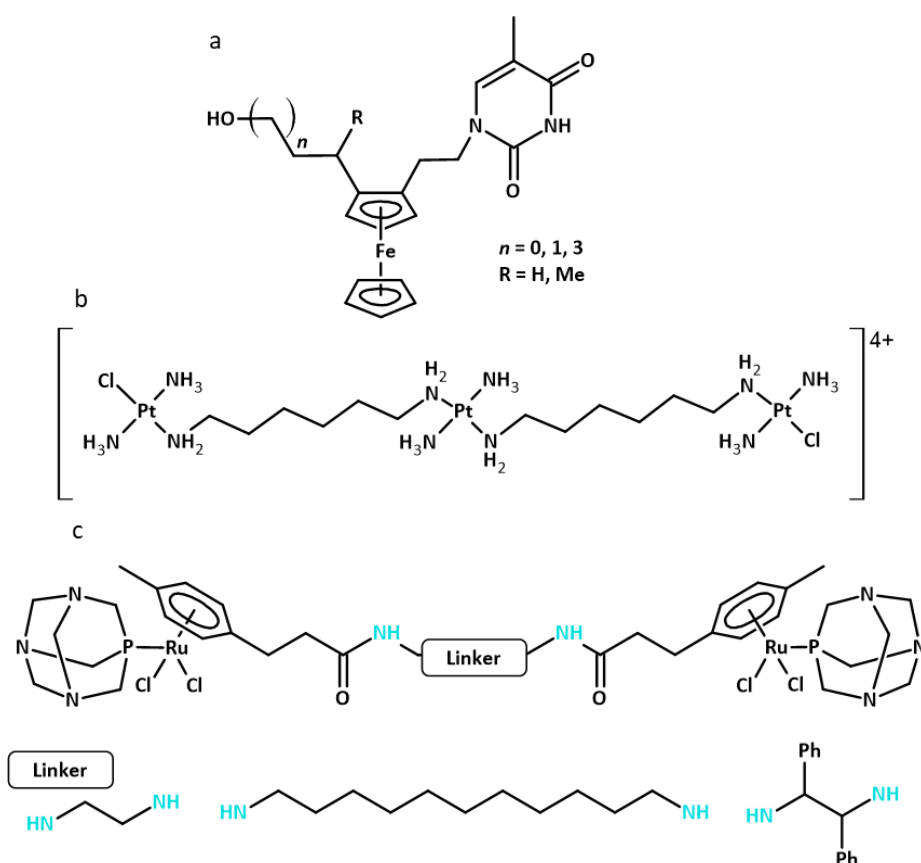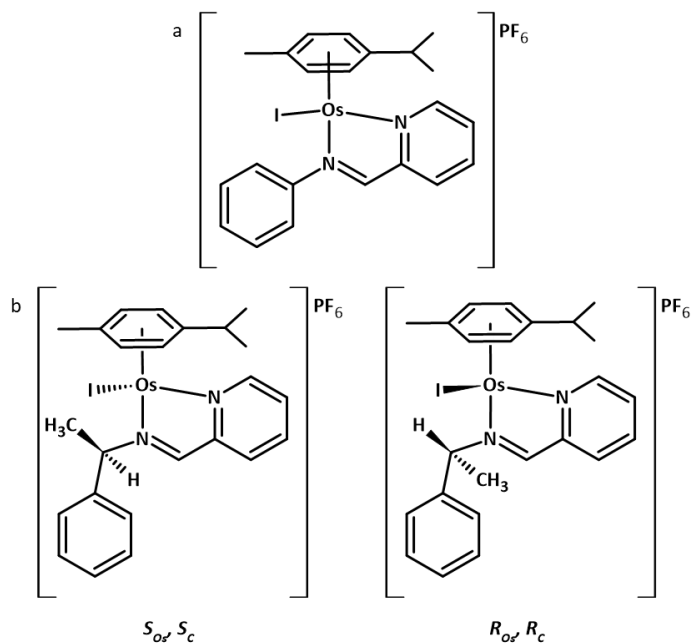
Figure 4-5: Osmium piano-stool complexes synthesised a). without and b). with an alkyl spacer to introduce a chiral carbon within the complex bidentate ligand to assess isomerism in transfer hydrogenation activity[31]. However limited antiproliferation studies were done[31–33].

4-1.4: Overview of work in Chapter 4

This chapter assessed the potential of a spacer bioisostere within the ImPy bidentate ligand of ruthenium piano-stool complexes by generating a series of $[Ru(\eta^6\text{-}p\text{-Cym})(ImPy)X]PF_6$ and $[Ru(\eta^6\text{-}p\text{-Cym})(ImPy\text{-}Bn)X]PF_6$ complexes. Physiochemical, biological and antiproliferative activity in a variety of cell lines was carried out to determine structure activity relationships. The best candidate pair, complexes **7** and **9**, were then taken forward for comparison and to understand differences in MOA in the EOC cell line A2780 with particular attention to DNA damage induced by the complexes.

4-2: Experimental section

4-2.1: Ligand and complex synthesis

ImPy ligands used in this chapter are shown in Figure 4-6. Ligands were synthesised using the synthetic scheme shown in Scheme 2-1, except for ImPy-4-OH which was previously synthesised[34]. Full synthetic information is given in Appendix II. Ligands **L1** and **L2** were previously used in Chapter 3.
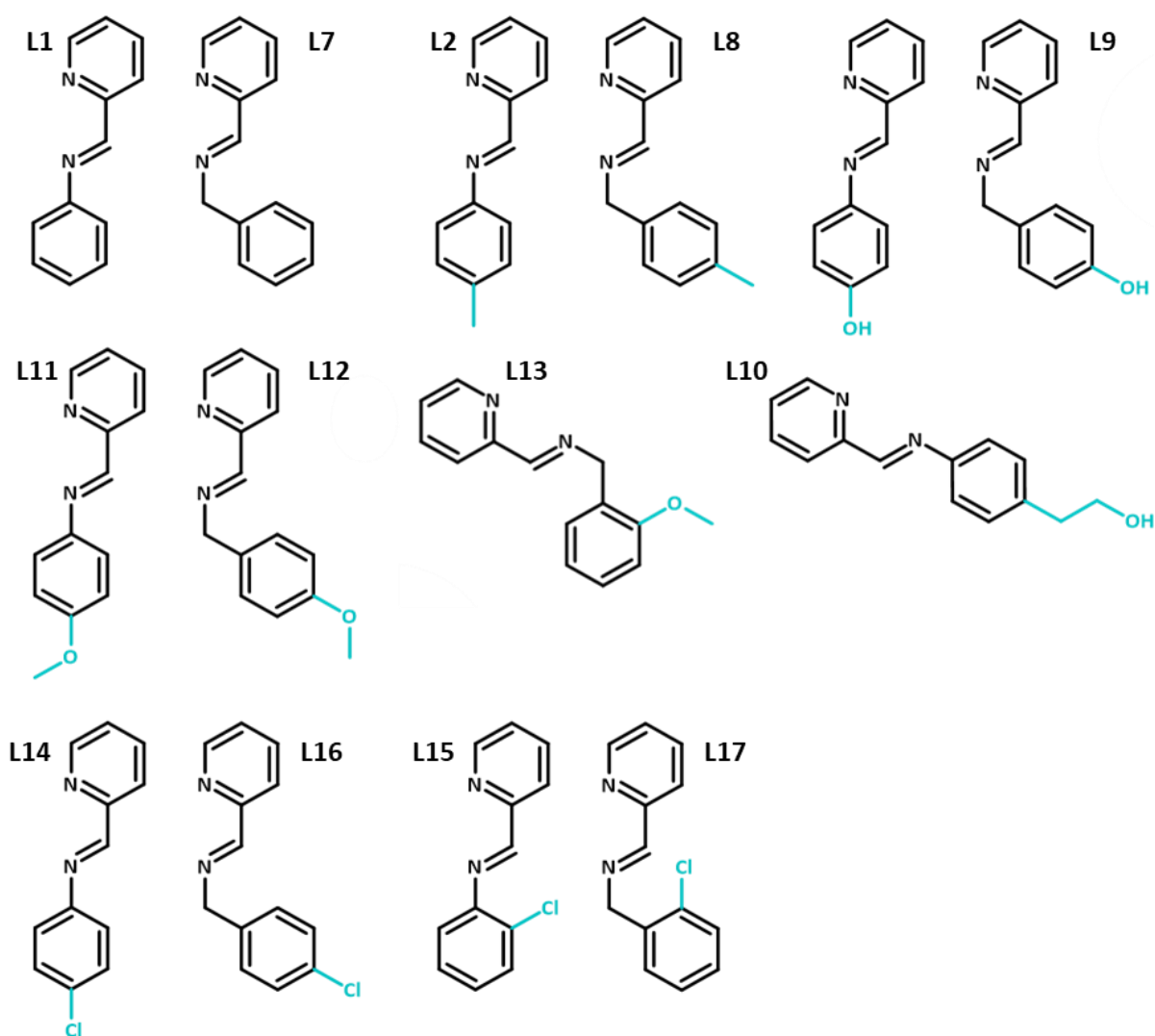
Figure 4-6: Structures of the 14 ligands used in Chapter 4 with the differing active groups highlighted in blue. Ligands are presented in pairs with and without the spacer.

Complexes were then synthesised using the synthetic scheme shown in Scheme 2-1. Complexes *1* and *2* were previously synthesized in Chapter 3.

4-2.1.1: *Complex 7-* Ru(L1)I(PF$_6$), [Ru(η^6-*p*-Cym)(ImPy)I]PF$_6$

According to reaction scheme 2-2, diiodo(p-cymene)ruthenium(II) dimer (126.8 mg, 0.13 mmol) was mixed with **L1** (47.24 mg, 0.26 mmol). Following which ammonium hexafluorophosphate (105.7 mg, 0.65 mmol) was added producing a solid weighing 104.9 mg (58.96%). ^{1}H NMR (400 MHz; DMSO-d$_6$) 0.96 (d, J=6.8 Hz, 3H), 1.00 (d, J=7.0 Hz, 3H), 2.36 (s, 3H), 2.60 (m, 1H), 5.60 (d, J=6.3 Hz, 1H), 5.66 (d, J=6.3 Hz, 1H), 5.80 (d, J=6.3 Hz, 1H), 6.01 (d, J=6.3 Hz, 1H), 7.63 (m, 3H), 7.83 (qd, J=5.8, 2.2 Hz, 1H), 7.87 (dd, J=8.1, 1.8 Hz, 2H), 8.27 (dd, J=7.9, 0.96 Hz, 1H), 8.31 (dd, J=8.2, 2.2 Hz, 1H), 8.88 (s, 1H), 9.56 (d, J=5.5 Hz, 1H). ^{13}C NMR (400 MHz; DMSO-d$_6$) 19.83, 21.51, 27.72, 31.01, 85.80, 85.95, 86.24, 86.26, 101.78, 107.54, 123.19, 128.42, 129.48, 130.01, 130.30, 139.62, 152.19, 154.55, 157.29, 167.35. m/z (ESI-MS) found a highest intensity peak for the fragment of 545.00, with a calculated of 545.00 (M+ [C$_{22}$H$_{24}$IN$_2$Ru]$^+$).

4-2.1.2: *Complex 8 -* Ru(L7)Cl(PF$_6$), [Ru(η^6-*p*-cym)(ImPy-Bn)Cl]PF$_6$

According to reaction scheme 2-2, dichloro(p-cymene)ruthenium(II) dimer (303.7 mg, 0.50 mmol) was mixed with **L7** (194.7 mg, 0.99 mmol). Following which ammonium hexafluorophosphate (404.2 mg, 2.48 mmol) was added, solid was precipitated and recrystalised using chilled ethanol and water producing a solid weighing 410.2 mg (63.05%). ^{1}H NMR (400 MHz; DMSO-d$_6$) δ 0.90 (d, J=7.0 Hz, 3H), 0.99 (d, J=6.7 Hz, 3H), 2.11 (s, 3H), 2.51 (m, 1H), 5.47 (dd, J=15.9, 1.2 Hz, 1H), 5.70 (dd, J=15.8, 1.7 Hz, 1H), 5.87 (d, J=9.2 Hz, 1H), 5.88 (d, J=9.1 Hz, 1H), 5.99 (d, J=6.1 Hz, 1H), 6.25 (d, J=6.2 Hz, 1H), 7.50 (m, 5H), 7.79 (qd, J= 5.81, 3.07 Hz, 1H), 8.22 (m, 2H), 8.44 (s, 1H), 9.54 (d, J=5.5 Hz, 1H). ^{13}C NMR (400 MHz; DMSO-d$_6$) δ 18.05, 18.38, 21.48, 22.03, 30.43, 57.60, 68.66, 83.86, 84.20, 84.39, 87.62, 103.71, 104.37,

128.25, 128.88, 129.06, 129.33, 129.89, 134.35, 139.70, 154.49, 155.85, 167.21. m/z (ESI-MS) found a highest intensity peak for the fragment of 467.08, with a calculated of 467.08 (M+ $[C_{23}H_{26}ClN_2Ru]^+$).

4-2.1.3: *Complex 9* - Ru(L7)I(PF$_6$), [Ru(η^6-*p*-cym)(ImPy-Bn)I]PF$_6$

According to reaction scheme 2-2, diiodo(p-cymene)ruthenium(II) dimer (505.7 mg, 0.51 mmol) was mixed with **L7** (186.5 mg, 1.02 mmol). Following which ammonium hexafluorophosphate (416.6 mg, 2.56 mmol) was added, solid was precipitated and recrystalised using chilled ethanol and water producing a solid weighing 214.1 mg (29.77%). ^{1}H NMR (400 MHz; DMSO-d$_6$) δ 0.90 (d, J=7.2 Hz, 3H), 1.07 (d, J=7.0, 3H) 2.39 (s, 3H), 2.70 (m, 1H), 5.49 (d, J=15.9 Hz, 1H), 5.71, (dd, J=16.0, 1.7 Hz, 1H), 5.96 (t, J=5.9 Hz, 2H), 6.05 (d, J=6.1 Hz, 1H), 6.16 (d, J=6.3, 1H), 7.51 (m, 5H), 7.73 (qd, J=5.5, 1.6 Hz, 1H), 8.17 (td, J=7.8, 1.2 Hz, 1H), 8.24 (dd, J=7.9, 1.4 Hz, 2H), 9.52 (d, J=5.5 Hz, 1H). ^{13}C NMR (400 MHz; DMSO-d$_6$) 20.57, 21.89, 22.50, 31.52, 70.52, 84.90, 85.51, 85.85, 87.31, 102.45, 107.33, 127.79, 128.26, 129.51, 129.67, 130.02, 130.52, 134.63, 139.79, 154.96, 157.45, 166.39. m/z (ESI-MS) found a highest intensity peak for the fragment of 559.02, with a calculated of 559.02 (M+ $[C_{23}H_{26}IN_2Ru]^+$).

4-2.1.4: *Complex 10* - Ru(L8)Cl(PF$_6$), [Ru(η^6-*p*-cym)(ImPy-Bn-4-Me)Cl] PF$_6$

According to reaction scheme 2-2, dichloro(p-cymene)ruthenium(II) dimer (110.1 mg, 0.18 mmol) was mixed with **L8** (75.6 mg, 0.36 mmol). Following which ammonium hexafluorophosphate (146.5 mg, 0.90 mmol) was added producing a solid weighing 183.0 mg (83.17%). ^{1}H NMR (400 MHz; DMSO-d$_6$) δ 0.91 (d, J=7.0 Hz, 3H), 1.00 (d, J=6.9 Hz, 3H), 2.13 (s, 3H), 2.36 (s, 3H), 2.55 (m, 1H), 5.39 (d, J=16.2 Hz, 1H), 5.68 (dd, J=16.1, 1.5 Hz, 1H), 5.88 (d, J=6.2 Hz, 1H), 5.91 (d, J=6.0 Hz, 1H), 6.05 (d, 6.1 Hz, 1H), 6.25 (d, J=6.2 Hz, 1H), 7.31 (d, J=8.0 Hz, 2H), 7.37 (d, J=8.00 Hz, 2H), 7.79 (dd, J=5.5, 4.7Hz, 1H), 8.21 (d, J=4.2 Hz, 2H), 8.36 (s, 1H), 9.54 (d, J=5.6 Hz, 1H). ^{13}C NMR (400 MHz; DMSO-d$_6$) δ 18.38, 20.89, 21.50, 22.00, 30.44, 68.38, 83.90, 84.16, 84.51, 87.57, 103.64, 104.35, 128.18, 129.28, 129.67, 129.92, 131.26,

138.24, 139.66, 154.52, 155.82, 166.60. m/z (ESI-MS) found a highest intensity peak for the fragment of 481.09, with a calculated of 481.10 (M+ [$C_{24}H_{28}ClN_2Ru$]$^+$).

4-2.1.5: Complex 11 - [Ru(η^6-*p*-Cym)(ImPy-4-OH)Cl]PF$_6$

According to reaction scheme 2-2, dichloro(p-cymene)ruthenium(II) dimer (86.04 mg, 0.14 mmol) was mixed with ImPy-4-OH (53.6 mg, 0.27 mmol). Following which ammonium hexafluorophosphate (110.2 mg, 0.68 mmol) was added producing a solid weighing 133.6 mg (80.08%). ^{1}H NMR (400 MHz; DMSO-d$_6$) δ 0.97 (dd, J=6.9, 4.7 Hz, 6H), 2.17 (s, 3H), 2.48 (m, 1H), 5.61 (s, 2H), 5.76 (d, J=6.2 Hz, 1H), 6.09 (d, J=6.2 Hz, 1H), 6.97 (dt, J=8.9, 2.5 Hz, 2H), 7.67 (dt, J=8.9, 2.5 Hz, 2H), 7.84 (qd, J=5.6, 1.6 Hz, 1H), 8.21 (d, J=7.7, 1.0 Hz, 1H), 8.28 (td, J=7.7, 1.2 Hz, 1H), 8.81 (s, 1H), 9.53 (d, J=5.5 Hz, 1H). ^{13}C NMR (400 MHz; DMSO-d$_6$) δ 18.33, 21.62, 21.70, 30.48, 84.56, 85.10, 86.46, 86.69, 103.75, 104.64, 115.73, 119.05, 124.30, 128.41, 129.36, 139.85, 143.60, 154.81, 155.86, 158.98, 165.00. m/z (ESI-MS) found a highest intensity peak for the fragment of 469.06, with a calculated of 469.06 (M+ [$C_{22}H_{24}N_2OClRu$]$^+$).

4-2.1.6: Complex 12 - Ru(L9)Cl(PF$_6$), [Ru(η^6-*p*-Cym)(ImPy-Bn-4-OH)Cl]PF$_6$

According to reaction scheme 2-2, dichloro(p-cymene)ruthenium(II) dimer (109.0 mg, 0.18 mmol) was mixed with **L9** (75.5 mg, 0.36 mmol). Following which ammonium hexafluorophosphate (145.1 mg, 0.89 mmol) was added producing a solid weighing 199.3 mg (89.16%). 1H NMR (400 MHz; DMSO-d$_6$) δ 0.98 (d, J=6.9 Hz, 6H), 2.16 (s, 1H), 2.49 (m, 1H), 4.64 (d, J=5.7 Hz, 2H), 5.44 (t, J=5.7 Hz, 1H), 5.60 (dd, J=9.0, 2.5 Hz, 2H), 5.76 (d, J=6.3 Hz, 1H), 6.10 (d, J=6.2 Hz, 1H), 7.56 (d, J=8.5 Hz, 2H), 7.77 (d, 8.5 Hz, 2H), 7.88 (qd, J= 5.8, 1.7 Hz, 1H), 8.27 (dd, J= 7.8, 1.3 Hz, 1H), 8.31 (td, J=7.6, 1.3 Hz, 1H), 8.91 (s, 1H), 9.57 (d, J=5.4 Hz, 1H). 13C NMR (400 MHz; DMSO-d$_6$) δ 18.32, 21.60, 21.72, 30.51, 62.25, 84.77, 85.11, 86.28, 86.53, 103.62, 104.97, 122.35, 127.12, 128.84, 129.97, 139.95, 144.50, 150.31, 154.58, 155.98, 167.32. m/z (ESI-MS) found a highest intensity peak for the fragment of 483.08, with a calculated of 483.08 (M+ [$C_{23}H_{26}N_2OClRu$]$^+$).

4-2.1.7: *Complex 13 -* Ru(L10)Cl(PF$_6$), [Ru(η^6-*p*-Cym)(ImPy-(CH$_2$)$_2$-4-OH)Cl]PF$_6$

According to reaction scheme 2-2, dichloro(p-cymene)ruthenium(II) dimer ((106.4 mg, 0.17 mmol) was mixed with **L10** (78.6 mg, 0.35 mmol). Following which ammonium hexafluorophosphate (141.6 mg, 0.87 mmol) was added producing a solid weighing 194.6 mg (87.23%). ^{1}H NMR (400 MHz; DMSO-d$_6$) δ 0.98 (d, J=6.9 Hz, 6H), 2.16 (s, 1H), 2.51 (m, 1H), 2.86 (t, J=6.8 Hz, 2H), 3.37 (s, 1H), 3.70 (t, J=6.9 Hz, 2H), 5.58 (d, J=6.2 Hz, 1H, 5.63 (d, J=6.3 Hz, 1H), 5.76 (d, J=6.2 Hz, 1H), 6.10 (d, J=6.4, 1H), 7.47 (d, J=8.4 Hz, 2H), 7.72 (d, J=8.4 Hz, 2H), 7.88 (qd, J=5.6, 2.7 Hz, 1H), 8.25 (dd, J=7.7, 1.3 Hz, 1H), 8.31 (td, J=7.7, 1.3 Hz, 1H), 8.89 (s, 1H), 9.57 (d, J=5.5 Hz, 1H). ^{13}C NMR (400 MHz; DMSO-d$_6$) δ 18.32, 21.58, 21.74, 30.50, 38.56, 61.77, 84.77, 85.08, 86.22, 86.60, 103.60, 104.94, 122.33, 128.79, 129.86, 139.94, 141.83, 149.78, 154.59, 155.97, 167.14. m/z (ESI-MS) found a highest intensity peak for the fragment of 497.09, with a calculated of 497.09 (M+ [C$_{24}$H$_{28}$N$_2$OClRu]$^+$).

4-2.1.8: *Complex 14 -* Ru(L11)Cl(PF$_6$), [Ru(η^6-*p*-Cym)(ImPy-4-OMe)Cl]PF$_6$

According to reaction scheme 2-2, dichloro(p-cymene)ruthenium(II) dimer (113.9 mg, 0.19 mmol) was mixed with **L11** (79.0 mg, 0.37 mmol). Following which ammonium hexafluorophosphate (151.1 mg, 0.93 mmol) was added producing a solid weighing 223.7 mg (95.77%). ^{1}H NMR (400 MHz; DMSO-d$_6$) δ 0.98 (d, J=6.9, 6H), 2.17 (s, 3H), 2.47 (m, 1H), 3.88 (s, 3H), 5.60 (d, J=5.9 Hz, 1H), 5.63 (d, J=6.3 Hz, 1H), 5.77 (d, J=6.3 Hz, 1H), 6.10 (d, J=6.3 , 1H), 7.17 (dt, J=9.0, 2.1 Hz, 2H), 7.78 (dt, J=8.9, 2.1 Hz, 2H), 7.86 (qd, J=5.6, 1.7 Hz, 1H), 8.23 (dd, J=7.7, 1.3 Hz, 1H), 8.30 (td, J=7.7, 1.2 Hz, 1H), 8.86 (s, 1H), 9.55 (d, J=5.4 Hz, 1H). ^{13}C NMR (400 MHz; DMSO-d$_6$) δ 18.32, 21.58, 21.75, 30.49, 55.67, 84.67, 85.07, 86.40, 86.55, 103.71, 104.77, 114.51, 124.16, 128.58, 129.60, 139.89, 144.88, 164.72, 155.92, 160.25, 165.98. m/z (ESI-MS) found a highest intensity peak for the fragment of 483.078, with a calculated of 483.08 (M+ [C$_{23}$H$_{26}$N$_2$OClRu]$^+$).

4-2.1.9: *Complex 15 -* Ru(L12)Cl(PF$_6$), [Ru(η^6-*p*-Cym)(ImPy-Bn-4-OMe)Cl]PF$_6$

According to reaction scheme 2-2, dichloro(p-cymene)ruthenium(II) dimer (113.1 mg, 0.18 mmol) was mixed with **L12** (83.6 mg, 0.37 mmol). Following which ammonium hexafluorophosphate (150.5 mg, 0.92 mmol) was added producing a solid weighing 201.3 mg (84.89%). ^{1}H NMR (400 MHz; DMSO-d$_6$) δ 0.92 (d, J=6.9 Hz, 3H), 1.01 (d, J=6.9 Hz, 3H) 2.13 (s, 3H), 2.56 (m, 1H), 3.80 (s, 3H), 5.35 (d, J=16.1 Hz, 1H), 5.68 (dd, J=16.1, 1.2 Hz, 1H), 5.90 (d, J=6.3 Hz, 1H), 5.92 (d, J=6.3 Hz, 1H), 6.09 (d, J=6.0 Hz, 1H), 6.25 (d, J=6.3 Hz, 1H), 7.05 (dt, J=8.7, 1.8 Hz, 2H), 7.39 (dt, J=8.5, 1.8 Hz, 2H), 7.78 (m, 1H), 8.20 (d, J=4.4 Hz, 2H), 8.33 (s, 1H), 9.54 (d, J=5.5 Hz, 1H). ^{13}C NMR (400 MHz; DMSO-d$_6$) δ 18.40, 21.51, 22.02, 30.45, 55.20, 68.07, 83.87, 84.14, 84.57, 87.61, 103.67, 104.31, 114.45, 126.14, 128.14, 129.23, 131.45, 139.66, 154.55, 155.83, 159.55, 166.25. m/z (ESI-MS) found a highest intensity peak for the fragment of 497.10, with a calculated of 497.09 (M+ [C$_{24}$H$_{28}$N$_2$OClRu]$^+$).

4-2.1.10: *Complex 16 -* Ru(L13)Cl(PF$_6$), [Ru(η^6-*p*-Cym)(ImPy-Bn-2-OMe)Cl]PF$_6$

According to reaction scheme 2-2, dichloro(p-cymene)ruthenium(II) dimer (111.8 mg, 0.37 mmol) was mixed with **L13** (82.6 mg, 0.37 mmol). Following which ammonium hexafluorophosphate (148.8 mg, 0.91 mmol) was added producing a solid weighing 147.4 mg (62.88%). ^{1}H NMR (400 MHz; DMSO-d$_6$) δ 0.95 (d, J=7.0 Hz, 3H), 1.01 (d, J=6.9 Hz, 3H), 2.17 (s, 3H), 2.57 (m, 1H), 2.81 (s, 3H), 5.20 (d, J=16.6 Hz, 1H), 5.77 (d, J=16.5 Hz, 1H), 5.09 (d, J=5.8 Hz, 2H), 6.14 (d, J=6.1 Hz, 1H), 6.26 (d, J=6.2 Hz, 1H), 7.07 (t, J=7.4 Hz, 1H), 1.18 (d, J=8.4 Hz, 1H), 7.40 (dd, J=7.4 , 1.6 Hz, 1H), 7.50 (m, 1H), 8.22 (m, 3H), 9,54 (d, J=5.5 Hz, 1H). ^{13}C NMR (400 MHz; DMSO-d$_6$) δ 18.48, 21.39, 21.96, 30.49, 55.50, 64.36, 83.34, 83.89, 85.12, 87.82, 103.84, 104.28, 111.66, 120.89, 121.66, 128.10, 129.21, 131.12, 131.91, 139.67, 154.53, 155.85, 157.83, 165.30. m/z (ESI-MS) found a highest intensity peak for the fragment of 497.09, with a calculated of 487.09 (M+ [C$_{24}$H$_{28}$N$_2$OClRu]$^+$).

4-2.1.11: *Complex 17* - Ru(L14)Cl(PF$_6$), [Ru(η^6-*p*-Cym)(ImPy-4-Cl)Cl]PF$_6$

According to reaction scheme 2-2, dichloro(p-cymene)ruthenium(II) dimer (94.3 mg, 0.15 mmol) was mixed with **L14** (66.7 mg, 0.31 mmol). Following which ammonium hexafluorophosphate (125.5 mg, 0.77 mmol) was added producing a solid weighing 179.3 mg (92.07%). ^{1}H NMR (400 MHz; DMSO-d$_6$) δ 0.97 (d, J=1.50 Hz, 3H), 0.99 (d, J=1.45 Hz, 3H), 2.36 (s, 3H), 2.59 (m, 1H), 5.59 (d, J=6.3 Hz, 1H), 5.71 (d, J=6.3 Hz, 1H), 5.79 (d, J=6.2 Hz, 1H), 6.01 (d, J=6.3 Hz, 1H), 7.72 (dt, J=8.8, 2.1 Hz, 3H), 7.84 (dt, J=8.8, 2.1 Hz, 3H), 7.90 (qd, J=5.5, 1.7 Hz, 1H), 8.27 (dd, J=7.6, 1.5 Hz, 1H), 8.23 (dd, J=7.6, 1.3 Hz, 1H), 8.32 (td, J=7.6, 1.1 Hz, 1H), 8.88 (s, 1H), 9.56 (d, J=5.5 Hz, 1H). ^{13}C NMR (400 MHz; DMSO-d$_6$) δ 18.34, 21.61, 21.77, 30.50, 84.75, 84.85, 86.06, 86.73, 103.89, 105.15, 124.38, 129.07, 129.59, 130.29, 134.07, 140.01, 150.46, 154.42, 156.06, 168.51. m/z (ESI-MS) found a highest intensity peak for the fragment of 487.03, with a calculated of 487.03 (M+ [C$_{22}$H$_{23}$Cl$_2$N$_2$Ru]$^+$).

4-2.1.12: *Complex 18* - Ru(L15)Cl(PF$_6$), [Ru(η^6-*p*-Cym)(ImPy-2-Cl)Cl]PF$_6$

According to reaction scheme 2-2, dichloro(p-cymene)ruthenium(II) dimer (110.0 mg, 0.18 mmol) was mixed with **L15** (77.8 mg, 0.36 mmol). Following which ammonium hexafluorophosphate (146.0 mg, 0.90 mmol) was added producing a solid weighing 201.8 mg (88.83%). ^{1}H NMR (400 MHz; DMSO-d$_6$) δ 0.95 (d, J=6.9 Hz, 3H), 1.00 (d, J=6.9 Hz, 3H), 2.12 (s, 3H), 2.60 (m, 1H), 5.36 (d, J=6.3 Hz, 1H), 5.72 (d, J=6.1 Hz, 1H), 5.80 (d, J=6.4 Hz, 1H), 6.13 (d, J=6.3 Hz, 1H), 7.59 (m, 2H), 7.85 (qd, J=7.8, 2.0 Hz, 2H), 7.97 (m, 1H), 8.36 (d, J=4.2 Hz, 2H), 9.09 (s, 1H), 9.67 (d, J=5.5 Hz, 1H). ^{13}C NMR (400 MHz; DMSO-d$_6$) δ 18.30, 21.39, 21.90, 30.57, 84.59, 85.53, 86.20, 86.99, 102.70, 105.77, 123.35, 124.78, 128.44, 129.79, 130.44, 130.64, 130.84, 140.32, 148.57, 153.85, 156.32, 172.81. m/z (ESI-MS) found a highest intensity peak for the fragment of 487.03, with a calculated of 487.03 (M+ [C$_{22}$H$_{23}$Cl$_2$N$_2$Ru]$^+$).

4-2.1.13: Complex 19 - [Ru(η^6-*p*-Cym)(ImPy-Bn-4-Cl)Cl]PF$_6$

According to reaction scheme 2-2, dichloro(p-cymene)ruthenium(II) dimer (110.7 mg, 0.18 mmol) was mixed with **L16** (83.4 mg, 0.36 mmol). Following which ammonium hexafluorophosphate (147.3 mg, 0.90 mmol) was added producing a solid weighing 161.9 mg (69.28%). ^{1}H NMR (400 MHz; DMSO-d$_6$) δ 0.92 (d, J=6.9 Hz, 3H), 1.10 (d, J=7.0 Hz, 3H), 2.11 (s, 3H), 2.57 (m, 1H), 5.46 (d, J=15.9 Hz, 1H), 5.47 (dd, J=16.0, 1.3 Hz, 1H), 5.91 (t, J=5.1 Hz, 2H), 6.11 (d, J=6.3 Hz, 1H), 6.25 (d, J=6.4 Hz, 1H), 7.50 (dt, J=8.5, 2.2 Hz, 2H), 7.56 (dt, J=8.5, 2.2 Hz, 2H), 7.80 (qd, J=5.7, 2.2 Hz, 1H), 8.18-8.25 (m, 2H), 8.44 (s, 1H), 9.54 (d, J=5.6 Hz, 1H). ^{13}C NMR (400 MHz; DMSO-d$_6$) δ 18.34, 21.49, 22.01, 30.45, 67.73, 84.10, 84.34, 84.44, 87.45, 103.46, 104.56, 128.29, 129.00, 129.34, 131.92, 133.23, 133.51, 139.71, 154.46, 155.84, 167.38. m/z (ESI-MS) found a highest intensity peak for the fragment of 501.04, with a calculated of 501.04 (M+ [C$_{23}$H$_{25}$Cl$_2$N$_2$Ru]$^+$).

4-2.1.14: Complex 20 - Ru(L17)Cl(PF$_6$), [Ru(η^6-*p*-Cym)(ImPy-Bn-2-Cl)Cl]PF$_6$

According to reaction scheme 2-2, dichloro(p-cymene)ruthenium(II) dimer (110.7 mg, 0.18 mmol) was mixed with **L17** (147.3 mg, 0.90 mmol). Following which ammonium hexafluorophosphate (147.3 mg, 0.90 mmol) was added producing a solid weighing 190.5 mg (81.39%). ^{1}H NMR (400MHz; DMSO-d$_6$) δ 0.97 (d, J=6.8 Hz, 3H), 1.04 (d, J=6.9 Hz, 3H), 2.17 (s, 3H), 2.63 (m, 1H), 5.40 (dd, J=17.3, 2.0 Hz, 1H), 5.92-6.02 (m, 3H), 6.2 (d, J=6.0 Hz, 1H), 3.60 (d J=6.3 Hz, 1H), 7.48-7.61 (m, 3H), 7.65 (dd, J=7.7, 1.4 Hz, 1H), 7.80 (qd, J=5.7, 2.4 Hz, 1H), 8.16 (t, J=1.8 Hz, 1H), 8.22 (m, 2H), 9.56 (d, J=9.6 Hz, 1H). ^{13}C NMR (400 MHz; DMSO-d$_6$) δ 18.43, 21.58, 21.96, 30.58, 66.08, 84.13, 84.90, 87.54, 103.68, 104.53, 128.18, 128.33, 129.50, 130.09, 131.32, 131.43, 133.19, 134.42, 139.73, 154.40, 155.91, 165.60. m/z (ESI-MS) found a highest intensity peak for the fragment of 501.04, with a calculated of 501.04 (M+ [C$_{23}$H$_{25}$Cl$_2$N$_2$Ru]$^+$).

4-2.2: Aqueous solution behaviour experimentation

4-2.2.1: ctDNA binding using UV-Vis spectrometry

Lyophilised ctDNA sodium salt was dissolved in 10% (v/v) methanol in PBS to prepare a 1 mg/mL stock solution, from which final assay titre concentrations ranging from 0.5 to 0.01 mg/mL were diluted. Complexes **7** and **9** were diluted to a final concentration of 150 µM of 3.75% (v/v) DMSO in PBS. The complexes and the ctDNA dilutions were mixed with a total volume of 200 µL in a clear 96 well plate with each titre concentration in quadruplicate. The plate was then shaken for 30 minutes at room temperature, following which UV-Vis spectra were collected.

4-2.2.2: 9-Ethyl Guanine binding using UV-Vis spectrometry

9-Ethyl Guanine (9EtG) was dissolved to prepare a 1200 µM stock solution in 5% (v/v) methanol in PBS, from which final assay titre concentrations ranging from 600 to 10 µM were diluted. Complexes **7** and **9** were diluted to a final concentration of 150 µM of 3.75% (v/v) DMSO in PBS. The complexes and the 9EtG dilutions were mixed with a total volume of 200 µL in a clear 96 well plate with each titre concentration in quadruplicate. The plate was then shaken for 30 minutes at room temperature, following which UV-Vis spectra were collected.

4-2.3: Cell Studies in A2780

For all following experiments, A2780 cells were treated with full media as a negative control. All treatments were used equipotently at IC$_{50}$ concentrations with CDDP and PTX as treatment standards, in addition to complexes **7** and **9**. Cells were exposed to treatment for 24 hours.

4-2.3.1: Metal localisation distribution by ICP-MS

Following treated cell pellet collection, cell fractions were collected using the FractionPREP™ Cell Fractionation Kit (BioVision, Inc.) according to manufacturer instructions[35]. Produced supernatants and

pellets for cytosol, nucleus, membrane/particulate, and cytoskeletal fractions were then frozen at 4°C until digestion for ICP-MS analysis as detailed in Chapter 2.

4-2.3.2: Alkaline comet assay

A 6 well plate was seeded with $1X10^6$ A2780 cells and incubated for 24 hours. Cells were then drugged with 2 mL of treatment. Following exposure, cells were washed with PBS and harvested by trypsinisation, the SCS was then centrifuged, media discarded, and cells were suspended in PBS (without calcium or magnesium). These SCS were then counted and diluted to $2X10^4$ cells per 1 mL. 800 μL of the SCD was added to 2.4 mL of 1% (m/v) low temperature agarose and mixed rapidly. Slides were preprepared by heating 1% (m/v) low-temperature agarose in distilled water to 100°C to become molten, then cooled to 40°C. When cooled, edge-scored dust-free frosted slides were coated on one side with the agarose and allowed to air dry until the agarose was solid. 1.2 mL of the cell agarose solution was added to each slide with each treatment done in duplicate and allowed to set. Following the setting of the SCD-treated slides, the cells were lysed in the dark at 4°C by submersion in lysis solution of 1.2 M NaCl, 100 mM Na_2EDTA, 0.1% (v/v) sodium lauryl sarcosinate, and 0.26 M NaOH in distilled water for 24 hours. Following lysis, slides were washed by submersion for 20 minutes in wash solution of 0.03 M NaOH and 2 mM Na_2EDTA in distilled water ensuring pH stayed above 12.3. The slides were then ran by horizontal electrophoresis for 25 minutes at a voltage of 20 volts (constant) in fresh wash solution. Following electrophoresis, the slides were washed with distilled water, stained with 1% (v/v) PI in distilled water for 20 min, then washed again with distilled water following which the comets were imaged on the EVOS. From the images, comet length and comet head size were measured using FIJI[36]. From this the comet tail moment was calculated measuring from the centre of the comet head to the end of the comet tail.

4-2.3.3: Gamma-H2A.X analysis by fluorescence microscopy

$6X10^4$ A2780 cells were seeded per well in a 24 well plate and incubated for 24 hours. Cells were then drugged with 500 μL of treatment in triplicate. Following exposure, cells were washed with PBS, fixed in 4% (v/v) formaldehyde in PBS for 30 minutes, then washed with TBS and permeabilised with a solution of 0.05% (v/v) Triton X-100 and 10 mg/mL BSA in TBS for 90 minutes. After permeabilisation, cells were washed thoroughly with TBS then stained with a solution of 10 mg/mL BSA, 1% (v/v) DAPI and 1% (v/v) gamma-H2A.X (Ser139) Monoclonal Antibody (CR55T33), PerCP-eFluor™ 710 in TBS for 3 hours at 4°C in the dark. After staining, cells were gently washed with TBS then imaged on the EVOS.

4-2.3.4: Gamma-H2A.X analysis by flow cytometry

$1X10^6$ A2780 cells were seeded per well in a 6 well plate and incubated for 24 hours. Cells were then drugged with 2 mL of treatment in triplicate. Following exposure, cells were washed with PBS, trypsinized and quenched with media to a SCS. The SCS was centrifuged at 1,000 RPM for 5 minutes and supernatant was removed. Cells were fixed in 4% (v/v) formaldehyde in PBS for 30 minutes, washed with TBS, then permeabilised in a solution of 0.05% (v/v) Triton X-100 and 10 mg/mL BSA in TBS for 90 minutes. After permeabilisation, supernatant was removed and cells washed with TBS, then stained with a solution of 10 mg/mL BSA and 1% (v/v) gamma-H2A.X (Ser139) Monoclonal Antibody (CR55T33), PerCP-eFluor™ 710 in TBS for 3 hours on ice. Cells were gently mixed by pipetting at regular intervals in longer incubation steps. After staining, stain solution was removed, and cells were gently washed with TBS and resuspended in fresh TBS then ran by flow cytometry.

4-2.3.5: HDAC inhibition activity assay

A black, glass bottom 96 well plate was seeded with $2X10^4$ A2780 cells per well and incubated for 24 hours. Cells were then drugged with six replicates per treatment. Following exposure, HDAC activity was assessed using the *in situ* HDAC activity by fluorescence kit (Sigma) per manufacturer's instructions using TriA as a positive control. Fluorescence intensity was measured using the blue channel settings.

4-3: Results

4-3.1: Physiochemical characterisation

4-3.1.1: Synthesis and characterisation of the iminopyridine ligands and ruthenium piano-stool complexes

Following ImPy ligand synthesis, imine bond formation was confirmed, and ligand structure was elucidated using ^{1}H, ^{13}C and 2D HSQC NMR experiments, specifically observing for the singlet imine proton shift at ~8.8 ppm for ligands without a spacer, and ~8.2 ppm with a spacer

The ligands were then used to synthesise the 16 complexes shown in Table 4-1. Following synthesis, complex structure was elucidated using ^{1}H, ^{13}C, COSY, HSQC and HMBC NMR, complimented with ESI-MS spectrometry, HPLC and elemental analysis. The experimental data was consistent with the proposed structures and purity was confirmed.

Table 4-1: Structure information for the 16 complexes synthesised and used in Chapter 4. The complexes highlighted in blue have a spacer, highlighted in blue in the right chemical structure.
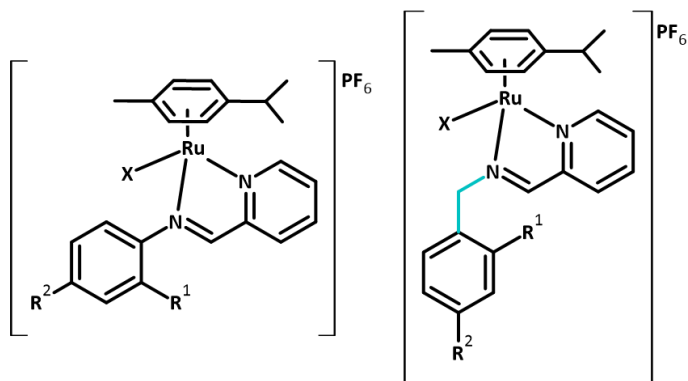
Complex	X	R^1	R^2	Spacer
1 - Ru(L1)Cl(PF$_6$), [Ru(η^6-*p*-Cym)(ImPy)Cl]PF$_6$	Cl	H	H	No
7 - Ru(L1)I(PF$_6$), [Ru(η^6-*p*-Cym)(ImPy)I]PF$_6$	I	H	H	No
8 - Ru(L7)Cl(PF$_6$), [Ru(η^6-*p*-Cym)(ImPy-Bn)Cl]PF$_6$	Cl	H	H	Yes
9 - Ru(L7)I(PF$_6$), [Ru(η^6-*p*-Cym)(ImPy-Bn)I]PF$_6$	I	H	H	Yes
2 - Ru(L2)Cl(PF$_6$), [Ru(η^6-*p*-Cym)(ImPy-4-CH$_3$)Cl]PF$_6$	Cl	H	CH$_3$	No
10 - Ru(L8)Cl(PF$_6$), [Ru(η^6-*p*-Cym)(ImPy-Bn-4-Me)Cl]PF$_6$	Cl	H	CH$_3$	Yes
11 - [Ru(η^6-*p*-Cym)(ImPy-4-OH)Cl]PF$_6$	Cl	H	OH	No
12 - Ru(L9)Cl(PF$_6$), [Ru(η^6-*p*-Cym)(ImPy-Bn-4-OH)Cl]PF$_6$	Cl	H	OH	Yes
13 - Ru(L10)Cl(PF$_6$), [Ru(η^6-*p*-Cym)(ImPy-(CH$_2$)$_2$-4-OH)Cl]PF$_6$	Cl	H	(CH$_2$)$_2$OH	No
14 - Ru(L11)Cl(PF$_6$), [Ru(η^6-*p*-Cym)(ImPy-4-OMe)Cl]PF$_6$	Cl	H	OMe	No
15 - Ru(L12)Cl(PF$_6$), [Ru(η^6-*p*-Cym)(ImPy-Bn-4-OMe)Cl]PF$_6$	Cl	H	OMe	Yes
16 - Ru(L3)Cl(PF$_6$), [Ru(η^6-*p*-Cym)(ImPy-Bn-2-OMe)Cl]PF$_6$	Cl	OMe	H	Yes
17 - Ru(L14)Cl(PF$_6$), [Ru(η^6-*p*-Cym)(ImPy-4-Cl)Cl]PF$_6$	Cl	H	Cl	No
18 - Ru(L15)Cl(PF$_6$), [Ru(η^6-*p*-Cym)(ImPy-2-Cl)Cl]PF$_6$	Cl	Cl	H	No
19 - Ru(L16)Cl(PF$_6$), [Ru(η^6-*p*-Cym)(ImPy-Bn-4-Cl)Cl]PF$_6$	Cl	H	Cl	Yes
20 - Ru(L17)Cl(PF$_6$), [Ru(η^6-*p*-Cym)(ImPy-Bn-2-Cl)Cl]PF$_6$	Cl	Cl	H	Yes

4-3.1.2: Complex interaction with biologically relevant matrixes

Evaluation of complex interaction with biologically relevant matrixes was assessed by UV-Vis spectroscopy to determine suitability for biological study (Table 4-2). No complex synthesised here exhibited an isosbestic point with 1:1 water to PBS, PBS, Albumin, human plasma or NEAA, further no precipitation of the complexes was seen in any matrix tested. Two significant trends between complexes with or without a spacer are apparent. There is a corelation between the possession of a spacer preventing interaction with GSH compared to its unlinked counterpart, seen by the unsubstituted (*1*, *7*, *8,* and *9*), methyl (*2* and *10*) and methoxy (*14* and *15*) complexes. A similar corelation is seen between the possession of a spacer and the prevention of interaction with media and full media shown by the unsubstituted (*1*, *7*, *8,* and *9*), hydroxyl (*12* and *13*) and methoxy (*14* and *15*) complexes. Interestingly interaction with GSH, media or full media is not prevented with the addition of the spacer in the chlorine (*17*, *18*, *19*, and *20*) complexes. Interestingly, several complexes including *7*, *9*, *11*, and *14* did not form an isosbestic point with water. Additionally, only complex *7* formed an isosbestic point with DMSO, all others either exhibited hyperchromism, hypochromism, or did not exhibit spectra changes.

Table 4-2: Summary of UV-Vis spectra changes of the complexes investigated in Chapter 4 with biologically relevant matrixes following 24 hours incubation. Abbreviations: dimethyl sulfoxide (DMSO), phosphate buffered saline (PBS), bovine serum albumin (BSA), glutathione (GSH), calf thymus DNA (ctDNA), non-essential amino acids (NEAA), no change (NC), isosbestic point (IP), hypochromism (↓), hyperchromism (↑), and no data (nd).

Complex	DMSO	H$_2$O	1:1 H$_2$O:PBS	PBS	BSA	GSH	Media	Full Media	ctDNA	Human plasma	NEAA
1	NC	IP	NC	↑	↑	IP	IP	IP	IP	↑	↑
7	IP	NC	↑	↑	NC	NC	↑	↑	IP	↑	NC
8	↓	IP	NC	NC	NC	NC	IP	IP	IP	NC	NC
9	↓	NC	NC	NC	NC	NC	IP	IP	IP	NC	NC
2	↑	IP	NC	NC	NC	IP	IP	IP	IP	NC	NC
10	↓	IP	NC	NC	NC	NC	IP	IP	IP	NC	NC
11	NC	**NC**	NC	NC	NC	IP	IP	IP	IP	NC	NC
12	↓	IP	NC	NC	NC	IP	NC	NC	IP	NC	NC
13	NC	IP	NC	NC	NC	IP	NC	NC	IP	NC	NC
14	NC	**NC**	NC	NC	NC	IP	IP	IP	IP	NC	NC
15	↑	IP	NC	NC	NC	NC	IP	IP	IP	NC	NC
16	NC	IP	NC	NC	NC	NC	IP	IP	*nd*	NC	NC
17	↑	IP	↑	NC	NC	IP	IP	IP	*nd*	NC	NC
18	NC	IP	NC	NC	NC	IP	IP	IP	IP	NC	NC
19	NC	IP	NC	NC	NC	IP	IP	IP	NC	NC	NC
20	NC	IP	NC	NC	NC	IP	IP	IP	NC	NC	NC

Lipophilicity

Following confirmation that the complexes were suitable for biological work, lipophilicity at physiological pH was determined by the shake flask method (Table 4-3). All complexes in this series exhibit a negative $LogD_{7.4}$ values ranging from -0.92 (complex **13**) to -0.21 (complex **9**). The use of the spacer exhibits a general increase in lipophilicity. This effect is more profound in complexes with unsubstituted or methyl substituted complexes with the $LogD_{7.4}$ increasing by half in several cases, for example from **7** to **9** which has an increase from -0.41 to -0.21. Yet, increase in lipophilicity with the addition of the spacer is not seen in all substitutions. For example, in the chlorine group, addition insignificantly increases lipophilicity from -0.24 to -0.23 (complexes **17** and **19**). However, the location of the spacer is highly important as there is a large decrease in lipophilicity between the hydroxyl containing complexes **12** and **13** from -0.50 to -0.92 where the spacer is before and after the phenyl ring respectively.

4-3.1.3: Density Functional Theory of the ruthenium complexes

With the addition of the spacer inducing several physiochemical changes, DFT lowest energy structures of **7** and **9** were calculated from which bond lengths, electron density and Mulliken partial charges were predicted. These structures highlight that without the spacer, the phenyl ring is rotated out of the ligand plane by 48.67°, away from the p-cymene ring and other ligands to prevent steric hinderance (Figure 4-7a and b). The addition of the spacer has no substantial effect on bond lengths around the ruthenium centre (Table 4-4).

Table 4-3: LogD$_{7.4}$ of the 16 complexes evaluated in this chapter determined by the shake flask method using PBS and n-octanol. Complexes highlighted in blue have a spacer.

Complex	LogD$_{7.4}$
1	-0.66
7	-0.41
8	-0.54
9	-0.21
2	-0.38
10	-0.29
11	-0.53
12	-0.50
13	-0.92
14	-0.50
15	-0.49
16	-0.45
17	-0.24
18	-0.53
19	-0.23
20	-0.40
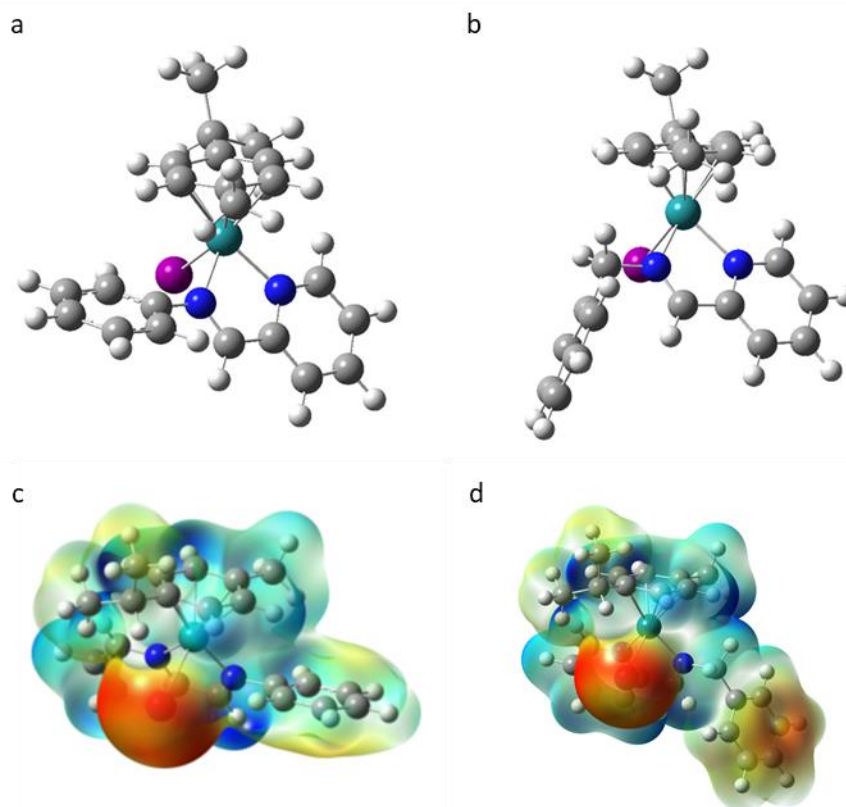
Figure 4-7: Calculated DFT structures of complexes a). **7**, b). **9**, in their lowest energy structures. c). and d). demonstrate Electrostatic Potential Surface (EPS) mapped onto Total Electron Density around the complex for **7** and **9** respectively, with colour scale corelating with electron density with blue being less electron dense and red being more electron dense, demonstrating that with the inclusion of the spacer, electron density increases in the phenyl ring. Renders produced by Dr J.P.C. Coverdale.

Table 4-4: Calculated DFT bond lengths (Å) determined from the lowest energy structures. Calculations performed by Dr J.P.C. Coverdale.

Complex	Ru-I (Å)	Ru-N(Ph) (Å)	Ru-N(Py) (Å)
7	2.73376	2.06667	2.08361
9	2.73290	2.06114	2.08063

Table 4-5: Calculated DFT Mulliken partial charges of select atoms determined from the lowest energy structures. Calculations performed by Dr J.P.C. Coverdale.

Complex	Ru	N(Ph)	N(Py)	I
7	-0.087	-0.523	-0.567	-0.043
9	-0.099	-0.476	-0.568	-0.033

In addition to the reduction of steric hinderance, the spacer removes any resonance effect across the ligand of complex **9** due to the spacer preventing the overlap of the p orbitals in the phenyl ring with the sp2 nitrogen in the imine bond, which extends to the rest of the ligand. This is shown by the alteration of the nitrogens' Mulliken partial charges and phenyl ring electron density (Table 4-5 and Figure 4-7c and d). In complex **7**, the Mulliken partial charges predicted are similar between the two nitrogens' being -0.567 in the pyridine and -0.523 in the imine bond. This alters to -0.567 and -0.476 respectively in complex **9**, showing a reduction in the electron density around the imine nitrogen. These changes in potential lead to an alteration in the electron density in the bidentate ligand of the complexes shown in where the surface (isovalue of 0.004) has been visualised to show red colouring as an increase in electron density and blue corresponds to a lower electron density from +0.05 to +0.18.

4-3.2: Cell Studies of ruthenium complexes with and without a spacer bioisostere

4-3.2.1: Antiproliferative activity screening

The complexes were screened in a variety of cell lines to assess their antiproliferative activity (Table 4-6, and selected complexes in Figure 4-9). There is a remarkable increase in potency with the use of the spacer in almost all the phenyl ring substituent variants tested. This is exemplified by complexes **7** (**(ImPy)I**) and **9** (**(ImPy-Bn)I**) the lung cell line A549 where activity improves >6.5X from >140 to 21.49 µM, and by 5.5X in the EOC line A2780 from 24 to 4.4 µM, respectively. Only the hydroxyl substituent containing complexes **11** and **12** did not exhibit antiproliferative activity improvement with the spacer with IC_{50} values >140 mM. However, as values are described as >140 µM, a potency improvement with the spacer may be occurring, but outside the range of this screen.

Table 4-6: Antiproliferative screening of the 16 complexes used in this chapter with efficacy displayed as IC$_{50}$ values (all units in µM unless stated otherwise) (N.D.: no data collected). Complexes highlighted in blue have a spacer.

Complex	A2780	A549	MIAPaCa	UFH001	HCT116 P53+/+	HCT116 P53-/-	MRC5
1	>140	>140	>140	>140	>140	>140	>140
7	24 (1)	>140	22.5 (0.2)	41 (3)	40 (4)	42 (3)	>140
8	72 (3)	56 (2)	68 (3)	>140	>140	124.8 (0.4)	>140
9	4.4 (0.2)	21.49 (0.09)	5.19 (0.05)	9 (2)	13.5 (0.1)	8 (2)	64.8 (0.8)
2	76 (2)	53 (4)	95.2 (0.4)	120.1 (0.4)	>140	137 (2)	>140
10	72 (2)	58 (1)	56 (2)	50 (3)	59.6 (0.2)	51 (3)	>140
11	>140	>140	>140	>140	>140	>140	N.D
12	>140	>140	>140	>140	>140	>140	N.D
13	>140	>140	>140	N.D.	N.D	N.D.	N.D
14	>140	81 (3)	>140	>140	>140	>140	N.D
15	75 (2)	46 (2)	99.3 (0.5)	80 (2)	>140	>140	N.D
16	54 (3)	51(3)	89 (2)	55 (1)	58 (3)	97 (3)	N.D
17	84 (1)	>140	120 (1)	>140	>140	>140	N.D
18	>140	>140	>140	>140	>140	>140	N.D
19	67 (3)	85 (4)	79 (3)	77 (2)	122 (3)	>140	N.D
20	56 (1)	43 (1)	94 (3)	78 (2)	71 (1)	73 (3)	N.D
CDDP	3 (1)	12 (1)	24 (3)	17.3 (0.7)	6 (1)	5.7 (0.4)	5.6 (0.7)
PTX	0.3 nM (0.02)	N.D.	N.D	N.D.	N.D.	N.D	N.D
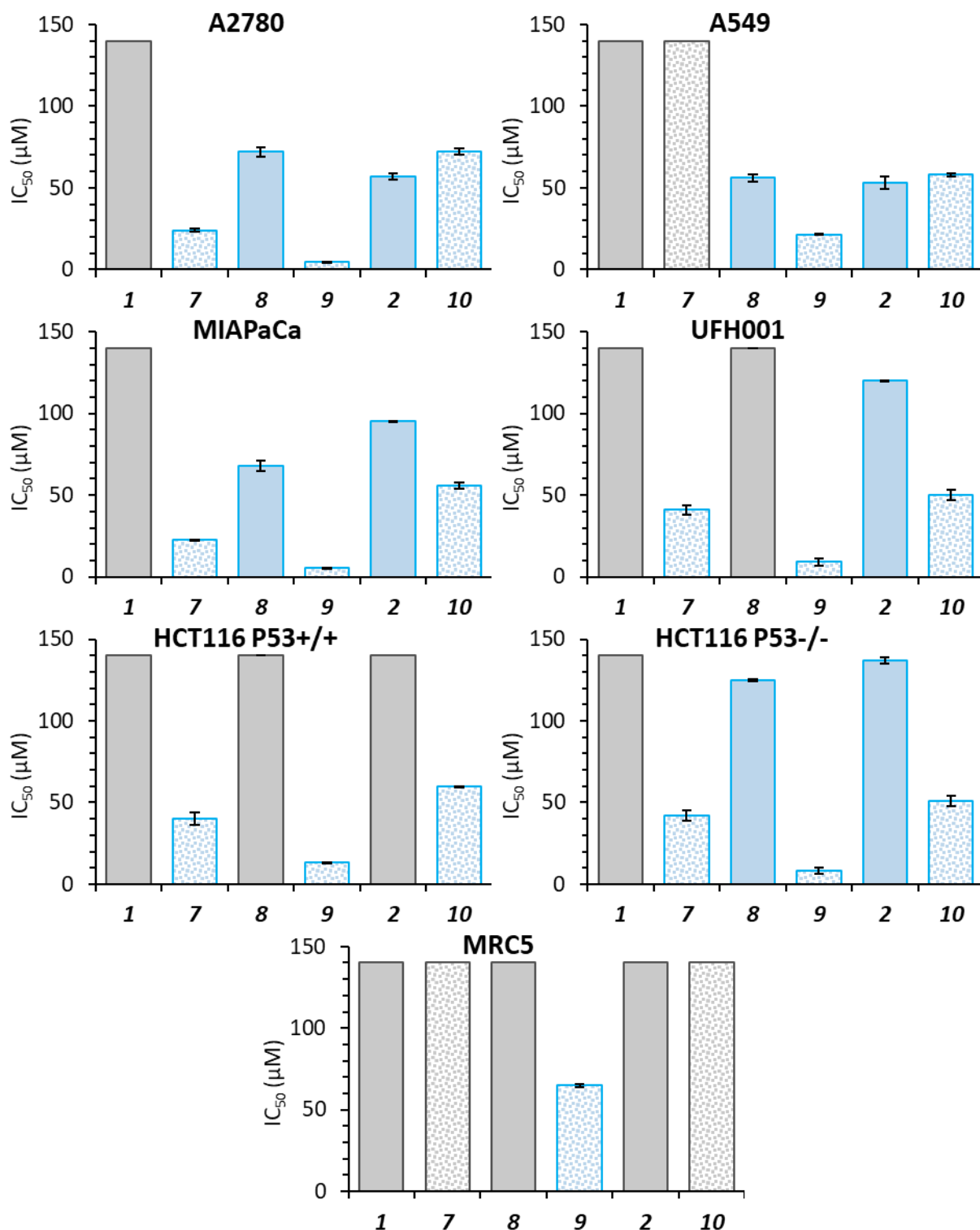
Figure 4-8: Antiproliferative screening of select pairs of complexes (*1* and *7, 8* and *9*, and *2* and *10*) used in this chapter with efficacy displayed as IC$_{50}$ values. Bars in grey indicate an IC$_{50}$ value of >140 µM. Patterned bars indicate complexes with a spacer.

One remarkable finding of the spacer containing complexes is that activity is not affected by p53 status in the colorectal cell lines HCT116 p53-/- and HCT116 p53+/+. For example, in the unsubstituted (*1*, *7*, *8*, and *9*) and methyl (*2* and *10*) derivatives, complexes with a spacer have a marginally improved or equivalent potency with the loss of p53. One outlier to this is complex *16 (ImPy-Bn-2-OMe)* which has a substantially lower potency in HCT116 p53-/- than in HCT116 p53+/+.

While the majority of the complexes in this series have phenyl ring substituents in the *para* position, complexes with *meta* substitutions were synthesised for the methoxy (*16*) and chloride (*20*) variants. Remarkably for both, activity was the same or substantially improved in almost all cell lines tested. This is demonstrated by the >2.4X increase in potency between the methoxy complexes *15 (ImPy-Bn-4-OMe)* and *16 (ImPy-Bn-2-OMe)* in HCT116 p53+/+ and the 2.0X increase between the chloride complexes *19 (ImPy-Bn-4-Cl)* and *20 (ImPy-Bn-2-Cl)*.

In addition to altering the ImPy ligand, the monodentate chlorine halogen ligand was substituted for iodine in the unsubstituted complexes. In A2780, the iodo complex was >5.8X more potent in the unlinked variants (*1* and *7*), and 16.4X more potent in the linked variant (*8* and *9*). Additionally, in this screen complex *9* was the most active in all cell lines exhibiting IC_{50} values <10 µM in four of the six cancerous cell lines screened.

Antiproliferative activity was determined in MRC5 to see if increased activity is also observed in normal cells. Of the six complexes tested in MRC5, all complexes had an IC_{50} of >140 µM in the normal line MRC5, except complex *9* with an IC_{50} of 64.8 µM. Yet this activity is still substantially lower than in the cancerous lines being 15X and 3X less potent in A2780 EOC and A549 lung cancer.

Complexes *7* (*(ImPy)I*) and *9* (*(ImPy-Bn)I*) were selected for further testing in A2780 due to being the best preforming pair with and without the spacer, but also being unsubstituted on the phenyl ring, reducing other areas of MOA influence.

4-3.2.2: Time dependant activity of complexes 7 and 9

The effect of time on biological activity was investigated by treating cells without recovery time (Figure 4-9). Without recovery time, *7* is 1.8X more effective than *9* with IC_{50} values of 20.32 μM and 37.51 μM, respectively. However, with recovery time, the potency of *7* decreases marginally with IC_{50} increasing by 1.18X to 24 μM, while the potency of *9* hugely increases with IC_{50} dropping by 8.5X to 4.4 μM.
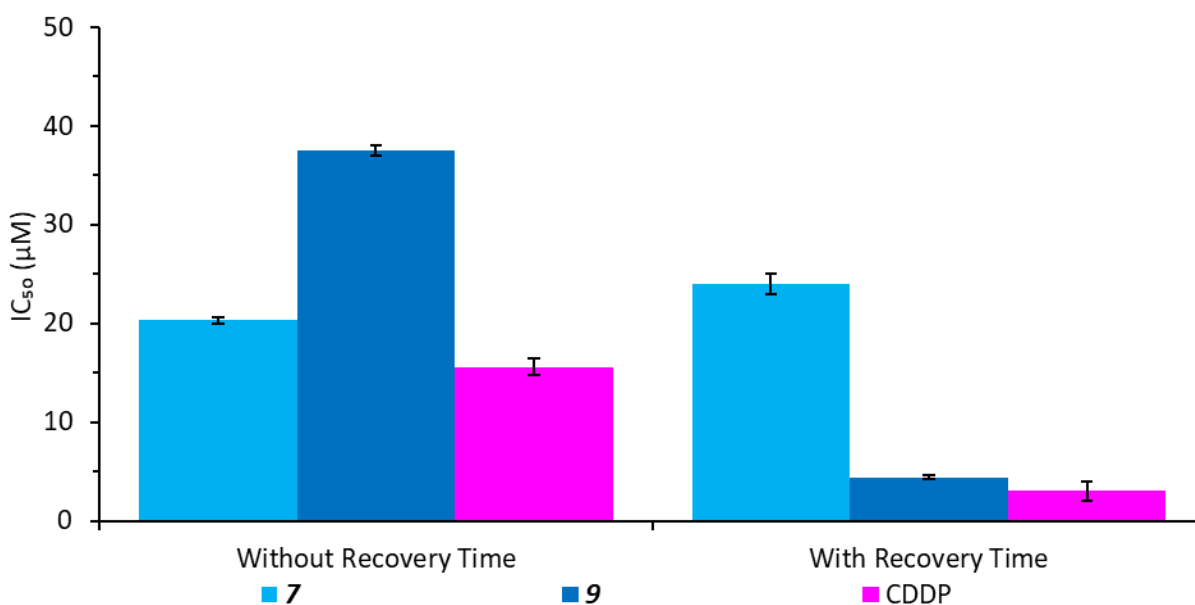
Figure 4-9: Comparison of IC_{50} values of *7*, *9* and CDDP after 24 hours of treatment with and without 72 hours of recovery time in full media in A2780.

4-3.3: Mode of action comparisons of complex 7 and 9

4-3.3.1: Mitochondrial polarisation studies

As ΔΨm depolarisation is a common MOA of ruthenium piano-stool complexes, ΔΨm was assessed by fluorescence microscopy using Rh123 staining (Figure 4-10). Fluorescence microscopy suggests that complexes *7* and *9* do not induce ΔΨm depolarisation, but the contrary with Rh123 fluorescence increasing for *7* (Figure 4-11). To investigate this, fluorescence intensity was used and agreed that *7*

significantly (p<0.001) increased Rh123 fluorescence while **9** treated cells exhibited no significant difference to the negative control or other comparator treatments.
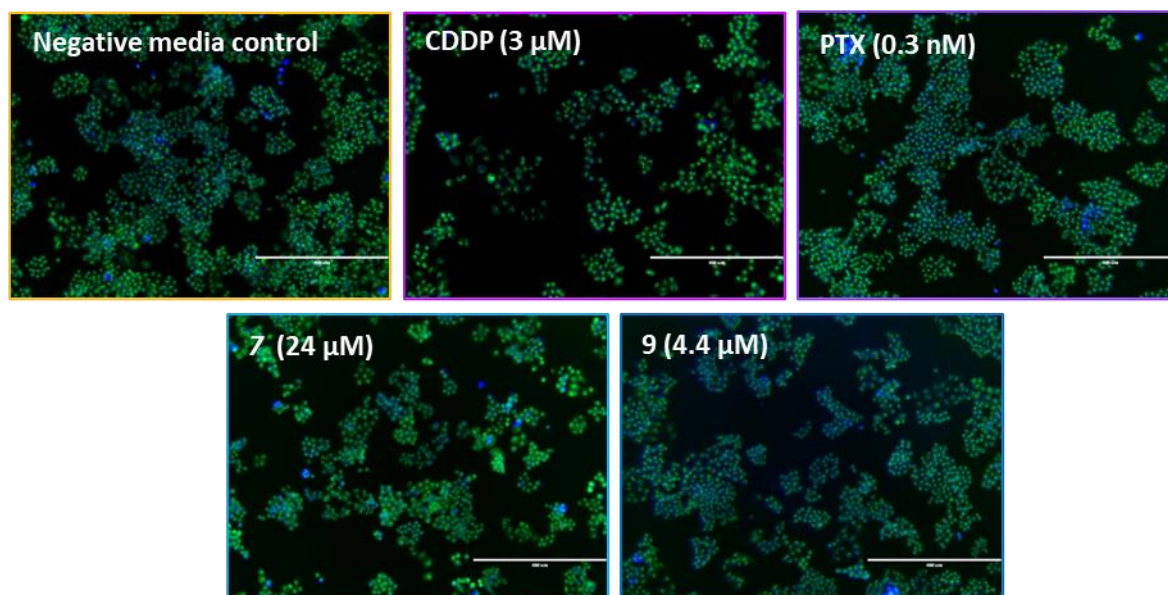
Figure 4-10: Determination of mitochondrial depolarisation of A2780 cells following treatment with a). media as the negative control, CDDP (3 µM), PTX (0.3 nM), **7** (24 µM), or **9** (4.4 µM) by fluorescence microscopy using Rh123 (green), DAPI (blue) and PI (red). Images presented as overlays of the green, blue, and red channels at 10X magnification (scale bar 400 µm).
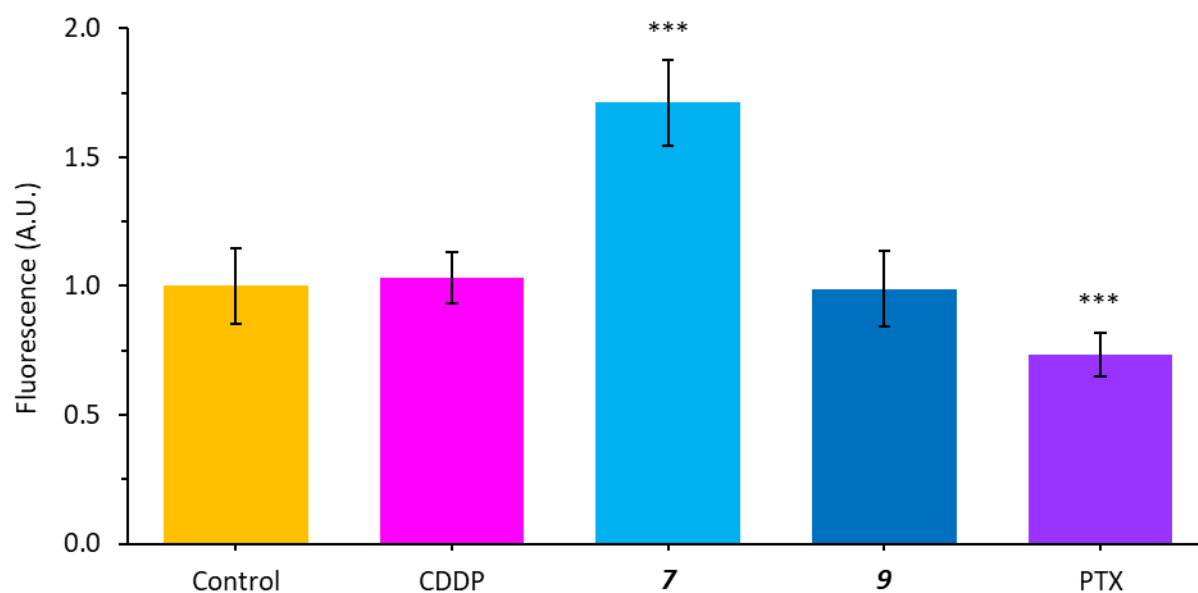
Figure 4-11: Determination of mitochondrial depolarisation of A2780 cells following treatment with media as the negative control, CDDP (3 µM), PTX (0.3 nM), **7** (24 µM), or **9** (4.4 µM) by fluorescence intensity using Rh123 normalised by protein content. (Significance determined by Welch t-test where * indicates p<0.05, ** indicates p<0.01, and *** indicates p<0.001 levels of significance).

4-3.3.2: ROS generation studies

Noting increase in ΔΨm polarisation in **7** treated cells, ROS generation was evaluated by DCFDA microscopy as these MOA are often interlinked (Figure 4-12). Hot spots of green fluorescence were induced by complex **7** but not complex **9**. To further probe low level ROS, fluorescence intensity was used (Figure 4-13). Intensity levels show that both complexes do significantly ($p<0.001$) increase ROS levels in cells, with **7** producing to a greater extent than **9**. However, neither are to the extent of the positive controls, consistent with the fluorescence microscopy data.
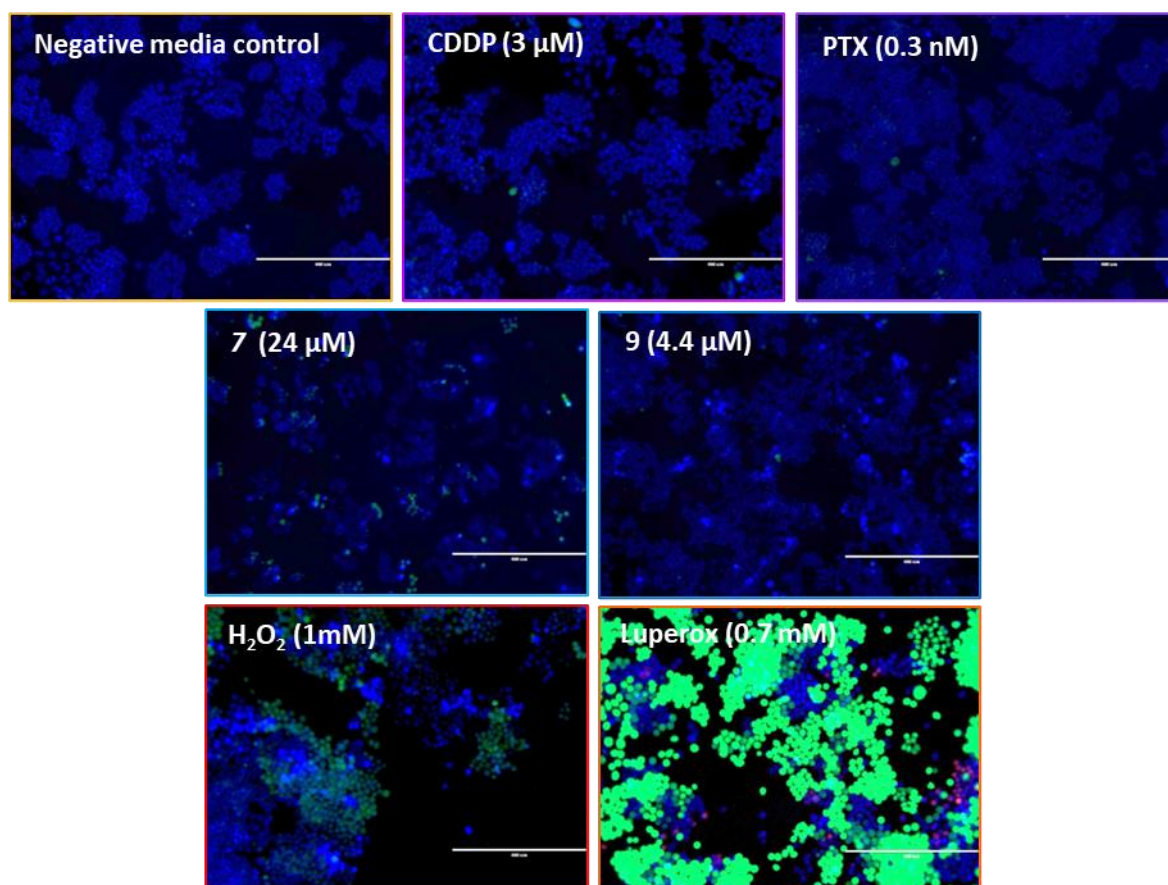
Figure 4-12: Determination of ROS generation by DCFDA of A2780 cells following treatment with media as the negative control, CDDP (3 μM), PTX (0.3 nM), **7** (24 μM), **9** (4.4 μM), 1 mM hydrogen peroxide, or 0.7 mM Luperox by fluorescence microscopy using DCFDA (green), DAPI (blue) and PI (red). Images presented as overlays of the green, blue, and red channels at 10X magnification (scale bar 400 μm).
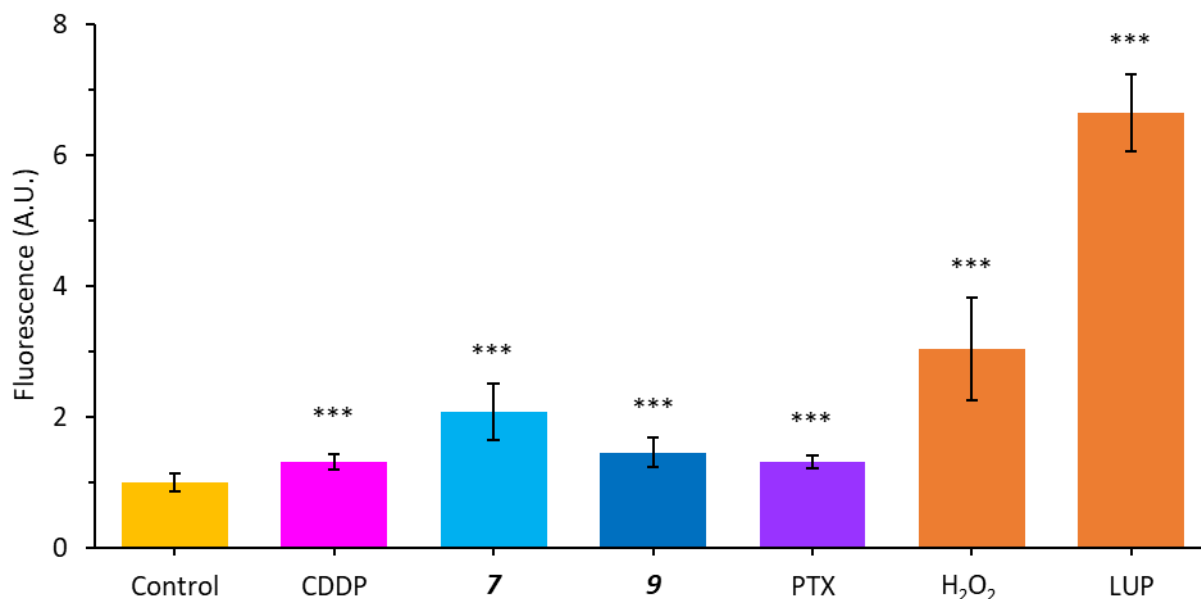
Figure 4-13: Determination of ROS generation in A2780 cells following treatment with media as the negative control, CDDP (3 μM), PTX (0.3 nM), **7** (24 μM), **9** (4.4 μM), or 0.7 mM Luperox by fluorescence intensity of DCFDA normalised by protein content. (Significance determined by Welch t-test where * indicates $p<0.05$, ** indicates $p<0.01$, and *** indicates $p<0.001$ levels of significance).

4-3.3.3: Cell cycle arrest induction

The inhibition of cell division is a key MOA in the prevention of cancer progression and can be indicative of other MOA, therefore cell cycle arrest was assessed by flow cytometry following staining with PI and RNase (Figure 4-14). Complex **7** did not induce significant cell cycle arrest, but there was a substantial increase ($p=0.06$) in the sub G_1 population by 10.2% and a significant ($p<0.05$) decrease in the S phase population. Complex **9** however did induce G_1 phase arrest with a significant ($p<0.05$) in the G_1 population through a significant ($p<0.05$) decrease in the S and G_2/M phases. This contrasts CDDP which exhibited significant ($P<0.001$) S phase and significant ($p<0.05$) sub G_1 arrest and PTX which did not induce significant arrest.

4-3.3.4: Apoptosis induction

As an important MOD, apoptosis was investigated via flow cytometry after staining with Annexin V and PI (Figure 4-15). Both complex **7** and **9** treatment induced significant late phase apoptosis ($p<0.001$ and

166

p<0.05 respectively). Furthermore, *7* induced significant (p<0.05) early apoptosis. However, both *7* and

9 treatment induce significant (p<0.001 and p<0.05 respectively) increase in the non-viable population.
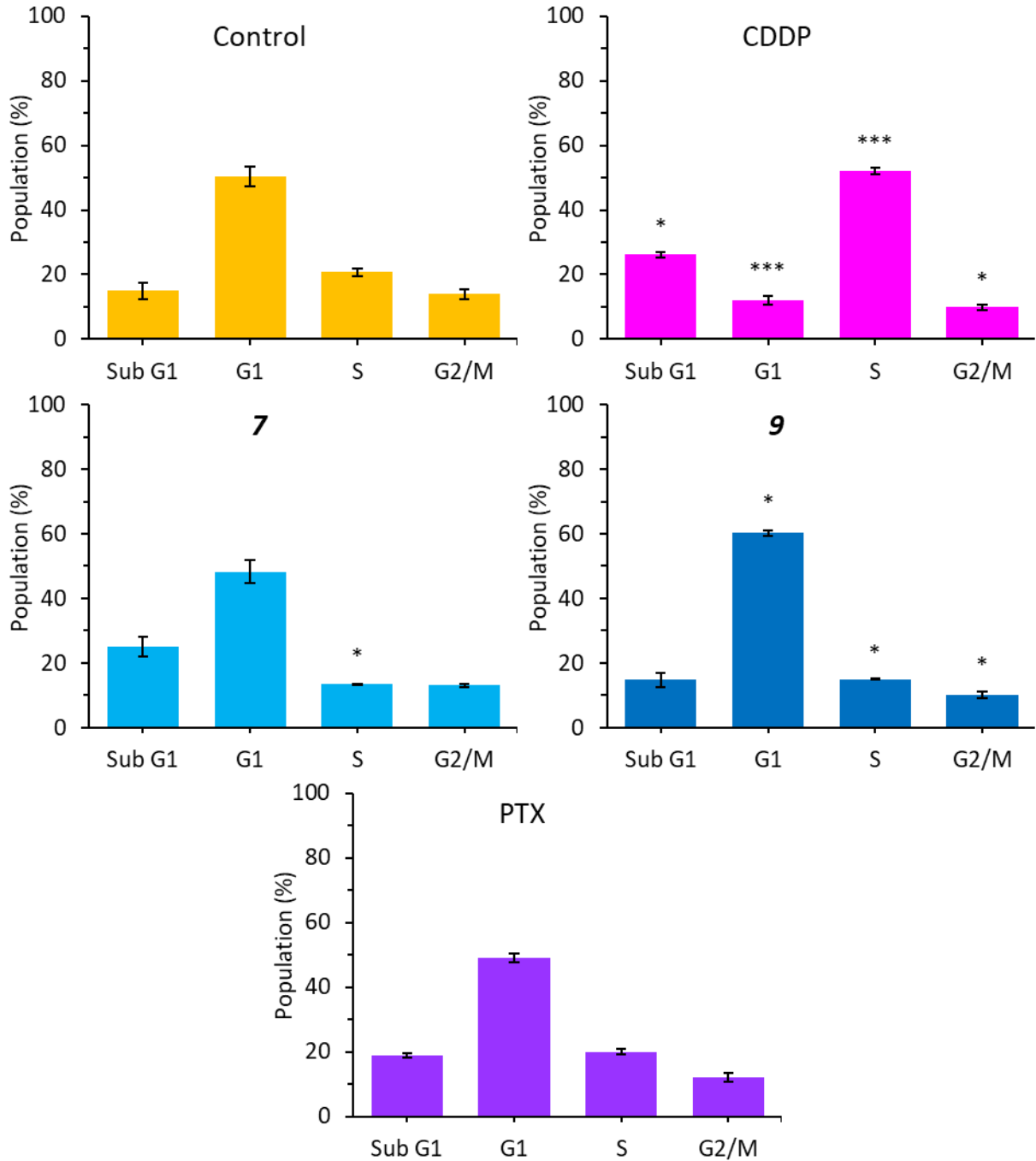
Figure 4-14: Cell cycle arrest of A2780 cells by flow cytometry treated with media as negative control, CDDP (3 µM), PTX (0.3 nM), *7* (24 µM), or *9* (4.4 µM), stained with PI and RNase. (Significance determined by Welch t-test where * indicates p<0.05, ** indicates p<0.01, and *** indicates p<0.001 levels of significance).
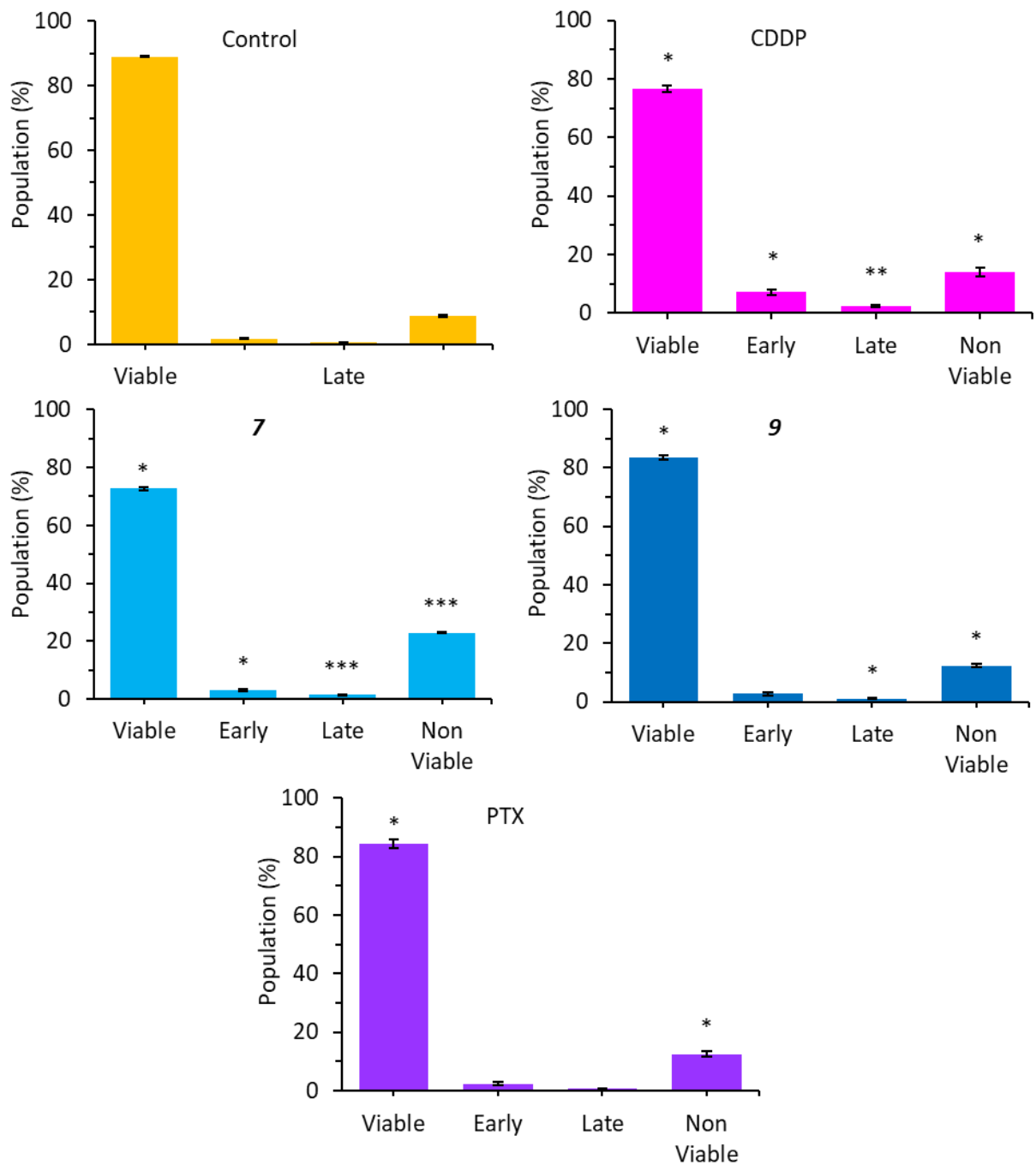
Figure 4-15: Apoptosis induction by flow cytometry of A2780 cells treated with media as negative control, CDDP (3 µM), PTX (0.3 nM), **7** (24 µM), or **9** (4.4 µM), stained with PI and Annexin V. (Significance determined by Welch t-test where * indicates p<0.05, ** indicates p<0.01, and *** indicates p<0.001 levels of significance).

4-3.3.5: Wound healing studies

As a model of invasion, wound healing was done using a 24 hours treatment and 72 hours recovery protocol (Figure 4-16 and Figure 4-17). Following 24 hours treatment, all treatments used apart from **9** significantly (p<0.05) prevented wound healing, with **7** exhibiting the best activity of all treatments tested with average wound closing of 0.01 mm.

Following 72 hours recovery, **7** and PTX continued to significantly (p<0.001) prevent wound closure. CDDP failed to prevalent wound closure being statistically no different to the control wounds. Further, **9** treatments statistically (p<0.05) increased wound closure.
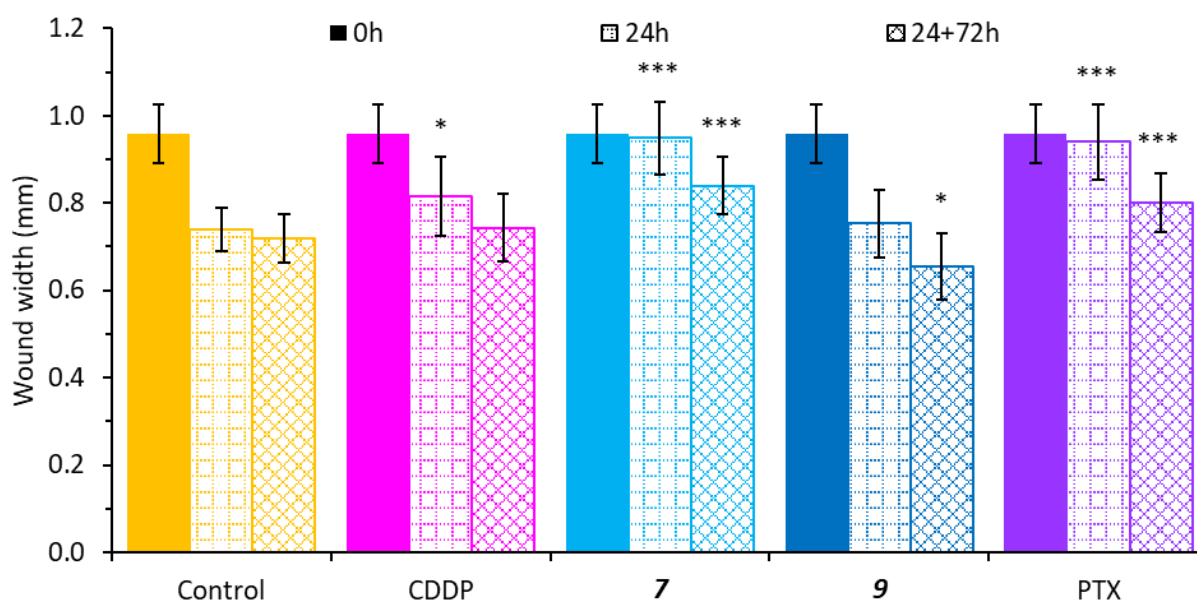
Figure 4-16: Measurements of wound widths of A2780 cell monolayers following treatment with media as the negative control, CDDP (3 µM), PTX (0.3 nM), **7** (24 µM), or **9** (4.4 µM), at 0 hours (monolayer wounding and start of treatment exposure), 24 hours (following treatment exposure) and 24+72 hours (total wound closure including 24 hours treatment and 72 hours recovery time). (Significance determined by Welch t-test where * indicates p<0.05, ** indicates p<0.01, and *** indicates p<0.001 levels of significance).
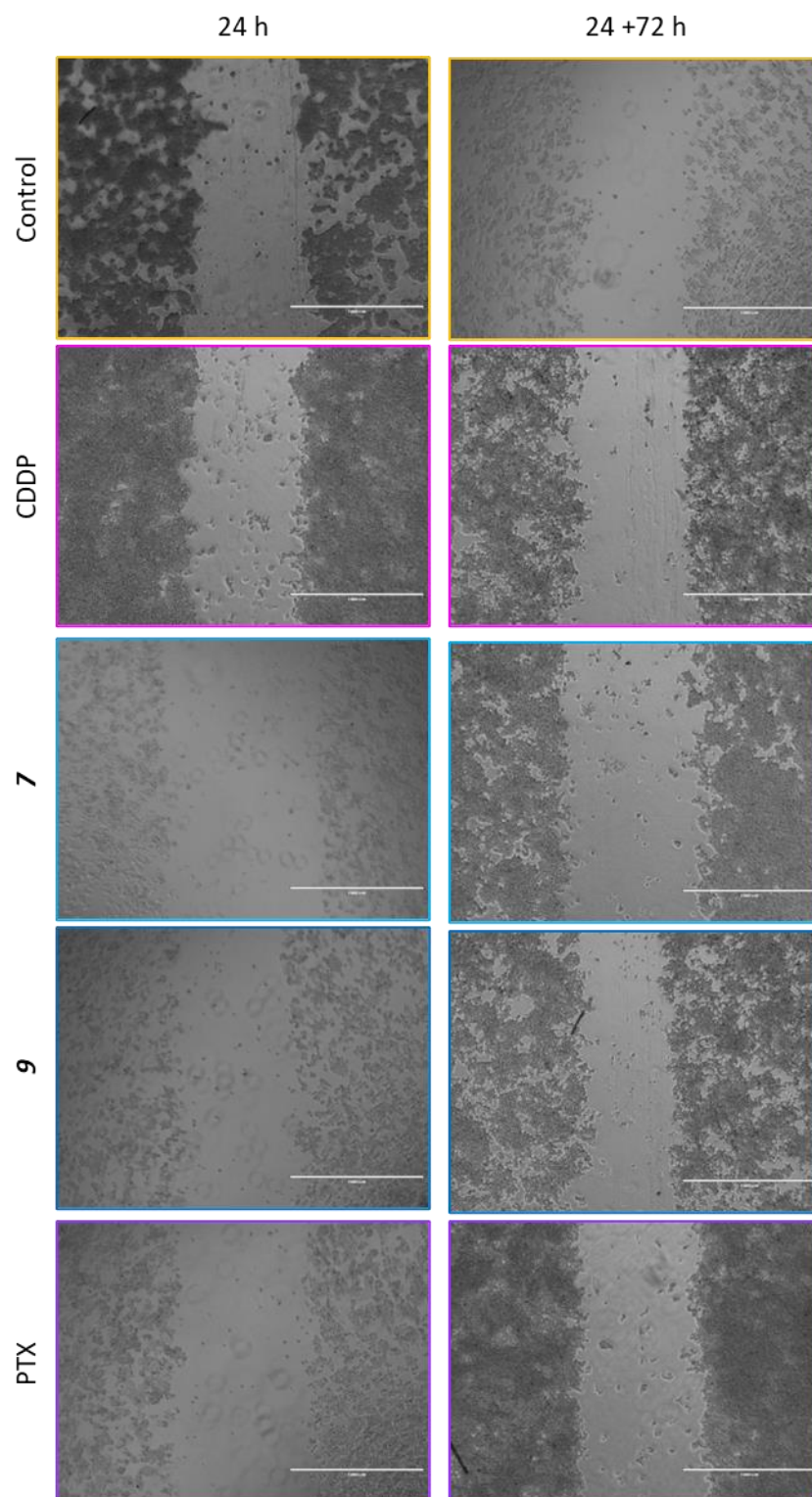
Figure 4-17: Images of the wound healing assay of A2780 cell monolayers following treatment with media as the negative control, CDDP (3 µM), PTX (0.3 nM), **7** (24 µM), or **9** (4.4 µM), at 24 hours (following treatment exposure) and 24+72 hours (total wound closure including 24 hours treatment and 72 hours recovery time). Images taken at 4X magnification, scale bar: 1000 µM.

4-3.3.6: Colony formation studies

Metastasis inhibition activity was simulated by the colony formation assay. Regarding colony number (Figure 4-18), when treated with complex **7** or CDDP there is a significant ($p<0.001$) decrease in colony formation with an average of three colonies. Complex **9** does not share this activity as on average over 200 colonies developed, however this was significantly ($p<0.01$) lower than the control.

Colony area was also measured to assess the effectiveness of growth following metastasis (Figure 4-19). Complex **7** and CDDP significantly ($p<0.001$) prevented the growth of colonies, therefore size could not be determined and were deemed 0 mm^2. Colonies that developed from cells treated with complex **9** were significantly ($p<0.001$) smaller than the control colonies by 0.02 mm^2.

4-3.3.7: Spheroids growth inhibition

Spheroids are a considerable problem in EOC often being the cause of many metastatic and recursion events . *In vitro*, they are also highly effective at modelling potential for *in vivo* experiments. Spheroid activity is shown in Figure 4-20 and Figure 4-21. All the treatments significantly ($p<0.05$) reduced spheroid area. Complex **7** activity was comparable to CDDP by reducing spheroid area by 9.5%, while **9** and PTX were slightly less effective reducing area by 8.2% and 7.9% respectively.
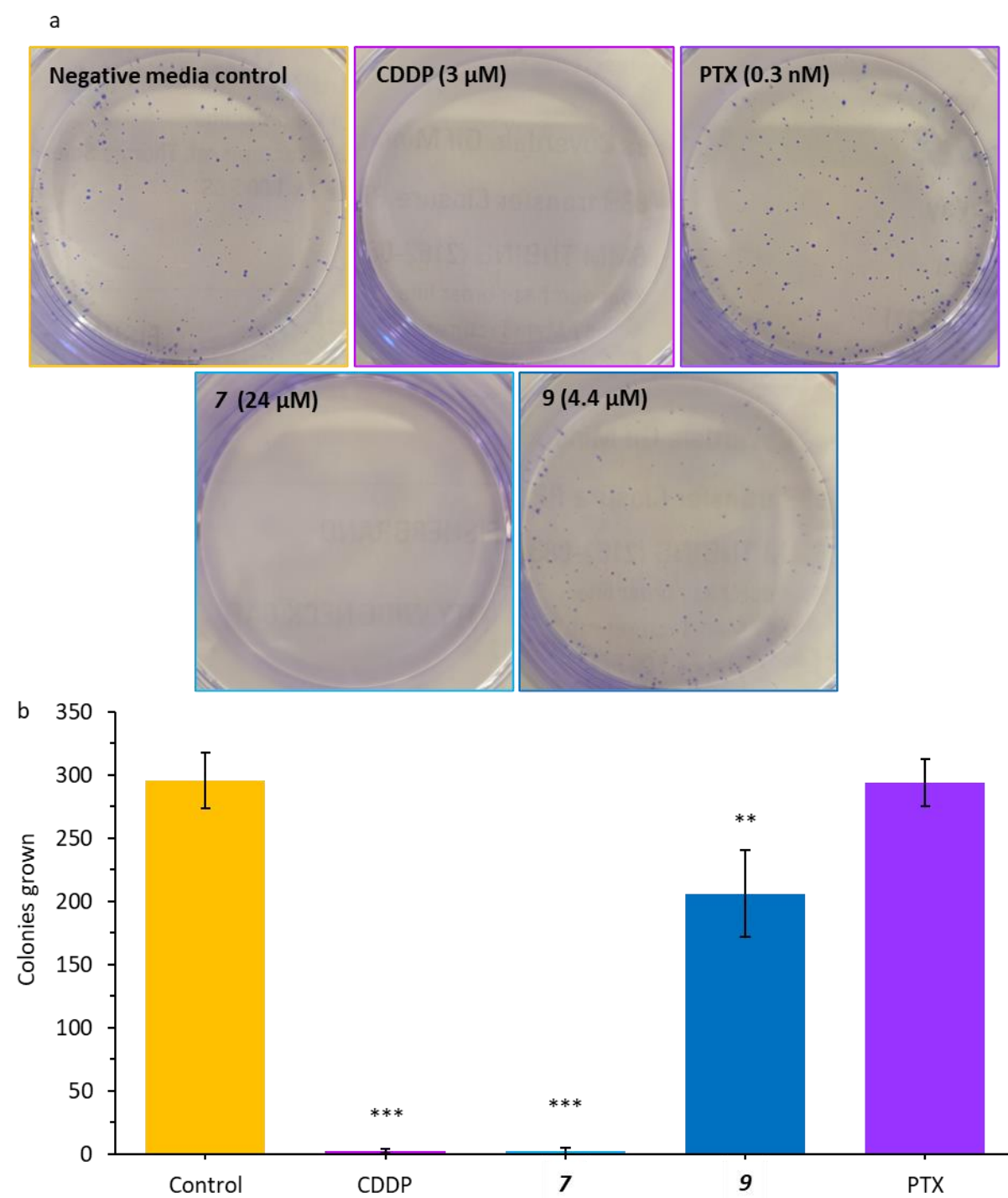
Figure 4-18: Colony formation a). well images and b). colony counts of A2780 cells following treatment with media as the negative control, CDDP (3 µM), PTX (0.3 nM), *7* (24 µM), or *9* (4.4 µM) following 24 hours exposure and 7 days colony growth time. Images taken at 1X magnification. (Significance determined by Welch t-test where * indicates p<0.05, ** indicates p<0.01, and *** indicates p<0.001 levels of significance).
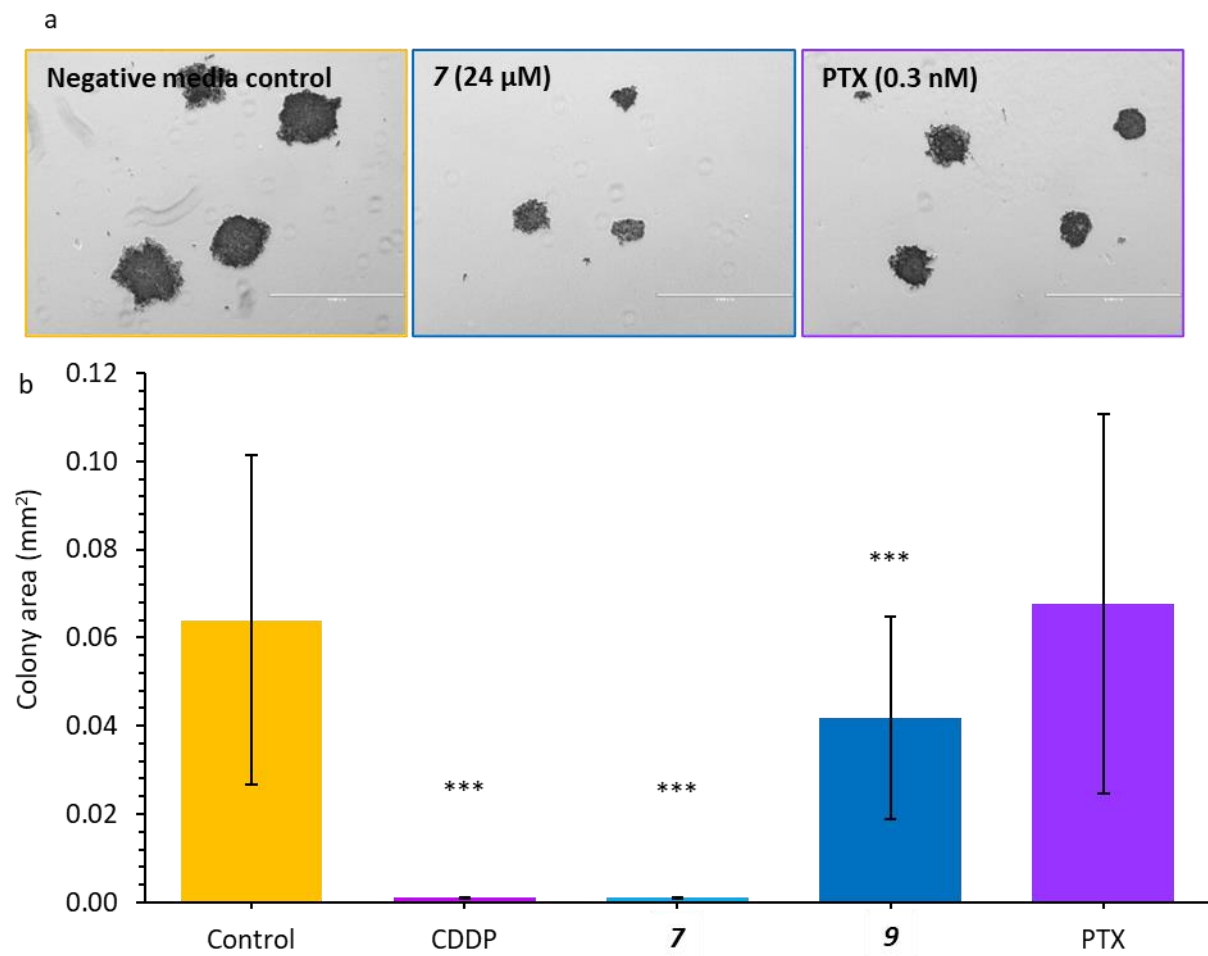
Figure 4-19: Colony density a). well images and b). colony counts of A2780 cells following treatment with media as the negative control, CDDP (3 µM), PTX (0.3 nM), **7** (24 µM), or **9** (4.4 µM) following 24 hours exposure and 7 days colony growth time. Images taken at 4X magnification. (Significance determined by Welch t-test *** indicates $p < 0.001$ level of significance).
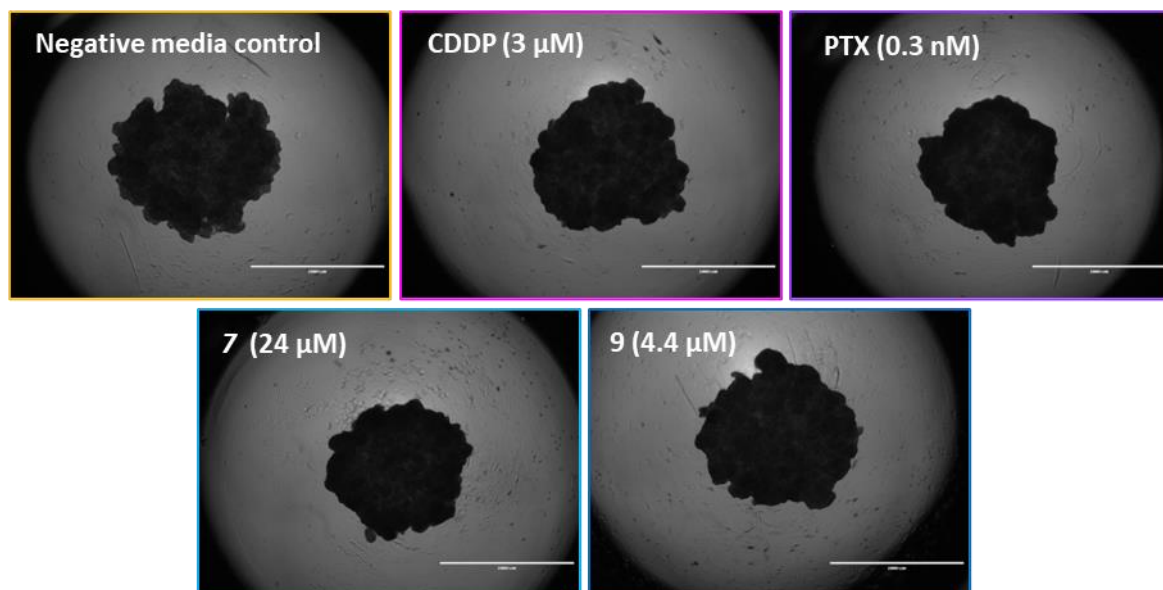
Figure 4-20: Microscopy of A2780 spheroids following treatment with media as the negative control, CDDP (3 μM), PTX (0.3 nM), *7* (24 μM), or *9* (4.4 μM). Images taken at 2X magnification, scale bar: 2000 μM.
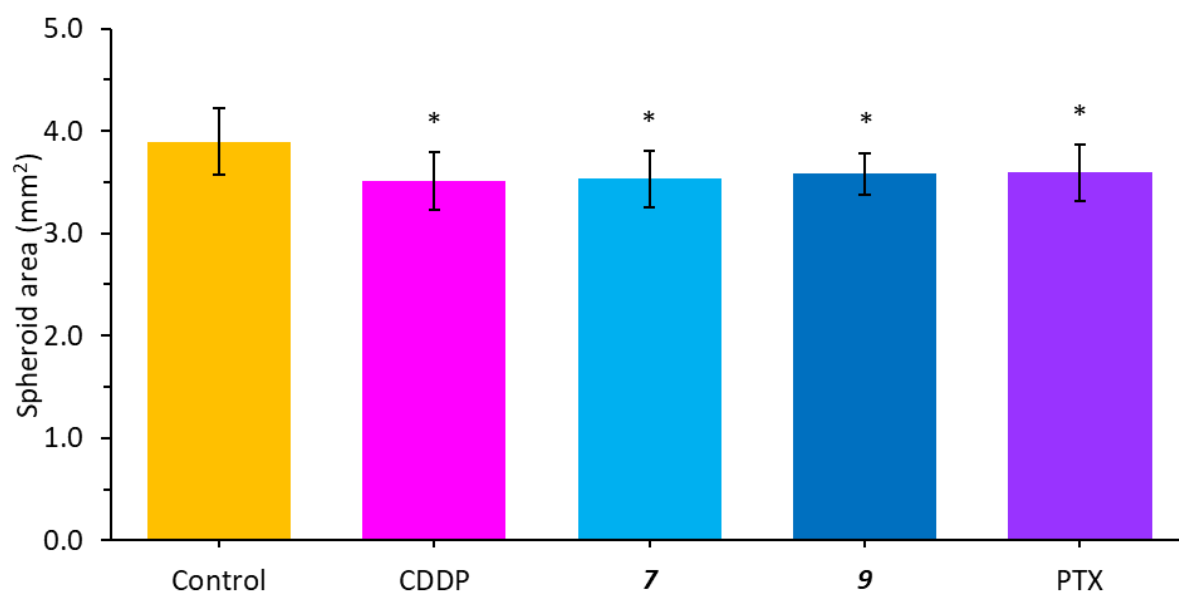
Figure 4-21: A2780 spheroids area following treatment with treated with media as the negative control, CDDP (3 μM), PTX (0.3 nM), *7* (24 μM), or *9* (4.4 μM). (Significance determined by Welch t-test where * indicates $p < 0.05$ level of significance).

4-3.3.8: Metal accumulation by inductively coupled plasma mass spectrometry

Metal accumulation by ICP-MS was determined allowing for insight into uptake/efflux and efficiency of a complex as an indirect method of complex accumulation as this method does not allow for identification of speciation. Total platinum and ruthenium accumulation is shown in Figure 4-22a and b respectively. Following treatment, there was significant uptake of platinum in the CDDP (0.069± 0.006 fmol/cell) treated cells, but not in **7** and **9** (0.0005 ±0.0003 fmol/cell and 0.00012 ±0.00003 fmol/cell, respectively). Remarkably, there was significantly (p<0.01) more ruthenium accumulation in **7** treated cells than **9** treated cells by 0.057f fmol/cell accumulating 0.290 ±0.001 fmol/cell and 0.23 ±0.02 fmol/cell, respectively. Additionally, the ruthenium complexes encouraged 3.2 to 7.8X more metal accumulation compared to CDDP.
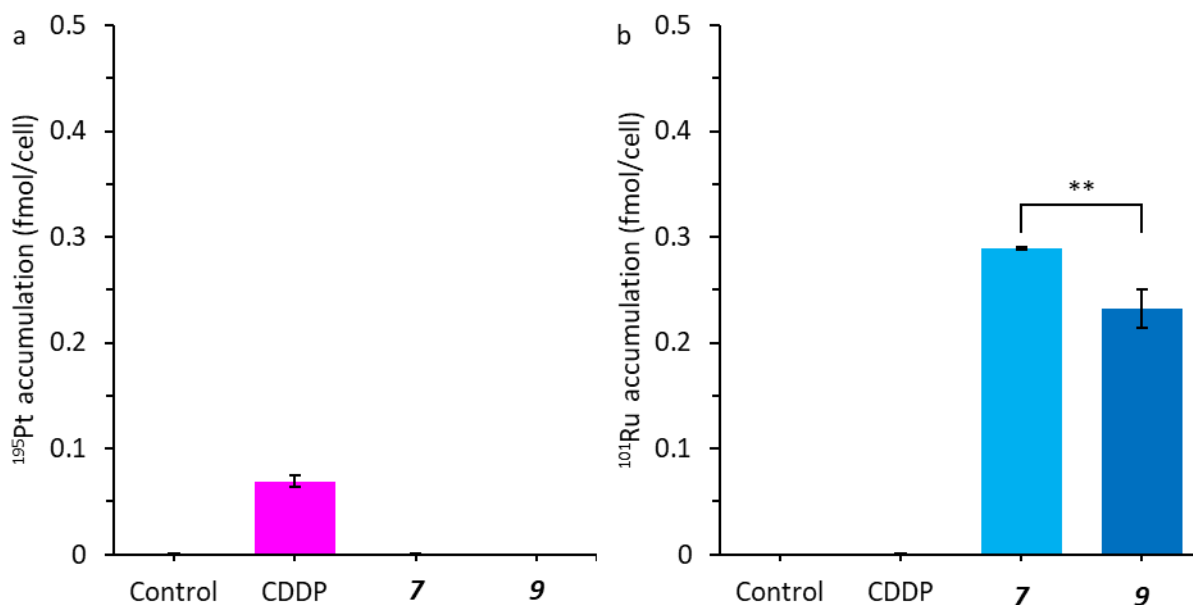
Figure 4-22: Metal accumulation of A2780 cells treated with media as negative control, CDDP (3 µM), **7** (24 µM) or **9** (4.4 µM) testing for a). platinum content and b). ruthenium content by ICP-MS. Significance determined by Welch t-test where ** indicates p<0.01 level of significance.

4-3.3.9: Cellular metal distribution by inductively coupled plasma mass spectrometry

In extension to the overall accumulation of platinum and ruthenium, the cellular localisation of platinum and ruthenium was assessed to observe if differing MOA of *7* and *9* is due to the localisation of the complexes. The fraction percentages are shown in Figure 4-23 and raw metal mass values are given in Appendix III. The negative control samples had minimal platinum and ruthenium content with measured mass per fraction per cell being less than 0.07 fg in all fractions. Cells exposed to CDDP had platinum mainly localise to the membrane & organelle fraction, followed by the cytosolic, cytoskeletal then nucleic fractions. Ruthenium localisation was similar in *7* and *9* treated cells which also had ruthenium mainly localise to the membrane & organelle fractions respectively with similar accumulation with other fractions.
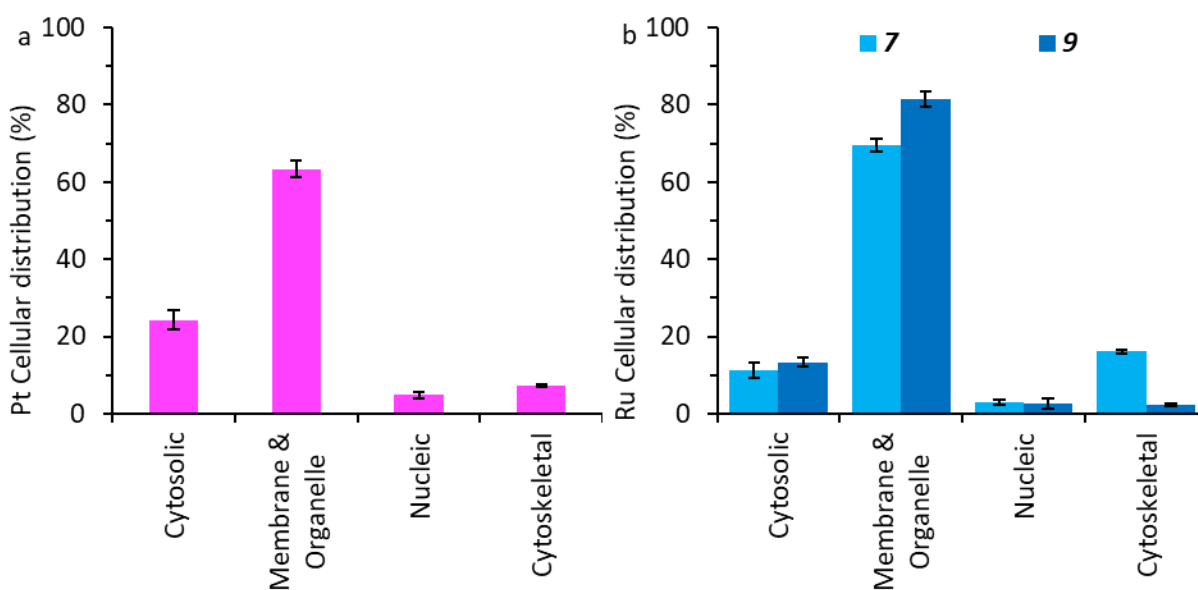
Figure 4-23: Metal distribution of A2780 looking for and treated with a). platinum with CDDP (3 µM) and b). ruthenium with *7* (24 µM), or *9* (4.4 µM) determined by ICP-MS.

4-3.4: DNA damage differences induced by complexes 7 and 9

4-3.4.1: Nuclear morphology studies

Nuclei morphology was assessed by DAPI at 40X magnification (Figure 4-24). Nuclear morphology is highly indicative of nuclear health and DNA damage. DAPI staining highlights that cells treated with CDDP, *7* and *9* have crescent shaped nuclei, in contrast to untreated and PTX treated cells that have round nuclei. In extension of this, complex *9* treated cells have less DAPI fluorescence than *7*, CDDP and control cells.
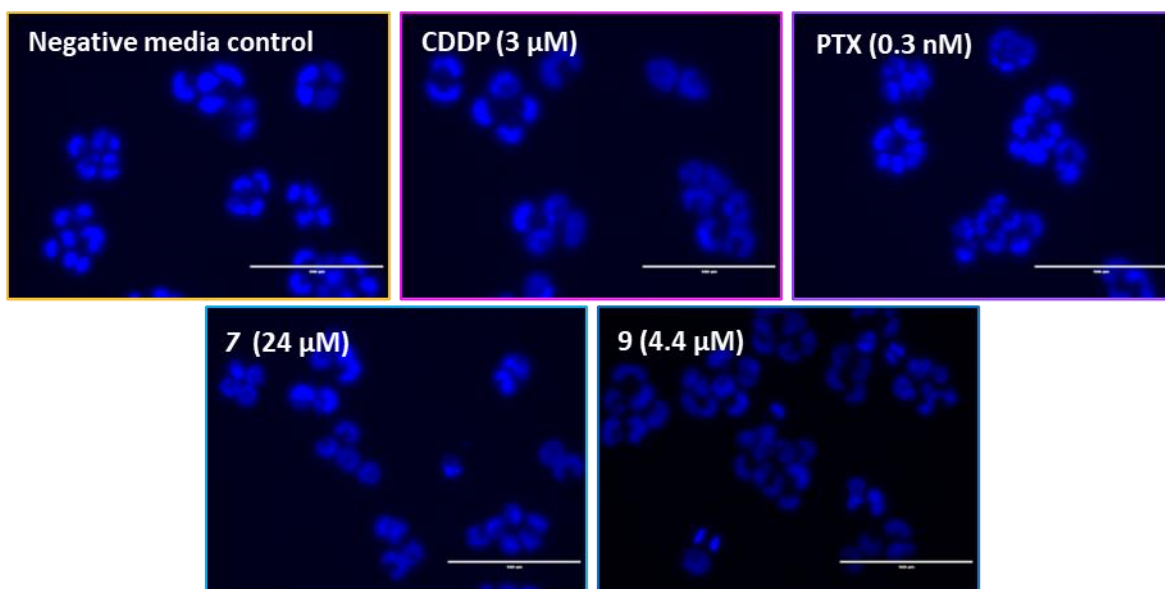
Figure 4-24: Nuclear morphology of A2780 cells stained with DAPI following treatment with media as the negative control, CDDP (3 µM), PTX (0.3 nM), *7* (24 µM), or *9* (4.4 µM) by fluorescence microscopy. Images taken at 40X magnification, scale bar: 100 µM.

4-3.4.2: ctDNA interaction by UV-Vis titration

Due to the indications that *7* and *9* may induce DNA damage and the development of an isosbestic point following 24 hours incubation with ctDNA, complex binding to DNA was assessed through ctDNA titration by UV-Vis (Figure 4-25). Both complexes interacted with ctDNA with both complexes inducing

a hyperchromic effect (increase in absorbance) at 320nm in the charge transfer band region, however hyperchromic is more pronounced with **7**-ctDNA interaction than with **9**-ctDNA.
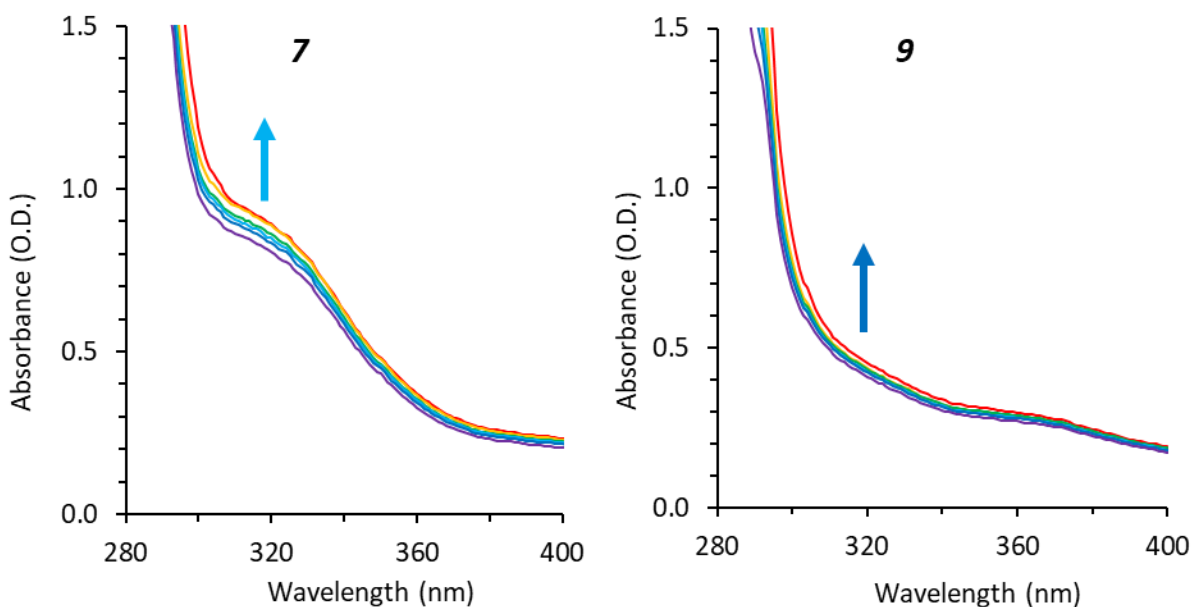
Figure 4-25: ctDNA concentration titration ranging from 0.01 to 0.5 mg/mL interaction studies by UV-Vis spectroscopy with 150 µM complex **7** or **9**.

4-3.4.3: 9-Ethyl Guanine interaction by UV-Vis titration

As both complexes exhibited interaction with ctDNA, interaction nucleotide interaction was assessed using 9-EtG by UV-Vis titration (Figure 4-26). Hyperchromism was not observed with the combination of 9-EtG with **7**. This is contrary to **9** which does exhibit a spectrum shift similar to that seen in the ctDNA interaction spectra in the charge transfer band region.
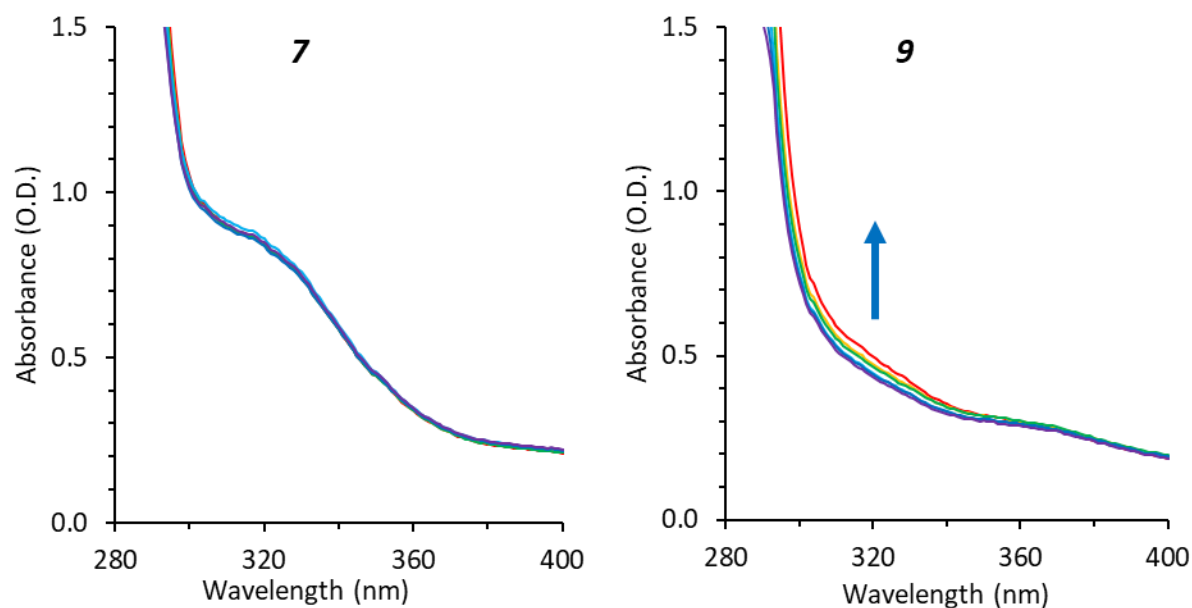
Figure 4-26: 9-Ethyl guanine concentration titration ranging from 10 to 600 µM interaction studies by UV-Vis spectroscopy with 150 µM complex *7* or *9*.

4-3.4.4: Alkaline comet assay

The alkaline comet assay assesses the extent of ssDNA and dsDNA breaks and other DNA damage using electrophoresis. With more strand breaks and damage, there is an increase in smaller fragments of DNA in the nucleus, which move faster through the agarose gel, allowing for the development of the comet tail (Figure 4-27). The from the average comet tail moments (Figure 4-28), CDDP demonstrated significant ($p<0.001$) comet tail moments 1.69X longer than untreated cells ($P<0.001$). PTX also induced significant ($P<0.05$) levels of DNA breaks. Complex *7* induced similar comet tails moments to the negative control, however complex *9* treatment caused significant ($p<0.001$) comet tail moments, 1.25X longer than the control comets.
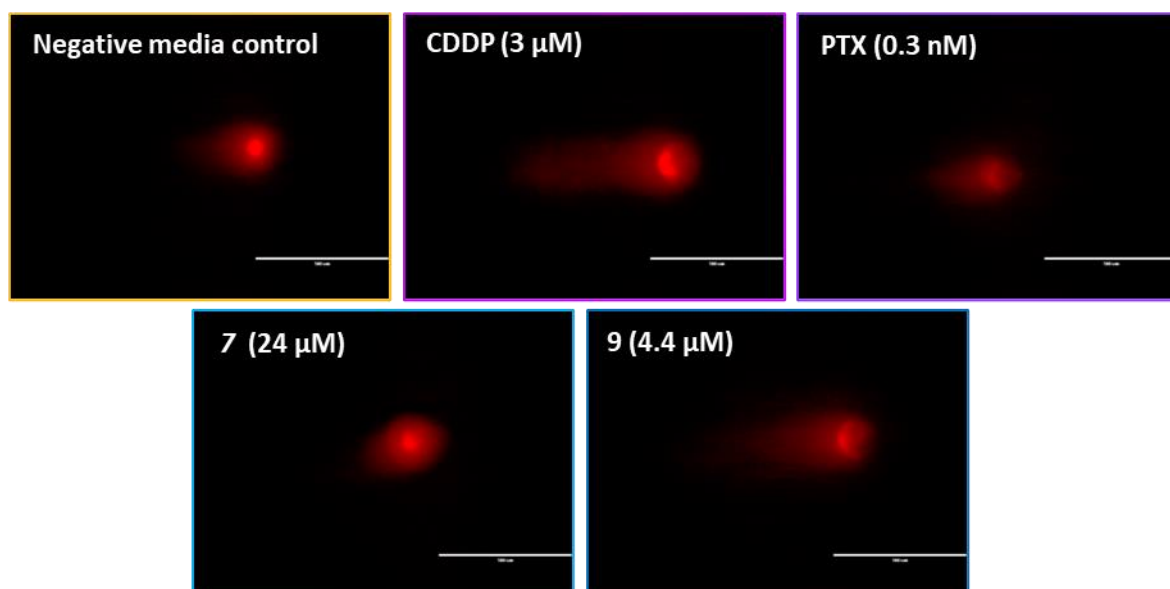
Figure 4-27: Images of A2780 nuclear comets stained with PI following treatment with media as the negative control, CDDP (3 µM), PTX (0.3 nM), *7* (24 µM), or *9* (4.4 µM). Images taken at 40X magnification, scale bar: 100 µM.
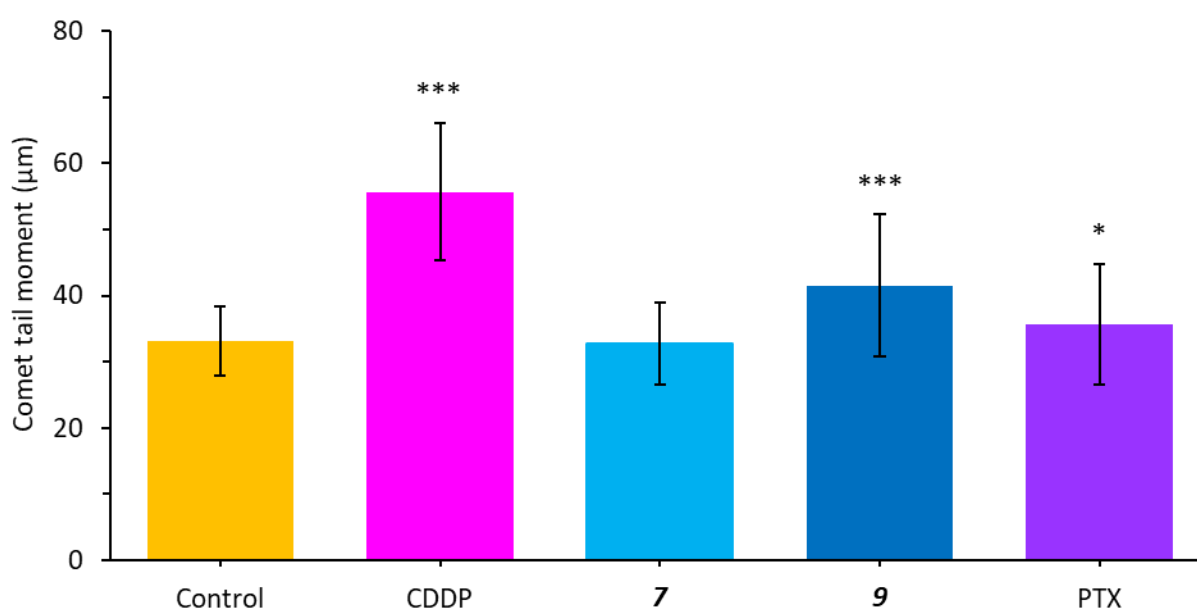
Figure 4-28: Comet tail moments of A2780 nuclei from the comet assay following treatment with media as the negative control, CDDP (3 µM), PTX (0.3 nM), *7* (24 µM), or *9* (4.4 µM). Significance determined by Welch t-test where * indicates $p<0.05$ and *** indicates $p<0.001$ levels of significance.

4-3.4.5: Gamma-H2A.X staining studies

Observing that ssDNA strand breakages were being induce, dsDNA breaks were investigated. When dsDNA damage occurs, one cellular response is the phosphorylation of the histone H2A.X at serine 139, known as gamma-H2A.X. This can be probed for and quantified using commercial fluorescence probes (Figure 4-29 and Figure 4-30). Cells in the control population exhibited very low levels of gamma-H2A.X staining which was not observed by fluorescence microscopy with a mean fluorescence intensity of $1.5X10^3$. CDDP treatment induced significantly ($p<0.01$) high levels of fluorescence with a mean intensity of $4.9X10^3$. Both **7** and **9** induced significant levels of fluorescence, however treatment with complex **7** induced more fluorescence that **9** with means of $3.5X10^3$ ($p<0.01$) and $2.8X10^4$ ($p<0.05$), exhibiting 2.4X and 1.9X more phosphorylation than the negative control respectively. PTX also induced a significant ($p<0.05$) level of fluorescence, however, this was lower than the other complexes tested here with a mean fluorescence intensity of $2.3X10^3$.
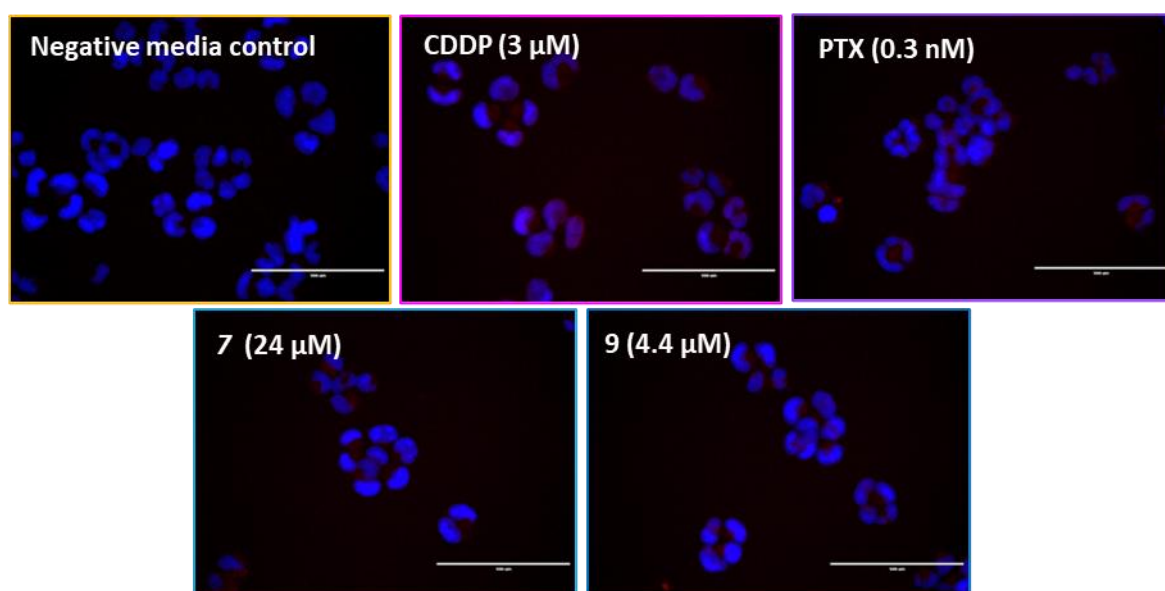
Figure 4-29: Double strand DNA breakage assessment via gamma-H2A.X phosphorylation of A2780 cells treated with media as the negative control, CDDP (3 µM), PTX (0.3 nM), **7** (24 µM), or **9** (4.4 µM). Cells were stained with gamma-H2A.X (Ser139) Monoclonal Antibody (CR55T33), (red) and DAPI (blue). Images presented as overlays of the red and blue channels 40X magnification (scale bar: 100 µm).
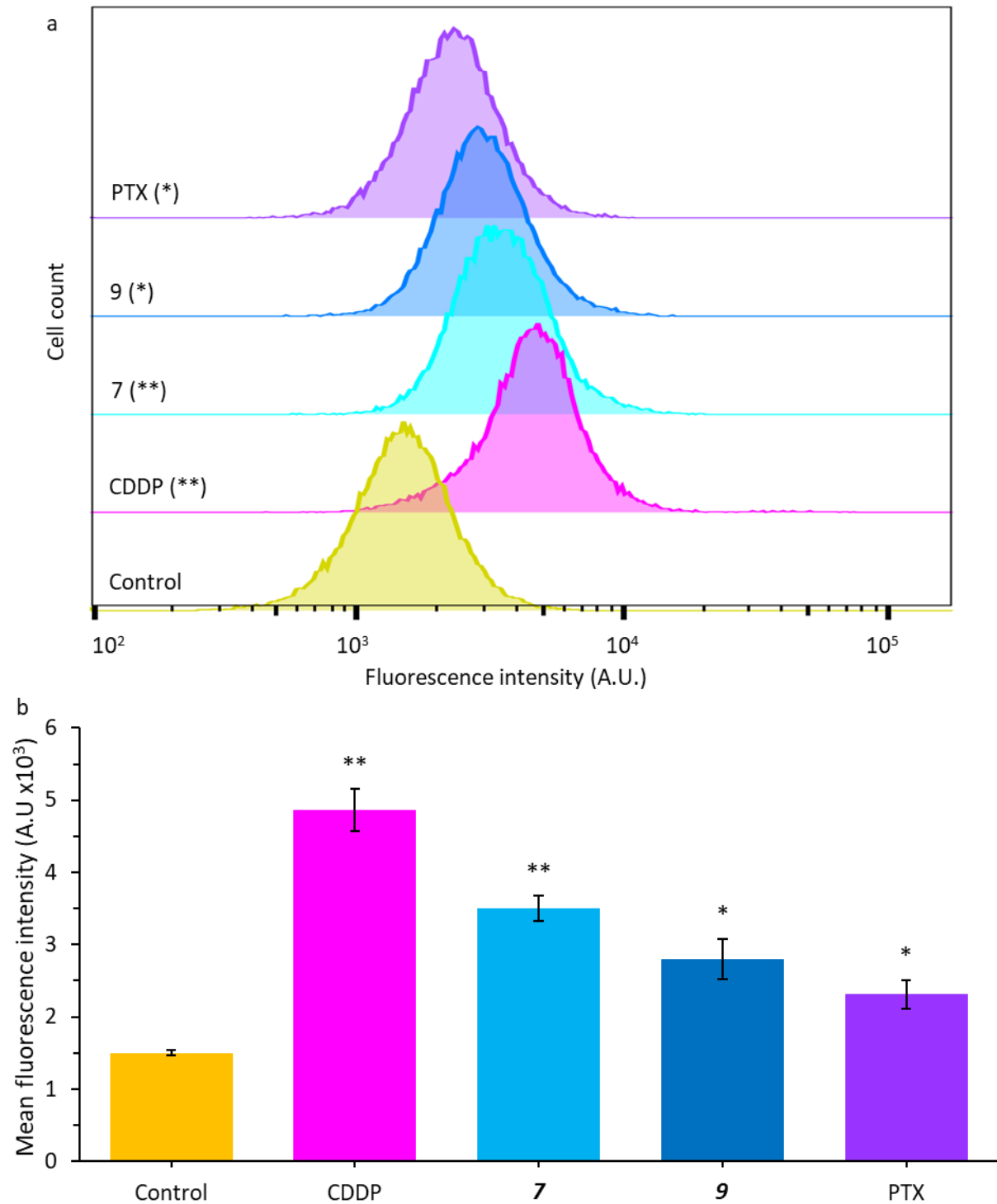
Figure 4-30: Gamma-H2A.X fluorescence intensity by flow cytometry of A2780 cells treated with media as the negative control, CDDP (3 µM), PTX (0.3 nM), **7** (24 µM), or **9** (4.4 µM). a). histograms of the fluorescence intensity of treated cells, b). mean fluorescence intensity of three biological replicates. (Significance determined by Welch t-test where * indicates $p<0.05$ and ** indicates $p<0.01$ levels of significance).

4-3.4.6: HDAC inhibition activity

With several assays suggesting higher-level DNA damage, quaternary DNA alteration through HDACi was assessed using fluorescence intensity, with fluorescence corelating linearly with HDAC inhibition (Figure 4-31). CDDP, **7** and the HDACi TriA significantly ($p < 0.05$, $p < 0.01$, and $p < 0.001$, respectively) reduced HDAC activity. While **9** did not induce significant ($p = 0.11$) decrease in activity, there was a small amount of inhibition.
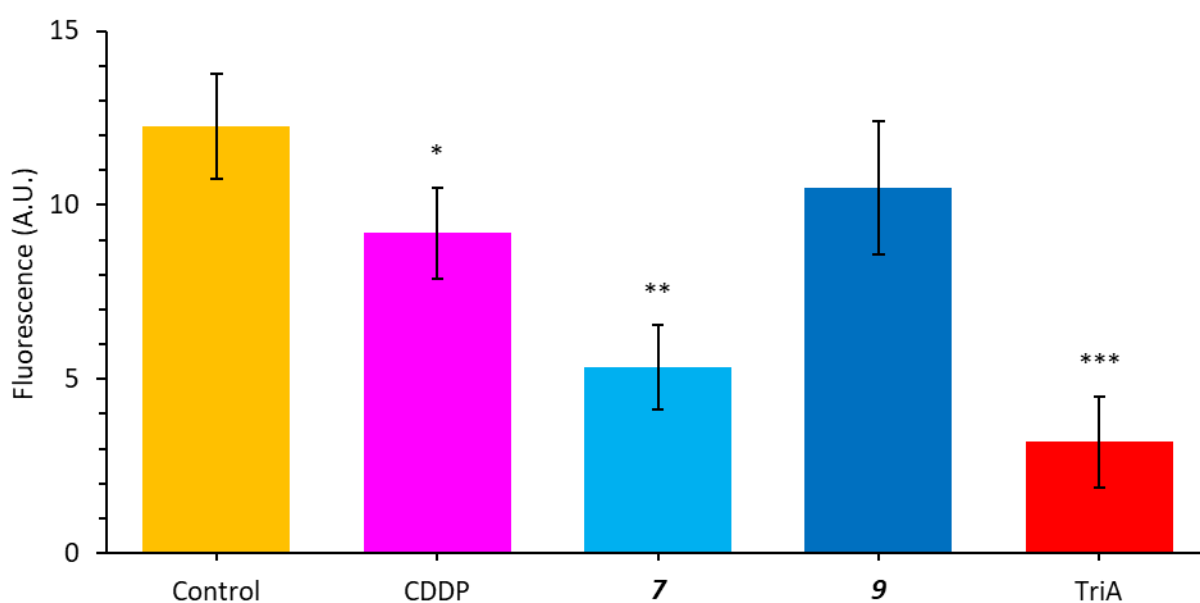
Figure 4-31: HDAC activity assay of A2780 cells with media as the negative control, CDDP (3 µM), PTX (0.3 nM), **7** (24 µM), **9** (4.4 µM) for 24 hours or 10 µM TriA for two hours as a positive control assessed by in situ HDAC activity fluorometric assay kit. (Significance determined by Welch t-test where * indicates $p < 0.05$, ** indicates $p < 0.01$, and *** indicates $p < 0.001$ levels of significance).

4-4: Discussion

Alkyl linkers/spacers/bridges are widely applied in many aspects of pharmacology to maximise treatment potential and allow additional properties[23,26–28]. Despite this, there is little research into the potential of a spacer within a bidentate ligand of piano-stool complexes. Here, the use of the spacer exhibited variety of effects that were divergent from their sister complexes without a spacer.

4-4.1: Physicochemical influences of the spacer in Ru(II) complexes

Biological matrix interaction by UV-Vis indicated none of the complexes interacted with 1:1 water to water, PBS, Albumin, plasma or NEAA, eliminating several transport and potential MOA including albumin conjugation and protein synthesis inhibition. Several complexes interacted with GSH, media and full media. There was a significant trend between the presence of a spacer and the prevention of interaction with these matrixes with all pairs losing one or more interactions with GSH and/or media. This is potentially explained by the DFT calculations.

In an atomic structure simulation, DFT calculations of **7** and **9** predict the spacer causes rotation of the phenyl ring out of the path of the *p*-cymene ring and iodine ligand. This leads to the disruption of the resonance by preventing the overlap of the p orbitals in the phenyl ring with the sp2 nitrogen in the imine bond, leading to reduced negativity of the ruthenium centre and iodine monodentate ligand. This provides some insight into the behaviours observed. Due to the iodine in **9** being more positive than **7**, becomes more strongly bonded to the ruthenium centre, improving bond stability. Increased ligand stability has two consequences; one being the increase in time to become active, and two being that it takes longer for the complex to be deactivated. This increase in stability is highly sought after as it corelated with increased potency, reduced side effects, extended therapeutic range and prevention with detoxicants such as GSH[37,38]. Noting the trends indicated by the loss of interaction with

biomolecules shared by several linked complexes here, it would be consistent that all the complexes in this series share loss of resonance.

As similarly seen in Chapter 3, several of these complexes aquated in water with the development of an isosbestic point. This is supportive of aquation being an activation step of these complexes. however, the iodo complexes and two oxygen-based R group complexes (**11** and **14**). The iodo complexes can be explained by steric hinderance surrounding the iodo ligand with slower aquation leading to slower clearance and increased potency[39]. On the contrary, oxygen-containing R group complexes, especially those in the *para* position, undergo poor aquation due to the electron donating group effects, leading to poor activation and antiproliferative activity[34]. Therefore, the inclusion of the spacer may increase the potency of these complexes by the distribution of the resonance across the ligand and the prevention of the extended effects of the electron donation of the oxygen group, allowing for their activation by aquation.

Additionally, several of these complexes exhibited spectra changes with DMSO. The only exception is complex **7** which exhibited an isosbestic point. While this can be problematic for DMSO based studies, this behaviour is similar to CDDP which can also form adduct species[40]. However, this isosbestic point is not seen in several other matrixes where DMSO concentration is <5%. Additionally, in antiproliferative screening, complex **7** is the second most active complex in this family. This suggests that this DMSO adduct is labile, and can be removed to form another species, likely water due to the aquation activation of these complexes[39,41,42].

Linkers have been previously shown to improve stability and potency. In the case of Titanocene dichloride modification to Oxali-Titanocene Y by the addition of two methoxybenzene groups through alkyl bridges from the bis-cyclopentadienyl group[37,43,44]. The flexibility provided by the bridge allows for the methoxy to bind to the aquated chlorine ligands, allowing for further complex stability and significant increased potency by 80X in renal cancer[37,43,44]. While this mechanism may not be employed

here, this further reinforces the idea that bridges and spacers can alter complex chemistry and improve the potency.

Similar to interaction differences, the addition of the spacer consistently exhibited a beneficial increase to lipophilicity of the complexes, or lipophilicity was maintained. Due to the spacer being lipophilic itself being a methyl derivative, it would be expected that the lipophilicity of the complexes would increase. This is seen in many organic and organometallic complexes[23,45,46]. In the unsubstituted and methyl substituted complexes lipophilicity increases consistent with aforementioned examples. This contrasts the oxygen and chlorine substituent complexes where lipophilicity remained unchanged. This may be due to the hydroxyl substituent contribute to a more hydrophilic nature while chlorine substituents contribute to a more lipophilic nature due to ionization and hydrogen bonding capabilities being present or not, respectively[47]. Therefore, when in combination with the spacer and disruption of resonance, increase in lipophilicity may not be seen due to the electron donating and withdrawing effects of these substituents. Due to the ionic nature of these complexes, they are expected to be hydrophilic. It has been documented that lipophilicities with LogP values between -5 and 0 favour the nuclei and lysosomes while if between 0 and +5, mitochondria and the ER are favoured[48,49]. Further that a LogP between 0 and +3 is favoured for optimal active transport[48,49]. Here, many of the complexes have a $logD_{7.4}$ close to 0 varying between -0.21 and -0.5 with the more potent complexes being more lipophilic. Comparing to similar ruthenium iminopyridine and osmium azopyridine complexes previously synthesised, these complexes exhibit a similar hydrophilicity exhibiting negative LogP values[33,34,50]. However, in these instances, potency did not corelate with lipophilicity. This contrasts with the findings in Chapter 3 of this work and in other published work. Therefore, while potency could potentially be improved with modification to increase lipophilicity, such as arene ring modification, it has been noted that potency is reliant on the type lipophilic moieties rather than the general increase lipophilicity[32,33,48,49,51].

4-4.2: Antiproliferative activity of complexes with and without a spacer

Antiproliferative screening demonstrated significant benefit of complexes possessing a spacer. This is exemplified by **7** and **9** where potency increased 5.5X. Potency can be attributed to the calculated loss of resonance, leading to decreased aquation of the complexes, as increased stability is often associated with improved potency by increasing the therapeutic time range[37]. This is further supported by the improved activity of **7** over **9** without recovery time. In addition, when the family of complexes is taken as a whole, the addition of the spacer is an additional compounding effect to other structural choices including phenyl ring substituent and monodentate species.

In addition to improved potency, other trends with the spacer are observed. In several complex pairs, the addition of a spacer improves potency in HCT116 p53-/- line. As p53 is the most commonly mutated oncogene in cancer involved in cell cycle, apoptosis, metabolism and DNA repair, its loss can hinder cytotoxic treatments[52]. Another trend seen is the consistent good potency of **7** and **9**, even in pancreatic and triple negative breast cancer (TNBC). Both are considered difficult cancers to treat. Pancreatic cancer treatment suffers from low drug efficacy, high toxicity, resistance, in addition to high metabolic, cellular and microenvironment heterogeneity[53,54]. TNBC treatment suffers from lack of targets and treatment guidelines in addition to being highly aggressive, heterogenous and metastatic[55,56]. Therefore, the ability of **7** and **9** to be highly effective in these both lines demonstrates their potential as non-specific treatments for a wide range of cancer types, including highly lethal variants.

Comparing chloro and iodo monodentate ligands; iodine activity is often superior to chlorine in regards to potency, as shown here and consistently in the literature due to their effects on aquation[57–59]. Aquation is often a required activation step for metallic complexes, including CDDP where the chlorine monodentate ligands are replaced with water[57,60]. From DFT calculations using $[(\eta^6\text{-bz})Ru(en)X]^{n+}$,

aquation occurs through interchange associative substitution which is hindered by heavier halides due to increased steric hinderance in the co-ordination sphere of the associative state (Scheme 4-1)[39]. Due to the increased size the formation of the intermediate is less likely due to steric hinderance, therefore aquation occurs at a decreased rate[61]. This explains the reduced aquation rate of iodo ligands in piano-stool complexes, and in extension improved potency. This also explains the lack of spectra changes by UV-Vis of the two iodo complexes in water. However, this trend is not always consistent as shown by Os-ImPy complexes where chloro ligands are often more potent than iodo ligands, which can be attributed to the effects of the osmium centre[32].
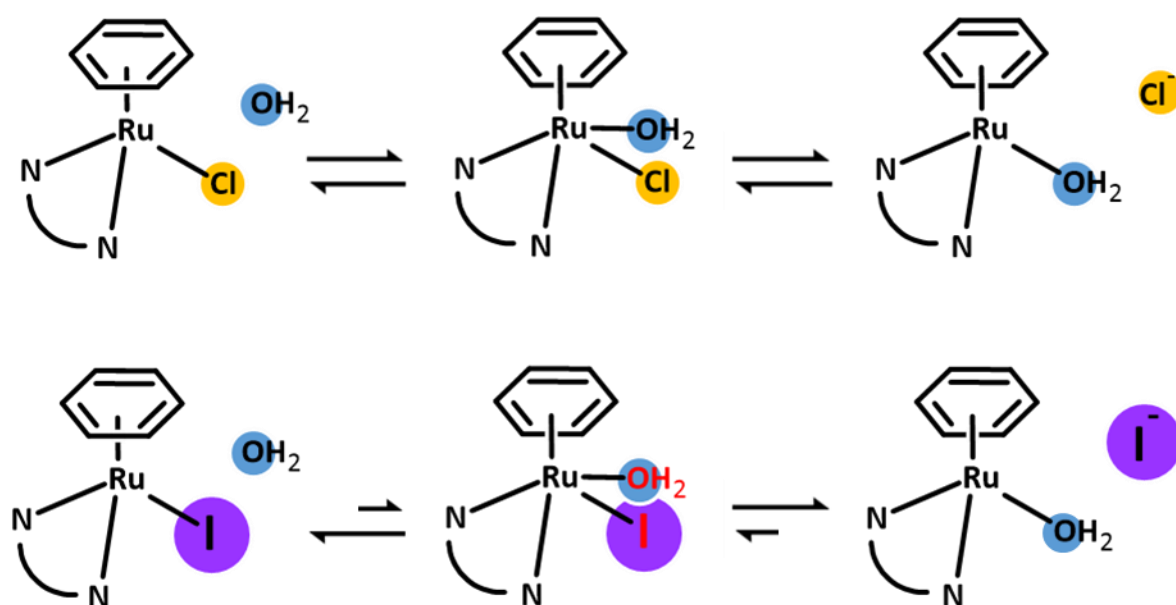
Scheme 4-1: Simplified model process of aquation of piano-stool complexes though interchange associative substitution where halide weight hinders aquation through steric hinderance[39].

Here, the delay in aquation induced by the spacer and the iodo monodentate ligand can contribute to the extension of complex stability and bioavailability. Many treatments seek stability by several methods such as those previously discussed including arene tethering and arene ring modification[37,39,43,44]. Therefore 'inbuilt' increased stabilisation a significant benefit, especially as these complexes do not appear to take advantage of the EPR effect as they are not indicated to bind to albumin by the UV-Vis experimentation.

Comparing the phenyl ring substituents, consistently **10 (p-CH₃)** followed by **16 (o-OCH₃)** were the most effective complexes. Efficacy is unlikely to be due to lipophilicity due to these complexes highly differing with **10** having a more lipophilic methyl group and **16** possessing a highly hydrophilic group[47]. Activity may be due to lack of GSH interaction, therefore reduced detoxification and by extension increase in the half-life[38]. Without further probing into the MOA of action of these complexes, reasons for their potency over other complexes cannot be fully ascertained. Yet without further improvement modifications, like Cl to I monodentate substitution to improve the potency, the further testing of **10** and **16** is not recommended[32,33].

Beneficially, only complex **9** was found to have an IC$_{50}$ value <140 µM in normal MRC5 cells. **9** exhibited an IC$_{50}$ of 64.8 µM. While this is can be classified as antiproliferative, this is minimal compared to its efficacy in cancerous cells by being 14.7X less potent than in A2780 and 3.0X less potent than in A549. This indicates that the presence of the spacer allows the benefit of improving potency in cancerous cells while maintaining tumour specificity and not centred around the structure of the bidentate ligand. Specificity of ruthenium complexes has been attributed to more selective uptake and activation of complexes in addition to MOA that utilise the biochemical differences between cancerous and normal cells[62–65]. However, many ruthenium complexes do not possess cancer cell specificity[58,66,67].

2D models of antiproliferative screening are highly effective for assessing initial antiproliferative activity and safety of prospective agents, but cannot evaluate the effectiveness of a treatment in a solid tumour [68]. 3D structures have been found to be more consistent with *in vivo* activity, histological structures and resistance profiles of tumours, and are comparable to patient models[69–72]. To assess the potential of **7** and **9** *in vivo*, activity in A2780 spheroids was assessed. Both complexes at IC$_{50}$ concentration achieved significantly reduced spheroid area by reducing area by ~10%, comparable to the clinically approved CDDP and PTX. Significant potency in EOC spheroids is particularly noteworthy, as spheroids are commonly found in the acetic fluid and peritoneum of metastatic EOC patients[70–72]. Furthermore, these spheroids are often found to be highly resistant to platinum complexes and PTX, theorised to be due

to being derived from the primary mass following received previous treatment, resulting in resistant residual cells that develop into spheroids[70]. Therefore, the ability of these complexes to penetrate spheroids is highly beneficial and highlights their potential in advanced disease progression.

4-4.3: Mode of action differences of complexes with a spacer

As many ruthenium piano-stool complexes depolarise ΔΨm, this was assessed using Rh123. Neither complex induced ΔΨm depolarisation, but *7* induced hyperpolarisation seen by the increase of Rh123 fluorescence. Hyperpolarisation been noted to be induced by several organometallic complexes by JC1 flow cytometry analysis (Figure 4-32)[73,74]. Hyperpolarisation naturally occurs in cancer cells compared to normal cells by having a mitochondrial inner membrane potential (Ψ_{IM}) of ~-200 mV and -139mV respectively[75,76]. This documented to be due to reduced ΔΨm dissipation, increased glycolysis and increased NADPH concentrations[75,76]. Hyperpolarisation is associated with the reversable, initial stages of apoptosis coupled with further increase of ROS species and reduced GSH, therefore is seen before induction of canonical apoptosis features such as caspase activation, phosphatidylserine externalisation and FAS signalling[73,77]. In addition, hyperpolarisation has been documented to be associated with type II autophagic death[73]. Therefore, ΔΨm hyperpolarisation induced in *7* treated cells would be consistent with antiproliferative activity seen with 24 hours. Furthermore, consistent the suggested delay in activation of *9* and antiproliferative activity studies.
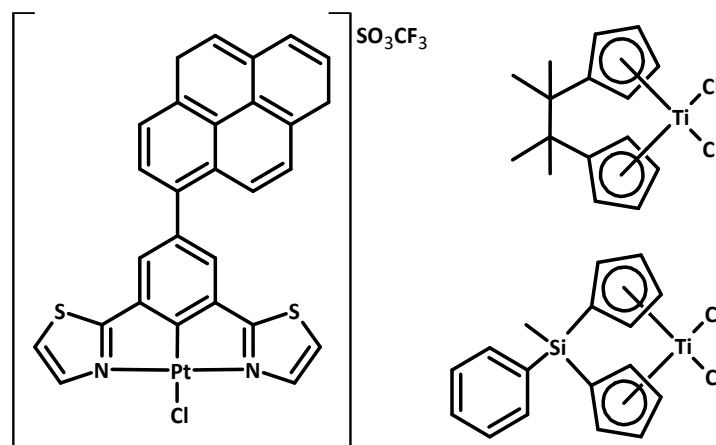
Figure 4-32: Organometallic complexes noted to induce mitochondrial hyperpolarisation by JC1 analysis.

Due to the increase in ΔΨm seen by **7**, ROS generation was assessed as fluctuations of ΔΨm of as little as 10% can increase ROS generation by 90% in normal cells[76]. This was shown to be consistent with **7** as an increase in ROS levels was observed by increasing DCFDA fluorescence by 208%, however despite **9** not inducing any mitochondrial changes ROS levels were increased by 146%. This suggests that the complexes induce ROS through a similar MOA. Organometallic complexes have been shown to generate ROS through a variety of mechanisms dependant on structure including redox cycling, detoxification inhibition, and mitochondrial damage. Direct generation relies on the ability of transition metals to redox cycle using a redox couple and generate superoxide from the oxidation of oxygen while reducing the other element of the redox couple, as seen with NADPH/NADP$^+$ as shown by hydrogenation catalytic complexes[78,79]. On the other hand, indirect generation relies on the damage to cellular systems such as mitochondrial hyperpolarisation as previously described, and ROS detoxification system damage. This can include biomolecules and enzymes such as GSH by catalytic GSSG formation and peroxiredoxin modulation shown by RM175 which can bind to the resolving cysteine Cys173 of Peroxiredoxin 1 during hydrogen peroxide detoxification[73,80,81]. However, there is debate on if ROS is generated by ΔΨm changes or if ΔΨm changes result in ROS generation[73].

Taking these mechanisms into consideration, these results may be due to a multitude of compounding factors. The most likely explanation is that at 24 hours exposure, complex **9**, due to lack of ΔΨm

alteration, likely has of redox activity inducing ROS. This would contrast **7** which exhibits higher levels of ROS, induces ROS through mitochondrial hyperpolarisation, GSH conjugation and exhibiting redox activity inducing ROS. Redox capability of these complexes could be assessed by cell free xylenol orange-based assays in future work[82].

During ΔΨm and ROS generation studies, **7** and **9** were noted to induce nuclear softening allowing the formation of convex nuclei. Furthermore, in **9** treated cells there is a decrease in DAPI fluorescence in comparison to the negative control. It must be noted that EOC has been documented to possess mildly convex nuclei as seen in the negative control induced by non-cytotoxic nuclear grooving inducing a bean-shaped morphology[83]. Nuclear softening is widely associated with DNA damage from aberrant structural protein expression, and genetic and chemical influences[84]. This often manifests as increased convexity[85]. Softening occurs due decreased actin and lamin A/C binding/expression, decreased lamina thickness, extent of chromatin condensation and nuclear protein expression[84,86]. Beyond this there is conflicting information on the reasoning behind morphological changes, due to the complexity of chromatin structures, DNA damage responses, and staining procedures[83,84,86]. CDDP binding has been documented to induce nuclear softening and global chromatin relaxation, also seen by in nuclear morphology changes in this work[87]. However, this then subsides to increased chromatin condensation, nuclear fragmentation associated with apoptosis, but increased stain fluorescence is maintained[88–90]. This demonstrates that nuclear morphology is a highly transient dependant on many factors. This suggests that while **7** and **9** both induce DNA damage, the extent or type of damage cannot be discerned from morphology.

With apoptotic death being considered the most effective method of fighting cancer bar surgery, and the primary MOD resultant from DNA, it was investigated by flow cytometry[91]. Results suggest that both complexes do induce apoptosis. Furthermore, are consistent with **9** taking longer to activate than **9** with **7** exhibiting more apoptosis than **9** in 24 hours. DNA damage is a significant inducer of intrinsic apoptosis especially though the activity of p53 which goes on to activate and inhibit many subsequent

biomolecules including PUMA, PAX, p53AIP1, APAF-1, miR-34A, BCL-2 and BCL-X$_L$[92,93]. However, apoptosis through p53-independent mechanisms can also occur through p73 which mediates PUMA and BAX to induce mitochondrial permeabilization and cytochrome C release, and Nur77 which can also affect mitochondria inducing cytochrome C release[93]. Considering the IC$_{50}$ values of **7** and **9** in the HCT116 p53+/+ and p53-/- cell lines, the induction of apoptosis from DNA damage does not to appear to rely on p53, further the potency of **9** further improved in HCT116 p53-/-. This is highly remarkable and highly beneficial as many cancers lack a functional p53[52]. However, DNA damage can also initiate necrosis and autophagy using PARP and mTorc/TSC2 respectively[93]. Considering the significant increase in the non-viable population, necrosis should also be considered as an MOD.

DNA damage can induce cell cycle arrest at any point in the cell cycle program. Similar ruthenium complexes with dimethylamine phenyl ring substituents that have been documented to induce DNA damage arrest in G$_1$, while CDDP has been demonstrated to induce arrest in both S phase and G$_2$/M[57,94,95]. G$_1$ arrest is the primary restriction point of cell cycle and the starting point of replication, therefore arrest here indicates that cell is too damaged, old, experiencing too many toxin signals and/or has an insufficient nutrient source for replication, forcing the cell into arrest, evaluated by cyclin-dependant kinases, RB, ATM and p53[96,97]. This contrasts later arrest such as S phase or G$_2$/M where progression is halted due to damage that occurs during replication such as replication fork stalling and structural damage evaluated by ATM, ATR, CHK1/2, WEE1, CDC25 and CDK2/1 or Aurora B, MCC and APC/C, respectively[96,97]. Here, **9** induced G$_1$ arrest by compromising the S phase population, indicating that **9** also induces DNA damaged in a similar fashion to similar ruthenium ImPy complexes[57]. However, complex **7** while not statistically significant at p=0.06 (likely due to the wider variance in the analysed samples), there was a substantial increase in the sub-G$_1$ population by 10.2% by similarly compromising the S phase population. This suggests, both complexes prevent initiation of cell cycle from the restriction point.

Due to the methodology of cell cycle arrest analysis by PI and RNase staining, Sub-G_1 analytically stems from cells with less PI fluorescence than the G_1 population, G2/M being double the G_1 peak from having double the DNA content from replication, and S being in-between from DNA being replicated and not having a full second copy of DNA (Figure 4-33)[98,99]. This is due to PI being a non-specific DNA intercalator and the amount of fluorescence being proportional to the amount of DNA in the cell[99]. The decrease in PI fluorescence of cells resulting in the sub-G_1 population could be due to decreased concentration of DNA for PI intercalation or prevention of DNA intercalation. While which cannot be ascertained from the flow cytometry data, the decrease fluorescence is still highly indicative of DNA damage, and further that the extent is far more than that exhibited by *9*, further supporting the faster activation/delayed activation of *7* and *9* respectively.

In this work, the wound healing assay has been used to evaluate invasion inhibition in parallel with the colony formation assay to evaluate metastasis. *7* was highly effective at inhibiting wound healing and colony formation, this highly contrasted *9* which was no more effective than the untreated control in wound healing and fractionally inhibited colony formation. While this differential behaviour further highlights that the presence of the spacer drastically alters the MOA of the complex, these results are contradictory to other results presented in this chapter. It would be expected that due to complex *9* having a lower IC_{50} with recovery time that *9* would be more effective in the wound healing assay and the colony formation assays due to having a 72- and 168-hour recovery time respectively. Therefore, lack of activity is unlikely due assay time. One reasoning may be due to the MOA of the complexes. Metastasis and invasion mechanisms are composed of a diverse array of signals, enzymes and proteins. Some examples include the alteration of adhesome including integrin and cadherin binding and expression, the employment of MMPs, and intercellular signalling changes of TGF-β signalling through SMAD2/3/4[100–103]. Furthermore, these MOA are often distinct from antiproliferative MOA. Therefore, it may be that the unlinked complex *7* can affect these antiinvasive and antimetastatic pathways while *9* cannot.
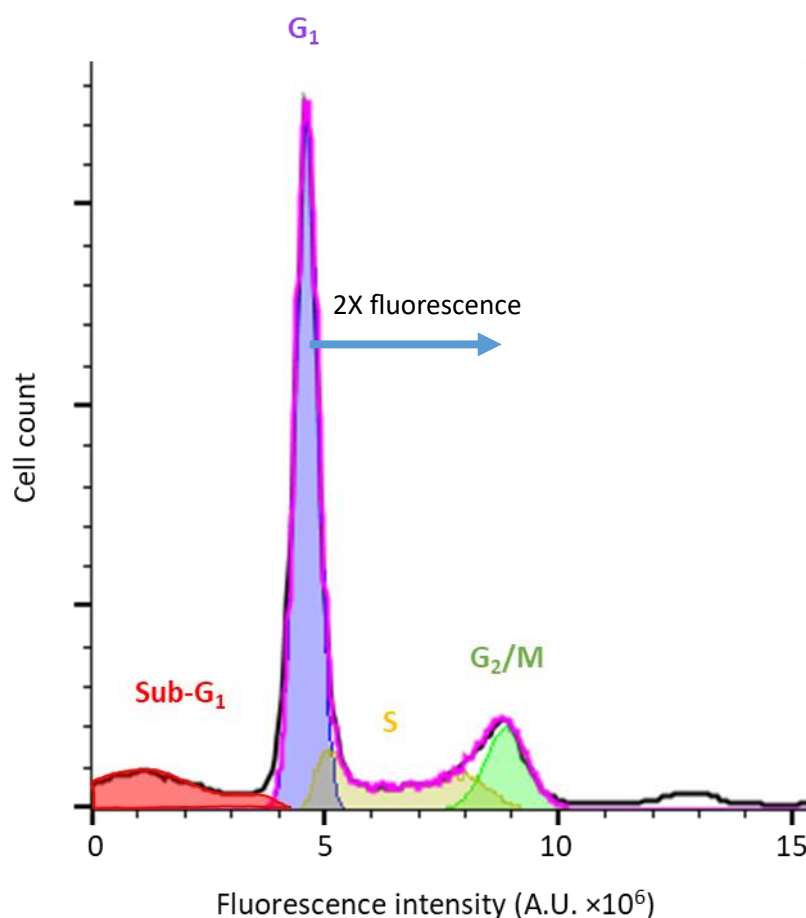
Figure 4-33: Representative cell cycle population proportions of untreated A2780 cells demonstrating the methodology of cell cycle determination by flow cytometry with PI and RNase staining. Demonstrating that there is twice as much PI fluorescence in the G_2/M population than in the G_1 population due to there being twice as much DNA to bind to.

ICP-MS work here demonstrates that the addition of the spacer reduces ruthenium accumulation. Following 24 hours exposure, there was a significant increased uptake of ruthenium in **7** treated cells over **9** treated cells by 0.057 fmol/cell. Noting that complex **9** has a higher lipophilicity than **7**, -0.21 and -0.41 respectively, this suggests that the accumulation of ruthenium of **9** treated cells should be higher. From an uptake perspective, increased lipophilicity aids transport across the CCM in a passive diffusion mechanism due to the phospholipid bilayer of the CCM[104]. Additionally, increased lipophilicity aids active uptake mechanisms, with LogP values between 0 and +3 is favoured for optimal active transport[48,49]. This suggests other factors are involved uptake including complex charge, electron density across the complex and steric behaviour of the spacer and the phenyl moeity[62,105]. Many similar

complexes use an active uptake mechanism to enter the cell, which has been demonstrated by temperature dependant accumulation assays[106,107]. As part of this method of analysis, efflux must also be considered. Considering that complex **7** interacts with GSH while complex **9** does not, this suggests that **7** may undergo more detoxification and efflux. However, other efflux mechanisms should be considered such as ATP-dependant ABC-transporters such as MRP2 and MRP1-5, which can contribute to the decreased levels of **9** ruthenium accumulation[107,108].

From metal accumulation data coupled with treatment efficacy; potency is dependent on ruthenium content, a trend seen by many complexes[57,62,105,109,110]. If this trend continues the recovery period, this predicts that **7** may be more vulnerable to efflux in the recovery period, consistent with GSH toxification as demonstrated by GSH UV-Vis interaction. Overall, this suggests that while the uptake of complex **9** is reduced in comparison to **7**, leading to the lower potency at 24 hours exposure only, there is indication that the efflux of complex **9** is also hindered in the recovery period. This would allow for a longer intracellular localisation, therefore be more beneficial as a long-term treatment.

The localisation of ruthenium caused by exposure to these complexes is similar; both **7** and **9** predominantly localise to the membrane and organelle fraction. These localisation patterns agree with localisation predictions from lipophilicity[48]. The membrane and organelle fraction of the kit used encompasses all cellular membrane proteins and organelles[35]. While localisation of the metal can be highly beneficial to understanding potential targets of a treatment, it is only indicative. For example, CDDP is canonically known as a DNA damaging agent, yet it is widely documented that only 1% of a total CDDP dose localises to the nucleus[111–115]. This is also supported by the data collected here with platinum of CDDP treated cells predominantly accumulating in the membrane and organelle fraction. Therefore, it is likely that **7** and **9** do not need to be primarily localised to the nucleus and DNA damage to induce significant DNA damage. This accumulation pattern could be due to other cellular pathways including other MOA, influx and efflux pathways and other intercellular transport pathways.

4-4.4: DNA damage differences induced by ImPy and ImPy-Bn complexes

Due to the indications that DNA damage induced by **7** and **9** DNA damaged was investigated further as a primary MOA of these complexes.

As ctDNA interaction was documented following 24 hours incubation with the formation of an isosbestic points for most of the complexes in this family, including complexes **7** and **9**, ctDNA titration binding assay was done to assess type of interaction. Both complexes interacted with ctDNA with a hyperchromic shift. This has been widely documented to corelate with DNA unwinding, as unwinding allows for increased π → π* excitement and increased absorbance[116]. In addition, hyperchromism has been documented to correspond to dsDNA groove binding, electrostatic interactions and in some cases covalent bonding[116–119]. This contrasts hypochromism which is associated with non-covalent intercalative binding[120]. This is consistent with **7** and **9** inducing DNA damage indicated by the nuclear morphology. Organic Schiff bases which have been used as the bidentate ligand in organometallic complexes have also been documented to induce hyperchromism with ctDNA though electrostatic binding[119]. This highly indicates that these complexes also due to having Schiff base bidentate ligands could be interacting to ctDNA through electrostatic binding unwinding DNA. To investigate DNA interactions more closely, interactions with 9-EtG, a commonly used analogue for nucleotide interactions with organometallic complexes[121–123]. Only complex **9** demonstrated a hyperchromic effect with 9-EtG, associated with electrostatic binding to oxygen and phosphate in addition to covalent binding to N7[124]. It has been documented that complexes which exhibit hard Lewis acid activity favour the negative charge of the phosphate sugar of the nucleotide and preferably bind to the highly basic nature of Guanine-N7[125]. Similar ruthenium complexes including RM175 have been documented to be hard Lewis acids[126]. This is highly suggestive that these complexes function as Lewis acids and preferentially bind to the phosphate backbone of ctDNA. Further, complex **9** then has the additional

benefit of being a hard enough Lewis acid to also interact with 9-EtG. Experimental data here suggests that this could be due to the broken resonance causing the increased Mulkin charge of the ruthenium, increasing its hardness as a Lewis acid.

Due to the strong chemical indications that complexes **7** and **9** have a DNA-based MOA though the damage of DNA unwinding and base damage, the ability of the complexes to induce *in vitro* DNA damage was investigated using the comet assay[127]. The differential behaviour of these complexes was consistent with previous experiments as **7** did not induce significant levels of DNA breakage while **9** did. Considering the results from the UV-Vis titration studies and the reduced levels of dsDNA stand breakage in complex **9** treated cells from the gamma-H2A.X analysis, alkali-labile adducts and ssDNA are like the most likely are the predominant form of DNA damage seen in the complex **9** treated comets. ssDNA breaks are low-level damages considering the scale of DNA damage that can occur and are routinely repaired using the Base Excision repair (BER) system[128,129]. BER relies on DNA N-glycosylases to sense and initiate the first stages by excising damaged bases forming abasic sites, following which APE1, DNA polymerase β, DNA ligase 1/3 and XRCC1 to cleave, repair and ligate DNA respectively[128–130]. However, this mechanism repairs scheduled ssDNA breaks that occur during replication and other DNA maintenance procedures. This contrasts BER triggered by PARP which detects unscheduled ssDNA breaks[130]. PARP1 binds to DNA through zinc finger motifs, and when ssDNA breaks are detected, PARP1 induces PARslyation of PARP enzymes, XRCC family enzymes and histones H1 and H2b using NAD^+ and ATP to initiate chromatin reorganisation and DNA repair[129,130]. This may explain the lesser extent of antiproliferative activity of **9** at 24 hours compared to **7** as the damage induced is less toxic and can be initially repaired through the BER system. However, overactivation of PARP1 in cells can cause the overconsumption of NAD^+ and ATP for PARslyation leading to the induction of apoptotic and necrosis has also been documented[131,132].

Due to substantial levels of DNA damage being evident in complex **9** treated cells, dsDNA break incidence was investigated by gamma-H2A.X fluorescence. Gamma-H2A.X is a histone variant with a

conserved SQ motif at the carboxy tail that is phosphorylated by ATM and ATR on Serine 139 when dsDNA breaks occur[133,134]. Due to its highly sensitive nature, it is routinely used by immunostaining and flow cytometry to assess dsDNA breaks in the cell[135]. While both complexes exhibited significant levels of dsDNA breaks, **7** induced more breaks following 24 hours exposure. However, it must be noted that taking consideration of the gamma-H2A.X fluorescence intensity with the comet assay, this suggests that while complex **9** does not induce dsDNA damage,

 7 does include dsDNA damage, their frequency is much lower than

This corelates with its more potent nature at 24 hours without recovery time as dsDNA breaks are considered to be the most lethal form of DNA damage[9,10]. Therefore, the more potent nature of **9** with recovery time could be due to the pathway to transform ssDNA breaks to dsDNA breaks. After ssDNA breaks develop, repair is attempted through PARP activation. However, if a high volume of ssDNA breaks occur, breaks can arise in close proximity on opposite strands, forming dsDNA breaks. Additionally, if repair fails and ssDNA breaks persist, when the cell progresses through cell cycle, replication fork stalling can occur causing dsDNA breaks[129,136]. However, this requires one; chance, and two; time, to allow the opportunity for two ssDNA breaks to occur in proximity and for cell cycle to occur respectively. Regarding cell cycle, within the 24 hour exposure period, A2780 cells have the opportunity to undergo a maximum of two cell cycles due to having a doubling time of ~16-18 hours[137,138]. Meaning, of the fraction of ssDNA breaks that do not get repaired, a further fraction may induce dsDNA breaks. However, when 72 hours recovery time is included, this increases chances for repair failures, fork stalling, and fatal dsDNA damage formation in addition to any dsDNA breaks that may occur directly from **9** interaction with DNA.

Moving away from direct DNA damage to chromosomal MOA, leucine and arginine rich histones which interact with and give a quaternary structure to DNA using acetyl and methyl groups are also associated with induction of genomic damage if dysregulated[139–141]. DNA-histone interactions are tightly

controlled by a variety of enzymes that add and remove the acetyl and methyl groups to histones including Histone AcetylTransferase, HDAC, Methyl Transferases and de-methylases[139–141]. Despite HDAC possessing a zinc finger motif, similar to PARP1, interaction with metallic complexes is often through an organic HDACi derivative active cargo moiety, and by extension having a similar binding mode as the HDACi it was derived from as seen with the SAHA derivative complexes[142–144]. However, some gold complexes have been found to inhibit HDAC through a novel mechanism of blocking entry and exit of the active site channel by porphyrin ring ligands[145,146]. Due to this potential, the ability of these complexes to inhibit HDAC was investigated. Complex *7* significantly inhibited *in situ* HDAC activity while *9* did not. This difference may be due to structural and physicochemical differences between *7* and *9*. The spacer potentially prevents interaction to the Zinc atom of the HDAC, the associated amino acids ASP267, ASP178 and His180, or other key amino acids in the hydrophobic binding channel including Tyr 306, Tyr745, Pro464, Phe583, His463 and Gly473 due spacer causing a bend in the bidentate ligand if behaviour is similar to previously examined metallic complexes[142,144]. Furthermore, the ability of *7* to induce HDAC inhibition without an organic HDACi moiety is highly remarkable. Resulting HDAC inhibition leads to increased acetylation of histones and the opening of the chromatin structure by weakening the electrostatic interaction between the histones and DNA[139]. Excessive unwinding can lead to underwinding; classified as negative supercoiling of DNA which allows for opening of DNA[147]. Underwinding is routinely achieved by Topoisomerases to introduce DNA relaxation for transcription and replication[148,149]. Yet, excessive underwinding reintroduces local tension, in addition to overwinding tension in flanking areas, genomic extension, formation of abnormal structures including palindromic hairpins, Z-DNA, R-loops and D-loops. In addition, if unwinding is too fast and forceful, can induce significant damage through electrostatic interactions[148–151]. Topoisomerases including TOP1, TOP1mt and TOP3 can ameliorate these disruptions by introducing transient breaks, but rely on undamaged DNA[149]. Therefore, if complex *7* is bound to the major grooves

of DNA, as shown by ctDNA binding, topoisomerases can stall, introducing dsDNA breaks as seen, providing a consistent MOA for **7**.

4-5: Conclusion

Linkers are widely used in pharmacology to allow the addition of active cargos, prevent steric hinderance and add extra functions to a molecule. Here, the use of a spacer within a ImPy bidentate piano-stool complexes was investigated. It was demonstrated that the methylene spacer can greatly improve anti-proliferative activity of $[Ru(\eta^6\text{-}p\text{-Cym})(ImPy)X]PF_6$ complexes up to 6.5X versus their unlinked counterpart. Structural and electron density calculations suggest that this due to the disruption of bidentate ligand resonance which induces a more positive ruthenium centre and monodentate I ligand. This leads to alterations in biochemical interactions, uptake, complex activation, and MOA. However, the addition of the spacer inhibits anti-invasive and antimetastatic activity.

The MOA of complex **7** and **9** is to induce DNA strand breaks. However, the presence of the spacer greatly alters how following 24 hours exposure. A potential mechanism for complex **7** may involve the underwinding of DNA through electrostatic groove binding coupled with inhibition of histone acetylation. DNA underwinding can lead to strand tension, the development of hairpins, Z-DNA, R-loops and D-loops, but also increased protein interaction stabilisation. This leads to the development of dsDNA breaks, which induces cell cycle arrest and apoptosis. In comparison, results suggest complex **9** interacts with DNA through electrostatic groove binding and adduct formation causing ssDNA breaks, following which DNA damage is detected, inducing cell cycle arrest. Following the opportunity to undergo cell cycle and DNA replication where BER can be induced to combat the ssDNA breaks inducing cell cycle arrest, potential excessive PARP1 recruitment due to the extent of ssDNA breaks, there may be induction of apoptosis through NAD^+ and ATP overconsumption.

In addition to these potential pathway differences, the time frame for damage of these complexes is significantly different and alters the longer-term MOA. With the disruption of resonance, there is a

predicted increase in activation time of these complexes, supported by the antiproliferative activity studies in A2780. This means that while complex *7* may undergo detoxification and cellular efflux during the recovery time, complex *9* can continue to induce DNA damage, meaning more ssDNA breaks can be induced and allow the development of more serious damage and triggering of prolonged stress responses. This is supported by the highly potent antiproliferative activity of *9* with recovery time. However, these predictions should be confirmed by assays with a 72-hour recovery time following treatment.

Noting these significant differences that can be seen with unmodified complexes, there is high potential for the use of spacers in other piano-stool organometallic complexes to further improve potency.

4-6: References

1. Peng, J. C. & Karpen, G. H. Epigenetic regulation of heterochromatic DNA stability. *Curr. Opin. Genet. Dev.* **18**, 204–211 (2008).
2. Sirajuddin, M., Ali, S. & Badshah, A. Drug–DNA interactions and their study by UV–Visible, fluorescence spectroscopies and cyclic voltametry. *J. Photochem. Photobiol. B Biol.* **124**, 1–19 (2013).
3. Banfalvi, G. Structural organization of DNA. *Biochem. Educ.* **14**, 50–59 (1986).
4. Kiwerska, K. & Szyfter, K. DNA repair in cancer initiation, progression, and therapy—a double-edged sword. *J. Appl. Genet.* **60**, 329–334 (2019).
5. O'Connor, M. J. Targeting the DNA Damage Response in Cancer. *Mol. Cell* **60**, 547–560 (2015).
6. Tchounwou, P. B., Dasari, S., Noubissi, F. K., Ray, P. & Kumar, S. Advances in Our Understanding of the Molecular Mechanisms of Action of Cisplatin in Cancer Therapy. *J. Exp. Pharmacol.* **13**, 303–328 (2021).
7. Aldossary, S. A. Review on pharmacology of cisplatin: Clinical use, toxicity and mechanism of resistance of cisplatin. *Biomed. Pharmacol. J.* **12**, 7–15 (2019).
8. Kopa, P., Macieja, A., Galita, G., Witczak, Z. J. & Poplawski, T. DNA Double Strand Breaks Repair Inhibitors: Relevance as Potential New Anticancer Therapeutics. *Curr. Med. Chem.* **26**, 1483–1493 (2019).
9. Alhmoud, J. F., Woolley, J. F., Al Moustafa, A.-E. & Malki, M. I. DNA Damage/Repair Management in Cancers. *Cancers (Basel).* **12**, 1–22 (2020).
10. Huang, R.-X. & Zhou, P.-K. DNA damage response signaling pathways and targets for radiotherapy sensitization in cancer. *Signal Transduct. Target. Ther.* **5**, 1–27 (2020).
11. Hainsworth, J. D. & Greco, F. A. Etoposide: Twenty years later. *Ann. Oncol.* **6**, 325–339 (1995).
12. Montecucco, A., Zanetta, F. & Biamonti, G. Molecular mechanisms of etoposide. *EXCLI J.* **14**, 95–108 (2015).
13. Xu, W. S., Parmigiani, R. B. & Marks, P. A. Histone deacetylase inhibitors: molecular mechanisms of action. *Oncogene* **26**, 5541–5552 (2007).
14. Ho, T. C. S., Chan, A. H. Y. & Ganesan, A. Thirty Years of HDAC Inhibitors: 2020 Insight and Hindsight. *J. Med. Chem.* **63**, 12460–12484 (2020).
15. Ramaiah, M. J., Tangutur, A. D. & Manyam, R. R. Epigenetic modulation and understanding of HDAC inhibitors in cancer therapy. *Life Sci.* **277**, 1–19 (2021).
16. Bouyahya, A. *et al.* Pharmacological Properties of Trichostatin A, Focusing on the Anticancer Potential: A Comprehensive Review. *Pharmaceuticals* **15**, 1–53 (2022).
17. Hanahan, D. & Weinberg, R. A. Hallmarks of Cancer: The Next Generation. *Cell* **144**, 646–674 (2011).
18. Manohar, S. & Leung, N. Cisplatin nephrotoxicity: a review of the literature. *J. Nephrol.* **31**, 15–25 (2018).
19. Coverdale, J. P. C., Laroiya-McCarron, T. & Romero-Canelón, I. Designing Ruthenium Anticancer Drugs: What Have We Learnt from the Key Drug Candidates? *Inorganics* **7**, 1–15 (2019).
20. Sheyi, R., de la Torre, B. G. & Albericio, F. Linkers: An Assurance for Controlled Delivery of Antibody-Drug Conjugate. *Pharmaceutics* **14**, 1–27 (2022).
21. de la Torre-Rubio, E. *et al.* Carbohydrate effect of novel arene Ru(II) phenanthroline-glycoconjugates on metastatic biological processes. *J. Inorg. Biochem.* **247**, 1–13 (2023).
22. Chellan, P. & Sadler, P. J. Enhancing the Activity of Drugs by Conjugation to Organometallic Fragments. *Chem. – A Eur. J.* **26**, 8676–8688 (2020).
23. Kedge, J. L. *et al.* Organometallic Nucleoside Analogues: Effect of Hydroxyalkyl Linker Length on Cancer Cell Line Toxicity. *Eur. J. Inorg. Chem.* **2017**, 466–476 (2017).
24. Can, D. *et al.* The [(Cp)M(CO)3] (M=Re, 99mTc) Building Block for Imaging Agents and Bioinorganic Probes: Perspectives and Limitations. *Chem. Biodivers.* **9**, 1849–1866 (2012).
25. Lee, H. Z. S. *et al.* Synthesis, Characterization, and Biological Properties of Osmium-Based Tamoxifen Derivatives – Comparison with Their Homologues in the Iron and Ruthenium Series. *Eur. J. Inorg. Chem.* **2015**, 4217–4226 (2015).
26. Adhikari, S., Hussain, O., Phillips, R. M., Kaminsky, W. & Kollipara, M. R. Neutral and cationic half-sandwich arene d 6 metal complexes containing pyridyl and pyrimidyl thiourea ligands with interesting bonding modes: Synthesis, structural and anti-cancer studies. *Appl. Organomet. Chem.* **32**, 1–13 (2018).
27. De Miranda, A. S. The methylation effect in medicinal chemistry. *Rev. Virtual Quim.* **3**, 228–232 (2011).
28. Schindler, T. *et al.* Structural Mechanism for STI-571 Inhibition of Abelson Tyrosine Kinase. *Science,* **289**,

1938–1942 (2000).

29. Sigel, A., Sigel, H., Freisinger, E. & Sigel, R. K. O. *Metallo-Drugs: Development and Action of Anticancer Agents*. (De Gruyter, 2018).

30. Murray, B. S. & Dyson, P. J. Recent progress in the development of organometallics for the treatment of cancer. *Curr. Opin. Chem. Biol.* **56**, 28–34 (2020).

31. Fu, Y. *et al.* Mirror-Image Organometallic Osmium Arene Iminopyridine Halido Complexes Exhibit Similar Potent Anticancer Activity. *Chem. – A Eur. J.* **19**, 15199–15209 (2013).

32. Fu, Y. *et al.* The contrasting chemical reactivity of potent isoelectronic iminopyridine and azopyridine osmium(ii) arene anticancer complexes. *Chem. Sci.* **3**, 2485–2494 (2012).

33. Fu, Y. Organometallic Osmium Arene Anticancer Complexes. (University of Warwick, 2011).

34. Romero-Canelón, I. DESIGN AND MECHANISM OF ACTION OF ORGANOMETALLIC ANTICANCER COMPLEXES. (University of Warwick, 2012).

35. BioVision. FractionPREP™ Cell Fractionation Kit | K270 | BioVision, Inc. https://www.biovision.com/products/cell-fractionation-kits/fractionpreptm-cell-fractionation-kit.html (2021).

36. Schindelin, J. *et al.* Fiji: an open-source platform for biological-image analysis. *Nat. Methods* **9**, 676–682 (2012).

37. Hartinger, C. G. & Dyson, P. J. Bioorganometallic chemistry—from teaching paradigms to medicinal applications. *Chem. Soc. Rev.* **38**, 391–401 (2009).

38. Romero-Canelón, I., Mos, M. & Sadler, P. J. Enhancement of Selectivity of an Organometallic Anticancer Agent by Redox Modulation. *J. Med. Chem.* **58**, 7874–7880 (2015).

39. Wang, F. *et al.* Controlling ligand substitution reactions of organometallic complexes: Tuning cancer cell cytotoxicity. *Proc. Natl. Acad. Sci.* **102**, 18269–18274 (2005).

40. Kerrison, S. J. S. & Sadler, P. J. Solvolysis of cis-[Pt(NH3)2Cl2] in dimethyl sulphoxide and reactions of glycine with [PtCl3 (Me2SO)] – as probed by 195 Pt nuclear magnetic resonance shifts and 195Pt– 15N coupling constants. *J. Chem. Soc., Chem. Commun.* **23** 861–863 (1977).

41. Rottenberg, S., Disler, C. & Perego, P. The rediscovery of platinum-based cancer therapy. *Nat. Rev. Cancer* **21**, 37–50 (2021).

42. Lau, J. K.-C. & Ensing, B. Hydrolysis of cisplatin—a first-principles metadynamics study. *Phys. Chem. Chem. Phys.* **12**, 10348–10355 (2010).

43. Strohfeldt, K. & Tacke, M. Bioorganometallic fulvene-derived titanocene anti-cancer drugs. *Chem. Soc. Rev.* **37**, 1174–1187 (2008).

44. Claffey, J., Hogan, M., Müller-Bunz, H., Pampillón, C. & Tacke, M. Oxali-Titanocene Y: A Potent Anticancer Drug. *ChemMedChem* **3**, 729–731 (2008).

45. Papadopoulou, M. V *et al.* Novel 3-Nitro-1H-1,2,4-triazole-Based Amides and Sulfonamides as Potential Antitrypanosomal Agents. *J. Med. Chem.* **55**, 5554–5565 (2012).

46. Wu, Y., Smith, A. E. & Reineke, T. M. Lipophilic Polycation Vehicles Display High Plasmid DNA Delivery to Multiple Cell Types. *Bioconjug. Chem.* **28**, 2035–2040 (2017).

47. Harrold, M. W. & Zavod, R. M. Chapter 2: Functional Group Characteristics and Roles. in *Basic Concepts in Medicinal Chemistry* (eds. Harrold, M. W. & Zavod, R. M.) 21–66 (American Society of Health-System Pharmacists, 2018).

48. Łakomska, I. *et al.* Use of 1,2,4-triazolo[1,5-a]pyrimidines to design new "piano-stool" ruthenium(II) compounds. *Polyhedron* **109**, 33–39 (2016).

49. Fandzloch, M. *et al.* New organometallic ruthenium(ii) complexes with purine analogs – a wide perspective on their biological application. *Dalt. Trans.* **50**, 5557–5573 (2021).

50. Fu, Y. *et al.* Structure–activity relationships for organometallic osmium arene phenylazopyridine complexes with potent anticancer activity. *Dalt. Trans.* **40**, 10553–10562 (2011).

51. Pastuszko, A., Majchrzak, K., Czyz, M., Kupcewicz, B. & Budzisz, E. The synthesis, lipophilicity and cytotoxic effects of new ruthenium(II) arene complexes with chromone derivatives. *J. Inorg. Biochem.* **159**, 133–141 (2016).

52. Fischer, M. Census and evaluation of p53 target genes. *Oncogene* **36**, 3943–3956 (2017).

53. Biancur, D. E. & Kimmelman, A. C. The plasticity of pancreatic cancer metabolism in tumor progression and therapeutic resistance. *Biochim. Biophys. Acta - Rev. Cancer* **1870**, 67–75 (2018).

54. Birhanu, G., Javar, H. A., Seyedjafari, E. & Zandi-Karimi, A. Nanotechnology for delivery of gemcitabine to treat pancreatic cancer. *Biomed. Pharmacother.* **88**, 635–643 (2017).

55. Omarini, C. *et al.* Neoadjuvant treatments in triple-negative breast cancer patients: where we are now and where we are going. *Cancer Manag. Res.* **10**, 91–103 (2018).
56. Jitariu, A.-A., Cîmpean, A. M., Ribatti, D. & Raica, M. Triple negative breast cancer: the kiss of death. *Oncotarget* **8**, 46652–46662 (2017).
57. Romero-Canelón, I., Salassa, L. & Sadler, P. J. The Contrasting Activity of Iodido versus Chlorido Ruthenium and Osmium Arene Azo- and Imino-pyridine Anticancer Complexes: Control of Cell Selectivity, Cross-Resistance, p53 Dependence, and Apoptosis Pathway. *J. Med. Chem.* **56**, 1291–1300 (2013).
58. Bolitho, E. M. *et al.* Elemental mapping of half-sandwich azopyridine osmium arene complexes in cancer cells. *Inorg. Chem. Front.* **8**, 3675–3685 (2021).
59. Coverdale, J. P. C. C. *et al.* In Vivo Selectivity and Localization of Reactive Oxygen Species (ROS) Induction by Osmium Anticancer Complexes That Circumvent Platinum Resistance. *J. Med. Chem.* **61**, 9246–9255 (2018).
60. Alderden, R. A., Hall, M. D. & Hambley, T. W. The Discovery and Development of Cisplatin. *J. Chem. Educ.* **83**, 728–734 (2006).
61. Mendoza-Ferri, M. G. *et al.* Influence of the Arene Ligand, the Number and Type of Metal Centers, and the Leaving Group on the in Vitro Antitumor Activity of Polynuclear Organometallic Compounds. *Organometallics* **28**, 6260–6265 (2009).
62. Nikolić, S. *et al.* Strong in Vitro Cytotoxic Potential of New Ruthenium–Cymene Complexes. *Organometallics* **34**, 3464–3473 (2015).
63. Bergamo, A. *et al.* In Vitro Cell Cycle Arrest, In Vivo Action on Solid Metastasizing Tumors, and Host Toxicity of the Antimetastatic Drug NAMI-A and Cisplatin. *J. Pharmacol. Exp. Ther.* **289**, 559–564 (1999).
64. Clarke, M. J. Ruthenium metallopharmaceuticals. *Coord. Chem. Rev.* **232**, 69–93 (2002).
65. de Lima, A. P. *et al.* The compound cis-(dichloro)tetrammineruthenium(III) chloride induces caspase-mediated apoptosis in K562 cells. *Toxicol. Vitr.* **24**, 1562–1568 (2010).
66. Nikolić, S. *et al.* Synthesis, characterization and biological evaluation of novel Ru(II)–arene complexes containing intercalating ligands. *J. Inorg. Biochem.* **160**, 156–165 (2016).
67. Chen, F. *et al.* Transfer Hydrogenation and Antiproliferative Activity of Tethered Half-Sandwich Organoruthenium Catalysts. *Organometallics* **37**, 1555–1566 (2018).
68. Abolhasani, M. H., Safavi, M., Goodarzi, M. T., Kassaee, S. M. & Azin, M. Identification and anti-cancer activity in 2D and 3D cell culture evaluation of an Iranian isolated marine microalgae Picochlorum sp. RCC486. *Daru* **26**, 105–116 (2018).
69. Perche, F. & Torchilin, V. P. Cancer cell spheroids as a model to evaluate chemotherapy protocols. *Cancer Biol. Ther.* **13**, 1205–1213 (2012).
70. Shield, K., Ackland, M. L., Ahmed, N. & Rice, G. E. Multicellular spheroids in ovarian cancer metastases: Biology and pathology. *Gynecol. Oncol.* **113**, 143–148 (2009).
71. Shishido, A. *et al.* Mesothelial cells facilitate cancer stem-like properties in spheroids of ovarian cancer cells. *Oncol. Rep.* **40**, 2105–2114 (2018).
72. Raghavan, S. *et al.* Formation of stable small cell number three-dimensional ovarian cancer spheroids using hanging drop arrays for preclinical drug sensitivity assays. *Gynecol. Oncol.* **138**, 181–189 (2015).
73. Giovannini, C. *et al.* Mitochondria hyperpolarization is an early event in oxidized low-density lipoprotein-induced apoptosis in Caco-2 intestinal cells. *FEBS Lett.* **523**, 200–206 (2002).
74. Mijatović, S. *et al.* Study of the anticancer properties of methyl- and phenyl-substituted carbon- and silicon-bridged ansa-titanocene complexes. *J. Organomet. Chem.* **751**, 361–367 (2014).
75. Hockenbery, D. M. Targeting mitochondria for cancer therapy. *Environ. Mol. Mutagen.* **51**, 476–489 (2010).
76. Bagkos, G., Koufopoulos, K. & Piperi, C. A new model for mitochondrial membrane potential production and storage. *Med. Hypotheses* **83**, 175–181 (2014).
77. Choroba, K. *et al.* Platinum(<scp>ii</scp>) complexes showing high cytotoxicity toward A2780 ovarian carcinoma cells. *Dalt. Trans.* **48**, 13081–13093 (2019).
78. Soldevila-Barreda, J. J., Romero-Canelón, I., Habtemariam, A. & Sadler, P. J. Transfer hydrogenation catalysis in cells as a new approach to anticancer drug design. *Nat. Commun.* **6**, 1–9 (2015).
79. Zhang, J. *et al.* Organometallic gold(I) and gold(III) complexes for lung cancer treatment. *Front. Pharmacol.* **13**, 1–19 (2022).
80. Dougan, S. J., Habtemariam, A., McHale, S. E., Parsons, S. & Sadler, P. J. Catalytic organometallic anticancer complexes. *Proc. Natl. Acad. Sci.* **105**, 11628–11633 (2008).

81.   Lin, Y. *et al.* Organometallic ruthenium anticancer complexes inhibit human peroxiredoxin I activity by binding to and inducing oxidation of its catalytic cysteine residue†. *Metallomics* **11**, 546–555 (2019).

82.   Kowol, C. R. *et al.* Mechanisms underlying reductant-induced reactive oxygen species formation by anticancer copper(II) compounds. *JBIC J. Biol. Inorg. Chem.* **17**, 409–423 (2012).

83.   Fischer, E. G. Nuclear Morphology and the Biology of Cancer Cells. *Acta Cytol.* **64**, 511–519 (2020).

84.   dos Santos, Á. & Toseland, C. P. Regulation of Nuclear Mechanics and the Impact on DNA Damage. *Int. J. Mol. Sci.* **22**, 1–18 (2021).

85.   Heckenbach, I. *et al.* Nuclear morphology is a deep learning biomarker of cellular senescence. *Nat. Aging* **2**, 742–755 (2022).

86.   Singh, I. & Lele, T. P. Nuclear Morphological Abnormalities in Cancer: A Search for Unifying Mechanisms. *Results Probl. Cell Differ.* **70**, 443–467 (2022).

87.   dos Santos, Á. *et al.* DNA damage alters nuclear mechanics through chromatin reorganization. *Nucleic Acids Res.* **49**, 340–353 (2021).

88.   Guo, Y. *et al.* Enhancing Cytotoxicity of a Monofunctional Platinum Complex via a Dual-DNA-Damage Approach. *Inorg. Chem.* **58**, 13150–13160 (2019).

89.   Forrest, R. A. *et al.* Activation of DNA damage response pathways as a consequence of anthracycline-DNA adduct formation. *Biochem. Pharmacol.* **83**, 1602–1612 (2012).

90.   Wang, L. & Eastmond, D. A. Catalytic inhibitors of topoisomerase II are DNA-damaging agents: induction of chromosomal damage by merbarone and ICRF-187. *Environ. Mol. Mutagen.* **39**, 348–356 (2002).

91.   Pfeffer, C. & Singh, A. Apoptosis: A Target for Anticancer Therapy. *Int. J. Mol. Sci.* **19**, 1–10 (2018).

92.   Galluzzi, L. *et al.* Molecular mechanisms of cell death: recommendations of the Nomenclature Committee on Cell Death 2018. *Cell Death Differ.* **25**, 486–541 (2018).

93.   Surova, O. & Zhivotovsky, B. Various modes of cell death induced by DNA damage. *Oncogene* **32**, 3789–3797 (2013).

94.   Chen, H., Landen, C. N., Li, Y., Alvarez, R. D. & Tollefsbol, T. O. Enhancement of Cisplatin-Mediated Apoptosis in Ovarian Cancer Cells through Potentiating G2/M Arrest and p21 Upregulation by Combinatorial Epigallocatechin Gallate and Sulforaphane. *J. Oncol.* **2013**, 1–9 (2013).

95.   Ghosh, S. Cisplatin: The first metal based anticancer drug. *Bioorg. Chem.* **88**, 1–20 (2019).

96.   Matthews, H. K., Bertoli, C. & de Bruin, R. A. M. Cell cycle control in cancer. *Nat. Rev. Mol. Cell Biol.* **23**, 74–88 (2022).

97.   Pietenpol, J. A. & Stewart, Z. A. Cell cycle checkpoint signaling: *Toxicology* **181**–**182**, 475–481 (2002).

98.   Zhu, H. Propidium Iodide Staining of Cells for FACS Analysis. *Bio-protocol* **2**, 1–2 (2012).

99.   Crowley, L. C., Chojnowski, G. & Waterhouse, N. J. Measuring the DNA content of cells in apoptosis and at different cell-cycle stages by propidium iodide staining and flow cytometry. *Cold Spring Harb. Protoc.* **2016**, 905–910 (2016).

100.   Hamidi, H. & Ivaska, J. Every step of the way: integrins in cancer progression and metastasis. *Nat. Rev. Cancer* **18**, 533–548 (2018).

101.   Fares, J., Fares, M. Y., Khachfe, H. H., Salhab, H. A. & Fares, Y. Molecular principles of metastasis: a hallmark of cancer revisited. *Signal Transduct. Target. Ther.* **5**, 1–17 (2020).

102.   Basu, M. *et al.* Invasion of ovarian cancer cells is induced byPITX2-mediated activation of TGF-β and Activin-A. *Mol. Cancer* **14**, 1–15 (2015).

103.   Conlon, G. A. & Murray, G. I. Recent advances in understanding the roles of matrix metalloproteinases in tumour invasion and metastasis. *J. Pathol.* **247**, 629–640 (2019).

104.   Alipour, E., Halverson, D., McWhirter, S. & Walker, G. C. Phospholipid Bilayers: Stability and Encapsulation of Nanoparticles. *Annu. Rev. Phys. Chem.* **68**, 261–283 (2017).

105.   Clède, S. *et al.* Influence of the Side-Chain Length on the Cellular Uptake and the Cytotoxicity of Rhenium Triscarbonyl Derivatives: A Bimodal Infrared and Luminescence Quantitative Study. *Chem. – A Eur. J.* **20**, 8714–8722 (2014).

106.   van Rijt, S. H., Romero-Canelón, I., Fu, Y., Shnyder, S. D. & Sadler, P. J. Potent organometallic osmium compounds induce mitochondria-mediated apoptosis and S-phase cell cycle arrest in A549 non-small cell lung cancer cells. *Metallomics* **6**, 1014–1022 (2014).

107.   Romero-Canelón, I., Pizarro, A. M., Habtemariam, A. & Sadler, P. J. Contrasting cellular uptake pathways for chlorido and iodido iminopyridine ruthenium arene anticancer complexes. *Metallomics* **4**, 1271–1279 (2012).

108.   Arnesano, F. & Natile, G. Mechanistic insight into the cellular uptake and processing of cisplatin 30 years

after its approval by FDA. *Coord. Chem. Rev.* **253**, 2070–2081 (2009).

109. Ballesta, A. *et al.* Kinetic analysis of the accumulation of a half-sandwich organo-osmium pro-drug in cancer cells. *Metallomics* **11**, 1648–1656 (2019).

110. Scolaro, C. *et al.* Tuning the hydrophobicity of ruthenium(ii)–arene (RAPTA) drugs to modify uptake, biomolecular interactions and efficacy. *Dalt. Trans.* **43**, 5065–5072 (2007).

111. Yu, F., Megyesi, J. & Price, P. M. Cytoplasmic initiation of cisplatin cytotoxicity. *Am. J. Physiol. Physiol.* **295**, 44–52 (2008).

112. Manohar, S. & Leung, N. Cisplatin nephrotoxicity: a review of the literature. *J. Nephrol.* **31**, 15–25 (2018).

113. Mandic, A., Hansson, J., Linder, S. & Shoshan, M. C. Cisplatin Induces Endoplasmic Reticulum Stress and Nucleus-independent Apoptotic Signaling *. *J. Biol. Chem.* **278**, 9100–9106 (2003).

114. Sancho-Martínez, S. M., Prieto-García, L., Prieto, M., López-Novoa, J. M. & López-Hernández, F. J. Subcellular targets of cisplatin cytotoxicity: An integrated view. *Pharmacol. Ther.* **136**, 35–55 (2012).

115. Arnesano, F., Losacco, M. & Natile, G. An Updated View of Cisplatin Transport. *Eur. J. Inorg. Chem.* **2013**, 2701–2711 (2013).

116. Fekri, R., Salehi, M., Asadi, A. & Kubicki, M. Spectroscopic studies, structural characterization and electrochemical studies of two cobalt (III) complexes with tridentate hydrazone Schiff base ligands: Evaluation of antibacterial activities, DNA-binding, BSA interaction and molecular docking. *Appl. Organomet. Chem.* **32**, 1–17 (2018).

117. Mukhopadhyay, S. *et al.* Synthesis, Structure, DNA/Protein Binding, and Anticancer Activity of Some Half-Sandwich Cyclometalated Rh(III) and Ir(III) Complexes. *Organometallics* **34**, 4491–4506 (2015).

118. Nisa, Z. un *et al.* Some newly synthesized ferrocene based esters: Characterization, DNA interaction and DFT studies. *J. Organomet. Chem.* **820**, 130–140 (2016).

119. Yildiz, E. A. *et al.* UV-Vis spectroscopic and colorimetric anion detection and fluorescence properties of new 3-amino-4-hydroxybenzenesulfonic acid-based Schiff bases depending on the strength and position of the electron donor substitution. *Phys. Scr.* **98**, 1–17 (2023).

120. Govender, P., Riedel, T., Dyson, P. J. & Smith, G. S. Regulating the anticancer properties of organometallic dendrimers using pyridylferrocene entities: synthesis, cytotoxicity and DNA binding studies. *Dalt. Trans.* **45**, 9529–9539 (2016).

121. Ruiz, J. *et al.* Palladium(II) and Platinum(II) Organometallic Complexes with the Model Nucleobase Anions of Thymine, Uracil, and Cytosine: Antitumor Activity and Interactions with DNA of the Platinum Compounds. *Inorg. Chem.* **45**, 6347–6360 (2006).

122. Barragán, F. *et al.* Photocontrolled DNA Binding of a Receptor-Targeted Organometallic Ruthenium(II) Complex. *J. Am. Chem. Soc.* **133**, 14098–14108 (2011).

123. Streciwilk, W. *et al.* Fluorescent organometallic rhodium(I) and ruthenium(II) metallodrugs with 4-ethylthio-1,8-naphthalimide ligands: Antiproliferative effects, cellular uptake and DNA-interaction. *Eur. J. Med. Chem.* **156**, 148–161 (2018).

124. Tabassum, S., Khan, R. A., Arjmand, F., Juvekar, A. S. & Zingde, S. M. Synthesis of carbohydrate-conjugate heterobimetallic CuII–Sn2IV and ZnII–Sn2IV complexes; their interactions with CT DNA and nucleotides; DNA cleavage, in-vitro cytotoxicity. *Eur. J. Med. Chem.* **45**, 4797–4806 (2010).

125. Tabassum, S. *et al.* Carbohydrate-conjugate heterobimetallic complexes: synthesis, DNA binding studies, artificial nuclease activity and in vitro cytotoxicity. *Carbohydr. Res.* **346**, 2886–2895 (2011).

126. Guo, W. *et al.* Transferrin Serves As a Mediator to Deliver Organometallic Ruthenium(II) Anticancer Complexes into Cells. *Inorg. Chem.* **52**, 5328–5338 (2013).

127. Collins, A. *et al.* Measuring DNA modifications with the comet assay: a compendium of protocols. *Nat. Protoc.* **18**, 929–989 (2023).

128. Hosoya, N. & Miyagawa, K. Targeting <scp>DNA</scp> damage response in cancer therapy. *Cancer Sci.* **105**, 370–388 (2014).

129. Lord, C. J. & Ashworth, A. The DNA damage response and cancer therapy. *Nature* **481**, 287–294 (2012).

130. Caldecott, K. W. Mammalian DNA base excision repair: Dancing in the moonlight. *DNA Repair,* **93**, 1–4 (2020).

131. Chen, A. PARP inhibitors: its role in treatment of cancer. *Chin. J. Cancer* **30**, 463–471 (2011).

132. Hossain, M., Lin, Y. & Yan, S. Single-Strand Break End Resection in Genome Integrity: Mechanism and Regulation by APE2. *Int. J. Mol. Sci.* **19**, 1–13 (2018).

133. Kuo, L. J. & Yang, L.-X. γ-H2AX - A Novel Biomarker for DNA Double-strand Breaks. *In Vivo,* **22**, 305–309 (2008).

134. Bai, D.-P., Zhang, X.-F., Zhang, G.-L., Huang, Y.-F. & Gurunathan, S. Zinc oxide nanoparticles induce apoptosis and autophagy in human ovarian cancer cells. *Int. J. Nanomedicine* **12**, 6521–6535 (2017).

135. Palla, V.-V. *et al.* gamma-H2AX: Can it be established as a classical cancer prognostic factor? *Tumor Biol.* **39**, 1–11 (2017).

136. Helleday, T., Petermann, E., Lundin, C., Hodgson, B. & Sharma, R. A. DNA repair pathways as targets for cancer therapy. *Nat. Rev. Cancer* **8**, 193–204 (2008).

137. Tudrej, P. *et al.* Establishment and Characterization of the Novel High-Grade Serous Ovarian Cancer Cell Line OVPA8. *Int. J. Mol. Sci.* **19**, 1–26 (2018).

138. Cowley, G. S. *et al.* Parallel genome-scale loss of function screens in 216 cancer cell lines for the identification of context-specific genetic dependencies. *Sci. Data* **1**, 1–12 (2014).

139. Audia, J. E. & Campbell, R. M. Histone Modifications and Cancer. *Cold Spring Harb. Perspect. Biol.* **8**, 1–13 (2016).

140. Waldmann, T. & Schneider, R. Targeting histone modifications—epigenetics in cancer. *Curr. Opin. Cell Biol.* **25**, 184–189 (2013).

141. Stratmann, A. & Haendler, B. Histone demethylation and steroid receptor function in cancer. *Mol. Cell. Endocrinol.* **348**, 12–20 (2012).

142. Hanif, M. *et al.* A Multitargeted Approach: Organorhodium Anticancer Agent Based on Vorinostat as a Potent Histone Deacetylase Inhibitor. *Angew. Chemie Int. Ed.* **59**, 14609–14614 (2020).

143. Kilpin, K. J. & Dyson, P. J. Enzyme inhibition by metal complexes: concepts, strategies and applications. *Chem. Sci.* **4**, 1410–1419 (2013).

144. Ye, R., Tan, C., Chen, B., Li, R. & Mao, Z. Zinc-Containing Metalloenzymes: Inhibition by Metal-Based Anticancer Agents. *Front. Chem.* **8**, 1–17 (2020).

145. Che, C.-M. & Siu, F.-M. Metal complexes in medicine with a focus on enzyme inhibition. *Curr. Opin. Chem. Biol.* **14**, 255–261 (2010).

146. Chow, K. H.-M. *et al.* A Gold(III) Porphyrin Complex with Antitumor Properties Targets the Wnt/β-catenin Pathway. *Cancer Res.* **70**, 329–337 (2010).

147. Deweese, J. E., Osheroff, M. A. & Osheroff, N. DNA topology and topoisomerases. *Biochem. Mol. Biol. Educ.* **37**, 2–10 (2009).

148. Tolstorukov, M. Y., Colasanti, A. V, McCandlish, D. M., Olson, W. K. & Zhurkin, V. B. A Novel Roll-and-Slide Mechanism of DNA Folding in Chromatin: Implications for Nucleosome Positioning. *J. Mol. Biol.* **371**, 725–738 (2007).

149. Sun, Y. *et al.* Excision repair of topoisomerase DNA-protein crosslinks (TOP-DPC). *DNA Repair,* **89**, 1–11 (2020).

150. Berghuis, B. A., Köber, M., van Laar, T. & Dekker, N. H. High-throughput, high-force probing of DNA-protein interactions with magnetic tweezers. *Methods* **105**, 90–98 (2016).

151. Gao, D. *et al.* Defect-Induced Double-Stranded DNA Unwinding on Graphene. *J. Phys. Chem. B* **125**, 2833–2840 (2021).

Chapter 5 - Atom Bioisosteres

Mode And Mechanism Of Action And Extracellular Matrix Interaction Differences Induced By Single Atom Bioisosteric Replacement In The Iminopyridine Ligand Of Ruthenium Piano-Stool Complexes

5-1: Introduction

5-1.1: The cell cytoplasmic membrane and beyond

The cell cytoplasmic membrane (CCM) is a highly integrated mechanostructure providing a robust, dynamic and flexible surface for the containment of intracellular structures, and as a communication and exchange platform between cells and the ECM[1]. To enable this, the CCM is in command of many essential functions including cell and tissue structure, transport, and intercellular communication and scaffolding.

The primary model used to demonstrate the CCM is the fluid mosaic model, first described in 1972[1,2]. To undergo its many functions, the CCM is highly complex, hierarchal, amphiphilic, asymmetrical, and an ever-changing structure of mainly lipids and proteins. The amphiphilic nature of the CCM stems from the phospholipid bilayer held together predominantly by hydrophilic interaction and Van de Waals forces, allowing for the positioning of polar and non-polar constituents to be anchored on and within[3]. There are several types of phospholipids in the bilayer, differing in head group, tail length, and tail chain saturation[4]. Depending on cell type, differing concentrations of lipids alters CCM functions by adjusting fluidity for environment and purpose specificity (Table 4-7)[5]. Further, the many assorted types of phospholipids have specialised functions within the CCM. One example, phosphatidylinositol, is key in CCM trafficking, golgi body functions, exocytosis, proliferation, and cell CCM curvature[5]. Another example is cholesterol, while not a lipid, it is a key regulator of lipids and an essential component for CCM rigidity, explaining why concentrations are lower in blood cells due to needing high CCM fluidity for transport[6].

Within the lipid bilayer, many types of protein reside, and are grouped by layer. Integral proteins constitute approximately one quarter of genes and are usually globular with areas of hydrophobicity to allow hydrophobic matching for integration through the CCM for anchorage as are used for ion and

nutrient transport, signalling, protection and adhesion[1,3,7]. One prime example is G-protein coupled receptors in their role in cancer development and treatment[8–10]. Examined in this work are the type I single membrane pass integrins. As heterodimers predominantly composed of α and β subunits, integrins traverse the CCM serve as the intermediate between the ECM and the cytoskeleton[11]. Varying combinations of heterodimers allows the binding of different ECM molecules, further binding can be specific for example α5β1 to fibronectin, or redundant such as αvβ3 to fibronectin, vitronectin, collagen, and others[12]. With alterations to binding through ECM stress, rigidity and downstream signalling through the LINC complex can be initiated, causing alterations in the nuclear pores, allowing YAP/TAZ translocation, chromatin remodelling and transcription alteration through the clutch theory[11]. This can lead to a range of effects including hippo pathway activation, actin polymerisation, increase in proliferation, stemness and mobility signalling and cell migaration[13,14].

Table 4-7: Proportional cell cytoplasmic membrane lipid composition of the cancerous lines HT-29, MDS-MB231 and Jurkat cells highlighting that differing cell types possess different membrane lipid compositions to aid cell function[5].

Lipid (%)	Colon Cancer (HT-29)	Breast Cancer (MDS-MB231)	T-Cell Leukaemia (Jurkat)
Phosphatidic acid	0.5	0.5	0.3
Phosphatidylinositol	4	4	12.5
Phosphatidylglycerol	0.5	0.5	0.3
Phosphatidylserine	4	4	7.5
Phosphatidylethanolamine	2	4	14
Phosphatidylcholine	9.5	12	40
Phosphatidylethanolamine-ether	7.3	10.5	3
Phosphatidylcholine-ether	16.8	1.5	3.4
Sphingomyelin	2.5	8.3	4
Diacylglycerol	25.8	51.7	0.5
Cholesterol	N/D	35	23

Peripheral proteins reside on the surfaces of the CCM through electrostatic bonding to the phospholipid head groups and glycosylated molecules[1]. This results in two dominant features; one, they can be removed from the CCM without damage, and two, are can be used in structural roles enabling curvature, binding, attachment and molecule transport[1,3]. One example is the annexin family which are calcium ion receptors utilised in cell cycle, exocytosis and apoptosis[15,16].

Associated proteins interact with the CCM, but do not directly interact with the lipid bilayer[3]. In parallel with the complexity of the CCM itself, this group is highly variable to associate with the CCM in a variety of ways. This family compasses mainly insoluble, structural the constituents of the ECM and cytoskeleton. The ECM mostly consists of water, structural proteins, enzymes, and growth factors, with significant variations occurring between tissues[17,18]. Structural proteins are used as fibrous scaffolds for cells, one example being collagen, which is the dominant scaffold being ~30% of all ECM[18]. Enzymes include MMP proteins which allow for structural modification of the ECM allowing for growth, angiogenesis, wound healing, and tissue regeneration in normal microenvironment, in addition to invasion, migration and metastasis in cancerous microenvironments[19].

In cancer, in line with mass dysregulation within the cell, the cell CCM and ECM is also highly dysregulated. Membrane lipid composition differs not only between cancerous and normal cells, but further between different cancerous cell types, and with additional fluctuation depending on cell needs at a particular point in disease progression[5]. This can manifest as altered levels of lipids, location and saturation, especially favouring increased lipid tail saturation for increase resistance to ROS damage, improve lipid raft number and capabilities for CCM presentation and has been noted in drug resistance[4,5]. Another example is phosphatidylethanolamine which has been observed to flip from localising from the inner CCM to the outer CCM in cancerous cells, preventing its use in detrimental activities including protein chaperoning for autophagy regulation and protease activity in apoptosis[5]. Yet, these advantages are coupled with the disadvantage of decreased CCM fluidity and prevention of

beneficial lipid functions. Protein contents can also vary depending on the phenotype required and can result from both genomic mutation and epigenetic dysregulation. For example, in EOC, α5β1, α6β4 and αVβ3 integrins have been shown to be upregulated[20]. This increases capability to bind to fibronectin, laminin and vitronectin, improving disease invasion properties, corelating with disease progression[12]. Highly dysregulated ECM and cell bonding in cancerous tissues, allows for disordered histology and improved capabilities for uncontrolled growth and spread[21]. It has been observed that a cancerous ECM is similar to an unresolved wound ECM, in which it becomes stiffer, and pressure increases in line with the increase in collagen and elastin expression[18]. In EOC, substantial increase in collagen-I, collagen-V and hyaluronan, in addition to increases in versican, fibronectin and tenascin-C and -X which have been associated with advanced disease progression and treatment inefficiency[17].

5-1.2: Organometallic complexes and the cytoplasmic membrane

The abnormalities of cancerous CCM can offer potential treatment specificity towards cancerous cells[4,5,22]. If the CCM is compromised sufficiently, cell death can be initiated through several MOD, including the type I death process anoikis. As a relatively new MOD discovered in the last 30 years, there has been great interest into the differences between anoikis and apoptosis mechanisms[23]. This MOD is centred around the loss of integrin binding to the ECM, leading to the activation of intrinsic and extrinsic apoptosis pathway activation through Bid/Bim and FAS/FAS ligand activation and upregulation respectively, culminating in Caspase 3 activation, subsequent target proteolysis and cell death[22,24].

However, there is concern when targeting the CCM that necrosis can occur. While necrosis is common in advanced solid tumours due to oxygen and nutrient deprivation, it can also be caused by chemotherapy and radiotherapy[25]. Necrosis leads to the release of cell content into the ECM including proinflammatory and growth factors, encouraging survival and growth in the surrounding area[25,26]. This

can lead to unfavourable repercussions including inflammation, tissue damage and treatment resistance[26,27].

Currently, there are a very limited number of ruthenium complexes that specifically target the CMM. The principal example is NAMI-A, which interrupts the $\alpha_5\beta_1$ integrin and fibronectin binding, preventing FAK autophosphorylation in addition to MMP2/9 inhibition and cytoskeleton remodelling, likely through integrin binding modification[28–30]. Unfortunately, the NAMI complexes are severely limited by their inactivity in primary tumours[31,32]. The activity of NAMI-A is viewed to be unique with minimal evidence of other organometallic complexes exhibiting similar behaviour. This indicates that there is potential to expand upon CCM targeting treatments against cancer.

5-1.3: Atom bioisosteric replacement

In Chapter 3, complex *6* was shown to have significant effect on SKOV3 cells and induce multiple MOA. Complexes with similar chemical structures have also been documented with dimethylamine phenyl ring substitution which have also been shown to be highly effective[33]. Especially in the case of the osmium piano-stool FY26, which can successfully achieve nanomolar IC_{50} values in many cancer cell lines with significant performance in the Sanger screen of 806 cancerous cell lines[34].

The comparison of carbon and nitrogen atom substitution has been explored in several functional groups of the bidentate ligand. The substitution of AzPy (nitrogen containing) to ImPy (carbon containing) has been shown to have slightly differing effects in osmium complexes when inhibiting the proliferation of A2780 cells, depending on the monodentate halogen, yet there is no substantial differences in the potency[33]. In comparison, the substitution of one co-ordinating atoms in two iridium piano stool complexes shown in Figure 4-34 was shown to have profound effects[35,36]. Despite there being no significant differences in key bond lengths, only differing in overall charge, complex behaviour significantly differed with the 2-phenylpyridine complex exhibiting significant adduct formation with 9-EtG and 9-methyl guanine, and substantial potency in A2780, while the bipyridine complexes did

not[35,36]. While this bioisosteric replacement can have significantly differing effects dependant on the function groups being altered, there has been minimal work in line with other minimal bioisosteric replacements and the evaluation of a single atom replacement of the phenyl ring, often favouring whole functional group substitution. Noting, the efficacy of the base bidentate structure shown in Figure 4-35, the efficacy of other R group atom variants may offer differing behaviour.
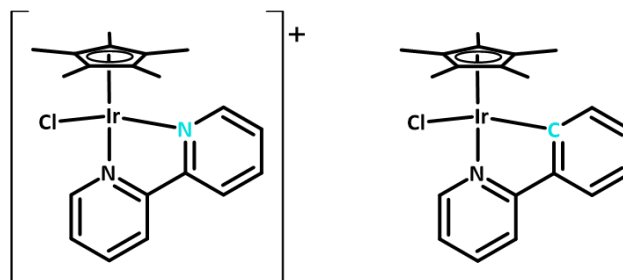
Figure 4-34: Two iridium based piano stool complexes with bioisosteric replacement of the atom involved in the ligand-metal coordination bond[35,36]
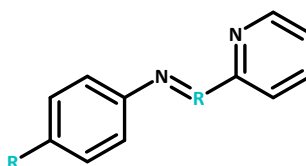
Figure 4-35: Structure of the bidentate ligand shown to have notable potency in multiple cell lines where R = CH or N.

5-1.4: Overview of work in Chapter 5

This chapter evaluates the bioisostere replacement in the phenyl ring of the bidentate ligand from hydrogen to an isopropyl, hydroxyl, methoxy, methylthio or dimethylamine group, assessing in the physiochemical and biological activity of the complexes. This was achieved by the synthesis and characterisation of the series, followed by antiproliferative activity screening in a variety of cell lines to determine structure activity relationships. The best candidates, complexes *6* and *22*, were then taken forward for comparison to understand differences in MOA in the EOC cell line A2780. Noting the significant effect on the adherence of cells treated with *6*, effects on the CCM were investigated further.

5-2: Experimental section

5-2.1: Iminopyridine ligand and complex synthesis

ImPy ligands used in this chapter are shown in Figure 4-36. Ligands were synthesised using the synthetic scheme shown in Scheme 2-1 except for ImPy-4-OH which was synthesised in previous work[37]. Ligands **L1**, **L6**, and **L11** were used in previous chapters. Full synthetic information is given in Appendix II.
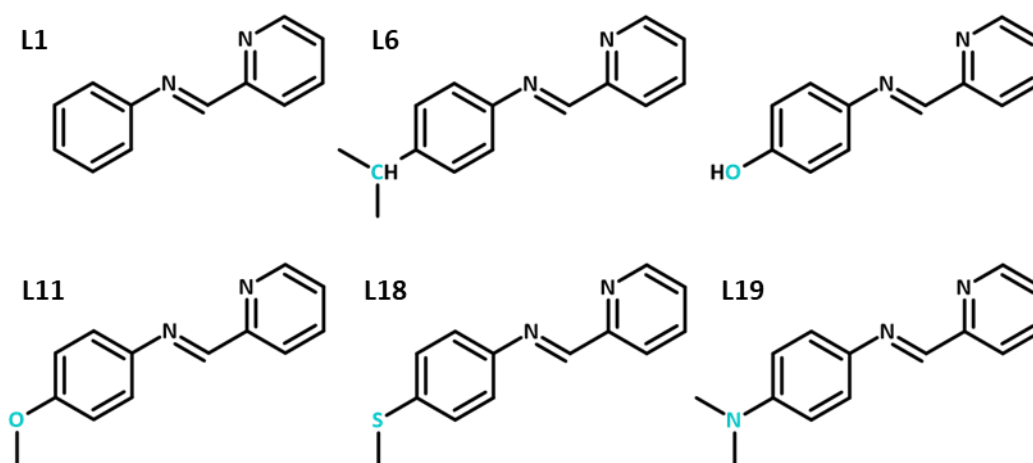
Figure 4-36: Structures of the six ligands used in Chapter 5. Atom bioisosteres are highlighted in blue.

Complexes were then synthesised using the synthetic scheme shown in Scheme 2-2. Synthetic information for complexes **1**, **6**, **11** and **14** are detailed in previous chapters.

5-2.1.1: *Complex 21 -* Ru(L18)Cl(PF$_6$), Ru(η^6-*p*-Cym)(ImPy-4-SMe)CI]PF$_6$

According to reaction Scheme 2-2 dichloro(p-cymene)ruthenium(II) dimer (108.6 mg, 0.18 mmol) was reacted with **L18** (81.0 mg, 0.35 mmol). Following which, ammonium hexafluorophosphate (144.5 mg, 0.89 mmol) was added producing a final solid weighing 182.6mg (83.55%). ^{1}H NMR (400 MHz; DMSO-d$_6$) δ 0.98 (d, J=6.8 Hz, 6H), 2.17 (s, 3H), 2.49 (m, 1H), 2.59 (s, 3H), 5.59 (d, J=6.2 Hz, 1H), 5.67 (d, 6.1 Hz, 1H), 5.77 (d, J=6.2 Hz, 1H), 6.11 (d, J=6.2 Hz, 1H), 7.49 (d, J=8.6 Hz, 2H), 7.77 (d, J=8.6 Hz, 2H), 7.78 (qd, J=5.7, 1.6 Hz, 1H), 8.25 (d, J=7.8 Hz, 1H), 8.31 (t, J=7.7 Hz, 1H), 8.89 (s, 1H), 9.56 (d, J=5.5 Hz, 1H).

^{13}C NMR (400 MHz; DMSO-d_6) δ 14.40, 18.33, 21.56, 21.76, 30.49, 84.68, 84.92, 86.22, 86.67, 103.84, 104.89, 123.13, 125.97, 128.75, 129.88, 139.91, 140.90, 148.43, 154.59, 155.96, 166.82. m/z (ESI-MS) found a highest intensity peak for the fragment of 499.06, with a calculated of 499.06 (M+ [$C_{23}H_{26}N_2SClRu$]$^+$).

5-2.1.2: *Complex 22* - Ru(L19)Cl(PF$_6$), [Ru(η^6-*p*-cym)(Imi-4-N(CH$_3$)$_2$)Cl] PF$_6$

According to reaction Scheme 2-2, dichloro(p-cymene)ruthenium(II) dimer (107.1 mg, 0.17 mmol) was reacted with **L19** (78.8 mg, 0.35 mmol). Following which, ammonium hexafluorophosphate (142.5 mg, 0.87 mmol) was added producing a final solid weighing 199.2mg (88.85%). ^{1}H NMR (400 MHz; DMSO-d_6) δ 0.98 (dd, J=6.9, 2.1 Hz, 6H), 2.18 (s, 3H), 2.45 (m, 1H), 3.06 (s, 6H), 5.61 (t, J=7.1 Hz, 2H), 5.76 (d, J=6.1 Hz, 1H), 6.09 (d, J=6.1 Hz, 1H), 6.9 (dt, J=9.0, 2.1 Hz, 2H), 7.69 (dt, J=9.1, 2.0 Hz, 2H), 7.79 (qd, J=5.6, 1.5 Hz, 1H), 8.17 (d, J=7.94 Hz, 1H), 8.25 (td, J=7.8, 1.3 Hz, 1H), 8.76 (s, 1H), 9.49 (d, J=5.4 Hz, 1H). ^{13}C NMR (400 MHz; DMSO-d_6) δ 18.31, 21.54, 21.74, 30.47, 39.87, 84.44, 85.00, 86.43, 86.72, 103.72, 104.27, 111.47, 124.12, 127.84, 128.67, 139.70, 140.45, 151.17, 155.09, 155.72, 162.07. m/z (ESI-MS) found a highest intensity peak for the fragment of 496.11, with a calculated of 496.02 (M+ [$C_{24}H_{29}N_3ClRu$]$^+$).

5-2.2: Cell studies in A2780

For all following experiments, A2780 cells were treated with full media as a negative control. All treatments were used equipotently at IC$_{50}$ concentrations with CDDP and PTX, as positive and as EOC gold standard of treatments, in addition to complexes *6* and *22*. Additional concentrations of *6* and *22* at 0.5X and 2X IC$_{50}$ were used for selected experiments. Cells were exposed to treatment for 24 hours unless stated otherwise.

5-2.2.1: Cell detachment studies

A2780 cells were seeded at 1.2×10^5 cells per well in 12 well plates and incubated for 24 hours. Cells were then treated equipotently in triplicate. Following exposure, supernatant was collected, wells were washed with 1000 μL of PBS three times and washes added to the supernatant population. This was termed the suspended population. Attached cells were then harvested by trypsinisation, termed the adherent population. Triplicates for suspended and attached populations were counted using a haemocytometer.

5-2.2.2: JC1 staining for mitochondrial polarisation by flow cytometry

A2780 cells were seeded at 1×10^6 cells per well in 6 well plates and incubated for 24 hours. Cells were then treated equipotently in triplicate for 24 hours. Positive populations were exposed to 5 μM Carbonyl Cyanide Chlorophenylhydrazone (CCCP) for 15 minutes were used as a positive control. Keeping the supernatant population, cells were washed with PBS and harvested by trypsinisation. SCS were then stained using the JC-1 Mitochondrial Membrane Potential Detection Kit (Biotium) per manufacturer's instructions. Samples were then ran by flow cytometry.

5-2.2.3: Temperature and time dependant metal accumulation by inductively coupled plasma mass spectrometry

A2780 cells were seeded at 4×10^6 per p100 dish and incubated for 24 hours. Following which cells were treated per the scheme shown in Figure 4-37 in triplicate. Following treatment, samples were collected, digested, and analysed per the protocol detailed in Chapter 2.
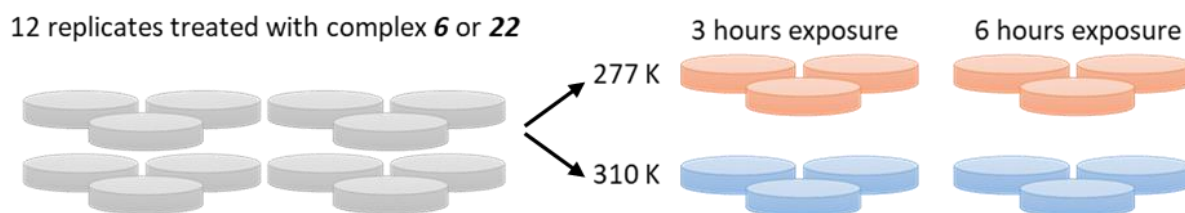
Figure 4-37: Diagram of the treatment conditions used for the temperature and time dependant metal accumulation studies. Briefly, twelve p100 dishes were treated at IC$_{50}$ concentration of **6** or **22**, these were then divided between four treatment conditions: 3 hours at 277 K, 6 hours at 277 K, 3 hours at 310 K and 6 hours at 310 K, allowing for triplicates for each test condition.

5-2.2.4: A2780 cell lysate collection

A2780 cells were seeded at $4X10^6$ cells per p100 dish and incubated for 24 hours. Following incubation, cells were then treated equipotently with the addition of **6** and **22** at 0.5 and 2X IC$_{50}$, and 0.1 µM STS in triplicate. Following exposure, cells were collected by trypsinisation, washed with PBS, and digested by incubation in 250 µL X2 Cell lysis buffer (Item J, Sigma) and 250 µL PBS on ice for 30 minutes. Following digestion, the solution was centrifuged at 12,000 RPM at 4°C for 30 minutes with the supernatant collected for further analysis. Cell lysates were then used to determine protein content by Bradford assay and Caspase 3/7 activity assay, detailed in Chapter 2.

5-2.2.5: Extracellular matrix binding assay

A2780 cells were seeded at $1.2X10^7$ cells per p150 dish and incubated for 24 hours. Following incubated cells were treated equipotently with CDDP, **6** or **22**. Following exposure, supernatant was collected, cells were washed with PBS and harvested using 15 mL 0.48 mM Versene solution. Collected cells were centrifuged at 1000 RPM for 5 minutes, supernatant was removed, cells were resuspended in 10 mL PBS then passed through a 70 µm cell strainer to ensure a SCS. SCS was then counted for each treatment from which $4.8X10^6$ cells were taken and centrifuged. After supernatant was removed, cells were resuspended in 3.2 mL of assay buffer from ECM Cell Adhesion Array Kit assay (SigmaAldrich) buffer to generate a SCD of $1.5X10^5$ cells per 100 µL. The binding assay was then conducted using the

ECM Cell Adhesion Array Kit (SigmaAldrich) shown in Figure 4-38. Absorbance was taken at 555 nm

exported to Microsoft Excel for processing.
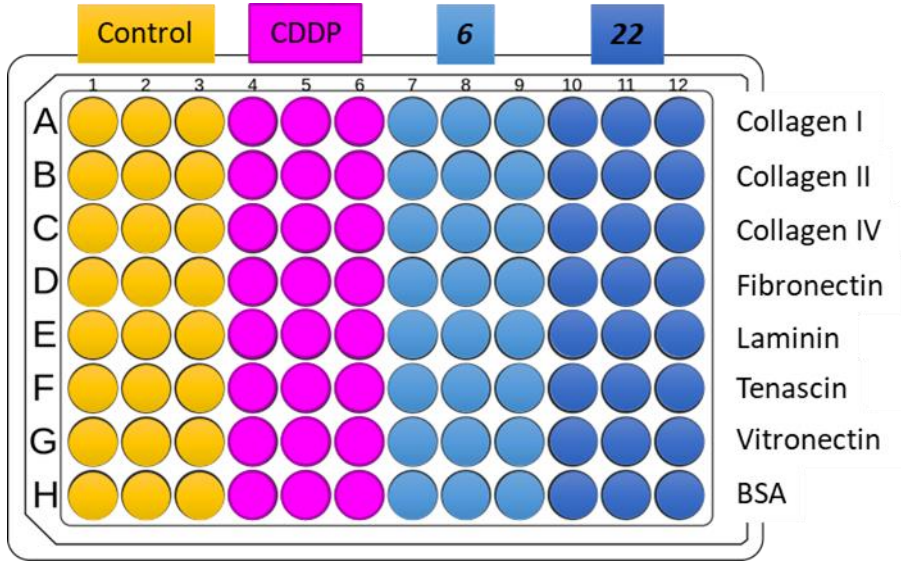
Figure 4-38: Plate layout for the extracellular matrix binding assay to allow for triplicates for each treatment for the eight extracellular proteins in the plate.

5-2.2.6: Transwell invasion assay

Protocol was based on the migration assay conducted by Bergamo and colegues[38]. A2780 cells were

seeded at $1X10^6$ cells per well in 6 well plates and incubated for 24 hours. Following incubation, cells

were treated equipotently in RPMI-1640 only supplemented with and 0.1% (w/v) BSA. Following

exposure, supernatant was collected, cells were collected with 1 mL 0.48 mM Versene solution. The

SCS were then centrifuged at 1000 RPM for 5 minutes, supernatant removed, washed with 2 mL PBS,

passed through a 70 µm cell strainer and centrifuged again. PBS wash was removed, cells were

resuspended in RPMI-1640 only supplemented with and 0.1% (w/v) BSA, counted and diluted to a SCD

of $5X10^4$ cells per 200 µL. SCD were then added to the top of a Greiner 24 well plate format 8 µm

ThinCert cell culture insert, with full media in the bottom of the well (Figure 4-39). Cells were incubated

for 2 or 24 hours to allow chemotaxis. Following chemotaxis, inserts were stained with 0.1% (v/v)

Biotracker 490 green membrane dye and 0.5% (v/v) DAPI in 80% (v/v) methanol in PBS for 1 hour using

200 μL in well insert and 1000 μL in the well. Following staining, cells were washed with PBS. The membranes were then removed and mounted on microscope slides using fluoromount and the bottom on the insert was imaged.
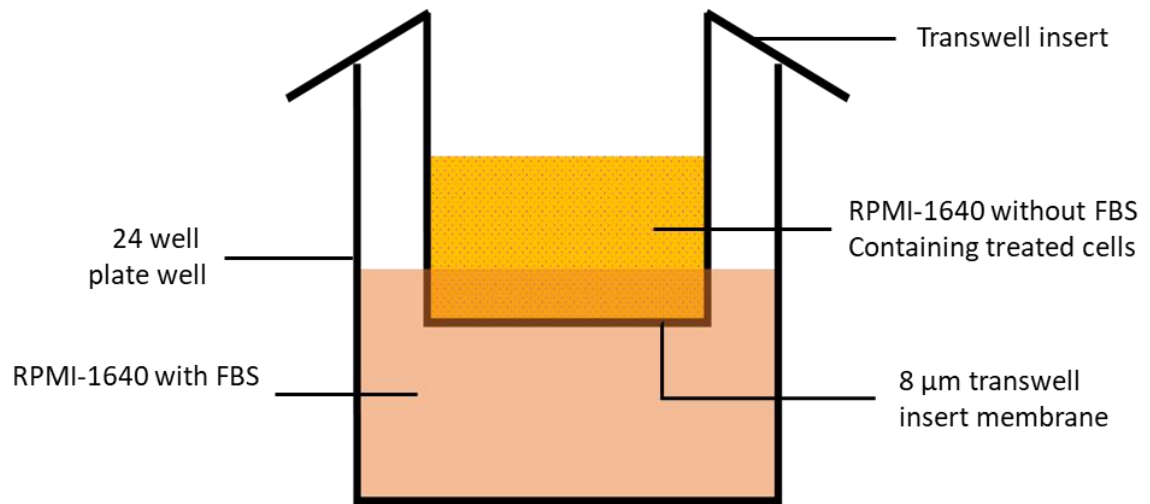
Figure 4-39: Diagram of the well format of the chemotactic Transwell assay.

5-3: Results
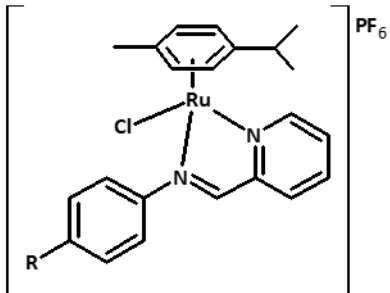
5-3.1: Physiochemical characterisation

5-3.1.1: Synthesis and characterisation

Following ImPy ligand synthesis, imine bond formation was confirmed, and ligand structure was elucidated using ^{1}H, ^{13}C and HSQC NMR experiments, specifically observing for the singlet imine proton shift at ~8.8 ppm.

The ligands were then used to synthesise the six complexes shown in Table 4-8. Following synthesis, complex structure was elucidated using ^{1}H, ^{13}C, COSY, HSQC and HMBC NMR, complimented with ESI-MS spectrometry, HPLC and elemental analysis. The experimental data was consistent with the proposed structures and purity was confirmed.

Table 4-8: Details of the six complexes and their structures compared in Chapter 5.

Complex	R
1 - Ru(L1)Cl(PF$_6$), [Ru(η^6-*p*-Cym)(ImPy)Cl]PF$_6$	H
6 - Ru(L6)Cl(PF$_6$), [Ru(η^6-*p*-Cym)(ImPy-4-*i*Pr)Cl]PF$_6$	CH(CH$_3$)$_2$
11 - [Ru(η^6-*p*-Cym)(ImPy-4-OH)Cl]PF$_6$	OH
14 - Ru(L11)Cl(PF$_6$), [Ru(η^6-*p*-Cym)(ImPy-4-OMe)Cl]PF$_6$	OCH$_3$
21 - Ru(L18)Cl(PF$_6$), [Ru(η^6-*p*-Cym)(ImPy-4-SMe)Cl]PF$_6$	SCH$_3$
22 - Ru(L19)Cl(PF$_6$), [Ru(η^6-*p*-Cym)(ImPy-4-NMe$_2$)Cl]PF$_6$	N(CH$_3$)$_2$

5-3.1.2: Interaction of ruthenium complexes with biologically relevant matrixes

Following synthesis, interaction of the complexes with biologically relevant matrixes was determined by UV-Vis spectroscopy (Table 4-9). Results indicate that all the complexes in this series interact with GSH, media, full media, and ctDNA. Additionally, all the complexes here except the oxygen-containing R group complexes exhibit an isosbestic point with water. Importantly, no isosbestic point was observed in 1:1 water and PBS, or PBS, only the sulphur containing complex **21** formed an isosbestic point with DMSO, and no precipitation occurred in any matrix.

Table 4-9: Summary of UV-Vis spectra changes of the complexes investigated in Chapter 5 with biologically relevant matrixes following 24 hours incubation. Abbreviations: dimethyl sulfoxide (DMSO), phosphate buffered saline (PBS), bovine serum albumin (BSA), glutathione (GSH), calf thymus DNA (ctDNA), non-essential amino acids (NEAA), no change (NC), isosbestic point (IP), hypochromism ($\downarrow$) and hyperchromism ($\uparrow$).

Complex	DMSO	H_2O	1:1 H_2O:PBS	PBS	BSA	GSH	Media	Full Media	ctDNA	Human plasma	NEAA
1	NC	IP	$\downarrow$	$\downarrow$	$\downarrow$	IP	IP	IP	IP	$\downarrow$	$\downarrow$
6	$\uparrow$	IP	NC	NC	NC	IP	IP	IP	IP	NC	NC
11	NC	NC	NC	NC	NC	IP	IP	IP	IP	NC	NC
14	NC	NC	NC	NC	NC	IP	IP	IP	IP	NC	NC
21	IP	IP	NC	NC	NC	IP	IP	IP	IP	NC	NC
22	$\uparrow$	IP	NC	NC	NC	IP	IP	IP	IP	NC	NC

5-3.1.3: Lipophilicity of the ruthenium complexes at physiologically relevant pH

Lipophilicity, being an important quality in the behaviour of a pharmacological agent, was determined by the shake flask method (Table 4-10). All the complexes in this series exhibit a negative $LogD_{7.4}$ value. The unsubstituted complex **1** was the most hydrophilic while the most lipophilic complex was complex **6**, followed by **22** and **21**. A loose trend can be seen between element substitution and lipophilicity with moving across the groups and down the periods of the periodic table increasing lipophilicity, however this trend can also be attributed to the addition of second methyl substituent.

Table 4-10: LogD$_{7.4}$ of the six complexes evaluated in this chapter determined by the shake flask method using PBS and n-octanol.

Complex	LogD$_{7.4}$
1	-0.66
6	-0.21
11	-0.53
14	-0.50
21	-0.32
22	-0.30

5-3.1.4: Density Functional Theory of the ruthenium complexes

With no differences being apparent in other physiochemical characterisations, DFT was used to calculate using the lowest energy structures (Figure 4-40). From these structures, bond length was calculated (Table 4-11). Calculations predict that the substitution of the phenyl ring ligand substituent does not change the bond lengths surrounding the ruthenium centre.

In addition, electron density and Mullikan partial charges were calculated (Figure 4-41 and Table 4-12. The atom change here was predicted to not induce any significant changes in the electron density or the partial charges of the complexes. The partial charges are predicted to only be altered in the phenyl ring which is to be expected.
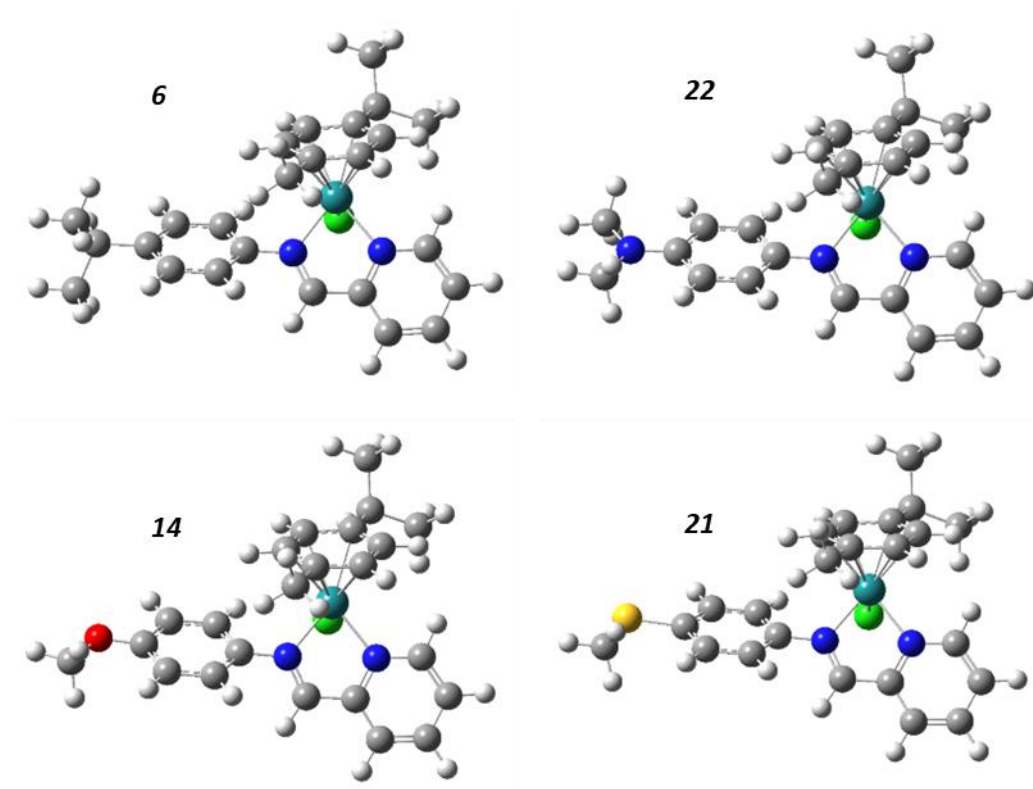
Figure 4-40: Calculated DFT structures of complexes *6, 22, 14*, and *21* in their lowest energy structures. Renders produced by Dr J.P.C. Coverdale.

Table 4-11: Calculated DFT bond lengths (Å) determined from the lowest energy structures. Calculations performed by Dr J.P.C. Coverdale.

Complex	Ru-Cl (Å)	Ru-Ph (Å)	Ru-Py (Å)
6	2.39089	2.06603	2.08433
14	2.39065	2.07352	2.08111
21	2.38976	2.06740	2.08377
22	2.39008	2.06885	2.08375
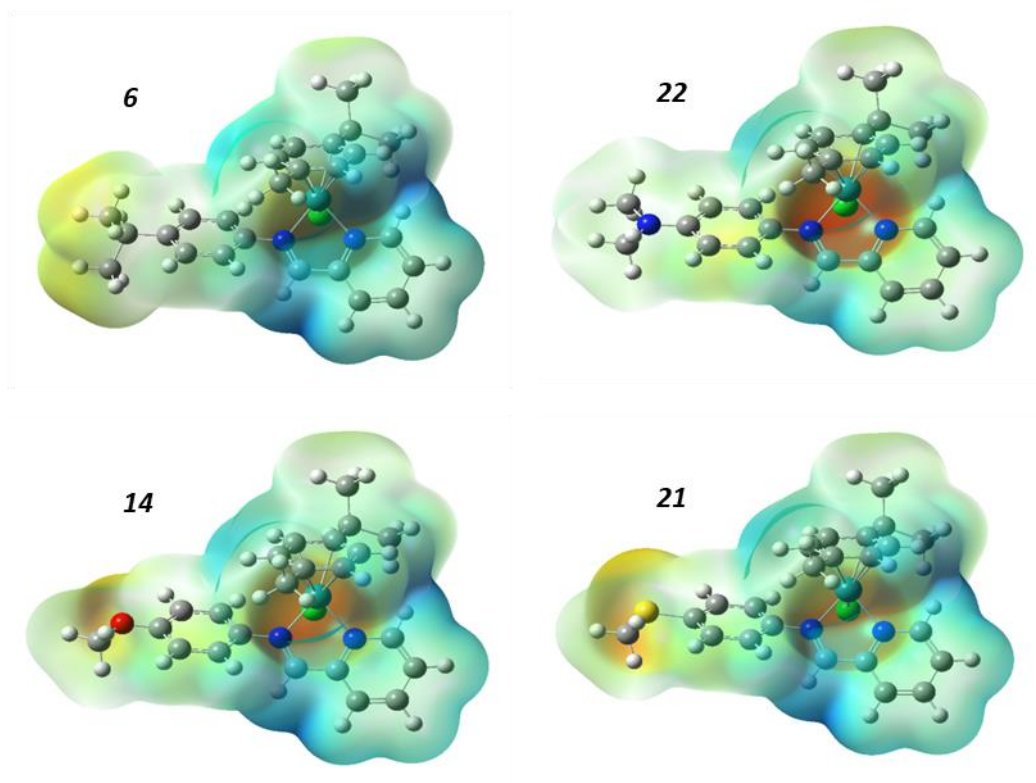
Figure 4-41: Electrostatic Potential Surface (EPS) mapped onto Total Electron Density of calculated DFT structures of complexes *6, 22, 14,* and *21* in their lowest energy structures demonstrating electron density around the complexes, with colour scale corelating with electron density with blue being less electron dense and red being more electron dense. Renders produced by Dr J.P.C. Coverdale.

Table 4-12: Calculated DFT Mulliken partial charges of select atoms determined from the lowest energy structures. Calculations performed by Dr J.P.C. Coverdale.

Complex	Ru	N-Ph	N-Py	Cl
6	0.100	-0.529	-0.573	-0.223
14	0.104	-0.530	-0.576	-0.229
21	0.100	-0.529	-0.573	-0.224
22	0.099	-0.529	-0.574	-0.223

5-3.2: *Cell Studies of atom bioisosteric replacement complexes*

5-3.2.1: Preliminary antiproliferative activity screening

Antiproliferative activity of the six complexes in this series were evaluated using the MTT method following 24 hours exposure and 72 hours recovery (Table 4-13 and Figure 4-42) expressed as IC_{50} values. As seen in previous chapters, there is a moderate trend of increasing lipophilicity with increasing antiproliferative activity with the most lipophilic complexes being *6 (-CH(CH₃)₂)* and *22 (-N(CH₃)₂)* also being the most active. Complexes *1, 11 (-OH), 14 (-OCH₃)* and *21 (-SCH₃)* exhibited no activity in all cell lines except for *14 (-OCH₃)* in A549 and *21 (-SCH₃)* in A2780 and HCT116 p53-/-. *6 (-CH(CH₃)₂)* and *22 (-N(CH₃)₂)* both show good activity in all cell lines tested here with *6* generally being between 1.3X and 3.2X more potent than *22* in MiaPaCa and HCT116 p53-/- respectively. Remarkably, *6* and *22* exhibit differential responses to the loss of P53 in the HCT116 lines with *6* increasing in potency by 1X.4, while *22* marginally decreases in potency by 0.9X.

Focusing on the EOC line A2780, no trend is apparent with the atom substitution and potency. Oxygen containing complexes are inactive in A2780 with both *11* and *14* having IC_{50} values above 140 µM. The other atom substitutions all produced a potency of below 100 µM in order of *22 < 6 < 21* with *22* being the most potent. While potency approximately halves for leading complexes *6* and *22* between the EOC lines A2780 and SKOV3, this is substantially less than the effect observed in CDDP treatment with potency in SKOV3 being 3.4X lower than in A2780. Remarkably, complexes *1*, *6* and *22* which were screened in the normal lung cell line MRC5 were ineffective with IC_{50} values >140 µM, in contrast to CDDP which had an IC_{50} value of 5.6 µM.

Table 4-13: Antiproliferative screening of the six complexes used in this chapter with efficacy displayed as IC$_{50}$ values (all units in μM unless stated otherwise) (*N.D.*: no data collected).

Complex	A2780	SKOV3	A549	MIAPaCa	UFH001	HCT116 p53+/+	HCT116 p53-/-	MRC5
1	>140	>140	>140	>140	>140	>140	>140	>140
6	44.6 (0.7)	84.5 (0.5)	52 (3)	45.97 (0.05)	47 (1)	30 (3)	21.9 (0.02)	>140
11	>140	*N.D.*	>140	>140	>140	>140	>140	*N.D.*
14	>140	*N.D.*	81 (3)	>140	>140	>140	>140	*N.D.*
21	82 (1)	*N.D.*	>140	>140	>140	>140	111 (1)	*N.D.*
22	25.9 (0.3)	66 (1)	33 (1)	60 (1)	72 (3)	63 (1)	69 (2)	>140
CDDP	3 (1)	11 (1)	12 (1)	24 (3)	17.3 (0.7)	6 (1)	5.7 (0.4)	5.6 (0.8)
PTX	0.3 nM (0.02)	0.56 nM (0.03)	*N.D.*	*N.D.*	*N.D.*	*N.D.*	*N.D.*	*N.D.*
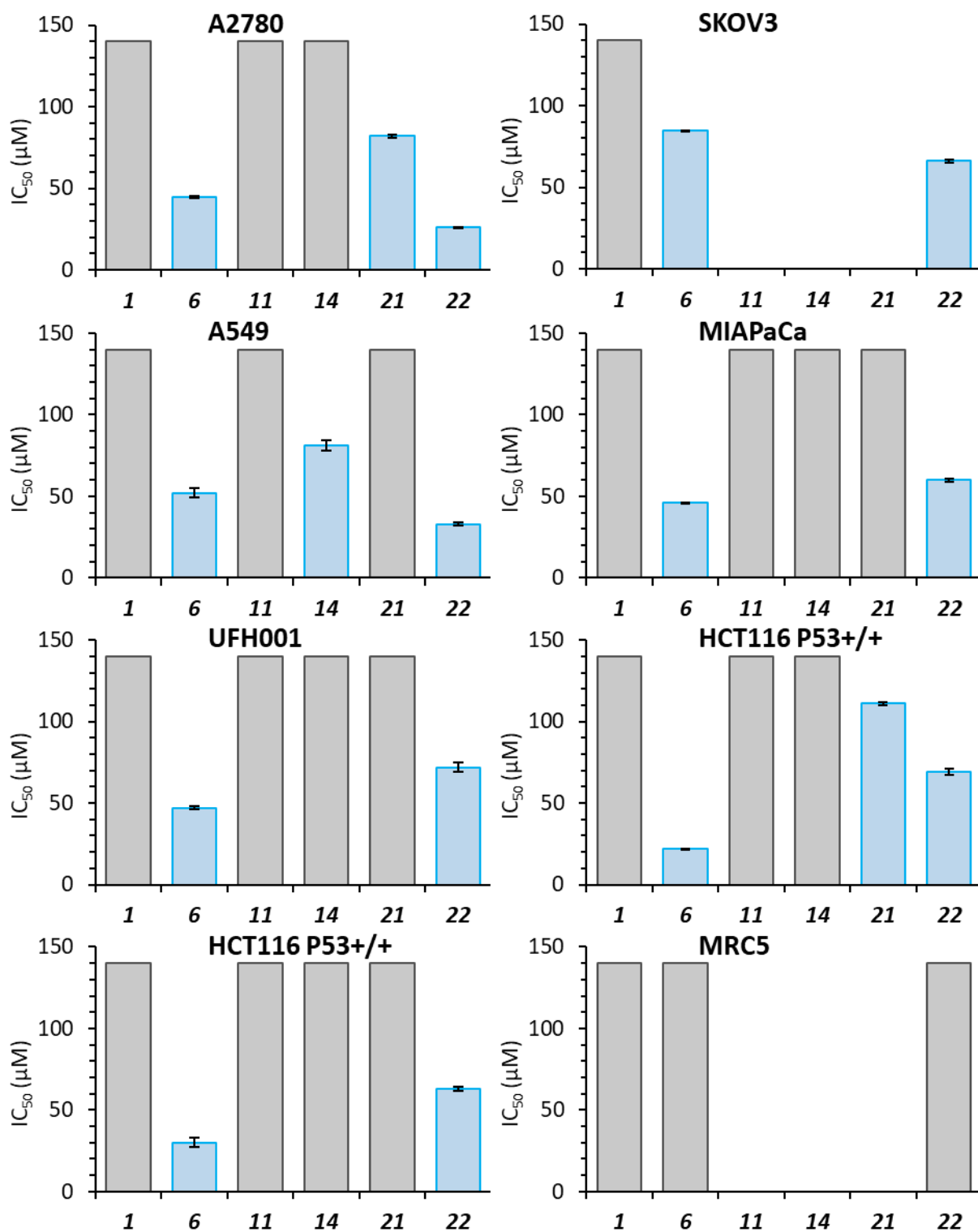
Figure 4-42: Antiproliferative screening of the six complexes used in this chapter with efficacy displayed as IC$_{50}$ values in μM. Bars in grey indicate an IC$_{50}$ value of >140 μM.

5-3.2.2: Antiproliferative activity without recovery time in A2780

To assess the effect of recovery on these complexes, the two main complexes of interest, **6** and **22**, were investigated with only 24 hours exposure time in the EOC line A2780. Complex **22** was 1X.7 more potent than **6** following 24 hours exposure and 72 hours recovery with IC_{50} values of 25.9 μM and 44.6 μM, respectively. However, without recovery time **6** is 2.5X more potent than **22** with an IC_{50} values of 24.1 μM (±0.4) and 60.5 μM (±0.1) (Figure 4-43).
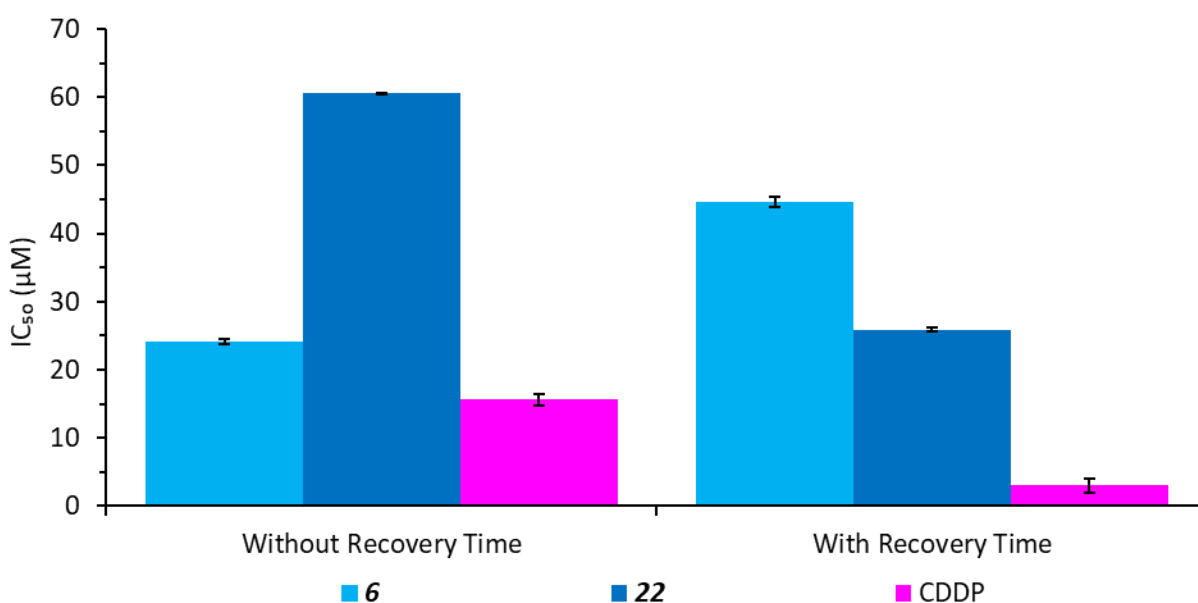
Figure 4-43: Comparison of IC_{50} values of *6, 22* and CDDP after 24 hours of treatment with and without 72 hours of recovery time in full media in A2780.

5-3.3: Preliminary differing mode of action screening of 6 and 22

To further observe the differing effects of the bioisosteric replacement of the within the phenyl group substitution on MOA in A2780, **6** and **22** were evaluated for further studies using 24+72 hour IC_{50} equipotent concentrations.

5-3.3.1: Mitochondrial polarisation studies using Rh123 by fluorescence microscopy

As ΔΨm depolarisation is a key MOA of ruthenium complexes, adherent cells were assessed with Rh123 microscopy (Figure 4-44). Treatment with *6* or *22* induced a decrease in Rh123 fluorescence even at 0.5X IC_{50}, which is not observed in CDDP and PTX treated cells. Notably, there was a significant loss of the *6* treated cell populations at 1X and 2X IC_{50} concentrations, however the remaining adherent cells maintained Rh123 fluorescence.

5-3.3.2: ROS generation studies

Noting the indications of ΔΨm depolarisation, DCFDA was used to assess the generation of ROS in treated cells by fluorescence microscopy (Figure 4-45) and fluorescence intensity (Figure 4-46). There was an increase in fluorescence by microscopy in *6* treated cells, which decreased with increased concentration. But as seen by the DAPI staining, the number of cells also decreased. *22* also exhibited a mild increase in DCFDA fluorescence at 1X and 2X IC_{50}.

Due to population loss of cells treated with 2X IC_{50} *6*, fluorescence intensity was measured. This highlighted that both *6* and *22* both induced a significant ($p<0.001$) increase in DCFDA fluorescence, with *6* inducing more fluorescence than *22.*
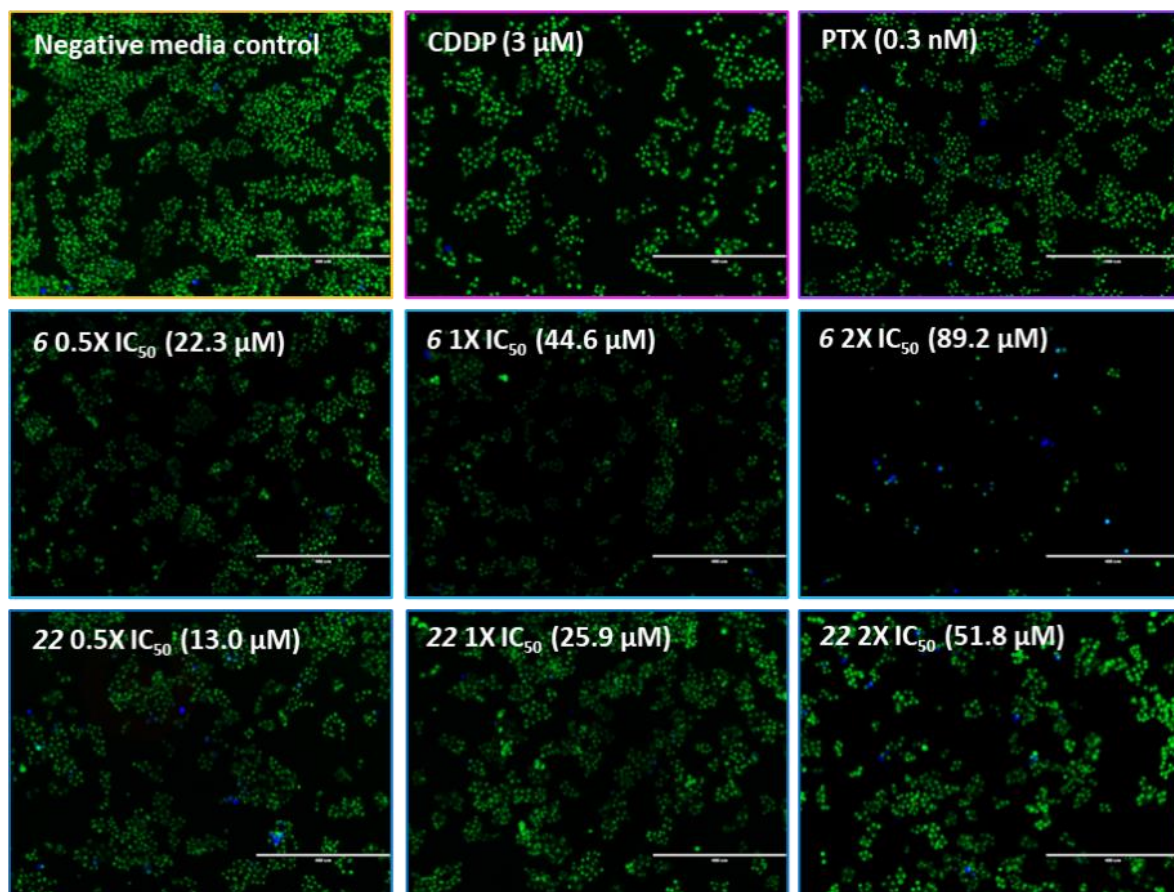
Figure 4-44: Determination of mitochondrial depolarisation by Rh123 of A2780 cells following treatment with media as a negative control, CDDP (3 µM), PTX (0.3 nM), **6** 0.5X, 1X, and 2X IC$_{50}$ (22.3, 44.6, and 89.2 µM), or **22** at 0.5X, 1X, and 2X IC$_{50}$ (13.0, 25.9, and 51.8 µM) by fluorescence microscopy using Rh123 (green), DAPI (blue) and PI (red). Images presented as overlays of the green, blue, and red channels at 10X magnification (scale bar 400 µm).
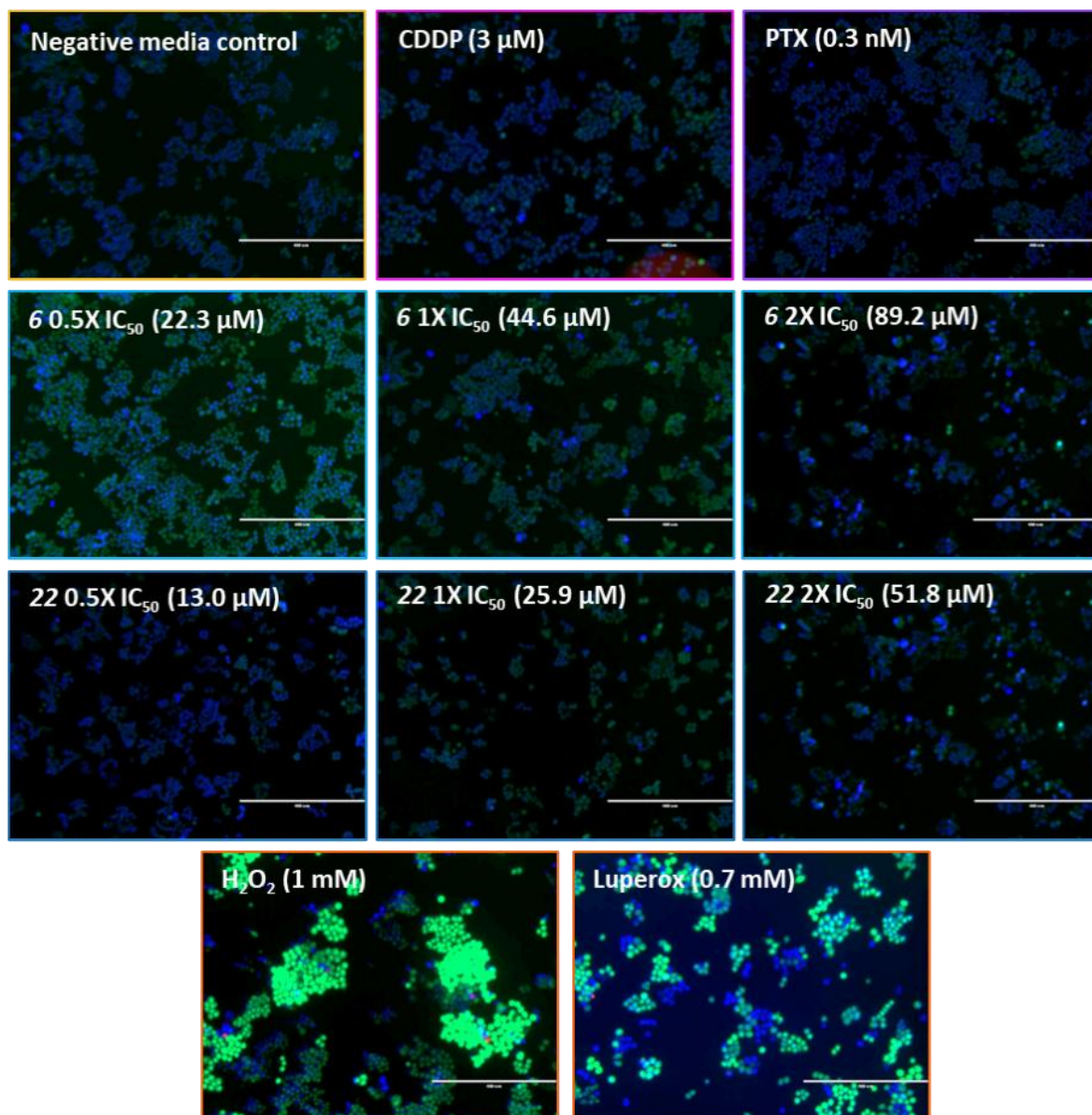
Figure 4-45: Determination of ROS generation by DCFDA of A2780 cells following treatment with media as a negative control, CDDP (3 µM), PTX (0.3 nM), **6** 0.5X, 1X, and 2X IC$_{50}$ (22.3, 44.6, and 89.2 µM), **22** at 0.5X, 1X, and 2X IC$_{50}$ (13.0, 25.9, and 51.8 µM), 1 mM hydrogen peroxide for 2 hours or 0.7 mM Luperox for 2 hours by fluorescence microscopy using DCFDA (green), DAPI (blue) and PI (red). Images presented as overlays of the green, blue, and red channels at 10X magnification (scale bar 400 µm).
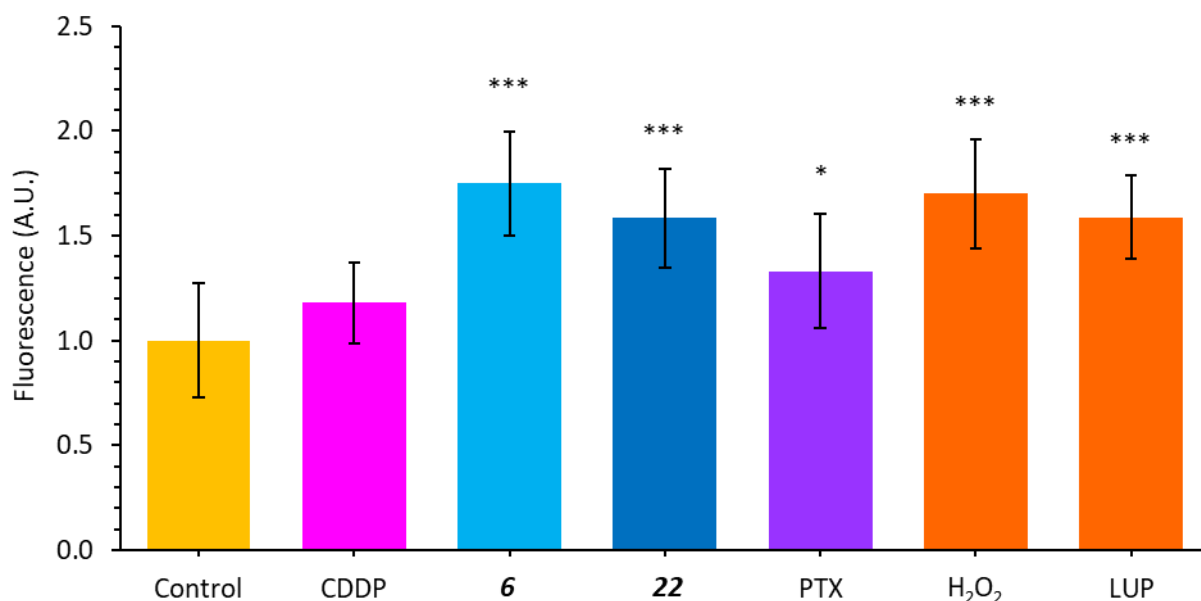
Figure 4-46: Determination of ROS generation in A2780 cells following treatment with media as a negative control, CDDP (3 µM), PTX (0.3 nM), *6* (44.6 µM), *22* (25.9 µM), 1 mM hydrogen peroxide for 2 hours, or 0.7 mM Luperox for 2 hours by fluorescence intensity of DCFDA normalised by protein content. (Significance determined by Welch t-test where * indicates $p<0.05$, ** indicates $p<0.01$, and *** indicates $p<0.001$ levels of significance).

5-3.3.3: Cell cycle analysis

Following equipotent treatment of A2780 cells, cell cycle arrest was investigated by flowcytometry using PI and RNase (Figure 4-47). Both *6* and *22* induced significant ($p<0.01$) G_1 arrest though a decrease in the G_2/M fraction. This contrasts both CDDP which induced G_2/M arrest and PTX which did not cause significant cell cycle arrest.

5-3.3.4: Apoptosis analysis

Apoptosis induction also by flow cytometry was assessed using PI and Annexin V. Both *6* and *22* increased the number of cells in the apoptotic populations (Figure 4-48). However, *6* caused a greater response with significant population increases in early, late and non-viable fractions, while *22* which induced a lesser response only in late and non-viable populations. The comparators all also induced significant early and late apoptosis.
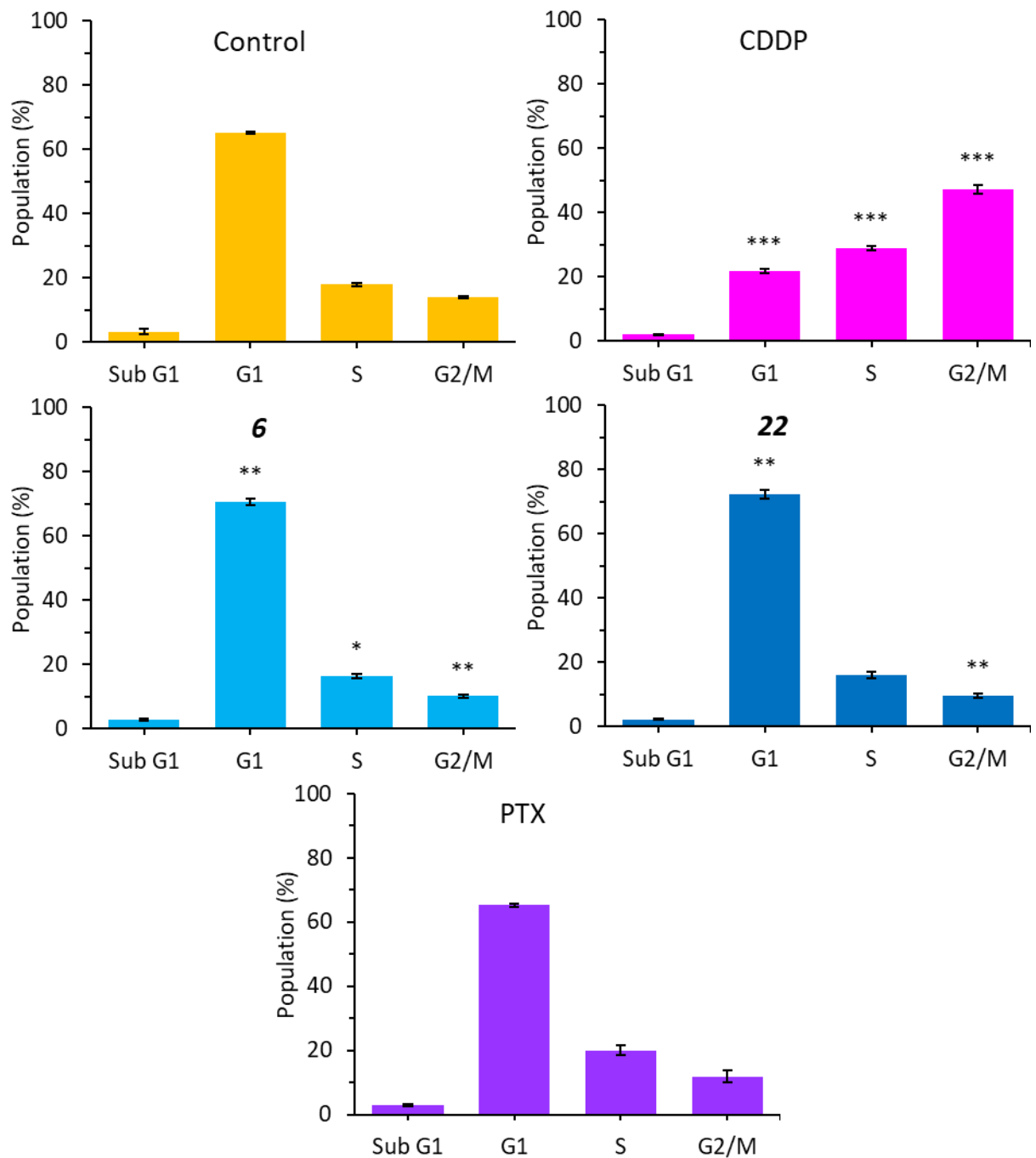
Figure 4-47: Cell cycle arrest of A2780 cells by flow cytometry treated with media as a negative control, CDDP (3 µM), PTX (0.3 nM), *6* (44.6 µM), or *22* (25.9 µM), stained with PI and RNase (significance determined by Welch t-test where * indicates p<0.05, ** indicates p<0.01, and *** indicates p<0.001 levels of significance).
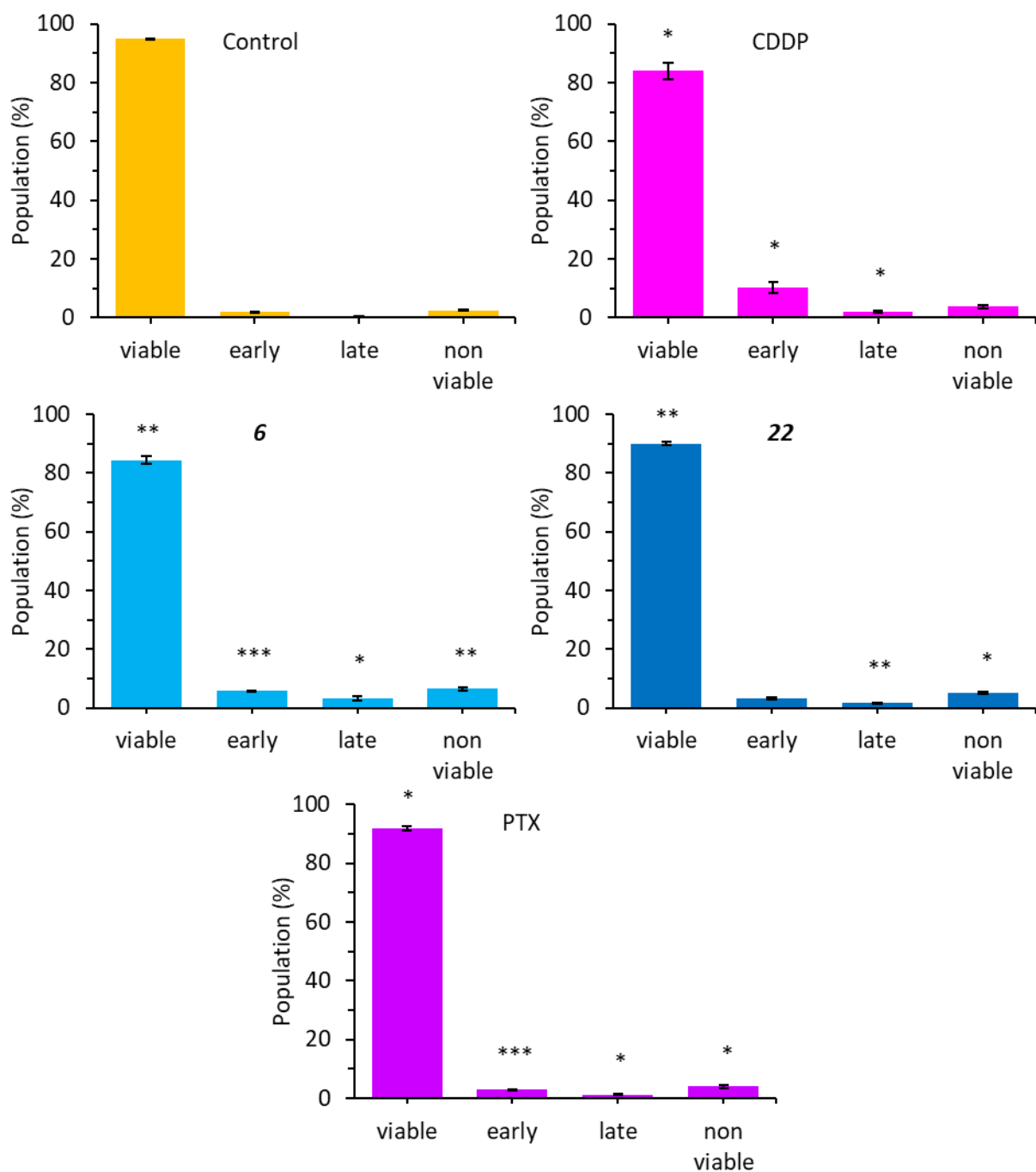
Figure 4-48: Apoptosis induction by flow cytometry of A2780 cells treated with media as a negative control, CDDP (3 µM), PTX (0.3 nM), **6** (44.6 µM), or **22** (25.9 µM), stained with PI and Annexin V (significance determined by Welch t-test where * indicates p<0.05, ** indicates p<0.01, and *** indicates p<0.001 levels of significance).

5-3.3.5: Wound healing studies

The potential for invasion inhibition was assessed using the wound healing assay (Figure 4-49 and Figure 4-50). Complex *6* was the most effective treatment tested significantly (p<0.001) preventing wound closure following the initial 24 treatment period and the following recovery period with a total closure of 0.14 mm. This highly contrasted complex *22* which initially significantly (p<0.001) inhibited wound closure initially during the exposure period, yet anti-invasive effects subsided and allowed wound closure following the 72-hour recovery period resulting in wound closure similar to the negative control. This was similarly seen for CDDP. Regarding PTX, wound closure was significantly (p<0.001) prevented during the exposure and recovery period, but was not as effective as *6* with a total closure of 0.16 mm.
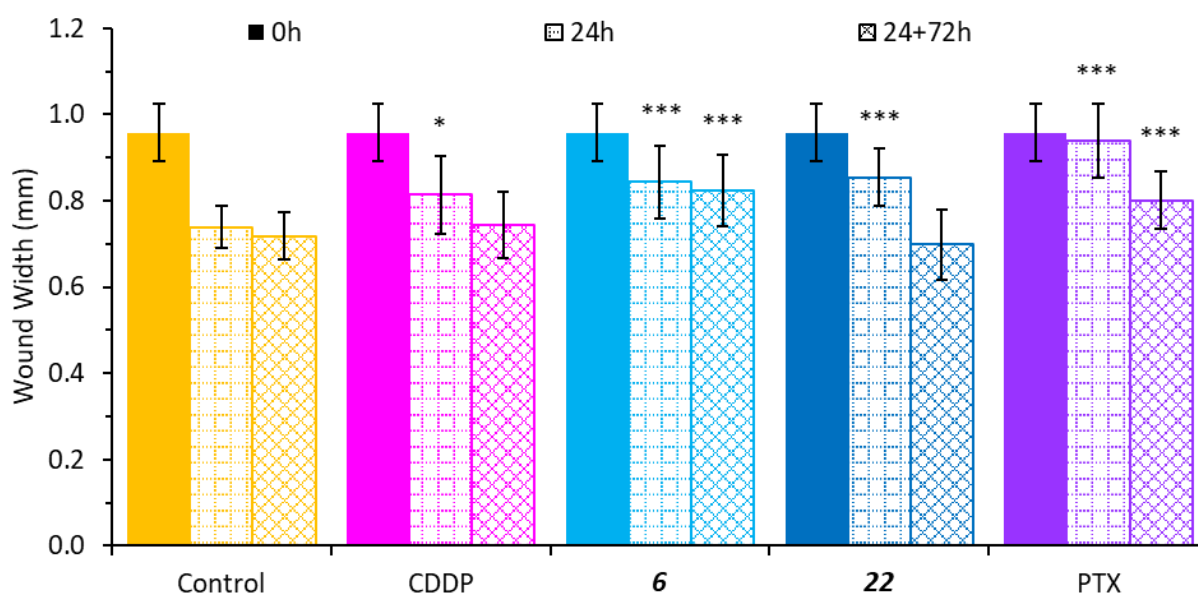
Figure 4-49: Measurements of wound widths of A2780 cell monolayers following treatment with media as a negative control, CDDP (3 μM), PTX (0.3 nM), *6* (44.6 μM) or *22* (25.9 μM) at 24 hours exposure and 24 + 72 hours recovery. Images taken at 4X magnification. (Significance determined by Welch t-test where * indicates p<0.05, ** indicates p<0.01, and *** indicates p<0.001 levels of significance).
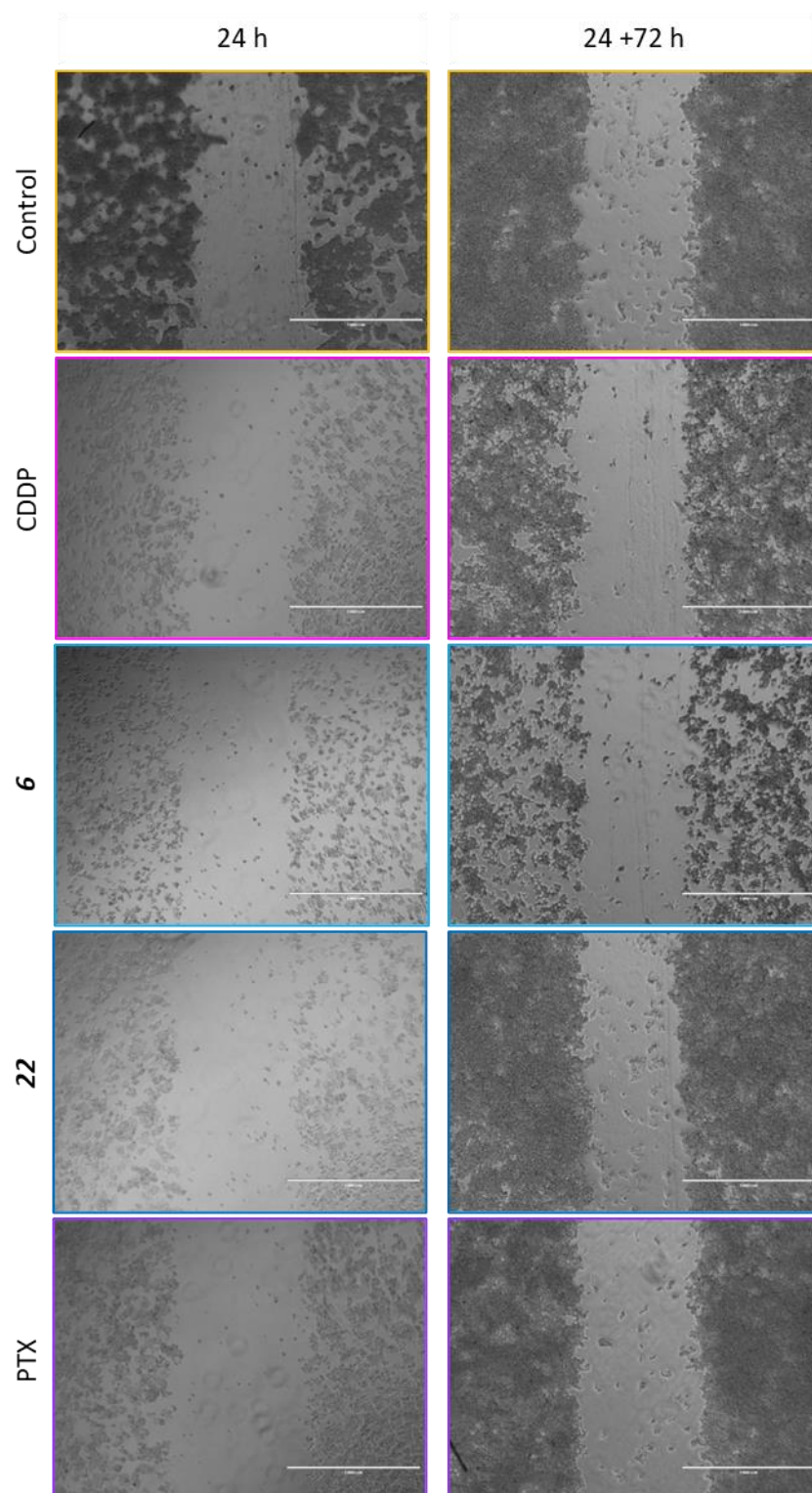
Figure 4-50: Images of the wound healing assay of A2780 cell monolayers following treatment with media as a negative control, CDDP (3 µM), PTX (0.3 nM), *6* (44.6 µM), or *22* (25.9 µM) at 24 hours exposure and 72 hours recovery. Images taken at 4X magnification, scale bar: 1000 µM

5-3.3.6: Colony formation studies

The colony formation was used to assess to assess antimetastatic potential (Figure 4-51). Complex **6** was significantly (P<0.001) effective at reducing colony formation by 71%. In contrast, **22** did not achieve a reduction in the number of colonies. The size of the colonies that developed were evaluated by area (Figure 4-52). Complex **6** significantly (p<0.001) reduced the density of colonies that developed being highly similar to CDDP. However, while **22** significantly (p<0.001) reduced the density of the colonies that developed, yet they were still of a notable size being half the size of the control colonies.

5-3.3.7: Spheroid growth inhibition

As a model of *in vivo* behaviour, spheroid area was used to assess inhibition of growth (Figure 4-54 and Figure 4-53). Both complexes **6** and **22** inhibited growth dose-dependently. Complex **6** was highly effective and induced significant (p<0.001) inhibition at 0.5X IC_{50} concentrations, but further dose increases did not remarkably improve activity. In contrast, complex **22** which only induced significant reduction at 2X IC_{50}. Remarkably, **6** was more effective at inhibiting growth compared to CDDP and PTX while **22** was only comparable at double concentrations.
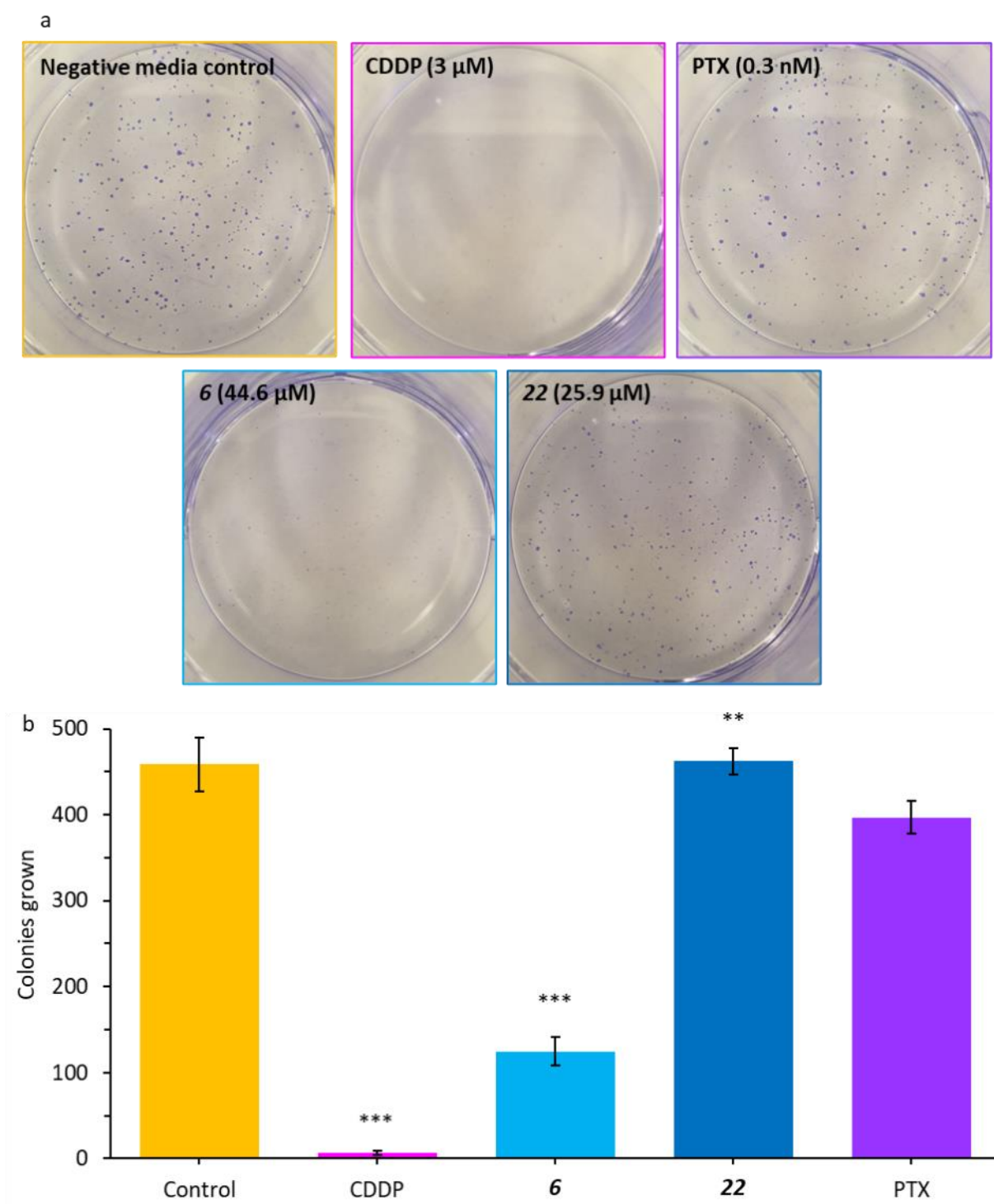
Figure 4-51: Colony formation a). well images and b). colony counts of A2780 cells following treatment with media as a negative control, CDDP (3 µM), PTX (0.3 nM), **6** (44.6 µM), or **22** (25.9 µM) following 24 hours exposure and 7 days colony growth time. Images taken at 1X magnification. b). graphical representation of the number of colonies grown (significance determined by Welch t-test where * indicates p<0.05, ** indicates p<0.01, and *** indicates p<0.001 levels of significance).
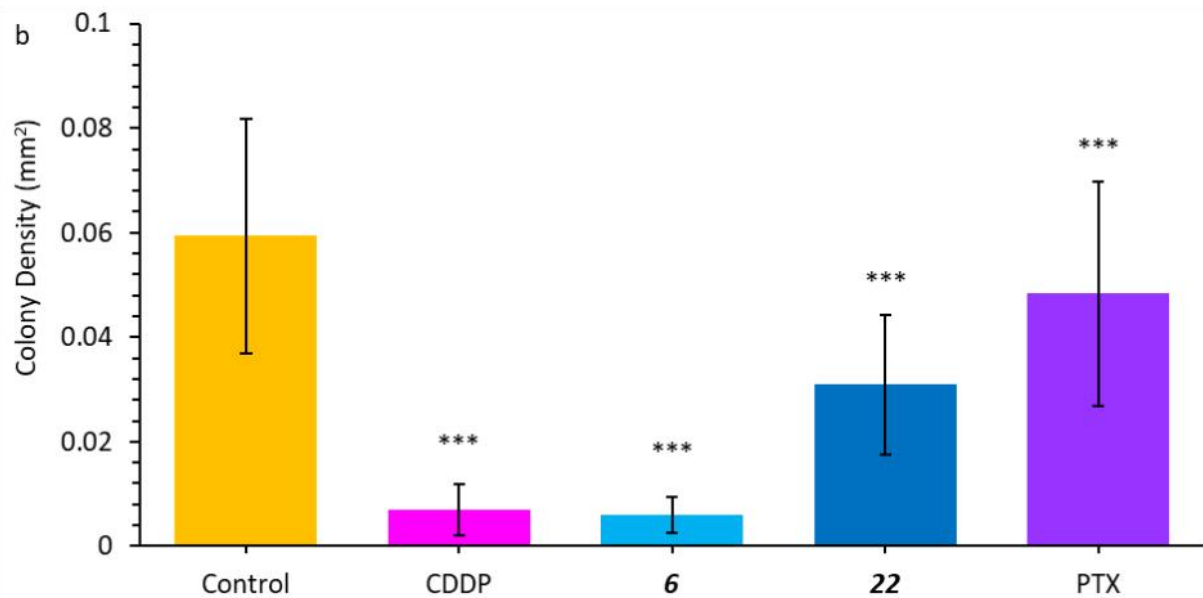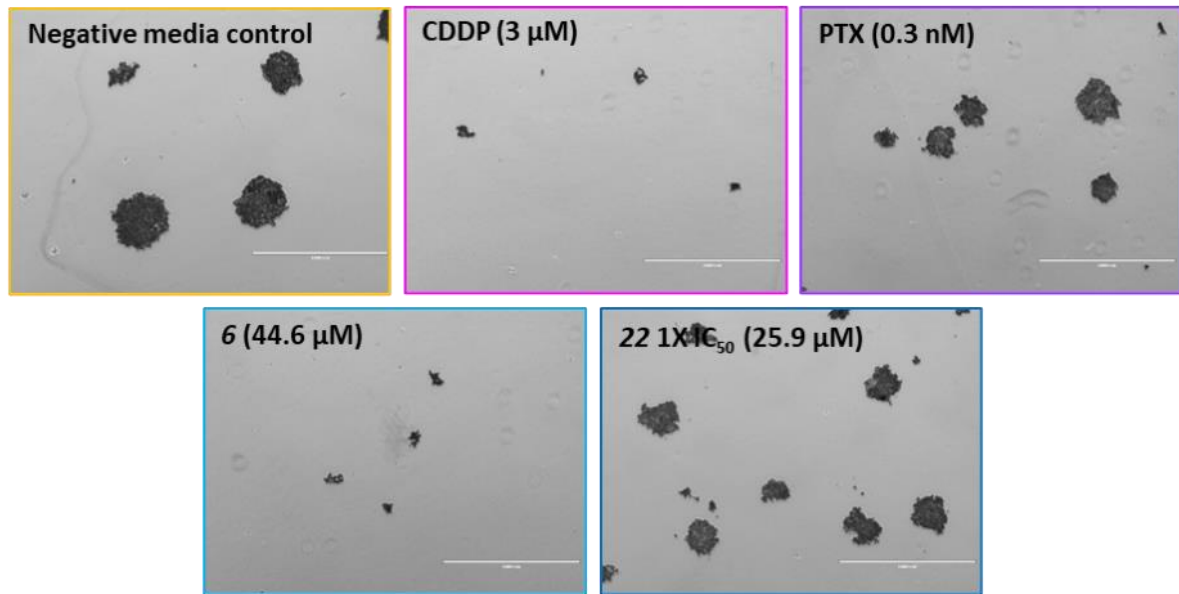
Figure 4-52: Colony density a). well images taken at 2X magnification, scale bar: 2000 μM. and b). graphical representation of the number of colonies grown of A2780 cells following treatment with media as a negative control, CDDP (3 μM), PTX (0.3 nM), *6* (44.6 μM), or *22* (25.9 μM) following 24 hours exposure and 7 days colony growth time. Significance determined by Welch t-test where * indicates $p<0.05$, ** indicates $p<0.01$, and *** indicates $p<0.001$ levels of significance.
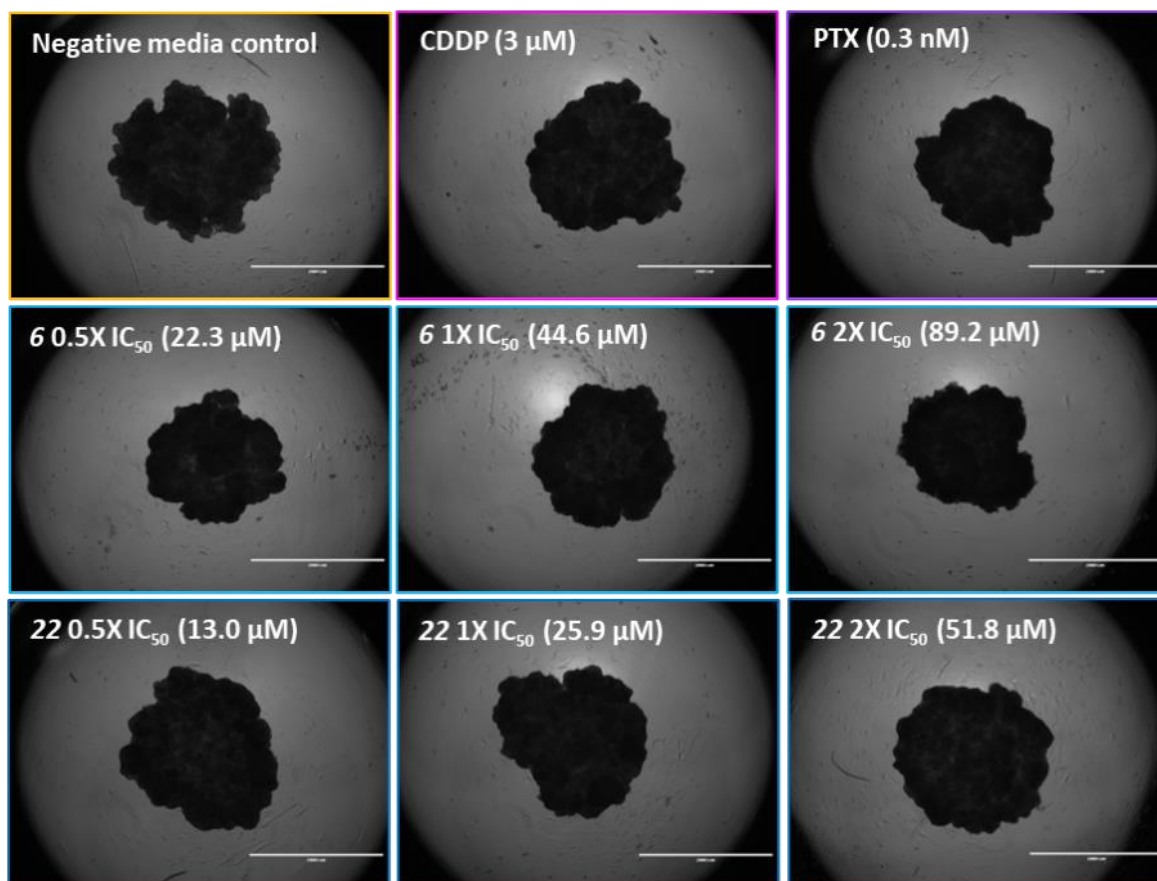
Figure 4-53: A2780 spheroids treated with media as a negative control, CDDP (3 μM), PTX (0.3 nM), *6* 0.5X, 1X, and 2X IC_{50} (22.3, 44.6, and 89.2 μM) or *22* at 0.5X, 1X, and 2X IC_{50} (13.0, 25.9, and 51.8 μM). Images taken at 2X magnification, scale bar: 2000 μM.
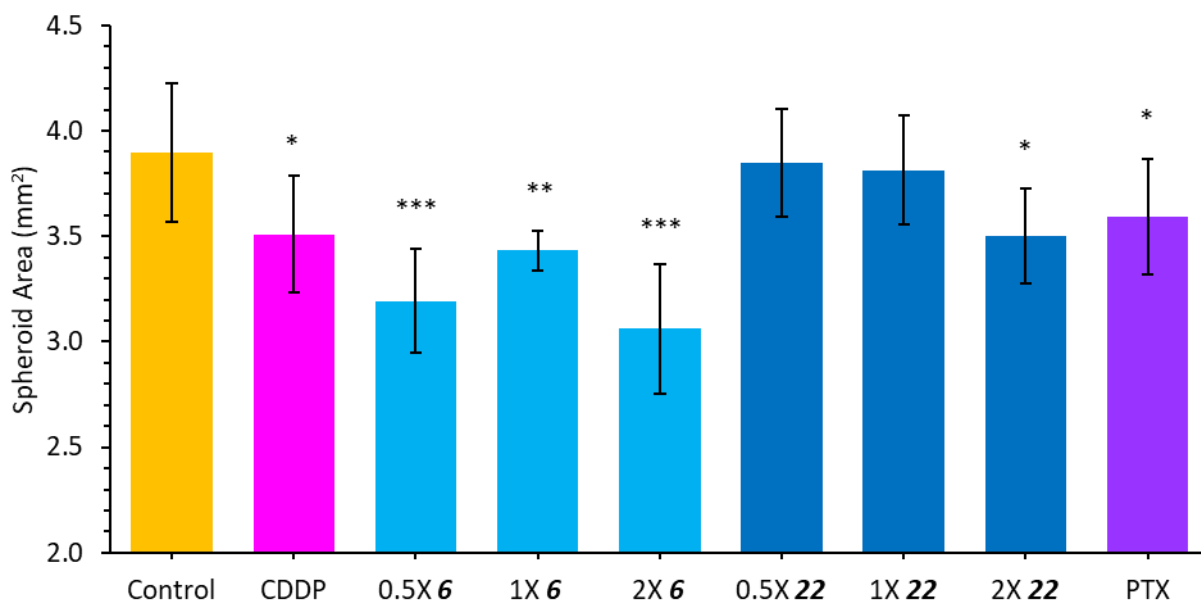
Figure 4-54: Area of A2780 spheroids following treatment with media as a negative control, CDDP (3 μM), PTX (0.3 nM), **6** 0.5X, 1X, and 2X IC$_{50}$ (22.3, 44.6, and 89.2 μM) or **22** at 0.5X, 1X, and 2X IC$_{50}$ (13.0, 25.9, and 51.8 μM). (Significance determined by Welch t-test where * indicates $p<0.05$, ** indicates $p<0.01$, and *** indicates $p<0.001$ levels of significance).

5-3.3.8: Protein content and Caspase 3/7 activity

Noting the significant apoptotic populations of complex **6** and **22** treated cells when analysed by flow cytometry, Caspase 3/7 activity was investigated and normalised by protein content (Figure 4-55). Significantly ($p<0.001$) lower protein content was only seen in **6** treated cells at 2X IC$_{50}$ treated cells, with all other treatments not exhibiting a significant difference to the negative control.

Complex **6** induced significantly ($p<0.001$) high levels of Caspase 3/7 activity at 0.5X IC$_{50}$ which decreased but maintained significance at 1X and 2X IC$_{50}$. This is contrary to **22** which exhibits a dose dependant increase in activity. Remarkably, both **6** and **22** induced significant ($p<0.01$) levels of activity even at 0.5X IC$_{50}$ doses and higher than the comparator CDDP at 1X IC$_{50}$.
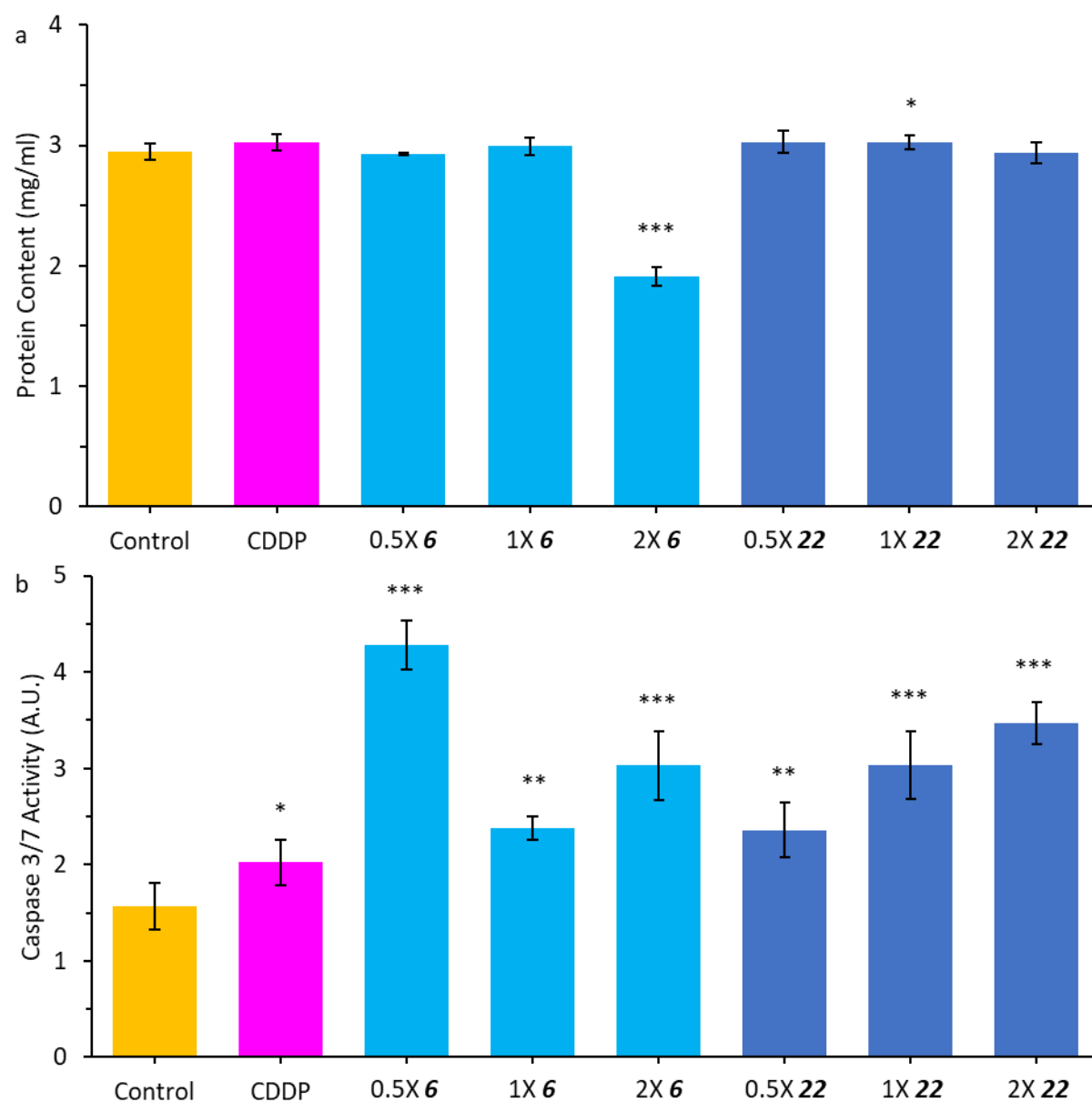
Figure 4-55: Cell lysates of A2780 cells treated with media as a negative control, CDDP (3 μM), **6** 0.5X, 1X, and 2X IC$_{50}$ (22.3, 44.6, and 89.2 μM) or **22** at 0.5X, 1X, and 2X IC$_{50}$ (13.0, 25.9, and 51.8 μM) tested for a). Protein content by Bradford assay and b). Caspase 3/7 activity normalised by protein content. (Significance determined by Welch t-test where * indicates $p<0.05$, ** indicates $p<0.01$, and *** indicates $p<0.001$ levels of significance).

5-3.3.9: Total metal accumulation by inductively coupled plasma mass spectrometry

With metal accumulation being able to indicate the uptake/efflux and efficiency of a complex, total metal accumulation of treated A2780 cells was evaluated by ICP-MS. Total uptake of platinum and ruthenium of treated cells are shown in Figure 4-56a and b respectively. Remarkably, *6* treated cells contained 2.3X more ruthenium than *22* treated cells, accumulating 0.51±0.04 fmol and 0.22±0.04 fmol per cell, respectively. Additionally, both *6* and *22* treated cells induced higher metal uptake than CDDP treated cells, with CDDP cells accumulating 0.069±0.006 fmol per cell.
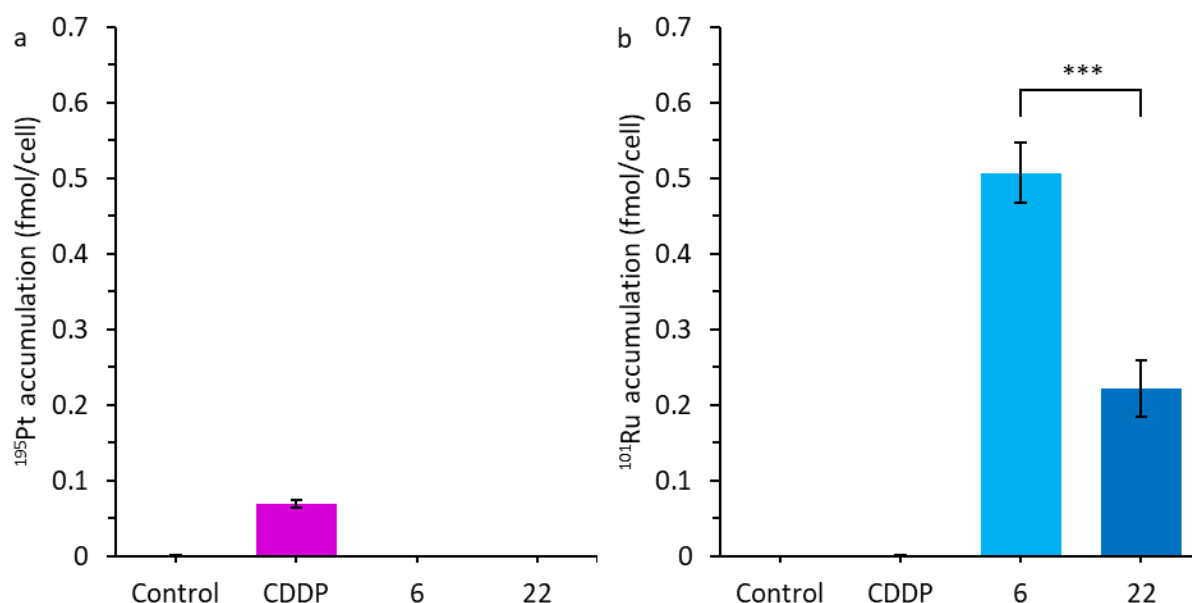
Figure 4-56: Metal accumulation of A2780 cells treated with media as a negative control, CDDP (3 µM), *6* (44.6 µM), or *22* (25.9 µM) looking for a). ^{195}Pt content and b). ^{101}Ru content determined by ICP-MS shown in femtomoles per cell (fmol/cell). Significance determined by Welch t-test where *** indicates $p < 0.001$ levels of significance).

5-3.3.10: Time and temperature dependant metal accumulation by inductively coupled plasma mass spectrometry

In addition to total uptake, temperature and time dependant ruthenium accumulation was also evaluated to evaluate passive and active accumulation (Figure 4-57). Very low accumulation of

ruthenium for both **6** and **22** were seen at 277 K compared to 310 K. Complex **6** at 277 K only achieved 5.9% and 6.5% of ruthenium accumulation at 310 K at three and six hours, respectively. Similarly, complex **22** only achieved 8.2% and 6.6% accumulation at 277K at three and six hours, respectively.

Furthermore, time interval accumulation also shows faster ruthenium accumulation with complex **6** treatment over **22**. At three hours (310 K), complex **6** treated cells contain 55.0% (0.28± 0.01 fmol) of the total ruthenium accumulation at 24 hours. This is substantially higher than in complex **22** treated cells at 310 K which only accumulate 32.1% (0.071± 0.004 fmol). This trend extended to the six-hour interval with 71.1% (0.4± 0.2 fmol) of total accumulation being complete for **6** in comparison to **22** which only achieves 51.6% (0.11± 0.02 fmol) of total accumulation.
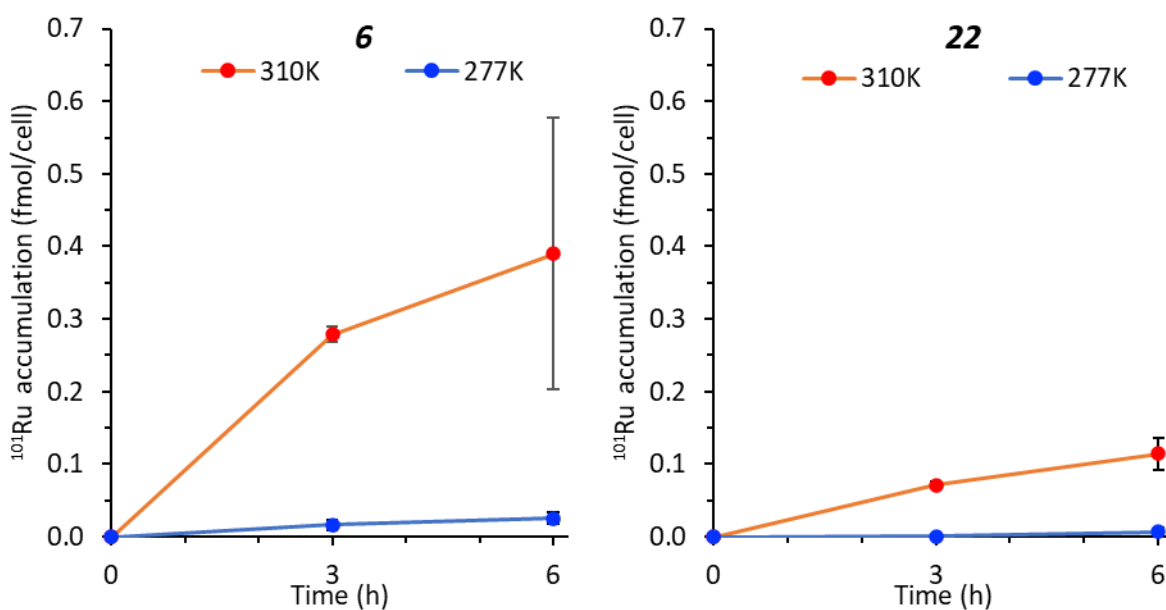
Figure 4-57: Temperature and time dependant ruthenium accumulation of A2780 cells treated a). **6** (44.6 μM) or b). **22** (25.9 μM) determined by ICP-MS shown in femtomoles per cell (fmol/cell).

246

5-3.4: Cytoplasmic membrane damage studies induced by 6 and 22

5-3.4.1: Attachment assay

Noting the indications of cellular detachment of complex **6** treated cells in the microscopy assays, cell attachment was assessed by counting the detached and suspended populations following 24 hours treatment exposure and three PBS washes, analogous to the washing protocols used for fluorescence microscopy (Figure 4-58). While both CDDP and **6** induced a significant (p<0.001) decrease in the attached population, consistent with previous results. Only **6** induced a significant (p<0.001) increase in the suspended population with ~ 8.5×10^6 cells per mL in suspension compared to the control with only 2.1×10^5 cells total in suspension.
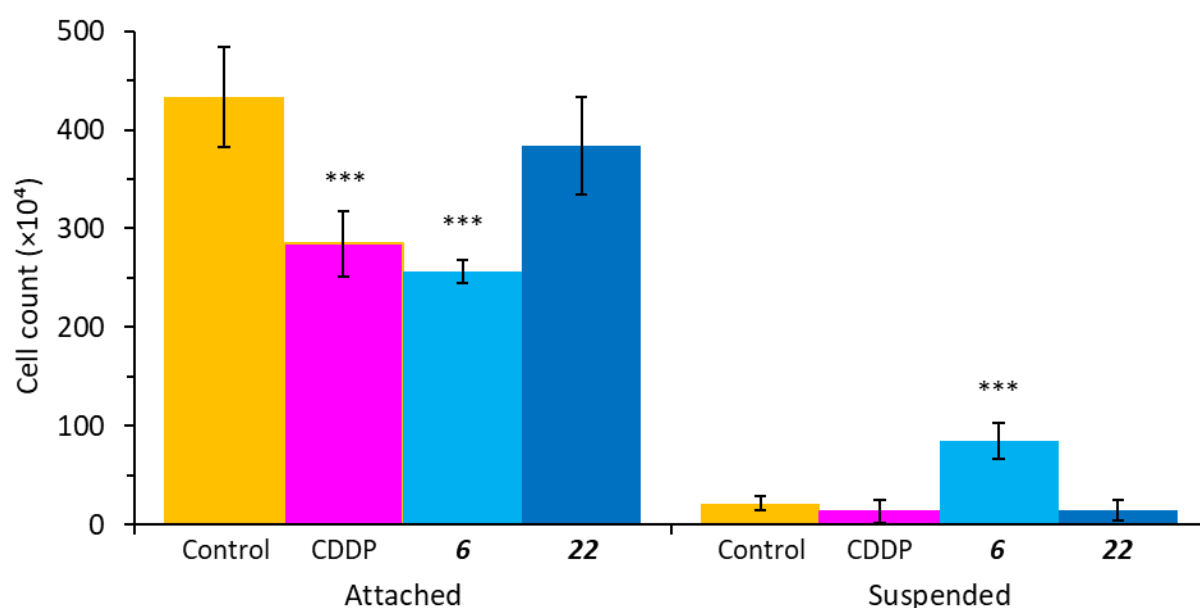
Figure 4-58: Attachment assay of A2780 cell treated with media as a negative control, CDDP (3 µM), PTX (0.3 nM), **6** (44.6 µM), or **22** (25.9 µM) comparing the attached and suspended population following three PBS washes. (Significance determined by Welch t-test where *** indicates p<0.001 levels of significance).

5-3.4.2: Mitochondrial polarisation by flow cytometry

Following the confirmation of cell detachment, ΔΨm was assessed using JC1 by flow cytometry using both the adherent and suspended cell populations (Figure 4-59). The decrease in PE fluorescence is corelated with the decrease in ΔΨm. Here, **6** at IC_{50} induced significant (P<0.001) ΔΨm depolarisation comparable to the positive control CCCP. This highly contrasts **22** which did not induce significant ΔΨm depolarisation at 1X IC_{50} but did at 2X IC_{50}. Both CDDP and PTX did achieve a significant decrease in ΔΨm polarisation, but this was marginal compared to **6** and CCCP.
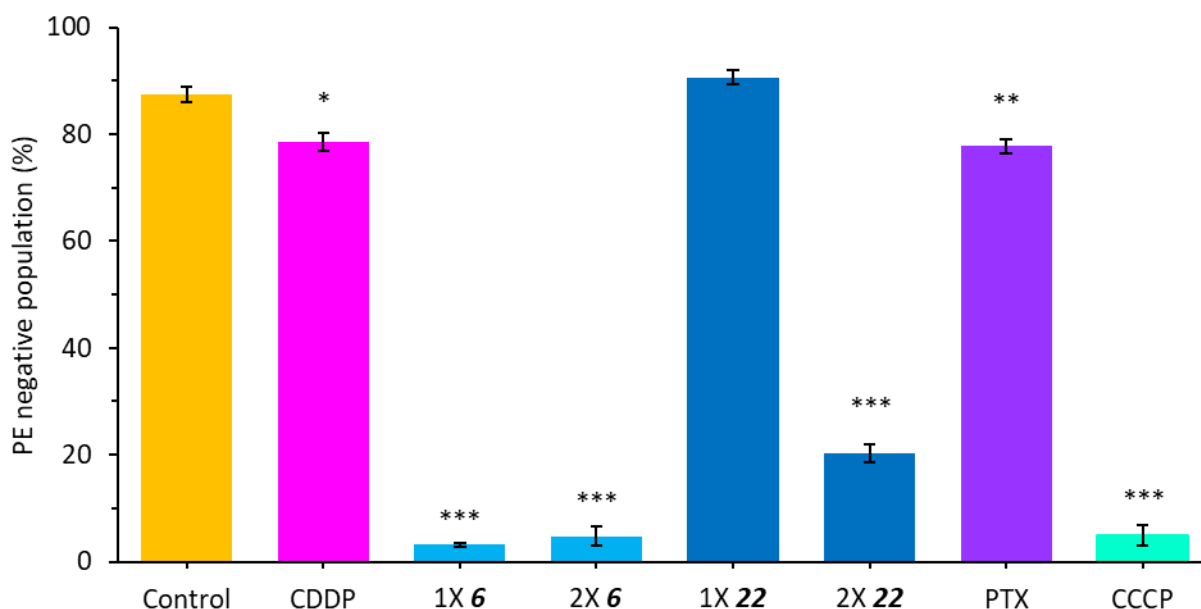
Figure 4-59: Mitochondrial polarisation assay by JC1 staining and flow cytometry of A2780 cells treated with media as a negative control, CDDP (3 μM), **6** 1X and 2X IC_{50} (44.6 and 89.2 μM), **22** at 1X and 2X IC_{50} (25.9 and 51.8 μM), or 5 μM CCCP (significance determined by Welch t-test where * indicates p<0.05, ** indicates p<0.01, and *** indicates p<0.001).

5-3.4.3: Cellular morphology by fluorescence microscopy

With reduced attachment predominantly due to CCM damage, morphology of the cell and CCM were evaluated using a lipophilic carbocyanine dye (Figure 4-60). Consistent with the detachment assay, at higher concentrations of **6**, a decreased population of adherent cells were seen. **6** induced a concentration dependant loss in CCM staining culminating in the complete loss in CCM staining at 2X

IC$_{50}$ in addition to reduced cell size. *22* did induce a decrease in fluorescence in comparison to the control at 0.5X IC$_{50}$, however further loss with increased concentration is not observed. CDDP nor PTX exhibited no alteration in fluorescence intensity or morphology.
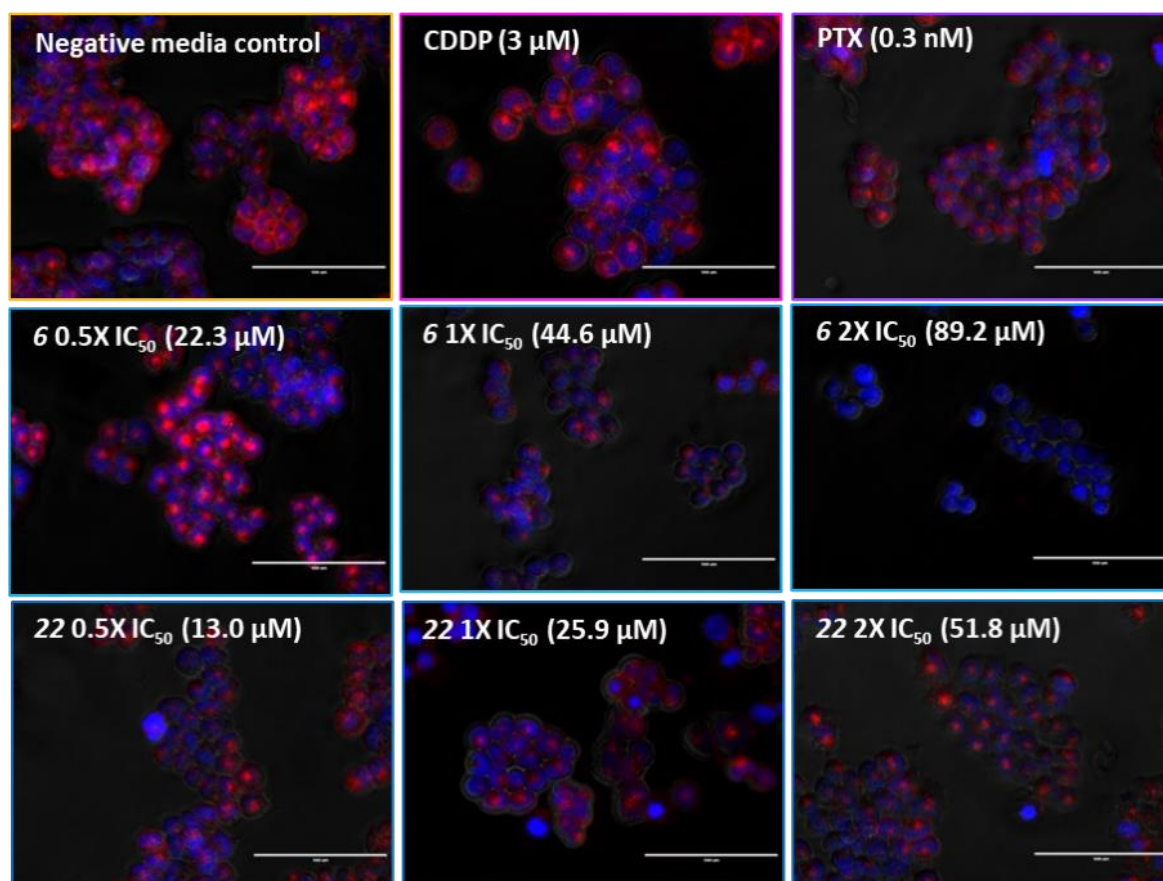
Figure 4-60: Cell morphology of A2780 cells following treatment with media as a negative control, CDDP (3 μM), PTX (0.3 nM), *6* 0.5X, 1X, and 2X IC$_{50}$ (22.3, 44.6, and 89.2 μM) or *22* at 0.5X, 1X, and 2X IC$_{50}$ (13.0, 25.9, and 51.8 μM) by fluorescence microscopy. Cells stained with DAPI (blue) and Cell Brite red membrane dye (red). Images presented as overlays of the blue, red, and transmission channels at 40X magnification (scale bar 100 μm).

5-3.4.4: Membrane integrity by flow cytometry

The loss of CCM dye fluorescence suggests that the CCM is being compromised. To evaluate if this was due to loss of integrity, analysis of the PI staining alone from the apoptosis assay was used (Figure 4-61). Although there was a significant (p<0.001) decrease in the PI negative population for both *6* and *22*,

this represents a 9% and 6% increase in the positive population, respectively, and is incomparable to the positive control STS with an increase of 75% in comparison to the negative control.
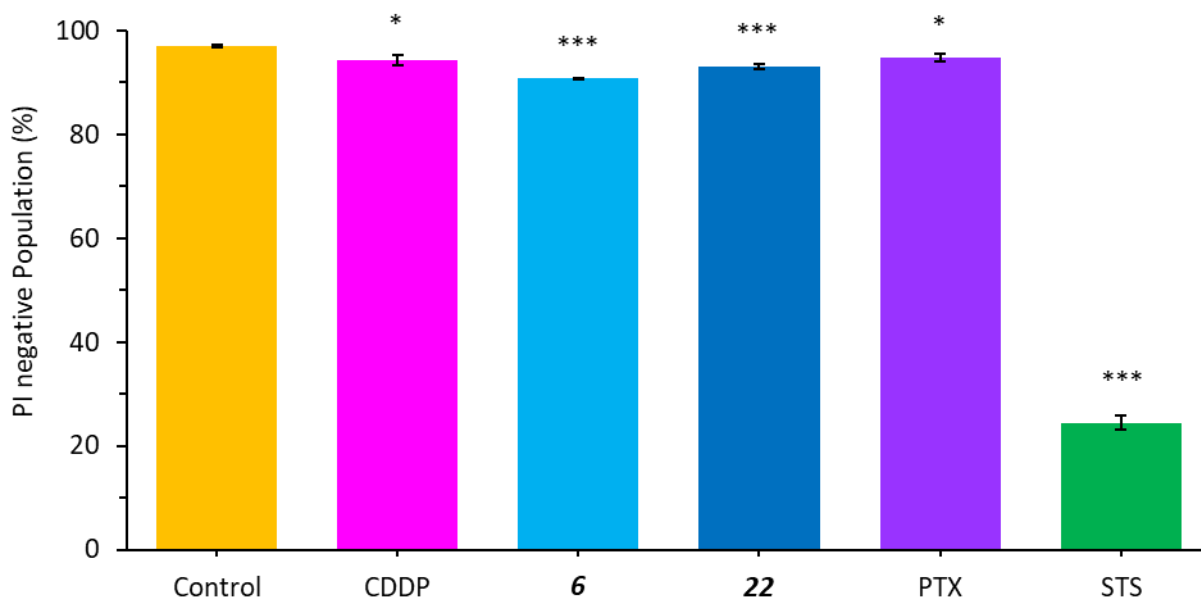
Figure 4-61: Membrane integrity by flow cytometry of A2780 cells treated with media as a negative control, CDDP (3 µM), PTX (0.3 nM), *6* (44.6 µM), or *22* (25.9 µM) or 0.1 µM STS, stained with PI and Annexin V. Only PI channel presented. (Significance determined by Welch t-test where * indicates p<0.05, ** indicates p<0.01, and *** indicates p<0.001 levels of significance).

5-3.4.5: Extracellular biomolecule binding assay

As cell binding is predominantly through integrins, reduction in attachment may be due to loss of integrins. This can be assessed by the evaluation of binding to different ECM proteins. Here, binding to collagen-I, collagen-II, collagen-IV, fibronectin, laminin, tenascin and vitronectin with BSA as a negative control was assessed using the ECM Cell Adhesion Array Kit (Figure 4-62). Base line ECM binding was established using the untreated control, demonstrating that the primary proteins tested here involved in A2780 adherence are collagen-I, fibronectin and laminin with absorbance levels greater than 1.0 A.U., followed by collagen-IV, tenascin and vitronectin (Figure 4-62a), consistent with the literature[17].

On average, treatment with *6* reduced ECM binding by 67%, compared to *22* which reduces binding by 38%. Evaluating the ECM proteins individually, treatment with *6* significantly (p<0.01) reduced binding

to all matrixes except collagen-II. Complex *22* exhibited a similar effect, but to a lesser extent. Notably, *6* reduced binding to collagen-I, fibronectin and laminin by 85%, 63% and 69%, respectively, while *22* reduced binding by 70%, 26% and 29%. Comparably, CDDP also reduced binding to all of the ECM proteins evaluated with a total reduced binding on 76%.

5-3.4.6: Transwell invasion

Noting the loss of attachment to several ECM proteins and cultureware and the inhibition of wound healing, the invasive potential of *6* and *22* treated cells was evaluated by Transwell chemotaxis. Following two hours of chemotaxis (Figure 4-63, left column), untreated cells achieved chemotaxis through the membrane, this was in significant contrast to CDDP, *6* and *22* treated cells which substantially reduced the chemotaxis of cells. Notably, *6* and *22* treated cells exhibit a reduction in green membrane dye fluorescence, similar to the results observed in the CCM morphology experimentation.

Following 24 hours of chemotaxis (Figure 4-63, right column), an increased number of untreated cells that achieved migration. Similarly, a substantial number of CDDP treated cells also achieved migration through the membrane with no reduction in CCM stain fluorescence reduction. This contrasts *6* and *22* treated cells. While further chemotaxis of *22* treated cells was prevented, CCM fluorescence is regained. This differs *6* treated cells where an increase in cells that achieved chemotaxis increased by approximately double, however the cells that do achieve migration do not regain CCM fluorescence.
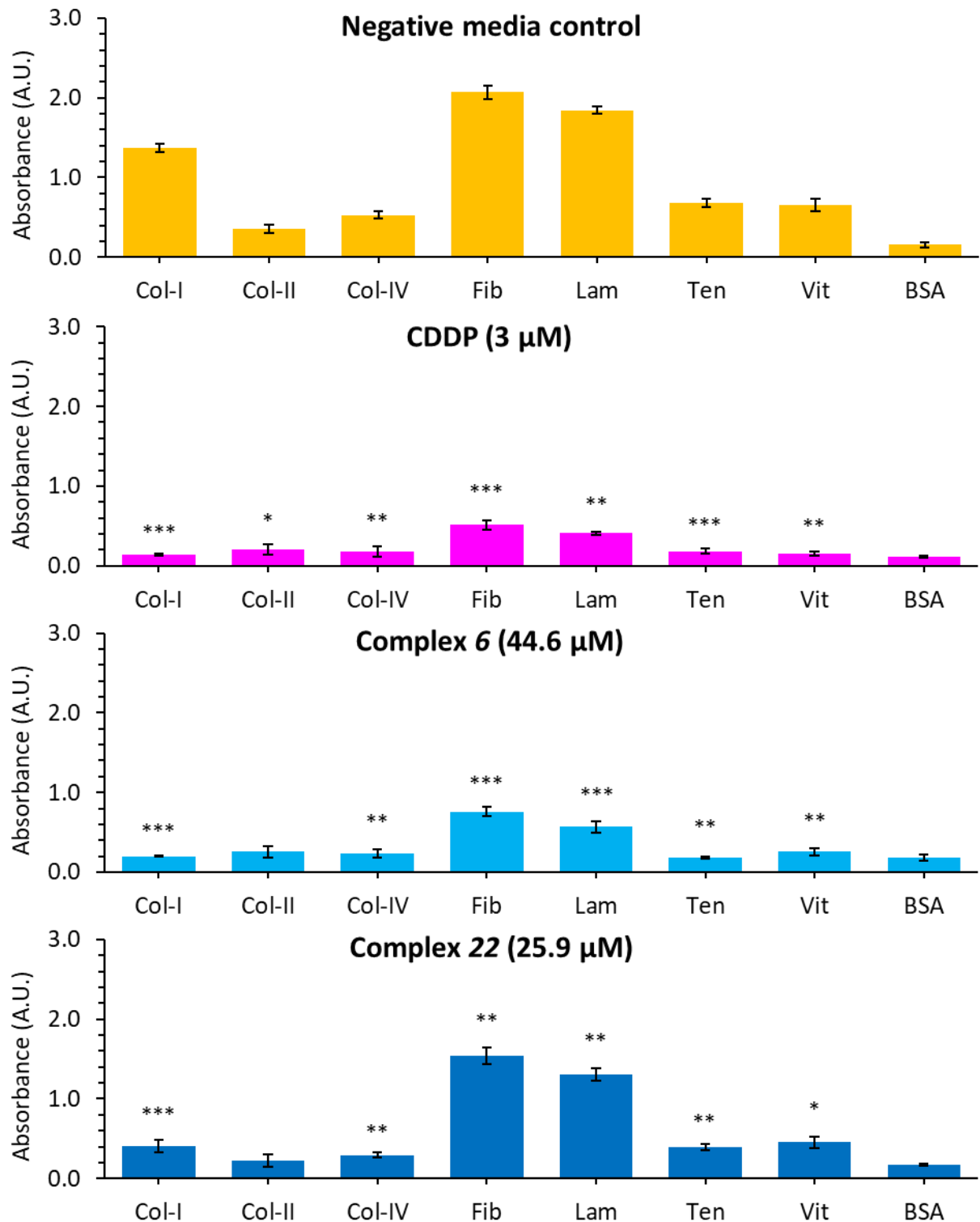
Figure 4-62: Extracellular matrix (ECM) assay to assess the binding capability of A2780 cells treated with media as a negative control, CDDP (3 µM), *6* (44.6 µM) or *22* (25.9 µM) to the ECM proteins collagen-I (Col I), collagen-II (Col II), collagen-IV (Col IV), fibronectin (Fib), laminin (Lam), tenascin (Ten) and vitronectin (Vit) with Bovine Serum Albumin (BSA) as a negative control. (Significance determined by Welch t-test where * indicates p<0.05, ** indicates p<0.01, and *** indicates p<0.001 levels of significance).
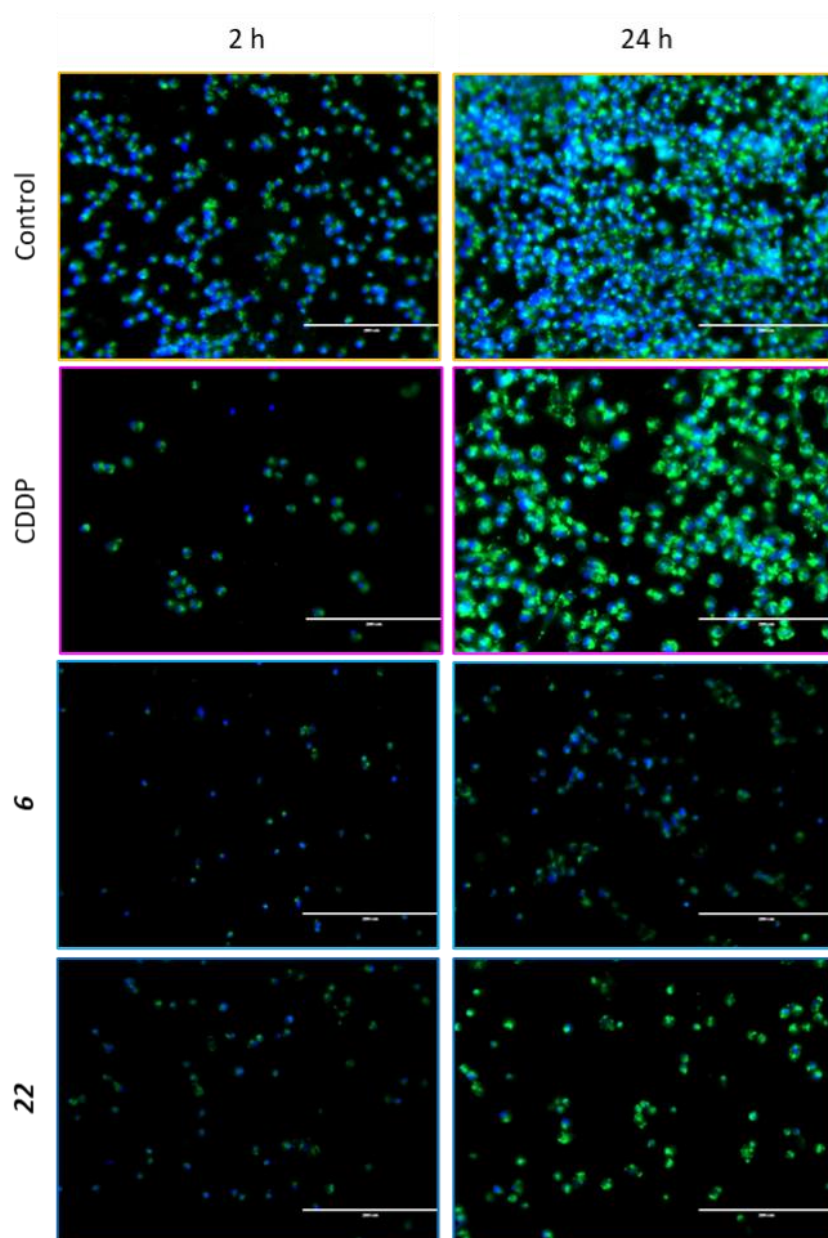
Figure 4-63: Transwell assay following 2 or 24 hours of invasion time of A2780 cells treated with media as a negative control, CDDP (3 µM), **6** (44.6 µM) or **22** (25.9 µM) stained with DAPI (blue) and Biotracker 490 green membrane dye (green). Images presented as overlays of the blue and green channels at 10X magnification, scale bar: 400 µM.

5-4: Discussion

The CCM is an essential component to the cell as the intermediate between the intercellular and extracellular matrixes. The compromise of the CCM and its adherence the ECM can lead to cellular death through type I and type III mechanisms. Select ruthenium complexes have been previously documented to be able to compromise the CCM leading to significant antiproliferative activity of cancer metastases[28,30,39]. In this work, the bioisosteric replacement phenyl ring substituent was investigated. Experimentation into the activity of the complexes **6** and **22** provide significant evidence that substitution from nitrogen to carbon can impact the antiproliferative activity and MOA in the EOC cell line A2780.

5-4.1: Physiochemical influences of bioisosteric replacement

In the previous chapters, bioisosteric replacements have been based around substitution and insertion of functional groups. In this chapter, the substitution of a singular atom was investigated to determine the possible effect of movement across the periodic table. By DFT calculation, typical periodic table trends are not observed with the substitution of the phenyl ring substituent with no significant differences observed in key bond length, Mulliken charges or electron density around the ruthenium centre, chlorine, or co-ordinated nitrogens. Charge effect appears to be very localized to the substitution and the phenyl ring. In similar AzPy complexes, electron donating phenyl substituent has been associated with improving antiproliferative activity, potentially through improved redox activity of the azo bond[40]. The ImPy bond of the complexes here may not have this similar redox activity, therefore the electron donating activity may have differing effects to the imine bond, considering that the highly donating hydroxyl is inactive while the dimethylamine group is highly active. This suggests that the nature of the substitution had a differing effect than those seen in AzPy complexes.

In line with the DFT structure predictions, the physicochemical interactions of the substituted complexes also do not differ between the complexes synthesised here interacting with GSH, media, full media, and ctDNA while not interacting with 1:1 water to PBS, PBS, BSA, human plasma, and NEAA. Like previous complexes assessed, interaction with GSH is expected due to interaction being through the charge transfer band at between 250 and 500 nm. This encompasses the bonds directly to the ruthenium centre, therefore the most likely interaction is through the labile chlorine bond. Noting the little change in bond length or electron density changes around the ruthenium centre, similar behaviour is to be expected between these complexes. Here all the complexes except the oxygen containing complexes **11** and **14** exhibited an isosbestic point in water, suggesting that the methylthio may have less of an electron donating effect than the hydroxyl and methoxy groups, still allowing the aquation and activation of the sulphur containing complex **21**[37]. However, the reduced activity of complex **21** suggests that aquation may be occurring at a reduced rate, but this should be explored through aquation NMR where a proportion of Cl:H_2O species can be evaluated. Additionally, complex **21** is the only complex to exhibit an isosbestic point in the DMSO matrix. This may be through the formation of a disulphide bond between the DMSO and the complex methylthio group. However, speciation of this should be evaluated by NMR spectroscopy following 24 hours incubation, as no change in speciation from the proposed complex is observed with NMR spectroscopy occurring within 12 hours (as part of NMR conducted in structure elucidation testing).

In contrast to the previous physiochemical results, substitution did appear to effect lipophilicity of the complexes with lipophilicity decreasing with increasing periodic group number in addition to increasing lipophilicity with increasing period number. While this could be due to atom substitution, this trend may be overshadowed by the loss of a methyl group due to valency moving across the elements with the carbon and nitrogen derivatives **6** and **22** having two methyl substituents, while the oxygen and sulphur derivatives **14** and **21** only have one. As shown with benzene and toluene, the addition of a singular methyl group can significantly increase lipophilicity[41]. Therefore, a larger panel of complexes

should be evaluated without differing methyl group substitutions should be evaluated to determine reasoning for this trend.

5-4.2: Potency differences due to bioisosteric replacement

Following physiochemical characterisation, complexes were assessed for antiproliferative activity in a panel of cell lines. Interestingly, bioisosteric substitution confers significant differences in antiproliferative activity in a similar trend to the lipophilicity. Of the complexes evaluated here, the unsubstituted complex *1* and oxygen containing complexes *11* and *14* conferred the worst activity being inactive with an IC_{50} of >140 µM in most cell lines. This was closely followed by the sulphur containing *21*. In contrast, the carbon and nitrogen containing complexes *6* and *21* exhibited significant activity in a variety of cells, with the *6* being more active in most cell lines. Observing this, potency increases with moving left across the groups of the periodic table *6*>*22*>*21*>*14* (C>N>S>O). As previously stated, this trend could be due to group effect, methyl number, lipophilicity, or a combination of these qualities in addition to any complex specific MOA the substituent may grant[42]. Of particular interest is the lack of activity of the oxygen and sulphur containing species, especially considering the enhancing effects oxygen containing species provide in similar azo complexes[40]. The inactive behaviour of these complexes may be due to the detoxifying actions of GSH. As GSH can target a variety of electrophilic agents, including many organometallic complexes[43–48]. Therefore, an additional oxygen and sulphur group, which are often a highly common targets for GSH, maybe provide a secondary point for GSH-adduct formation for cell export, leading to decreased activity.

Of these complexes in this series, none exhibit substantial decrease in activity with the loss of p53. On the contrary, both *6* and *21* exhibit an increase in potency, however, this is more profound for *21*. With the loss of p53 often associated with reduced treatment response of DNA targeting treatments, this suggests that these complexes may not target DNA, or if DNA is targeted it may be via a MOA not

associated with p53[49]. This is also supported by the improved activity of *6* in the MiaPaCa where DNA repair is less frequently hindered through mutation damage[50,51].

Focusing on EOC specifically, there is a considerable difference in the activity of *6* and *22* in A2780 and SKOV3, with the complexes being twice as active in A2780. Noting improvement of activity of *6* with the loss of p53 in the comparison HCT116 cell lines, and minor decrease in activity of *22*, the activity difference should not be attributed to the loss of p53 in SKOV3[52–56]. Noting the documented difficulty in treating SKOV3 due to increased GSH levels, reduced apoptotic signalling, aberrant PUMA expression and Smac release, and increased anti-apoptotic protein levels including BCL-x_L and MCL-1, as these complexes are indicated to induce apoptosis and interact with GSH, this may explain why these complexes suffer from decreased activity in SKOV3[57–59]. However, it must be observed that the impact of activity nullification of this series is fractional compared to CDDP which suffers from a 73% decrease in activity in SKOV3 against A2780, compared to 47.3% and 60.8% decrease for *6* and *22*, respectively. This suggests that while there is overlap between the intrinsic CDDP resistance mechanisms in SKOV3, these mechanisms are not as effective against *6* and *22* as they are against CDDP.

Despite having remarkable antiproliferative activity in all cancerous cell lines, *6* and *22* both are inactive in the normal cell line MRC5 having a lung specificity value of >2.7 and >4.2 and ovarian specificity of >3.3 and >5.4, respectively (specificity value = ratio of IC_{50} for MRC5 human lung fibroblasts ÷ IC_{50} of cancerous line), where a greater number corelates with increased specificity[33]. This specificity is highly beneficial by providing an intrinsic specificity for cancerous cells. This has the potential to limit toxicity in non-cancerous cells and systemic damage, a consistence hinderance of non-targeted chemotherapies[60–62]. This is also consistent with other similar organometallic complexes, and provides a substantial benefit over other organometallic complexes that do not exhibit specificity[63–65].

Noting the remarkable activity of *6* and *22*, activity of the complexes was assessed without recovery time. Interestingly, the antiproliferative activity of the complexes alters with *6* becoming 2.5X potent

than **22** without recovery, while **22** becomes 1.7X more active than **6** with recovery. This is highly indicative of these complexes possessing differential MOA despite their similarities in physiochemical characterisation. This could be due to a combination of differential accumulation, efficacy of the MOA being activated, and damage recovery between the complexes.

While the potency of **6** and **22** may not be as high as CDDP, there is a consistent trend of *in vitro* ruthenium organometallic complex antiproliferative studies not corelating with *in vivo* studies. This is seen with both NAMI-A and RAPTA complexes which both do not have remarkable antiproliferative activities in vitro often exhibiting antiproliferative activity greater than 300 and 50 µM respectively, while achieving significantly effective *in vivo* activity[31,32,66]. Therefore, both complexes **6** and **22** here having lower IC_{50} values than published values for other treatments in further study and clinical trial is highly remarkable, demonstrating that these complexes may have high potential for in vivo study in the future.

5-4.3: Preliminary mode of action evaluation of 6 and 22

Following the identification of the two lead candidates; **6** and **22**, initial MOA of screening was preformed to identify key differences between the carbon and nitrogen complexes in the EOC cell line A2780.

To further evaluate the antiproliferative activity of these complexes, spheroid growth following 24 hours exposure was evaluated. As spheroids pose significant problem in EOC patients, good anti-spheroid activity is important[67–69]. Complex **6** was more effective than both comparator treatments, even at 0.5X IC_{50} concentrations, while **22** was only effective at 2X IC_{50} concentration. This is reflective of the time-dependant activity of these complexes with **6** being more potent following 24 hours exposure. Sustained remission is difficult to achieve in EOC patients due to spheroids present in free fluid which are frequently highly resistant to first line therapies[67]. Spheroid activity is associated with the ability to penetrate into the mass and the ability to combat differing tumour microenvironments

within one tumour including oxygen and nutrient differences[70]. The significant activity of **6** is remarkable suggesting potential against primary and metastatic tumours by substantial penetration into the spheroid but also to combat differing microenvironments of a tumour. Additionally, the improved activity of **6** over **22** highlights a substantial differential MOA despite only differing in one peripheral atom, highlighting the benefits of bioisosteric replacement exploration.

As previously shown in Chapter 3, complex **6** was highly effective at inducing ΔΨm depolarisation in SKOV3. Following Rh123 staining, comparable results were not observed in A2780 with adherent cells maintaining fluorescence therefore maintaining ΔΨm, albeit to a decreased extent[71]. However, these results came at the reduction of the adherent cell population at higher concentrations, indicating adherence issues. To confirm ΔΨm in A2780, JC1 staining was used on the whole population, including the suspended cells by flow cytometry. JC1 is a highly sensitive quantitative stain for the polarisation of the ΔΨm where the stain forms J aggregates which fluoresces red when polarised, but monomerises and fluoresces green when depolarised and is highly effective in flow cytometry applications[72]. Of particular interest, **6** treated cells exhibit significant levels of ΔΨm depolarisation comparable to CCCP, a proton shuttling compound which permeabilises the mitochondrial membrane to protons[73]. Therefore, while this may disagree with the A2780 Rh123 results, it is comparable to the SKOV3 Rh123 results. This suggests that in A2780, during the progression of the MOA of **6**, loss of adherence occurs in parallel or before ΔΨm loss. In comparison, **22** only manages to induce significant depolarisation at 2X IC$_{50}$, in agreement with the Rh123 results, indicating that the MOA of **22** is not as efficient as **6** following 24 hours exposure and that ΔΨm depolarisation MOA has dependence on the phenyl ring substituents. ΔΨm depolarisation could potentially explain the specificity for cancerous cells. In cancer, mitochondria are often hyperpolarised and overworked, while mitochondrial health is maintained and more tolerable to fluctuations in normal cells[74]. Therefore, the ability of these complexes to induce ΔΨm depolarisation in healthy cells may be reduced.

With ΔΨm depolarisation being indicated as a MOA of **6**, ROS generation in A2780 cells was evaluated by DCFDA staining as these MOA often appear together due to mitochondrial damage. As shown by the increase in DCFDA fluorescence, both complex **6** and **22** induced significant ROS generation, with no significant (p=0.21) difference between the two treatments at IC_{50}. This is consistent with previous evidence of **6** in SKOV3, indicating a similar MOA of ROS generation across the two cell lines. Further, similarity in activity between the two complexes suggests that ROS generating activity is not dependant on the phenyl ring substituent and not entirely dependent on mitochondrial damage. This would be consistent with ROS generation being dependant on the redox capabilities of ruthenium and redox cycling, rather than the activity of the phenyl ligand[75,76]. This is also supported by the DFT predictions of the ruthenium centre and its surrounding ligands exhibiting similar bond lengths, electron densities and Mulliken charges, therefore could be expected exhibit similar properties.

Being an essential MOD, apoptosis was investigated by flow cytometry. Results suggest that apoptosis occurs at 1X IC_{50} concentrations of **6** and **22** with a 6.5% and 2.8% increase in phosphatidylserine presenting cells respectively. Additionally, in agreement with previous results, **6** induced higher levels of cell death than **22**. The presentation of phosphatidylserine is a final stage of apoptotic processes due to relying on Caspase-3 cleavage dependant activation of Xkr8 to flip phosphatidylserine from the inner CCM to the outer CCM phagocytosis initiation[77,78]. This suggests that despite the indications the CCM is being compromised for adherence, other ATP-dependant processes occurring at the CCM are still able to occur.

To confirm apoptotic signalling pathways, Caspase 3/7 activity was measured. While both **6** and **22** induced significant levels of Caspase 3/7 activity, **22** induced a significantly (p<0.05) higher activity levels at IC_{50} following 24 hours exposure. This is contradictory to the antiproliferative activity at 24 hours and apoptosis assay by flow cytometry assay. This could be due to **6** treated cells requiring less Caspase 3/7 activity to initiate apoptosis than **22** at 24 hours, or **6** inducing cell death by additional

caspase-independent mechanisms, which would agree with the suggestions of other MOD occurring in SKOV3 cells as shown in Chapter 3. Conjugation of GSH and induction of ROS allows predisposes cells to type II MOD ferroptosis which relies on the oxidation of CCM lipids which is caspase independent[79,80]. Additionally, the ΔΨm depolarisation seen with **6** can initiate mitophagy to selectively remove damaged mitochondria, which is also caspase independent, and can be encouraged by lower caspase levels[81]. This highlights the differential MOA of the two complexes.

A second reasoning for this activity discrepancy may be due to the nature of the previous assays. Here, antiproliferative activity was measured using the MTT assay, which relies on the conversion of MTT to formazan by mitochondrial oxidoreductase and dehydrogenase enzymes using NAD(P)H as an electron donor[82,83]. Noting the ΔΨm depolarisation of **6** treated cells, there may be less conversion of MTT to formazan, resulting in a lower IC_{50} value. Similarly, the annexin V-PI flow cytometry bias can occur. Apoptosis by flow cytometry is determined by CCM qualities; phosphatidylserine presentation and CCM integrity[84]. However, if the CCM is sufficiently compromised, annexin V stain can penetrate the cell to bind to phosphatidylserine on the inner CCM and fluoresce. This can lead to a false increase in the late apoptotic population through compromise of the non-viable population. Comparing the PI positive populations of **6** and **22** treated cells, while there is a statistically significant (p<0.05) difference, the PI positive population of complex **6** treated cells is still less than 10% and the populations differ by 2.3%. This suggests that the primary reasoning in differing Caspase 3/7 activity is likely due to differing MOA rather than experimental shortfalls.

Cell cycle arrest by flow cytometry indicates that both **6** and **22** induce a G_1 arrest to a similar extent when treated equipotently by inducing a decrease in G_2/M population. G_1 arrest is canonical of several traits including DNA damage, nutrient restriction, toxin signalling and age initiated by signalling from cyclin-dependant kinases and other tumour suppressor genes[85,86]. Here, in the case of **6** and **22** it is possible that arrest could be initiated by downstream signalling of type I death through P130CAS

cleavage by Caspase 3 and P21WAF/CCP1 transcription inhibition, leading to G_1 arrest[87]. Yet, considering the many inducers of G_1 arrest, it is not possible to determine a singular cause, or if multiple mechanisms compound to induce arrest. The latter is more likely due to the multifrontal MOA of these complexes and other similar organometallic complexes and the highly interconnected signalling pathways on cyclin dependant kinase–RB–E2F axis in addition to P130CAS cleavage pathways to induce G_1 arrest[33,88–90].

ICP-MS can be used to assess the influx/efflux and total accumulation of a complex. However as an indirect method by measuring the metal, not the complex, no information on speciation can be ascertained[91]. A2780 cells treated with **6** and **22** showed a substantial increase in ruthenium content, further, that cells treated with **6** exhibited a significantly higher concentration of ruthenium compared to **22** treated cells. This supports that potency is correlated with ruthenium uptake with **6** being more potent than **22** at 24 hours, a trend often seen with organometallic complexes[33,92–95].

In extension to total ruthenium accumulation of these complexes, time and temperature dependant accumulation was done to assess energy-dependant uptake and uptake efficiency[96,97]. Time dependant assays show that ruthenium accumulates faster in **6** treated cells than in **22** treated cells. This suggests that the uptake of complex **6** is more efficient than **22**, and/or that the efflux of **6** is less effective than **22**. Further, temperature dependant accumulation demonstrates that neither complex has substantial ruthenium accumulation at 277 K while having considerable uptake at 310 K. This suggests that both complexes rely on an active uptake due to both complexes having 7% total accumulation at 6 hours at 277K. Work here also agrees with previous results for **22**, despite differences in treatment concentration explaining differences in total accumulation, similar conclusions are made with accumulation being energy dependant with A2780 cells experiencing decreased accumulation at colder temperatures[97].

Influx/efflux mechanisms in cancer cells are highly important in resistance mechanisms, and highly notable in EOC where 80% of advanced disease patients develop resistance to first line therapies with relapse within two years[98,99]. CDDP uptake has been previously observed to be a predominantly active process, requiring ATP, with minor reliance on passive diffusion, demonstrated by decreased accumulation in decreased temperature experiments and inhibition/saturation of ATP-dependant transporters including CRT1 and Na^+/K^+ ion transporters[97,99,100]. Meaning both complexes **6** and **22** could utilise one or several of these transporters in their uptake.

In addition, there is also increased efflux of CDDP though MRP1-5, MRP-2 and ATP7A[97,100]. ATP-dependant efflux was previously suggested to be a potential mechanism of **22** expulsion following co-treatment with the ATP-depleting agent antimycin A[97]. The requirement of ATP depletion for accumulation is consistent with other results seen here. ΔΨm depolarisation induced by **6** can lead to a decreased output of ATP in the cell through aerobic respiration. Therefore, potentially, once **6** enters into the cell, decreased ATP levels can lead to the decreased efflux though ATP-dependant ABC-transporters such as MRP2 and MRP1-5[97,100]. However, noting the ATP-dependant presentation of phosphatidylserine seen in the apoptosis assay, this suggests that despite adherence reduction and CCM contraction, ATP-dependant processes can still occur at the CCM and efflux is dependent on multiple requirements other than ATP. Further the higher IC_{50} values of **6** following 72 hours recovery and the interaction with GSH suggest that higher **6** accumulation is more likely due to increased uptake rather than decreased efflux.

Metastasis and invasion are key mechanisms in the progression of cancer development, meaning their inhibition is highly sought after in treatment. Complex **6** was highly effective at preventing both colony formation and invasion, used for evaluating metastasis and invasion respectively[101,102]. This contrasts **22** which exhibited no difference to the untreated control. This further highlights the significant impact of bioisosteric replacements and that despite not affecting any of the physicochemical characteristics

evaluated here that an anti-metastatic/invasive MOA is lost with the substitution of carbon with nitrogen. Similarly seen with the complexes evaluated in Chapter 4, contradictory behaviour between potency and antiinvasive/antimetastatic behaviour is seen. Due to the increasing antiproliferative activity of *22* with the use of recovery time, it could be expected that in turn antiproliferative activity would continue in the wound healing and colony formation assays leading to reduced closure and formation. However, this does not occur. Noting the behaviour of the two complexes studied in this work, evidence suggests that antimetastatic and antiinvasive behaviour is not centred around the central survival pathways and antiproliferative pathways activated by these complexes. Instead, complex *6* is able to effect additional pathways, or complex *22* is not able to effect pathways involved in invasion, migration, and metastasis. This could include interference with MMP enzymes, membrane adhesion proteins/glycoproteins such as CD44, selectins, N-Cadherin and integrins, epithelial-mesenchymal transition, prevention of anoikic death, or a combination of one or more pathways and molecules not included here due to the complexity of invasive, migratory, and metastatic mechanism[103–105]. This is potentially suggestive of why other ruthenium complexes such as NAMI-A possess anti-metastatic activity without antiproliferative activity.

Notably, the antimetastatic and antiinvasive behaviour differs between SKOV3 and A2780 for *6* treated cells. This may be due to differing surface adhesion molecules present. One example is mesothelin, a ~40 kDa cell surface glycoprotein, has been widely associated with and over expressed in more invasive and aggressive EOC and pancreatic cancers by acting as a CA125 receptor, mediating cell adhesion and activating the NFκB/MAPK/PI3K pathways preventing apoptosis[106–108]. SKOV3 expresses mesothelin on the CMM while A2780 is mesothelin negative[109,110]. However, due to the highly complex nature of invasion and metastasis, the lesser response in the colony formation and wound healing assay in SKOV3 in Chapter 3 compared to A2780 evaluated here may be due to one or many other components that differ between A2780 and SKOV3.

5-4.4: Cytoplasmic membrane differences induced by bioisosteric replacement

After noting the reduced attached cell populations and CCM effects in previous assays, the CCM was investigated in more detail. Cell detachment following 24 hours exposure to complex *6*, *22* or CDDP demonstrates that of the treatments evaluated here, only *6* treated cells exhibit an increase in the detached population. Plastics for tissue culture has been highly developed to allow for optimal growth of cells. Cultureware, including the plasticware used in this work, is primarily polystyrene, surface treated to generate highly energetic oxygen groups including hydroxyl, carboxyl and aldehyde groups (Figure 4-64), by exposure to corona discharge or other methods[111,112]. These oxygen groups allow for the binding of predominantly fibronectin, in addition to other ECM proteins from media serum or cellular secretions, to which cells attach[113]. EOC cells have been shown to secrete collagen-I, collagen-XI and fibronectin in addition to other proteins and proteoglycans to improve binding[17]. Furthermore that the predominant ECM protein scaffolds for EOC are collagen-I, fibronectin and laminin[17]. This suggests that the detachment of *6* may be due to the disruption of these cell-cell and cell-plasticware/ECM adhesion junctions with a predominant culprit potentially being compromised in fibronectin binding, but also possibly disruption to the phospholipid bilayer that these junctions reside in.
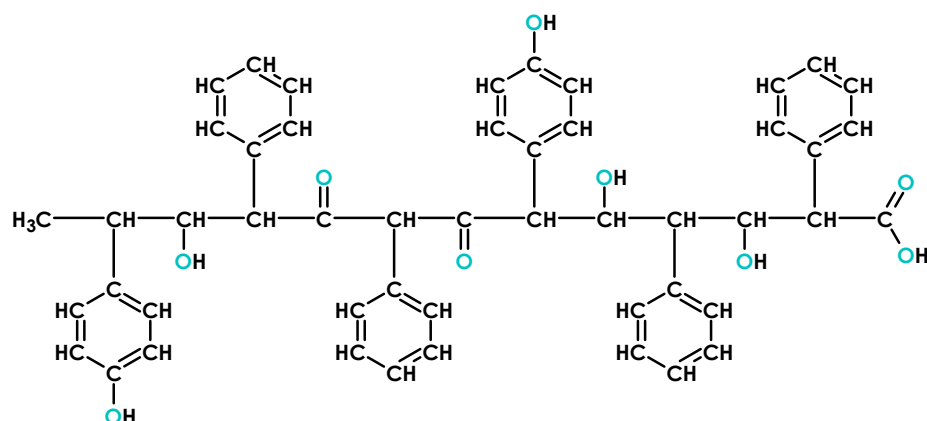
Figure 4-64: Model molecular structure of the surface of polystyrene tissue culture plasticware following treatment with corona discharge or other methods[111,112]. The oxygen groups in blue are common binding points to which extracellular matrix proteins or cells can directly bind to allowing for cell monolayer adherence.

With the cell detachment of A2780 cells treated with complex *6* demonstrated, CCM morphology was evaluated with a lipophilic carbocyanine dye which fluoresces when intercalated into the CCM, showing cell morphology but can provide insight into the condition of the CCM (Figure 4-65)[114,115]. Remarkably, with increased concentrations of complex *6*, there was decreased CCM fluorescence in addition to reduced cell size. While *22* treated cells exhibited some decrease in fluorescence, it was not to the extent of *6*. This agrees with the protein content assay where decreased protein levels were seen with increased *6* treatment levels also indicating decreased cell size. It could be assumed that decrease in fluorescence is due compromise in the CCM preventing proper dye intercalation. While this is partially supported by a statistically significant decrease in CCM integrity by PI fluorescence, this only reflects 6.1% of the total *6* treated population exhibiting substantial increase in PI fluorescence. This is not representative of the CCM fluorescence loss which occurs consistently across the observed population. It has been previously noted in pseudo-membrane studies that alterations in the membrane including increased rigidity and acyl hydrophobic mismatching can reduce fluorescence by preventing correct dye intercalation into the phospholipid bilayer[116]. This is highly suggestive of a contraction of the CCM, encouraging compression of the lipid molecules which can contribute to increased CCM rigidity, preventing intercalation shown in Figure 4-65.
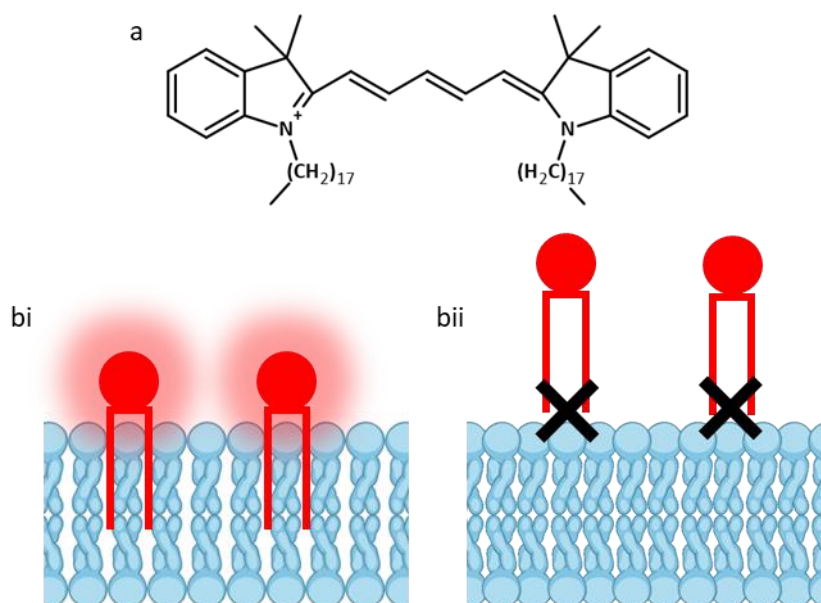
Figure 4-65: a). structure of carbocyanine dye DiI, from which the stain used in this study is derived[114]. b). graphical representation of the mechanism of DiI binding[116]. i). when the membrane is in a disordered liquid state, this allows for gaps to allow for dye intercalation, ii). however, when the membrane becomes more rigid this prevents the intercalation of the dye into the membrane. Due to the mechanism of these dyes, they only fluoresce when intercalated, therefore can provide details on membrane rigidity inversely corelated to dye fluorescence.

Membrane rigidity has been inversely corelated to the uptake of platinum complexes, with increased rigidity of the CCM being a common feature in resistant cells[117]. Further, induced rigidity has been associated with the reduction of ATP-dependant transporter efficacy, including P-Glycoprotein and other ABC transporters. In previous work, membrane rigidity induced by cholesterol introduction, substantially reduced the efficiency of P-Glycoprotein, regardless of level expression[118]. P-Glycoprotein localises to lipid rafts of the CCM due to the preference of liquid-ordered phase membranes, meaning that a balance of CCM rigidity and fluidity is required for function. It was suggested that the increased in rigidity due to cholesterol was impeded P-Glycoprotein function via lipid raft composition disruption. Similar effects have been seen with other membrane changes including lipid phase, thickness and fluidity impeding ABC transporter activity, possibly through ATPase activity of the transporter[119–121]. This could explain the increased accumulation of ruthenium in *6* treated cells in comparison to *22* treated cells, as CCM contraction inducing rigidity could be hindering efflux of the complex through

disruption of ABC transporters via lipid raft structure. In addition, the potential to disrupt P-Glycoprotein function regardless of expression levels is highly significant in the treatment of resistant disease where P-Glycoprotein is often upregulated to assist in the efflux of chemotherapies, as well as the potential of other efflux mechanisms utilised by the cell[98]. This also indicates that *6* has the potential to be effective in resistant disease.

With the indications of complex *6* inducing reduction in adherence, CCM contraction without substantial CCM integrity loss and suggested induced rigidity, ECM binding was investigated, as loss of binding to the ECM is a primary inductor of the type I death mechanism anoikis[122]. When treated with *6* or *22* there was a significant loss of binding to all ECM proteins tested except Collagen-II. The insignificant loss in binding to Collagen-II may be due to the already low levels of Collagen-II present[17]. In EOC, it has been documented that the primary ECM proteins utilised are Collagen-I, Collagen-XI, hyaluronan, Fibronectin and Laminin[17]. As previously discussed, Fibronectin is the primary protein in cell adherence to cultureware through the highly energetic oxygen groups[113]. Therefore, the decreased binding to Fibronectin may explain the reduced bringing to the plasticware. Additionally, Collagen-I has been associated with increased steering ques for migration. Therefore, significant binding loss induced by complex *6* is remarkable due to potentially inhibiting migration, which is supported by wound healing and colony formation assay. However, this is contradictory regarding complex *22* which induces significant Collagen-I loss without any significant reduction in colony formation or wound healing.

One possible explanation for this binding behaviour could be explained by the spheroid assay. Spheroids are often indicted in the development of peritoneal metastasises through by binding through $\beta 1$ integrin connections, hyaluronic acid and CD44[68]. The $\beta 1$ integrin monomer is seen in several integrin dimers which bind several ECM proteins including Collagen-I ($\alpha 1\beta 1$, $\alpha 2\beta 1$, $\alpha 3\beta 1$), Fibronectin ($\alpha 5\beta 1$) and Laminin ($\alpha 3\beta 1$, $\alpha 6\beta 1$, $\alpha 7\beta 1$), all which are upregulated in EOC ECM[122–124]. Here, binding was significantly reduced to all three was significantly reduced upon exposure to both *6* and *22*. Yet, while

Collagen-I was reduced to a similar extent, binding to Fibronectin and Laminin was significantly (p≤0.001) lower by 40% in the **6** treated population in comparison to **22** treated cells. Fibronectin and Laminin binding is heavily associated with the metastasis and invasion of EOC cells[17]. This indicates that Fibronectin and Laminin disconnection are likely significant in the anti-metastatic and antiinvasive MOA of **6**, but also the predominant cause of reduction of adhesion in the microscopy assays conducted here.

Noting the reduction in integrin binding and the suggestion of metastasis and invasion prevention with complex **6**, intravasation and extravasation capability was assessed by a chemotactic Transwell assay. In comparison to both the negative control and CDDP, **6** and **22** achieved a remarkable decrease in the migration of cells at both two and 24 hours and was substantially better than CDDP. The lack of CDDP migration activity, but the significant loss of binding the in ECM assay suggests that both **6** and **22** also interfere with other ECM binding components outside the ECM panel. Potential candidates include other proteins, glycoproteins and proteoglycans of the ECM of the CCM surface including selectins, cadherins, and other integrins including $\alpha_V\beta_1$, $\alpha_V\beta_3$, and $\alpha_4\beta_1$, CD44V, CD24 and L1CAM[125]. Another potential reasoning may be due to **6** and **22** treatment preventing the development of invadopodia, F-actin protrusions used for transendothelial migration through endothelial membranes[126]. If CCM fluidity is reduced, formation of the invadopodia may be impeded through cytoskeletal disruption and prevention of correct F-actin polymerisation. This is supported by the cells that have transmigrated through the insert exhibiting CCM fluorescence, indicating that the cells that have migrated may have retained sufficient CCM fluidity for dye intercalation and to form invadopodia and penetrate the insert pores.

These results agree with previous experiments **6** and **22** with decreased migration due to decreased ECM binding. However, these results also highlight that although **22** can enable short term invasion inhibition, it is eventually lost demonstrated by the intended time frames of the wound healing and

colony formation assay, instead there is a shift to increased cytotoxicity over invasion, highlighting significant MOA differences of the two complexes evaluated here. Differing effect of bioisosteres on metastasis and invasion has previously been observed in the piano-stool complexes RM175 and the osmium variant AFAP51, where RM175 has significant antimetastatic properties in breast cancer cell lines while AFAP51 did not, but no explanation was provided[127]. However, this does further exemplify the significance of bioisosteric screening.

Remarkably, both *6* and *22* reduce transendothelial migration while CDDP did not. While this may be contradictory to the results from the wound healing assay, colony formation and ECM binding assay for CDDP, this could be possible due to two reasons previously discussed. One, being due to other ECM components being utilised that have not been evaluated here, or two, invadopodia still being able to develop. This is supported by previous work of CDDP having widely varied responses effect on invasion and metastasis from preventing through ET1, BTG1 and the Wnt/β-catenin pathway in nasopharyngeal carcinoma, to no effect, to encouraging the development of invasive and metastatic phenotypes through promoted epithelial-mesenchymal transition, increased N-Cadherin and Vimentin, decreased E-Cadherin and ERK pathway activation in EOC[128–131]. The high prevalence of resistant metastatic EOC in relapsed patients which receive platinum therapies is highly indicative that CDDP does not prevent metastasis in patients, therefore indicates that transendothelial migration is not inhibited[132–137].

Table 4-14: Summary of complexes **6** and **22** including their qualities determined through the experiments conducted in Chapter 5 in A2780 EOC cells treated at equipotent IC_{50} (★ denotes improved activity over CDDP).

Quality	Complex 6	Complex 22
Name	[Ru(η^6-*p*-Cym)(ImPy-4-*i*Pr)Cl]PF$_6$	[Ru(η^6-*p*-Cym)(ImPy-4-NMe$_2$)Cl]PF$_6$
LogD$_{7.4}$	-0.21	-0.30
Biological interactions	GSH, media, full media	GSH, media, full media
IC$_{50}$ in A2780 (24h) (24+72 h)	24.1µM 44.6 µM	60.5 µM 25.9 µM
Spheroid activity	Yes, 1.13X decrease ★	No, 1.02X decrease
ΔΨm depolarisation	Yes, 96.8% of cells ★	No, 9.38% of cells
ROS Generation	Yes, 1.75X increase ★	Yes, 1.58X increase ★
Cell cycle arrest	G$_1$ arrest	G$_1$ arrest
Apoptosis induction	Early: 5.79%, Late: 3.31%, Non-viable: 6.50% ★	Early: 3.12%, Late: 1.72%, Non-viable: 5.14% ★
Caspase activity	Yes, 1.51X increase ★	Yes, 1.93X increase ★
Metal accumulation	51.2 fg/mL, active uptake ★	22.4 fg/mL, active uptake ★
CMM fluorescence	Substantial loss of fluorescence ★	Small loss of fluorescence
Detachment	Yes, 3.9X increase in detached cells ★	No, 1.4X decrease in detached cells
ECM binding	67% decrease in attachment	38% decrease in attachment
Antiinvasive	Yes, 0.14 mm total closure ★	No, 0.26 mm total closure
Antimetastatic	Yes, 125 colonies ★	No, 462 colonies
Antimigratory	Yes ★	Yes ★

5-5: Conclusion

The work in this chapter further demonstrates the significant effect of bioisosteric replacement in the alteration of potency and MOA. Significant differences were observed in complex potency in several differing cancerous cell lines highlighting the potency of nitrogen and carbon containing ligands. In addition to differing potency, when the carbon containing isopropyl (**6**) and nitrogen containing dimethylamine (**22**) complexes were compared several similar and differing qualities were found and are highlighted in Table 4-14. Furthermore, several qualities of **6** were found to be an improvement over CDDP. Most notable effect of **6** was on the CCM, inducing profound cell detachment, antiinvasive, antimetastatic and antimigratory mechanisms of treated cells **6**, potentially through the loss of fibronectin and laminin binding, in addition to other ECM components.

Loss of ECM binding is an uncommon MOA of ruthenium complexes. NAMI-A is one such example which has been shown to interfere with the β_1 integrin subunit preventing dominantly preventing Fibrin and collagen binding and inhibiting FAK Try397 autophosphorylation[28–30,138]. Despite the extreme differences in between NAMI-A and complex **6** regarding structures, properties and antiproliferative activity, there appears to be some similarity between their MOA. These differences suggest the benefit of a comparable study between NAMI-A and complex **6**. This would provide a more in-depth mechanism of **6** including key molecular targets by assessing the CCM in more detail by exploring CCM lipid quantification and activity against the integrin unit β1.

5-6: References

1. Nicolson, G. L. Cell Membrane Fluid–Mosaic Structure and Cancer Metastasis. *Cancer Res.* **75**, 1169–1176 (2015).
2. Singer, S. J. & Nicolson, G. L. The Fluid Mosaic Model of the Structure of Cell Membranes. *Science,* **175**, 720–731 (1972).
3. Nicolson, G. L. & Ferreira de Mattos, G. The Fluid–Mosaic model of cell membranes: A brief introduction, historical features, some general principles, and its adaptation to current information. *Biochim. Biophys. Acta - Biomembr.* **1865**, 184135–184143 (2023).
4. Skotland, T., Kavaliauskiene, S. & Sandvig, K. The role of lipid species in membranes and cancer-related changes. *Cancer Metastasis Rev.* **39**, 343–360 (2020).
5. Szlasa, W., Zendran, I., Zalesińska, A., Tarek, M. & Kulbacka, J. Lipid composition of the cancer cell membrane. *J. Bioenerg. Biomembr.* **52**, 321–342 (2020).
6. Maxfield, F. R. & Tabas, I. Role of cholesterol and lipid organization in disease. *Nature* **438**, 612–621 (2005).
7. Hegde, R. S. & Keenan, R. J. The mechanisms of integral membrane protein biogenesis. *Nat. Rev. Mol. Cell Biol.* **23**, 107–124 (2022).
8. Thomas, R. & Weihua, Z. Rethink of EGFR in Cancer With Its Kinase Independent Function on Board. *Front. Oncol.* **9**, 1–16 (2019).
9. Peterson, Y. K. & Luttrell, L. M. The Diverse Roles of Arrestin Scaffolds in G Protein–Coupled Receptor Signaling. *Pharmacol. Rev.* **69**, 256–297 (2017).
10. Sriram, K. & Insel, P. A. G Protein-Coupled Receptors as Targets for Approved Drugs: How Many Targets and How Many Drugs? *Mol. Pharmacol.* **93**, 251–258 (2018).
11. Kechagia, J. Z., Ivaska, J. & Roca-Cusachs, P. Integrins as biomechanical sensors of the microenvironment. *Nat. Rev. Mol. Cell Biol.* **20**, 457–473 (2019).
12. Hamidi, H. & Ivaska, J. Every step of the way: integrins in cancer progression and metastasis. *Nat. Rev. Cancer* **18**, 533–548 (2018).
13. Cai, X., Wang, K.-C. & Meng, Z. Mechanoregulation of YAP and TAZ in Cellular Homeostasis and Disease Progression. *Front. Cell Dev. Biol.* **9**, 1–12 (2021).
14. Swaminathan, V. & Waterman, C. M. The molecular clutch model for mechanotransduction evolves. *Nat. Cell Biol.* **18**, 459–461 (2016).
15. Monje-Galvan, V. & Klauda, J. B. Peripheral membrane proteins: Tying the knot between experiment and computation. *Biochim. Biophys. Acta - Biomembr.* **1858**, 1584–1593 (2016).
16. Mirsaeidi, M., Gidfar, S., Vu, A. & Schraufnagel, D. Annexins family: insights into their functions and potential role in pathogenesis of sarcoidosis. *J. Transl. Med.* **14**, 1–9 (2016).
17. Cho, A., Howell, V. M. & Colvin, E. K. The Extracellular Matrix in Epithelial Ovarian Cancer – A Piece of a Puzzle. *Front. Oncol.* **5**, 1–16 (2015).
18. Frantz, C., Stewart, K. M. & Weaver, V. M. The extracellular matrix at a glance. *J. Cell Sci.* **123**, 4195–4200 (2010).
19. Jabłońska-Trypuć, A., Matejczyk, M. & Rosochacki, S. Matrix metalloproteinases (MMPs), the main extracellular matrix (ECM) enzymes in collagen degradation, as a target for anticancer drugs. *J. Enzyme Inhib. Med. Chem.* **31**, 177–183 (2016).
20. Villegas-Pineda, J. C. *et al.* Integrins and haptoglobin: Molecules overexpressed in ovarian cancer. *Pathol. - Res. Pract.* **211**, 973–981 (2015).
21. Khalili, A. A. & Ahmad, M. R. A Review of Cell Adhesion Studies for Biomedical and Biological Applications. *International Journal of Molecular Sciences* vol. 16 18149–18184 (2015).
22. Taddei, M. L., Giannoni, E., Fiaschi, T. & Chiarugi, P. Anoikis: an emerging hallmark in health and diseases. *J. Pathol.* **226**, 380–393 (2012).
23. Frisch, S. & Francis, H. Disruption of epithelial cell-matrix interactions induces apoptosis. *J. Cell Biol.* **124**, 619–626 (1994).
24. Paoli, P., Giannoni, E. & Chiarugi, P. Anoikis molecular pathways and its role in cancer progression. *Biochim. Biophys. Acta - Mol. Cell Res.* **1833**, 3481–3498 (2013).
25. Grivennikov, S. I., Greten, F. R. & Karin, M. Immunity, Inflammation, and Cancer. *Cell* **140**, 883–899

(2010).

26. D'Arcy, M. S. Cell death: a review of the major forms of apoptosis, necrosis and autophagy. *Cell Biol. Int.* **43**, 582–592 (2019).

27. Hou, J. *et al.* PD-L1-mediated gasdermin C expression switches apoptosis to pyroptosis in cancer cells and facilitates tumour necrosis. *Nat. Cell Biol.* **22**, 1264–1275 (2020).

28. Pelillo, C. *et al.* Inhibition of adhesion, migration and of α5β1 integrin in the HCT-116 colorectal cancer cells treated with the ruthenium drug NAMI-A. *J. Inorg. Biochem.* **160**, 225–235 (2016).

29. Sava, G. *et al.* Dual Action of NAMI-A in inhibition of solid tumor metastasis: selective targeting of metastatic cells and binding to collagen. *Clin. Cancer Res.* **9**, 1898–905 (2003).

30. Leijen, S. *et al.* Phase I/II study with ruthenium compound NAMI-A and gemcitabine in patients with non-small cell lung cancer after first line therapy. *Invest. New Drugs* **33**, 201–214 (2015).

31. Bergamo, A., Riedel, T., Dyson, P. J. & Sava, G. Preclinical combination therapy of the investigational drug NAMI-A+ with doxorubicin for mammary cancer. *Invest. New Drugs* **33**, 53–63 (2015).

32. Bacac, M. *et al.* The hydrolysis of the anti-cancer ruthenium complex NAMI-A affects its DNA binding and antimetastatic activity: an NMR evaluation. *J. Inorg. Biochem.* **98**, 402–412 (2004).

33. Romero-Canelón, I., Salassa, L. & Sadler, P. J. The Contrasting Activity of Iodido versus Chlorido Ruthenium and Osmium Arene Azo- and Imino-pyridine Anticancer Complexes: Control of Cell Selectivity, Cross-Resistance, p53 Dependence, and Apoptosis Pathway. *J. Med. Chem.* **56**, 1291–1300 (2013).

34. Hearn, J. M. *et al.* Pharmaco-genomic investigations of organo-iridium anticancer complexes reveal novel mechanism of action. *Metallomics* **10**, 93–107 (2018).

35. Liu, Z. *et al.* Contrasting Reactivity and Cancer Cell Cytotoxicity of Isoelectronic Organometallic Iridium(III) Complexes. *Inorg. Chem.* **50**, 5777–5783 (2011).

36. Liu, Z. & Sadler, P. J. Organoiridium Complexes: Anticancer Agents and Catalysts. *Acc. Chem. Res.* **47**, 1174–1185 (2014).

37. Romero-Canelón, I. DESIGN AND MECHANISM OF ACTION OF ORGANOMETALLIC ANTICANCER COMPLEXES. (University of Warwick, 2012).

38. Bergamo, A. *et al.* In vivo tumour and metastasis reduction and in vitro effects on invasion assays of the ruthenium RM175 and osmium AFAP51 organometallics in the mammary cancer model. *J. Inorg. Biochem.* **104**, 79–86 (2010).

39. Eisenhauer, E. A. *et al.* New response evaluation criteria in solid tumours: Revised RECIST guideline (version 1.1). *Eur. J. Cancer* **45**, 228–247 (2009).

40. Fu, Y. *et al.* Organometallic osmium arene complexes with potent cancer cell cytotoxicity. *J. Med. Chem.* **53**, 8192–8196 (2010).

41. Sun, S. & Fu, J. Methyl-containing pharmaceuticals: Methylation in drug design. *Bioorganic Med. Chem. Lett.* **28**, 3283–3289 (2018).

42. Pastuszko, A., Majchrzak, K., Czyz, M., Kupcewicz, B. & Budzisz, E. The synthesis, lipophilicity and cytotoxic effects of new ruthenium(II) arene complexes with chromone derivatives. *J. Inorg. Biochem.* **159**, 133–141 (2016).

43. Aktara, M. N., Nayim, S., Sahoo, N. K. & Hossain, M. The synthesis of thiol-stabilized silver nanoparticles and their application towards the nanomolar-level colorimetric recognition of glutathione. *New J. Chem.* **43**, 13480–13490 (2019).

44. Kar, B. *et al.* GSH-resistant and highly cytoselective ruthenium(ii)-p-cymene-(imidazo[4,5-f][1,10]phenanthrolin-2-yl)phenol complexes as potential anticancer agents. *Dalt. Trans.* **50**, 10369–10373 (2021).

45. Kausar, H. *et al.* Cucurbitacin B potently suppresses non-small-cell lung cancer growth: Identification of intracellular thiols as critical targets. *Cancer Lett.* **332**, 35–45 (2013).

46. Mondal, A. & Paira, P. Hypoxia efficient and glutathione-resistant cytoselective ruthenium(ii)-p-cymene-arylimidazophenanthroline complexes: biomolecular interaction and live cell imaging. *Dalt. Trans.* **49**, 12865–12878 (2020).

47. Mondal, A. *et al.* DNA targeting half sandwich Ru(ii)-p-cymene-N^N complexes as cancer cell imaging and terminating agents: influence of regioisomers in cytotoxicity. *Dalt. Trans.* **50**, 979–997 (2021).

48. Blair, I. A. Analysis of endogenous glutathione-adducts and their metabolites. *Biomed. Chromatogr.* **24**, 29–38 (2010).

49. Fischer, M. Census and evaluation of p53 target genes. *Oncogene* **36**, 3943–3956 (2017).

50. Lohse, I. *et al.* BRCA1 and BRCA2 mutations sensitize to chemotherapy in patient-derived pancreatic

cancer xenografts. *Br. J. Cancer* **113**, 425–432 (2015).

51. Skripova, V., Vlasenkova, R., Zhou, Y., Astsaturov, I. & Kiyamova, R. Identification of New Regulators of Pancreatic Cancer Cell Sensitivity to Oxaliplatin and Cisplatin. *Molecules* **27**, 1289–1299 (2022).

52. UK Health Security Agency. Cell line profile Ovarian Cancer Cell Like A2780. *ECACC catalogue* https://www.culturecollections.org.uk/media/113526/a2780-cell-line-profile.pdf.

53. Lee, J.-G., Ahn, J.-H., Jin Kim, T., Ho Lee, J. & Choi, J.-H. Mutant p53 promotes ovarian cancer cell adhesion to mesothelial cells via integrin β4 and Akt signals. *Sci. Rep.* **5**, 1–12 (2015).

54. Lu, X., Errington, J., Curtin, N. J., Lunec, J. & Newell, D. R. The impact of p53 status on cellular sensitivity to antifolate drugs. *Clin. cancer Res.* **7**, 2114–2123 (2001).

55. Mullany, L. K. *et al.* Specific TP53 Mutants Overrepresented in Ovarian Cancer Impact CNV, TP53 Activity, Responses to Nutlin-3a, and Cell Survival. *Neoplasia* **17**, 789–803 (2015).

56. Yaginuma, Y. & Westphal, H. Abnormal structure and expression of the p53 gene in human ovarian carcinoma cell lines. *Cancer Res.* **52**, 4196–4199 (1992).

57. Yuan, Z. *et al.* The p53 Upregulated Modulator of Apoptosis (PUMA) Chemosensitizes Intrinsically Resistant Ovarian Cancer Cells to Cisplatin by Lowering the Threshold Set by Bcl-xL and Mcl-1. *Mol. Med.* **17**, 1262–1274 (2011).

58. Kelland, L. R. *et al.* Mini-review: discovery and development of platinum complexes designed to circumvent cisplatin resistance. *J. Inorg. Biochem.* **77**, 111–115 (1999).

59. Mon, M. T., Yodkeeree, S., Punfa, W., Pompimon, W. & Limtrakul, P. Alkaloids from *Stephania venosa* as Chemo-Sensitizers in SKOV3 Ovarian Cancer Cells *via* Akt/NF-κB Signaling. *Chem. Pharm. Bull.* **66**, 162–169 (2018).

60. Olver, I. *et al.* The timeliness of patients reporting the side effects of chemotherapy. *Support. Care Cancer* **26**, 3579–3586 (2018).

61. Qiao, J., Liu, Z. & Fu, Y.-X. Adapting conventional cancer treatment for immunotherapy. *J. Mol. Med.* **94**, 489–495 (2016).

62. Oun, R., Moussa, Y. E. & Wheate, N. J. The side effects of platinum-based chemotherapy drugs: a review for chemists. *Dalt. Trans.* **47**, 6645–6653 (2018).

63. Hildebrandt, J. *et al.* Highly Cytotoxic Osmium(II) Compounds and Their Ruthenium(II) Analogues Targeting Ovarian Carcinoma Cell Lines and Evading Cisplatin Resistance Mechanisms. *Int. J. Mol. Sci.* **23**, 4976–5005 (2022).

64. Păunescu, E., Soudani, M., Clavel, C. M. & Dyson, P. J. Varying the metal to ethacrynic acid ratio in ruthenium(ii)/osmium(ii)-p-cymene conjugates. *J. Inorg. Biochem.* **175**, 198–207 (2017).

65. Teixeira-Guedes, C., Brás, A. R., Teixeira, R. G., Valente, A. & Preto, A. Ruthenium(II)–Cyclopentadienyl-Derived Complexes as New Emerging Anti-Colorectal Cancer Drugs. *Pharmaceutics* **14**, 1293–1313 (2022).

66. Murray, B. S., Babak, M. V, Hartinger, C. G. & Dyson, P. J. The development of RAPTA compounds for the treatment of tumors. *Coord. Chem. Rev.* **306**, 86–114 (2016).

67. Shield, K., Ackland, M. L., Ahmed, N. & Rice, G. E. Multicellular spheroids in ovarian cancer metastases: Biology and pathology. *Gynecol. Oncol.* **113**, 143–148 (2009).

68. Shishido, A. *et al.* Mesothelial cells facilitate cancer stem-like properties in spheroids of ovarian cancer cells. *Oncol. Rep.* **40**, 2105–2114 (2018).

69. Raghavan, S. *et al.* Formation of stable small cell number three-dimensional ovarian cancer spheroids using hanging drop arrays for preclinical drug sensitivity assays. *Gynecol. Oncol.* **138**, 181–189 (2015).

70. Ruppen, J. *et al.* A microfluidic platform for chemoresistive testing of multicellular pleural cancer spheroids. *Lab Chip* **14**, 1198–1205 (2014).

71. Huang, M., Camara, A. K. S., Stowe, D. F., Qi, F. & Beard, D. A. Mitochondrial Inner Membrane Electrophysiology Assessed by Rhodamine-123 Transport and Fluorescence. *Ann. Biomed. Eng.* **35**, 1276–1285 (2007).

72. Perelman, A. *et al.* JC-1: alternative excitation wavelengths facilitate mitochondrial membrane potential cytometry. *Cell Death Dis.* **3**, 430–430 (2012).

73. Kane, M. S. *et al.* Current mechanistic insights into the CCCP-induced cell survival response. *Biochem. Pharmacol.* **148**, 100–110 (2018).

74. Grasso, D., Zampieri, L. X., Capelôa, T., Van de Velde, J. A. & Sonveaux, P. Mitochondria in cancer. *Cell Stress* **4**, 114–146 (2020).

75. Soldevila-Barreda, J. J., Romero-Canelón, I., Habtemariam, A. & Sadler, P. J. Transfer hydrogenation

catalysis in cells as a new approach to anticancer drug design. *Nat. Commun.* **6**, 1–9 (2015).

76. Zhang, J. *et al.* Organometallic gold(I) and gold(III) complexes for lung cancer treatment. *Front. Pharmacol.* **13**, 1–19 (2022).

77. Mariño, G. & Kroemer, G. Mechanisms of apoptotic phosphatidylserine exposure. *Cell Res.* **23**, 1247–1248 (2013).

78. Segawa, K. & Nagata, S. An Apoptotic 'Eat Me' Signal: Phosphatidylserine Exposure. *Trends Cell Biol.* **25**, 639–650 (2015).

79. Cao, J. Y. & Dixon, S. J. Mechanisms of ferroptosis. *Cell. Mol. Life Sci.* **73**, 2195–2209 (2016).

80. Li, J. *et al.* Ferroptosis: past, present and future. *Cell Death Dis.* **11**, 1–13 (2020).

81. Youle, R. J. & Narendra, D. P. Mechanisms of mitophagy. *Nat. Rev. Mol. Cell Biol.* **12**, 9–14 (2011).

82. Ghasemi, M., Turnbull, T., Sebastian, S. & Kempson, I. The MTT Assay: Utility, Limitations, Pitfalls, and Interpretation in Bulk and Single-Cell Analysis. *Int. J. Mol. Sci.* **22**, 12827–12857 (2021).

83. Chacon, E., Acosta, D. & Lemasters, J. J. Primary Cultures of Cardiac Myocytes as In Vitro Models for Pharmacological and Toxicological Assessments. in *In Vitro Methods in Pharmaceutical Research* (eds. Castell, J. V & Gómez-Lechón, M. J. B. T.) 209–223 (Elsevier, 1997).

84. Crowley, L. C., Marfell, B. J., Scott, A. P. & Waterhouse, N. J. Quantitation of Apoptosis and Necrosis by Annexin V Binding, Propidium Iodide Uptake, and Flow Cytometry. *Cold Spring Harb. Protoc.* **11**, 953–957 (2016).

85. Matthews, H. K., Bertoli, C. & de Bruin, R. A. M. Cell cycle control in cancer. *Nat. Rev. Mol. Cell Biol.* **23**, 74–88 (2022).

86. Pietenpol, J. A. & Stewart, Z. A. Cell cycle checkpoint signaling: *Toxicology* **181–182**, 475–481 (2002).

87. Pérez-Sayáns, M. *et al.* The role of p21Waf1/CIP1 as a Cip/Kip type cell-cycle regulator in oral squamous cell carcinoma (Review). *Med. oral* **18**, 219–225 (2013).

88. Chen, H., Landen, C. N., Li, Y., Alvarez, R. D. & Tollefsbol, T. O. Enhancement of Cisplatin-Mediated Apoptosis in Ovarian Cancer Cells through Potentiating G2/M Arrest and p21 Upregulation by Combinatorial Epigallocatechin Gallate and Sulforaphane. *J. Oncol.* **2013**, 1–9 (2013).

89. Ghosh, S. Cisplatin: The first metal based anticancer drug. *Bioorg. Chem.* **88**, 1–20 (2019).

90. Kent, L. N. & Leone, G. The broken cycle: E2F dysfunction in cancer. *Nat. Rev. Cancer* **19**, 326–338 (2019).

91. Galé, A. *et al.* Beyond Single-Cell Analysis of Metallodrugs by ICP-MS: Targeting Cellular Substructures. *Int. J. Mol. Sci.* **22**, 9468–9480 (2021).

92. Ballesta, A. *et al.* Kinetic analysis of the accumulation of a half-sandwich organo-osmium pro-drug in cancer cells. *Metallomics* **11**, 1648–1656 (2019).

93. Nikolić, S. *et al.* Strong in Vitro Cytotoxic Potential of New Ruthenium–Cymene Complexes. *Organometallics* **34**, 3464–3473 (2015).

94. Clède, S. *et al.* Influence of the Side-Chain Length on the Cellular Uptake and the Cytotoxicity of Rhenium Triscarbonyl Derivatives: A Bimodal Infrared and Luminescence Quantitative Study. *Chem. – A Eur. J.* **20**, 8714–8722 (2014).

95. Scolaro, C. *et al.* Tuning the hydrophobicity of ruthenium(ii)–arene (RAPTA) drugs to modify uptake, biomolecular interactions and efficacy. *Dalt. Trans.* **43**, 5065–5072 (2007).

96. van Rijt, S. H., Romero-Canelón, I., Fu, Y., Shnyder, S. D. & Sadler, P. J. Potent organometallic osmium compounds induce mitochondria-mediated apoptosis and S-phase cell cycle arrest in A549 non-small cell lung cancer cells. *Metallomics* **6**, 1014–1022 (2014).

97. Romero-Canelón, I., Pizarro, A. M., Habtemariam, A. & Sadler, P. J. Contrasting cellular uptake pathways for chlorido and iodido iminopyridine ruthenium arene anticancer complexes. *Metallomics* **4**, 1271–1279 (2012).

98. Pokhriyal, R., Hariprasad, R., Kumar, L. & Hariprasad, G. Chemotherapy Resistance in Advanced Ovarian Cancer Patients. *Biomark. Cancer* **11**, 1–19 (2019).

99. Eljack, N. D. *et al.* Mechanisms of cell uptake and toxicity of the anticancer drug cisplatin. *Metallomics* **6**, 2126–2133 (2014).

100. Arnesano, F. & Natile, G. Mechanistic insight into the cellular uptake and processing of cisplatin 30 years after its approval by FDA. *Coord. Chem. Rev.* **253**, 2070–2081 (2009).

101. Franken, N. A. P., Rodermond, H. M., Stap, J., Haveman, J. & van Bree, C. Clonogenic assay of cells in vitro. *Nat. Protoc.* **1**, 2315–2319 (2006).

102. Riahi, R., Yang, Y., Zhang, D. D. & Wong, P. K. Advances in Wound-Healing Assays for Probing Collective Cell Migration. *J. Lab. Autom.* **17**, 59–65 (2012).

103. Nakayama, K., Nakayama, N., Katagiri, H. & Miyazaki, K. Mechanisms of Ovarian Cancer Metastasis: Biochemical Pathways. *Int. J. Mol. Sci.* **13**, 11705–11717 (2012).
104. Majidpoor, J. & Mortezaee, K. Steps in metastasis: an updated review. *Med. Oncol.* **38**, 3 (2021).
105. Reymond, N., d'Água, B. B. & Ridley, A. J. Crossing the endothelial barrier during metastasis. *Nat. Rev. Cancer* **13**, 858–870 (2013).
106. Rump, A. *et al.* Binding of Ovarian Cancer Antigen CA125/MUC16 to Mesothelin Mediates Cell Adhesion*. *J. Biol. Chem.* **279**, 9190–9198 (2004).
107. Lv, J. & Li, P. Mesothelin as a biomarker for targeted therapy. *Biomark. Res.* **7**, 1–18 (2019).
108. Hassan, R., Kreitman, R. J., Pastan, I. & Willingham, M. C. Localization of Mesothelin in Epithelial Ovarian Cancer. *Appl. Immunohistochem. Mol. Morphol.* **13**, 243–247 (2005).
109. Klapdor, R. *et al.* Characterization of a Novel Third-Generation Anti-CD24-CAR against Ovarian Cancer. *Int. J. Mol. Sci.* **20**, 660–675 (2019).
110. Li, M. *et al.* Mesothelin is a malignant factor and therapeutic vaccine target for pancreatic cancer. *Mol. Cancer Ther.* **7**, 286–296 (2008).
111. Curtis, A. S., Forrester, J. V, McInnes, C. & Lawrie, F. Adhesion of cells to polystyrene surfaces. *J. Cell Biol.* **97**, 1500–1506 (1983).
112. Ramsey, W. S., Hertl, W., Nowlan, E. D. & Binkowski, N. J. Surface treatments and cell attachment. *In Vitro* **20**, 802–808 (1984).
113. Reid, L. M. & Rojkind, M. [21] New Techniques for Culturing Differential Cells: Reconstituted basement membrane rafts. in *Cell Culture* (eds. Jakoby, W. B. & Pastan, I. H.) vol. 58 263–278 (Academic Press, 1979).
114. Li, Y. *et al.* Direct labeling and visualization of blood vessels with lipophilic carbocyanine dye DiI. *Nat. Protoc.* **3**, 1703–1708 (2008).
115. Axelrod, D. Carbocyanine dye orientation in red cell membrane studied by microscopic fluorescence polarization. *Biophys. J.* **26**, 557–573 (1979).
116. Lubart, Q. *et al.* Lipid vesicle composition influences the incorporation and fluorescence properties of the lipophilic sulphonated carbocyanine dye SP-DiO. *Phys. Chem. Chem. Phys.* **22**, 8781–8790 (2020).
117. Martinho, N., Santos, T. C. B., Florindo, H. F. & Silva, L. C. Cisplatin-Membrane Interactions and Their Influence on Platinum Complexes Activity and Toxicity. *Front. Physiol.* **9**, 1–15 (2019).
118. dos Santos, S. M., Weber, C.-C., Franke, C., Müller, W. E. & Eckert, G. P. Cholesterol: Coupling between membrane microenvironment and ABC transporter activity. *Biochem. Biophys. Res. Commun.* **354**, 216–221 (2007).
119. Wang, F. *et al.* Cetuximab enhanced the efficacy of chemotherapeutic agent in ABCB1/P-glycoprotein-overexpressing cancer cells. *Oncotarget* **6**, 40850–40865 (2015).
120. Sharom, F. J. Complex Interplay between the P-Glycoprotein Multidrug Efflux Pump and the Membrane: Its Role in Modulating Protein Function. *Front. Oncol.* **4**, 1–19 (2014).
121. Neumann, J., Rose-Sperling, D. & Hellmich, U. A. Diverse relations between ABC transporters and lipids: An overview. *Biochim. Biophys. Acta - Biomembr.* **1859**, 605–618 (2017).
122. Adeshakin, F. O. *et al.* Mechanisms for Modulating Anoikis Resistance in Cancer and the Relevance of Metabolic Reprogramming. *Front. Oncol.* **11**, 1–21 (2021).
123. Nishiuchi, R. *et al.* Ligand-binding specificities of laminin-binding integrins: A comprehensive survey of laminin–integrin interactions using recombinant α3β1, α6β1, α7β1 and α6β4 integrins. *Matrix Biol.* **25**, 189–197 (2006).
124. Schaffner, F., Ray, A. M. & Dontenwill, M. Integrin α5β1, the Fibronectin Receptor, as a Pertinent Therapeutic Target in Solid Tumors. *Cancers,* **5**, 27–47 (2013).
125. Sökeland, G. & Schumacher, U. The functional role of integrins during intra- and extravasation within the metastatic cascade. *Mol. Cancer* **18**, 12 (2019).
126. Borriello, L. *et al.* The role of the tumor microenvironment in tumor cell intravasation and dissemination. *Eur. J. Cell Biol.* **99**, 151098 (2020).
127. Bergamo, A. *et al.* In vivo tumour and metastasis reduction and in vitro effects on invasion assays of the ruthenium RM175 and osmium AFAP51 organometallics in the mammary cancer model. *J. Inorg. Biochem.* **104**, 79–86 (2010).
128. Yin, P., Song, G. & Jiang, Z. Cisplatin suppresses proliferation, migration and invasion of nasopharyngeal carcinoma cells in vitro by repressing the Wnt/β-catenin/Endothelin-1 axis via activating B cell translocation gene 1. *Cancer Chemother. Pharmacol.* **81**, 863–872 (2018).

129. Latifi, A. *et al.* Cisplatin treatment of primary and metastatic epithelial ovarian carcinomas generates residual cells with mesenchymal stem cell-like profile. *J. Cell. Biochem.* **112**, 2850–2864 (2011).

130. Lee, T. K. *et al.* Lupeol Suppresses Cisplatin-Induced Nuclear Factor-κB Activation in Head and Neck Squamous Cell Carcinoma and Inhibits Local Invasion and Nodal Metastasis in an Orthotopic Nude Mouse Model. *Cancer Res.* **67**, 8800–8809 (2007).

131. Lee, T. K. *et al.* Correction: Lupeol Suppresses Cisplatin-Induced Nuclear Factor-κB Activation in Head and Neck Squamous Cell Carcinoma and Inhibits Local Invasion and Nodal Metastasis in an Orthotopic Nude Mouse Model. *Cancer Res.* **76**, 2052–2053 (2016).

132. NICE. Ovarian cancer: recognition and initial management. *[Online]* https://www.nice.org.uk/guidance/cg122 (2011).

133. Cancer Research, U. K. Ovarian cancer statistics. *[Online]* https://www.cancerresearchuk.org/health-professional/cancer-statistics/statistics-by-cancer-type/ovarian-cancer#heading-Zero (2022).

134. Hirose, S. *et al.* Retrospective analysis of sites of recurrence in stage I epithelial ovarian cancer. *J. Gynecol. Oncol.* **29**, 1–11 (2018).

135. Al-Alem, L. & Curry, T. E. Ovarian cancer: involvement of the matrix metalloproteinases. *Reproduction* **150**, 55–64 (2015).

136. Lheureux, S., Gourley, C., Vergote, I. & Oza, A. M. Epithelial ovarian cancer. *Lancet* **393**, 1240–1253 (2019).

137. Rocconi, R. P. *et al.* Long-Term Follow-Up of Gemogenovatucel-T (Vigil) Survival and Molecular Signals of Immune Response in Recurrent Ovarian Cancer. *Vaccines* **9**, 894–910 (2021).

138. Khoshnoodi, J., Pedchenko, V. & Hudson, B. G. Mammalian collagen IV. *Microsc. Res. Tech.* **71**, 357–370 (2008).

Chapter 6 - Conclusions and Future Work

Future Chemical And Biological Experimentation Of Bioisosteres In Ruthenium Piano-Stool Complexes Against Cancer

6-1: Conclusions of bioisosteric replacements used in this work

Bioisosteric replacement is a powerful tool in drug design with small structural changes inducing significant mechanism and potency changes. In metallic complexes, they are widely used to improve potency and shift MOA[1–6]. In this work, the use of bioisosteric replacement was highly effective at achieving both with surprising and beneficial results.

In Chapter 3, the effectiveness of methyl bioisosteres was evaluated and the MOD of complex **6** [Ru(η^6-*p*-Cym)(ImPy-4-*i*Pr)Cl]PF$_6$ was investigated. Results of this chapter highlight that the position of the methyl group can hinder the chemical reactivity of the complex due to steric hindrance in the *ortho* position. Therefore, for future work in similar complexes, phenyl substituents in this position are not recommended. Additionally, MOD screening of complex **6** demonstrates the highly multimodal MOA of this complex inducing $\Delta\Psi$m depolarisation, ROS induction and G$_1$ arrest leading to apoptosis with minor autophagy and ferroptosis. Further experimentation also demonstrated that complex **6** used in combination treatment with other toxic and non-toxic treatments can significantly taking advantage of ferroptotic mechanisms improve antiproliferative activity in EOC.

In Chapter 4, the potential of a spacer within the ImPy ligand of ruthenium piano-stool complexes was assessed. Antiproliferative screening demonstrated the significant potential of the spacer being able to increase the potency in most variants evaluated. To further ascertain the difference between the unlinked and linked complexes, **7** [Ru(η^6-*p*-Cym)(ImPy-Ph)I]PF$_6$ and **9** [Ru(η^6-*p*-Cym)(ImPy-Bn)I]PF$_6$ were taken forward for MOA screening. Initial MOA and DNA damage screening of these complexes highlighted the significant difference in mechanisms between the two complexes. This difference is suggested to be resultant of the disrupted resonance of complex **9**. Experiments suggests that complex **7** has a short, aggressive MOA inducing dsDNA breaks, while complex **9** has a longer, gentler MOA

inducing ssDNA breaks that accumulate over time. With this knowledge, complexes can be adjusted to allow activation time of future complexes.

In Chapter 5, the effect of atom bioisosteric replacement on the phenyl ring of ImPy ruthenium piano-stool complexes was considered. While no physiochemical differences were induced by atom replacement in the ImPy ligand substituent, antiproliferative activity was found to be substantially different between the different complexes. The most effective complexes **6** [Ru(η^6-*p*-Cym)(ImPy-4-iPr)Cl]PF$_6$ and **22** [Ru(η^6-*p*-Cym)(ImPy-4-N(CH$_3$)$_2$)Cl]PF$_6$ were then taken forward for MOA comparison screening. The most remarkable result from MOA comparison screening was the effect on the CCM, with complex **6** possessing significant antimetastatic, antiinvasive and antimigratory activity in addition to antiproliferative in comparison to **22** which did not share these MOA. This highlights the importance of screening of potential complexes as even one small difference in a complex can have significant repercussions in activity.

6-2: Potential future work using bioisosteric replacements in organometallics

There were some limits to the work done during this project and would be worth considering for future work. These can be divided into further chemical work and further biological work.

6-2.1: Potential future chemistry

A variety of physiochemical experiments were conducted including DFT, UV-Vis and LogD$_{7.4}$. However, further experimentation of the complexes here would be warranted. This would include the x-ray crystallography of the lead complexes would be warranted to support the findings of the DFT calculations. This would be particularly useful for the work done in Chapter 4 to confirm the disruption of resonance across the ImPy-Bn ligand. Additional NMR experiments for biomolecule interactions would also be warranted to confirm binding and elucidate the nature of interaction. For example, the interaction of complex **6** with GSH in addition to complexes **7** and **9** to ctDNA and 9EtG. Results of this would contribute to the explanation of the molecular MOA of these complexes.

Figure 6-1: a). Complex [Ru(η^6-p-Cym)(ImPy-Bn-iPr)I]PF$_6$ that would warrant further examination. b). Osmium complex FY26 developed by Dr Ying Fu.
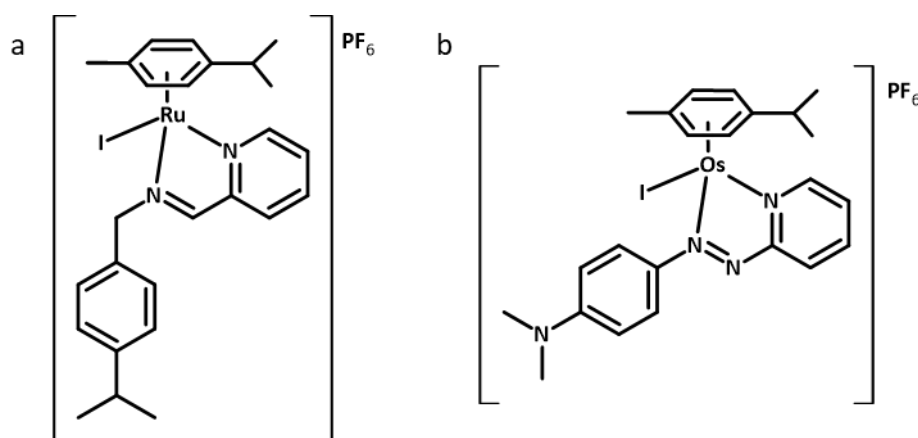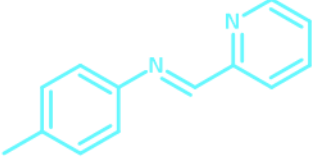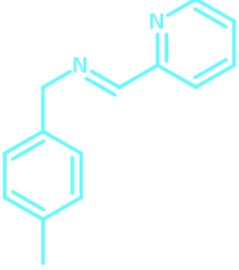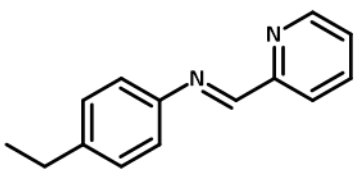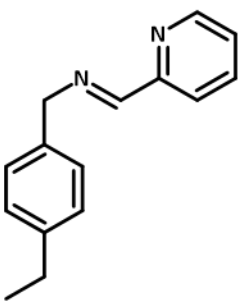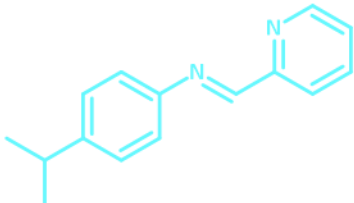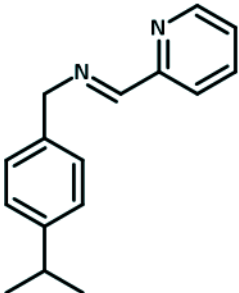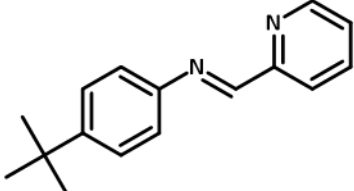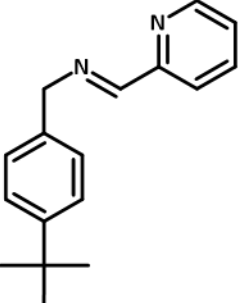

Within the scope of this project, three families, totalling 22 complexes from 19 ligands were

synthesised. Culminating all the work here, one particular complex of interest would be [Ru(η^6-p-Cym)(ImPy-Bn-iPr)I]PF$_6$ (Figure 6-a). Due to the beneficial effects noted from Chapter 4 by using a CH$_2$ spacer and an iodo monodentate ligand shown by complex **9**, combined with the significant MOA demonstrated by the bioisosteric replacement on the phenyl ring shown by complex **6**, this complex has the potential to be highly potent. However, noting the loss of antiinvasive and antimetastatic activity of linked complexed, the MOA of this complex cannot be predicted considering the MOA of **6**.

In extension to [Ru(η^6-p-Cym)(ImPy-Bn-iPr)I]PF$_6$, examination of the series of complexes shown in Table 4-15 would be highly warranted. This series would evaluate the methyl moiety by saturation of a single phenyl ring substitution. The work in Chapter 3 demonstrated the significant increase in potency between complex **2** and **6**, and it would be expected that this trend would continue with full saturation to the *tert*-butyl- substituent. This coupled with the potential of the CH$_2$ spacer would be highly interesting to investigate to observe if CCM and antimetastatic based MOA are maintained or shifted to other MOA.
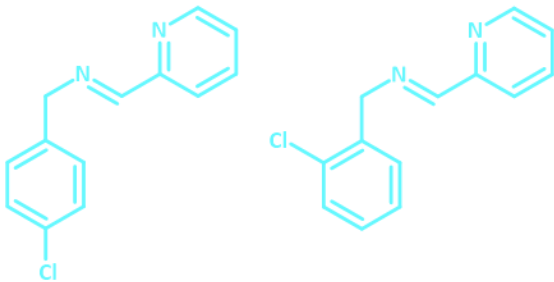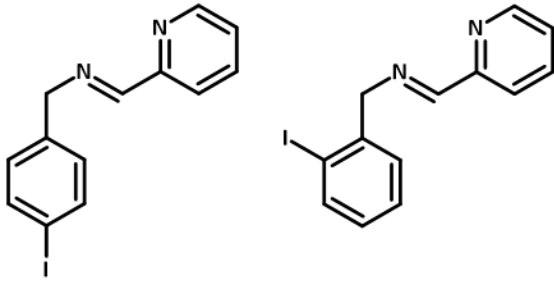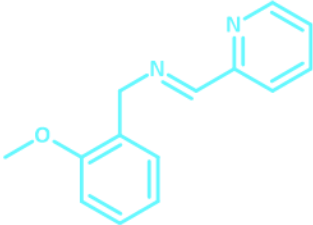
Table 4-15: A series of complexes for potential future experimentation based on the cumulative evidence of complexes **6** and **9** to improve the potency of ruthenium piano-stool complexes. Ligands in blue denote ligands synthesised in this work.

Ligands worthy of future consideration		Aniline/amine derivative	Oher information
		Ligands already synthesised in this work	Cl monodentate ligand variant synthesised in this work. Consider I variant
		4-Ethylaniline / 4-Ethylbenzyl amine in reaction shown in Scheme 2-1	Both Cl and I monodentate ligand variants should be considered
		Unlinked ligand already synthesised in this work / 4-isopropylbenzyl amine in reaction shown in Scheme 2-1	Cl monodentate ligand variant synthesised in this work. Consider I variant
		4-tert-Butylaniline / 4-tert-butylbenzyl amine in reaction shown in Scheme 2-1	Both Cl and I monodentate ligand variants should be considered

In this work, there was limited work on the use of halogens as bioisosteric replacements in the phenyl ring with only chlorine being explored. Early work not discussed in this thesis has highlighted the potential of iodine as a phenyl ring substituent (Table 4-16). Comparison to chlorine and potentially

other halogens such as fluorine and bromine would also potentially be interesting to investigate electron withdrawal from the phenyl ring and the subsequent effect on potency, especially in complexes with a CH_2 spacer due to the disrupted resonance. In extension of this, the iodo counterpart of complex *16* may also warrant further investigation due to the increased potency the phenyl ring substituent in the *ortho* position offered in linked complexes.

Table 4-16: A series of complexes for future potential experimentation based on the antiproliferative screening in Chapter 4. Ligands in blue denote ligands synthesised in this work.

Ligands worthy of future consideration	Aniline/amine derivative	Other information
	Ligands already synthesised in this work	Cl monodentate ligand variant synthesised in this work. Consider I variant.
	4-Iodo benzylamine / 2-Iodobenzyl amine in reaction shown in Scheme 2-1	Both Cl and I monodentate ligand variants should be considered
	Ligand already synthesised in this work in reaction shown in Scheme 2-1	Cl monodentate ligand variant synthesised in this work. Consider I variant.

In addition to the ligands suggested other bioisosteric replacements of the rest of the complex were not investigated here. One such example is the metal centre. Here, ruthenium was used due to its iron mimicking, prodrug and MOA properties[7,8]. However, other metals such as osmium and iridium have

also been found to be highly effective in similar structures[16,19,20–28]. The principal example which is structurally similar to the complexes investigated here is FY26 (Figure 6-b) which has exhibited nanomolar IC_{50} concentrations in many different cancerous cell lines and significant efficacy in *in vivo* work[19–21]. This may be due the aqueous chemistry behaviour of the metals. It has been documented that third row metals are much more inert than second row metals, and in the case of ruthenium and osmium, the latter can react 100X slower in hydrolysis/aquation and biomolecule reactions[22,23]. Therefore, in complexes such as *6* where a delay in reactivity could be of benefit to prevent reaction with GSH, media and full media, an increase in potency could be seen.

Other arene rings in variable complexity from benzene to biphenyl to multiring structures can also be evaluated. However, alteration of the arene ring bioisostere has been extensively reviewed in the literature and some trends have been observed[6,16,24–26]. For example, in several papers biphenyl complexes have higher antiproliferative activity than *p*-cymene complexes with some potency increases being up to 5.8X, with further extension to terphenyl being more potent[6,24]. Other ring structures including pentamethylcyclopentadiene and pentamethylcyclopentadiene-biphenyl have also been investigated, yet in these structures, smaller ring structures are more potent[16]. Therefore, it can be concluded that the effect of the phenyl ring is highly dependent on the complex and the screening cell line. From similar complexes evaluated in the literature, if other arene ring structures were to be investigated to increase potency, a biphenyl ring would be recommended.

6-2.2: Potential future biology

A wide variety of biological experiments were conducted in this work, however, there are still some questions regarding the MOA of these complexes. In Chapter 3, while several MOD were evaluated for complex *6*, however, this was only a selection of possible MOD. While not all MOD are appropriate to evaluate such as immune system-based death including NEtosis and pyroptosis, other mechanisms such as mitochondrial parthantosis and mitoptosis should be investigated in future work[27]. In addition,

noting the significant indications of anoikic death in Chapter 5, the molecular mechanisms of this should be investigated with specific attention to signalling molecules and essential integrins used in the induction of anoikis such as analysis of the β1 integrin and integrins associated with fibronectin binding, PERK and Beclin1, and comparison to NAMI-A by evaluation of FAK autophosphorylation[7,28–31]. Other MOD should also be confirmed with further molecular work confirming the extent of autophagy by for example monitoring of phosphorylation ATG16L1 using an pATG16L1s278 antibody and ferroptosis by for example monitoring ACSL4/TFRC/PTGS2/CHAC1 regulation, DAMP release, or degradation of GPX4/ARNTL/VDAC[32–35].

For Chapter 4, the biggest limitation of this work is the time frame selected for these experiments. For the preliminary MOA and DNA damage experiments, analysis was conducted immediately following 24 hours exposure. This time frame was chosen for comparability with other results in this thesis, previous work and the literature[5,17,36,37]. However, for complex *9* and other similar spacer complexes, this may not be the most appropriate timeframe due to delayed activation. Therefore, repeats of selected experiments including ssDNA and dsDNA damage, ΔΨm and ROS induction and ruthenium accumulation assays should be considered to assess the longer MOA of the spacer complexes.

Noting the significant antiproliferative of complex *9* and if similar activity of the proposed complexes in Table 4-15 and Table 4-16. Following more in-depth determination of the MOA of these complexes, they should be considered for *in vivo* studies to assess not only the antiproliferative, but also any pharmacokinetic properties and side effects that may develop.

Overall, the work in this thesis demonstrates that bioisosteric replacements in organometallic complexes are not only diverse but can yield unpredictable results. Here, the potential of the CH_2 spacer and the isopropyl bioisosteres to increase potency and shift the MOA has been demonstrated. Furthermore, the other trends observed can be used to inform the future of complex design and broaden the field of the use of precious in the fight against cancer.

6-3: References

1. Gottschaldt, M. *et al.* Sugar-Selective Enrichment of a D-Glucose-Substituted Ruthenium Bipyridyl Complex Inside HepG2 Cancer Cells. *ChemBioChem* **11**, 649–652 (2010).
2. Kacsir, I. *et al.* Ruthenium Half-Sandwich Type Complexes with Bidentate Monosaccharide Ligands Show Antineoplastic Activity in Ovarian Cancer Cell Models through Reactive Oxygen Species Production. *Int. J. Mol. Sci.* **22**, 1–38 (2021).
3. Vessières, A. *et al.* A ferrocenyl derivative of hydroxytamoxifen elicits an estrogen receptor-independent mechanism of action in breast cancer cell lines. *J. Inorg. Biochem.* **104**, 503–511 (2010).
4. Aird, R. E. *et al.* In vitro and in vivo activity and cross resistance profiles of novel ruthenium (II) organometallic arene complexes in human ovarian cancer. *Br. J. Cancer* **86**, 1652–1657 (2002).
5. Romero-Canelón, I., Salassa, L. & Sadler, P. J. The Contrasting Activity of Iodido versus Chlorido Ruthenium and Osmium Arene Azo- and Imino-pyridine Anticancer Complexes: Control of Cell Selectivity, Cross-Resistance, p53 Dependence, and Apoptosis Pathway. *J. Med. Chem.* **56**, 1291–1300 (2013).
6. Fu, Y. *et al.* The contrasting chemical reactivity of potent isoelectronic iminopyridine and azopyridine osmium(ii) arene anticancer complexes. *Chem. Sci.* **3**, 2485–2494 (2012).
7. Leijen, S. *et al.* Phase I/II study with ruthenium compound NAMI-A and gemcitabine in patients with non-small cell lung cancer after first line therapy. *Invest. New Drugs* **33**, 201–214 (2015).
8. Guichard, S. M. *et al.* Anti-tumour activity in non-small cell lung cancer models and toxicity profiles for novel ruthenium(II) based organo-metallic compounds. *Biochem. Pharmacol.* **71**, 408–415 (2006).
9. Fu, Y. *et al.* Mirror-Image Organometallic Osmium Arene Iminopyridine Halido Complexes Exhibit Similar Potent Anticancer Activity. *Chem. – A Eur. J.* **19**, 15199–15209 (2013).
10. Fu, Y. *et al.* Organometallic osmium arene complexes with potent cancer cell cytotoxicity. *J. Med. Chem.* **53**, 8192–8196 (2010).
11. Hearn, J. M. *et al.* Potent organo-osmium compound shifts metabolism in epithelial ovarian cancer cells. *Proc. Natl. Acad. Sci.* **112**, 3800–3805 (2015).
12. van Rijt, S. H., Romero-Canelón, I., Fu, Y., Shnyder, S. D. & Sadler, P. J. Potent organometallic osmium compounds induce mitochondria-mediated apoptosis and S-phase cell cycle arrest in A549 non-small cell lung cancer cells. *Metallomics* **6**, 1014–1022 (2014).
13. Liu, Z. *et al.* The Potent Oxidant Anticancer Activity of Organoiridium Catalysts. *Angew. Chemie Int. Ed.* **53**, 3941–3946 (2014).
14. Wang, X. *et al.* A ferroptosis-inducing iridium(III) complex. *Sci. China Chem.* **63**, 65–72 (2020).
15. Li, J. *et al.* Half-Sandwich Iridium and Ruthenium Complexes: Effective Tracking in Cells and Anticancer Studies. *Inorg. Chem.* **57**, 13552–13563 (2018).
16. Štarha, P., Habtemariam, A., Romero-Canelón, I., Clarkson, G. J. & Sadler, P. J. Hydrosulfide Adducts of Organo-Iridium Anticancer Complexes. *Inorg. Chem.* **55**, 2324–2331 (2016).
17. Hearn, J. M. *et al.* Pharmaco-genomic investigations of organo-iridium anticancer complexes reveal novel mechanism of action. *Metallomics* **10**, 93–107 (2018).
18. Du, Q. *et al.* Potent Half-Sandwich Iridium(III) and Ruthenium(II) Anticancer Complexes Containing a P^O-Chelated Ligand. *Organometallics* **37**, 2880–2889 (2018).
19. Kumar, S. A. *et al.* Dose- and time-dependent tolerability and efficacy of organo-osmium complex FY26 and its tissue pharmacokinetics in hepatocarcinoma-bearing mice. *Metallomics* **13**, 1–11 (2021).
20. Ballesta, A. *et al.* Kinetic analysis of the accumulation of a half-sandwich organo-osmium pro-drug in cancer cells. *Metallomics* **11**, 1648–1656 (2019).
21. Romero-Canelón, I., Mos, M. & Sadler, P. J. Enhancement of Selectivity of an Organometallic Anticancer Agent by Redox Modulation. *J. Med. Chem.* **58**, 7874–7880 (2015).
22. Gatti, A. *et al.* Half-Sandwich Arene Ruthenium(II) and Osmium(II) Thiosemicarbazone Complexes: Solution Behavior and Antiproliferative Activity. *Organometallics* **37**, 891–899 (2018).
23. Peacock, A. F. A. *et al.* Tuning the Reactivity of Osmium(II) and Ruthenium(II) Arene Complexes under Physiological Conditions. *J. Am. Chem. Soc.* **128**, 1739–1748 (2006).
24. Coverdale, J. P. C. C. *et al.* In Vivo Selectivity and Localization of Reactive Oxygen Species (ROS) Induction by Osmium Anticancer Complexes That Circumvent Platinum Resistance. *J. Med. Chem.* **61**, 9246–9255 (2018).

25. Coverdale, J. P. C. *et al.* Asymmetric transfer hydrogenation by synthetic catalysts in cancer cells. *Nat. Chem.* **10**, 347–354 (2018).
26. Soldevila-Barreda, J. J., Romero-Canelón, I., Habtemariam, A. & Sadler, P. J. Transfer hydrogenation catalysis in cells as a new approach to anticancer drug design. *Nat. Commun.* **6**, 1–9 (2015).
27. Galluzzi, L. *et al.* Molecular mechanisms of cell death: recommendations of the Nomenclature Committee on Cell Death 2018. *Cell Death Differ.* **25**, 486–541 (2018).
28. Taddei, M. L., Giannoni, E., Fiaschi, T. & Chiarugi, P. Anoikis: an emerging hallmark in health and diseases. *J. Pathol.* **226**, 380–393 (2012).
29. Pelillo, C. *et al.* Inhibition of adhesion, migration and of α5β1 integrin in the HCT-116 colorectal cancer cells treated with the ruthenium drug NAMI-A. *J. Inorg. Biochem.* **160**, 225–235 (2016).
30. Khoshnoodi, J., Pedchenko, V. & Hudson, B. G. Mammalian collagen IV. *Microsc. Res. Tech.* **71**, 357–370 (2008).
31. Sava, G. *et al.* Dual Action of NAMI-A in inhibition of solid tumor metastasis: selective targeting of metastatic cells and binding to collagen. *Clin. Cancer Res.* **9**, 1898–905 (2003).
32. Chen, X., Comish, P. B., Tang, D. & Kang, R. Characteristics and Biomarkers of Ferroptosis. *Front. Cell Dev. Biol.* **9**, 1–9 (2021).
33. Tian, W. *et al.* An antibody for analysis of autophagy induction. *Nat. Methods* **17**, 232–239 (2020).
34. Yuan, H., Li, X., Zhang, X., Kang, R. & Tang, D. Identification of ACSL4 as a biomarker and contributor of ferroptosis. *Biochem. Biophys. Res. Commun.* **478**, 1338–1343 (2016).
35. Wang, C.-W. & Klionsky, D. J. The Molecular Mechanism of Autophagy. *Mol. Med.* **9**, 65–76 (2003).
36. Romero-Canelón, I. DESIGN AND MECHANISM OF ACTION OF ORGANOMETALLIC ANTICANCER COMPLEXES. (University of Warwick, 2012).
37. Romero-Canelón, I., Pizarro, A. M., Habtemariam, A. & Sadler, P. J. Contrasting cellular uptake pathways for chlorido and iodido iminopyridine ruthenium arene anticancer complexes. *Metallomics* **4**, 1271–1279 (2012).

Appendix I – Complex Guide

Complex	Ligand	Short structure	Full structure
1	L1	Ru(L1)Cl(PF$_6$)	[Ru(η^6-p-Cym)(ImPy)Cl]PF$_6$
2	L2	Ru(L2)Cl(PF$_6$)	[Ru(η^6-p-Cym)(ImPy-4-Me)Cl]PF$_6$
3	L3	Ru(L3)Cl(PF$_6$)	[Ru(η^6-p-Cym)(ImPy-3-Me)Cl]PF$_6$
4	L4	Ru(L4)Cl(PF$_6$)	[Ru(η^6-p-Cym)(ImPy-2-Me)Cl]PF$_6$
5	L5	Ru(L5)Cl(PF$_6$)	[Ru(η^6-p-Cym)(ImPy-3,5-DiMe)Cl]PF$_6$
6	L6	Ru(L6)Cl(PF$_6$)	[Ru(η^6-p-Cym)(ImPy-4-iPr)Cl]PF$_6$
7	L1	Ru(L1)I(PF$_6$)	[Ru(η^6-p-Cym)(ImPy)I]PF$_6$
8	L7	Ru(L7)Cl(PF$_6$)	[Ru(η^6-p-Cym)(ImPy-Bn)Cl]PF$_6$
9	L7	Ru(L7)I(PF$_6$)	[Ru(η^6-p-Cym)(ImPy-Bn)I]PF$_6$
10	L8	Ru(L8)Cl(PF$_6$)	[Ru(η^6-p-Cym)(ImPy-Bn-4-Me)Cl]PF$_6$
11	ImPy-4-OH	Ru(ImPy-4-OH)Cl(PF$_6$)	[Ru(η^6-p-Cym)(ImPy-4-OH)Cl]PF$_6$
12	L9	Ru(L9)Cl(PF$_6$)	[Ru(η^6-p-Cym)(ImPy-Bn-4-OH)Cl]PF$_6$
13	L10	Ru(L10)Cl(PF$_6$)	[Ru(η^6-p-Cym)(ImPy-(CH$_2$)$_2$-4-OH)Cl]PF$_6$
14	L11	Ru(L11)Cl(PF$_6$)	[Ru(η^6-p-Cym)(ImPy-4-OMe)Cl]PF$_6$
15	L12	Ru(L12)Cl(PF$_6$)	[Ru(η^6-p-Cym)(ImPy-Bn-4-OMe)Cl]PF$_6$
16	L13	Ru(L13)Cl(PF$_6$)	[Ru(η^6-p-Cym)(ImPy-Bn-2-OMe)Cl]PF$_6$
17	L14	Ru(L14)Cl(PF$_6$)	[Ru(η^6-p-Cym)(ImPy-4-Cl)Cl]PF$_6$
18	L15	Ru(L15)Cl(PF$_6$)	[Ru(η^6-p-Cym)(ImPy-2-Cl)Cl]PF$_6$
19	L16	Ru(L16)Cl(PF$_6$)	[Ru(η^6-p-Cym)(ImPy-Bn-4-Cl)Cl]PF$_6$
20	L17	Ru(L17)Cl(PF$_6$)	[Ru(η^6-p-Cym)(ImPy-Bn-2-Cl)Cl]PF$_6$
21	L18	Ru(L18)Cl(PF$_6$)	[Ru(η^6-p-Cym)(ImPy-4-SMe)Cl]PF$_6$
22	L19	Ru(L19)Cl(PF$_6$)	[Ru(η^6-p-Cym)(ImPy-4-NMe$_2$)Cl]PF$_6$
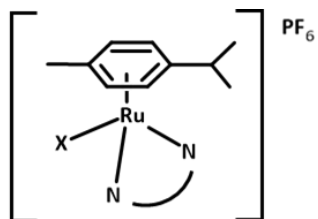
Complex 1
Ru(L1)Cl(PF$_6$)
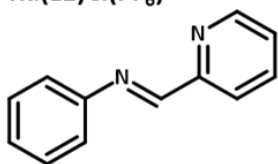
Complex 2
Ru(L2)Cl(PF$_6$)
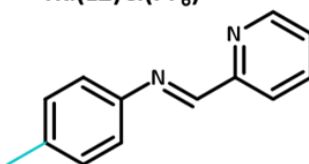
Complex 3
Ru(L3)Cl(PF$_6$)
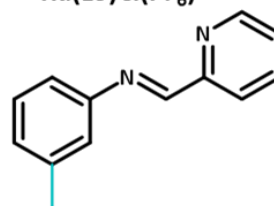
Complex 4
Ru(L4)Cl(PF$_6$)
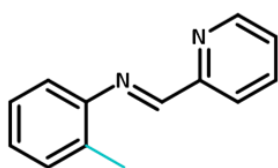
Complex 5
Ru(L5)Cl(PF$_6$)
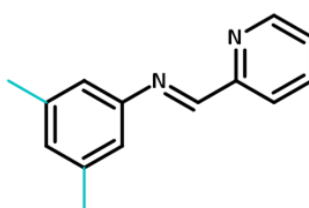
Complex 6
Ru(L6)Cl(PF$_6$)
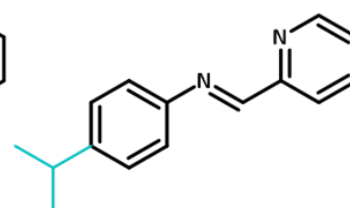
Chapter 4: Spacer Bioisosteres
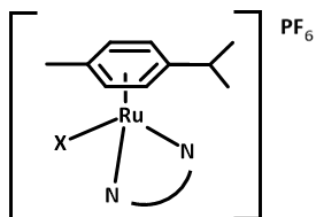
Complex 1   X = Cl
Ru(L1)Cl(PF$_6$)
Complex 7   X = I
Ru(L1)I(PF$_6$)
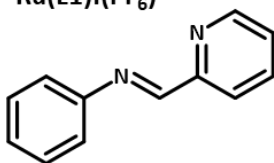
Complex 8   X = Cl
Ru(L7)Cl(PF$_6$)
Complex 8   X = I
Ru(L7)I(PF$_6$)
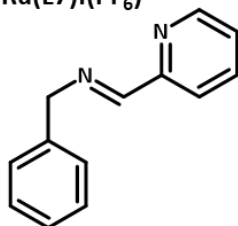
Complex 2   X = Cl
Ru(L2)Cl(PF$_6$)
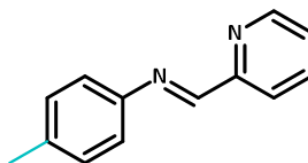
Complex 10   X = Cl
Ru(L8)Cl(PF$_6$)
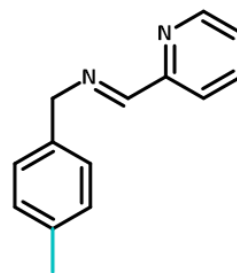
Complex 11   X = Cl
Ru(ImPy-4OH)Cl(PF$_6$)
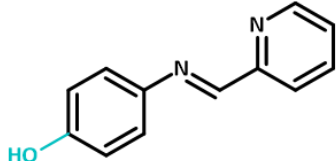
Complex 12   X = Cl
Ru(L9)Cl(PF$_6$)
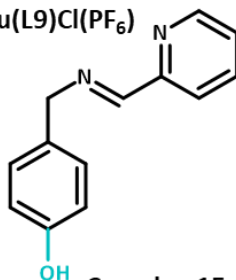
Complex 13   X = Cl
Ru(L10)Cl(PF$_6$)
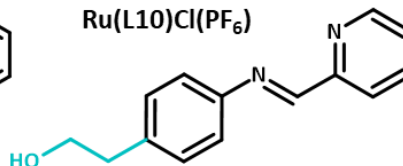
Complex 14   X = Cl
Ru(L11)Cl(PF$_6$)
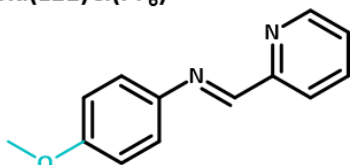
Complex 15   X = Cl
Ru(L12)Cl(PF$_6$)
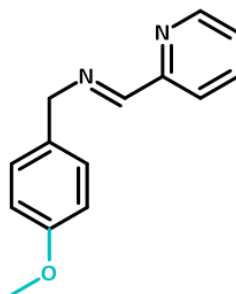
Complex 16   X = Cl
Ru(L13)Cl(PF$_6$)
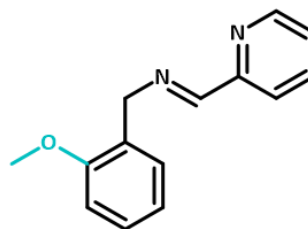
Complex 17   X = Cl
Ru(L14)Cl(PF$_6$)
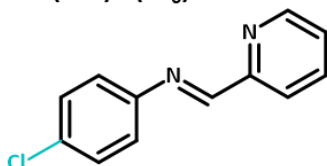
Complex 19   X = Cl
Ru(L16)Cl(PF$_6$)
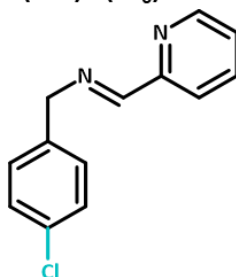
Complex 18   X = Cl
Ru(L15)Cl(PF$_6$)
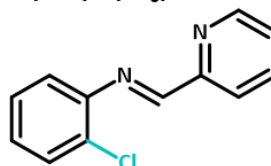
Complex 20   X = Cl
Ru(L17)Cl(PF$_6$)
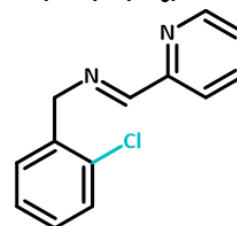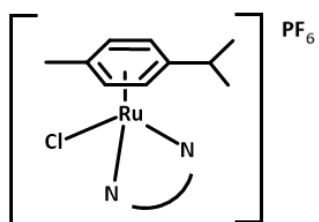
Complex 1
Ru(L1)Cl(PF₆)
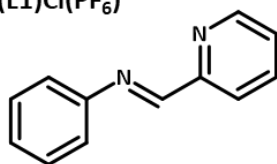
Complex 6
Ru(L6)Cl(PF₆)
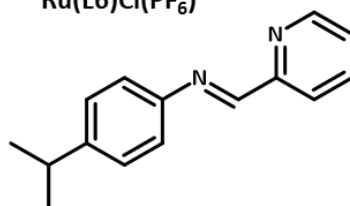
Complex 1
Ru(ImPy-4OH)Cl(PF₆)
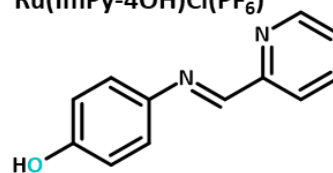
Complex 14
Ru(L1)Cl(PF₆)
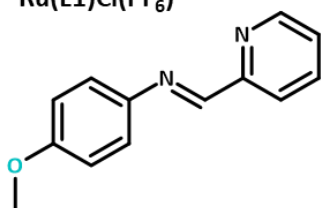
Complex 21
Ru(L18)Cl(PF₆)
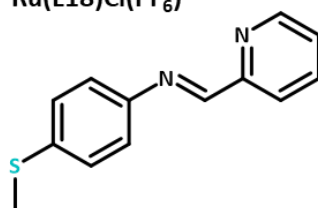
Complex 22
Ru(L19)Cl(PF₆)
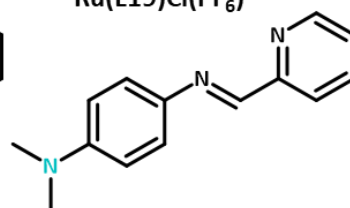
Appendix II – Bidentate Ligands Synthesis Methodology

Chapter 3: Methyl Bioisosteres

L1 - ImPy

Aniline (204.4 mg, 2.20 mmol) was dissolved in up to 5 mL of acetonitrile to which one mol equivalent of 2-pyridinecarboxaldehyde (235.1 mg, 2.20 mmol) was added. This reaction was left to stir at room temperature for 24 hours. The acetonitrile was removed by rotary evaporation producing a liquid crude product weighing 381.5 mg (95%). ^{1}H NMR (400 MHz; DMSO-d_6) δ 7.29 (tt, J=7.4, 1.7 Hz, 1H), 7.33 (dt, J=7.3, 1.3 Hz, 2H), 7.44 (m, 2H), 7.52 (d, J=4.8, 1.23 Hz, 1H), 7.94 (td, J=7.8, 1.6 Hz, 1H), 8.16 (dt, J=7.5, 1.0 Hz, 1H), 8.59 (s, 1H), 8.72 (d, J=4.9 Hz, 1H). ^{13}C NMR (400 MHz; DMSO-d_6) δ 160.80, 153.99, 150.49, 149.68, 137.04, 129.32, 126.73, 125.65, 121.19, 121.12. m/z (ESI) found a highest intensity peak for the fragment of 183.09, with a calculated of 182.22 (M+ [$C_{12}H_{10}N_2$]).

L2 – ImPy-4-Me

p-Toluidine (219.5 mg, 2.05 mmol) was dissolved in up to 5 mL of acetonitrile to which one mol equivalent of 2-pyridinecarboxaldehyde (219.4 mg, 2.05 mmol) was added. This reaction was left to stir at room temperature for 24 hours. The acetonitrile was removed by rotary evaporation producing a solid crude product weighing 389.2 mg (97%). ^{1}H NMR (400 MHz; DMSO-d_6) δ 2.33 (s, 3H), 7.26, (m, 4H), 7.52 (qd, J=4.8, 1.2 Hz, 1H), 7.95 (td, J=7.8, 1.6 Hz, 1H), 8.15 (dt, J=8.0, 1.0 Hz, 1H), 8.59 (s, 1H), 8.71, (dq, J=4.5, 0.7 Hz, 1H). ^{13}C NMR (400 MHz; DMSO-d_6) δ 20.63, 121.06, 121.16, 125.52, 129.83,

136.33, 137.04, 147.83, 149.66, 154.15, 159.80. m/z (ESI) found a highest intensity peak for the fragment of 196.25, with a calculated of 197.11 (M+ [$C_{13}H_{12}N_2$]).

L3 – ImPy-3-Me

m-Toluidine (218.4 mg, 2.04 mmol) was dissolved in up to 5 mL of acetonitrile to which one mol equivalent of 2-pyridinecarboxaldehyde (193.3 mg, 2.04 mmol) was added. This reaction was left to stir at room temperature for 24 hours. The acetonitrile was removed by rotary evaporation producing a solid crude product weighing 374.1mg (93%). ^{1}H NMR (400MHz; DMSO-d_6) δ 2.34 (s, 3H), 7.11 (m, 3H), 7.31 (t, J=7.6 Hz, 1H), 7.52 (qd, J=4.5, 1.0 Hz, 1H), 7.94 (td, J=7.8, 1.5 Hz, 1H), 8.14 (d, J=7.9 Hz, 1H), 8.57 (s, 1H), 8.72 (dq, J=4.8, 0.8 Hz, 1H). ^{13}C NMR (400 MHz; DMSO-d_6) δ 20.92, 118.15, 121.12, 121.66, 125.59, 137.39, 129.11, 137.02, 138.69, 149.67, 150.49, 154.05, 160.52. m/z (ESI) found a highest intensity peak for the fragment of 197.11, with a calculated of 197.10 (M+ [$C_{13}H_{12}N_2$]).

L4 – ImPy-2-Me

o-Toluidine (218.4 mg, 2.04 mmol) was dissolved in up to 5 mL of acetonitrile to which one mol equivalent of 2-pyridinecarboxaldehyde (193.3 mg, 2.04 mmol) was added. This reaction was left to stir at room temperature for 24 hours. The acetonitrile was removed by rotary evaporation producing a solid crude product weighing 337.7 mg (84%). ^{1}H NMR (400 MHz; DMSO-d_6) δ 2.32 (s, 3H), 7.10 (d, J=7.6 Hz, 1H), 7.17 (td, J=7.3, 1.2 Hz, 1H), 7.23 (dd, J=7.5, 1.3 Hz, 1H), 7.27, (d, J=7.3Hz, 1H), 7.53 (qd, J=4.8, 1.1 Hz, 1H), 7.96 (td, J=7.7, 1.5 Hz, 1H), 8.47 (s, 1H), 8.72 (dq, J=4.8, 0.8 Hz, 1H). ^{13}C NMR (400 MHz; DMSO-d_6) δ 17.50, 117.63, 121.16, 125.61, 126.38, 126.94, 130.23, 131.64, 137.06, 149.50, 149.64, 154.13, 160.01. m/z (ESI) found a highest intensity peak for the fragment of 197.11, with a calculated of 197.11 (M+ [$C_{13}H_{12}N_2$]).

L5 – ImPy-3,5-Me₂

3,5-Dimethylaniline (230.5 mg, 1.90 mmol) was dissolved in up to 5 mL of acetonitrile to which one mol equivalent of 2-pyridinecarboxaldehyde (203.8 mg, 1.90 mmol) was added. This reaction was left to stir at room temperature for 24 hours. The acetonitrile was removed by rotary evaporation producing a solid crude product weighing 391.8 mg (98%). ^{1}H NMR (400 MHz; DMSO-d₆) δ 2.30 (s, 6H), 6.93 (s, 1H), 6.94 (s, 2H), 7.52 (qd, J=4.8, 1.3 Hz, 1H), 9.75 (td, J=7.8, 1.6 Hz, 1H), 8.13 (dt, J=7.9, 1.0 Hz, 1H), 8.55 (s, 1H), 8.71 (dq, J=4.8, 0.7 Hz, 1H). ^{13}C NMR (400 MHz; DMSO-d₆) δ 20.85, 118.77, 121.07, 125.56, 128.18, 137.04, 138.42, 148.41, 149.68, 150.50, 154.08, 160.24. m/z (ESI) found a highest intensity peak for the fragment of 481.10, with a calculated of 481.10 (M+ [C₁₄H₁₄N₂]).

L6 – ImPy-4-CH(CH₃)₂

4-Isopropylaniline (241.1 mg, 1.78 mmol) was dissolved in up to 5 mL of acetonitrile to which one mol equivalent of 2-pyridinecarboxaldehyde (191.0 mg, 1.78 mmol) was added. This reaction was left to stir at room temperature for 24 hours. The acetonitrile was removed by rotary evaporation producing a solid crude product weighing 385. 8mg (96%). ^{1}H NMR (400 MHz; DMSO-d₆) δ 1.22 (d, J=6.9 Hz, 6H), 2.92 (m, 1H), 7.30 (m, 4H), 7.52 (qd, J=5.9, 4.8, 1.0 Hz, H1), 7.94 (td, J=7.6, 1.4Hz, 1H), 8.15 (d, J=7.9 Hz, 1H), 8.60 (s, 1H), 8.71 (d, J=4.6 Hz, 1H). ^{13}C NMR (400 MHz; DMSO-d₆) δ 23.88, 33.05, 121.06, 121.19, 125.52, 127.16, 137.02, 147.23, 148.17, 149.65, 149.65, 154.16, 159.89. m/z (ESI) found a highest intensity peak for the fragment of 225.14, with a calculated of 225.14 (M+ [C₁₅H₁₆N₂]).

Chapter 4: Spacer Bioisosteres

L7 – ImPy-Bn

Benzylamine (218.4 mg, 2.04 mmol) was dissolved in up to 5 mL of acetonitrile to which one mol equivalent of 2-pyridinecarboxaldehyde (218.1 mg, 2.04 mmol) was added. This reaction was left to stir

at room temperature for 24 hours. The acetonitrile was removed by rotary evaporation producing a liquid crude product weighing 215.1 mg (54%). ^{1}H NMR (400 MHz; DMSO-d$_6$) δ 2.08 (s, 2H), 4.84 (d, J=1.4 Hz, 2H), 7.26 (m, 1H), 7.35 (d, J=4.5 Hz, 4H), 7.46, (qd, J=4.8 Hz, 1.30, 1H), 7.86 (td, J=7.7, 1.5 Hz, 1H), 7.99 (dt, J=7.9, 1.0 Hz, 1H), 8.49 (s, 1H), 8.65 (dq, J=4.9, 0.8 Hz, 1H). ^{13}C NMR (400 MHz; DMSO-d$_6$) δ 30.68 63.72, 120.53, 125.23, 126.94, 128.07, 128.43, 136.91, 139.09, 149.42, 154.11, 162.68. m/z (ESI) found a highest intensity peak for the fragment of 197.11, with a calculated of 197.11 (M+ [$C_{13}H_{12}N_2$]).

L8 - ImPy-Bn-4-Me

4-Methylbenzylamine (230.5 mg, 1.90 mmol) was dissolved in up to 5 mL of acetonitrile to which one mol equivalent of 2-pyridinecarboxaldehyde (203.76 mg, 1.90 mmol) was added. This reaction was left to stir at room temperature for 24 hours. The acetonitrile was removed by rotary evaporation producing a solid crude product weighing 396.7 mg (99%). ^{1}H NMR (400 MHz; DMSO-d$_6$) δ 2.28 (s, 3H), 4.79 (s, 2H), 7.15 (d, J=7.8 Hz, 2H), 7.22 (d, J=8.1 Hz, 2H), 7.46 (qd, J=4.8, 1.3 Hz, 1H), 7.86 (td, J=7.7, 1.7 Hz, H1), 7.97 (dt, J=7.8, 1.1 Hz, 1H), 8.46 (s, 1H), 8.65 (dq, J=4.8, 0.8 Hz, 1H).^{13}C NMR (400 MHz; DMSO-d$_6$) δ 20.69, 30.69, 63.45, 120.48, 125.19, 128.04, 128.97, 135.98, 136.90, 149.40, 154.13, 162.42. m/z (ESI) found a highest intensity peak for the fragment of 211.12, with a calculated of 211.12 (M+ [$C_{14}H_{15}N_2$]).

L9 – ImPy-Bn-4-OH

4-Hydroxybenzylamine (236.4 mg, 1.92 mmol) was dissolved in up to 5 mL of acetonitrile to which one mol equivalent of 2-pyridinecarboxaldehyde (205.0 mg, 1.92 mmol) was added. This reaction was left to stir at room temperature for 24 hours. The acetonitrile was removed by rotary evaporation producing a solid crude product weighing 374.7mg (92%). ^{1}H NMR (400 MHz; DMSO-d$_6$) δ 4.53 (d, J=5.7 Hz, 2H), 5.23 (t, J=5.7 Hz, 1H), 7.32 (dt, J=8.3, 1.9 Hz, 2H), 7.39 (dt, J=8.5, 2.1 Hz, 2H), 7.53 (qd,

J=4.9, 1.2 Hz, 1H), 7.96 (td, J=7.8, 1.8 Hz, 1H), 8.16 (dt, J=7.9, 1.0 Hz, 1H), 8.60 (s, 1H), 8.72 (dq, J=4.8, 1.0 Hz, 1H). ^{13}C NMR (400 MHz; DMSO-d_6) δ 62.54, 120.95, 121.13, 125.60, 127.40, 137.07, 141.33, 148.98, 149.69, 154.09, 160.21. m/z (ESI) found a highest intensity peak for the fragment of 213.10, with a calculated of 213.10 (M+ [$C_{13}H_{13}N_2O$]).

L10 – ImPy-(CH$_2$)$_2$-4-OH

4-Aminophenethyl alcohol (264.4 mg, 1.60 mmol) was dissolved in up to 5 mL of acetonitrile to which one mol equivalent of 2-pyridinecarboxaldehyde (171.4 mg, 1.60 mmol) was added. This reaction was left to stir at room temperature for 24 hours. The acetonitrile was removed by rotary evaporation producing a liquid crude product weighing 368.7 mg (91%). ^{1}H NMR (400 MHz; DMSO-d_6) δ 2.75 (t, J=7.0 Hz, 2H), 3.63 (m, 2H), 4.68 (t, J=5.2 Hz, 1H), 7.28 (m, 4H), 7.52 (qd, J=4.8, 1.3 Hz, 1H), 7.94 (td, J=7.7, 1.7 Hz, 1H), 8.15 (dt, J=7.9, 1.0 Hz, 1H), 8.59 (s, 1H), 8.71 (dq, J=4.8, 0.9 Hz, 1H). ^{13}C NMR (400 MHz; DMSO-d_6) δ 38.57, 62.11, 121.04, 121.10, 125.54, 129.81, 137.04, 138.51, 148.31, 149.66, 154.14, 159.93. m/z (ESI) found a highest intensity peak for the fragment of 227.124, with a calculated of 227.12 (M+ [$C_{14}H_{15}N_2O$]).

L11 - ImPy-4-OMe

4-Methoxyaniline (237.2 mg, 1.93 mmol) was dissolved in up to 5 mL of acetonitrile to which one mol equivalent of 2-pyridinecarboxaldehyde (206.3 mg, 1.93 mmol) was added. This reaction was left to stir at room temperature for 24 hours. The acetonitrile was removed by rotary evaporation producing a liquid crude product weighing 335.7 mg (82%). ^{1}H NMR (400 MHz; DMSO-d_6) δ 3.78 (s, 3H), 6.99 (m, 2H), 7.38 (m, 2H), 7.48 (qd, J=4.8, 1.2 Hz, 1H), 7.91 (td, J=7.8, 1.6 Hz, 1H), 8.12 (d, J=7.93 Hz, 1H), 8.62 (s, 1H), 8.69 (dq, J=4.8, 0.9 Hz, 1H). ^{13}C NMR (400 MHz; DMSO-d_6) δ 55.30, 114.50, 120.83, 122.80, 125.23, 136.90, 143.02, 149.58, 154.39, 158.19, 158.58. m/z (ESI) found a highest intensity peak for the fragment of 213.10, with a calculated of 213.10 (M+ [$C_{13}H_{13}N_2O$]).

L12 – ImPy-Bn-4-OMe

4-Methoxybenzylamine (242.5 mg, 1.77 mmol) was dissolved in up to 5 mL of acetonitrile to which one mol equivalent of 2-pyridinecarboxaldehyde (189.4 mg, 1.77 mmol) was added. This reaction was left to stir at room temperature for 24 hours. The acetonitrile was removed by rotary evaporation producing a liquid crude product weighing 387.3 mg (97%). ^{1}H NMR (400 MHz; DMSO-d$_6$) δ 3.73 (s, 3H), 4.77 (s, 2H), 6.91 (m, 2H), 7.26 (m, 2H), 7.46 (qd, J=4.9, 1.3 Hz, 1H), 7.86 (m, 1H), 7.97 (dt, J=7.9, 1.1 Hz, 1H), 8.45 (s, 1H), 8.64 (dq, J=4.8, 0.8 Hz, 1H). ^{13}C NMR (400 MHz; DMSO-d$_6$) δ 55.03, 63.16, 133.82, 120.46, 125.16, 129.35, 130.93, 136.88, 149.39, 154.16, 158.30, 162.18. m/z (ESI) found a highest intensity peak for the fragment of 249.10, with a calculated of 249.10 (M+ [$C_{14}H_{14}N_2O$]).

L13 - ImPy-Bn-2-OMe

2-Methoxybenzylamine (242.5 mg, 1.77 mmol) was dissolved in up to 5 mL of acetonitrile to which one mol equivalent of 2-pyridinecarboxaldehyde (189.4 mg, 1.77 mmol) was added. This reaction was left to stir at room temperature for 24 hours. The acetonitrile was removed by rotary evaporation producing a liquid crude product weighing 377.5 mg (94%). ^{1}H NMR (400 MHz; DMSO-d$_6$) δ 3.80 (s, 3H), 4.80 (s, 2H), 6.93 (td, J=7.4, 1.0 Hz, 1H), 7.01 (d, J=7.8 Hz, 1H), 7.27 (m, 2H), 7.46 (qd, J=4.9, 1.3 Hz, 1H), 7.86 (td, J=7.8, 1.6 Hz, 1H), 7.99 (dt, J=7.9, 1.0 Hz, 1H), 8.40 (s, 1H), 8.64 (dq, J=4.9, 1.0 Hz, 1H). ^{13}C NMR (400 MHz; DMSO-d$_6$) δ 55.33, 58.15, 110.69, 120.34, 120.47, 125.16, 126.64, 128.43, 129.28, 136.89, 149.37, 154.18, 156.88, 162.66. m/z (ESI) found a highest intensity peak for the fragment of 249.10, with a calculated of 249.10 (M+ [$C_{14}H_{14}N_2ONa$]).

L14 - ImPy-4-Cl

4-Chloroaniline (245.5 mg, 1.92 mmol) was dissolved in up to 5 mL of acetonitrile to which one mol equivalent of 2-pyridinecarboxaldehyde (206.1 mg, 1.92 mmol) was added. This reaction was left to stir at room temperature for 24 hours. The acetonitrile was removed by rotary evaporation producing a

liquid crude product weighing 368.9 mg (89%). ^{1}H NMR (400 MHz; DMSO-d$_6$) δ 7.43 (td, J=46.2, 8.7 Hz, 4H), 7.54 (qd, J=4.9, 1.1 Hz, 1H), 7.96 (td, J=7.8, 1.4 Hz, 1H), 8.15 (d, J=8.0 Hz, 1H), 8.60 (s, 1H), 8.73 (dq, J=4.8, 0.8 Hz, 1H). ^{13}C NMR (400 MHz; DMSO-d$_6$) δ 121.37, 123.02, 125.83, 129.26, 131.04, 137.11, 149.26, 149.75, 153.80, 161.58. m/z (ESI) found a highest intensity peak for the fragment of 217.05, with a calculated of 217.05 (M+ [C$_{12}$H$_{10}$N$_2$Cl]).

L15 – ImPy-2-Cl

2-Chloroaniline (235.5 mg, 1.85 mmol) was dissolved in up to 5 mL of acetonitrile to which one mol equivalent of 2-pyridinecarboxaldehyde (197.7 mg, 1.85 mmol) was added. This reaction was left to stir at room temperature for 24 hours. The acetonitrile was removed by rotary evaporation producing a liquid crude product weighing 398.8 mg (100%). ^{1}H NMR (400 MHz; DMSO-d$_6$) δ 7.28 (td, J=7.5, 1.7 Hz, 1H), 7.32 (dd, J=7.9, 1.7 Hz, 1H), 7.40 (td, J=7.5, 1.4 Hz, 1H), 7.55 (dd, J=6.5, 1.4 Hz, 1H), 7.57 (qd, J=4.8, 1.2 Hz, 1H), 7.99 (td, J=7.7, 1.5 Hz, 1H), 8.19 (td, J=7.8, 1.0 Hz, H1), 8.54 (s, 1H), 8.75 (dq, J=4.7, 0.9 Hz, 1H). ^{13}C NMR (400 MHz; DMSO-d$_6$) δ 120.32, 121.60, 126.08, 127.56, 128.31, 128.94, 129.76, 137.21, 147.91, 149.80, 153.61, 162.79. m/z (ESI) found a highest intensity peak for the fragment of 217.05, with a calculated of 217.05 (M+ [C$_{12}$H$_{10}$N$_2$Cl]).

L16 - ImPy-Bn-4-Cl

4-Chlorobenzylamine (245.5 mg, 1.73 mmol) was dissolved in up to 5 mL of acetonitrile to which one mol equivalent of 2-pyridinecarboxaldehyde (185.7 mg, 1.73 mmol) was added. This reaction was left to stir at room temperature for 24 hours. The acetonitrile was removed by rotary evaporation producing a solid crude product weighing 338.9 mg (85%). ^{1}H NMR (400 MHz; DMSO-d$_6$) δ 4.84 (s, 2H), 7.38 (dt, J=8.8, 2.5 Hz, H), 7.42 (dt, J=8.8, 2.3 Hz, 2H), 7.48 (qd, J=4.8, 1.3 Hz, 1H), 7.88 (td, J=7.6, 1.7 Hz, 1H), 7.99 (dt, J=7.9, 1.0 Hz, 1H), 8.50 (s, 1H), 8.66 (dq, J=4.8, 1.0 Hz, 1H). ^{13}C NMR (400 MHz; DMSO-

d_6) δ 62.68, 120.55, 125.31, 128.37, 129.85, 131.50, 136.95, 138.21, 149.45, 154.00, 163.09. m/z (ESI) found a highest intensity peak for the fragment of 231.07, with a calculated of 231.07 (M+ [$C_{13}H_{12}N_2Cl$]).

L17 – ImPy-Bn-2-Cl

2-Chlorobenzylamine (282.0 mg, 1.99 mmol) was dissolved in up to 5 mL of acetonitrile to which one mol equivalent of 2-pyridinecarboxaldehyde (213.3 mg, 1.99 mmol) was added. This reaction was left to stir at room temperature for 24 hours. The acetonitrile was removed by rotary evaporation producing a liquid crude product weighing 443.9 mg (89%). ^{1}H NMR (400 MHz; DMSO-d_6) δ 4.93 (d, J=1.2 Hz, 2H), 7.35 (m, 2H), 7.49 (m, 3H), 7.88 (td, J=7.9 Hz, 1H), 8.01 (dt, J=8.0, 1.03 z, 1H), 8.48 (s, 1H), 8.66 (dq, J=4.8, 0.9 Hz, 1H). ^{13}C NMR (400 MHz; DMSO-d_6) δ 60.72, 120.59, 125.37, 127.42, 128.94, 129.24, 130.38, 132.73, 136.39, 136.97, 149.45, 153.93, 163.62. m/z (ESI) found a highest intensity peak for the fragment of 231.07, with a calculated of 231.07 (M+ [$C_{13}H_{12}N_2Cl$]).

Chapter 5: Atom Bioisosteres

L18 - ImPy-4-SMe

4-(Methylthio)aniline (252.2mg, 2.01mmolol) was dissolved in up to 5mL of acetonitrile to which one mol equivalent of 2-pyridinecarboxaldehyde (215.8mg, 2.01mmolol) was added. This reaction was left to stir at room temperature for 24 hours. The acetonitrile was removed by rotary evaporation producing a liquid crude product weighing 398.0mg (87%). ^{1}H NMR (400 MHz; DMSO-d_6) δ 2.50 (s, 3H), 7.33 (m, 4H), 7.51 (qd, J=4.8, 1.2 Hz, 1H), 7.94 (td, J=7.7, 1.5 Hz, 1H), 8.14 (d, J=7.9 Hz, 1H), 8.62 (s, 1H), 8.71 (dq, J=5.8, 0.9 Hz, 1H). ^{13}C NMR (400 MHz; DMSO-d_6) δ 14.89, 121.10, 121.99, 125.51, 126.75, 136.87, 136.98, 147.19, 149.65, 154.10, 159.83. m/z (ESI) found a highest intensity peak for the fragment of 229.08, with a calculated of 229.08 (M+ [$C_{13}H_{13}N_2S$]$^+$).

L19 - ImPy-4-NMe₂

Protocol was conducted per the methodology outlined by Hindo *et al*[1]. Briefly, 4-dimethylaminopyridine (690.6mg, 5.07mmolol) was added to 3mL of ethanol under nitrogen atmosphere. To this 1 equimolar equivalent of 2-pyridinecarboxaldehyde (543.1mg, 5.07mmolol) was slowly added. This solution was allowed to mix under nitrogen for 10 minutes. This solution was then refluxed for 40 minutes. This reaction was then allowed to cool, then the ethanol was removed by rotary evaporation producing a dark green solid weighing 1104.5 mg (97%). ^{1}H NMR (400 MHz; DMSO-d_6) δ 2.95 (s, 6H), 6.77 (dt, J=9.0, 2.2 Hz, 2H), 7.36 (dt, J=9.0, 2.2 Hz, 2H), 7.45 (qd, J=4.82, 1.21 Hz, 1H), 7.90 (m, 1H), 8.11 (dt, J=7.9, 1.0 Hz, 1H), 8.63 (s, 1H), 8.67 (dq, J=4.8, 1.0 Hz, 1H). ^{13}C NMR (400 MHz; DMSO-d_6) δ 40.09, 112.45, 120.40, 122.84, 124.69, 136.77, 138.48, 149.47, 149.94, 154.72, 154.89. m/z (ESI) found a highest intensity peak for the fragment of 226.13, with a calculated of 226.13 (M+ [$C_{14}H_{16}N_3$]$^+$).

References

1.   Hindo, S. S. *et al.* Small Molecule Modulators of Copper-Induced Aβ Aggregation. *J. Am. Chem. Soc.* **131**, 16663–16665 (2009).

Appendix III – Metal Content Distribution Raw Values (Chapter 4)

Raw metal accumulation of platinum or ruthenium determined by ICP-MS in fg/cell of the fractions of A2780 cells produced using the FractionPREP™ Cell Fractionation Kit (BioVision, Inc.). A2780 cells were treated with treated with media as negative control, CDDP, *7* or *9* equipotently.

Pt content	Cytosol	Membrane	Nucleus	Skeleton
Control	0.006 (0.002)	0.044 (0.031)	0.008 (0.013)	0.012 (0.027)
CDDP	2.910 (0.205)	7.683 (1.527)	0.590 (0.132)	0.898 (0.187)

Ru content	Cytosol	Membrane	Nucleus	Skeleton
Control	0.007 (0.001)	0.062 (0.043)	0.059 (0.094)	0.005 (0.004)
7	5.213 (2.416)	32.226 (12.803)	1.380 (0.618)	7.563 (3.184)
9	3.587 (0.453)	22.087 (5.099)	0.723 (0.200)	0.630 (0.221)